High-Chromium Ferritic and Martensitic Steels for Nuclear Applications

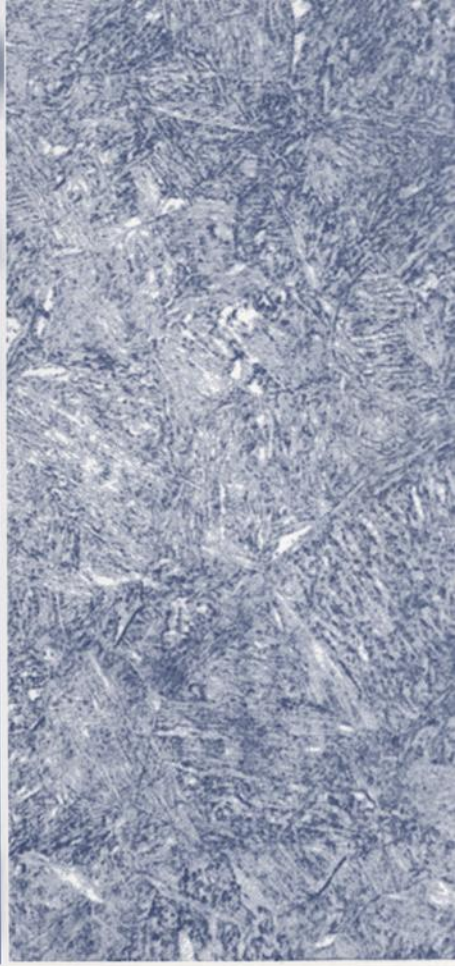

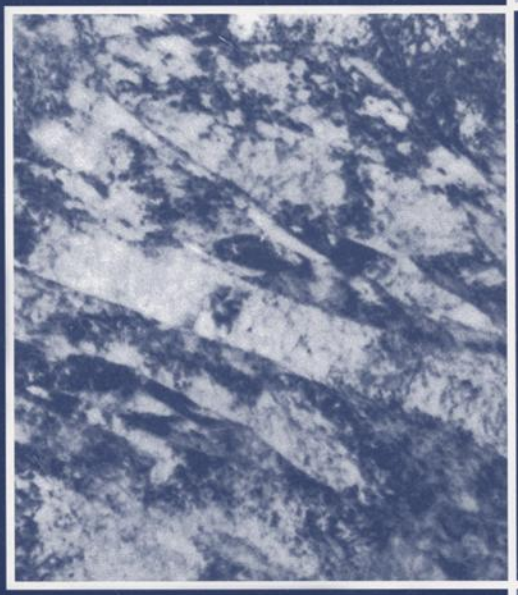

Ronald L. Klueh and
Donald R. Harries

ASTM

High-Chromium Ferritic and Martensitic Steels for Nuclear Applications

Ronald L. Klueh and
Donald R. Harries

ASTM Stock Number: MONO3

ASTM
100 Barr Harbor Drive
P.O. Box C700
West Conshohocken, PA 19428–2959

Printed in the U.S.A.

Library of Congress Cataloging-in-Publication Data

Klueh, R. L., 1936–
High-chromium ferritic and martensitic steels for nuclear applications / Ronald L. Klueh and Donald R. Harries.
p. cm.—(Monograph ; 3)
"ASTM stock number: MONO3."
Includes index.
ISBN 0-8031-2090-7
1. Steel, Stainless. 2. Steel alloys. 3. Nuclear reactors—Materials—Effects of radiation on. I. Harries, Donald R., 1930- . II. Title. III. Series: Monograph (American Society for Testing and Materials) ;
TA479.S7.K56 2001
620.1'728—dc21 2001033490

Printed in Bridgeport, NJ
June 2001

Foreword

THIS PUBLICATION, *High-Chromium Ferritic and Martensitic Steels for Nuclear Applications,* was sponsored by ASTM Committee E10 on Nuclear Technology and Applications. The authors were Ronald L. Klueh and Donald R. Harries. This is Monograph 3 in ASTM's monograph series.

Acknowledgments

DURING THE COURSE of preparing this monograph, we contacted and were greatly aided by many research workers throughout the world, some of whom we knew personally and others who we knew only by reputation. In addition, The Institute of Materials, The Institution of Mechanical Engineers, and The British Nuclear Energy Society in London kindly provided many useful references and copies of published papers as well as the loan of the proceedings of relevant conferences. The individuals who aided us are too numerous to mention, but we are most grateful for their kind and generous assistance. Thanks are also due to those who critically and constructively reviewed the manuscript, including the anonymous reviewers selected by ASTM and colleagues at the Oak Ridge National Laboratory who reviewed the respective chapters.

We particularly wish to acknowledge the following individuals: Dr. Roger Stoller, who recommended ASTM as the publisher for the book, and who, as Chairman of the ASTM Publications Committee, reviewed the final manuscript; Ms. Megan Baily, who took copies of the many figures from various sources and produced electronic versions for publication; Ms. Kathy Dernoga, Manager of New Publications for ASTM, who worked with us from the beginning; and Ms. Monica Siperko and Mr. David Jones of ASTM, who took the final manuscript and worked to turn it into this publication.

A large volume of published work has been cited, and the majority of the illustrations used have been copied from these publications. The authors of the original papers are referenced in the individual figures, and their efforts are gratefully appreciated. We are also indebted to the following publishers for permission to use copyrighted material: Academic Press, AEA Technology, ASM International, American Society for Testing and Materials (ASTM), Blackwell Science Ltd, British Nuclear Energy Society, ECN-NRG The Netherlands, Elsevier Science Limited, Forschungszentrum Karlsruhe GmbH, G+B Publishing Services S.A., Inforum GmbH, SEC-CEN Belgium, The Institution of Nuclear Engineers, The Institute of Materials, The Minerals, Metals & Materials Society (TMS), and World Scientific Publishing Co Pte Ltd.

The work was carried out as research sponsored by the Office of Fusion Energy Sciences, U.S. Department of Energy, under contract DE-AC05-00OR22725 with U.T.-Battelle, LLC.

CONTENTS

Preface

The high-chromium (9–12 wt%) ferritic/martensitic steels were developed during the first half of the last century and have a long history of use in the power-generation industry as boiler and turbine materials as well as for other applications. The original steels were based on 12% Cr and 9 and 12% Cr-Mo compositions, but the need for reduced generating costs in power plants (higher efficiencies, which means higher temperatures) has resulted in the development of more highly alloyed steels with progressively enhanced creep-rupture strengths. These developments have allowed the maximum operating temperatures in the boilers to be increased from less than 450 to 620°C and the 10^5 h creep-rupture strengths to be raised from around 40 to 140 MPa. Advanced steels of this type are now being developed with a target operating temperature of 650°C and a 10^5 h creep-rupture strength of 180 MPa.

High-chromium Cr-Mo steels were selected for use in steam generators of nuclear power plants during the 1960s, and steels with additions of V, Nb, and/or W and with oxide dispersions were subsequently chosen and evaluated as fuel element core component (ducts and cladding) materials in sodium-cooled fast breeder reactors. Since the late 1970s, the steels have also been considered as potential first wall and breeding blanket structural materials in fusion reactor systems. The fission (in-core) and fusion reactor applications require steels that are resistant to radiation damage induced by bombardment from high-energy neutrons as well as to retain adequate toughness and elevated-temperature strength during service. The requirement for safe and routine operation and decommissioning of a fusion plant and the disposal of radioactive wastes has also demanded the development of steels with enhanced radioactive decay characteristics. This development of "reduced-activation" steels, containing W, V, Mn, Ta, and Ti and without Mo, Nb, Ni, and other radiologically undesirable elements and possessing an appropriate combination of the other desirable properties, is still progressing.

This monograph presents a detailed review of the development of the high-chromium ferritic/martensitic steels for exposure to the high-energy neutron environment of a fission or fusion reactor, and the book should be of most interest for people involved in the use of the steels for nuclear applications. However, to provide a baseline for understanding the irradiation effects on the steels, it is first necessary to understand the basic properties of the steels under nonnuclear conditions. Therefore, many of the chapters are devoted to such considerations, and it is hoped that this information will be of interest to readers beyond those involved in nuclear applications.

1

Introduction

Most of the information on ferritic/martensitic steels for nuclear applications comes from studies on commercial Cr-Mo steels, primarily 9–12% Cr, 1–2% Mo, 0.1–0.2% C with small amounts of V, Nb, W, Ni, etc. (Compositions throughout the book will be in wt% unless otherwise stated.) These were the ferritic steels considered first for fast breeder fission reactors in the early 1970s and then in the late 1970s for fusion applications. The steels became of interest because of their swelling resistance compared to austenitic stainless steels, which were the primary candidates for both applications up to that time [1,2].

In recent years, most of the developmental studies on the ferritic/martensitic steels for nuclear applications have been for fusion, and much of the discussion in this book will be on that application. Since the mid-1980s, the fusion materials programs in Japan, the European Union, and the USA have been developing ferritic/martensitic steels that would lessen the environmental impact of the irradiated and activated steel after the service lifetime of a fusion reactor. As discussed throughout this book, these new "reduced-activation" ferritic/martensitic steels display the same general behavior as the conventional steels, but there are quantitative differences. Often, some of the properties of the reduced-activation steels are better than those of the conventional steels.

The amount of data available for reduced-activation steels either in the unirradiated or irradiated condition is not as extensive as for the conventional steels, since many of the conventional steels are used for elevated-temperature applications to 550 to 600°C in the power-generation and petrochemical industries. As a result, the metallurgical characteristics and mechanical and physical properties of the conventional steels are reasonably well understood, and comprehensive mechanical properties compilations are available.

Fusion applications require information on some mechanical properties that differ from those normally measured (e.g., thermal fatigue). However, from the wealth of data available, indications are that a range of ferritic/martensitic steels have properties that make them viable candidates for fusion applications to 550 to 600°C. The maximum operating temperature will be determined by the creep properties and, under some circumstances, by the compatibility with the operating media (i.e., water, liquid lithium, liquid Pb-Li eutectic, etc.) of the fusion power plant. The major difference in the fission and fusion environments and the environments of most other applications is the neutron flux of the nuclear applications. Fast fission and fusion applications differ in this respect—a much higher-energy neutron flux is produced by fusion neutrons.

Chapter 2 provides some information on fission and fusion systems for which the high-chromium ferritic/martensitic steels are to be used. In fast reactors, ferritic/martensitic steels are considered primarily in the fuel subassembly as fuel pin cladding and wrapper material. The use of these steels as structural materials for a fusion reactor first wall and blanket structure provides a much bigger challenge, and considerable work on determining a range of properties has been carried out for this application. Much of the work on irradiated steels for both fast fission and fusion applications has been on steels irradiated in fast reactors. Because in recent years the development of fast fission reactors has been de-emphasized while work on the fusion application continued, much of the emphasis of the discussion in this book is on the fusion application. However, most of the information obtained in the fusion program applies for fast fission applications, because most neutron irradiations were carried out in fission reactors, and mostly in fast reactors.

This book will show that fission and fusion reactors present a difficult challenge for the materials community, but it will also demonstrate that considerable progress has been made. The following two sections of this chapter will provide a brief introduction to some of the ways ferritic/martensitic steels will help meet the challenge.

ADVANTAGES AND LIMITATIONS OF MARTENSITIC STEELS FOR FUSION

Austenitic stainless steels were the first structural materials considered for both fast fission and fusion applications. To reach higher operating temperatures (≥700°C) in a fusion plant, superalloys and refractory metal (Nb, Mo, V, and Ti) alloys were considered. Ferritic/martensitic steels were not considered originally for fission because of elevated-temperature strength and coolant compatibility considerations. They were not considered originally for fusion because of the fear of possible complications caused by the interaction of a ferromagnetic material within the high magnetic fields in a fusion plant. The steels were considered only after preliminary calculations [3–5] indicated that possible problems caused by a ferromagnetic material can be handled in the reactor design.

Two types of problems are of concern with the use of a ferromagnetic material in the high magnetic field of a fusion reactor: (1) the effect of the field perturbation caused by the ferromagnetic material on the plasma, and (2) the magnetostatic forces on the ferromagnetic structure due to the mag-

netic field. Early calculations [3–5] indicated that the field pertubations were small and confined to the end region and on the same order of magnitude as the field ripples produced by the central cell magnets. Based on the calculations of the magnetostatic forces on a ferritic steel pipe in the magnetic field of the machine, the stresses were found to be small but not negligible, and it was concluded that they must be incorporated in the stress analysis of the design [3–5]. Similar results have been obtained by later calculations [6–10]. It must be emphasized that the favorable conclusions on the ferromagnetic interactions were reached from simplified calculations (e.g., the calculation of stresses on a coolant pipe, etc.). No comprehensive analysis of ferromagnetic effects for the blanket structure and primary coolant circuit has been attempted, although such studies are presently in progress in Japan [9]. Experimental work is also in progress in Japan, where a ferritic steel liner is being installed in a small tokamak vessel [10].

As a result of work during the last 20 years or so, most of the refractory metals have been eliminated for use as the structural material of the first wall and blanket structures because of inadequate physical or mechanical properties or because they did not meet the reduced-activation criteria to be discussed below. Austenitic stainless steels are considered unsuitable for a fusion power plant because of high swelling rates and high thermal stresses caused by the low thermal conductivity and high thermal expansion coefficient. Austenitic stainless steels are still considered as the structural material for experimental fusion machines, such as the International Thermonuclear Test Reactor (ITER). At present, there are only three materials considered viable candidates for structural components for a fusion power plant: vanadium alloys, SiC/SiC composites, and ferritic/martensitic steels.

Martensitic steels containing 9–12% Cr with about 1% Mo, 0.1–0.2% C and combinations of small amounts of V, W, Nb, etc., have the strength, including elevated-temperature strength, and thermal properties (conductivity and expansion coefficient) that result in excellent resistance to thermal stresses [1]. Creep strength of these types of steels is adequate to 550 to 600°C, and they have been used at these temperatures in the power-generation and chemical and petrochemical industries.

Because of the widespread use in industrial applications, the technology for production and fabrication of all types of product forms exists [11]. All conventional melting practices as well as various special melting techniques, including electron-beam, electroslag, and vacuum melting, have been used to produce the steels. The steels are hot and cold workable by all methods. Forgings up to 70 tons have been produced, and the steels can be rolled to thin sheet and strip. Standard heat treatment facilities are adequate for the normalizing and tempering or quenching and tempering conditions that the steels require before use.

Any structural material used for fabrication of a fusion power plant would have to receive the appropriate code approval for the country in which the plant was constructed (i.e., ASME Boiler and Pressure Vessel Code, etc.). Conventional ferritic/martensitic steels of the type being considered for fusion have been approved for design by code bodies in the USA, Europe, and Japan. In the USA, modified 9Cr-1Mo (nominally Fe-9Cr-1Mo-0.25V-0.06Nb-0.1C) and 2¼Cr-1Mo (nominally Fe-2.25Cr-1Mo-0.1C) steels are included in the ASME Boiler and Pressure Vessel Code Section VIII for petrochemical and chemical pressure vessels and in Section III for nuclear pressure vessels, including high-temperature liquid metal fast fission reactor systems, as described in ASME Code Case N-47.

Welding will be required in the fabrication of a fusion power plant, and ferritic/martensitic steels are readily weldable. However, stringent procedures are required to obtain quality welds with maximum properties. For the 9–12% Cr steels, a preheat of 150 to 450°C [12–14] is generally required. In some cases, interpass temperature control can be used to prevent transformation to untempered martensite. Finally, a post-weld heat treatment (PWHT) is required as soon as possible after welding to temper the martensite in the high-chromium (5 to 12%) steels. (Low-chromium steels, e.g., 2¼Cr-1Mo, are weldable with fewer restrictions.) Welding will be discussed in detail in Chapter 7.

A fusion power plant will require field erection, which means that for a 9–12% Cr structural steel the preheat and PWHT will be performed in the field. The technology of field fabrication is well developed [15]. Pressure vessels for nuclear and petrochemical applications have been built in compliance with the ASME Code. Examples of large structures that have been fabricated in the field include: (1) nuclear containment vessels 46 m in diameter, over 73 m high, weighing over 6350 tons with the entire structure given a PWHT in the field; (2) 91-m-high heavy water columns up to 8.5-m diameter (1900 metric tons) with the entire structure given a field PWHT; and (3) coal-conversion vessels 59-m high with unit weights of 760 metric tons and wall thicknesses up to 89 mm [15]. Therefore, the technology for field fabrication of a steel fusion structure will not have to be developed.

Of the three materials presently considered for fusion applications, ferritic steels have the advantage for the construction of the massive structure of a fusion power plant based on past experience. For both vanadium and SiC/SiC composites, the techniques for constructing such a structure (joining, etc.) must still be developed. In addition, these materials have numerous problems that must be solved before the feasibility of their use can be proved. Besides the problem of a ferromagnetic material in high magnetic fields discussed above, the most serious problem faced by ferritic/martensitic steels is the effect of neutron irradiation on the fracture behavior, which will be discussed in detail in later chapters.

LOW- AND REDUCED-ACTIVATION CONSIDERATIONS

The safety of a fusion power plant depends on (1) the structural integrity of the plant and the probability of its failure, (2) the radioactive decay heat generated in the absence of coolant, and (3) the paths for dispersion of radioactivity to the plant surroundings during an accident. The ideal structural material for accident conditions, as well as normal operations, would be a "low-activation" material, that is, one that would not activate (would not become radioactive), would activate to a benign level, or, alternatively, one that would quickly decay (within minutes or hours) to a benign

level after activation [16]. A low-activation material would negate the consequences of a loss of coolant accident or any other incident that could cause an accidental release of radioactive debris. Such a material would also allow for "hands-on" maintenance of the plant, instead of the much more complicated and expensive remote maintenance required with a radioactive plant.

At present, no "low-activation" structural materials as defined above exist. A recent study (discussed in detail in Chapter 2) [17] indicates that the activation of SiC, which has often been labeled "low activation," is considerably lower than a V-5Cr-5Ti alloy and OPTIFER, a Cr-W ferritic/martensitic steel developed for "reduced activation" in the European Union. Indeed, according to the study [17], the activity of SiC about 100 y after shutdown is higher than that of V-5Cr-5Ti and OPTIFER. Therefore, safety will need to be engineered into a fusion structure constructed from a vanadium alloy, a SiC/SiC composite, or a reduced-activation ferritic steel.

Environmental effects will be produced from the disposal of fusion reactor components when they are replaced during operation or following the decommissioning of the plant [16]. This radioactive waste will have to be disposed of in a safe manner harmless to the environment. Depending on the elements present, the decay of induced radioactivity in a conventional ferritic/martensitic steel can take thousands of years. Such highly radioactive nuclear waste is disposed of by deep geological storage. To improve this situation, programs in Europe, Japan, the Soviet Union, and the USA were started in the mid-1980s to develop "low-activation" or "reduced-activation" ferritic steels [18–26] with the objective of shallow land burial or recycle of the material after its service lifetime and after some suitable "cooling-off" (radioactivity decay) period, usually assumed to be 100 years. In the USA, a Department of Energy Panel used U.S. Nuclear Regulatory Commission 10 CFR Part 61 guidelines to suggest that wastes at least meet the criteria for shallow land burial [16]. The 10 CFR Part 61 guidelines were set up for storage and disposal of low-level nuclear wastes from fission reactors, and it is not known how they might apply to fusion wastes generated many years in the future.

It should be noted that the term "low activation" is often used interchangeably with "reduced activation" to describe the vanadium alloys, SiC/SiC composites, and ferritic/martensitic steels developed to ease radioactive disposal, even though they do not meet the criteria for low activation as described above (i.e., a material that does not activate or activates to a very low level). As presently defined, a reduced- or low-activation steel is one that will be disposed of by shallow land burial (according to the 10CFR Part 61 guidelines). As an alternative, recycling has been suggested [18]. The composition of such a steel needs to be adjusted to contain only elements that form radioactive products that decay rapidly (in tens or hundreds of years rather than thousands of years) to low levels. Calculations were made to determine which elements must be replaced in conventional Cr-Mo steels to obtain a rapid decay of induced radioactivity levels after irradiation in a fusion reactor [16]. Such calculations indicated that the common alloying elements used in steels that must be eliminated or minimized include Mo, Nb, Ni, Cu, and N [16].

As discussed in Chapter 2, reduced-activation ferritic steels were developed [18–30] by replacing molybdenum in conventional Cr-Mo steels by tungsten and/or vanadium, and by replacing niobium by tantalum. Alloy development studies have shown that reduced-activation steels can be produced that offer the promise of fast-induced radioactivity decay and whose properties compare favorably with the conventional candidate materials. Final radioactivity levels for such a "reduced-activation" or "low-activation" steel is calculated to be over two orders-of-magnitude lower than for conventional Cr-Mo steels after a "cooling-off" period. It may be possible to recycle such a steel or to dispose of it by shallow land burial, instead of the much more expensive deep geological disposal, thus providing a substantial economic benefit for fusion power. Even if deep geological burial is necessary, reduced-activation steels would be of benefit because of reduced personnel exposure during the waste-disposal process.

In the development work on the reduced-activation materials, steels have been produced without adding any of the restricted elements (i.e., Nb, Ni, Mo, N) to demonstrate that the mechanical and physical properties of the steels would be as good or better than the properties of the conventional steels [22–30]. In those instances where special effort was made to lower the restricted elements, emphasis was focused mainly on eliminating niobium because of the very low concentrations (<1 wppm) of that element that will be required to meet criteria for shallow land burial or recycling [31]. Besides the elements Mo, Nb, Ni, Cu, and N, other elements (e.g., Co, Bi, Cd, Ag, etc.) that could appear as tramp impurities must be restricted to extremely low levels if the goals of shallow land burial or recycling are to be achieved [32–34].

This chapter introduced some important considerations for the conventional high-chromium ferritic/martensitic steels in relation to the nuclear applications for which they are being considered. It also introduced the new steels being developed to better adapt this type of steel to that application. In the following chapters, these and other aspects of the steels will be examined in detail.

REFERENCES

[1] S. N. Rosenwasser et al., J. Nucl. Mater., 85 & 86 (1979) 177.
[2] D. R. Harries, in: Proceedings of Topical Conference on Ferritic Steels for Use in Nuclear Energy Technologies, Eds. J. W. Davis and D. J. Michel (The Metallurgical Society of AIME, Warrendale, PA, 1984) 141.
[3] H. Attaya, K. Y. Yuan, W. G. Wolfer, and G. L. Kulcinski, in: Proceedings of Topical Conference on Ferritic Steels for Use in Nuclear Energy Technologies, Eds. J. W. Davis and D. J. Michel (The Metallurgical Society of AIME, Warrendale, PA, 1984) 169.
[4] T. Lechtenberg, C. Dahms, and H. Attaya, in: Proceedings of Topical Conference on Ferritic Steels for Use in Nuclear Energy Technologies, Eds. J. W. Davis and D. J. Michel (The Metallurgical Society of AIME, Warrendale, PA, 1984) 179.
[5] J. Rawls, W. Chen, E. Chung, J. Dillassandro, P. Miller, S. Rosenwasser and L. Thompson, Assessment of Martensitic Steels as Structural Materials in Magnetic Fusion Devices, General Atomic Report GA-A15749, January 1980.
[6] L. V. Boccaccini, P. Norajitra, and P. Ruatto, Fusion Engineering and Design 27 (1995) 407.
[7] L. V. Boccaccini and P. Ruatto, Fusion Technology (1997) 1519.

[8] T. Takagi, J. Tani, P. Ruatto, B. Krevet, and L. V. Boccacini, IEEE Transactions on Magnetics, 32 (3) (1996) 1054.
[9] M. Sato, Y. Miura, S. Takeji, H. Kimura, and K. Shiba, J. Nucl. Mater. 258-263 (1998), 1253.
[10] T. Nakayama, M. Abe, T. Tadokoro, and M. Otsuka, J. Nucl. Mater. 271 & 272 (1999) 491.
[11] J. Z. Briggs and T. D. Parker, The Super 12% Cr Steels, 2nd Edition (Climax Molybdenum Co., Ann Arbor, MI, 1982).
[12] J. R. DiStefano and V. K. Sikka, Summary of Modified 9Cr-1Mo Steel Development Program: 1975-1985, Oak Ridge National Laboratory Report, ORNL-6303, October 1986.
[13] J. F. King et al., Weldability of Modified 9Cr-1Mo Steel, Oak Ridge National Laboratory Report, ORNL-6299, August 1986.
[14] F. Brühl and H. Müsch, in: Proceedings of Topical Conference on Ferritic Steels for Use in Nuclear Energy Technologies, Eds. J. W. Davis and D. J. Michel (The Metallurgical Society of AIME, Warrendale, PA, 1984) 253.
[15] J. E. Bonta and O. G. Sikora, in: Application of 2¼Cr-1Mo Steel for Thick-Wall Pressure Vessels, ASTM STP 775, Eds. G. S. Sangdahl and M. Semchyshen (American Society for Testing and Materials, 1982) 255.
[16] R. W. Conn, E. E. Bloom, J. W. Davis, R. E. Gold, R. Little, K. R. Schultz, D. L. Smith, and F. W. Wiffen, Panel Report on Low Activation Materials for Fusion Applications, UCLA Report PPG-728, (University of California at Los Angeles, 1983).
[17] K. Ehrlich, S. W. Cierjacks, S. Kelzenberg, and A. Möslang, in: Effects of Radiation on Materials: 17th Volume, ASTM STP 1270, Eds. D. S. Gelles, R. K. Nanstad, A. S. Kumar, and E. A. Little (American Society for Testing and Materials, Philadelphia, 1996) 1109.
[18] G. J. Butterworth and O. N. Jarvis, J. Nucl. Mater., 122 & 123 (1984) 982.
[19] N. M. Ghoniem, A. Shabaik, and M. Z. Youssef, in: Proceedings of Topical Conference on Ferritic Steels for Use in Nuclear Energy Technologies, Eds. J. W. Davis and D. J. Michel (The Metallurgical Society of AIME, Warrendale, PA, 1984) 201.
[20] R. L. Klueh and E. E. Bloom, Nucl. Eng. Design/Fusion, 2 (1985) 383.
[21] D. S. Gelles, in: Optimizing Materials for Nuclear Applications, Eds. F. R. Garner, D. S. Gelles, and F. W. Wiffen (The Metallurgical Society, Warrendale, PA, 1985) 63.
[22] D. Dulieu, K. W. Tupholme, and G. J. Butterworth, J. Nucl. Mater., 141-143 (1986) 1097.
[23] M. Tamura, H. Hayakawa, M. Tanimura, A. Hishinuma, and T. Kondo, J. Nucl. Mater. 141-143 (1986) 1067.
[24] T. Noda, F. Abe, H. Araki, and M. Okada, J. Nucl. Mater., 141-143 (1986) 1102.
[25] C. Y. Hsu and T. A. Lechtenberg, J. Nucl. Mater., 141-143 (1986) 1107.
[26] K. Anderko, K. Erhlich, L. Schäfer, and M. Schirra, CeTa, Ein Entwicklungsschritt zu einem schwack aktivierbaren martensitischen Chromstahl, KfK Report 5060, June 1993, Kernforschungszentrum Karlsruhe GmbH.
[27] R. L. Klueh and P. J. Maziasz, Met. Trans., 20A (1989) 373.
[28] D. S. Gelles, in: Reduced Activation Materials for Fusion Reactors, ASTM STP 1047, Eds. R. L. Klueh, D. S. Gelles, M. Okada, and N. H. Packan (ASTM, Philadelphia, 1990) 113.
[29] H. Kayano, H. Kurishita, A. Kimura, M. Narui, M. Yamazaki, and Y. Suzuki, J. Nucl. Mater., 179-181 (1991) 425.
[30] K. Ehrlich, S. Kelzenberg, H. -D. Röhrig, L. Schäfer, and M. Schirra, J. Nucl. Mater. 212-215 (1994) 678.
[31] N. Yamanouchi, M. Tamura, H. Hayakawa, A. Hishinuma, and T. Kondo, J. Nucl. Mater. 191-194 (1992), 822.
[32] G. J. Butterworth and L. Giancarli, J. Nucl. Mater. 155-157 (1988), 575.
[33] G. J. Butterworth, J. Nucl. Mater. 179-181 (1991), 133.
[34] D. Murphy and G. J. Butterworth, J. Nucl. Mater. 191-194 (1992), 1444.

2

Development of High (7–12%) Chromium Martensitic Steels

The development of 9–12% chromium steels is reported to have originated in 1912 with the manufacture of a 12% Cr:2–5% Mo steel for steam turbine blades by Krupp and Mannesmann in Germany [1,2]. However, in 1912–13 Brearley in the U.K., while attempting to develop high-temperature steels for gun barrels, accidentally discovered that martensitic steels containing 13% Cr and 0.2% C did not rust [3]; the stainless characteristics of high-chromium steels were also recognized by Haynes in the USA and by Strauss and Maurer in Germany at about the same time. The high-chromium, high-carbon martensitic steels were hard and had a sharp cutting edge and were subsequently developed commercially for applications such as cutlery knives and tableware in competition with austenitic stainless steels as well as for razors, scalpel blades, and heat-resisting tools and bearings [4].

The 9 and 12% Cr transformable steels with lower carbon (0.1% max) contents and additions of Mo, W, V, Nb, N and other elements, possessing higher creep-rupture strengths combined with good oxidation and corrosion resistance at elevated temperatures, have subsequently been developed. These steels have been used or considered for use in petrochemical and chemical plants, gas turbine engineering, aircraft and aerospace industries, electrical power plants, and as nuclear fission and fusion reactor components. The steel compositions are given in Tables 2.1 and 2.2.*

The petrochemical and chemical processing industries utilize the steels in the form of thin tubular products in hydrogen desulfurization systems and in plants for the combustion of oil and the containment of various chemical products. The 9Cr-1Mo (T9) type of steel [5], possessing fairly moderate creep-rupture strength, was initially developed in the 1930s for such applications. However, the principal uses of the high-chromium martensitic steels are currently for components in gas turbines and in the boilers and turbines in steam power plants. The development and usage of the 9–12% Cr steels for these applications, as well as the 7–12% Cr steels for core components in fast breeder reactors and as potential first wall and breeder blanket structural materials in fusion reactor systems, are surveyed in this chapter.

* The steels in Tables 2.1 and 2.2 are designated according to their principal alloying elements (Cr, Mo, W, V, Nb, etc.) contents; for example, 9Cr-1MoVNb is the designation for the modified 9Cr-1Mo steel, which contains (by weight) 9% Cr, 1% Mo, and lesser amounts of V and Nb. Trade names (e.g., Firth Vickers FV448, Nippon Steel NSCR9, Sandvik Steel HT9, etc.) and/or related specification codes (AISI, ASME, Werkstoff, DIN, etc.) are also given where appropriate, while the newer steels are indicated by the designations assigned by their developers.

GAS TURBINES

The simple 12Cr and the 9 and 12Cr-Mo steels in the hardened-and-tempered condition have been used widely at moderate stresses and temperatures in the chemical and power plant industries. However, the introduction of gas turbine engines of the jet and prop-jet types for powering military and civil aircraft during and in the years immediately following the Second World War, and subsequently in land-based, marine, and aerospace power installations, led to the requirement for steels possessing good corrosion resistance and superior mechanical properties at high temperatures. This provided the impetus for the progressive development and utilization of several high-chromium martensitic steels, ranging from the plain 12Cr through the 12Cr-MoVNb (high-carbon FV448 and H46), 12Cr-NiMoV (M152), and 12Cr-MoV (FV607) to the 12Cr-MoVNbWCo (FV535 and H53) grades, with enhanced tensile proof and ultimate stresses and creep-rupture strengths at temperatures up to 550°C and times of $\leq 10^4$ h for gas turbine disks (diameters and thicknesses typically 1600 to 1950 and 240 to 550 mm, respectively), compressor wheels, blades, bolts and/or sheet structures [6–10]. A super-clean 12Cr-2.6Ni-2MoVNbN steel has been developed for heavy duty gas turbine applications in Japan [11], and the 12Cr-MoVNbW (COST Steel "E") is being evaluated as a potential disk material in Europe [12]. Recent developments in electro slag refining (ESR) involving high nitrogen pressures (pressurized ESR) have also enabled 12Cr steels with nitrogen levels as high as 0.3% to be produced [13]. These steels have been considered for use as disk materials in gas turbines; they possess high tensile strength and ductility, improved toughness, and promising short-term (10 000 h) creep-rupture strength up to 600°C [14].

STEAM POWER PLANTS

The majority of large fossil-fired power plants were operated at sub-critical steam conditions (pressures ≤22 MPa) prior to about 1990; the main steam temperature was standardized at 540°C worldwide, although 565°C was the standard for coal-fired plants in Europe, particularly in the U.K., with the steam pressure being typically 18 MPa. However, the need to develop fossil-fired power plants with reduced generating costs and acid rain and greenhouse gas productions was widely recognized in the late 1970s and early 1980s and subsequently led to the design and construction of supercritical or ultrasupercritical (USC) and combined cycle power plants with improved

TABLE 2.1—Compositions of commercial and developmental 9% Cr martensitic steels.

Steel Type	Designation	Country Of Origin	Analysis (wt. %)										
			C	Si	Mn	Cr	Ni	Mo	V	Nb	W	N	B
9Cr-1Mo	9Cr -1Mo*	UK	0.10	0.70	0.50	9.5	0.20	1.0					
	T9	Japan	≤0.15	0.25-1.00	0.30-0.60	8.0-10.0		0.90-1.10					
	EM10*	France	0.10	0.30	0.50	9.0	0.20	1.0					
9Cr-2Mo	HCM9M*	Japan	0.07	0.30	0.45	9.0		2.0					
	NSCR9*	Japan	0.08	0.25	0.50	9.0	0.10	1.6	0.15	0.05		0.030	0.003
	EM12	Belgium/ France	0.08-0.12	0.30-0.50	0.90-1.20	9.0-10.0		1.9-2.1	0.25-0.35	0.35-0.45			
	JFMS*	Japan	0.05	0.67	0.58	9.6	0.94	2.3	0.12	0.06			
9Cr-MoVNb	Tempaloy F-9	Japan	0.04-0.08	0.25-1.00	0.40-0.80	8.0-9.5		0.90-1.1	0.15-0.45	0.20-0.60			≤0.005
	T91	USA	0.08-0.12	0.20-0.50	0.30-0.60	8.0-9.5	≤0.40	0.85-1.05	0.18-0.25	0.06-0.10		0.030-0.070	
9Cr-MoVNbW	COST 'B'*	Europe	0.17	0.10	0.10	9.5	0.10	1.5	0.25	0.05		0.005	0.010
	E911*	Europe	0.10	0.20	0.40	9.0	0.20	1.0	0.20	0.08	1.0	0.070	
	TF1*	Japan	0.12	0.20	0.50	9.0	0.80	0.60	0.26	0.06	1.6	0.050	0.003
	TB9 (NF616) (T92)	Japan	0.07-0.13	≤0.05	0.30-0.60	8.5-9.5	≤0.40	0.30-0.60	0.15-0.25	0.04-0.09	1.5-2.0	0.050-0.070	0.001-0.006

*typical composition

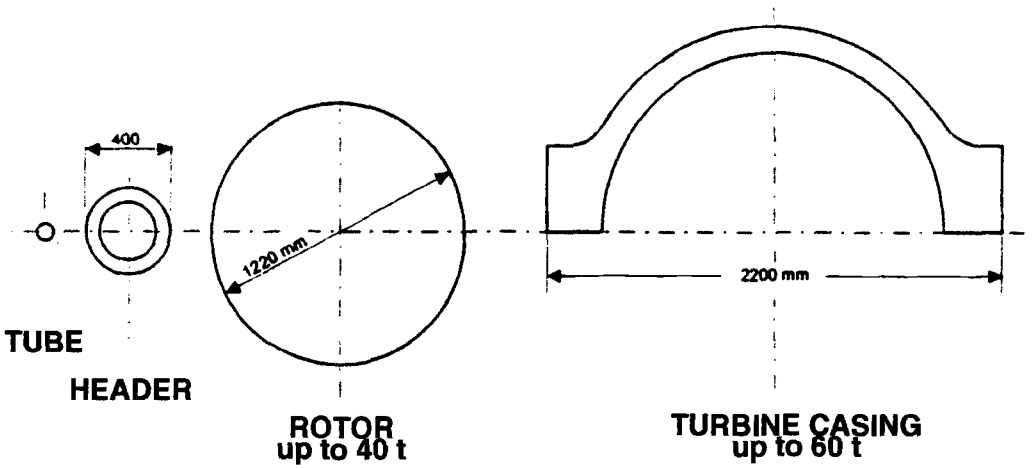

FIG. 2.1—Comparison of section dimensions of steam plant components [15].

thermal efficiencies. The requirement for operation with advanced (higher temperature and pressure) steam cycles in turn resulted in the establishment of a number of coordinated research and development activities in Japan [spearheaded since 1980 by The Electric Power Development Company Limited (EPDC)], the USA [the Electrical Power Research Institute (EPRI) Project RP 1403 initiated in 1985], and in Europe [Cooperation in Science and Technology (COST) 501 Programme initiated in the early 1980s]. These studies have focused on the development of highly alloyed 9-12Cr steels for boiler (superheater and reheater tubing and large-diameter, thick-walled pipes for steam lines and headers) and turbine (rotors, casings and valves, blades, bolts, etc.) components for operation at inlet steam temperatures up to 620 or 630°C and pressures of 30 to 34 MPa, with further developments for applications up to 650°C. The requirements of the materials for the steam turbine components differ from those of boilers in that they must be met with very large section sizes; the relative dimensions of boiler tubes, headers, turbine rotors, and turbine rotor inner casings are indicated in Fig. 2.1 [15].

The general requirements of the steels may be summarized as follows [16]:

- Ease of fabrication of large forged and cast components and of weldability for tubes and pipes.
- Through hardening and uniformity of mechanical properties in rotor forgings with diameters up to and in excess of 1.2 m.
- High creep and rupture strengths at temperatures of 600°C; a creep-rupture strength of 100 MPa at 600°C and 10^5 h has been the target for turbine components.
- High toughness and resistance to both embrittlement and softening during long-term service at elevated temperatures.
- Resistance to steam oxidation and also to fireside corrosion in the case of boiler tubes.

The respective programs have been described and the information and data generated reported in technical publications and proceedings of many international conferences held during the past 15 to 20 years [17–37].

Boiler Components

The compositions of newly developed higher-strength ferritic/martensitic steels are included in Tables 2.1 and 2.2, and the progress in their development for boiler applications is depicted in Fig. 2.2 [38]. It should be emphasized that there are considerable uncertainties in predicting the long-term creep-rupture strengths of the steels by extrapolation of short-term data usually obtained by testing in air. The complications arise as a consequence of scatter in the experimental data, microstructural changes that occur during testing and affect the deformation and fracture, and oxidation, which reduces the effective load-bearing cross-section. These effects and the various extrapolation procedures employed have been described elsewhere [39,40]. Nevertheless, progressive improvements in creep resistance have been achieved by close control of the major and minor alloying element concentrations so as to: (a) optimize the constitution and δ-ferrite content by additions of the austenite-stabilizing elements Cu and Co, (b) maximize the solid solution strengthening by W, Mo, and N, (c) stabilize the martensite dislocation structure and the $M_{23}C_6$ type precipitates by B additions, and (d) enhance the precipitation strengthening by the formation of fine particles of VN and Nb(CN), which are highly resistant to coarsening.

Many different steels, including 0.5Cr-MoV, 1.0Cr-0.5 Mo (T11), 2.25Cr-1Mo (P/T 22), and 9-12Cr, have been used worldwide for boiler tubing and steam piping in thermal power plants. The high-chromium steels have superior strength and oxidation resistance compared to the low-alloy steels. Furthermore, the 12Cr steels have better oxidation resistance than the 9Cr materials, and higher-strength versions of the former are therefore more suitable for use in the high-temperature parts of superheaters, which are susceptible to heavy corrosion and also, in some cases, for reheater tubing [41]. The temperature of the steam piping does not exceed

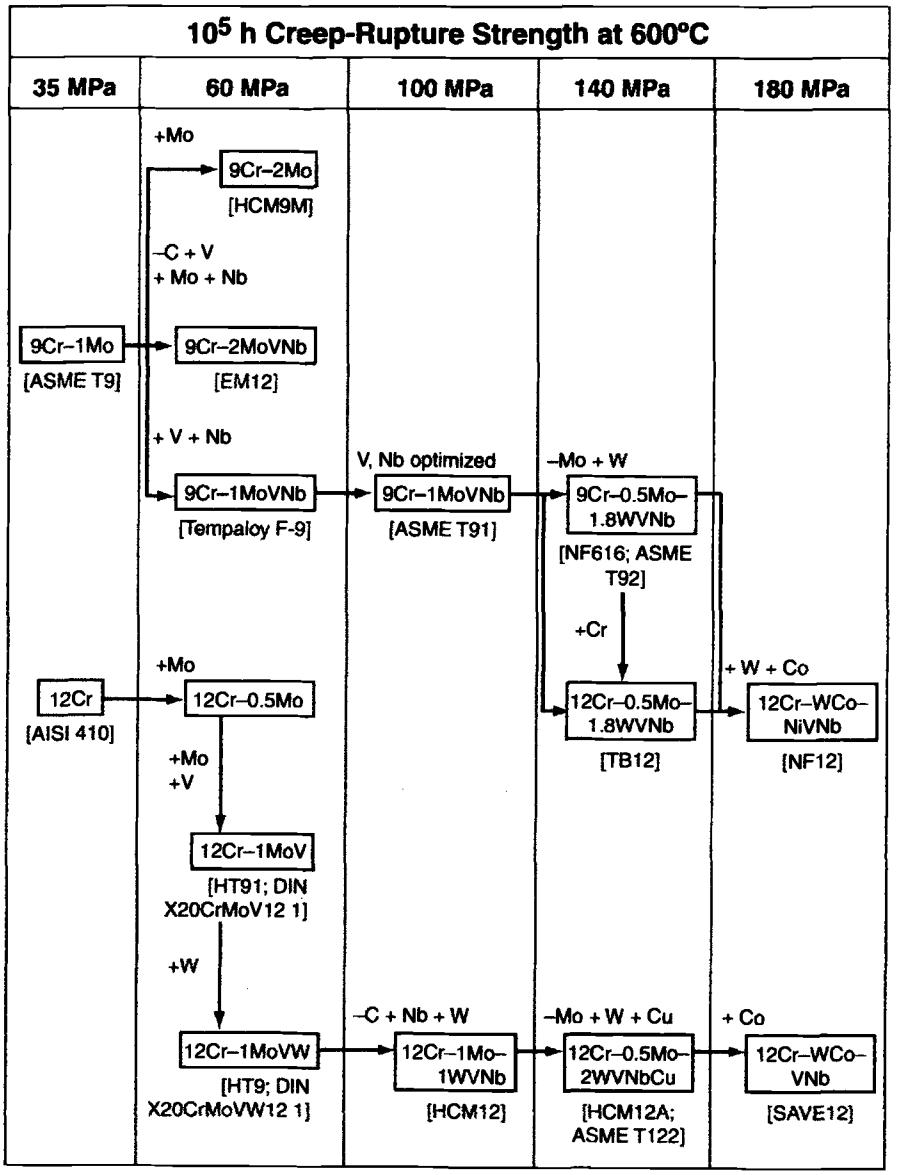

FIG. 2.2—Development of 9–12% chromium ferritic/martensitic steels [38].

TABLE 2.2—Compositions of commercial and developmental 12% Cr martensitic steels.

Steel Type	Designation	Country of Origin	Analysis (wt. %)											
			C	Si	Mn	Cr	Ni	Mo	V	Nb	W	N	B	Others
12Cr	AISI 403	US/UK	≤0.15	0.20-0.35	0.46-0.53	11.5-13.0								0.015 Cu 0.05 Al
	AISI 410	US/UK	≤0.15	≤1.0	≤1.0	11.5-13.0								
	FI*	UK	0.10	0.18	0.41	12-13	0.49							
12Cr-MoV	FV607*	UK	0.13	0.40	0.77	11.16	0.62	0.89	0.27					
	CRM12*	UK	0.19	0.45	0.54	11.80	0.40	0.96	0.30					
	X20CrMoV 12 1 (W.Nr.1.4922)	Germany	0.17-0.23	≤0.50	≤1.0	10.0-12.5	0.30-0.80	0.80-1.20	0.25-0.35					
	X22CrMoV 12 1 (W.Nr.1.4923) HT91 (SS2317)	Germany Sweden	0.18-0.24	0.10-0.50	0.30-0.80	11.0-12.5	0.30-0.80	0.80-1.20	0.25-0.35					
	LAPELLOY*	USA	0.30	0.25	1.0	12.0	0.30	2.75	0.25					
12Cr-MoVW	AISI 422*	USA	0.23	0.40	0.60	12.5	0.70	1.0	0.25		1.0			
	AL 419*	USA	0.25	0.30	1.0	11.5	0.50	0.50	0.40		2.5	0.10		
	HT9*	Sweden	0.20	0.38	0.60	11.95	0.60	1.0	0.30		0.52			
12Cr-MoVNb	H46*	UK	0.15	0.40	0.60	12.0	0.50	0.50	0.30	0.25		0.050		
	TAF*	Japan	0.18	0.30	0.50	10.5		1.5	0.20	0.15			0.030	
	FV448*	UK	0.10	0.46	0.86	10.7	0.65	0.60	0.14	0.26		0.050		
	W.Nr.1.4914	Germany	0.11-0.19	0.15-0.65	0.20-1.25	10.0-12.0	0.50-1.20	0.40-1.00	0.10-0.70	0.10-0.60		0.03-0.09		
	MANET I*	Europe	0.13	0.37	0.82	10.6	0.80	0.77	0.22	0.16		0.020	0.0085	0.015 Cu 0.05 Al 0.053 Zr
	MANET II*	Europe	0.10	0.17	0.81	9.97	0.66	0.61	0.24	0.15		0.024	0.007	≤0.02 Al 0.017 Zr
	X19CrMoVNbN 11 1 (W.Nr.1.4913)	Germany	0.16-0.22	0.10-0.50	0.30-0.80	10.0-11.5	0.30-0.80	0.50-1.00	0.10-0.30	0.15-0.50		0.05-0.19	≤0.01	
	GE*	USA	0.19	0.30	0.65	10.5	0.60	1.0	0.20	0.085		0.060		
	TR1100 (TMK1)*	Japan	0.14	0.05	0.50	10.2	0.60	1.5	0.20	0.06		0.040		
	EP450	Russia	0.10-0.15	0.50	0.80	11.0-13.5	0.05-0.30	1.2-1.8	0.10-0.30	0.30-0.60			0.004	
	COST 'F'	Europe	0.11	0.03	0.52	10.2	0.60	1.4	0.18	0.05		0.056	0.001	
	TOS 101*	Japan	0.18			11.0	0.40	1.0	0.20	0.07		0.050		
	TOS-301*	Japan	0.14			10.0	0.50	1.0	0.20	0.10		0.050		

TABLE 2.2—(cont'd).

Steel Type	Designation	Country of Origin	Analysis (wt. %)											
			C	Si	Mn	Cr	Ni	Mo	V	Nb	W	N	B	Others
12Cr-MoVNbW	HCM12	Japan	≤ 0.14	≤ 0.50	0.40-0.70	11.0-13.0		0.80-1.2	0.20-0.30	≤ 0.20	0.8-1.2			
	TB12*	Japan	0.08	0.05	0.50	12.0	0.10	0.50	0.20	0.05	1.8	0.050	0.003	
	TR1150 (TMK2)*	Japan	0.13	0.05	0.50	10.7	0.70	0.40	0.17	0.06	1.8	0.045		
	TR1200*	Japan	0.12	0.05	0.50	11.0	0.80	0.15	0.20	0.08	2.5	0.060		
	TF2*	Japan	0.18	0.05	0.50	11.0	0.10	0.20	0.20	0.08	2.4	0.025	0.015	
	TF3*	Japan	0.18	0.05	0.50	10.5	0.10	0.20	0.20	0.08	2.4	0.025	0.015	
	PNC-FMS*	Japan	0.12	0.05	0.60	11.0	0.40	0.50	0.20	0.05	2.0	0.050		
	GE (Mod)*	USA	0.14	0.03	0.60	10.0	0.70	1.0	0.18	0.045	1.0	0.040		
	COST 'E'*	Europe	0.12	0.10	0.45	10.4	0.75	1.1	0.18	0.045	0.8	0.052	0.0002	
	TOS 107*	Japan	0.14			10.0	0.70	1.0	0.20	0.05	1.0	0.050		
	TOS 202*	Japan	0.16	0.07	0.50	11.0	0.70	1.0	0.20	0.20	1.1	0.050		
	TOS 302*	Japan	0.12			10.0	1.0	1.1	0.20	0.1	0.8	0.050		
12Cr-MoVNbWCu	HCM 12A (P122)	Japan	0.07-0.14	≤ 0.50	≤0.70	10.0-12.5	≤ 0.50	0.25-0.60	0.15-0.30	0.04-0.10	1.5-2.5	0.040-0.10	≤0.005	0.3-1.7 Cu ≤0.04 Al
	Tempaloy F-12M*	Japan	0.15	0.20	0.10	12.0	0.30	0.70	0.25	0.10	1.0	0.075	0.006	1.0 Cu
12Cr-MoVNbWCo	HR1200*	Japan	0.11	0.05	0.60	11.0	0.50	0.15	0.20	0.08	2.6	0.025	0.015	3.0 Co
	FV535	UK	0.06-0.11	0.10-0.70	0.60-1.15	9.8-11.2	0.20-0.80	0.50-1.00	0.10-0.35	0.20-0.45	≤0.70	0.010-0.035	0.005-0.012	5.0-7.0 Co
	TOS 110*	Japan	0.11			10.0	0.20	0.70	0.20	0.05	1.8	0.020	0.010	3.0 Co
	TOS 203*	Japan	0.11			10.5	0.60	0.10	0.20	0.10	2.5	0.030	0.010	1.0 Co 0.2 Re
	TOS 303*	Japan	0.12			10.0	0.20	0.70	0.20	0.05	1.8	0.020	0.006	3.0 Co
	NF 12*	Japan	0.08	0.20	0.50	11.0		0.20	0.20	0.07	2.6	0.050	0.004	2.5 Co
	SAVE 12*	Japan	0.10	0.30	0.20	11.0			0.20	0.07	3.0	0.040		3.0 Co 0.07 Ta 0.04 Nd
12Cr-MoNiV	M152*	USA	0.10	0.25	0.65	11.7	2.65	1.6	0.28					

*typical composition.

that of the steam, and the oxidation resistance of the 9Cr steels is satisfactory for these components; however, a steel with high yield and creep-rupture strengths is advantageous for application as thick-walled (typically ≈230 mm) steam pipes as thinner sections can be used and thermal stress and fatigue loading are thereby minimized.

The X20CrMoV 12 1 (HT91) [42] steel has been utilized widely for superheater tubes, steam pipes, and thick-section boiler headers at steam pressures up to 25 MPa and temperatures of 540 and 560°C in European power plants; there is also extensive service experience on the duplex (tempered martensite plus δ-ferrite) 9Cr-2Mo (HCM 9M) steel [43,44] for similar applications at temperatures up to about 593°C in Japan and the 9Cr-2MoVNb (EM12) steel for superheaters at temperatures up to 600°C in France [45]. The modified 9Cr-1Mo steel (T/P/F 91) [46,47], in which the V and Nb contents have been optimized, is being increasingly used throughout the world for superheater tubing, headers, and piping with conventional steam conditions and also for advanced plants with steam inlet temperatures up to 593°C. This steel can be readily fabricated and welded and has a favorable combination of properties (high yield and creep-rupture strengths and allowable stresses) against which those of newer steels have to be judged. The T/P91 steel has thus been the basis for the further development in Japan of advanced grades, such as the 9Cr-MoVNbW (NF616; TB9; P92) [48,49], 12Cr-MoVNbW (HCM 12) [50,51], and the 12Cr-MoVNbWCu (HCM 12A) [52–54] steels for USC applications as large-diameter, thick-walled pipes [NF616 (T92)and HCM 12A (T122)] [55] and superheater and reheater tubes (HCM 12), while the 9Cr-MoVNbWN (E911) [56,57] steel, first evaluated as a rotor steel, is in an advanced stage of development as a tube and pipe material in Europe. The predicted 10^5 h/600°C creep-rupture strength of the E911 steel is slightly lower (105 MPa [39] and 108 MPa [58]) than that of the NF616 (P92) steel (112 to 130 MPa [39,48,58,59]) but superior to that of the modified 9Cr-1Mo (P91) steel (94 [58] and 87 MPa [60]). Two new 12Cr-MoVNbWCo boiler steels (NF12 [38,61,62] and SAVE 12 [38, 63]) with 10^5 h/600°C creep-rupture strength of ≈180 MPa have been laboratory tested in Japan; the SAVE 12 steel has small additions of Ta and Nd, which are reputed to enhance the creep-rupture strength in the 600 to 650°C temperature range [63].

Other developments being pursued include the elimination of welding in the production of complex-shaped boiler components by manufacturing the header and nozzle as one unit by hot isostatic pressing (HIPping) of E911 steel powders [57].

Turbine Components

The designations and compositions of the steels utilized for steam turbine components together with the newer high-chromium martensitic steels developed for these applications are also included in Tables 2.1 and 2.2.

Rotors

1.0Cr-MoV, 3.5Ni-CrMo(V) and conventional 12Cr steels have been used for turbine rotor forgings in subcritical plants as they have adequate creep-rupture strength, thermal-fatigue resistance, hardenability, and toughness for operation with steam inlet temperatures up to 540 to 565°C. Tungsten-containing 12Cr steels, such as AISI 422, GE, and the modified GE steel, possessing improved properties compared to the 1.0Cr-MoV steel, were developed for turbine rotors in the USA in the 1950s and 1960s, and the GE steel has been used successfully in supercritical plants with a steam temperature of 565°C for more than 25 years [64]. However, the creep-rupture properties of these steels are inadequate for operation in supercritical and USC plants operating at 595 to 650°C. Also, the 12Cr steels developed in the late 1940s and 1950s for gas turbine applications were not considered suitable for large rotor forgings and other steam turbine components as they were susceptible to segregation, had relatively poor forgeability and weldability as well as fracture toughness, and were microstructurally unstable [65]. Thus, while the steels had high creep-rupture strengths at ≥550°C for times of $\approx 10^4$ h appropriate to jet engines, their rupture strengths decreased rapidly at the times of $\approx 10^5$ h required for steam turbines.

The development of ferritic/martensitic rotor steels with improved creep-rupture strengths at ≥565°C was initiated in Japan in the 1950s; the development was focused on the 12Cr-MoV type, and a 12Cr-MoVNbB steel (TAF) [19,26,66] was used for the manufacture of small rotor forgings. Subsequent investigations during the 1970s led to the development of the 12Cr-MoVNb (TR1100; TMK1 [19,26,66,67] and TOS 101 [68,69]) and 12Cr-MoVNbWN (TR1150, TMK2 [19,26,66,67] and TOS 107 [68,69]) steels designed for use at 593 and 620°C, respectively, and the more highly alloyed 12Cr-MoVNbW (TR1200 [19,26]) and 12Cr-MoVNbWCoB (HR1200 [61,70] and TOS 110 [68,69]) steels aimed at inlet steam temperatures ≥630°C; the TMK1 and TMK2 steels have been used for the manufacture of turbine rotor forgings for Japanese supercritical steam power plants operating at ≥593°C [67].

Several new turbine rotor steels [9.5Cr-MoVNbB (Steel "B"), 10.5Cr-MoVNbWN (Steel "E") and 10.2Cr-MoVNbN (Steel "F")] have also been developed as part of the European COST 501 program [65,71]. The steels have been used for the manufacture of prototype rotor forgings and sectioned for characterization studies and short- and long-term mechanical property investigations, while Steel "F" rotors have been manufactured and operated at high steam temperatures and pressures in Danish power plants.

The high-pressure/low-pressure combination (HLP) rotor shafts are used widely in the steam turbine side of the combined-cycle power plants. The increases in power generation capacity of the combined-cycle plants necessitate an increase in the size of the HLP turbines, and their diameters may well approach 2000 mm in the near future. Several 2.0-2.5Cr-MoNiV steels have been successfully developed for such large turbines [72]. However, further increases in section size will result in higher stresses and the need for greater toughness in the center portions, which cannot be met with the low-alloy steels. High-purity 9Cr-MoVNiNbN steels have therefore been evaluated as potential rotor forging materials in large HLP turbines [73].

Attempts have been made to enhance the creep resistance of the 10-12Cr rotor steels by the direct addition of thermally stable carbides [(W,Ti)C and (W,Nb)C] to the melt under nonoxidizing conditions; the objective is to produce a fine

dispersion of precipitates in the matrix so as to reinforce that produced by the normal solid-state heat treatments.

Casings and Valve Bodies

Modified 9Cr-1Mo steels with increased nitrogen contents (G-X12CrMoVNb 9 1 [64,71] and G-X12CrMoVNbN 10 1 1 based on COST Steel "E"[15,71]) in the form of large castings have been used in Europe for valve chests and casings of HP and intermediate pressure (IP) turbines with main and reheat temperatures of 580 to 600°C; these replace the previous standard conditions of 540 to 565°C using low-alloy (1.0Cr-MoV, 1.25Cr-0.5Mo, and 2.25Cr-1Mo) steel castings [15,64]. The production and properties of the modified 9Cr-1Mo steel (F91) in the form of a thick (400 to 500 mm) forging for turbine valves have also been investigated [75]. Other steels developed in Japan for casings and valve bodies include 9Cr-MoVNbW (TF1) [26] and 12Cr-MoVNb (TOS 301) [69]; the use of the 9Cr-MoVNbW [NF616 (T/P 92)] steel in the cast form has also been considered [76], while the 12Cr-MoV-NbW (TOS 302) and 12Cr-MoVNbWCo (TOS 303) cast steels have been proposed for operation at steam temperatures of 600 and 630°C, respectively [69].

Turbine Blades

A variety of 12Cr-MoV (Lapelloy), 12Cr-MoVNbW (AL 419 and AISI 422) [1], and 12Cr-MoVNb (H46 [6], FV448 [7] and X19CrMoVNbN) steels have been used extensively for steam turbine blades, but they have insufficient creep-rupture strengths at temperatures above 550°C for application in USC power plants. The 12Cr-MoVNbWNB (TF2) steel [26] has been developed in Japan for use at higher temperatures, but a Ni-Cr-Co superalloy [Refractaloy 26: 0.08% C (max), 35–39% Ni, 16–20% Cr, 18–22% Co, 2.5–3.5% Mo, 2.5–3.5% Ti, 0.25% Al (max), balance Fe] has been employed successfully at temperatures above 570°C in the USA [64].

Bolts

The bolts used in modern steam turbines range in length from 300 to 1000 mm and in diameter from 40 to 150 mm. They operate at temperatures in the creep range and are often slackened and retightened after service periods of 30 to 80 000 h for maintenance purposes. The requirements of the bolt materials include high tensile yield and creep relaxation strengths and high fracture toughness, adequate ductility to avoid creep crack formation, and resistance to stress corrosion cracking in the steam environment [71,77–79]. High-chromium martensitic steels such as the 12Cr-MoNiV (X12CrNiMo 12 1), 12Cr-MoV (X22CrMoV 12 1), and 11Cr-MoVNbN (X19CrMoVNb 11 1) grades have been favored in Europe for bolts in steam turbines operating at temperatures in the range 450 to 565°C [71,78–80]. Other steels considered for bolting include 12Cr-MoNiV (M152) and 12Cr-MoVNb-WCu (FV535), while the 12Cr-MoVNb (H46) and 12Cr-MoVW (AISI 422) steels have been employed widely in the USA [64], and the 12Cr-MoVNbW (TF3) is favored in Japan [66]. However, tests have been carried out as part of the COST 501 and EPRI RP 1403 projects [71,78,79] on the higher creep-rupture strength 9-10Cr-MoVNb(W)N(B) steels, including the TAF, P91, and the COST rotor steels, to qualify them as bolt materials in thermal power stations operating at 600°C. The results of 1000 h screening tests showed that the relaxation behavior of these newer steels are comparable or inferior to those of the 11Cr-MoVNbN (X19CrMoVNb 11 1) steel despite their superior creep-rupture strengths and ductilities at 550 to 600°C [79]. The high-chromium martensitic steels are, consequently, only considered for use as turbine bolts up to a maximum temperature of 550 to 560°C, with nickel-base alloys such as Nimonic 80A [0.10% C (max), 18–21% Cr, 3.0% Fe (max), 2.0% Co (max), 1.8–2.7% Ti, 1.0–1.8% Al, balance Ni] and Refractaloy 26 favored for higher-temperature applications [64,81].

FAST BREEDER REACTORS

Nuclear Fission

The only fissionable material that occurs naturally is uranium with an atomic weight of 235, that is, ^{235}U; natural uranium contains 0.7% ^{235}U, the remainder being mainly ^{238}U. An example of one of the many possible fission reactions when an atom of ^{235}U absorbs a neutron (n) is:

$$^{235}U_{92} + {}^{1}n_0 \rightarrow {}^{94}Sr_{38} + {}^{140}Xe_{54} + 2\,{}^{1}n_0 + \approx 160\ \text{MeV} \quad (2.1)$$

The two fission fragments (^{94}Sr and ^{140}Xe) are highly radioactive and share the kinetic energy of about 160 MeV, which is available principally as heat. Each neutron created by the fission has an average kinetic energy of about 2 MeV (corresponding to a speed of 2×10^7 m/s). Some of these fission or fast neutrons are lost by being absorbed in materials other than the ^{235}U atoms and by escaping from the fuel, but the chain reaction can be maintained in fuel highly enriched in the fissile isotopes in fast reactors provided sufficient neutrons remain to produce as many new fissions in the next generation as there were in the first. However, in thermal reactors, the fast neutrons are slowed down to thermal energies (about 0.025 eV at ambient temperature, corresponding to a speed of 2×10^3 m/s) by repeated collisions with the low atomic weight atoms of a moderator, such as light water (H_2O), heavy water (D_2O), graphite (C), and beryllia (BeO). The slow or thermal neutrons are capable of sustaining the chain reaction in natural uranium fuel or fuel only slightly enriched with respect to the fissile ^{235}U isotope.

The fission and thermal neutrons may also breed plutonium from the nonfissionable ^{238}U isotope, as follows:

$$^{238}U_{92} + {}^{1}n_0 \rightarrow {}^{239}U_{92} + \gamma \quad (2.2)$$

$$^{239}U_{92} \rightarrow {}^{239}Np_{93} + {}^{0}\beta_{-1} \quad (2.3)$$

$$^{239}Np_{93} \rightarrow {}^{239}Pu_{94} + {}^{0}\beta_{-1} \quad (2.4)$$

The ^{239}Pu fissions readily and can be used together with ^{235}U to fuel both fast and thermal reactors.

Radiation Damage

The components located in or near the reactor core are bombarded with neutrons having a spectrum of energies mainly in the range above about 10 keV in fast reactors and range from approximately 2 MeV down to 0.025 eV in thermal reactors. As described in more detail in Chapter 8, radiation damage is produced in nonfissile materials used for fuel element cladding and core structural components as a result of: (a) the displacement of atoms from their equilibrium lattice

positions by energetic neutron-atom collisions and the formation of Frenkel defects (vacancies and interstitials), and (b) the creation of solid and gaseous impurity atoms by (n,γ), (n,α), and (n,p) transmutation reactions. The damage in ferrous and nonferrous metals and alloys is manifested as void formation and swelling, microchemical and microstructural changes, irradiation or in-reactor creep, radiation hardening and embrittlement, and reductions in fracture toughness and fatigue endurance. These effects are discussed in Chapters 9 to 17 in respect of the high-chromium ferritic/martensitic steels.

Reactor Components and Materials

The 12Cr (AISI 403) and wrought 9Cr-1Mo steels have been used for the pressure tube end fittings in the Canadian CANDU reactors [82] and in the evaporators and parts of the superheaters in the UK Advanced Gas-Cooled Reactors (AGRs) [83], respectively. The high-chromium martensitic steels have found few other applications in thermal reactors, their main development having been directed towards fast breeder reactor usage.

Several prototype sodium-cooled fast breeder reactors have been constructed and operated as fuel element subassembly test facilities and also to establish the viability of commercial fast reactor core component designs under fully representative conditions without compromising the main objective of demonstrating that they could reliably generate electricity for the national grids. These reactors include the Dounreay Fast Reactor (DFR) and Prototype Fast Reactor [PFR] (UK), RAPSODIE, PHÉNIX and Super-PHÉNIX (France), KNK-2 (Germany), EBR-II and the Fast Flux Test Facility [FFTF] (USA), BN5 (10), BOR60, BN350 and BN600 (Russia), JOYO and MONJU (Japan) and FBTR (India); however, many of these reactors have now ceased operation.

The 9Cr-1Mo steel has been utilized as internal sleeves for the repair of leaks in the welds between the 2.25Cr-1MoNb steel steam tubes and 2.25Cr-1Mo steel tube plates in the evaporator units and also for the replacement superheater and reheater tube bundles in PFR [83,84]. However, the successful operation of fast reactors is also dependent on the performance of the materials used in the construction of the fuel and breeding blanket assemblies. Thus, the subassembly fuel pin cladding and wrappers (or ducts) in a commercial fast reactor have to endure prolonged service at elevated temperatures and a maximum displacement per atom (dpa) dose of 150 to 200 dpa (see Chapter 8) if the fuel is to achieve an economic target burn-up of 15 to 20% of the heavy atoms.

The prototype fast breeder reactors usually commenced operation with conventional austenitic steels as the core component structural materials. However, these steels exhibited significant irradiation-induced void swelling and irradiation creep that could lead to dimensional instability and core distortion [85]. These problems may be exemplified by reference to the PFR [600 MW(th), 250 MW(e)] fuel element subassembly shown in Fig. 2.3 [85,86]. PFR employed a nominally free-standing core design in which 78 subassemblies were cantilevered from the bottom core support structure. Each subassembly consisted of 325 or 265 fuel pins with outside diameters of 5.84 and 6.60 mm, respectively, containing a stack of mixed-oxide (UO_2:PuO_2) annular pellets; the pins

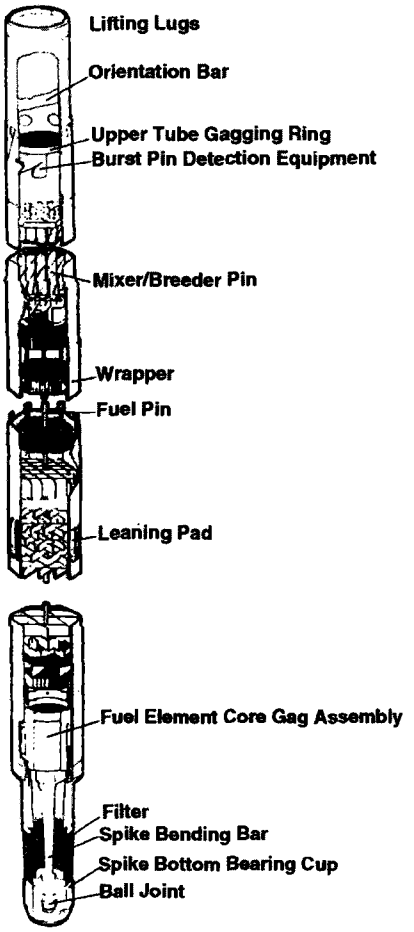

FIG. 2.3—PFR standard core subassembly [86,87].

were held in grids spaced at intervals along their length and enclosed within a hexagonal wrapper approximately 2.75 m long, 142 mm across the flats, and 3 mm wall thickness. The wrapper served to channel the sodium coolant flow (inlet and outlet temperatures of 400 and 560°C, respectively) over the fuel pin bundles and provided the structural strength and stiffness of the assemblies. The design temperature ranges for the wrapper and cladding (mid-wall) for the fuel element subassemblies in PFR (Row 1) were 420 to 550°C and 430 to 700°C, respectively.

The void swelling produced both axial and radial expansion of the cladding and wrapper so that, in the extreme, the coolant flow between the pins would be reduced, resulting in increases in temperature and possible failure, together with difficulties in removal or insertion during refueling unless sufficient clearance was allowed. In addition, differential void swelling due to gradients in neutron flux and temperature across a subassembly caused wrapper bowing, while the wrapper faces dilated (or bulged) due to irradiation creep under the influence of the internal coolant pressure. The subassembly bowing, dilatation and length, illustrated in Fig. 2.4, were important in determining the design, operation, and burn-up limits for the fuel elements. However, irradiation creep could be beneficial in certain circumstances by reducing interaction loads between neighboring subassem-

blies in the free-standing PFR core design or between the subassemblies and the core restraint structure in constrained core designs, such as those adopted for FFTF, PHÉNIX, and BN-350.

It became essential, therefore, to select or develop wrapper materials exhibiting consistently low void swelling and irradiation creep rates that were not excessively high if the burnup targets in the fuel were to be achieved [85]. Furthermore, the fuel pin cladding had to retain sufficient "in-reactor" creep strength and ductility to avoid premature failure under the stresses imposed by fission product gas release and fuel-clad mechanical interaction.

These requirements led to extensive post-irradiation examination and test programs on the subassembly components, as well as on specimens irradiated in rigs in experimental fast reactors, such as DFR, RAPSODIE, EBR II, FFTF, BR-10, BOR-60, and JOYO, and in the prototypes being undertaken in Europe [86–90], the USA [91,92], Russia [93,94], and Japan [95]. The data obtained in these studies enabled component material design rules to be formulated and materials with progressively increased resistance to void swelling, such as cold-worked unstabilized (based on Type 316: 0.08% C max.; 16.0–18.0% Cr; 10.0–14.0% Ni; 2.0–3.0% Mo) and Ti- or Nb-stabilized austenitic steels, precipitation-hardened intermediate nickel-base alloys and the high-chromium ferritic/martensitic steels, to be identified.

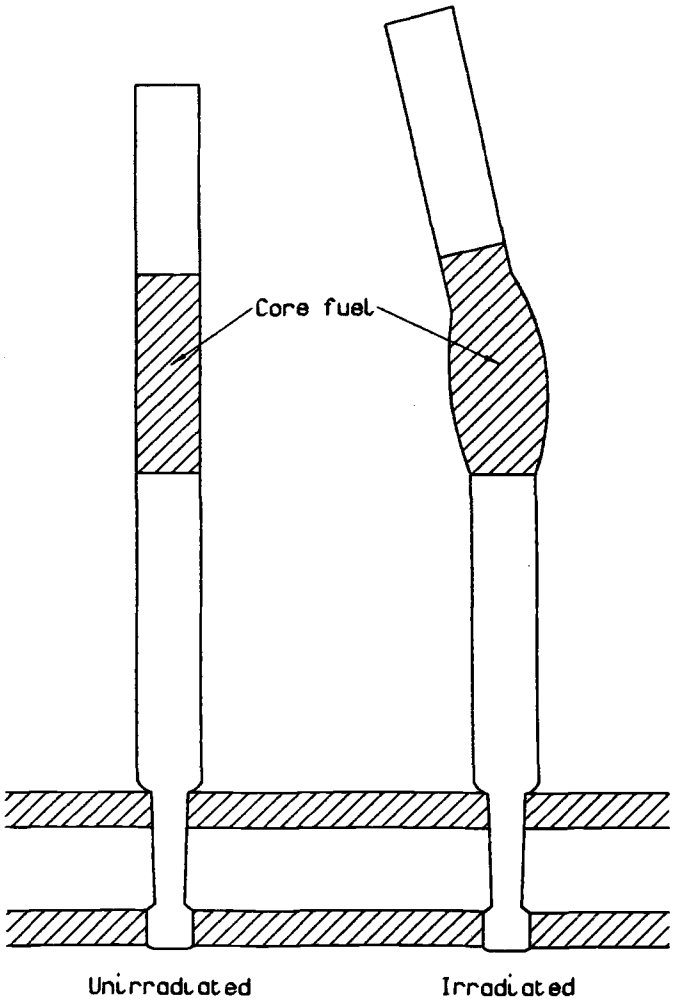

FIG. 2.4—Fast reactor core fuel element subassembly bowing, dilatation, and length increase resulting from irradiation.

Many wrought ferritic/martensitic steels have been employed or considered for application as wrappers (ducts) and, to a lesser extent, cladding in the core fuel element subassemblies in sodium-cooled fast reactors in Europe, the USA, Russia, and Japan [87–99]. They include (see Tables 2.1 and 2.2): plain 12Cr (FI) in the U.K. and a fully ferritic, non-transformable 17Cr (F17) in France, 9Cr-1Mo (EM10) and duplex 9Cr-2Mo (EM12) in France, 12Cr-1MoV (FV607 and CRM12) in the U.K., 1.4923 in Germany and EP450 in Russia), 9Cr-1MoVNb [modified 9Cr-1Mo (T91) in the USA and France], 12Cr-MoVNb (FV448 in the U.K. and 1.4914 in Germany), 12Cr-1MoVW (HT9) in the USA, and 12Cr-MoVNbW (PNC-FMS) in Japan.

The heat treatments specified for the 9–12% Cr ferritic-martensitic steels for nonnuclear conventional engineering applications are aimed at maximizing the tensile proof and creep-rupture strengths. However, a high thermal creep strength has not been a primary requirement for the wrappers, as the operating temperatures are below or at the lower end of the creep range for these materials and the components are not highly stressed during normal operation. A reduced creep strength was therefore acceptable, provided that increased fracture toughness and good high-temperature ductility, coupled with adequate formability and weldability, could be achieved. Consequently, extensive studies, involving modifications of the compositions and initial heat treatments, were carried out to develop the optimum combination of properties for some of the steels intended for use as wrappers [89,98,99].

Significant increases in toughness [low impact ductile-brittle transition temperature (DBTT) and high upper shelf energy (USE)], albeit with large reductions in creep-rupture strengths, have been effected by: (a) avoiding the formation of δ-ferrite and ensuring fully martensitic structures in the 12% Cr steels by close control of the nickel and chromium equivalent element concentrations; the single phase 9Cr-1Mo (EM10) steel has also been preferred to the previously considered duplex 9Cr-2Mo (EM12) steel [89]; (b) specifying a low nitrogen content (0.01% max) for the 1.4914 steel [99], although this benefit was not maintained after reactor exposure [89]; and (c) optimizing the austenitizing and tempering treatments to refine the prior austenite grain size and reduce the strength of the matrix of the 12% Cr [98] and 9% Cr [89] steels. For example, a reduction in the sub-size Charpy V-notch impact DBTT of the FV448 steel from −10 to −50°C was effected by changing from the manufacturer's recommended [1020°C/1 h, air cool (AC) plus 700°C/1 h, AC] to the high toughness wrapper (1100°C/1 h, AC plus 750°C/6 h, AC) heat treatment for the FV448 steel [89,98]; there was an associated decrease in the creep-rupture strength (550°C, 10^4 h) from approximately 260 to 200 MPa [98]. The applications of the high-chromium martensitic steels in fast reactor driver fuel element subassemblies are summarized in Table 2.3.

The high-chromium ferritic/martensitic steels have shown excellent dimensional stability (void swelling ≤0.5%) at high displacement doses [132 dpa for an FV448 steel wrapper in PFR and 142 and 115 dpa for EM10 and 1.4914 steel wrappers, respectively, in PHÉNIX] based on length and across-flats measurements on irradiated wrappers and density

TABLE 2.3—Application of high chromium ferritic/martensitic steels for driver subassembly structural components in sodium-cooled fast breeder reactors.

Reactor	Country	Cladding Steel/Alloy[a]	Wrapper Steel[a]	Reference
PFR	U.K.	STA Nimonic PE16	FV448	87, 90
PHÉNIX	France	CW 15Cr-5NiTiMoB	EM10	87, 90
PHÉNIX	Germany (DEBENE)	CW and CWA 1.4970 Mod.[b]	1.4914[b]	87, 90 96, 97
FFTF	U.S.A.	HT9	HT9	91, 92
BN-350 BN-600	Russia	CW ChS-68	EP450	93, 94
Long life cores (proposed)	Japan	PNC-FMS	PNC-FMS	95

[a] Solution treated and aged (STA) Nimonic PE16: 17% Cr, 43% Ni, 3% Mo, 2.5% Ti + Al, balance Fe.
Cold worked (CW) and cold worked and aged (CWA) 1.4970 austenitic steel and modified versions: 15% Cr, 15% Ni, 1.2% Mo, 0.40% Ti, 0.005% B.
Cold worked (CW) ChS-68 austenitic steel: 15.0, 16.5% Cr, 14.0–15.5% Ni, 1.9–2.5% Mo, 0.2–0.3% Ti, 0.001–0.005% B.
The following are ferritic/martensitic steels:
HT9: 12% Cr, 0.6% Ni, 1% Mo, 0.30% V, 0.5% W.
PNC-FMS: 11% Cr, 0.4% Ni, 0.5% Mo, 2.0% W, 0.2% V, 0.05% Nb, 0.05% N.
FV448: 10.7% Cr, 0.65% Ni, 0.60% Mo, 0.15% V, 0.25% Nb.
EM10: 9% Cr, 0.20% Ni, 1.0% Mo.
1.4914: 10.5% Cr, 0.85% Ni, 0.55% Mo, 0.25% V, 0.20% Nb, ≤0.010% N, ≤0.0015% B.
EP450: 11.0–13.5% Cr, 0.05–0.30% Ni, 1.2–1.8% Mo, 0.3–0.6% Nb, 0.1–0.3%V, 0.004% B.
[b] Experimental subassemblies.

determinations on specimens machined from irradiated wrappers or exposed in irradiation rigs [90]. In addition, 20 subassemblies consisting of STA Nimonic PE16 clad pins in FV448 steel wrappers loaded in the PFR core in the late 1980s reached 15 at% burn-up and 110 dpa, while one subassembly successfully achieved 19 at% burn-up and 155 dpa by the time the reactor was finally shut down in 1994 [87]. Also, cold-worked (CW) 15Cr:15NiTiMoB austenitic steel clad pins in EM10 steel wrappers reached burn-ups of about 17 at% and 146 dpa in PHÉNIX [90], while the EP-450 ferritic/martensitic steel clad pins in EP-450 wrappers achieved burn-ups of 12 at% with an associated displacement dose of 45 dpa in BN-350 and 15 at% and 144 dpa in BOR-60 [93,94].

A major limitation of the high-chromium ferritic/martensitic steels, in common with other body-centered-cubic (bcc) steels, is that they exhibit a ductile-brittle transition temperature (DBTT) in which the energy of fracture increases with increasing temperature on passing through the transition, followed by an upper-shelf region of relatively constant or slightly decreasing high fracture energies. The steels also suffer radiation embrittlement in that the DBTT increases and the upper-shelf energy (USE) is reduced by neutron irradiation; these changes correspond to a reduction in fracture toughness in fracture mechanics terminology, with decreased resistance to crack initiation in the transition region and ductile crack growth from preexisting flaws in the upper-shelf region. However, it has been established that the DBTTs of the irradiated high-chromium steels are not markedly dependent on the steel type and displacement dose (10 to 100 dpa) in the wrapper operating temperature range of 400 to 560°C, the irradiation-induced shifts being relatively small [90]. These effects will be discussed in detail in Chapters 14 and 15.

Oxide Dispersion-Strengthened Steels

The high-chromium ferritic/martensitic steels have limited thermal creep-rupture strengths at temperatures above 550°C and were, for this reason, considered unlikely to meet the target burn-ups for cladding operating at temperatures up to 670 or 700°C in commercial fast reactors. Consequently, the development of oxide dispersion-strengthened (ODS) steels possessing higher strengths at elevated and ambient temperatures for fuel element cladding and other applications has been pursued in Europe, the USA, Japan, and Russia [88,100–107]. The steels initially investigated had ferritic matrices containing 13% Cr and 1.5% Mo [88,100–102] and 11–13% Cr and 3% W [106] with titania (Ti_2O_3) and/or yttria (Y_2O_3) dispersions. The commercial manufacture involved the mechanical alloying of rapidly solidified alloy and ultra fine oxide powders, followed by consolidation by hot extrusion, rolling, or hot isostatic pressing (HIPping). The extruded and HIPped products generally have a very fine grain size (<1μm), and the uniaxial creep-rupture strengths and ductilities are enhanced if the matrix grains have a high aspect ratio (grain length:diameter ≥15) [108]. The large columnar structure is usually obtained by zone annealing, which also produces a strong texture due to secondary recrystallization (also referred to as exaggerated grain growth) [109–113]. However, an equiaxed grain structure is required for the fuel element cladding application so as to obtain good biaxial creep strengths and ductilities in the tubes [114].

FUSION REACTORS

Nuclear Fusion

Considerable effort is being expended worldwide to develop fusion as a long-term energy source. The most suitable fusion reaction occurs between the nuclei of the two heavy isotopes of hydrogen—deuterium (D) and tritium (T)—to form a helium nucleus and the release of a neutron and energy:

$$^2D_1 + {}^3T_1 \rightarrow {}^4He_2\,(3.5\ MeV) + {}^1n_0\,(14.1\ MeV) \qquad (2.5)$$

The fuel changes from a gas to a plasma at a temperature below the ≥100 million degrees celsius required for the D-T fusion reaction, and the hot plasma has to be magnetically confined within a vacuum vessel and isolated from the vessel

walls. The most promising magnetic confinement systems are toroidal (ring shaped), and the most advanced of these is the tokamak reactor. However, inertially confined fusion systems, in which the energy is produced by the repeated ignition of D-T pellets, have also been studied.

The deuterium fuel is abundant and can be readily extracted from seawater. Tritium does not occur naturally; relatively small amounts of tritium can be obtained as a by-product from heavy water thermal reactors, such as CANDU, but sufficient quantities to fuel the fusion reactor may be bred from lithium in the blanket surrounding the vacuum vessel in a tokamak reactor. Natural lithium contains 7.3 and 92.7% of the isotopes ^6Li and ^7Li, respectively, and the principal tritium breeding reactions are as follows:

$$^6Li_3 + {}^1n_0 \rightarrow {}^3T_1 + {}^4He_2 + 4.8\ MeV \quad (2.6)$$

$$^7Li_3 + {}^1n_0 \rightarrow {}^3T_1 + {}^4He_2 + {}^1n_0 - 2.9\ MeV \quad (2.7)$$

A tritium breeding ratio greater than unity is possible with natural lithium, as the breeding reaction with ^7Li releases a neutron capable of inducing the tritium breeding reaction with ^6Li. The primary neutron required for tritium breeding is obtained from the D-T reaction so that the consumables are deuterium and lithium, and the overall fusion breeding process may be represented by:

$$^2D_1 + {}^6Li_3 \rightarrow 2\ {}^4He_2 + 22.4\ MeV \quad (2.8)$$

Reactor Systems and Components

A schematic of a commercial D-T tokamak fusion power reactor (CFPR) is shown in Fig. 2.5. Many small and large [Joint European Torus (JET) in the U.K. [115], Tokamak Fusion Test Reactor (TFTR) in the USA [116] and JAERI Tokamak-60 (JT-60) in Japan [117]] experimental tokamaks have been constructed and operated. The principal objectives of these tokamaks have been to achieve plasma fusion physics conditions approaching breakeven (that is, net energy production) and to evaluate the behavior of various material components; however, D-T experiments have only been performed in JET [118] and TFTR.

A team was established in 1983 to define the Next European Torus (NET), envisaged as one of the main steps between JET and CFPR, and to initiate the technological developments necessary for its design and construction as well as those required in the longer term for a fusion power demonstration reactor (DEMO). The evolution of the NET objectives, schedule, parameters, and operation scenarios has been fully documented [119] and the selection of structural materials for the components exposed to the most onerous operating conditions [first wall, impurity control systems (limiter and divertor), and tritium breeding blanket] and associated test programs described [120–122]. The NET project was superseded in the mid-to-late 1980s by the International Thermonuclear Experimental Reactor (ITER) project involving the USA, Japan, the former USSR, and Europe [123,124].

The plasma-facing components in D-T tokamak reactors are subjected during service to:

- Mechanical and electromagnetic loadings and alternating thermal stresses induced by the surface and volumetric heating and pulsed nature of the operation.
- Irradiation with high-energy (14.1 MeV) fusion neutrons producing displaced atoms and helium, hydrogen, and solid transmutation products, leading to changes in bulk properties.
- Bombardment with ions and energetic neutral atoms from the plasma, resulting in surface (physical and chemical sputtering) and near-surface (gas bubble formation and blistering) damage. The damage is exacerbated in the event of plasma instabilities (disruptions) and by run-away and arcing effects; however, the metallic first wall has to be protected against these surface effects by graphite, beryllium, or other materials in the form of tiles or deposits.

The Fe-Cr-Ni and Fe-Cr-Mn austenitic and the Cr-Mo ferritic/martensitic steels, other metallic (vanadium, niobium, molybdenum, titanium, tantalum, etc.,) base alloys, and SiC/SiC composites have been considered as potential structural materials for the first wall and tritium breeding blanket components in the magnetically (D-T tokamak) [120–122, 125–135] and inertially [136–138] confined fusion reactor systems and included in the various national and community fusion materials research and development programs. The high-chromium (9–12%) steels initially included in these programs were essentially those being evaluated and developed for fuel element subassembly wrapper and cladding applications in the fast fission reactors. They included HT9 and the modified 9Cr-1Mo (T/P91) in the USA, JFMS (Japanese Ferritic Martensitic Steel) in Japan, a 12Cr-1.6Mo (1KH12M2S2) steel in Russia, and FV448, 1.4914, EM12, and other grades in Europe [121,127]. Type 316L (0.03% C; 17.0% Cr; 12.5% Ni; 2.5% Mo) austenitic steel and the fully martensitic MANET I followed by MANET II steels (based on the 1.4914 and FV448 specifications—see Table 2.2) were originally chosen as alternative first wall and breeder structural component materials for NET with a first wall target fluence of 2.8 MWy m^{-2} [120,121]. The composition (except for increased B, N, and Zr concentrations) and properties of the MANET I steel were generally comparable to those of the standard 1.4914 steel, while the MANET II steel, with reduced C, Al, and Zr contents, exhibited superior toughness properties and creep characteristics [139]. The martensitic steels, in addition to being more resistant to irradiation-induced void swelling, creep, and high-temperature helium embrittlement than the austenitic steels, have greater resistance to thermal stress development and fatigue because of their higher thermal conductivities and lower thermal expansion coefficients [121].

The ITER D-T tokamak device (illustrated in Fig. 2.6) is characterized by a low operating temperature (150 to 250°C), a moderate neutron (first) wall loading of 0.5–1.0 MW m^{-2}, an integrated (first) wall loading of 0.3 MWy m^{-2} (corresponding to a maximum displacement dose of about 3 dpa and helium and hydrogen gas production of 30 to 40 and 160 to 170 appm, respectively, in steel), a strongly pulsed operational mode (pulses of 1000 s duration with a total of 3 to 4 $\times$ 10^4 cycles), and with no requirement for tritium breeding [124]. Type 316LN austenitic steel (0.03% C max, 17.0–18.0% Cr, 12.0–12.5% Ni, 2.30–2.70% Mo, 0.06–0.08% N, 0.001–0.002% B, 0.30% Cu max, 0.25% Co max, 0.15%Nb+Ta+Ti max), which has been used as a fuel element cladding material in fast fission reactors, is deemed to be suitable for fulfilling the moderate demands of the water-cooled first wall in ITER.

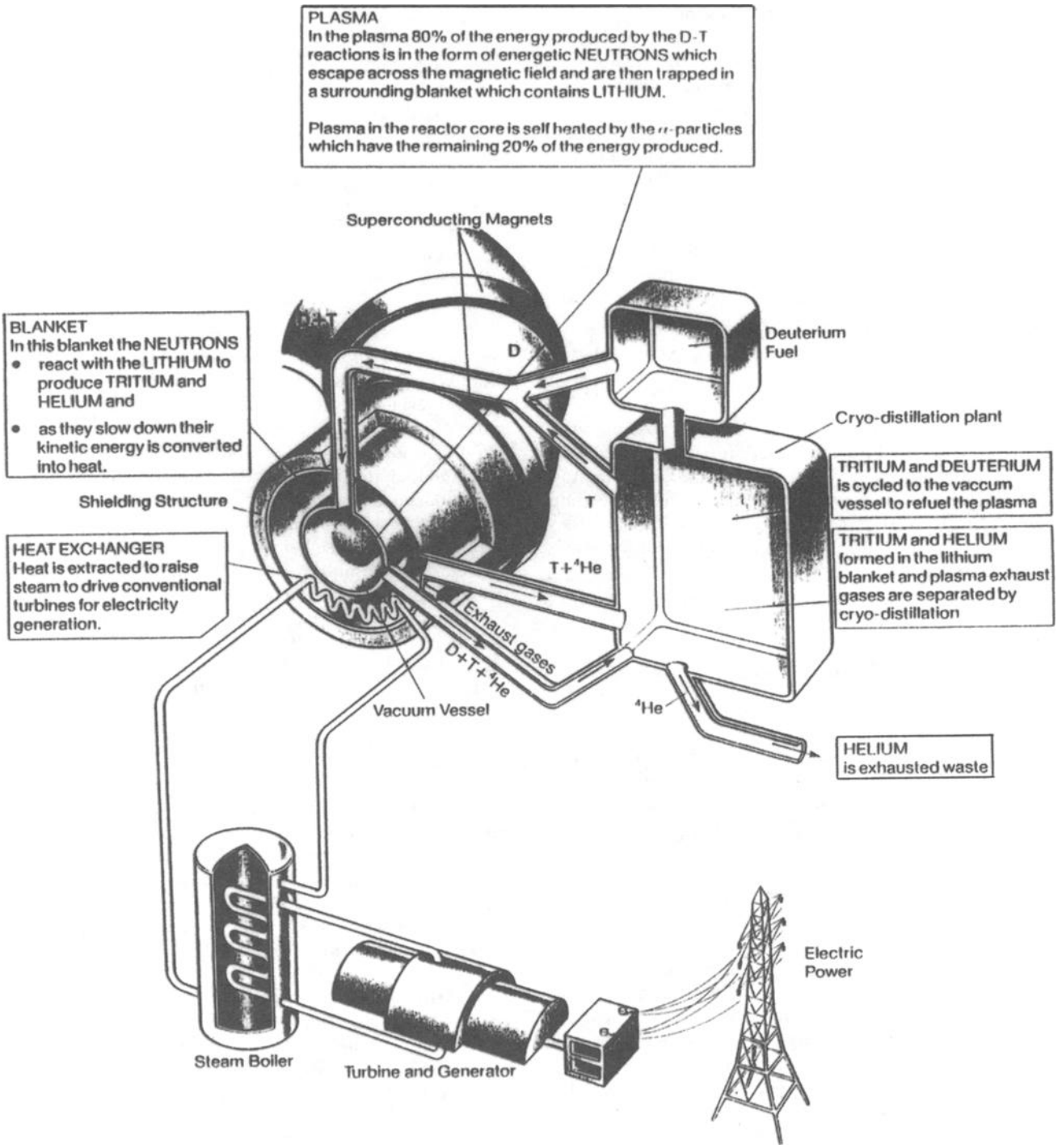

FIG. 2.5—Schematic of a fusion power reactor.

Tritium Breeding Blanket Concepts

Considerable design and associated research and development effort has also been devoted in Europe to the DEMO fusion power reactor-relevant solid ceramic and liquid metal tritium breeding modules to be tested and irradiated in ITER [140]. The various blanket concepts include:

1. Solid breeder blankets based on the use of lithiated ceramics, such as the oxide (Li_2O), aluminate (Li_4AlO_2), orthosilicate (Li_4SiO_4), and metazirconate (Li_2ZrO_3), cooled with high-temperature, high-pressure water [141] or high-pressure helium [142,143] and incorporating beryllium as a neutron multiplier to achieve a tritium breeding ratio in excess of unity. The two helium-cooled blanket configurations, in which helium is also used to purge the tritium from the breeding material, differ in the following respects: (a) The breeder inside tube (BIT) design [142] uses lithium aluminate or metazirconate in the form of annular pellets contained in tubes surrounded by beryllium blocks, the coolant being outside the tubes, (b) The ortho-silicate breeder and

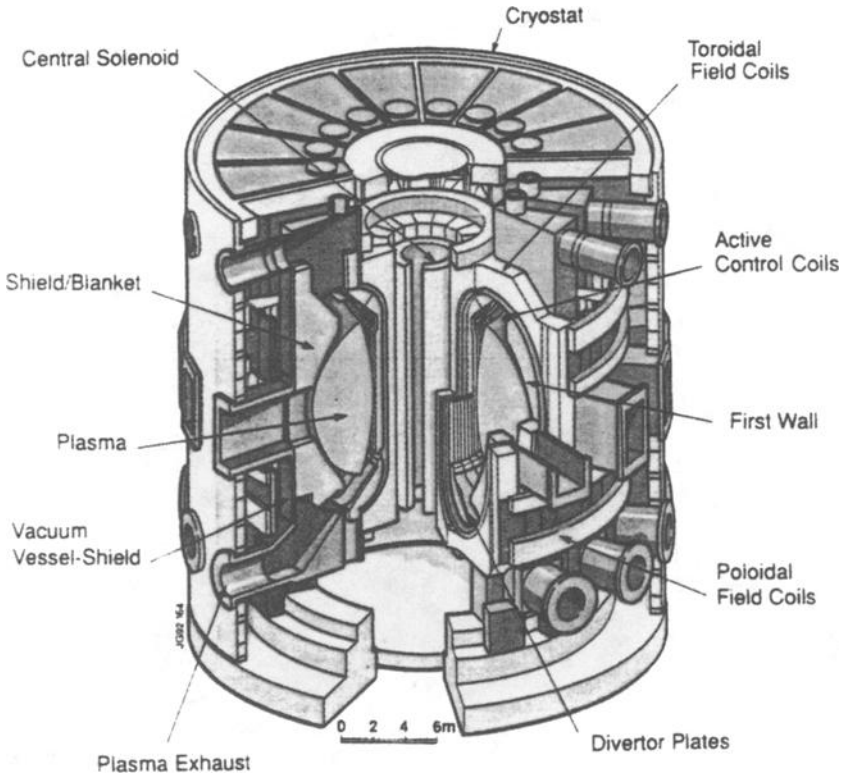

FIG. 2.6—The ITER device—schematic.

beryllium neutron multiplier are in the form of pebbles located between diffusion-bonded (welded) plates containing channels for two independent cooling systems in the breeder outside tube (BOT) [143] concept.

The outboard blanket segment (of which there are 48 in total) in the BOT design is shown in Fig. 2.7, and an isometric view of a poloidal portion of the outboard blanket segment around the torus equatorial plane is presented in Fig. 2.8 [143].

2. Liquid metal blankets utilizing the lithium-lead eutectic ($Li_{17}Pb_{83}$) both as breeder and coolant [144] and a water-cooled $Li_{17}Pb_{23}$ design [145]. The liquid metal velocity in the self-cooled concept is high (<1 m/s) and a major issue here is the magnetohydrodynamic (MHD) pressure drop in the magnetic field and the resulting high mechanical stresses produced in the ducts; however, the pressure drop can be reduced by about three orders of magnitude by using an oxide insulator coating on the channel walls to prevent current flow in the structural material. The liquid metal is semi-stagnant (velocity <0.01 m/s) in the water-cooled concept.

Further development is now restricted to the helium-cooled solid ceramic BOT [143] and water-cooled $Li_{17}Pb_{83}$ [145] concepts, with a high-chromium martensitic steel proposed as the structural material. An average neutron wall loading of 2.2 MWm^{-2} and a continuous operational mode have been specified for the DEMO reactor; the envisaged operating temperature range and target fluence for the steel structure in the helium-cooled solid ceramic blanket sectors are 200 to 550°C and 5 MWy m^{-2}, with a corresponding maximum displaced atom dose of approximately 70 dpa and helium and hydrogen gas generations by (n,α) and (n,p) reactions of about 700 and 3500 appm, respectively [140].

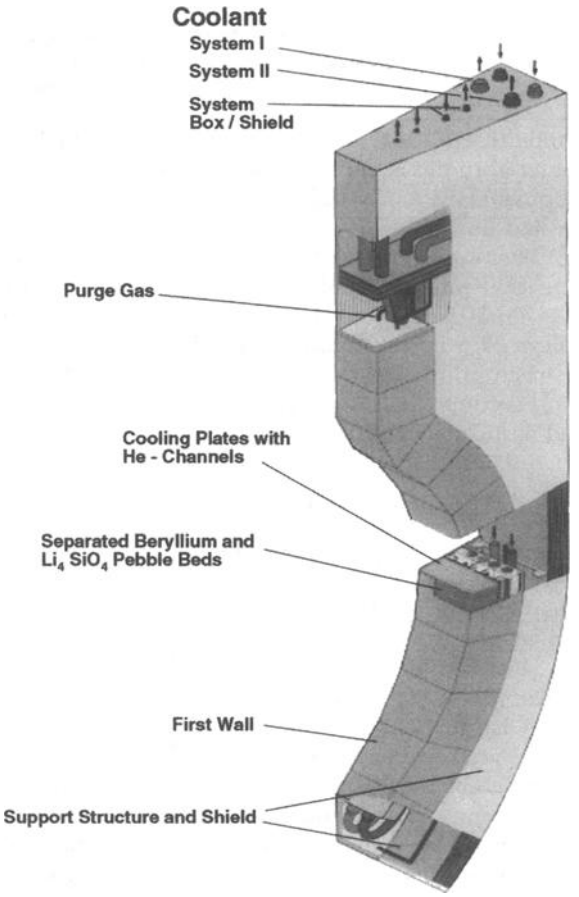

FIG. 2.7—Outboard blanket segment in the Breeder Outside Tube (BOT) concept [143].

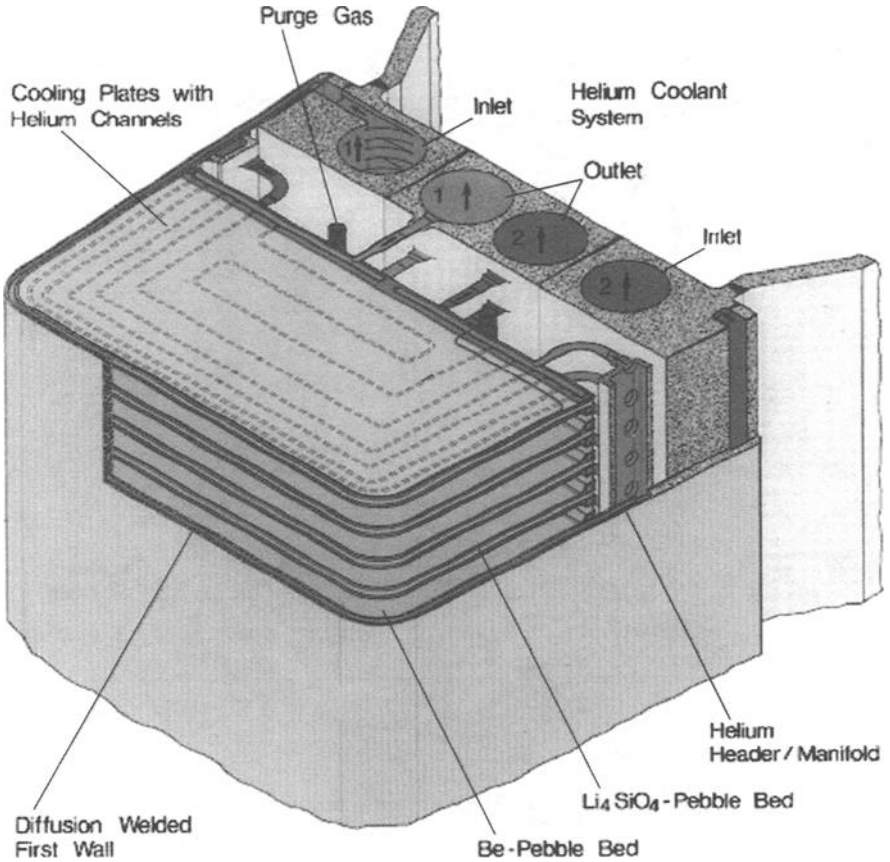

FIG. 2.8—Isometric view of a poloidal portion of the outboard blanket segment around the torus equatorial plane in the breeder outside tube (BOT) concept [143].

Liquid lithium has not been considered as a tritium breeding material in the European fusion reactor breeder blanket development, primarily because of its high reactivity with water, and its use has only been entertained for self-cooled fusion reactor designs in the USA [146]. A high-chromium martensitic steel was initially perceived as the structural material in the American liquid lithium blanket designs, but a vanadium alloy is now favored [147]. The use of a vanadium alloy structural material with liquid lithium for cooling and tritium breeding was also considered previously for an enhanced performance phase (EPP) in ITER [123].

Reduced-Activation Steels

There is no highly radioactive product in fusion as in fission. However, the fast and thermal neutrons in fission reactors and the high-energy (14.1 MeV) fusion neutrons can be absorbed by the nonfissile core component and structural materials in the respective systems, in some instances causing transmutation of the absorbing atoms and generating radioactive isotopes of the same or neighboring elements. These activated atoms decay back to stable isotopes, usually accompanied by the emission of β or γ radiation. Depending on the element, the emission may continue long after the irradiation has ceased, and the activations have major radiological implications with respect to the safe and routine operation and decommissioning of the plant and disposal of the radioactive material wastes.

The fusion reactor materials programs in Europe, the USA, Japan, and Russia have thus included the development of ferritic/martensitic and austenitic steels with enhanced radioactive decay characteristics, the objectives being to maximize the safety advantages of fusion and enable material and component maintenance, waste management, and recycling scenarios to be established [148–150]. The principal approaches adopted in this development are: (a) the replacement of the radiologically undesirable Mo, Nb, and Ni in the existing commercial steels by elements such as W, V, Mn, Ta, and Ti, which have equivalent or similar effects on the constitution and structures, and (b) the removal of the impurities that adversely influence the induced activities and dose rates when present in low concentrations in the steels. Isotopic tailoring, involving the removal of the undesirable isotopes in the major and minor alloying elements in the steels, appears feasible [151] but has not been actively pursued for a number of technical reasons, and the approach is less economic than that of elemental tailoring [152].

Relevant parameters and simplified radiological criteria for the respective scenarios have been proposed and are reproduced in Table 2.4 [148].

The inventory codes and cross-section and decay libraries developed in Europe, the USA, and Japan for predicting the radionuclide inventories of materials exposed in fusion reactor systems have been summarized [148]. FISPACT is an advanced inventory code for fusion applications and is available as part of the European Activation System, desig-

TABLE 2.4—Relevant parameters for low- and reduced-activation materials [147].

Safety	Prevention of any release of activity, which would necessitate off-site emergency action, interpreted as: • Prompt dose at site boundary due to complete release of inventory: <2 Sv. • Early dose at 1 km associated with accidental release of 100 kg of activated materials: <50 mSv. • Maximum early dose: 100 mSv. • Off-site releases: $<10^{14}$ Bq.
Maintenance	Remote maintenance: Dose rate inside plasma chamber $<1 \times 10^4$ Gy h^{-1} after 1 day cooling or integrated dose $<1 \times 10^7$ Gy based on doses which can be tolerated by electronic components.
Waste Disposal	Maximum doses to inadvertent intruders and members of the public for near-surface burial: • 5 and 0.25 mSv·y^{-1} (10CFR61, U.S.A.) [153]. Maximum annual individual risk for a single facility of 10^{-6} (Authorizing Departments, U.K.), equivalent to a health risk associated with a dose of 0.1 mSv. For 50 y interim storage [154]:

	Dose rate, mSv h^{-1}	Decay heat, W m^{-3}
Low level waste:	<2	<1
Medium level waste:	<20	<10
High level waste:	>20	>10

Recycling	"Hands-on" contact dose rate after 100 y cooling: • 25→10 μSv h^{-1}. Remote recycling limit (ability to remelt and refabricate remotely): • <10 mSv h^{-1} after 50 y cooling. Dose rate and decay heat after 50 y interim storage: • <2 mSv h^{-1} and <1W m^{-3} [154]. Residual activity for unrestricted release: • $<10^3$ Bq kg^{-1}.

TABLE 2.5—Basic compositions of reduced-activation ferritic and martensitic steels.

USA	CEC	Japan
2-9Cr-V	9Cr-W-V-Ta-N	2-15Cr-W
2-9Cr-W	12Cr-W-V-Ta-N	2-3Cr-W-V-Ta
2-12Cr-W-V	9-10Cr-W-V-Ta-Ti-Ce	7-9Cr-W-V-Ta
9Cr-W-Mn	9Cr-W-V-Mn-Ti	11Cr-W-V-Ta
9Cr-V-Mn		
12Cr-W-Mn		
12Cr-V-Mn		

nated EASY [155]; this also includes activation and decay libraries, a subsidiary library of biological hazard data, and reference neutron spectra for a fusion reactor first wall, blanket, shield and magnetic coils. Sequential reactions [A (n,x) B → A (x,n) C where x is a charged particle such as a proton (p), deuteron (d), α-particle (α) , triton (t), etc.] may also contribute to the residual activities, dose rates and decay heats in some circumstances [156], and pseudo cross sections for the relevant reactions are now included in the activation codes.

The results of the neutronic calculations have demonstrated that the radioactivity induced in conventional 9–12% Cr martensitic steels, such as HT9 and MANET, following exposure for 2.5 year (y) in a fusion power reactor with a neutron (first) wall loading of 5 MWm^{-2} do not satisfy any of the criteria in Table 2.4 [154,157,158].

The basic compositions of the reduced-activation ferritic and martensitic steels investigated in the European [159–165], USA [166–172], and Japanese [173–177] fusion materials programs are summarized in Table 2.5; the analyses of the martensitic steels which, on present evidence, appear to have reasonably stable microstructures and favorable combinations of strength, toughness, and resistance to radiation damage are given in Table 2.6. EUROFER [163] has now replaced the MANET II steel (see Table 2.2) as the reference structural material for the European DEMO breeding blanket concepts [140]. Furthermore, the Japanese modified F82H and JLF-1 steels form the basis of a continuing International Energy Agency (IEA) Collaborative Program to evaluate and develop these reduced activation transformable steels for use in fusion reactors [180].

Increasing attention is also being given in Europe and Japan to the development of the ODS ferritic/martensitic steels for eventual structural component applications at temperatures of 600°C and above in DEMO fusion reactor blankets [182]. The physical metallurgy research and development of material manufacturing and component fabrication routes are centered on the "conventional" ODS (9Cr-Mo+Y_2O_3) steels [183] as well as on reduced activation (9Cr-W+Y_2O_3 [183] and 8Cr-2W+Y_2O_3 +Ti [184]) versions.

The effects of individual alloying additions in the steels on the contact γ-dose rate, induced activity, and decay heat relative to the contributions from the iron base have been calculated as a function of time after reactor shutdown for a fusion reactor first wall with a neutron loading of 2 MWm^{-2} for 2.5 y [185] using FISPACT and the EAF-3 cross-section library [186]. The results confirm that Cr (any concentration), V (≤8%), Mn (≤1%), Ta (≈1%), and Si (< 0.4%) are

TABLE 2.6—Typical/nominal compositions (wt%) of reduced-activation martensitic steels with favorable combination of properties.

Program	Designation	C	Si	Mn	Cr	W	V	Ta	N	B	Ref.
CEC	LA12TaLC	0.09	0.03	1.0	8.9	0.8	0.40	0.10	0.02		159–161
	EUROFER	0.10–0.12	0.05 max	0.4–0.6	8.0–9.0	1.0–1.2	0.20–0.30	0.06–0.10	0.02–0.04	0.004–0.006	150, 163, 164
Japan	F82H	0.10	0.20	0.50	8.0	2.0	0.20	0.04	<0.01	0.003	150, 173, 178, 179
	JLF-1	0.10	0.08	0.45	9.0	2.0	0.20	0.07	0.05		150, 176, 180
USA	9Cr-2WVTa	0.10	0.30	0.40	9.0	2.0	0.25	0.07			150, 168 170, 171

acceptable while Mo (> 100 ppm), Nb (> 1 ppb), and Ni (> 50 ppm) are unacceptable alloying additions; C, B, and Ti in the concentrations normally present in the steels do not detrimentally affect the activation parameters of the iron base. The data also suggest that tungsten may not be the ideal substitute for molybdenum in the steels as the dose rate after 100 y cooling with 1% W exceeds that for iron by up to two orders of magnitude; also, significant transmutations of W to Os and Re and Ta to W and Hf can occur with fusion neutrons [187].

Other data on steels, based on the individual element γ-dose rate contribution of 25 $\mu Sv h^{-1}$ at 100 y, also show that the allowable concentrations of the elements Pd, Sn, Gd, Dy, Yb, Lu, Hf, Ir, Bi, Ag, Eu, Tb, and Ho as well as Nb, are re-

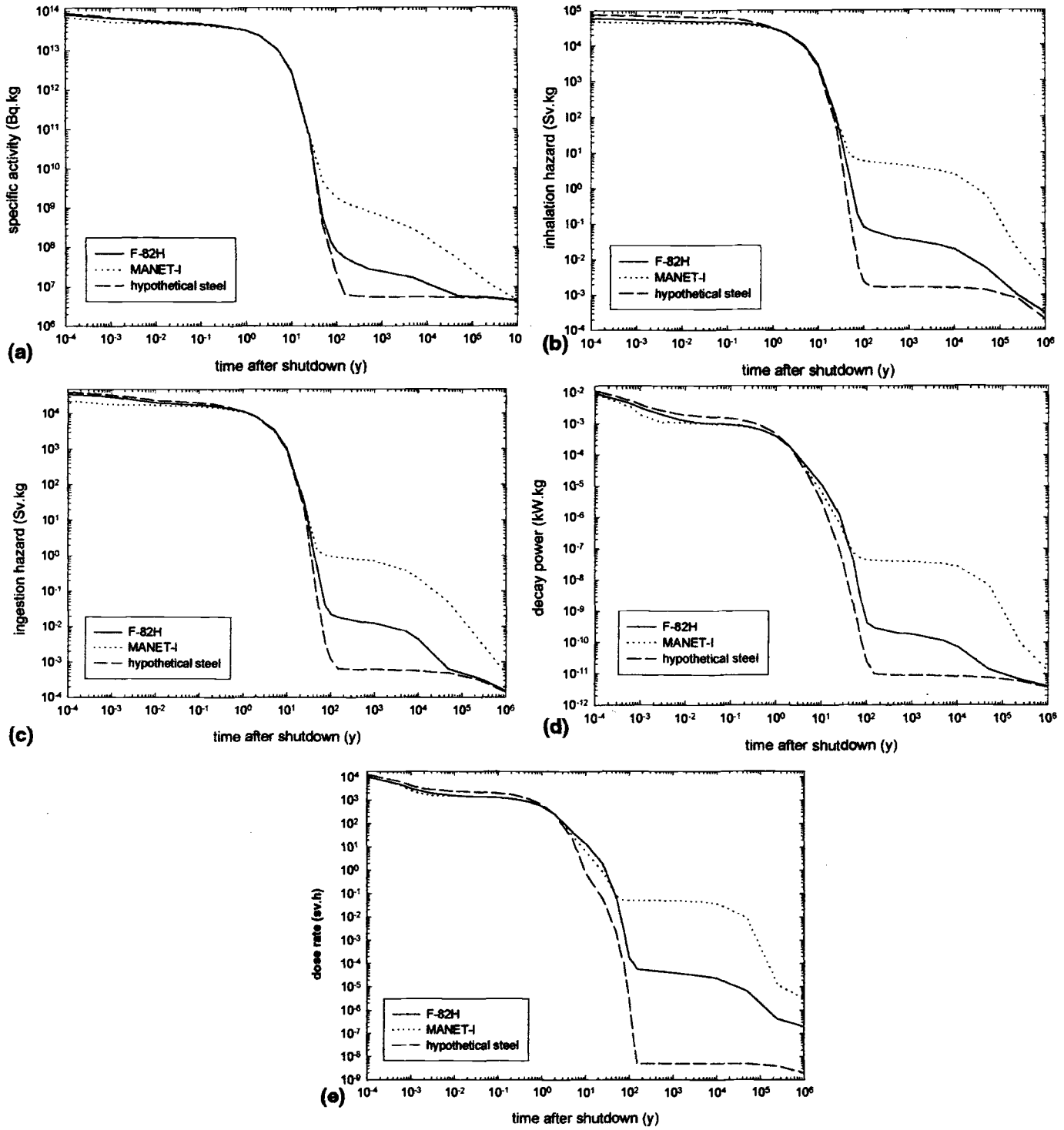

FIG. 2.9—Activation property comparison for MANET I, F82H and a hypothetical steel showing the (a) specific activity, (b) contact γ-dose rate, (c) ingestion hazard, (d) inhalation hazard, and (e) decay power [192].

stricted to < 1 ppm, with particularly stringent limitations applying to Ag, Eu, Tb, Ho, Nb, and Bi [188].

A reduced-activation high-purity 9Cr-WVTa steel exhibits slightly higher activation, contact γ-dose rate, and decay heat for about 1 y after reactor exposure to 2.5 $MWym^{-2}$ (2.5 y with a neutron wall loading of 1 MWm^{-2}) compared with those for a conventional high-chromium martensitic steel [189]. However, the activation, dose rate, and decay heat of the reduced-activation steel are two-to-four orders of magnitude lower after cooling for approximately 100 y and satisfy the criteria for these parameters for recycling and the dose rate and decay heat criteria for classification as low-level waste given in Table 2.4 [148]. The data for the reduced-activation steel containing 0.019% N and 0.76% W also show that the long-term (>100 y) specific activity is determined by the ^{14}C formed by transmutation of nitrogen and that the tungsten dominates the γ-dose rate [182]; the nitrogen content has to be restricted to a maximum of 0.005 wt.% to avoid the activity increase due to ^{14}C.

The dose rates computed for a series of 8.5–9.5Cr-WVTa developmental steels are about one order of magnitude lower than those for conventional 10-12Cr-MoVNb steels after cooling for approximately 100 y following exposure for 2.5 y with a neutron wall loading of 5 MWm^{-2} but are still greater than a "hands-on" recycling limit of 25 μSvh^{-1} [163]. The long-term activity in these steels is dominated by the iron base, the alloying elements tungsten and tantalum, and the niobium impurity; the sequential reactions in the Cr, V, Mn, and N can be neglected as they only result in second-order effects.

Activation calculations have also been performed using EASY (FISPACT 4.1 activation code [190] linked with the EAF-4.1 cross section, decay, and other data libraries [191]) for the MANET I, F82H, and a hypothetical (assuming no impurities) 9Cr-2WVTa steel in a central blanket position in a water-cooled $Li_{17}Pb_{83}$ fusion reactor design [192]; a total neutron flux of 2.25×10^{18} nm^{-2} s^{-1} and a continuous 5 y exposure was assumed in the computations. The changes in the specific activities, contact γ-dose rates, residual decay powers, and biological hazard potentials (ingestion and inhalation hazards) of the three steels with time after shutdown are compared in Fig. 2.9 [192]. The results confirm some of the earlier observations cited above and show that in terms of activation response the hypothetical steel is marginally inferior and the MANET I steel is slightly superior to the F82H steel at short time scales. However, the steels exhibit diverging behavior after prolonged cooling times, the MANET I being consistently inferior and the hypothetical steel consistently the best with regard to the activation properties after approximately 100 y. The poorer activation response of the F82H steel beyond 100 y is due to the nitrogen (800 ppm assumed in this case).

The maximum allowable impurity concentrations in the steels have been calculated for a number of known radiologically detrimental elements, the criterion adopted being that the impurity should not contribute more than 10% of the activation response of the hypothetical steel at any post-shutdown time [192]. The results for 19 critical elements are listed in Table 2.7 [192] and confirm that the tolerable concentrations of elements such as Nb, Ag, and various lanthanides and actinides are less than 10^{-8} % (that is, less than 0.1 wppm).

The activation response functions of the F82H steel have also been compared with those of other potential fusion reactor structural materials, namely a SiC composite and a vanadium alloy (V-4Ti-3.3Cr) [193]. The specific activity and contact γ-dose rate responses for the three materials are shown in Fig. 2.10. The materials in order of decreasing activation property in the time period 10^{-4} to approximately 100 y are steel, vanadium alloy, and SiC. However, the order is generally reversed after 100 y cooling, with the SiC exhibiting the poorest response and the steel the best. It follows, therefore, that the choice of structural material for a DEMO or fusion power reactor is a compromise between several competing criteria [193].

Preliminary investigations have been carried out to determine if the required "hands-on" elemental concentration limits can be achieved. A 5-ton heat of an 8Cr-2WVTa reduced activation steel produced in Japan using "NKK pure iron" and

TABLE 2.7—Allowable concentrations of impurity elements in reduced-activation martensitic steel [192].

	Limiting Concentration (%)					
Element	Specific Activity Limit	Dose Rate Limit	Ingestion Hazard Limit	Inhalation Hazard Limit	Decay Power Limit	Most Stringent Limit
N	2.59×10^{-4}	no limit	6.77×10^{-5}	1.43×10^{-4}	1.08×10^{-4}	6.77×10^{-5}
Al	2.30×10^{-1}	1.06×10^{-5}	7.07×10^{-3}	3.60×10^{-1}	1.16×10^{-2}	1.06×10^{-5}
K	4.86×10^{-5}	1.51×10^{-2}	9.22×10^{-7}	3.09×10^{-8}	4.17×10^{-6}	3.09×10^{-8}
Ca	6.60×10^{-4}	9.18×10^{-3}	1.25×10^{-5}	4.19×10^{-7}	5.67×10^{-5}	4.19×10^{-7}
Co	1.85×10^{-3}	1.65×10^{-5}	8.97×10^{-5}	5.19×10^{-5}	2.09×10^{-5}	1.65×10^{-5}
Ni	1.12×10^{-3}	6.69×10^{-3}	1.05×10^{-3}	6.04×10^{-4}	1.25×10^{-3}	6.04×10^{-4}
Cu	5.05×10^{-4}	9.75×10^{-3}	4.64×10^{-4}	2.66×10^{-4}	5.51×10^{-4}	2.66×10^{-4}
Nb	6.39×10^{-4}	8.43×10^{-9}	6.20×10^{-5}	9.03×10^{-6}	8.21×10^{-6}	8.43×10^{-9}
Mo	7.42×10^{-4}	5.53×10^{-6}	1.27×10^{-4}	8.44×10^{-5}	5.87×10^{-4}	5.53×10^{-6}
Ag	2.45×10^{-4}	3.99×10^{-9}	1.60×10^{-5}	4.08×10^{-6}	2.93×10^{-6}	3.99×10^{-9}
Cd	4.18×10^{-3}	8.41×10^{-6}	1.07×10^{-5}	3.27×10^{-6}	2.61×10^{-4}	3.27×10^{-6}
Nd	3.43×10^{-4}	2.80×10^{-4}	4.84×10^{-4}	3.50×10^{-5}	3.23×10^{-4}	3.50×10^{-5}
Sm	2.14×10^{-5}	1.10×10^{-6}	2.81×10^{-5}	1.92×10^{-6}	1.37×10^{-5}	1.10×10^{-6}
Eu	4.24×10^{-5}	3.99×10^{-9}	1.68×10^{-6}	1.51×10^{-7}	3.80×10^{-7}	3.99×10^{-9}
Tb	5.09×10^{-5}	1.53×10^{-9}	6.38×10^{-6}	4.94×10^{-7}	1.05×10^{-6}	1.53×10^{-9}
Ho	1.02×10^{-4}	1.72×10^{-9}	7.03×10^{-6}	3.80×10^{-7}	1.04×10^{-6}	1.72×10^{-9}
Ir	6.62×10^{-5}	3.68×10^{-8}	4.62×10^{-5}	7.91×10^{-6}	8.25×10^{-6}	3.68×10^{-8}
Bi	2.81×10^{-2}	7.04×10^{-7}	3.00×10^{-4}	1.84×10^{-4}	2.51×10^{-4}	7.04×10^{-7}
U	1.65×10^{-4}	2.52×10^{-4}	1.55×10^{-7}	2.53×10^{-9}	9.49×10^{-7}	2.53×10^{-9}

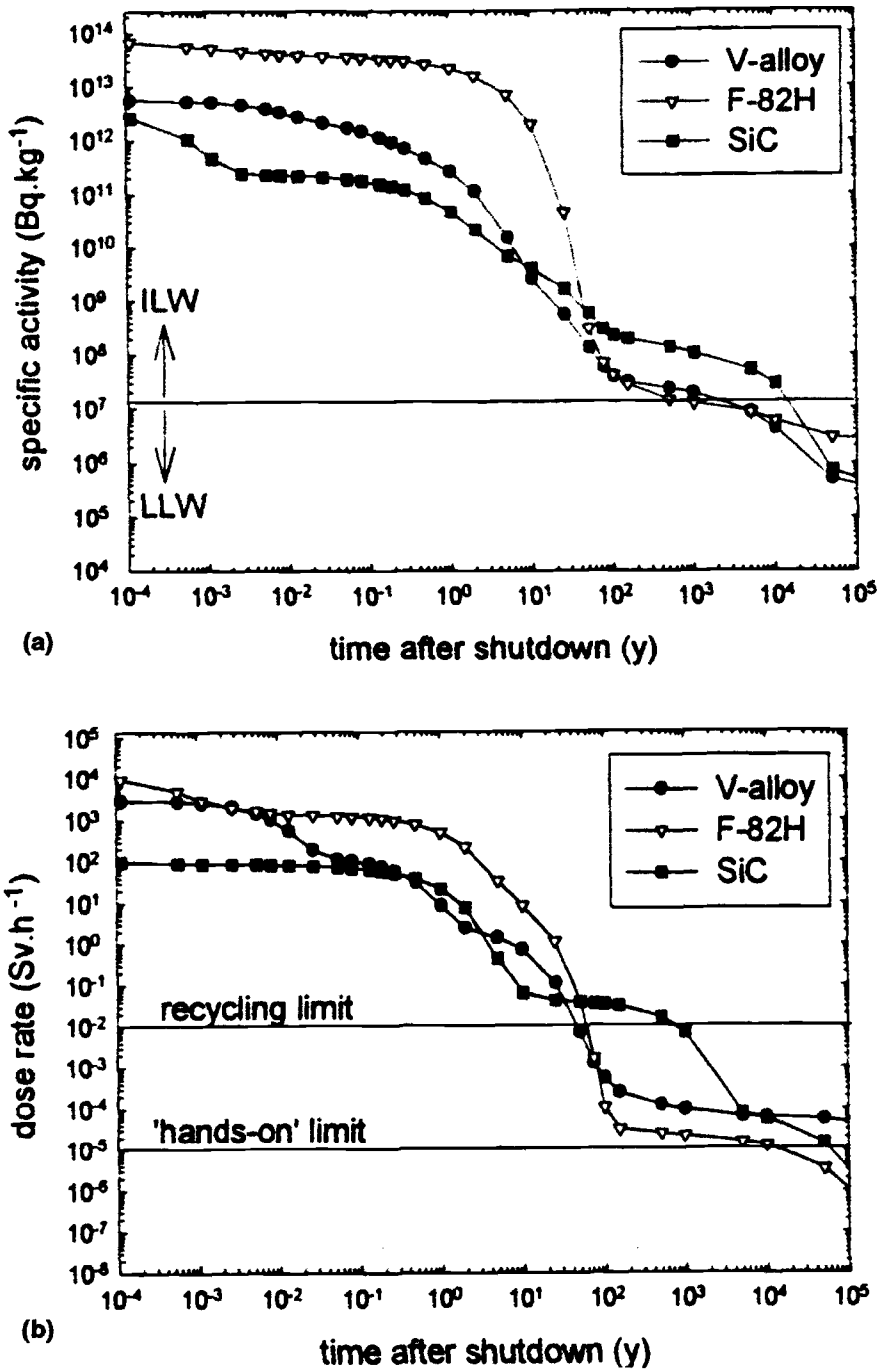

FIG. 2.10—Comparison of (a) specific activity and (b) contact γ-dose rate for F82H steel, a V-4Ti-3.3Cr alloy and a SiC/SiC composite [192].

ultra high-purity electrolytic chromium [150] was analyzed for the elements in Table 2.7 using inductively coupled mass spectrometry (ICMS) [194]. The results were compared with the criterion that "impurity elements be restricted to levels that would allow attainment of a surface γ dose rate not exceeding 25 μSvh^{-1} at 100 y cooling time for material subjected to a first wall neutron fluence of 12 $MWym^{-2}$" [195]. It was established that the niobium content of 2 to 3 wppm was over an order of magnitude above the allowable limit. The cobalt (≈20 wppm) also exceeded the limit of 0.16 wppm, while the concentration of molybdenum (20 wppm) was close to the limit of 18 wppm; the ICMS detection limits for silver and bismuth were just above the allowable concentrations (0.011 and 0.14 wppm, respectively), so that the contents of these two elements may or may not have been above the limits.

It follows that the production of reduced-activation martensitic steels with the niobium and other radioactively undesirable elements maintained at the low concentrations required to meet the "hands-on" dose rate recycling and additional targets has not been entirely successful hitherto.

Nevertheless, the experience gained in the development and production of nickel and cobalt based superalloys suggests that the required low concentrations of impurities in the reduced-activation steels may be achieved by selecting high-purity raw materials, the use of vacuum induction melting, and vacuum arc refining techniques, and avoiding impurity pick-up during processing and fabrication [196]. Furthermore, it appears that elemental analytical techniques such as glow discharge and inductively coupled mass spectrometry have sufficient sensitivity for the quantification of the impurity elements at the reduced concentrations required to achieve "low" activation in these steels.

REFERENCES

[1] Z. Briggs and T. D. Parker, The Super 12% Cr Steels (Climax Molybdenum Co., New York, 1965).

[2] Anon, Super 12% Cr Steels-An Update (Climax Molybdenum Co., New York, 1983).

[3] H. Brearley, Knotted String-Autobiography of a Steelmaker (Longmans, London, 1941).

[4] J. H. G. Moneypenny, Stainless Iron and Steel (Chapman and Hall, London, 1926).

[5] L. Egnell, in: High Temperature Properties of Steels (The Iron and Steel Inst., London, Publication 97, 1967) 153.

[6] D. A. Oliver and G. T. Harris, in: High Temperature Steels and Alloys for Gas Turbines (The Iron and Steel Inst., London, Special Report No. 43, 1952) 46.

[7] H. W. Kirkby and R. J. Truman, in: High Temperature Properties of Steels (The Iron and Steel Inst., London, Publication 97, 1967) 361.

[8] G. L. Briggs, A. E. Marsh, and J.W.S. Stafford, in: High Temperature Properties of Steels (The Iron and Steel Inst., London, Publication 97, 1967) 387.

[9] W. T. Davies and B. Hall, in: High Temperature Properties of Steels (The Iron and Steel Inst., London, Publication 97, 1967) 561.

[10] T. Angeliu, E. L. Hall, M. Larsen, A. Linsebigler, and C. Mukira, in: Advanced Heat Resistant Steel for Power Generation, Eds. R. Viswanathan and J. Nutting (The Inst. of Materials, London, Book 708, 1999) 234.

[11] Y. Fukui, M. Shiga, S. Nakamura, and K. Hidaka, in: Clean Steel: Superclean Steel, Eds. J. Nutting and R. Viswanathan (The Inst. of Materials, London, Book 635, 1996) 123.

[12] K.-H. Schonfeld and H. Wagner, in: Advanced Heat Resistant Steel for Power Generation, Eds. R. Viswanathan and J. Nutting (The Inst. of Materials, London, Book 708, 1999) 375.

[13] G. Stein and J. Menzel, in: Second Int. Conf. on Improved Coal-Fired Power Plants, Vol. 2, Eds. A. F. Armor, J. A. Bartz, G. Touchton, and L .J. Valverde A. (EPRI, Palo Alto, CA, 1988) 57.

[14] H. Berns and F. Krafft, in: Rupture Ductility of Creep Resistant Steels, Ed. A. Strang (The Inst. of Metals, London, Book No. 522, 1991) 116.

[15] D. V. Thornton and K.-H. Mayer, in: Advanced Heat Resistant Steel for Power Generation, Eds. R. Viswanathan and J. Nutting (The Inst. of Materials, London, Book 708, 1999) 349.

[16] R. B. Scarlin, in: Advances in Turbine Materials, Design and Manufacturing, Eds. A. Strang, W. M. Banks, R. D. Conroy, and M. J. Goulette (The Inst. of Materials, London, Book 689, 1997) 242.

[17] A. Armor, W. Bakker, R. Jaffee and G. Touchton (Eds.), in: First Int. Conf. on Improved Coal-Fired Power Plants, (EPRI, Palo Alto, CA, 1986).

[18] COST-EPRI Workshop on Creep-Resistant 9-12 Cr Steels, (EPRI, Palo Alto, CA, 1986).

[19] T. Fujita, Metals Progress 8 (1986) 33.

[20] A. F. Armor, J. A. Bartz, G. Touchton, and L. J. Valverde A. (Eds.), Second Int. Conf. on Improved Coal-Fired Power Plants, (EPRI, Palo Alto, CA, 1988).

[21] High Temperature Materials for Power Engineering (Kluwer Academic Publishers, Dordrecht, The Netherlands, 1990).

[22] Steam Plant for the 1990s (Inst. Mech. Engngs., London, 1990).

[23] F. Masuyama, Materials Technology for Ultra Supercritical Power Plants, Nishiyama Memorial Technology Lectures, No. 133 (Iron Steel Inst. Japan, 1990) 89.

[24] A. Strang (Ed.), Rupture Ductility of Creep Resistant Steels (The Inst. of Metals, London, Book No. 522, 1991).

[25] K. Natesan and D. J. Tillack (Eds.), First Int. Conf. on Heat Resistant Materials (ASM Int., Materials Park, OH, 1991).

[26] T. Fujita, Advanced Materials & Processes 4 (1992) 42.

[27] F. Masuyama, CAMP-Iron Steel Inst. Japan 5 (1992) 811.

[28] D. Coutsouradis, J. H. Davidson, J. Ewald, P. Greenfield, T. Khan, M. Malik, D. B. Meadowcroft, V. Regis, R. B. Scarlin, F. Schubert, and D. V. Thornton (Eds.), Materials for Advanced Power Engineering, 1994, Parts I and II (Kluwer Academic Publishers, Dordrecht, The Netherlands, 1994).

[29] E. Metcalfe (Ed.), EPRI/National Power Conf. on New Steels for Advanced Plant up to 620°C (EPRI, Palo Alto, CA, 1995).

[30] A. Strang (Ed.), Performance of Bolting Materials in High Temperature Plant Applications (The Inst. of Materials, London, Book 607, 1995).

[31] J. Nutting and R. Viswanathan (Eds.), Clean Steel: Superclean Steel (The Inst. of Materials, London, Book 635, 1996).

[32] Int. Conf. on Advanced Steam Plant (Inst. Mech. Engngs., London, 1997).

[33] A. Strang and D. J. Gooch (Eds.), Microstructural Development and Stability in High Chromium Ferritic Power Plant Steels (The Inst. of Materials, London, Book 667, 1997).

[34] A. Strang, W. M. Banks, R. D. Conroy, and M. J. Goulette (Eds.), Advances in Turbine Materials, Design and Manufacturing (The Inst. of Materials, London, Book 689, 1997).

[35] A. Strang, J. Cawley, and G. W. Greenwood (Eds.), Microstructural Stability of Creep Resistant Alloys for High Temperature Plant Applications (The Inst. of Materials, London, Book 682, 1998).

[36] R. Viswanathan and J. Nutting (Eds.), Advanced Heat Resistant Steel for Power Generation, (The Inst. of Materials, London, Book 708, 1999).

[37] A. Strang and M. McLean (Eds.), Modelling of Microstructural Evolution in Creep Resistant Materials (The Inst. of Materials, London, Book 723, 1999).

[38] F. Masuyama, in: Advanced Heat Resistant Steels for Power Generation, Eds. R. Viswanathan and J. Nutting (The Inst. of Materials, London, Book 708, 1999) 33.

[39] P. J. Ennis, in: Advances in Turbine Materials, Design and Manufacturing, Eds. A. Strang, W. M. Banks, R. D. Conroy, and M. J. Goulette (The Inst. of Materials, London, Book 689, 1997) 296.

[40] P. J. Ennis, Y. Wouters, and W. J. Quadakkers, in: Advanced Heat Resistant Steels for Power Generation, Eds. R. Viswanathan and J. Nutting (The Inst. of Materials, London, Book 708, 1999) 457.

[41] F. Masuyama, H. Haneda and B. W. Roberts, in: First Int. Conf. on Improved Coal-Fired Power Plants, Eds. A. Armor, W. Bakker, R. Jaffee and G. Touchton (EPRI, Palo Alto, CA, 1986) 5-83.

[42] G. Kalwa, K. Haarmann, and J. K. Janssen, in: Topical Conference on Ferritic Alloys for Use in Nuclear Energy Technologies, Eds. J. W. Davis and D. J. Michel (Met Soc. AIME, Warrendale, PA, 1984) 235.

[43] T. Yukitoshi, K. Nishida, T. Oda, and T. Daikoku, ASME J. of Pressure Vessel Tech. 98 (1976) 173.
[44] T. Daikoku, F. Masuyama, K. Uehara, K. Ishikawa, H. Watanabe, M. Okada, and T. Tsuchiya, A New Boiler Tube Material HCM9M, Mitsubishi Heavy Industries Ltd., Technical Review, February 1982.
[45] Ph. Berge, J. R. Donati, F. Pellicani and M. Weisz, in: Ferritic Steels for High Temperature Applications, Ed. A. K. Khare (ASM, Warren, PA, 1981) 100.
[46] V. K. Sikka, in: Topical Conference on Ferritic Alloys for Use in Nuclear Energy Technologies, Eds. J. W. Davis and D. J. Michel (Met Soc. AIME, Warrendale, PA, 1984) 317.
[47] B. W. Roberts and D. A. Canonico, in: First Int. Conf. on Improved Coal-Fired Power Plants, Eds. A. Armor, W. Bakker, R. Jaffee and G. Touchton (EPRI, Palo Alto, CA, 1986) 5-55.
[48] Data Package for NF616 Ferritic Steel (9 Cr-0.5 Mo-1.8 W-Nb-V) Second Edition, Nippon Steel Corporation, March 1994.
[49] H. Naoi, H. Mimura, M. Ohgami, H. Morimoto, T. Tanaka, Y. Yazaki and T. Fujita, in: Proc. EPRI/National Power Conf. on New Steels for Advanced Plant up to 620°C, Ed. E. Metcalfe (EPRI, Palo Alto, CA, 1995) 8.
[50] F. Masuyama, H. Haneda, T. Daikoku, and T. Tsuchiya, Development and Application of a High-Strength 12% Cr Steel Tubing with Improved Weldability, Mitsubishi Heavy Industries Ltd., Technical Review, October 1986.
[51] A. Iseda, Y. Sawaragi, and F. Masuyama, in: First Int. Conf. on Heat Resistant Materials, Eds. K. Natesan and D. J. Tillack (ASM Int., Materials Park, OH, 1991) 577.
[52] A. Iseda, A. Natoria, Y. Sawaragi, K. Ogawa, F. Masuyama, and T. Yokoyama, Thermal and Nuclear Power 45 (1993) 900.
[53] Y. Sawaragi, A. Iseda, K. Ogawa, F. Masuyama, and T. Yokoyama, in: EPRI/National Power Conf. on New Steels for Advanced Plant up to 620°C, Ed. E. Metcalfe (EPRI, Palo Alto, CA, 1995) 45.
[54] Y. Sawaragi, K. Miyata, S. Yamamoto, F. Masuyama, N. Komai, and T. Yokoyama, in: Advanced Heat Resistant Steel for Power Generation, Eds. R. Viswanathan and J. Nutting (The Inst. of Materials, London, Book 708, 1999) 144.
[55] F. Masuyama, in: EPRI/National Power Conf. on New Steels for Advanced Plant up to 620°C, Ed. E. Metcalfe (EPRI, Palo Alto, CA, 1995) 98.
[56] J. Orr and L. Woollard, in: Microstructural Development and Stability in High Chromium Ferritic Power Plant Steels, Eds. A. Strang and D. J. Gooch (The Inst. of Materials, London, Book 667, 1997) 53.
[57] J. Orr, L. W. Buchanan, and H. Eversons, in: Advanced Heat Resistant Steel for Power Generation, Eds. R. Viswanathan and J. Nutting (The Inst. of Materials, London, Book 708, 1999) 65.
[58] J. Hald, in: Modelling of Microstructural Evolution in Creep Resistant Materials, Eds. A. Strang and M. McLean (The Inst. of Materials, London, Book 723, 1999) 1.
[59] A. Zielinska-Lipiec, A. Czyrska-Filemonowicz, P. J. Ennis, and O. Wachter, in: Modelling of Microstructural Evolution in Creep Resistant Materials, Eds. A. Strang and M. McLean (The Inst. of Materials, London, Book 723, 1999) 79.
[60] W. Bendick, K. Haarmann, M. Ring, and M. Zschau, in: Ninth Int. Conf. on Creep Resistant Materials (Hradec and Moraviu, Czech Republic, 1996) 276.
[61] T. Fujita, in: EPRI/National Power Conf. on New Steels for Advanced Plant up to 620°C, Ed. E. Metcalfe (EPRI, Palo Alto, CA, 1995) 190.
[62] M. Ohgami, Y. Hasegawa, H. Naoi, and T. Fujita, in: Int. Conf. on Advanced Steam Plant (Inst. Mech. Engngs., London, 1997) 115.
[63] M. Igarashi and Y. Sawaragi, in: Int. Conf. on Power Engineering-'97, 2 (1997) 107.
[64] B. B. Seth, in: Advanced Heat Resistant Steel for Power Generation, Eds. R. Viswanathan and J. Nutting (The Inst. of Materials, London, Book 708, 1999) 519.
[65] R. W. Vanstone, in: Microstructural Stability of Creep Resistant Alloys for High Temperature Plant Applications, Eds. A. Strang, J. Cawley, and G. W. Greenwood (The Inst. of Materials, London, Book 682, 1998) 457.
[66] T. Fujita, Y. Nakabayashi, A. Suzuki, S. Kinoshita, M. Kohno, T. Tsuchiyama, A. Hizume, Y. Takeda, T. Fujikawa, and Y. Takano, in: COST-EPRI Workshop on Creep-Resistant 9-12 Cr Steels (EPRI, Palo Alto, CA, 1986).
[67] T. Tsuchyama, O. Matsumoto, O. Ishiyama, Y. Yasumoto, and T. Abe, in: Advanced Heat Resistant Steel for Power Generation, Eds. R. Viswanathan and J. Nutting (The Inst. of Materials, London, Book 708, 1999) 408.
[68] Y. Tsuda, M. Yamada, R. Ishii, and O. Watanabe, in: Advances in Turbine Materials, Design and Manufacturing, Eds. A. Strang, W. M. Banks, R. D. Conroy, and M. J. Goulette (The Inst. of Materials, London, Book 689, 1997) 283.
[69] M. Miyazaki, M. Yamada, Y. Tsuda, and R. Ishii, in: Advanced Heat Resistant Steel for Power Generation, Eds. R. Viswanathan and J. Nutting (The Inst. of Materials, London, Book 708, 1999) 574.
[70] K. Hidaka, Y. Fukui, S. Nakamura, R. Kaneko, Y. Tanaka, and T. Fujita, in: Advanced Heat Resistant Steel for Power Generation, Eds. R. Viswanathan and J. Nutting (The Inst. of Materials, London, Book 708, 1999) 418.
[71] D. V. Thornton and K.-H. Mayer, in: Advances in Turbine Materials, Design and Manufacturing, Eds. A. Strang, W. M. Banks, R. D. Conroy, and M. J. Goulette (The Inst. of Materials, London, Book 689, 1997) 203.
[72] T. Nakada, T. Tsuchiyama, M. Miyakawa, O. Matsumoto, H. Nakashima, O. Ishiyama, and T. Abe, in: Advanced Heat Resistant Steel for Power Generation, Eds. R. Viswanathan and J. Nutting (The Inst. of Materials, London, Book 708, 1999) 365.
[73] Y. Tanaka, T. Azuma, Y. Shudo, S. Ono, Y. Ikeda, and T. Ishiguro, in: Advanced Heat Resistant Steel for Power Generation, Eds. R. Viswanathan and J. Nutting (The Inst. of Materials, London, Book 708, 1999) 397.
[74] P. Bates, M. A. Walsh, and S. Price, in: Advanced Heat Resistant Steel for Power Generation, Eds. R. Viswanathan and J. Nutting (The Inst. of Materials, London, Book 708, 1999) 309.
[75] Y. Yamamoto, S. Seo, J. Matsumoto, Y. Kadoya, T. Nishimura, and R. Magoshi, in: Advanced Heat Resistant Steel for Power Generation, Eds. R. Viswanathan and J. Nutting (The Inst. of Materials, London, Book 708, 1999) 560.
[76] T. Honda, T. Kusano, T. Osada, K. Hirano, and T. Takemoto, in: Advanced Heat Resistant Steel for Power Generation, Eds. R. Viswanathan and J. Nutting (The Inst. of Materials, London, Book 708, 1999) 119.
[77] R. D. Townsend, in: Performance of Bolting Materials in High Temperature Plant Applications, Ed. A. Strang (The Inst. of Materials, London, Book 607, 1995) 15.
[78] K.-H. Mayer and H. König, in: Performance of Bolting Materials in High Temperature Plant Applications, Ed. A. Strang (The Inst. of Materials, London, Book 607, 1995) 150.
[79] D. V. Thornton, in: Performance of Bolting Materials in High Temperature Plant Applications, Ed. A. Strang (The Inst. of Materials, London, Book 607, 1995) 419.
[80] J. Orr, in: Performance of Bolting Materials in High Temperature Plant Applications, Ed. A. Strang (The Inst. of Materials, London, Book 607, 1995) 115.
[81] H. Schaff, in: Performance of Bolting Materials in High Temperature Plant Applications, Ed. A. Strang (The Inst. of Materials, London, Book 607, 1995) 410.
[82] R. R. Hosbons, in: Topical Conference on Ferritic Alloys for Use in Nuclear Energy Technologies, Eds. J. W. Davis and D. J. Michel (Met. Soc. AIME, Warrendale, PA, 1984) 91.

[83] J. Orr and S. J. Sanderson, in: Topical Conference on Ferritic Alloys for Use in Nuclear Energy Technologies, Eds. J. W. Davis and D. J. Michel (Met. Soc. AIME, Warrendale, PA, 1984) 261.
[84] F. S. Dickinson, A. F. Taylor, P. W. Jackson, and R. W. Smith, in: Topical Conference on Ferritic Alloys for Use in Nuclear Energy Technologies, Eds. J. W. Davis and D. J. Michel (Met. Soc. AIME, Warrendale, PA, 1984) 269.
[85] J. F. W. Bishop, in: Dimensional Stability and Mechanical Behaviour of Irradiated Metals and Alloys, Vol. 2 (British Nuclear Energy Society, London, 1984) 115.
[86] D. R. Harries, J. Standring, W. D. Barnes, and G. J. Lloyd, in: Effects of Irradiation on Materials: Eleventh Conference, ASTM STP 782, Eds. H. R. Brager and J. S. Perrin (American Society for Testing and Materials, Philadelphia, PA, 1982) 1197.
[87] C. Brown, R. J. Lilley, and G. C. Crittenden, Nucl. Engineer 35 (1994) 122.
[88] M. Lippens, K. Ehrlich, V. Levy, C. Brown, and A. Calza Bini, in: Materials for Nuclear Core Applications, Vol. I (British Nuclear Energy Society, London, 1987) 177.
[89] K. Q. Bagley, E. A. Little, V. Levy, A. Alamo, K. Ehrlich, K. Anderko, and A. Calza Bini, Nucl. Energy 27 (1988) 295.
[90] C. Brown, V. Levy, J. L. Séran, K. Ehrlich, R. J. C. Roger, and H. Bergmann, in: Fast Reactors and Related Fuel Cycles-FR '91, Vol. I (Atomic Energy Society of Japan, Tokyo, 1991) Paper 7.5.
[91] A. J. Lovell, A. L. Fox, W. H. Sutherland, and S. L. Hecht, in: Reliable Fuels for Liquid Metal Reactors (American Nuclear Society, LeGrange Park, IL, 1987) 3-25.
[92] D. S. Gelles, in: EUROMAT 96: Materials and Nuclear Power, (The Inst. of Materials, London, 1996) 281.
[93] V. S. Khabarov, A. M. Dvoriashin, and S. I. Porollo, in: Technical Committee Meeting on: Influence of High Dose Irradiation on Advanced Reactor Core Structural and Fuel Materials, IAEA-TECDOC-1039 (IAEA, Vienna, 1998) 139.
[94] V. M. Poplavsky and L. M. Zabudko, in: Technical Committee Meeting on: Influence of High Dose Irradiation on Advanced Reactor Core Structural and Fuel Materials, IAEA-TECDOC-1039 (IAEA, Vienna, 1998) 7.
[95] S. Nomura, S. Shikakura, S. Ukai, I. Seshimo, M. Harada, I. Shibahara, and M. Katsuragawa, in: Fast Reactors and Related Fuel Cycles-FR '91, Vol. I (Atomic Energy Society of Japan, Tokyo, 1991) Paper 7.4.
[96] K. Ehrlich and G. Mühling, in: Reliable Fuels for Liquid Metal Reactors (American Nuclear Society, 1987) 4-1.
[97] E. Materna-Morris and K. Ehrlich, in: Proc. Technical Committee Meeting on: Influence of High Dose Irradiation on Advanced Reactor Core Structural and Fuel Materials, IAEA-TECDOC-1039 (IAEA, Vienna, 1998) 129.
[98] E. A. Little, D. R. Harries, F. B. Pickering, and S. R. Keown, Metals Tech. 4 (1977) 205.
[99] K. Anderko, K. David, W. Ohly, M. Schirra, and C. Wassilew, in: Topical Conference on Ferritic Alloys for Use in Nuclear Energy Technologies, Eds. J. W. Davis and D. J. Michel (Met. Soc. AIME, Warrendale, PA, 1984) 299.
[100] J.-J. Huet, L. Coheur, L. De Wilde, J. Gedopt, W. Hendrix, and W. Vandermeulen, in: Topical Conference on Ferritic Alloys for Use in Nuclear Energy Technologies, Eds. J. Davis and D. J. Michel (Met. Soc. AIME, Warrendale, PA, 1984) 329.
[101] J.-J. Huet, L. Coheur, A. De Bremaeker, L. De Wilde, J. D. Gedopt, W. Hendrix, and W. Vandermeulen, Nucl. Tech. 70 (1985) 215.
[102] L. De Wilde, J. Gedopt, S. De Burbure, A. Delbrassine, C. Driesen, and B. Kazimierzak, in: Materials for Nuclear Reactor Core Applications, Vol. 1 (British Nuclear Energy Society, London, 1997) 271.
[103] A. Alamo, J. Decours, M. Pigoury, and C. Foucher, in: Structural Applications of Mechanical Alloying (American Society for Metals, Materials Park, OH, 1990) 89.
[104] S. D. Antolovich, R. W. Stusrud, R. A. Mackay, D. L. Anton, T. Khan, R. D. Kissinger, and D. L. Klarstrom (Eds.), Superalloys 1992 (The Minerals, Metals and Materials Society, Warrendale, PA, 1992).
[105] A. Alamo, H. Regle, and J. L. Bechade, in: Advances in Powder Metallurgy and Particulate Materials 7 (1992) 169.
[106] S. Ukai, M. Harada, M. Inoue, S. Nomura, S. Shikakura, M. Fujiwara, T. Nishida, and K. Asabe, Trans. Amer. Nucl. Soc. 66 (1992) 186.
[107] D. M. Jaeger and A. R. Jones, in: Materials for Advanced Power Engineering 1984, Part II, Eds. D. Coutsouradis, J. H. Davidson, J. Ewald, P. Greenfield, T. Khan, M. Malik, D. B. Meadowcroft, V. Regis, R. B. Scarlin, F. Schubert, and D. V. Thornton (Kluwer Academic Publishers, Dordrecht, The Netherlands, 1994) 1507.
[108] E. Artz, in: New Materials and Mechanical Alloying Techniques, Eds. E. Artz and L. Schultz (Deutsche Gesellschaft fur Materialkunde eV, 1989) 185.
[109] C. P. Jongenburger and R. F. Singer, in: New Materials and Mechanical Alloying Techniques, Eds. E. Artz and L. Schultz (Deutsche Gesellschaft für Materialkunde eV, 1989) 157.
[110] J. M. Marsh and J. W. Martin, Mater. Sci. Technol. 7 (1991) 183.
[111] P. J. Evens, J. W. Martin and E. A. Little, Mater. Sci. Technol. 8 (1992) 531.
[112] M. A. Miodownik, J. W. Martin, and E. A. Little, Mater. Sci. Technol. 10 (1994) 102.
[113] M. Mujahid and J. W. Martin, Mater. Sci. Technol. 10 (1994) 703.
[114] S. Ukai, M. Harada, K. Okada, M. Inoue, S. Nomura, S. Shikakura, K. Asabe, T. Nishida, and M. Fujiwara, J. Nucl. Mater. 204 (1993) 65.
[115] K. J. Dietz, J. Nucl. Mater. 155-157 (1988) 8.
[116] H. F. Dylla, M. A. Ulrickson, D. K. Owens, D. B. Heifetz, B. E. Mills, A. E. Pontau, W. R. Wampler, B. L. Doyle, S. R. Lee, R. D. Watson, and C. D. Croessmann, J. Nucl. Mater 155-157 (1988) 15.
[117] H. Takatsu, T. Ando, M. Yamamoto, T. Arai, K. Kodama, M. Ohkubo. M. Shimizu, and the JT-60 Team, J. Nucl. Mater. 155-157 (1988) 27.
[118] The JET Team (P.-H. Rebut presenter), Plasma Phys. Contr. Fusion 34 (1992) 1749.
[119] The NET Team, NET (Next European Torus) Predesign Report, Fus. Eng. Design 21 (1993).
[120] D. R. Harries, J.-M. Dupouy, and C. H. Wu, J. Nucl. Mater. 133-134 (1985) 25.
[121] D. R. Harries, Rad. Effects 101 (1987) 3.
[122] P. Schiller and J. Nihoul J. Nucl. Mater. 155-157 (1988) 41.
[123] ITER Joint Central Team (W.B. Gauster presenter), J. Nucl. Mater. 212-215 (1994) 3.
[124] Technical Basis for the ITER Final Design Report, Cost Review and Safety Analysis (FDR), ITER EDA Documentation Series No. 16 (IAEA, Vienna, 1998).
[125] Starfire-A Commercial Tokamak Fusion Power Plant Study, Argonne National Laboratory Report ANL/FPP-80-1, 1980.
[126] A Demonstration Tokamak Power Plant Study (DEMO), Argonne National Laboratory Report ANL/FPP/82-1, 1982.
[127] D. R. Harries, in: Topical Conference on Ferritic Alloys for Use in Nuclear Energy Technologies, Eds. J. W. Davis, and D. J. Michel (Met. Soc. AIME, Warrendale, PA, 1984) 141.
[128] J. D. Gordon, J. K. Garner, N. M. Ghoniem, and J. F. Parmer, in: Topical Conference on Ferritic Alloys for Use in Nuclear Energy Technologies, Eds. J. W. Davis and D. J. Michel (Met. Soc. AIME, Warrendale, PA, 1984) 157.

[129] H. Attaya, K. Y. Yuan, W. G. Wolfer, and G. L. Kulcinski, in: Topical Conference on Ferritic Alloys for Use in Nuclear Energy Technologies, Eds. J. W. Davis and D. J. Michel (Met. Soc. AIME, Warrendale, PA, 1984) 169.
[130] A. Kohyama, K. Asakura, and N. Igata, J. Nucl. Mater. 141-143 (1986) 921.
[131] C. A. English and D. J. Mazey, Nucl. Energy 29 (1990) 67.
[132] A. G. Ioltukhovsky, V. P. Kondrat'ev, M. V. Leont'eva-Smirnova, S. N. Votinov, V. K. Shamardin, A. P. Povstyanko, and T. M. Bulanova, J. Nucl. Mater. 233-237 (1996) 299.
[133] A. F. Rowcliffe, E. E. Bloom, R. H. Jones, D. L. Smith, F. W. Wiffen, and W. R. Johnson, in: Sixteenth Int. Conf. on Fusion Energy 1996, Vol. 3 (International Atomic Energy Agency, Vienna, 1997) 489.
[134] E. E. Bloom, J. Nucl. Mater. 258-263 (1998) 7.
[135] K. Ehrlich, Phil. Trans. R. Soc. Lond. A357 (1999) 595.
[136] M. J. Monsler, J. Hovingh, A. L. Cook, T. G. Frank and G. A. Moses, Nucl. Tech. Fusion 1 (1981) 302.
[137] M. Ragheb, G. H. Miley, J. F. Stubbins, and C. Choi, J. Fusion Energy 4 (1985) 239.
[138] W. J. Hogan (Ed.), Energy from Inertial Fusion, VICL 95-00117 (IAEA, Vienna, 1995).
[139] K. Ehrlich, D. R. Harries, and A. Möslang (Eds.), Characterization and Assessment of Ferritic/Martensitic Steels, Forschungszentrum Karlsruhe, FZKA Report 5626, February 1997.
[140] M. Dalle Donne, D. R. Harries, G. Kalinin, R. Mattas, and S. Mori, J. Nucl. Mater. 212-215 (1994) 69.
[141] E. Proust, L. Anzidei, et al., Fus. Technol. 19 (1991) 944.
[142] M. Eid, M. Ferrari, and E. Proust (Eds.), Helium-Cooled Ceramic Breeder-In-Tube Blanket Line, EU Reference Conceptual Design and Performance Presentation, CEA Report DMT 94/576 (SERMA/LCA/1682); ENEA Report RI-RCT 94/2, December 1994.
[143] M. Dalle Donne (Compiler), European DEMO BOT Solid Breeder Blanket, Kernforschungszentrum Karlsruhe, KfK Report 5429, November 1994.
[144] S. Malang and K. Schleisiek (Compilers), Dual Coolant Blanket Concept, Kernforschungszentrum Karlsruhe, KfK Report 5424, November 1994.
[145] L. Giancarli (Ed.), Water-Cooled Pb-17Li DEMO Blanket Line, EU Reference Conceptual Design and Performance Presentation, CEA Report DMT 94/538 (SERMA/1678), December 1994.
[146] Tokamak Power Systems Studies-FY 1986: A Second Stability Power Reactor, Argonne National Laboratory Report ANL/FPP-86-1, 1986.
[147] D. L. Smith and G. D. Morgan, Blanket Comparison and Selection Study: Final Report, Argonne National Laboratory Report ANL/FPP-84-1, 1984.
[148] D. R. Harries, G. J. Butterworth, A. Hishinuma, and F. W. Wiffen, J. Nucl. Mater. 191-194 (1992) 92.
[149] D. R. Harries and G. J. Butterworth, in: 1st. Int. Conf.on Ultra High Purity Base Metals (UHPM-94), Eds. K. Abiko, K. Hirokawa, and S. Takaki (Japan Inst. Metals, Tokyo, 1995) 101.
[150] A. Kohyama, A. Hishinuma, D. S. Gelles, R. L. Klueh, W. Dietz, and K. Ehrlich, J. Nucl. Mater. 233-237 (1996) 138.
[151] M. Z. Youssef and R. W. Conn, Nucl. Tech./Fusion 3 (1983) 361.
[152] R. W. Conn, K. Okula, and A. W. Johnson, Nucl. Tech. 41 (1978) 389.
[153] D. G. Doran, J. Nucl. Mater. 191-194 (1992) 1439.
[154] P. Rocco and M. Zucchetti, J. Fus. Energy 12 (1993) 201.
[155] R. A. Forrest and J. Kopecky, The European Activation System (EASY), IEA Advisory Group Meeting on FENDL-2, Vienna, November 1991.
[156] S. Cierjacks and J. Hino, J. Nucl. Mater. 170 (1990) 134.
[157] P. Rocco and M. Zucchetti, Fus. Eng. Design 15 (1992) 235.
[158] P. Rocco and M. Zucchetti, J. Nucl. Mater. 212-215 (1994) 649.
[159] D. Dulieu, K. W. Tupholme, and G. J. Butterworth, J. Nucl. Mater. 141-143 (1986) 1097.
[160] K. W. Tupholme, D. Dulieu, and G. J. Butterworth, J. Nucl. Mater. 155-157 (1988) 650.
[161] K. W. Tupholme, D. Dulieu, and G. J. Butterworth, J. Nucl. Mater. 179-181 (1991) 684.
[162] K. Anderko, K. Ehrlich, L. Schäfer, and M. Schirra, CETA-Ein Entwicklungsschritt zu einem schwach aktivierbaren martensitischen Chromstahl, Kernforschungszentrum Karlsruhe, KfK Report 5060, June 1993.
[163] K. Ehrlich, S. Kelzenberg, H.-D. Röhrig, L. Schäfer, and M. Schirra, J. Nucl. Mater. 212-215 (1994) 678.
[164] K. Ehrlich and B. van der Schaaf, in: IEA Working Group on Reduced Activation Ferritic-Martensitic Steels, Eds. F. Abe, A. Hishinuma, A. Kohyama, and M. Suzuki, Vol. II (Japan Atomic Energy Research Institute, Tokai Research Establishment, Tokai, Japan, 1993) 24.
[165] G. Filacchioni, L. Pilloni, and F.Attwa, in: IEA Working Group on Reduced Activation Ferritic-Martensitic Steels, Eds. F. Abe, A. Hishinuma, A. Kohyama, and M. Suzuki, Vol. II (Japan Atomic Energy Research Institute, Tokai Research Establishment, Tokai, Japan, 1993) 164.
[166] R. L. Klueh and E. E. Bloom, Nucl. Eng. Design/Fusion 2 (1985) 383.
[167] D. S. Gelles, in: Optimizing Materials for Nuclear Applications, Eds. F. A. Garner, D. S. Gelles, and F. W. Wiffen (The Metallurgical Society, Warrendale, PA, 1985) 63.
[168] R. L. Klueh, D. S. Gelles, and T. A. Lechtenberg, J. Nucl. Mater. 141-143 (1986) 1081.
[169] C. Y. Hsu and T. A. Lechtenberg, J. Nucl. Mater. 141-143 (1986) 1107.
[170] R. L. Klueh and P. J. Maziasz, Met. Trans. 20A (1989) 373.
[171] R. L. Klueh, Met. Trans. 20A (1989) 463.
[172] D. S. Gelles, in: Reduced Activation Materials for Fusion Reactors, ASTM STP 1047, Eds. R. L. Klueh, D. S. Gelles, M. Okada, and N. H. Packan (ASTM, Philadelphia, PA, 1990) 113.
[173] M. Tamura, H. Hayakawa, M. Tanimura, A. Hishinuma, and T. Kondo, J. Nucl. Mater. 141-143 (1986) 1067.
[174] T. Noda, F. Abe, H. Araki, and M. Okada, J. Nucl. Mater. 141-143 (1986) 1102.
[175] F. Abe, H. Araki, and T. Noda, Mat. Sci. Tech. 6 (1990) 714.
[176] F. Abe, T. Noda, H. Araki, and S. Nakazawa, J. Nucl. Mater. 179-181 (1991) 663.
[177] F. Abe and S. Nakazawa, Met. Trans. 23A (1992) 3025.
[178] M. Tamura, H. Hayakawa, M. Tanimura, A. Hishinuma, and T. Kondo, J. Nucl. Mater. 155-157 (1988) 620.
[179] M. Yamanouchi, M. Tamura, H. Hayakawa, A. Hishinuma, and T. Kondo, J. Nucl. Mater. 191-194 (1992) 822.
[180] A. Kohyama, Y. Kohno, K. Asakura, and H. Kayano, J. Nucl. Mater., 212-215 (1994) 684.
[181] R. L. Klueh and D. R. Harries (Eds.), Proc. IEA Workshop on Ferritic-Martensitic Steels, Oak Ridge National Laboratory, ORNL/M-2990, 1993.
[182] B. van der Schaaf, in: Proc. IEA Workshop/Working Group Meeting on Ferritic/Martensitic Steels, ECN Nuclear Research, Petten, Netherlands, October 1998, Prepared by R.L. Klueh, ORNL M-6627.
[183] V. Lambard and A. Alamo, in: Proc. IEA Workshop/Working Group Meeting on Ferritic/Martensitic Steels, ECN Nuclear Research, Petten, Netherlands, October 1998, Prepared by R. L. Klueh, ORNL M-6627.
[184] A. Hishinuma, in: Proc. IEA Workshop/Working Group Meeting on Ferritic/Martensitic Steels, ECN Nuclear Research, Petten, Netherlands, October 1998, Prepared by R.L. Klueh, ORNL M-6627.

[185] J.-Ch. Sublet and G. J. Butterworth, J. Nucl. Mater. 212-215 (1994) 695.
[186] J. Kopecky, H. A. J. van der Kamp, H. Gruppelaar, and D. Nierop, The European Activation File EAF-3 with Neutron Activation and Transmutation Cross Sections, ECN Petten, Report C-92-058, September 1992.
[187] C. A. B. Forty, G. J. Butterworth, and J.-Ch. Sublet, J. Nucl. Mater. 212-215 (1994) 640.
[188] R. A. Forrest, M. G. Sowerby, and D. A. J. Endacott, in: Fusion Technology 1990, Eds. B. E. Keen, M. Huguet, and R. Hemsworth, Vol. 1 (North Holland, Amsterdam, 1991) 797.
[189] J.-Ch. Sublet and G. J. Butterworth, in: Fusion Technology 1992, Eds. C. Ferro, M. Gasparotto and H. Knoepfel, Vol. 2 (North Holland, Amsterdam, 1993) 1774.
[190] R. A. Forrest and J.-Ch. Sublet, FISPACT 4.1 User Manual, UKAEA Report FUS 287, 1995.
[191] J. Kopecky and D. Nierop, The European Activation File EAF-4. Summary Documentation, ECN Petten Report C-95-072, December 1995.
[192] C. B. A. Forty, J. Fus. Energy 16 (1997) 277.
[193] C. B. A. Forty and N. P. Taylor, in: Topical Conf. on Materials and Nuclear Power (The Inst. of Materials, London, 1996) 519.
[194] R. L. Klueh, E. T. Chang, M. L. Grossbeck, and E. E. Bloom, J. Nucl. Mater., Vol. 280 (2000) 353.
[195] D. Murphy and G. J. Butterworth, J. Nucl. Mater. 191-194 (1992) 1444.
[196] G. J. Butterworth and S. R. Keown, J. Nucl. Mater. 186 (1992) 283.

3

Physical Metallurgy of High-Chromium Steels

The high (9–12%) chromium steels are either fully austenitic or have a duplex (austenite plus δ-ferrite) structure at austenitizing temperatures in the range 850 to 1200°C. The austenite phase transforms to martensite during air cooling or rapid quenching to ambient temperature, and the steels are subsequently tempered to obtain a good combination of strength, ductility, and toughness. The physical metallurgical basis of the development of the high-chromium martensitic steels has been reviewed elsewhere [1–3]; the factors determining the constitution, transformation, and tempering characteristics are briefly surveyed in this chapter.

CONSTITUTION

The γ-Fe loop in the Fe-Cr equilibrium diagram (Fig. 3.1) [4] is closed if the chromium content exceeds about 12%; however, the austenite-stabilizing elements (C, N, Ni, Mn, Cu, Co) extend the γ-phase field, while the ferrite-forming elements (Cr, Mo, Nb, V, W, Si, Ti, Al) contract it [5–7]. The austenite in low-carbon, low-nitrogen 9 and 12% Cr steels is stable at the normal austenitizing temperatures of 850 to 1200°C and 950 to 1150°C, respectively. The tempering resistance of the steels is increased by the addition of the ferrite-forming elements and, consequently, highly alloyed commercial steels may contain some δ-ferrite. The ferrite phase inhibits austenite grain growth, but it adversely influences the strength and, directly or indirectly, the toughness [8–10], particularly if present as films between the grains of the austenite, which is subsequently transformed to martensite and tempered. The duplex (martensite plus δ-ferrite) structure of a 12Cr-2WV steel with 0.1% C is illustrated in Fig. 3.2.

The formation of δ-ferrite can be avoided by the addition of the austenite-forming elements; thus, the balancing of the constitution to ensure 100% austenite at the austenitizing temperature may be effected using the data in Table 3.1 [11]. Carbon is the cheapest austenite former, but is not always favored, as it decreases the toughness and impairs the weldability and corrosion resistance [3]. Furthermore, higher austenitizing temperatures are required to dissolve carbides of the MC type (where M is V, Nb, Ti, or Ta), resulting in coarser prior austenite grain sizes and reductions in toughness and creep ductility. Nitrogen can also be utilized as an austenite stabilizer, but the amount required is generally excessive. Nickel, although less effective than carbon and nitrogen, is usually used in steels for non-nuclear applications, as it has fewer adverse effects.

Manganese has been considered as an alternative; however, it is inferior to nickel as an austenite stabilizer, and 0.1% C, 12% Cr steels contain some δ-ferrite even with an addition of 6% manganese [12,13]. The high-manganese steels are also prone to embrittlement during thermal aging and/or irradiation, possibly as a consequence of chi (χ)-phase formation [12]. Cobalt may also be employed, but it is expensive and, in common with nickel, has to be minimized in steels for component applications in fusion reactor systems because of the high residual radioactivity induced by neutron irradiation. The difficulty in eliminating δ-ferrite in the 12% Cr martensitic steels is one of the factors contributing to the lower (7 to 10%) chromium steels being favored for nuclear fusion applications.

The ferrite-forming elements V, Nb, Ta, Ti, and Al are also effective in removing the austenite formers carbon and/or nitrogen from solution as insoluble carbides and nitrides, thereby indirectly affecting the constitution of the steels [14]. The concentration of the elements that are soluble during austenitizing of the high-chromium steels may be estimated using the following solubility relationships derived for low-alloy or austenitic steels [15,16]:

$$\log [Nb][C] = -9{,}350/T + 4.55 \quad (3.1)$$

$$\log [Ti][C] = -6{,}780/T + 2.97 \quad (3.2)$$

$$\log [Nb][N] = -11{,}600/T + 4.84 \quad (3.3)$$

$$\log [Ti][N] = -15{,}188/T + 3.93 \quad (3.4)$$

$$\log [V][N] = -7{,}840/T + 3.02 \quad (3.5)$$

$$\log [Al][N] = -6{,}770/T + 1.03 \quad (3.6)$$

where [Nb], [C], etc., are in wt% and T is the temperature in K.

The solubility products of Nb(CN), VN, and AlN in austenite have been modified by taking account of the interaction parameters between the alloying element chromium and the interstitials carbon (e_C^{Cr}) and nitrogen (e_N^{Cr}), as follows [17,18]:

$$\log [Nb][C + 6/7N] = -6770/T + 2.26 - 1/2(e_C^{Cr}) + e_N^{Cr}[Cr] \quad (3.7)$$

$$\log [V][N] = -10\,500/T + 5.20 - e_N^{Cr}[Cr] \quad (3.8)$$

$$\log [Al][N] = -6770/T + 1.03 - e_N^{Cr}[Cr] \quad (3.9)$$

The interaction parameters are given by [19]:

$$e_C^{Cr} = -180/T + 0.09 \quad (3.10)$$

$$e_N^{Cr} = -145.8/T - 0.056 + 0.017\log (T) \quad (3.11)$$

The solubility curves for VN, Nb(CN), and AlN in a 11% Cr martensitic steel at 1100°C are reproduced in Fig. 3.3 [17,18].

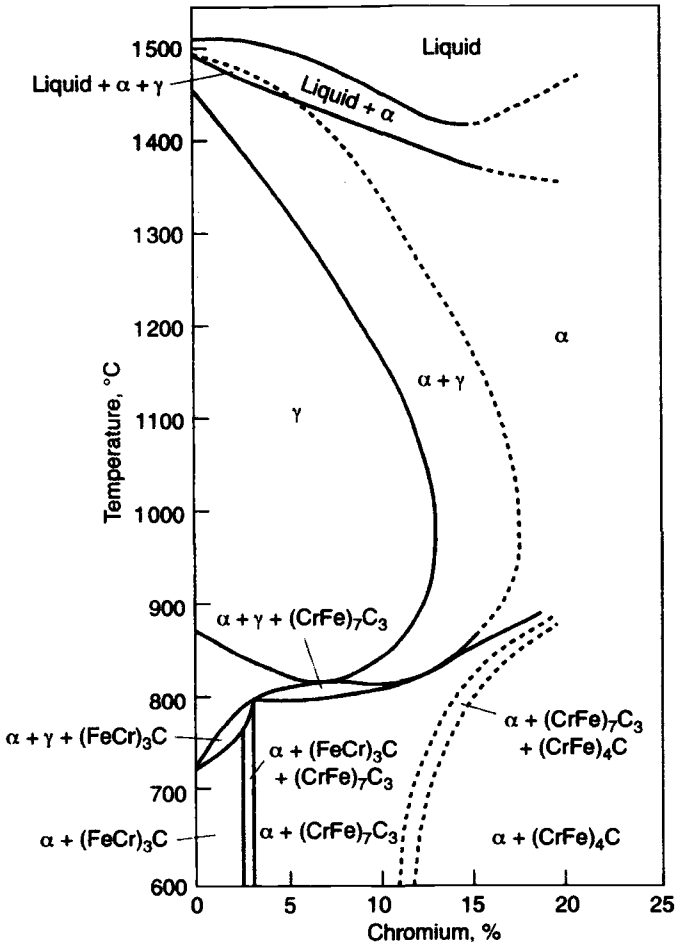

FIG. 3.1—Effect of chromium on the constitution of Fe-Cr-C alloys containing 0.1% C [4]; note that $(CrFe)_4C$ is $M_{23}C_6$ carbide [4].

FIG. 3.2—Duplex [about 25% δ-ferrite (light etching) and 75% martensite] microstructure of a normalized-and-tempered 12Cr-2WV reduced-activation steel.

The solubility of VN is significantly greater than for AlN and Nb(CN), and complete dissolution of the VN in the high-chromium steels is likely at 1100°C and lower austenitizing temperatures. The AlN may also be completely soluble during the austenitizing treatment as the steels generally contain relatively small amounts of aluminium. However, Nb(CN) may remain undissolved at the usual austenitizing temperatures, and particles of this phase are also effective in preventing excessive austenite grain growth.

The experimentally determined solubility product for TaC in the austenite in an 8Cr-2WVTa (F82H) reduced activation steel in the range 950 to 1250°C is significantly higher than in γ-iron and is given by [20]:

$$\log [Ta][C] = -7{,}027/T + 3.16 \qquad (3.12)$$

The solubility curves at 950 and 1050°C, the stoichiometric line for TaC [Ta:C = 15.065] and typical tantalum and carbon plus nitrogen contents of the F82H and 9Cr-2WVTaN (JLF-1) steels are shown in Fig. 3.4. The TaC in the F82H steel is completely soluble at an austenitizing temperature of 1050°C, whereas the solubility may be exceeded in some JLF-1 steels at this temperature. Fine particles of TaC that are insoluble at the austenitizing temperature and a high density of finely dispersed TaC precipitates produced by aging at 950°C, due to the reduced solubility at this temperature, and may limit austenite grain growth in these steels [20,21].

TRANSFORMATION

The constitution of the steels (compositions given in Tables 2.1 and 2.2) at ambient temperature following cooling from the austenitizing temperature may be predicted from the

TABLE 3.1—Effects of alloying additions on the constitution of high chromium steels [11].

Element	Change in δ-ferrite Content, % per Mass % Alloy Addition
N	−220
C	−210
Ni	−20
Co	−7
Cu	−7
Mn	−6
W	+3
Mo	+5
Si	+6
Cr	+14
V	+18
Al	+54

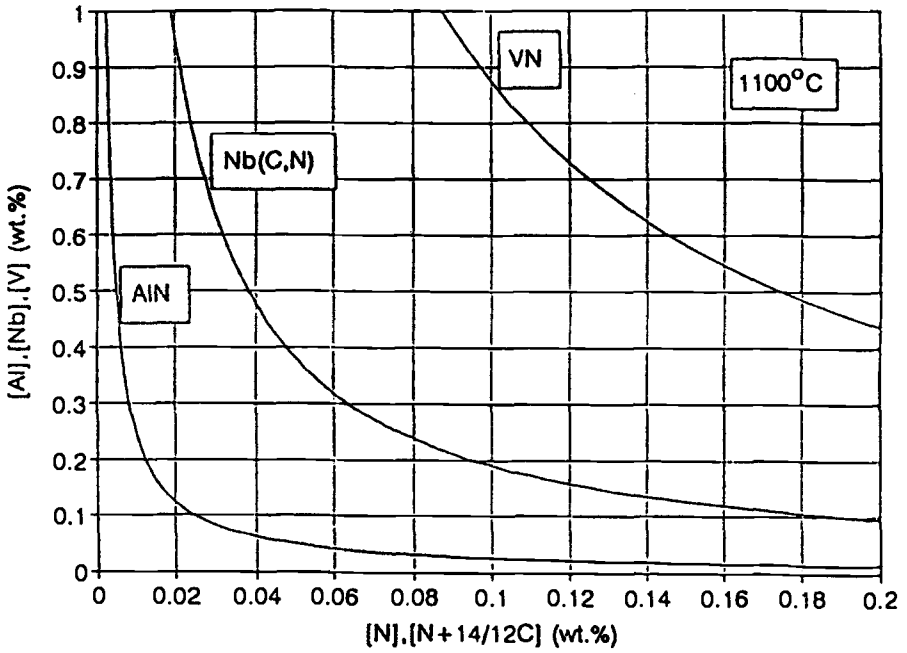

FIG. 3.3—Solubility curves at 1100°C for vanadium nitride, niobium carbo-nitride, and aluminium nitride in austenite in a 11% Cr steel [17,18].

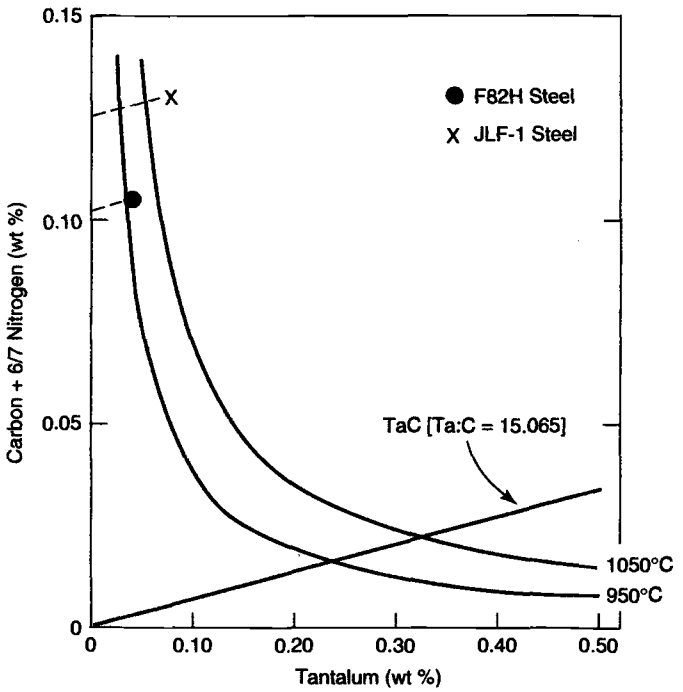

FIG. 3.4—Solubility curves for tantalum carbide in austenite in F82H (8Cr-2WVTa) steel at 950 and 1050°C [20], together with the stoichiometric line for TaC and typical Ta and C + 6/7N contents of the F82H and JLF-1 (9Cr-2WVTaN) reduced activation steels.

Schaeffler-Schneider diagram (Fig. 3.5) [22,23] using the following nickel and chromium equivalents of the alloying elements [14,24]:

$$\text{Ni equivalent (wt\%)} = (\%\text{Ni}) + (\%\text{Co}) + 0.5(\%\text{Mn}) + 0.3(\%\text{Cu}) + 30(\%\text{C}) + 25(\%\text{N}) \quad (3.13)$$

$$\text{Cr equivalent (wt\%)} = (\%\text{Cr}) + 2(\%\text{Si}) + 1.5(\%\text{Mo}) + 5(\%\text{V}) + 1.75(\%\text{Nb}) + 0.75(\%\text{W}) + 1.5(\%\text{Ti}) + 5.5(\%\text{Al}) + 1.2(\%\text{Ta}) + 1.2(\%\text{Hf}) + 1.0(\%\text{Ce}) + 0.8(\%\text{Zr}) + 1.2(\%\text{Ge}) \quad (3.14)$$

Some of the 9% Cr [EM10, T91, TB9 (NF616) and E911] and 12% Cr (FI, FV448, 1.4914, MANET II, and TR1150) steels are predicted to be fully martensitic, while others are predicted to have duplex martensite plus δ-ferrite (HCM9M, NSCR9, EM12, JFMS, Tempaloy F-9, MANET I, HCM12, TB12, and HCM12A), duplex martensite plus retained austenite (GE and HR1200), or three-phase martensite plus austenite plus δ-ferrite (HT9) structures on cooling to ambient temperature. These predictions are consistent with the experimental observations. In particular, the structure of the rapidly cooled HT9 (12Cr-1MoVW) steel is reported to consist of martensite laths with high dislocation densities [Fig. 3.6(a)] [25], small amounts of retained austenite in the form of islands, and δ-ferrite grains having low dislocation densities [26].

It has also been established that the δ-ferrite formation in the high-chromium martensitic steels is suppressed by main-

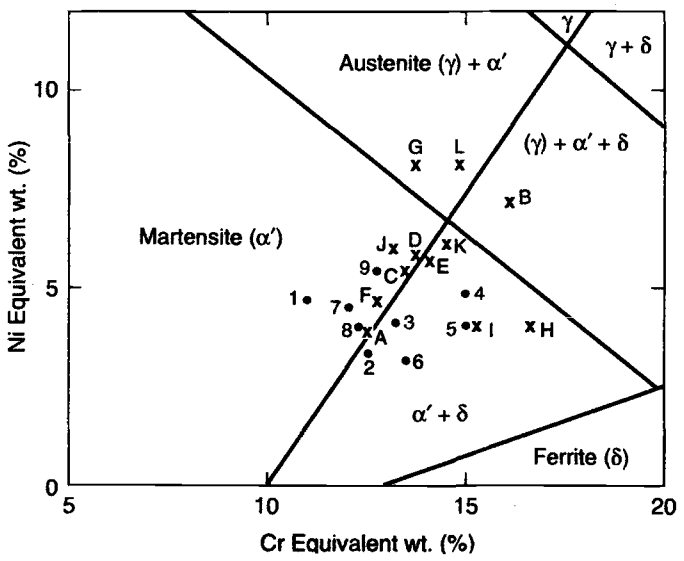

9% Cr Steels (•)

1. EM10
2. HCM9M
3. NSCR9
4. EM12
5. JFMS
6. TEMPALOY F-9
7. T91
8. TB9 (NF616)
9. E911

12% Cr Steels (x)

A. FI
B. HT9
C. FV448
D. 1.4914
E. MANET I
F. MANET II
G. GE
H. HCM12
I. TB12
J. TR1150
K. HCM12A
L. HR1200

FIG. 3.5—Schaeffler-Schneider diagram [22].

taining a Cr equivalent element content of ≤9 wt% [27]; the Cr equivalent in this case is given by [28]:

$$\begin{aligned}\text{Cr equivalent (wt\%)} = {} & (\%\text{Cr}) + 6(\%\text{Si}) \\ & + 4(\%\text{Mo}) + 11(\%\text{V}) + 5(\%\text{Nb}) \\ & + 1.5(\%\text{W}) + 8(\%\text{Ti}) + 12(\%\text{Al}) \\ & - 4(\%\text{Ni}) - 2(\%\text{Co}) - 2(\%\text{Mn}) \\ & - (\%\text{Cu}) - 40(\%\text{C}) - 30(\%\text{N})\end{aligned} \qquad (3.15)$$

The austenite present at the austenitizing temperature should transform fully to martensite on cooling [29]. The alloying additions made to balance the constitution or improve the tempering resistance of the steels also lower the martensite start (M_S) and finish (M_f) temperatures, resulting in a tendency for retained austenite to be present if the M_S temperature is close to or below room temperature [11]. The retained austenite increases the toughness of high-chromium transformable steels but, in other respects, it is undesirable as distortion occurs during its transformation and it decreases the strength. It follows that the composition of the steel must be adjusted not only to control the constitution but also to maintain the M_S-M_f temperature range above ambient. The coefficients of the elements in the Ni and Cr equivalent relationships (Eqs 3.13 to 3.15) are not the same as those for the effects on the M_S and M_f temperatures. A general indication of the influence of alloying elements on the M_S temperature can, however, be obtained from empirically established equations, the following being examples [1,29,30]:

$$\begin{aligned}M_S\ (^\circ\text{C}) = {} & 550 - 450(\%\text{C}) - 11(\%\text{Si}) \\ & - 33(\%\text{Mn}) - 20(\%\text{Cr}) - 17(\%\text{Ni}) \\ & - 15(\%\text{Mo}) - 20(\%\text{V}) - 11(\%\text{Nb}) \\ & - 10(\%\text{W}) - 10(\%\text{Cu}) + 15(\%\text{Co})\end{aligned} \qquad (3.16)$$

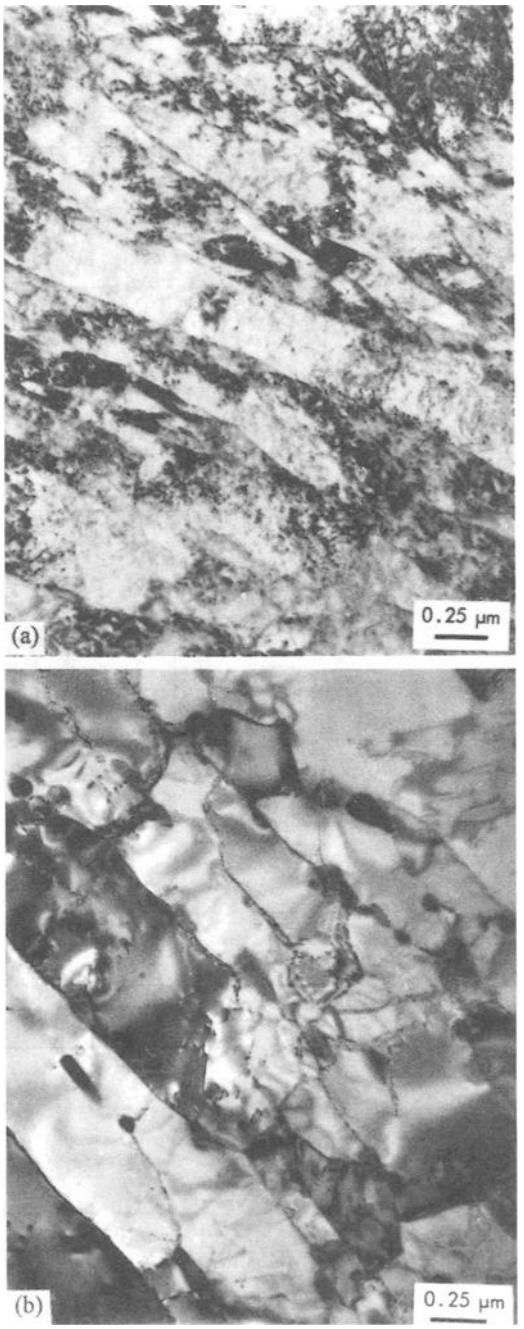

FIG. 3.6—Transmission electron micrographs of 12Cr-1MoVW (HT9) steel in (a) normalized and (b) normalized-and-tempered conditions [25].

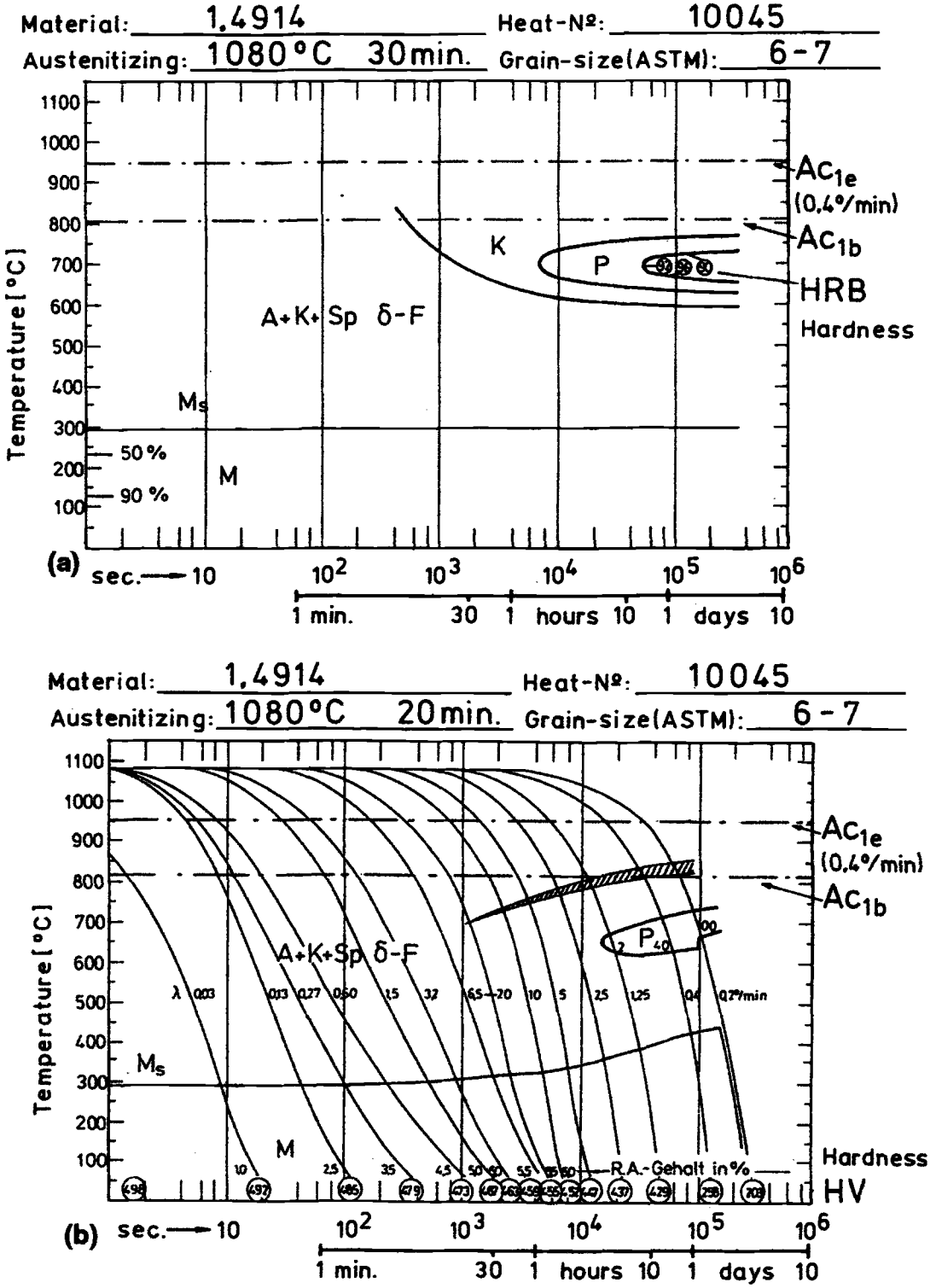

FIG. 3.7—(a) Isothermal transformation (TTT) and (b) continuous cooling transformation (CCT) diagrams for 1.4914 (12Cr-MoVNb) martensitic steel (A = Austenite, K = Carbide, Sp δ-F = Trace of ferrite, M = Martensite, P = Pearlite, Ac_{1b} = Start of austenite formation on heating, Ac_{1e} = Completion of austenite formation on heating, λ=Cooling rate (°C.min^{-1}) from 800–500°C [30].

$$M_S\,(°C) = 635 - 474[(\%C) + 0.86(\%N) - 0.15(\%Nb + \%Zr) - 0.066(\%Ta + \%Hf)] - [17(\%Cr) + 33(\%Mn) + 21(\%Mo) + 17(\%Ni) + 39(\%V) + 11(\%W)]. \quad (3.17)$$

Cobalt is unusual in that it raises the M_S temperature as well as being an austenite former capable of balancing the constitution; it is therefore an important addition in steels containing large concentrations of the ferrite-forming elements [31].

The phase transformations and precipitation reactions that occur during anisothermal and isothermal treatments are important in regard to heat treatment and normal fabrication and welding procedures. The continuous cooling transformation (CCT) and isothermal time-temperature-transformation (TTT) characteristics of the high-chromium (8 to 14%) conventional and reduced-activation ferritic/martensitic steels have been extensively studied using several techniques, including dilatometry, thermoelectric power, and optical and electron microscopy [21,30,32–34]. The CCT and TTT (displaying the characteristic C-curve behavior) diagrams for the 12Cr-MoVNb (1.4914) steel are compared in Fig. 3.7 [30], and the CCT diagram for the reduced activation F82H (7.5Cr-2WVTa) steel is shown in Fig. 3.8 [21].

The M_S and M_f temperatures for the high-chromium steels usually range from 250 to 350°C and 80 to 190°C, respectively, but much higher M_S ($\leq$ 450°C) and M_f ($\leq$ 260°C) temperatures have been determined for some of the developmental reduced-activation steels [21,30,34]. These observations and the CCT diagrams demonstrate that the steels are air hardenable, with the martensite being formed in thick sections because the pearlite transformation is greatly retarded and bainite is not formed even within extended time periods. The martensite produced is typical low-carbon lath martensite; the hardness of the as-quenched martensite in the high-chromium ferritic/martensitic steels increases linearly with increasing interstitial carbon and nitrogen contents [21,30,35] and is given by [30]:

$$Hv_{30} = (\%C) + 0.63[(\%N) - 0.15(\%Nb) + (\%Zr)] - 0.066[(\%Ta) + (\%Hf)] \quad (3.18)$$

Furthermore, the martensite hardness is not significantly dependent on the chromium, tungsten, vanadium, and tantalum contents, austenitizing temperature, and microstructural characteristics (prior austenite grain size and martensite lath width and length) of 8 and 11% Cr reduced-activation steels [21].

Double austenitizing treatments (950 to 965°C for 2 h, air cooled plus 1075°C for 0.5 h, air cooled) have been developed for the 12Cr-MoVNb (MANET II) and other high-chromium martensitic steels to produce a more uniform prior austenite grain size and martensite lath structure and, thereby, greater homogeneity in properties after subsequent tempering at 750°C [36]. In addition, a double austenitizing treatment (1200°C for 9 h, water quenched plus 1070°C for 10 h, air cooled) may be applied to modified 9Cr-1Mo (F91) steel forgings to refine the grain size and enhance the ambient temperature tensile proof stress and 600°C creep-rupture properties in the tempered (750°C for 11 h) condition [37].

TEMPERING

It is essential that the tempering of the martensite is performed at temperatures below the Ac_1 (the temperature at which the $\alpha \rightarrow \gamma$ transformation commences on heating) to avoid reaustenitization and thereby achieve the optimum combination of strength and toughness. Nickel, manganese,

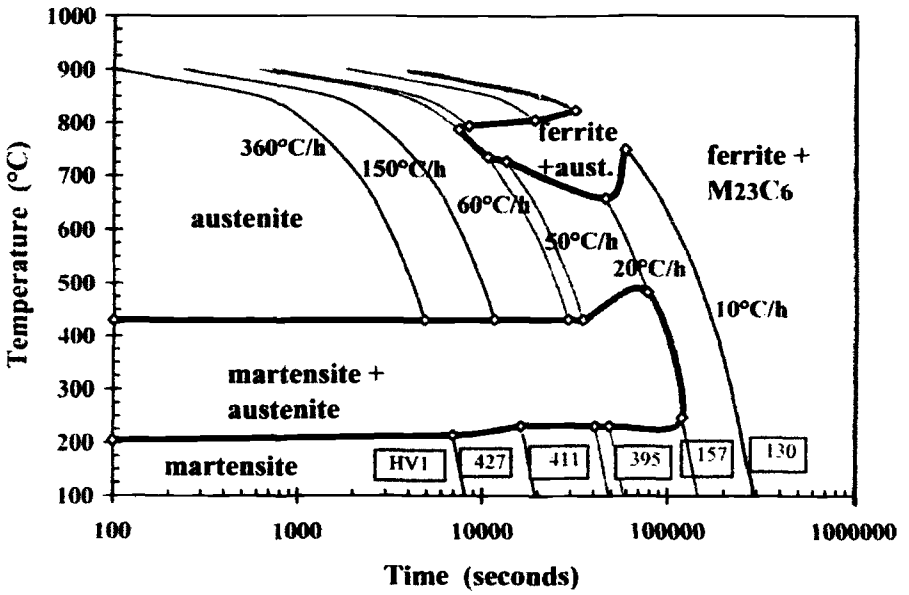

FIG. 3.8—Continuous cooling transformation (CCT) diagram for low-carbon F82H (8Cr-2WVTa) steel determined after austenitization at 1050°C for 0.5 h [21].

and, to a lesser extent, copper all lower the Ac_1 temperature, while the ferrite-forming elements Si, Mo, V, and Al increase it, as shown by the data in Table 3.2 [11,29]. The concentration of nickel has to be restricted to about 2% to prevent reaustenitization at temperatures below about 700°C and enable the tempering to be performed at reasonable temperatures. Measured Ac_1 and Ac_3 (the temperature at which the $\alpha \rightarrow \gamma$ transformation is complete) temperatures in the ranges 760 to 850°C and 870 to 960°C, respectively, are quoted for conventional [30] and reduced-activation [21,30,34] steels. The respective Ac_1 and Ac_3 temperatures for a series of 9Cr-0.8WTa reduced-activation steels are comparable and the transformation behavior on heating is not significantly dependent on the interstitial element and tantalum concentrations [21]; however, increased chromium (11%) and tungsten (2 to 3%) contents result in higher transformation temperatures.

Retarded softening occurs during tempering of a simple, low-carbon 12% Cr steel at temperatures up to about 500°C, while pronounced softening occurs at 500 to 550°C (Fig. 3.9) [3,11]; the rate of softening decreases progressively above 550°C. The hardness changes at different tempering temperatures can be correlated with the microstructural changes as follows [3,38–40]:

<350°C—A fine dispersion of M_3C (Fe_3C) precipitates forms and grows to a dendritic morphology and then to a plate-like Widmanstätten distribution. The chromium content of the Fe_3C increases to about 20% with the possibility of M_7C_3 being formed *in situ* from the Cr-enriched Fe_3C [41]. Both these effects slow down the growth rate of the Fe_3C and thereby retard softening.

≈450–500°C—Fine needles of M_2X [predominantly $Cr_2(CN)$] nucleate primarily on the dislocations within the martensite laths and retard the softening, but the precipitation is not sufficiently intense to produce secondary hardening.

500–550°C—The M_7C_3 and M_2X phases coarsen, with a resulting rapid decrease in hardness.

>550°C—The M_7C_3 and M_2X are replaced by Cr-rich $M_{23}C_6$ precipitates, which nucleate on the martensite lath and prior austenite grain boundaries, and the rate of decrease of hardness slows down. The dislocation density decreases relative to that of the "as-quenched" martensite, and sub-structures consisting of low-angle boundaries and dislocation arrays begin to form.

≥650°C—The $M_{23}C_6$ precipitates at the tempered lath martensite boundaries grow, leading to a further reduction in dislocation density and pronounced sub-grain formation across the martensite laths.

≥750°C—The sub-cells within the martensite laths grow into fairly equiaxed sub-grains with little or no trace of the original lath martensite structure. Growth of the $M_{23}C_6$ precipitates continues, but clearly defined dislocation networks may still be present. Virtually all the carbon in solution in the steels is precipitated as $M_{23}C_6$ on tempering for ≥1 h at 700 to 780°C [25].

It follows that overaging during tempering of these steels is associated with the removal of M_2X from within the martensite laths and the growth of the grain boundary $M_{23}C_6$; these processes allow the dislocations to form polygonal networks. Further coarsening results in the sub-boundaries becoming unpinned and growth of equiaxed areas of ferrite occurs with the boundaries being composed of well-defined dislocation arrays. This has been referred to as recrystallization during tempering, but it is really only a form of sub-grain growth [3].

TABLE 3.2—Effects of alloying elements on the Ac_1 temperature of 12% Cr steels [11,29].

Element	Change in Ac_1 (°C) per Mass %
Ni	−30
Mn	−25
Co	−5
Si	+25
Mo	+25
Al	+30
V	+50

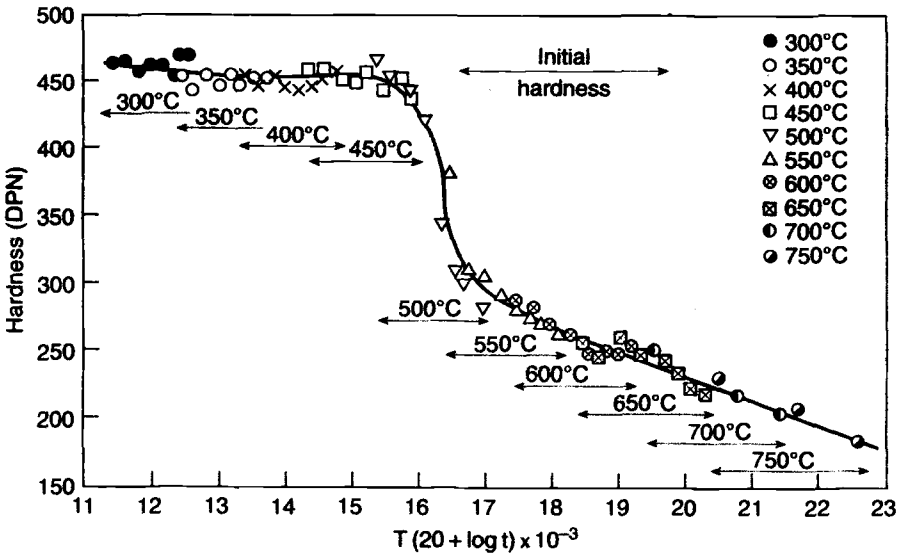

FIG. 3.9—Tempering characteristics of a 12Cr-0.14C steel [3,11].

Carbide precipitation on the tangled dislocations in δ-ferrite, which is frequently present in wrought products as bands of polygonal grains (Fig. 3.2), takes place on tempering at temperatures above about 500°C. The ferrite is rich in Cr, Mo, and the other ferrite formers as a result of partitioning, and intragranular precipitates of the M_2X [$(CrMo)_2(CN)$] phase in the form of large needles and intergranular $M_{23}C_6$ are produced [25,38,42–44]; these coarsen gradually and generally persist to the highest tempering temperatures.

The tempering characteristics of simple high-chromium steels are modified by alloying additions [3,38,39,45]. Thus, the presence of 0.02 to 0.03% nitrogen causes the hexagonal Cr_2N (M_2X) phase to form in preference to the rhombohedral M_7C_3 and thereby increases the intensity of the secondary hardening and overaged hardness. Carbon is also effective in promoting secondary hardening by increasing the volume fraction of the M_2X phase. Nickel, which is present in the majority of the 12% Cr steels to balance the constitution, accelerates carbide overaging and thus slightly decreases the tempering resistance.

The ferrite formers Mo, W, and V are soluble in the M_2X and increase its lattice parameter and the associated coherency strains, resulting in true secondary hardening and increased tempering resistance (Fig. 3.10) [46]. However, silicon increases the coherency strains and the tempering resistance by dissolving in the matrix and decreasing its lattice parameter [7]. Vanadium, niobium, tantalum, and titanium form carbides, nitrides, or carbonitrides [VC, VN, Nb(CN), Ta(CN), and TiN/TiC] at higher temperatures than those at which M_2X precipitates; these phases are very stable and increase the resistance to overaging and tempering. Any soluble V, Nb, Ta, and Ti also produce solid-solution strengthening and retard recovery and growth of the sub-grains at the highest tempering temperatures.

The solubilities of various carbides and nitrides in ferritic steels have been documented and reviewed [47]; the solubility relationships for VN and AlN in ferrite in a 11% Cr steel are quoted [17] as follows:

$$\log [V][N] = -7830/T + 5.54 \quad (3.19)$$

$$\log [Al][N] = -10062/T + 5.80 \quad (3.20)$$

where [V], [Al], and [N] are in wt%.

The solubility curves for VN in the ferrite at 600 and 750°C are shown in Fig. 3.11, with the stoichiometric line for VN (V:N = 3.64) included. The VN is much less soluble in the ferrite than in the austenite phase (Fig. 3.3); however, it is still significant at tempering temperatures of about 750°C, with the solubility being a maximum along the stoichiometric line. Precipitation of VN and [Nb(CN)] occurs during creep or exposure at lower temperatures due to the reduced solubilities. VC has an even higher solubility than VN, and precipitation in low-vanadium steels is less likely. AlN is less soluble than VN, and AlN precipitation may take place in steels with relatively high aluminum contents. It follows that, in addition to the tempering temperature and time, the extent of the precipitation during tempering depends on the carbon, nitrogen, and other alloying element contents of the steels. The effect of carbon content is illustrated in Fig. 3.12; there is significantly more precipitation in the higher (0.2%) carbon 12Cr-1MoVW steel [Fig. 3.12(a)] compared to the lower (0.1%) carbon 9Cr-1MoVNb steel [Fig. 3.12(b)] [25].

In summary, the microstructures of the conventional and reduced activation high-chromium martensitic steels in the

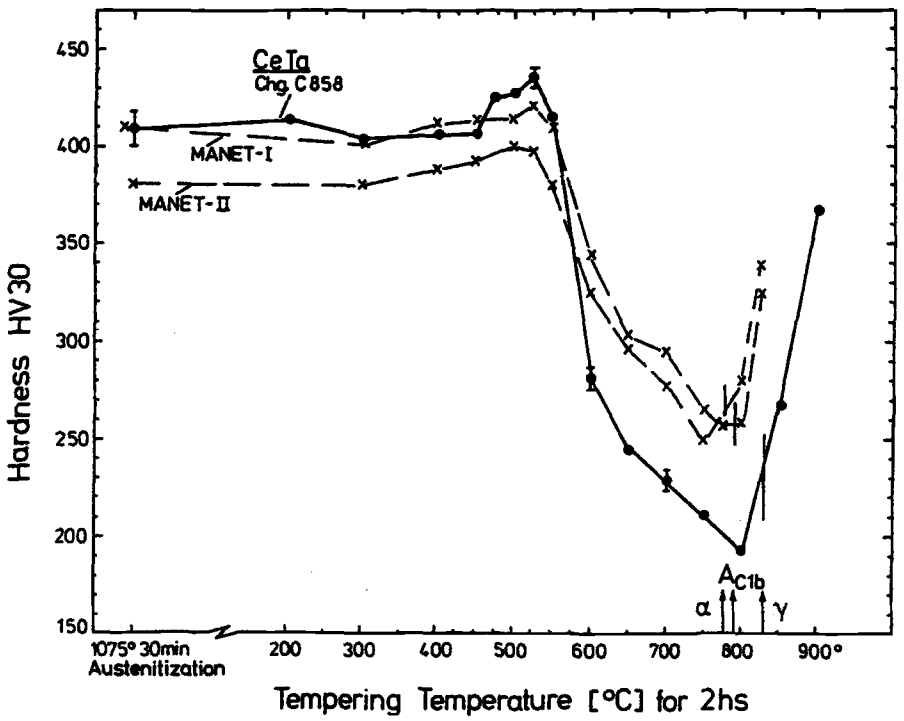

FIG. 3.10—Tempering curves for MANET I, MANET II, and reduced-activation CeTa (9.6Cr-0.8WVTaCe) martensitic steels [46].

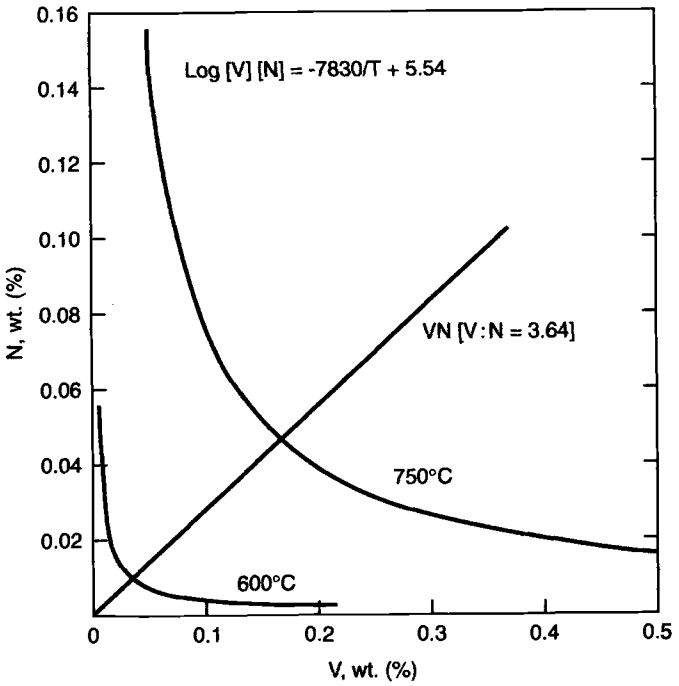

FIG. 3.11—Solubility curves for vanadium nitride in ferrite at 600 and 750°C with respect to 11 wt% Cr in the steel [17].

normalized-and-tempered condition are generally similar, as illustrated in Fig. 3.13(a) and (b). They consist of: (a) martensite laths (Fig. 3.14) about 1 μm wide and ≥5μm long [Fig. 3.6(b)] [25], containing dislocations with a Burgers vector $1/2a_0<111>$ and a density of approximately 1×10^{14} m^{-2} [48] and (b) coarse $M_{23}C_6$ particles located at prior austenite and ferrite grain boundaries with finer precipitates within the laths and at the martensite lath and sub-grain boundaries; M_2X precipitates rich in chromium and isomorphous with $(CrMoWV)_2(CN)$ within the martensite laths and δ-ferrite phase; primary (Nb,Ta)X; and fine secondary (V,Nb,Ta)X. Further details concerning the nature and characteristics of the precipitates in the tempered steels are given in Chapter 4.

The development of higher creep-rupture strength 9–12% Cr steels containing various combinations of N, Mo, W, V, Co, Cu, Nb, and Ta (surveyed in Chapter 2) is based on optimizing the constitution and δ-ferrite content, increasing the stability of the martensite dislocation structure, and maximizing the solid solution and precipitation hardening. The intensity of the precipitation hardening by carbides and nitrides of the V(CN) and Nb(CN) types is enhanced in steels having the appropriate stoichiometric ratios [49]. In addition, significant increases in hardness and strength of the low-carbon steels after tempering at relatively low temperatures of about 500°C are produced by precipitation of metallic copper in steels containing up to 4% Cu, NiAl in steels with Ni and ≤1.5% Al, and NiTi in steels with additions of Ni and Ti [50,51]. The precipitation of M_2X is intensified with increased additions of Mo and/or equivalent amounts of W [Mo equivalent = %Mo + 0.5 (%W)]. High (≤3.5%) concentrations of these elements, together with cobalt additions to balance the increased δ-ferrite-forming tendencies, increase the level of the tempering curve as a result of precipitation reactions at 600 to 650°C in which the M_2X formation is replaced by intermetallic compounds based on the Mo-Cr-Co ("R") phase [52] as well as Laves phases [Fe_2Mo, Fe_2W, $(FeCr)_2(MoW)$, and, possibly, Fe_3Co and M_7Mo_6 in the overtempered condition]. The tungsten-containing intermetallic compounds appear to coarsen at a slower rate than the molybdenum variant, resulting in higher strength, ductility, and toughness.

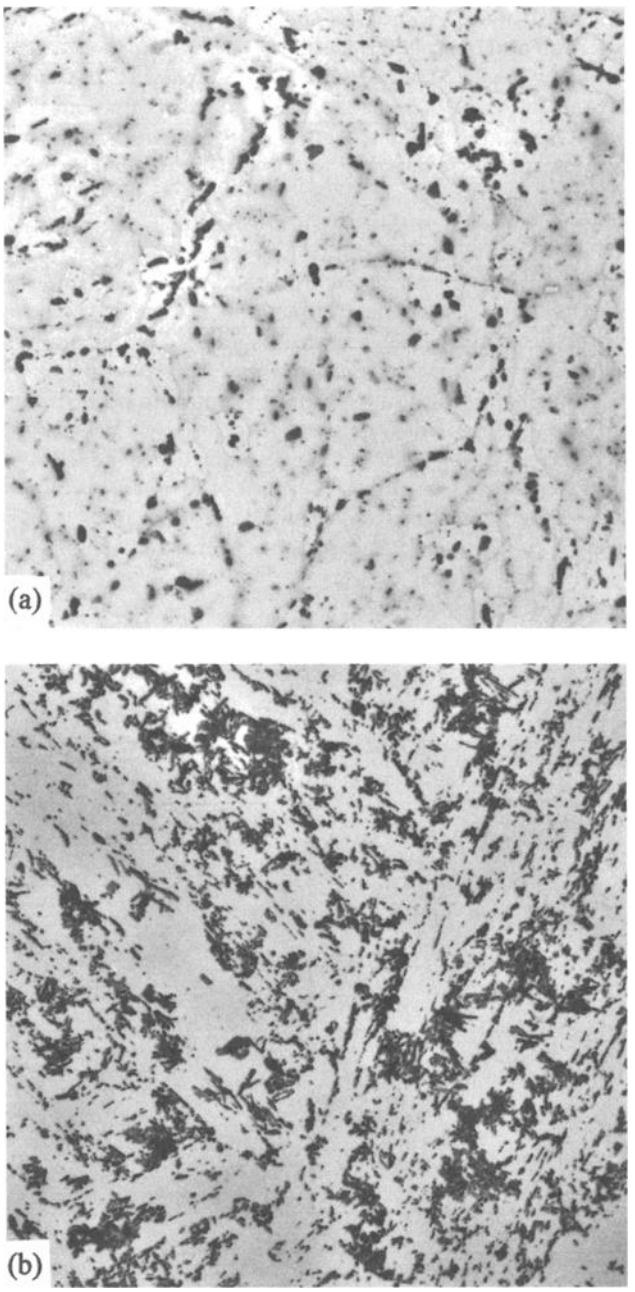

FIG. 3.12—Electron micrographs (extraction replicas) of normalized-and-tempered (a) 9Cr-1MoVNb (0.1% C) and (b) 12Cr-1MoVW (0.2% C) steels [25].

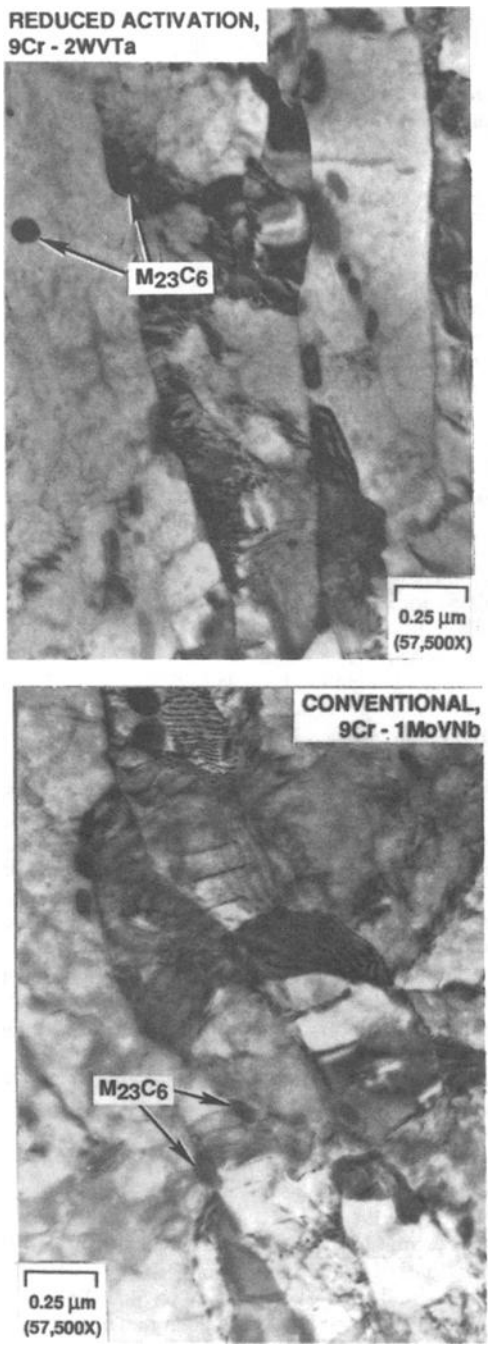

FIG. 3.13—Electron micrographs of normalized-and-tempered (a) reduced-activation 9Cr-2WVTa and (b) conventional 9Cr-1MoVNb steels.

Ausaging, a heat treatment that involves controlled isothermal aging at 700°C for 120 h after austenitization and before rapid cooling to ambient temperature and subsequent tempering of the martensite at 700°C for 4 h, has been developed to produce uniform precipitation of vanadium nitride and thereby enhance the stability of the sub-grain structure and the tensile proof strength and impact properties of high nitrogen (0.15 to 0.18%) and vanadium (0.6 to 0.8%) 12% Cr steels [53].

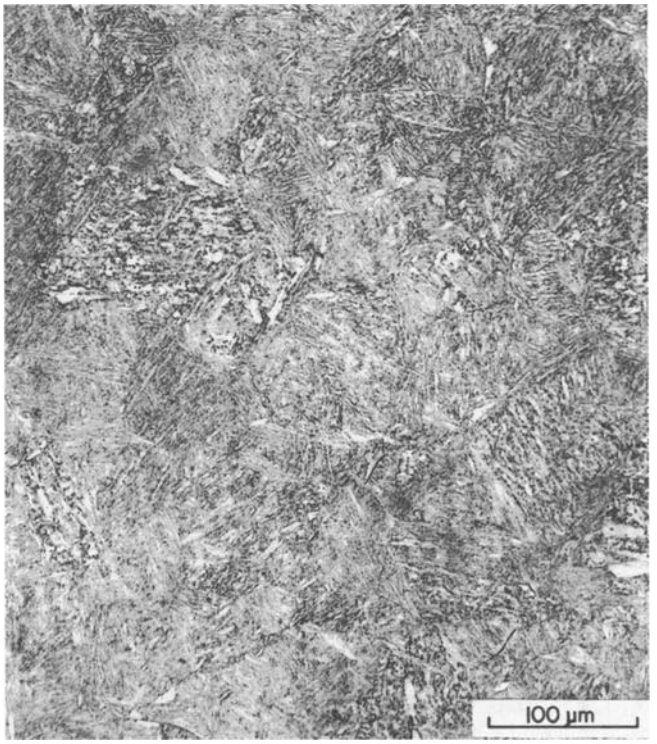

FIG. 3.14—Optical microstructure of normalized-and-tempered 12Cr-1MoVW (HT9) steel [25].

REFERENCES

[1] F. B. Pickering, Int. Met. Reviews, No. 211 (1976) 227.
[2] J. Orr, F. R. Beckitt, and G. D. Fawkes, in: Ferritic Steels for Fast Reactor Steam Generators, Vol. 1, Eds. S. F. Pugh and E. A. Little (British Nuclear Energy Soc., London, 1978) 91.
[3] F. B. Pickering, in: Microstructural Developments and Stability in High Chromium Ferritic Power Plant Steels, Eds. A. Strang and D. J. Gooch (The Inst. of Materials, London, Book No. 667, 1997) 1.
[4] W. Tofaute, A. Sponheuer, and H. Bennek, Archiv für Eisenhüttenwesen 8 (1935) 499.
[5] V. G. Rivlin and G. V. Raynor, Int. Met. Reviews 1 (1980) 21.
[6] D. Peckner and I. M. Bernstein (Eds.), Handbook of Stainless Steels (McGraw-Hill, New York, 1977).
[7] F. B. Pickering, in: Stainless Steels '84 (The Inst. of Metals, London, 1985) 2.
[8] K. Anderko, K. David, W. Ohly, M. Schirra, and C. Wassilew, in: Topical Conference on Ferritic Steels for Use in Nuclear Energy Technologies, Eds. J. W. Davis and D. J. Michel (The Met. Soc. AIME, Warrendale, PA, 1984) 299.
[9] B. A. Chin and R. C. Walkaways, in: Topical Conference on Ferritic Steels for Use in Nuclear Energy Technologies, Eds. J. W. Davis and D. J. Michel (The Met. Soc. AIME, Warrendale, PA, 1984) 347.
[10] K. Anderko, L. Schäfer, and E. Materna-Morris, J. Nucl. Mater. 179-181 (1991) 492.
[11] K. J. Irvine, D. J. Crowe, and F. B. Pickering, J. Iron Steel Inst. 195 (1960) 386.
[12] D. S. Gelles, in: Reduced Activation Materials for Fusion Reactors, ASTM STP 1047, Eds. R. L. Klueh, D. S. Gelles, M. Okada, and N. H. Packan (ASTM, Philadelphia, 1990) 113.
[13] R. L. Klueh, unpublished research.

[14] J. Z. Briggs and T. D. Parker, The Super 12% Chromium Steels (Climax Molybdenum Co., New York, 1965).
[15] F. B. Pickering, private communication.
[16] S. R. Keown and F. B. Pickering, in: Creep Strength in Steel and High Temperature Alloys (The Metals Society, London, 1974) 134.
[17] V. Foldyna and Z. Kuboň, in: Performance of Bolting Materials in High Temperature Plant Applications, Ed. A. Strang (The Inst. of Materials, London, Book 607, 1995) 175.
[18] V. Foldyna, Z. Kuboň, A. Jakovová, and V. Vodárek, in: Microstructural Developments and Stability in High Chromium Ferritic Power Plant Steels, Eds. A. Strang and D. J. Gooch (The Inst. of Materials, London, Book No. 667, 1997) 73.
[19] J. Kunze, cited by: V. Foldyna and Z. Kuboň, in: Performance of Bolting Materials in High Temperature Plant Applications, Ed. A. Strang (The Inst. of Materials, London, Book 607, 1995) 175.
[20] M. Tamura, K. Shinozuka, K. Masamura, K. Ishizawa, and S. Sugimoto, J. Nucl. Mater. 258-263 (1998) 1158.
[21] A. Alamo, J-C. Brachet, A. Castaing, C. Lepoittevin, and F. Barcelo, J. Nucl. Mater. 258-263 (1998) 1228.
[22] H. Schneider, Foundry Trades J. 108 (1960) 562.
[23] W. B. Delong, Metal Progress 77 (1960) 98.
[24] K. Anderko, cited by: M. Schirra, Stahl und Eisen 112 (1992) 117.
[25] J. M. Vitek and R. L. Klueh, Met. Trans. 14A (1983) 1047.
[26] T. Lauritzen, W. L. Bell and S. Vaidyanathan, in: Topical Conference on Ferritic Alloys for Use in Nuclear Energy Technologies, Eds. J.W. Davis and D.J. Michel (The Met. Soc. AIME, Warrendale, PA, 1984) 623.
[27] A. Iseda, Y. Sawaragi, S. Kato and F. Masuyama, in: Proc. 5th Int. Conf. on Creep of Materials (ASM Int., Materials Park, OH, 1992) 389.
[28] P. Patriarca, S. D. Harkness, J. M. Duke and L. R. Cooper, Nucl. Tech. 28 (1976) 516.
[29] F. B. Pickering, Physical Metallurgy and the Design of Steels (Applied Science Publishers, London, 1978).
[30] H. Finkler and M. Schirra, Steel Research, 67 (1996) 328.
[31] K. J. Irvine, J. Iron Steel Inst. 200 (1962) 820.
[32] J-C. Brachet, in: Heat Treatment of Materials: Heat and Surface '92, Ed. I. Tamura, (Japan Soc. for Heat Treatment, Tokyo, 1992) 89.
[33] J-C. Brachet, L. Gavard, C. Boussidan, C. Lepoittevin, S. Denis and C. Servant, J. Nucl. Mater. 258-263 (1998) 1307.
[34] L. Pilloni, F. Attura, A. Calza-Bini, G. De Santis, G. Filacchioni, A. Carosi, and S. Amato, J. Nucl. Mater. 258-263 (1998) 1329.
[35] J. Orr and D. Burton, in: Materials for Advanced Power Engineering 1994, Part 1, Eds. D. Coutsouradis, J. H. Davidson, J. Ewald, P. Greenfield, T. Khan, M. Malik, D. B. Meadowcroft, V. Regis, R. B. Scarlin, F. Schubert, and D. V. Thornton (Kluwer Academic Publishers, Dordrecht, The Netherlands, 1994).
[36] M. Schirra, P. Graf, S. Heger, H. Meinzer, W. Schweiger, and H. Zimmermann, MANET II, Untersuchungsergebnisse zum Umwandlungs- und Vergütungsverhalten und Prüfung mechanischer, Kernforschungszentrum Karlsruhe Report KfK 5177, May 1993.
[37] A. Jakovová, M. Filip, V. Foldyna, V. Vodárek, and A. Korčák, in: Advanced Heat Resistant Steels for Power Generation, Eds. R. Viswanathan and J. Nutting (The Inst. of Materials, London, Book 708, 1999) 322.
[38] E. A. Little, D. R. Harries, F. B. Pickering, and S. R. Keown, Metals Tech. 4 (1977) 208.
[39] J. Nutting, in: Topical Conference on Ferritic Steels for Use in Nuclear Energy Technologies, Eds. J. W. Davis and D. J. Michel (The Met. Soc. AIME, Warrendale, PA, 1984) 3.
[40] A. Strang and D. J. Gooch, Eds., Microstructural Developments and Stability in High Chromium Ferritic Power Plant Steels (The Inst. of Materials, London, Book No. 667, 1997).
[41] F. B. Pickering, in: Proc. 4th Int. Conf. on Electron Microscopy (Springer Verlag, Berlin, 1958) 665.
[42] E. A. Little and L. P. Stoter, in: Effects of Radiation on Materials: Proceedings of Eleventh International Symposium, ASTM STP 782, Eds. H. R. Brager and J. S. Perrin, (American Society for Testing and Materials, Philadelphia, PA, 1982) 207.
[43] V. S. Agueev, V. N. Bykov, A. M. Dvoryashin, V. N. Golovanov, E. A. Medvedeva, V. V. Romaneev, V. K. Shamardin, and A. N. Vorobiev, in: Effects of Radiation on Materials: 14th International Symposium, Vol. I, ASTM STP 1046, Eds. N. H. Packan, R. E. Stoller, and A. S. Kumar (American Society for Testing and Materials, Philadelphia, PA, 1989) 98.
[44] Y. Hosoi, N. Wade, S. Kunimitsu, and T. Urita, J. Nucl. Mater. 141-143 (1986) 461.
[45] B. S. Greenwell and S. M. Beech, in: Rupture Ductility of Creep Resistant Steels, Ed. A. Strang (The Inst. of Metals, London, Book No. 522, 1991) 103.
[46] S. Cierjacks, K. Ehrlich, E. Materna-Morris, L. Schäfer, M. Schirra, and C. Wassilew, in: Proc. IEA Workshop on Ferritic-Martensitic Steels, Vol. II, Eds. F. Abe, A. Hishinuma, A. Kohyama, and M. Suzuki, (Japan Atomic Energy Research Inst., Tokai Research Establishment, Tokai, Japan, 1993) 125.
[47] T. Gladman, Physical Metallurgy of Microalloyed Steels (The Inst. of Materials, London, Book No. 615, 1997).
[48] R. Schäublin, P. Spätig, and M. Victoria, J. Nucl. Mater. 258-263 (1998) 1178.
[49] H. Berns and F. Krafft, in: Rupture Ductility of Creep Resistant Steels, Ed. A. Strang (The Inst. of Metals, London, Book No. 522, 1991) 116.
[50] K. J. Irvine and F. B. Pickering, in: Metallurgical Developments in High Alloy Steels (The Iron and Steel Inst., London, Special Report No. 86, 1964) 34.
[51] F. B. Pickering, in: Low Alloy Steels (The Iron and Steel Inst., London, Publication No. 114, 1968) 131.
[52] D. J. Dyson and S. R. Keown, Acta Met. 17 (1969) 1095.
[53] A. Göecmen, P. J. Uggowitzer, C. Solenthaler, M. O. Speidel, and P. Ernst, in: Microstructural Stability of Creep Resistant Alloys for High Temperature Plant Applications, Eds. A. Strang, J. Cawley, and G. W. Greenwood (The Inst. of Materials, London, Book 682, 1998) 311.

4

Thermal Stability

Thermal aging after the initial normalizing (or quenching) and tempering treatments (discussed in Chapter 3) produces additional precipitation and interfacial segregation of trace impurities and alloying elements, which can significantly affect the toughness and susceptibility to cracking and high-temperature deformation of the high-chromium martensitic steels. The current understanding of the effects of thermal aging with and without simultaneous stress application and the factors that influence the toughness and fracture behavior and creep-rupture characteristics are reviewed in this chapter.

PRECIPITATION

The phases precipitated in the following steels during tempering and subsequent aging at temperatures in the range 400 to 750°C or creep-rupture testing at 550 to 700°C are summarized in Table 4.1: (a) wrought 9Cr-1Mo [1–9], 9Cr-2Mo (EM12 [10–12], and JFMS [13]), modified 9Cr-1Mo (T91 [14–23]), 12Cr (FI [24,25]), 12Cr-1MoV (FV607 [24], CRM12 [25], and X20CrMoV12.1 [23,26,27]), 12Cr-1MoVW (HT9 [14,15,28]), 12Cr-1MoVNb (FV448, 1.4914, and similar compositions [22,24,25,29–31]) and 13Cr-2MoVNb [32] ferritic/martensitic steels, the reduced activation grades (F82H and Ta-free F82 [15,33,34]) and other 9–12% Cr steels containing up to 4% W [35,36] and including E911, NF616, HCM12, HCM12A, and TB12M [21,23,37], and (b) 10.5Cr-1MoVNb and 10Cr-1Mo1WVNb casting steels [38,39].

The phases have been characterized by X-ray diffraction of extracted residues and by high-resolution analytical electron microscopy (AEM) of extraction replicas and thin foils using convergent beam microdiffraction, energy dispersive X-ray (EDX), electron energy loss spectroscopy (EELS), and other micro-analytical techniques.

The microstructural developments in the 9–12% Cr steels containing V, Nb, Mo, and W in the normalized-and-tempered condition and following aging and creep straining for 10 000 to 30 000 h at 600 to 650°C are compared in Table 4.2 [23].

The principal and most stable carbide formed in these steels is $M_{23}C_6$, but variable and smaller quantities of other carbides, nitrides, and carbonitrides may also be produced during normalizing (or quenching) and tempering. Further precipitation and spheroidization of these phases occur during aging or creep straining, the extent depending on the steel composition, temperature, time, and applied load. The M_2X precipitates in the normalized-and-tempered steels are gradually replaced by MX, Z, and Laves phases during prolonged high-temperature aging or creep straining. The Laves phases [Fe_2Mo, Fe_2W and $Fe_2(Mo,W)$ in steels containing Mo, W, and Mo plus W, respectively] are the main precipitates formed at temperatures in the range 450 to 650°C, the precipitate volume fractions increasing with increasing molybdenum and tungsten contents. The time-temperature-precipitation (TTP) curves for the Laves phase formation in the modified 9Cr-1Mo (T91), 12Cr-1MoVW (HT9), and reduced activation steels F82H and F82 are reproduced in Fig. 4.1 [15]; the noses of the curves for the T91 and HT9 steels are at 550 to 600°C, while the corresponding temperatures for the reduced-activation steels are ≥650°C. The precipitation in the fully martensitic steels is relatively slow, the Laves phase being nucleated on the acicular Cr_2N particles within the martensite laths and formed around the $M_{23}C_6$ precipitates at the prior austenite grain and lath boundaries [8]. However, the formation of the Laves phase (Fe_2Mo) in the δ-ferrite in the dual phase 9–12% Cr, 1–2% Mo steels occurs at an early stage of aging, the noses of the TTP curves being at 550 to 650°C [40,41]. Silicon also enhances the rate of the Laves phase formation during thermal aging of standard [42] and modified [19] 9Cr-1Mo steels, while small additions of tantalum retard the precipitation of the Fe_2W phase in the Fe-Cr-W system [15].

The measured compositions of the metal fractions in the $M_{23}C_6$ and Laves phase precipitates in the 9Cr-1MoVNb (T91) and 9Cr-MoVNbW (E911) steels in the normalized-and-tempered and/or aged at 600, 650, and 700°C conditions are given in Table 4.3 [21].

Chi (χ) phase has been detected in a 12Cr-4Mo steel [43] and a 12Cr-6Mn steel after thermal aging for times up to 5000 h at 400 and 520°C [44,45]; this phase can incorporate carbon and be considered as a carbide ($M_{18}C$) or behave as an intermetallic compound ($Fe_{35}Cr_{12}Mo_{10}$) [46]. It has also been reported to form in Fe-Cr-W alloys [47].

Aging for extended periods at temperatures between 400 and 550°C can result in the precipitation of coherent particles of α′ (Cr-rich ferrite) with an associated reduction in ductility (475°C embrittlement); however, such effects are not normally encountered in wrought, fully martensitic steels containing ≤12% Cr [48,49].

The α′-ferrite in the two-phase (γ+δ) steels is enriched in Cr, Mo, Si, W, and other ferrite-forming elements and depleted in Ni, Mn, and the other austenite (γ) stabilizing elements during austenitization; the γ-phase is similarly enriched in the austenite-stabilizing elements and depleted in the ferrite-forming elements. This alloy partitioning results

TABLE 4.1—Precipitation in normalized-and-tempered, aged, and creep-rupture tested high-chromium martensitic steels.

Precipitate Phase	Crystal Structure and Lattice Parameter	Typical Composition	Distribution of Precipitates
$M_{23}C_6$	fcc a =1.066 nm	$(Cr_{16}Fe_6Mo)C_6$ $(Cr_4Fe_{12}Mo_4Si_2WV)C_6$	Coarse particles at prior austenite grain and martensite lath boundaries and fine intra-lath particles
MX	f.c.c. a = 0.444-0.447 nm	NbC, NbN, VN, (CrV)N, Nb(CN) and (NbV)C	Undissolved particles and fine precipitates at martensite lath boundaries
M_2X	Hexagonal a = 0.478 nm c = 0.444 nm	Cr_2N, Mo_2C and W_2C	Martensite lath boundaries (Cr_2N and Mo_2C); prior austenite grain boundaries (Mo_2C); intra-lath (Mo_2C and W_2C); δ-ferrite in duplex steels [Cr_2(CN) and $(CrMo)_2$(CN)]
Z-phase	Tetragonal a = 0.286 nm c = 0.739 nm	(CrVNb)N	Large plate-like particles in the matrix after creep straining at 600°C
η-carbide	Diamond cubic a = 1.07-1.22 nm	M_6C $(Fe_{39}Cr_6Mo_4Si_{10})C$	Prior austenite grain and martensite lath boundaries and intra-lath
Vanadium carbide	f.c.c. a = 0.420 nm	V_4C_3	Low number density in matrix
Laves	Hexagonal a = 0.4744 nm c = 0.7725 nm	Fe_2Mo Fe_2W and Fe_2(MoW)	Prior austenite grain and martensite lath boundaries and intra-lath; δ-ferrite in duplex steels
Chi (χ)	b.c.c. a = 0.892 nm.	$M_{18}C$ or $Fe_{35}Cr_{12}Mo_{10}C$	Intra-martensite lath; δ-ferrite in duplex steels

in the precipitation of large needles of the M_2X phase [Cr_2(CN) and $(CrMo)_2$(CN)] in the δ-ferrite during tempering [24] and promotes the formation of the intermetallic (χ and Laves) compounds and the α′ phase in the δ-ferrite during prolonged aging or service at lower temperatures [43].

The microstructural evolution in the high-chromium power plant and reduced activation martensitic steels, including δ-ferrite stability, austenite-ferrite transformation temperatures, and precipitation of metastable and equilibrium phases as a function of the solute contents and temperature, has also been investigated by computer modeling [23,37,50–52]. These mathematical modeling approaches have become progressively more successful and offer the possibility of describing the changes in the phases and their proportions over extended time periods and developing structure-property relationships. The most thermodynamically stable phases in the steels (that is, the equilibrium condition where the free energy is a minimum) and their fraction as a function of temperature are predicted using available thermochemical data (THERMOCALC Software Package [53]). Examples of the data for the 9Cr-MoVNbW (P92;NF616) and modified 9Cr-1Mo (P91) steels are shown in Fig. 4.2 [37]; these data indicate that little or no Laves phase forms at temperatures above about 720 and 490°C in the respective steels.

Since the equilibrium state is reached only after long times, the models have to incorporate the kinetics of the precipitation reactions. Thus, thermochemical data in combination with classical nucleation and growth theories are being used

TABLE 4.2—Microstructural developments in 9–12Cr-MoWVNb steels during aging and creep straining at 600°–650°C [23].

	Normalized and Tempered	Aged, 10 000–30 000 h	Strained, 10 000–30 000 h
Hardness	High	95% of N & T	70-80% of N & T
Optical Microscopy	Tempered martensite; $M_{23}C_6$; δ-ferrite, depending on grade	Tempered martensite; $M_{23}C_6$; partly decomposed δ-ferrite	Tempered martensite; $M_{23}C_6$; partly decomposed δ-ferrite
Electron Microscopy Dislocation density	High	Low	Very low
Sub-grain/ martensite lath size	Small lath width	Martensite lath transformation to sub-grains	Sub-grains fully recovered
$M_{23}C_6$	On lath bound aries, typically 50–150 nm	Partly coarse ned on sub-grain boundaries	Partly coarsened on sub-grain boundaries
MX	Finely dispersed (20–50 nm)	Finely dispersed (20–50 nm)	Finely dispersed (20–50 nm)
Laves phase	None	Medium and large sized precipitates (200–500 nm)	Large sized precipitates (≈500 nm)

to predict the sequence in which the phases are formed, their fraction as a function of time and temperature and the distribution of particle sizes for each phase [51,54,55]. However, no reliable models describing the effects of temperature and time on the evolution of the dislocation density and sub-grain size appear to be available at present.

The computed TTP diagram for the Laves phase for the 9% Cr-MoVNbW (P92, NF616) steel is reproduced in Fig. 4.3 [37] and shows the characteristic C-curve kinetics. The calculated amounts of tungsten in the precipitates increase to an equilibrium value, which depends on the aging temperature (Fig. 4.4) [37], and are in good agreement with the values measured by EDX during aging at 600°C. The estimated concentrations of the tungsten in the different phases in the P92 steel aged at 600 and 650°C are listed in Table 4.4 [37]; the data confirm those in Table 4.3 in showing that the molybde-

TABLE 4.3—Compositions (wt. %) of the metal fractions in the $M_{23}C_6$ and laves phase precipitates in the T91 and E911 steels [21].

Precipitate	Steel	Condition	Cr	Fe	Mo	W
$M_{23}C_6$	T91	N & T	68	26	6	...
		Aged at 600 or 650°C	69–71	21–24	7–8	...
	E911	N & T	65	27	2	6
		Aged at 600, 650 or 700°C	67–68	16–23	4–8	6–11
Laves phase	E911	Aged at 600, 650 or 700°C	6–11	21–33	12–13	47–55

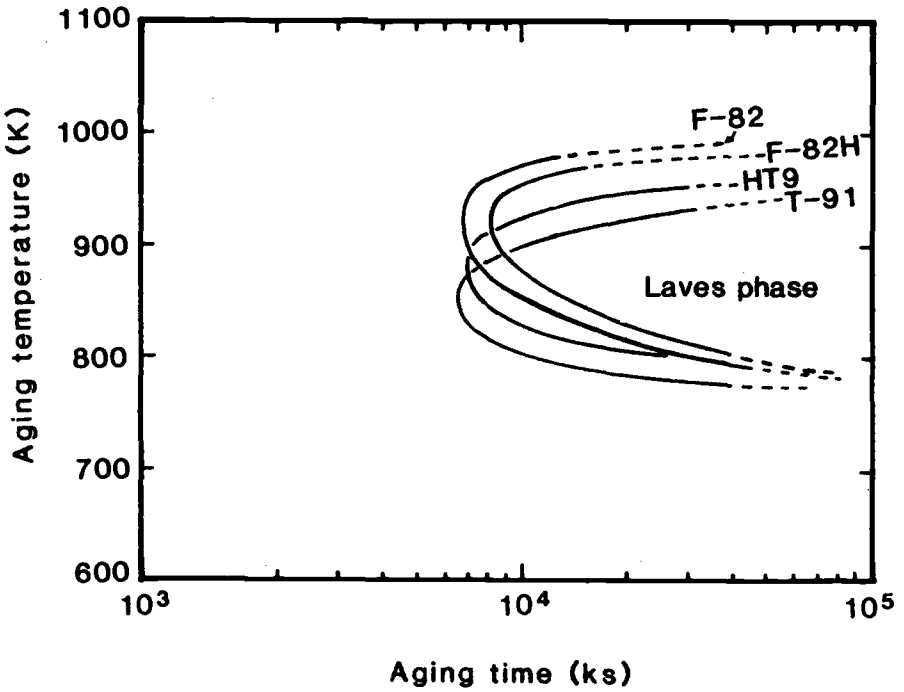

FIG. 4.1—TTP diagrams for the Laves phase in the modified 9Cr-1Mo (T91), 12Cr-1MoVW (HT9), F82H, and F82 steels [15]. NbC (T91) and $M_{23}C_6$ (all four steels) were present in the structures before aging.

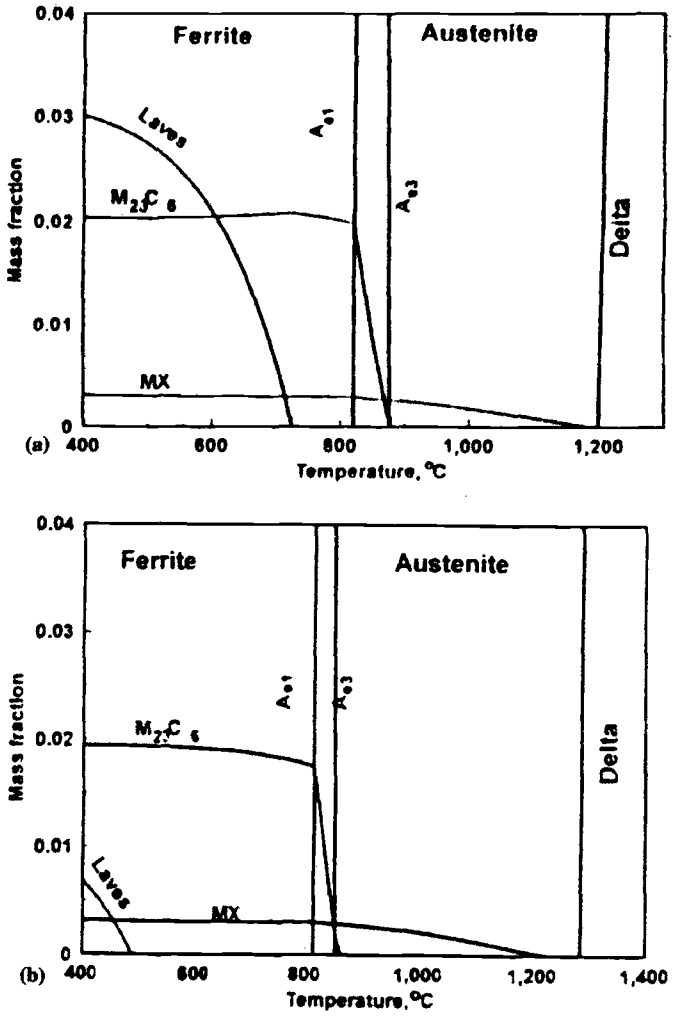

FIG. 4.2—THERMOCALC prediction of equilibrium phases in (a) 9Cr-MoVNbW (P92) and (b) modified 9Cr-1Mo (P91) steels [37].

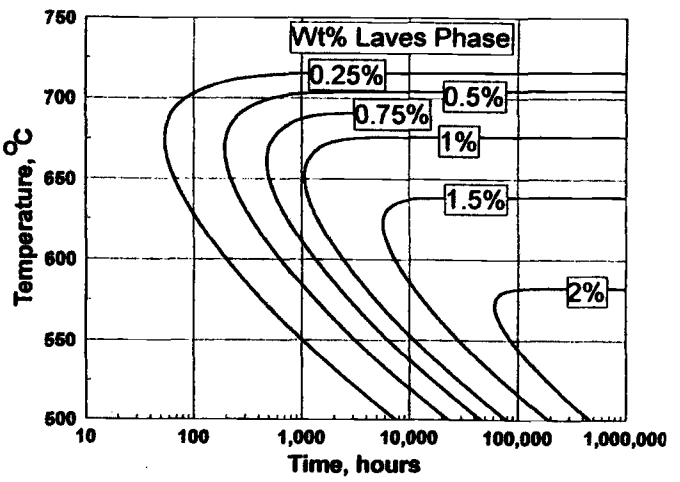

FIG. 4.3—Computed TTP diagram for the Laves phase in P92 (NF616) steel [37].

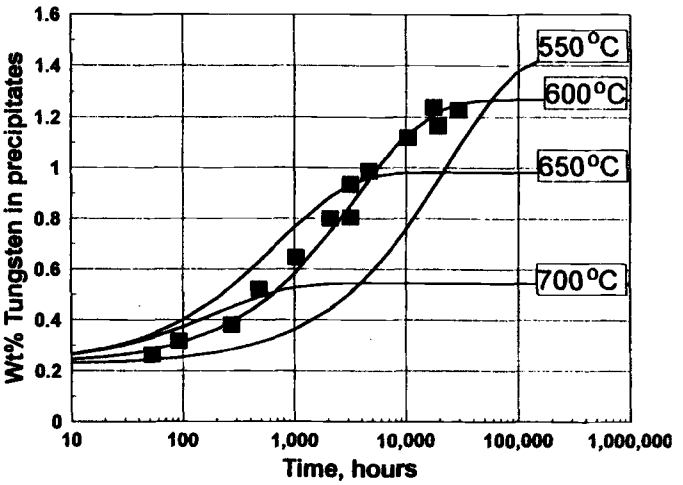

FIG. 4.4—Computed kinetics of tungsten precipitation in P92 (NF616) steel aged at 550, 600, 650, and 700°C [37].

TABLE 4.4—Computed partitioning of tungsten (wt. %) in the various phases in P92(NF616) steel aged at 600° and 650°C [37].

Time	W in $M_{23}C_6$	W in Laves Phase		W in Solution in Matrix	
		600°C	650°C	600°C	650°C
10 h	0.250	0	0	1.6	1.6
Equilibrium	0.300	0.95	0.7	0.6	0.85

num and tungsten contents of the $M_{23}C_6$ precipitates remain constant or increase during aging, thereby demonstrating that the Mo and W in the Laves phase come from the ferrite matrix and not from the "as-tempered" carbides.

Models describing the correlations between the microstructural parameters and the thermal creep strengths are under development. For example, a composite model that predicts the creep strain as a function of the sizes and volume fractions of second phases, dislocation density, and sub-grain size is available [56].

SEGREGATION

Significant progress in the understanding of elemental segregation and its effects on the properties of alloy steels has been made during the past 25 to 30 years. This has resulted from (a) the development and application of Auger Electron Spectroscopy (AES), with facilities for *in situ* fracture at low temperatures in high vacuum so that the composition of the first few atomic layers of the surfaces can be analyzed, (b) high-resolution scanning transmission electron microscopy (STEM) with a spatial resolution of ≈3 nm, and (c) advances in AEM, which have enabled complex microstructures to be quantitatively examined. However, AES cannot be performed on the duplex (tempered martensite plus δ-ferrite) steels to provide information on grain boundary segregation because they do not fracture intergranularly.

It has been demonstrated that interfacial segregation of alloying and impurity elements in the fully martensitic high-chromium steels can occur during cooling from the austenitization temperature and as a result of tempering and

aging. The concentrations of some alloying elements and trace impurities at lath and prior austenite grain boundaries in a 12Cr-MoVNb (1.4914) martensitic steel are enhanced during cooling at critical rates from the austenitization temperature of 1075°C by a non-equilibrium segregation process. It has been shown experimentally [29,57,58] that silicon, boron, and phosphorus segregate at critical cooling rates of 20–50, 250, and 50°C s^{-1}, respectively, while some of the other alloying elements segregate at lower rates of 2.5°C s^{-1} (Mo), 3.0°C s^{-1} (V), and 1.5°C s^{-1} (Nb). This type of segregation is believed to result from the formation of solute atom-thermal vacancy pairs at high temperatures and their subsequent diffusion during cooling to interfaces where the vacancies are annihilated; a theoretical model of this process has been formulated [59,60], developed further, and applied to the high-chromium martensitic steels [57,61]. However, desegregation may also occur during subsequent high-temperature tempering treatments, with the exact rates being dependent on the diffusivities of the particular elements in the steel matrices.

Phosphorus concentrations almost two orders of magnitude higher than those in the bulk are produced on intergranular facets in HT9 steel (0.016% P) during slow cooling or water quenching from a tempering temperature of 750°C, the segregation being less pronounced in the latter case [62]. Phosphorus, chromium, and silicon also segregate at the prior austenite grain boundaries of 9Cr and 9Cr-1Mo steels (0.061 and 0.025% P) during tempering [4,6–8], the extent of the segregation depending on the presence of molybdenum in the steel and the tempering temperature (Fig. 4.5) [6]; there is, however, no enhancement of this segregation at the martensite lath boundaries [7,8]. Most of the phosphorus and about half of the chromium at the grain boundaries is present in the first two or three monolayers, implying extremely localized elemental segregation, but the remaining chromium persists to a depth of about ten monolayers and is probably present in a precipitate form [8].

The majority of the systematic AES, STEM, and AEM studies of the changes in interfacial composition induced during aging have been carried out on 9Cr-1Mo steel. The observations of the increased segregation produced at interfaces in this and other steels during aging may be summarized as follows:

- Phosphorus displaces sulfur at the prior austenite grain boundaries of normalized-and-tempered HT9 steel (0.018% P) during aging at 540°C for 240 h [63].
- Phosphorus and chromium segregate in a commercial 12% Cr steel (0.02% P) aged at 500 to 675°C, producing enrichment ratios (interfacial:bulk concentrations) of about 700 and <2, respectively [64].
- Phosphorus, chromium, and molybdenum segregate at or adjacent to the prior austenite grain boundaries (as in the normalized-and-tempered condition) (Fig. 4.6) and at the martensite lath boundaries of 9Cr-1Mo steel (0.061% P) aged at 550°C for 1000 h [7]; the Mo, Cr, Si, and P are also enriched in the Laves phase (Fe_2Mo) formed at the boundaries.
- Silicon, phosphorus, molybdenum, and chromium segregation is observed at intergranular and, to a lesser extent, transgranular areas on the fracture surfaces of 9Cr-1Mo steels (0.025% P) aged at 500 to 550°C for times up to and in excess of 20 000 h [4,6,8]. Most of the chromium and an increasing proportion of the phosphorus are incorporated into the $M_{23}C_6$ and Fe_2Mo precipitates, respectively, during aging. The effect of aging at 500°C on the estimated amounts of phosphorus segregated in elemental form and incorporated in the Laves phase at the grain boundaries, as measured by scanning auger microprobe (SAM) analysis,

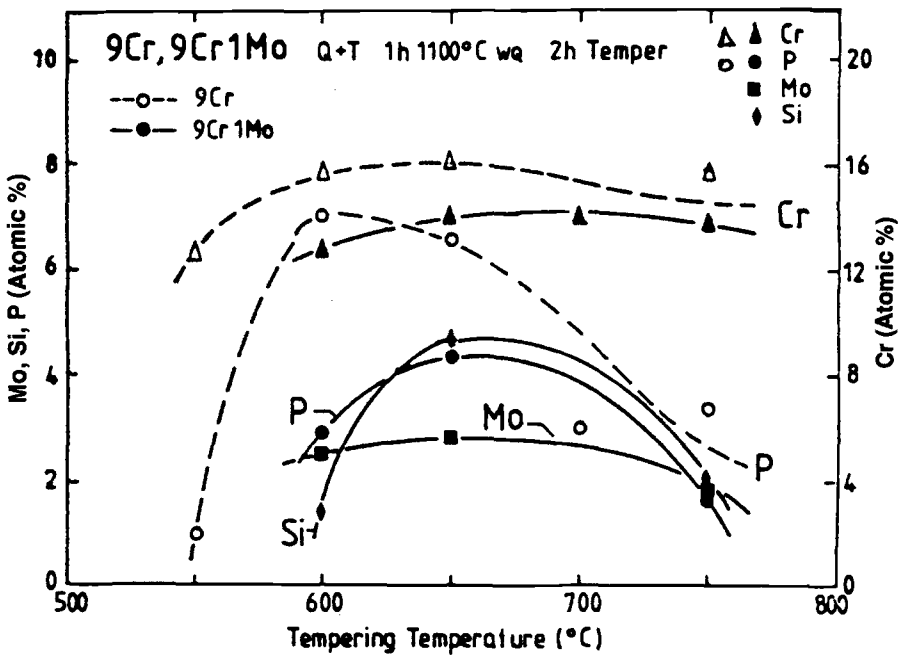

FIG. 4.5—Effect of molybdenum on the grain boundary composition during tempering of 9Cr-1Mo steel [6].

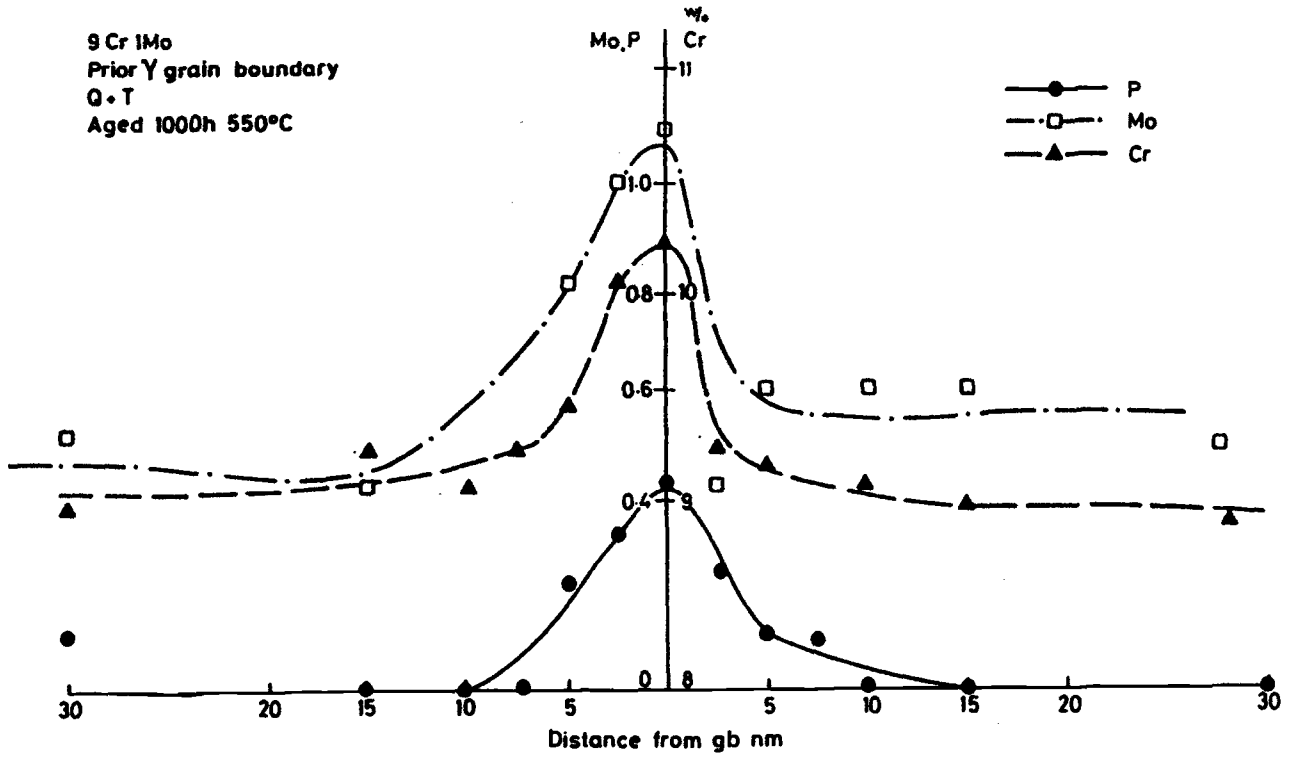

FIG. 4.6—Composition profiles for P, Mo, and Cr across prior austenite grain boundaries in aged 9Cr-1Mo steel as determined by high-resolution STEM analysis [7].

is shown in Fig. 4.7 [8]. The phosphorus attains levels of 1 to 2% in the Laves phase; M_6C precipitates absorb phosphorus more readily than some of the other phases, but significant concentrations of this element are not found in the $M_{23}C_6$ or Cr_2N particles.

- Phosphorus segregates at $M_{23}C_6$/matrix interfaces in the tempered 9Cr-1Mo steel [6,65]; however, the effect of further aging on the magnitude of this interfacial segregation does not appear to have been examined.
- Chromium also segregates at the prior austenite grain boundaries in the 12Cr-MoVNb (MANET) steel during aging at 700°C, and 1 mm size aggregates, tentatively identified as Cr-C complexes, have been detected in the matrix by small angle neutron scattering (SANS) [66]. In addition, long range fluctuations in the chromium concentration in the matrix of the normalized-and-tempered 12Cr-MoVNb (1.4914) steel have been observed by atom probe field ion microscopy (APFIM) following aging at 400°C for 17 000 h and at 500 and 550°C for 10 000 h [67].

The enhanced concentrations of phosphorus and other elements at the prior austenite grain boundaries observed after tempering result from either non-equilibrium and/or equilibrium segregation, while the interfacial segregation induced during aging occurs by the latter process. The driving force for the equilibrium segregation is the minimization of the free energy of the system when misfitting atoms diffuse from the matrix to the more accommodating sites at the prior austenite grain and lath boundaries. The thermodynamic modeling of the process in an ideal binary system with no solute-solute interactions [68] and in a ternary system where such interactions may have an important influence [69,70] have been suc-

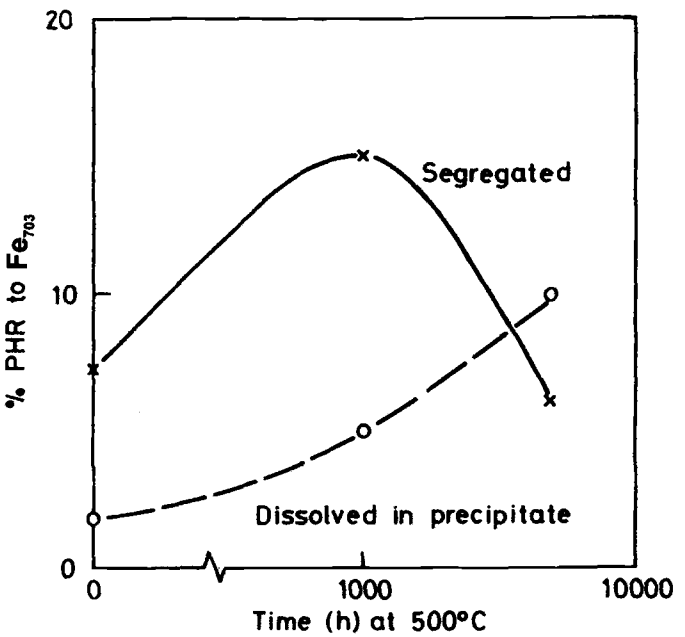

FIG. 4.7—Estimated amounts of phosphorus segregated in elemental form and dissolved in the Laves phase Fe_2Mo in the 9Cr-1Mo steel aged at 500°C [8]. [%PHR to Fe_{703} is the variation in the phosphorus peak height ratio (PHR) to iron peak at an Auger electron energy of 703 eV (Fe_{703}).]

cessful in providing a description of many aspects of the segregation behavior. However, these models cannot be readily applied to multi-component systems, such as the metastable high-chromium martensitic steels; this is because the microstructural changes occurring during tempering and subsequent aging also produce changes in the matrix compositions and, hence, the thermodynamic reference state [65]. In addition, other factors such as the diffusion kinetics, precipitation of particles at or near interfaces, chemical interactions, and site competition must be taken into account.

There is still considerable uncertainty concerning the role of alloying elements such as chromium and molybdenum in the equilibrium segregation of phosphorus. The observations of Cr, Mo, and P segregates at interfaces in steels may be attributed to co-segregation due to the high interaction energies of Cr-P and Mo-P complexes [69–71]. It has also been suggested [72] that site competition between C, N, and P is an important factor, with the chromium enhancing phosphorus segregation by removing carbon and nitrogen from solution to form carbonitrides. However, molybdenum (and vanadium and tungsten) in certain concentration ranges retard the phosphorus segregation in steels, possibly because the Mo-P interaction is so strong that precipitation occurs, with the result that the solubility of the phosphorus is reduced and the tendency to segregate thereby decreased. The beneficial effect of molybdenum is lost if it is incorporated into a carbide or intermetallic compound, and the rate of segregation of the phosphorus is then controlled by the rate of formation of the carbide or intermetallic compound. Likewise, phosphorus and tin in the lower alloy content steels may be immobilized by additions of the rare earth elements lanthanum and, to a lesser extent, cerium, which have high affinities for these impurities [73].

Stress-driven interfacial segregation can occur as a consequence of the interaction between the stress field of a loaded crack and solute atoms in the matrix. This interaction imposes a drift flow of under- and over-sized solutes that determines the migration in the vicinity of the crack tip; thus, enhanced segregation to the crack as well as the grain boundary ahead of the crack can result. A kinetic model of this process [74] has provided a satisfactory explanation of the stress-relief cracking within the heat affected zones (HAZs) of low-alloy steel welds at 300 to 650°C due to the stress-driven segregation of sulfur [75–77].

The effect of stress on elemental segregation in the high-chromium ferritic and martensitic steels has not been investigated. However, enhanced segregation of phosphorus in a 3.5Cr-MoV steel after aging at 340°C for 3 h under an applied tensile elastic stress of 80 MPa has been detected by AES [78]. Some enhancement of the interfacial concentrations of nitrogen and carbon are also found, but the grain boundary segregation of sulfur, evident after slow cooling (0.3°C s^{-1}) from 1100°C, is not affected by the subsequent aging at 340°C with or without stress application.

MECHANICAL PROPERTIES AND FRACTURE BEHAVIOR

A reduction in fracture toughness occurs when low-alloy steels are held in or slowly cooled through a critical temperature range, typically 300 to 600°C [6,65,79]. The embrittlement is manifested as an increase in the impact ductile-brittle transition temperature (DBTT) and is associated with a change in the low-temperature brittle fracture mode from transgranular cleavage to intergranular as depicted in Fig. 4.8. The equilibrium segregation of the impurity elements phosphorus, tin, and antimony to the prior austenite grain boundaries in otherwise relatively stable microstructures, and the resultant reductions in the intergranular cohesive strengths are primarily responsible for this process of reversible temper embrittlement (RTE) in the low-alloy steels [79–82]. The high-chromium martensitic steels also exhibit this type of embrittlement after aging, but the controlling factors and underlying mechanisms differ somewhat from those responsible for the RTE in low-alloy steels.

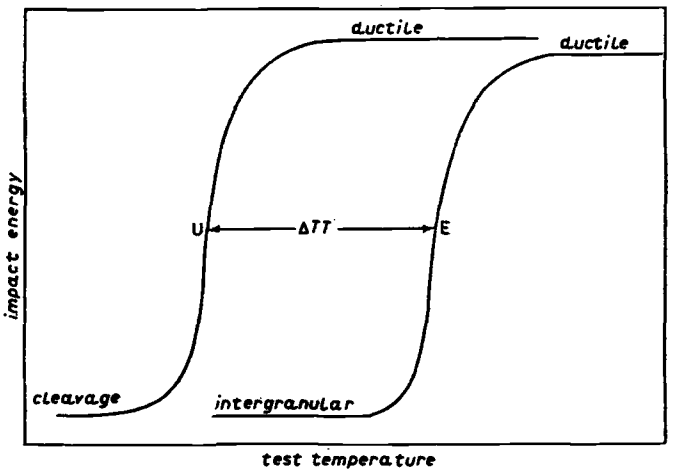

FIG. 4.8—Schematic illustration of the effect of RTE on the Charpy V-notch impact DBTT and low-temperature fracture mode [65]. U = unembrittled, E = embrittled.

Tensile

The tensile proof and ultimate stresses decrease progressively with increasing tempering temperature in the range 600 to 750°C for a series of 12Cr steels as shown in Fig. 4.9 [24]; there are associated increases in ductilities, particularly in the tempering temperature range 700 to 750°C, coincident with the rapid decrease in dislocation density, the formation of sub-grains, and the destruction of the martensite lath structure. The fractures remain fully ductile.

It has been suggested [83] that the 0.2% proof stresses ($\sigma_{0.2}$) of the normalized-and-tempered 12Cr steels are determined by the ferrite grain size (d) according to the Hall-Petch type of relationship plus a strengthening (σ_p) due to the precipitated carbides (and nitrides) described by an Orowan type of equation [84]:

$$\sigma_{0.2} = A' + B'd^{-1/2} + \sigma_p \quad (4.1)$$

$$\sigma_p = \frac{C'}{\lambda} \cdot \ln \frac{D}{2b} \quad (4.2)$$

where λ is the precipitate spacing, D is the precipitate particle diameter, b is the Burgers vector of the slip dislocation, and A′, B′, and C′ are constants.

There is also a good quantitative relationship between the ambient temperature tensile proof stresses and the carbon

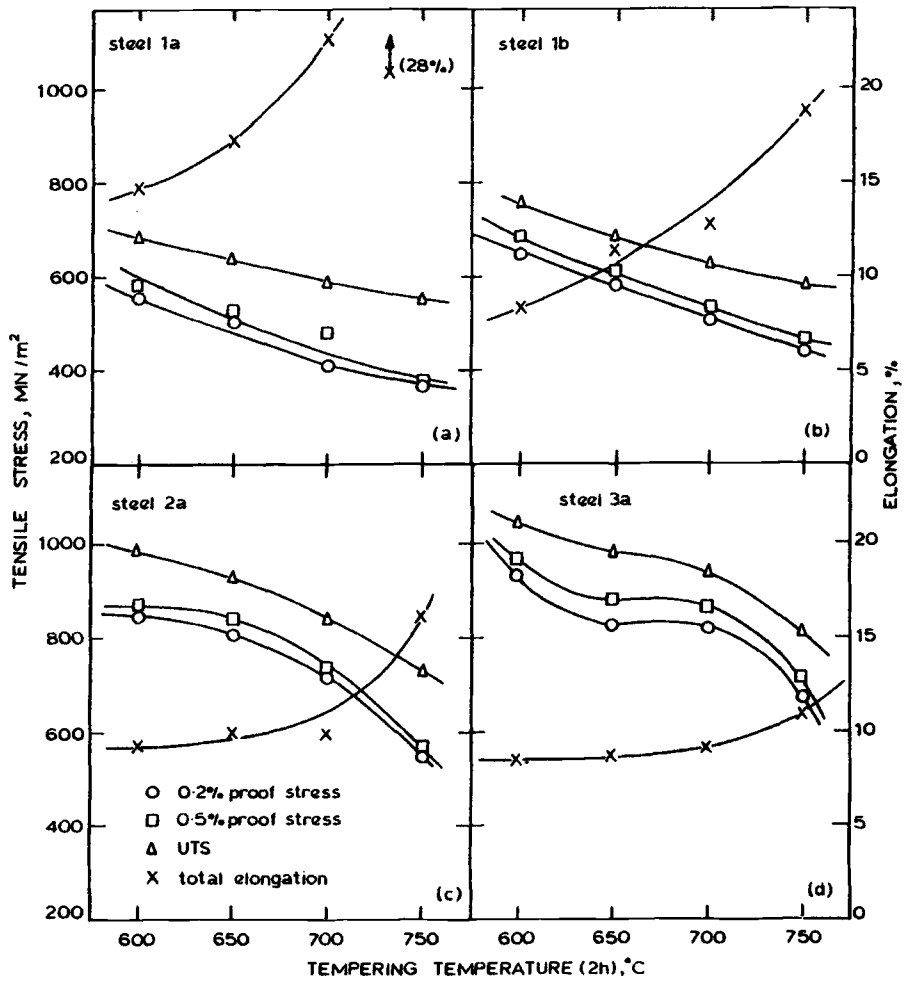

FIG. 4.9—Effects of tempering on the room temperature tensile properties of 12Cr steels [24]: (a) Steel 1a = 0.046C, 12Cr (FI), (b) Steel 1b = 0.10C, 12Cr (FI), (c) Steel 2a = 12Cr-MoV (FV607) and (d) Steel 3a = 12Cr-MoVNb (FV448).

and nitrogen contents of 12Cr-MoV steels tempered for 1 h at 650°C [83]:

$$\sigma_{0.2} = 710 + 770\,(C + N) \qquad (4.3)$$

where $\sigma_{0.2}$ is in MPa and C and N are in wt%. This equation simply reflects the increased strengthening due to the increased volume fraction of precipitates with increasing carbon and nitrogen contents.

In general, thermal aging has a relatively small effect on the ambient temperature tensile strengths and ductilities of the fully martensitic 9Cr-1Mo steel aged at 500 and 550°C for 1000 and 5000 h [1,8], modified 9Cr-1Mo steel aged at 482, 538, and 593°C for ≤50 000 h [85,86], and model 9Cr-1Mo alloys with various concentrations of phosphorus (<0.005% and 0.025–0.031%) and silicon (< 0.01% and 0.065 to 0.066%) and aged for 5000 h at 550°C [42]. However, the tensile reduction of area values and true strains to fracture of 9Cr-1Mo steels decrease after aging at 550°C for up to 5000 h (Fig. 4.10) [4,11,87], with the non-uniform (necking) elongation being primarily affected. Aging at the higher temperatures of 649 and 704°C produces reductions in strength and increases in the ductility of the modified 9Cr-1Mo steel [86]. Extensive brittle failures were not found in any of these tests, which were conducted above the DBTTs for the stress and strain conditions applied. Nevertheless, there is a partial change in fracture mode from micro-void coalescence to "chisel" type fracture with increasing aging time for the standard and model 9Cr-1Mo steels [8,42], and some secondary intergranular cracking is also produced in this type of steel when tested in both the tempered and aged conditions [4,87].

The duplex EM12 steel exhibits significant hardening, manifested as increases in tensile yield and ultimate strengths and reductions in ductility, following aging at temperatures in the range 400 to 600°C for times up to 30 000 h [10]. These changes in properties are attributed to the precipitation of the Laves phase (Fe_2Mo) in the δ-ferrite grains, the observed recovery of the properties after ≥1000 h at 550, and 600°C being due to overaging of the particles.

Impact

The prior austenite grain size and the tempered strength essentially determine the impact and toughness properties of the normalized-and-tempered high-chromium martensitic steels [24,88]. The effects of heat treatment on the impact

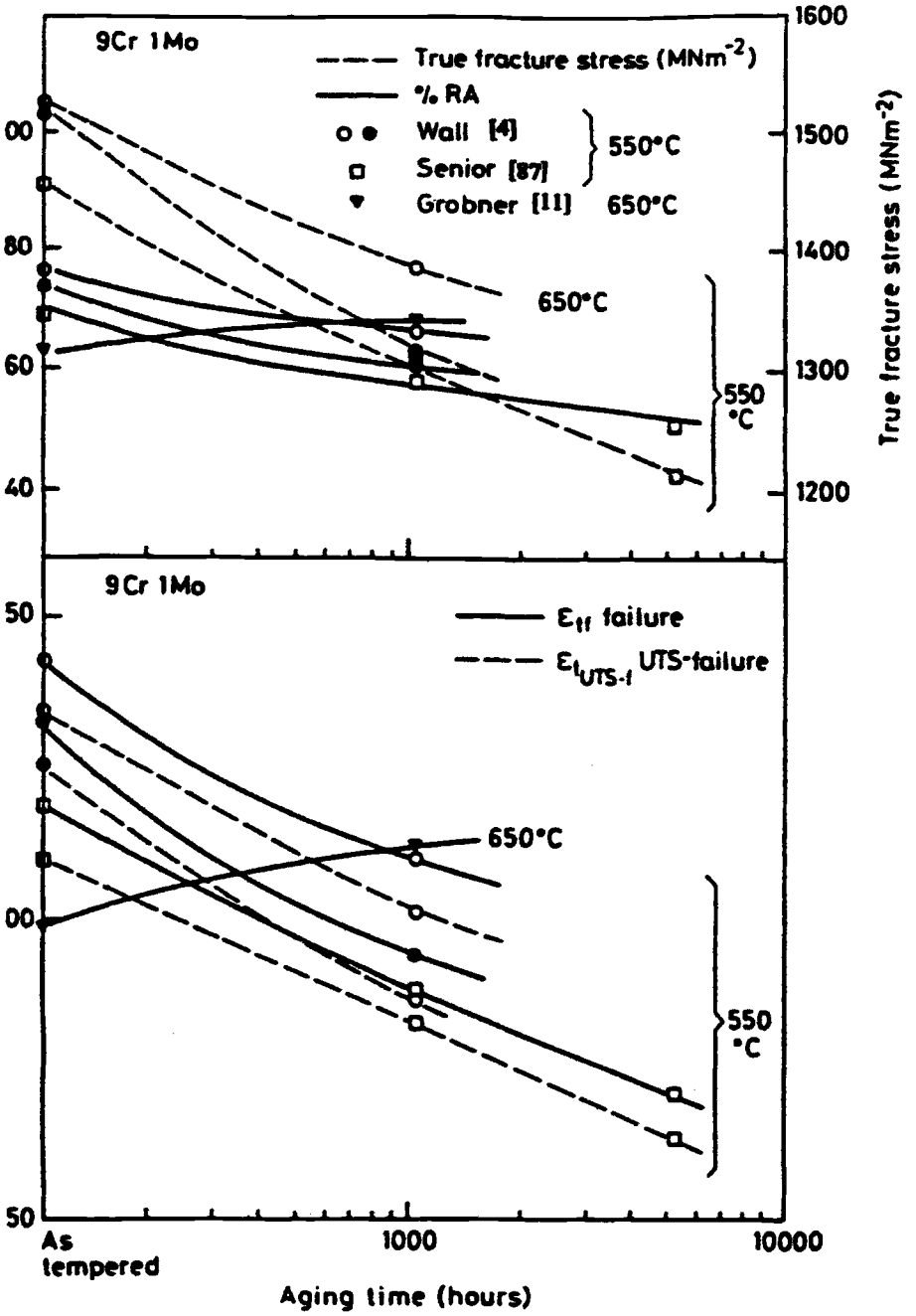

FIG. 4.10—Effects of thermal aging on the tensile ductility of 9Cr-1Mo steels [4,11,87].

DBTT curves of plain 12Cr (FI), 12Cr-MoV (FV607) and 12Cr-MoVNb (FV448) steels are shown in Fig. 4.11(a), (b), (c), and (d), respectively [24].

Increasing the austenitizing temperature from 950 to 1000°C and 950 to 1050°C, for a constant tempering condition of 750°C for 2 h, produces increases (ΔTs) in DBTTs from −85 to −60°C for the FI [Fig. 4.11(a)] and −90 to −60°C for the FV607 [Fig. 4.11(b)] steels, respectively, and no significant effects on the upper shelf energies (USEs). The ΔTs are due solely to the increase in prior austenite grain size with increasing austenitizing temperature (Fig. 4.12) [24] as the tempered strengths are comparable.

For a given austenitizing temperature of 1050°C, decreasing the tempering temperature from 750 to 650°C (time of 2 h) results in a ΔT of 45°C for the FV607 steel (from −60 to −15°C) together with a large reduction in the USE [Fig. 4.11(b)]; these effects are due to the increased tempered strength resulting from the lower tempering temperature and not to prior austenite grain-size variations.

An increase in austenitizing temperature from 1020 to 1100°C has very little effect on the prior austenite grain size of the 12% Cr-MoVNb (FV448) steel (Fig. 4.12) due to the inhibition of the grain growth by undissolved NbC particles [24]; however, increasing the strength by reducing the tem-

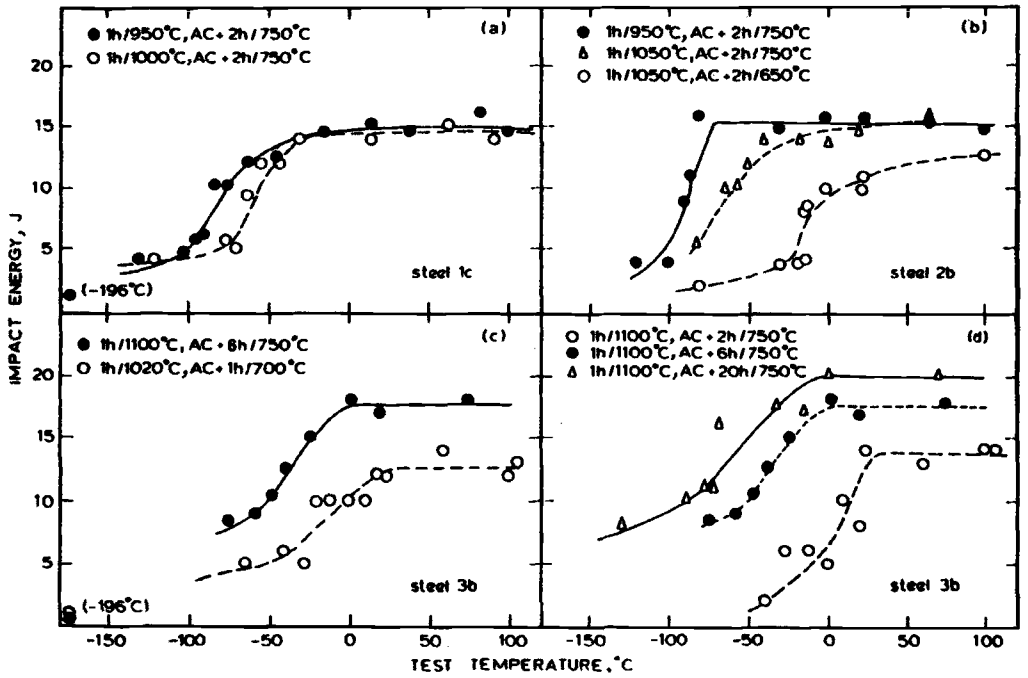

FIG. 4.11—Effects of heat treatment variations on the sub-size Charpy V-notch ductile-brittle transition curves of 12Cr steels [24]: (a) Steel 1c = 0.15C, 12Cr (FI), (b) Steel 2b = 12Cr-MoV (FV607), (c) and (d) Steel 3b = 12Cr-MoVNb (FV448).

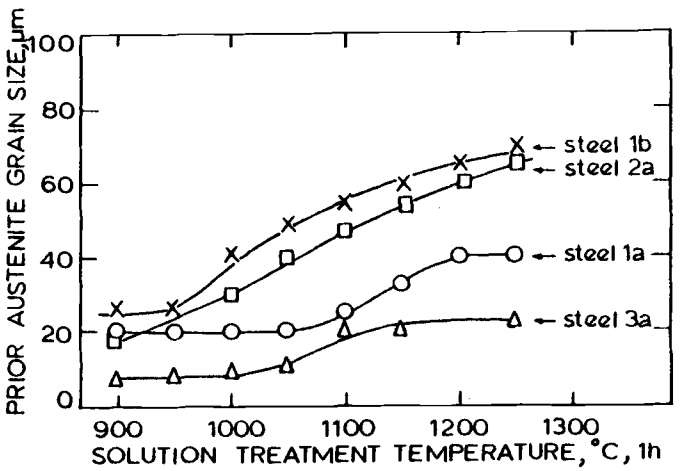

FIG. 4.12—Prior austenite grain growth characteristics of 12Cr steels [24]: Steel 1a = 0.046C; 12Cr (FI), Steel 1b = 0.10C; 12Cr (FI), Steel 2a = 12Cr-MoV (FV607), Steel 3a = 12Cr-MoVNb (FV448).

pering temperature and time from 750°C for 6 h to 700°C for 1 h produces a ΔT of 35°C (from −30 to +5°C) and a major reduction in the USE [Fig. 4.11(c)]. Similarly, increasing the tempered strength by decreasing the tempering time from 20 to 6 to 2 h at 750°C after austenitizing at 1100°C for 1 h results in ΔTs of 35 and 70°C (from −65 to −30 to +5°C) and large decreases in the USE [Fig. 4.11(d)].

An analysis of these impact and the corresponding tensile data show that a change in prior austenite grain size of $d^{-1/2} = 1\ mm^{-1/2}$ results in a change in DBTT of 23°C, while a ΔT of 2–5°C is produced for a tensile proof stress increase of 10 MPa [24]. Also, the USE values for the sub-size Charpy V-notch specimens of the 12Cr-MoV and 12Cr-MoVNb steels decrease by approximately 1 J for every 30 MPa increase in proof stress brought about by decreased tempering.

As stated in Chapter 3, the presence of δ-ferrite adversely affects the strength and toughness of the normalized-and-tempered high-chromium martensitic steels [83]. However, a δ-ferrite content of 0.5% in a 11Cr-MoVNb steel decreases the DBTT relative to that of a fully martensitic steel, while larger amounts of δ-ferrite in 12-14Cr-MoVNb and 12Cr-MoVW (HT9) steels produce increases in DBTT and reductions in USE [89–92]. These effects are attributed to the formation of massive dendritic carbides (mainly $M_{23}C_6$) at the δ-ferrite-matrix interfaces during cooling at critical rates from the austenitizing temperature [90–92]; the carbides initiate cleavage fractures which then propagate in the δ-ferrite grains at temperatures below the ductile-brittle transition and also nucleate ductile dimple fractures at temperatures corresponding to the upper shelf regions. Only isolated carbides are formed at the δ-ferrite grain boundaries in the steel containing 0.5% δ-ferrite, and the fracture processes are not adversely affected [90]. However, it is possible that the deleterious dendritic carbide structures may develop in the steels during prolonged aging or service exposure at high temperature, even when these structures are not formed during cooling from the austenitizing temperature [92].

Thermal aging produces increases in the Charpy V-notch impact DBTT and reductions in the USE of the high-chromium martensitic steels [4,6,86,87]. These effects are illustrated for the 9Cr-1Mo [4], modified 9Cr-1Mo [93], and 12Cr-MoV [94] fully martensitic steels in Fig. 4.13. The ΔTs

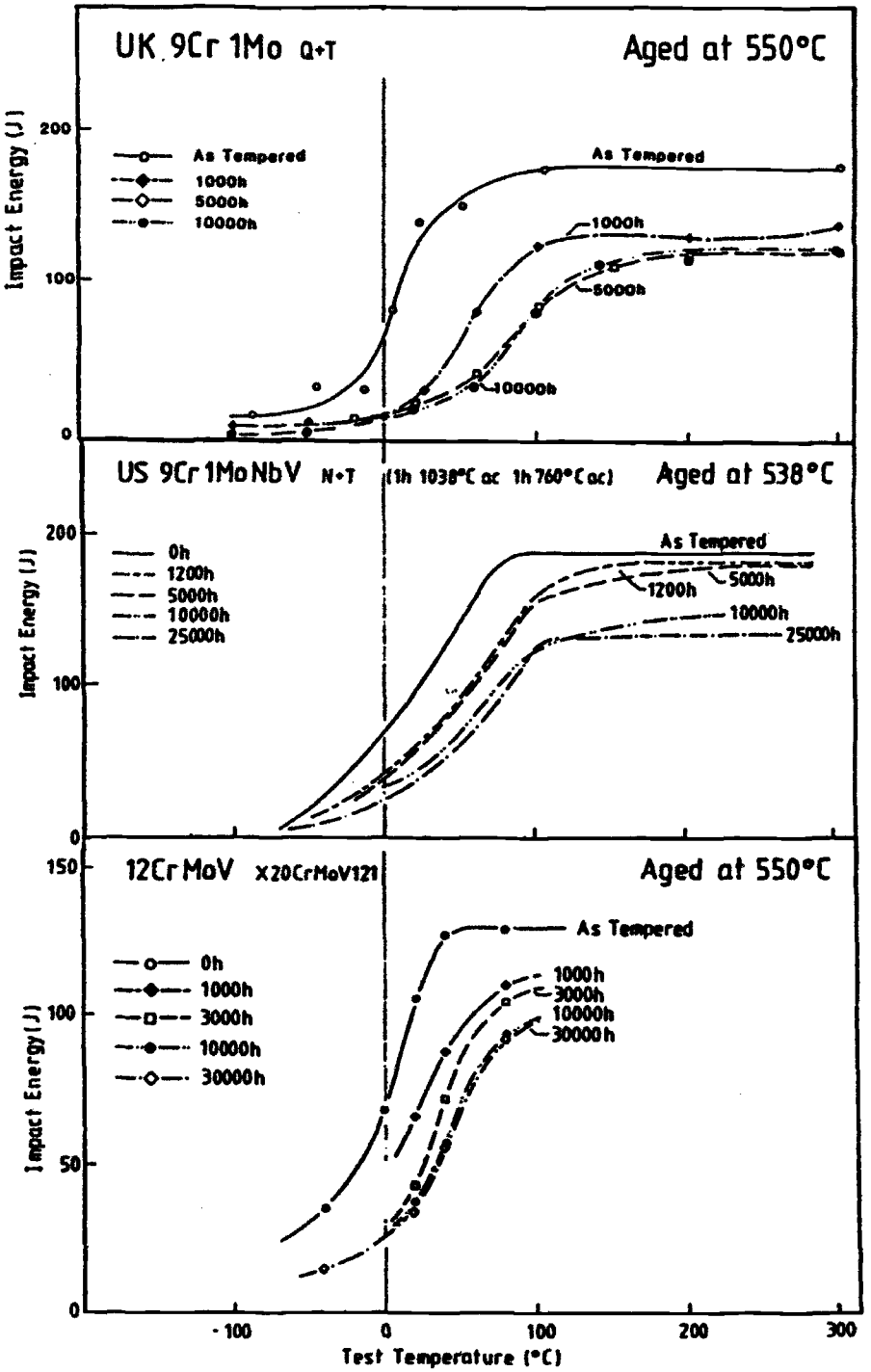

FIG. 4.13—Charpy V-notch impact transition curves for 9Cr-1Mo [4], modified 9Cr-1Mo [93], and 12Cr-MoV [94] steels aged at about 550°C.

produced by aging are listed for several steels in Table 4.5; the magnitude of the embrittlement is dependent on the steel composition and initial structure, aging temperature, and time, and the induced microstructural and local compositional changes.

The effects of aging temperature and time on the 67.8 J (50 ft-lb) DBTT of low (0.11%) and high (0.40%) silicon heats of the modified 9Cr-1Mo steel (the DBTTs of the normalized and tempered steels were −27 and −4°C, respectively) are shown in Fig. 4.14 [86]. The DBTTs increase with aging up to maxima and recover after long exposure times at 482, 538, and 593°C; however, the high silicon steel shows more rapid embrittlement and the recovery is less pronounced than in the low-silicon steel. The maximum embrittlement is produced by aging at 538°C for 25 000 h, the ΔTs for the low- and high-silicon grades being about 70 and 60°C, respectively. Smaller ΔTs are produced after aging for short and intermediate periods at 649 and 704°C, but the embrittlement, par-

TABLE 4.5—Effects of thermal aging on the increase (ΔT) in the Charpy V-notch impact ductile-brittle transition temperature (DBTT) of high-chromium martensitic steels.

Steel	Phosphorus Content (%)	Aging Temp (°C)	Aging Time (h)	ΔT (°C)	Reference
HT9 (12Cr-1MoVW)	0.018	500	240	10	63
	0.015	550	1000	30-50	28
	0.018	450	10000	0	15
		500	..	10	
		550	..	10	
		600	..	15-20	
		650	..	50	
X20CrMoV12.1 (12Cr-1MoV)	<0.018; <0.035	550	5000	<15	26
T91 (9Cr-1MoVNb)	0.010 (0.11% Si)	482	10000*	50	86
		538	25000*	70	
		593	25000*	60	
		649	1200*	25	
		704	50000*	30-35	
	0.010 (0.40% Si)	482	50000*	30-35	86
		538	25000*	60	
		593	1200*	45	
		649	5000*	35	
		704	50000*	20-25	
	0.006	<450	10000	0	15
		500	..	20	
		550	..	40	
		600	..	75-80	
		650	..	10	
F82H (8Cr-2WVTa)	0.005	<450	10000	0	15
		500	..	5	
		550	..	35	
		600	..	60	
		650	..	90	
F82 (8Cr-2WV)	0.003	<450	10000	0	15
		500	..	15	
		550	..	60	
		600	..	60	
		650	..	105	
9 & 12 Cr-2W	<0.002	600	1000	20-25	35

*Times to achieve maximum embrittlement during aging (duration ≤ 75,000 h).

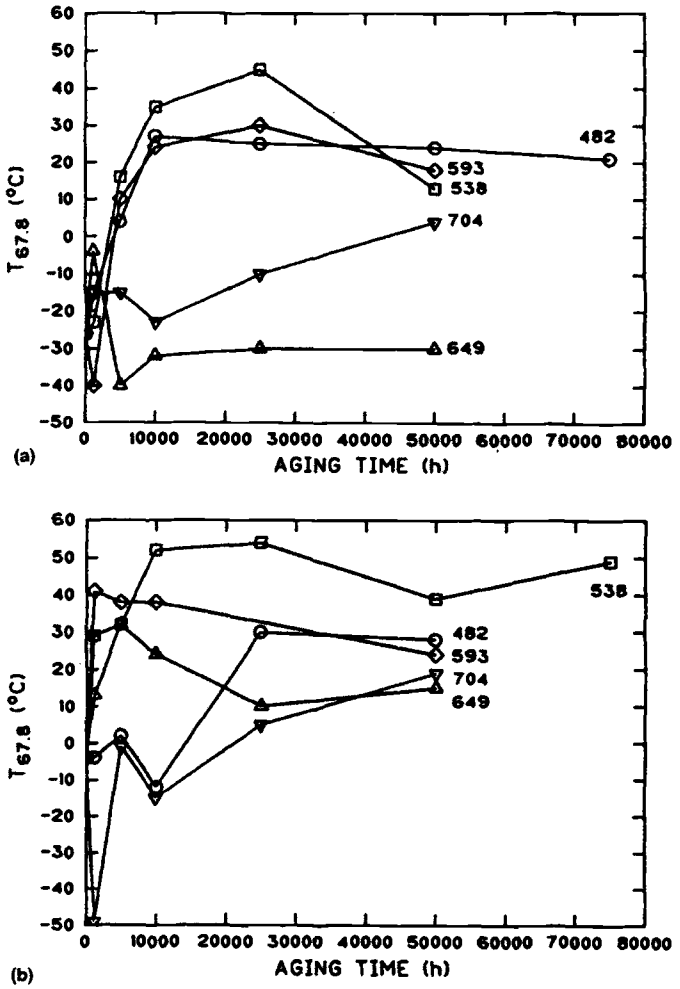

FIG. 4.14—DBTT measured at 67.8 J (50 ft.lb) as a function of aging time (≤75,000 h) and temperature (482, 538, 593, 649, and 704°C) for modified 9Cr-1Mo steel [86]. Top 0.11% Si, Bottom 0.40% Si.

ticularly of the high-silicon steel, approaches that induced at the lower temperatures after long aging times.

The Charpy V-notch impact transition curves for the 0.40% silicon-modified 9Cr-1Mo steel [93] have been reanalyzed, and the variations in the DBTT (100 J) and USE with aging temperature and time are illustrated in Fig. 4.15 [6]. The changes in the DBTT and USE exhibit similar kinetics, and the data confirm that the maximum effects are produced after aging at 500 to 550°C. The kinetics of the process are enhanced at the higher aging temperatures, but the magnitudes of the embrittlement are reduced; the transitory nature of the embrittlement is also evident, with the DBTT and USE recovering on prolonged exposure (≥10,000 h at ≥550°C).

It has been claimed that "475°C embrittlement," manifested as increases in the DBTT and reductions in the USE in notched impact tests and increases in the hardness at ambient temperature, is produced in weldments, particularly in the HAZs, of various 11-13Cr martensitic steels following isothermal aging at 340 to 600°C for times up to about 7000 h [95]. The effects are most pronounced after aging at 425°C, and the data suggest that this type of embrittlement might still occur during prolonged aging even at temperatures below 340°C. The magnitude of the embrittlement may be reduced by decreasing the chromium, nickel, and silicon contents, increasing the purity, and electron beam melting of the steels.

Creep and Creep-Rupture

The creep-rupture strengths of the highly alloyed 9 to 12% Cr martensitic steels are determined primarily by (i) solid-solution strengthening by Cr, Mo, and W and (ii) precipitation

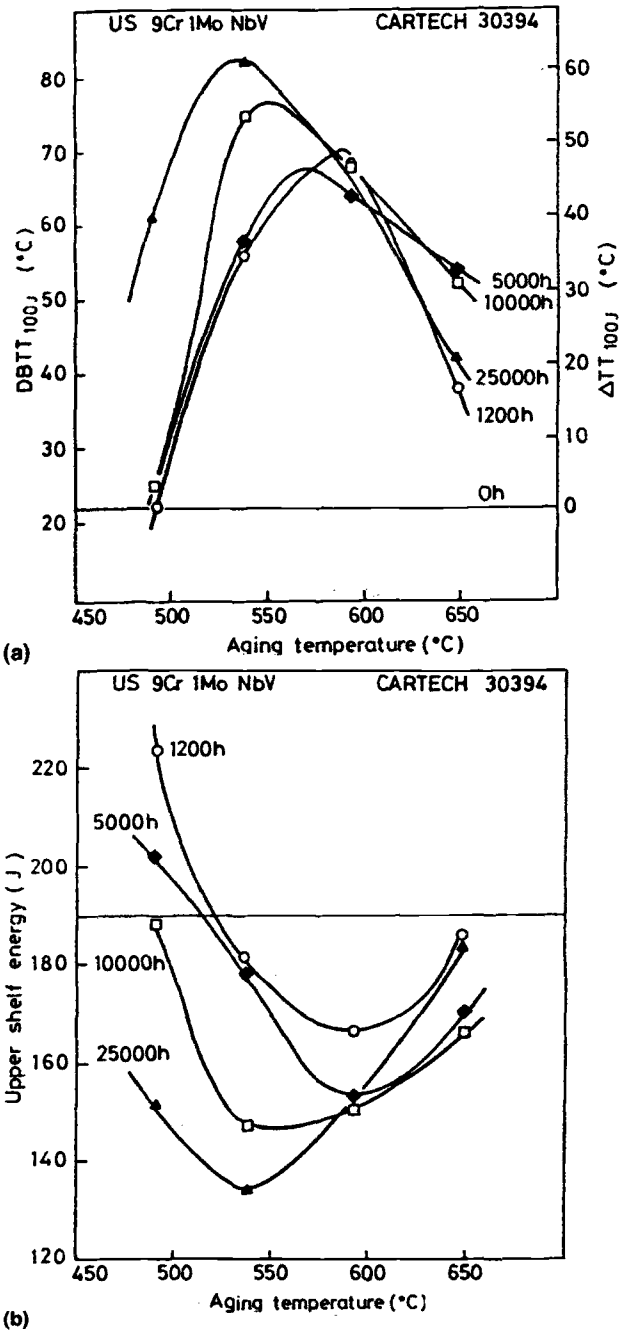

FIG. 4.15—Effect of aging temperature and time on the Charpy V-notch impact DBTT and USE of modified 9Cr-1Mo steel (0.40% Si) [6,93].

hardening by (a) the fine, stable MX phases produced during tempering and (b) the formation of VN and Nb(CN) particles during creep exposure due to the lower solubilities of these phases in the tempered martensite matrix at a testing temperature of about 600°C than in the austenite at the normalizing temperature and in the ferrite at the tempering temperature [21,22]. The precipitation of the Laves phases [Fe_2Mo; Fe_2W; $Fe_2(Mo,W)$] during the early stages of the creep-rupture tests may also produce some strengthening, but this subsequently decreases as a result of coarsening of the particles and the reduction in the chromium, molybdenum, and tungsten concentrations in solution when these elements are incorporated into the $M_{23}C_6$ and Laves phase particles.

The majority of steels with chromium contents ≤13% show inflections in the applied stress-rupture time curves, which are manifested as rapid reductions in creep-rupture strengths accompanied by corresponding increases in rupture ductilities during prolonged ($\leq 10^5$ h) exposure tests at 550°C; this was first reported in the 1960s [96,97] and has been termed "sigmoidal behavior." The characteristics of the sigmoidal behavior depend on the steel composition, initial heat treatment, and test temperature, the inflections generally occurring at shorter durations and lower stresses with increasing test temperature. This behavior is illustrated for two 12Cr-MoVNb steels containing 0.52 and 1.15% Ni in Fig. 4.16 [31]. It is due [31,98,99] in these and some other high-chromium martensitic steels to the progressive softening and recovery of the dislocation structure as a result of the coarsening of the $M_{23}C_6$ particles, the formation of Z-phase and the dissolution of M_2X and secondary MX precipitates under the combined influences of thermal exposure, applied stress, and plastic strain accumulation during creep; these processes are accelerated in the steel with the higher nickel content.

The microstructural degradation and the associated transition from precipitation to solid solution strengthening may be minimized in the 12Cr steels by restricting the nickel content to 0.5% (max), decreasing the niobium concentration to limit the precipitation of the Z-phase and thereby promote the retention of the fine, beneficial M_2X and secondary MX precipitates in the matrix [99].

Significant increases in the continuously measured creep rates of the MANET I steel after 10 000 to 20 000 h at 600°C, a few hundred hours at 650°C, and about 10 h at 700°C have also been reported [100]; this creep instability behavior is associated with a hyper-stoichiometric Al:N ratio (2.7) in the steel (0.054% Al; 0.02% N). This factor, coupled with the very low solubility of AlN in the ferritic matrix in high-chromium steels at temperatures of 600 to 700°C [22], results in little or no nitrogen being left in solution for the formation of the precipitation strengthening VN and Nb(CN) phases during the creep testing. However, the creep strengths of the MANET II steel (0.004–0.012% Al; 0.027–0.032% N) at 450 to 700°C and up to 10 000 h show little or no scatter and are, due to their hypo-stoichiometric Al:N ratio and the excess nitrogen in solution available for precipitation as VN and Nb(CN), superior to those of the MANET I steel [101]. Furthermore, the MANET II steel does not exhibit instabilities in its creep behavior.

A constant creep strength, termed "inherent creep strength" (ICS), may be achieved after long-term creep deformation at elevated temperature as a result of the microstructural degredation [102]. The creep-rupture strengths of Cr-Mo steels containing 1 to 12% Cr decrease towards a common level with increasing test temperature and time [103]. The ICS is determined by the composition of the ferrite matrix and is not dependent on the initial (as heat treated) microstructure. It is enhanced by solid-solution strengthening by molybdenum, the maximum ICS for a 0.2% carbon, high-chromium creep-resistant steel being achieved with 0.03% Mo [102].

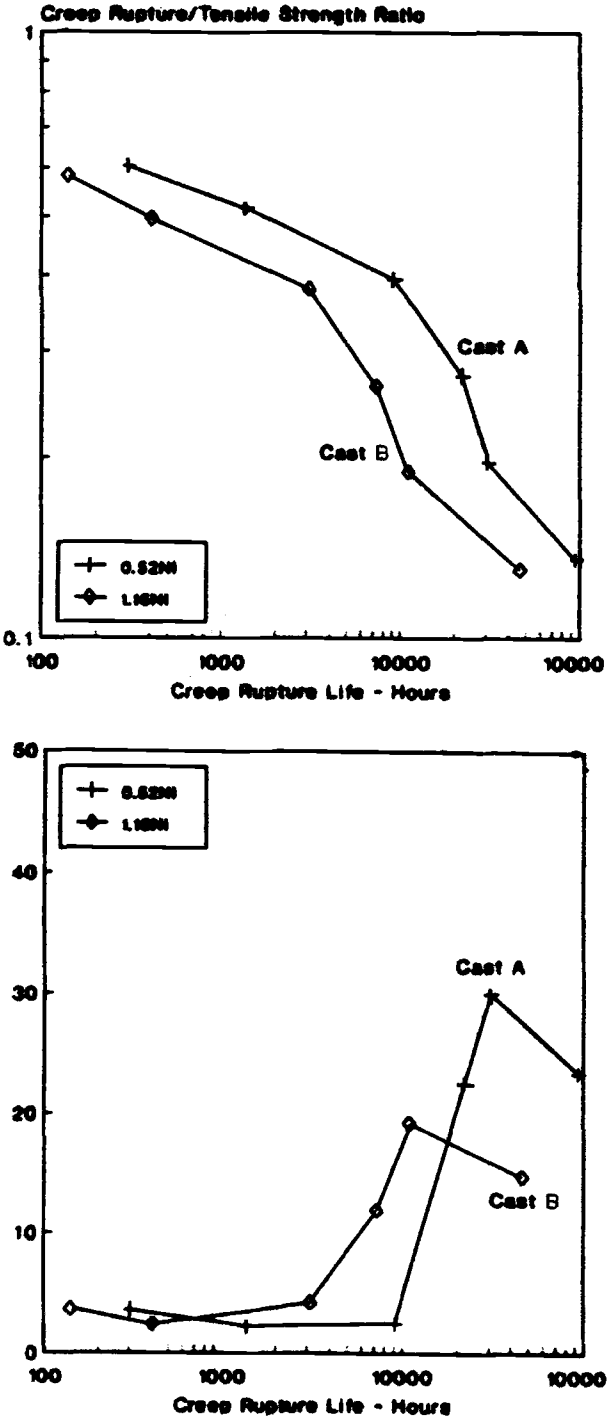

FIG. 4.16—Creep-rupture properties of 12Cr-MoVNb steels at 660°C [31].

Tungsten is also beneficial as it produces a more stable microstructure [104]; that is, recovery of the martensite structure and the associated decrease of the dislocation density proceeds more slowly in the tungsten-containing P92 (NF616) than in the modified 9Cr-1Mo (P91) steel [104], which in turn is more microstructurally stable than some of the other high-chromium martensitic steels [102].

Fracture

The embrittlement of the 12Cr-1MoVW (HT9) steel produced by aging for 1000 h at 550°C (see Table 4.5) is associated with increased grain boundary carbide precipitation and a tendency to form secondary intergranular cracks [28], while the aging-induced embrittlement of the 9Cr-1Mo steel (Fig. 4.13) is accompanied by a progressive change in fracture mode from cleavage or quasi-cleavage to intergranular at temperatures below the ductile-brittle transition temperature [3,4,6,9]. The latter behavior is also evident in bend tests at temperatures ranging from −196 to +50°C on blunt-notched specimens of the 9Cr-1Mo steel aged at 550°C for 1000 and 5000 h [105], and the brittle intergranular fracture can occur on a limited scale even in the upper-shelf region [4]. However, the majority of the steels for which impact embrittlement data are presented in Table 4.5 exhibit a transgranular cleavage or quasi-cleavage fracture mode with little or no intergranular cracking in the brittle, lower-shelf energy régime after aging.

The embrittlement and the associated grain boundary fracture in the aged high-chromium steels can be explained in terms of the following mechanisms [4,6]: (i) brittle separation of precipitate-free regions of the boundaries containing phosphorus segregates, (ii) decohesion at carbide precipitate/matrix interfaces to which phosphorus has segregated, and (iii) cleavage along internal boundaries of the brittle Laves phase. The embrittlement and intergranular failures produced by aging of the HT9 [22] and other high-chromium martensitic steels [59,80] may be explained by mechanisms (i) and (ii), as it appears that the Laves phase is not formed in these steels. The embrittlement of the 9Cr-1Mo steel after aging has been investigated in detail by STEM, AEM, and scanning electron microscopy (SEM) techniques, and the microstructural and local compositional changes correlated with the Charpy impact properties and fracture behavior [3,4,6,8,87]. It was established that the interfacial segregation of chromium, molybdenum, and silicon leads to the almost continuous precipitation of thin sheets of the Laves $Fe_2(Mo,Si)$ phase at the grain and lath boundaries during aging at 500 and 550°C, and that failure occurs by mechanism (iii). As illustrated in Fig. 4.7, interfacial elemental segregation of phosphorus occurs during the initial stages of aging, but increasing amounts of phosphorus are absorbed in the Laves phase at longer times and result in further reductions in the local fracture strength [105]. The recovery of the toughness after prolonged aging is associated with spheroidization of the Laves phase. Thus, contrary to the behavior of low-alloy steels in which the RTE is primarily due to the grain boundary segregation of phosphorus, the embrittlement in the aged 9Cr-1Mo and most probably other high-chromium martensitic steels is microstructurally dominated, with the phosphorus segregation having a secondary but, nevertheless, important influence.

In contrast to the observations on the 9Cr-1Mo steel cited above, the Laves phase is precipitated as discontinuous films and globular particles at the grain and lath boundaries in the modified 9Cr-1Mo steel [86]. The phosphorus contents of the standard 9Cr-1Mo steel heats examined were also much higher (0.061 and 0.025%) [7,8] than those of the modified 9Cr-1Mo steels (0.006 and 0.010%) [15,86] and reduced activation steels (≤0.005%) [15,35]. Consequently, the extent of the interfacial segregation and absorption of phosphorus into the Laves phase may have been more pronounced in the standard 9Cr-1Mo steel, thereby enhancing the reductions in the grain boundary cohesive strength. Thus, while intergranular fractures are not commonly produced in many of the aged high-chromium steels, there is no doubt that the formation of the Laves phase contributes to the observed embrittlement. Although the precise mechanism responsible for the embrittlement has not been identified [86], it is probable that the Laves phase precipitation and phosphorus segregation facilitate transgranular cleavage in these steels by lowering the fracture stress at the martensite lath boundaries.

The results of extensive STEM and AEM studies of the ductile void nucleation and growth processes in 9Cr-1Mo steel [65,87] have confirmed earlier predictions [1,4] that the reductions in the Charpy V-notch impact USEs and tensile ductilities produced by aging are associated with the $M_{23}C_6$ and Laves Fe_2Mo particles located at the martensite lath boundaries. The $M_{23}C_6$ particles are primarily responsible for the ductile fracture in the "as-tempered" steel; voids form at these carbides and grow, finally coalescing and linking up with larger cavities nucleated at inclusions. Phosphorus segregation to the carbide/matrix interfaces during the initial stages of aging at 550°C weakens the interface, thereby allowing void nucleation to occur at lower levels of deformation and resulting in reduced ductility and ductile fracture toughness. Voids form readily on the Laves particles produced at the lath boundaries during more prolonged aging and increase the number of nucleation sites; however, the incorporation of phosphorus into the Fe_2Mo leads to a partial recovery of the carbide/matrix interfacial strength.

Finally, the embrittlement produced by thermal aging can be minimized or suppressed by controlling the residual elements in the high-chromium fully martensitic steels [6]. Reducing the silicon content delays or inhibits the Laves phase formation, thereby slowing down the rate of embrittlement and promoting more rapid recovery. Decreasing the bulk phosphorus content to about 0.005% would also be beneficial in reducing the amount of intergranular fracture and, hence, the ΔT as well as maintaining a high upper-shelf toughness.

REFERENCES

[1] S. J. Sanderson, in: Ferritic Steels for Fast Reactor Steam Generators, Eds. S. F. Pugh and E. A. Little (British Nuclear Energy Society, London, 1977) 120.

[2] R. D. Leapman, S. J. Sanderson, and M. J. Whelan, Metal Sci. 12 (1978) 215.

[3] J. M. Titchmarsh, M. Wall, and B. C. Edwards, in: Proc. Workshop on Analytical Electron Microscopy, Eds. D. B. Williams and D. C. Joy (San Francisco Press, San Francisco, CA, 1984) 247.

[4] M. Wall, Temper Embrittlement in 9% Cr Steels, Ph.D. Thesis, Imperial College, University of London, 1985.
[5] J. M. Titchmarsh C. M. Shepherd, and I. A. Vatter, The Measurement of Chemical Composition with High Spatial Resolution Using a Dedicated Scanning Transmission Electron Microscope, UKAEA Report AERE-R 12317, February 1987.
[6] M. Wall, A Review of Thermal Aging Effects in High Chromium Ferritic Steels, UKAEA Report AERE-R 12812, January 1987.
[7] I. M. Vatter and J. M. Titchmarsh, Transmission Electron Microscope Investigation of Boundary Composition in 9%Cr-1%Mo Steel, UKAEA Report AERE-R12562, February 1987.
[8] C. A. Hippsley and N. P. Haworth, Mat. Sci. and Tech. 4 (1988) 791.
[9] J. A. Hudson, S. G. Druce, G. Gage, and M. Wall, J. Theor. Appl. Fracture Mech. 10 (1988) 123.
[10] P. Billard, J. R. Donati, D. Guttmann, M. Guttmann, S. Licheron, and J. C. Van Duysen, in: Ferritic Alloys for Use in Nuclear Energy Technologies, Eds. J. W. Davis and D. J. Michel (Met. Soc. AIME, Warrendale, PA, 1984) 425.
[11] P. J. Grobner and W. C. Hagel, Metall. Trans. 11A (1980) 633.
[12] M. Pelletier, R. M. Vilar, and G. Cizeron, J. Nucl. Mater. 105 (1982) 237.
[13] M. Suzuki, A. Hishinuma, P. J. Maziasz, and T. Sawai, J. Nucl. Mater. 170 (1990) 270.
[14] J. M. Vitek and R. L. Klueh, Metall. Trans., 14A (1983) 1047.
[15] M. Tamura, H. Hayakawa, A. Yoshitake, A. Hishinuma, and T. Kondo, J. Nucl. Mater. 155-157 (1988) 620.
[16] W. B. Jones, C. R. Hills, and D. H. Polonis, Metall. Trans. 22A (1991) 1049.
[17] K. Tokuno, K. Hamada, R. Uemori, T. Takeda, and K. Itoh, Scripta Metall. et Mater. 25 (1991) 871.
[18] K. Tokuno, K. Hamada, and T. Takeda, J. Metals 44(4) (1992) 25.
[19] P. J. Maziasz and R. L. Klueh, in: Effects of Radiation on Materials: 16th International Symposium, ASTM STP 1125, Eds. A. S. Kumar, D. S. Gelles, R. K. Nanstad, and E. A. Little, (American Society for Testing and Materials, Philadelphia, PA, 1992) 1135.
[20] C. R. Brinkman, B. G. Gieseke, and P. J. Maziasz, in: Microstructures and Mechanical Properties of Aging Material, Eds. P. K. Liaw, R. Viswanathan, K. L. Murty, E. P. Simonen, and D. Frear (The Minerals, Metals and Materials Soc., Warrendale, PA, 1993) 107.
[21] J. Orr and L. Woollard, in: Microstructural Development and Stability in High Chromium Ferritic Power Plant Steels, Eds. A. Strang and D. J. Gooch (The Inst. of Materials, London, Book 667, 1997) 53.
[22] V. Foldyna, Z. Kuboň, A. Jakovová, and V. Vodárek, in: Microstructural Development and Stability in High Chromium Ferritic Power Plant Steels, Eds. A. Strang and D. J. Gooch (The Inst. of Materials, London, Book 667, 1997) 73.
[23] H. Cerjak, V. Foldyna, P. Hofer, and B. Schaffernak, in: Microstructural Development and Stability in High Chromium Ferritic Power Plant Steels, Eds. A. Strang and D. J. Gooch (The Inst. of Materials, London, Book 667, 1997) 145.
[24] E. A. Little, D. R. Harries, F. B. Pickering, and S. R. Keown, Metals Tech. 4 (1977) 205.
[25] E. A. Little and L. P. Stoter, in: Effects of Irradiation on Materials: Eleventh Conference, ASTM STP 782, Eds. H. R. Brager and J. S. Perrin (American Society for Testing and Materials, Philadelphia, PA, 1982) 207.
[26] E. Tolksdorf, K. Schneider, and H. W. Grünling, in: Ferritic Alloys for Use in Nuclear Energy Technologies, Eds. J. W. Davis and D. J. Michel (Met. Soc. AIME, Warrendale, PA, 1984) 371.
[27] H. Berns and F. Krafft, in: Rupture Ductility of Creep Resistant Steels, Ed. A. Strang (The Inst. of Metals, London, Book No. 522, 1991) 116.
[28] T. Lechtenberg, W. M. Garrison, and J. M. Hyzak, in: Ferritic Alloys for Use in Nuclear Energy Technologies, Eds. J. W. Davis and D. J. Michel (Met. Soc. AIME, Warrendale, PA, 1984) 365.
[29] R. G. Faulkner, G. J. Adetunji, W. E. Voice, E. Materna-Morris, K. Ehrlich, and K. Anderko, in: Materials for Nuclear Reactor Core Applications, Vol. I (British Nuclear Energy Society, London, 1987) 253.
[30] E. Materna-Morris, M. Schirra, and K. Ehrlich, in: Materials for Nuclear Reactor Core Applications, Vol. I (British Nuclear Energy Society, London, 1987) 263.
[31] A. Strang and V. Vodárek, in: Microstructural Development and Stability in High Chromium Ferritic Power Plant Steels, Eds. A. Strang and D. J. Gooch, (The Inst. of Materials, London, Book 667, 1997) 31.
[32] V. S. Agueev, V. N. Bykov, A. M. Dvoryashin, V. N. Golovanov, E. A. Medvendeva, V. V. Romaneev, V. K. Sharmardin, and A. N. Vorobiev, in: Effects of Radiation on Materials: 14th International Symposium, ASTM STP 1046, Vol. I, Eds. N. H. Packan, R. E. Stoller, and A. S. Kumar (American Society for Testing and Materials, Philadelphia, PA, 1989) 98.
[33] M. Tamura, H. Hayakawa, M. Tanimura, A. Hishinuma, and T. Kondo, J. Nucl. Mater. 141-143 (1986) 1067.
[34] Y. Kohno, D. S. Gelles, A. Kohyama, M. Tamura, and A. Hishinuma, J. Nucl. Mater. 191-194 (1992) 868.
[35] F. Abe, H. Araki, T. Noda, and M. Okada, J. Nucl. Mater. 155-157 (1988) 656.
[36] A. Kimura, H. Kayano, T. Misawa, and H. Matsui, J. Nucl. Mater. 212-215 (1994) 690.
[37] B. Nath, E. Metcalfe, and J. Hald, in: Microstructural Development and Stability in High Chromium Ferritic Power Plant Steels, Eds. A. Strang and D. J. Gooch (The Inst. of Materials, London, Book 667, 1997) 123.
[38] R. W. Vanstone, H. Cerjak, V. Foldyna, J. Hald, and K. Spiradek, in: Microstructural Development and Stability in High Chromium Ferritic Power Plant Steels, Eds. A. Strang and D. J. Gooch (The Inst. of Materials, London, Book 667, 1997) 93.
[39] K. H. Mayer, H. Cerjak, P. Hofer, E. Letofsky, and F. Schuster, in: Microstructural Development and Stability in High Chromium Ferritic Power Plant Steels, Eds. A. Strang and D. J. Gooch (The Inst. of Materials, London, Book 667, 1997) 105.
[40] T. Fujita, K. Asakura, and Y. Otoguro, Metall. Trans. 12A (1981) 1071.
[41] Y. Hosoi, N. Wade, S. Kunimitsu, and T. Urita, J. Nucl. Mater. 141-143 (1986) 461.
[42] G. R. Jordan, S. J. Andrews, and C. A. Hippsley, Mat. Sci. and Tech. 9 (1993) 1115.
[43] F. B. Pickering, Physical Metallurgy and the Design of Steels (Applied Science Publishers Ltd., London, 1983).
[44] R. D. Griffin, R. A. Dodd, G. L. Kulcinski, and D. S. Gelles, Metall. Trans. 21A (1990) 1853.
[45] R. D. Griffin, D. S. Gelles, R. A. Dodd, and G. L. Kulcinski, J. Nucl. Mater. 179-181 (1991) 714.
[46] H. J. Goldschmidt, Interstitial Alloys (Butterworths, London, 1967).
[47] H. J. Goldschmidt, J. Inst. Metals 97 (1969) 173.
[48] R. Lagneborg, Trans. Amer. Soc. Metals 60 (1967) 67.
[49] P. J. Grobner, Metall. Trans. 4 (1973) 251.
[50] J. Hald and Z. Kuboň, in: Microstructural Development and Stability in High Chromium Ferritic Power Plant Steels, Eds. A. Strang and D. J. Gooch (The Inst. of Materials, London, Book 667, 1997) 159.
[51] J. D. Robson and H. K. D. H. Bhadeshia, in: Microstructural Development and Stability in High Chromium Ferritic Power Plant Steels, Eds. A. Strang and D. J. Gooch (The Inst. of Materials, London, Book 667, 1997) 179.
[52] J.-C. Brachet, L. Gavard, C. Boussidan, C. Lepoittevin, S. Denis and C. Servant, J. Nucl. Mater. 258-263 (1998) 1307.

[53] B. Sundman, B. Jansson and J.-O. Andersson, Calphad 9 (1985) 153.
[54] J. D. Robson and H. K. D. H. Bhadeshia, Mat. Sci. Tech 13 (1997) 631 and 640.
[55] J. D. Robson and H. K. D. H. Bhadeshia, in: Microstructural Stability of Creep Resistant Alloys for High Temperature Plant Applications, Eds. A. Strang, J. Cawley and G. W. Greenwood (The Inst. of Materials, London, Book 682, 1998) 395.
[56] P. Polcik, S. Straub, D. Henes and W. Blum, in: Microstructural Stability of Creep Resistant Alloys for High Temperature Plant Applications, Eds. A. Strang, J. Cawley and G. W. Greenwood (The Inst. of Materials, London, Book 682, 1998) 405.
[57] R. G. Faulkner, Acta. Met. 35 (1987) 2905.
[58] R. G. Faulkner, L. Schäfer, G. J. Adetunji, and E. A. Little, J. Nucl. Mater. 155-157 (1988) 612.
[59] T. M. Williams, A. M. Stoneham, and D. R. Harries, Met. Sci., 10 (1976) 14.
[60] D. R. Harries and A. D. Marwick, Phil. Trans. Roy. Soc. A295 (1980) 197.
[61] R. G. Faulkner, J. Mat. Sci. 16 (1981) 373.
[62] J. M. Hyzak and W. M. Garrison, in: Ferritic Alloys for Use in Nuclear Energy Technologies, Eds. J. W. Davis and D. J. Michel (Met. Soc. AIME, Warrendale, PA, 1984) 385.
[63] R. H. Jones and M. T. Thomas, in: Ferritic Alloys for Use in Nuclear Energy Technologies, Eds. J. W. Davis and D. J. Michel (Met. Soc. AIME, Warrendale, PA, 1984) 395.
[64] P. Lemble, A. Pineau, J. L. Castagne, P. Dumoulin, and M. Guttmann, Met. Sci. 13 (1979) 496.
[65] M. Wall, in: Proc. Int. School of Physics Enrico Fermi, Course CVI, Current Trends in the Physics of Materials, Eds. G. F. Chiarotti, F. Fumi, and M. P. Tosi (North Holland, Amsterdam, 1990) 161.
[66] R. Coppola, F. Fiori, E. A. Little and M. Magnani, J. Nucl. Mater. 245 (1997) 131.
[67] E. Camus, N. Wanderka, S. Welzel, E. Materna-Morris and H. Wollenberger, Mater. Sci. Eng. A250 (1998) 37.
[68] D. McLean, Grain Boundaries in Metals (Oxford University Press, Oxford, U.K., 1957).
[69] M. Guttmann, Met. Sci. 10 (1976) 337.
[70] M. Guttmann, Phil. Trans. Roy. Soc. A295 (1980) 169.
[71] B. C. Edwards, B. L. Eyre, and J. M. Titchmarsh, in: Advances in the Physical Metallurgy and Application of Steels (The Metals Society, London, 1981) 246.
[72] H. Erhart and H. J. Grabke, Met. Sci. 15 (1981) 401.
[73] M. P. Seah, P. J. Spencer, and E. D. Hondros, Met. Sci. 13 (1979) 307.
[74] H. Rauh, Stress-Driven Solute Segregation Near Crack Tips: Theoretical Modelling and Application to the Intergranular Fracture of Heterogeneous Materials, UKAEA Report AERE Report R 13735, January 1990.
[75] C. A. Hippsley, H. Rauh, and R. Bullough, Acta Metall. 32 (1984) 1381.
[76] C. A. Hippsley, Acta Metall. 35 (1987) 2399.
[77] H. Rauh, C. A. Hippsley, and R. Bullough, Acta Metall. 37 (1989) 269.
[78] A. M. Ilyin and V. N. Golovanov, J. Nucl. Mater. 233-237 (1996) 233.
[79] S. F. Pugh, An Introduction to Grain Boundary Fracture in Metals (The Inst. of Metals, London, Book No. 464, 1991).
[80] C. J. McMahon, Met. Sci. Eng. 25 (1976) 233.
[81] C. L. Briant and S. K. Banjeri, Int. Met. Rev. 23 (1978) 164.
[82] B. C. Edwards, B. L. Eyre, and G. Gage, Acta Metall. 28 (1980) 335.
[83] F. B. Pickering, in: Microstructural Development and Stability in High Chromium Ferritic Power Plant Steels, Eds. A. Strang and D.J. Gooch (The Inst. of Materials, London, Book 667, 1997) 1.
[84] K. Onel and J. Nutting, Met. Sci. 13 (1979) 573.
[85] J. R. DiStefano and V. K. Sikka, Summary of Modified 9Cr-1Mo Steel Development Program: 1975-1985, Oak Ridge National Laboratory, ORNL-6303, October 1986.
[86] D. J. Alexander, P. J. Maziasz, and C. R. Brinkman, in: Microstructures and Mechanical Properties of Aging Material, Eds. P. K. Liaw, R. Viswanathan, K. L. Murty, E. P. Simonen, and D. Frear (The Minerals, Metals and Materials Soc., Warrendale, PA, 1993) 343.
[87] B. Senior, Ductile Fracture of 9%Cr 1%Mo Steel, Ph. D. Thesis, University of Liverpool, September 1985.
[88] E. A. Little, D. R. Harries and F. B. Pickering, in: Ferritic Steels for Fast Reactor Steam Generators, Eds. S. F. Pugh and E. A. Little (British Nuclear Energy Society, London, 1977) 136.
[89] B. A. Chin and R. C. Wilcox, in: Ferritic Alloys for Use in Nuclear Energy Technologies, Eds. J. W. Davis and D. J. Michel (Met. Soc. AIME, Warrendale, PA, 1984) 347.
[90] E. Materna-Morris, Scanning Microscopy 4 (1990) 287.
[91] K. Anderko, L. Schäfer and E. Materna-Morris, J. Nucl. Mater. 179-181 (1991) 492.
[92] E. Materna-Morris and H. Finkler, Prakt. Metallogr. 30 (1993) 441.
[93] V. K. Sikka, in: Pressure Vessels and Piping: Materials for Nuclear Steam Generators, (American Society of Mechanical Engineers, New York, 1985) .
[94] J. W. Schinkel, P. F. Rademakers, B. R. Drenth, and C. P. Sheepens, in: Production, Fabrication and Application of Ferritic Steels for High Temperature Applications, Ed. A. K. Khare (American Society for Metals, Metals Park, OH, 1985) 131.
[95] Yu. I. Kazennov, E. A. Krylov, A. V. Minaev, R. H. Gibadullin, and V. V. Brovko, J. Nucl. Mater. 233-237 (1996) 305.
[96] J. H. Bennewitz, in: Proc. Joint Int. Creep Conf. (Inst. Mech. Engng., London, 1963) S-81.
[97] T. Marrison and A. Hogg, J. Metal Soc. 151 (1972).
[98] A. Strang, V. Foldyna, A. Jakobová, Z. Kuboň, V. Vodárek and J. Lenert, in: Advances in Turbine Materials, Design and Manufacturing, Eds. A. Strang, W. M. Banks, R. D. Conroy and M. J. Goulette, (The Inst. of Materials, London, Book 689, 1997) 603.
[99] A. Strang and V. Vodárek, in: Microstructural Stability of Creep Resistant Alloys for High Temperature Plant Applications, Eds. A. Strang, J. Cawley, and G. W. Greenwood, (The Inst. of Materials, London, Book 682, 1998) 117.
[100] M. Schirra and K. Anderko, Steel Research No. 6 (1990) 242.
[101] M. Schirra, P. Graf, S. Heger, H. Meinzer, and W. Schweiger, MANET II, Untersuchungsergebnisse zum Umwandlungs-und Vergütungsverhalten und Prüfung mechanischer Eigenschaften, Kernforschungszentrum Karlsruhe, KfK Report 5177, May 1993.
[102] K. Kimura, H. Kushima, F. Abe, K. Yagi, and H. Irie, in: Advances in Turbine Materials, Design and Manufacturing, Eds. A. Strang, W. M. Banks, R. D. Conroy, and M. J. Goulette, (The Inst. of Materials, London, Book 689, 1997) 257.
[103] F. Abe and K. Yagi, in: Advances in Turbine Materials, Design and Manufacturing, Eds. A. Strang, W. M. Banks, R. D. Conroy, and M. J. Goulette (The Inst. of Materials, London, Book 689, 1997) 750.
[104] P. J. Ennis, A. Zieliñska-Lipiec, and A. Czyrska-Filemonowicz, in: Microstructural Stability of Creep Resistant Alloys for High Temperature Plant Applications, Eds. A. Strang, J. Cawley, and G. W. Greenwood, (The Inst. of Materials, London, Book 682, 1998) 135.
[105] M. Wall, C. E. Lane and C. A. Hippsley, Acta Metall. and Mater. 42 (1994) 1295.

5

Oxidation, Corrosion, and Compatibility

This chapter is primarily devoted to considerations of the oxidation, corrosion, and compatibility of the high-chromium martensitic steels in environments currently appropriate for D-T tokamak fusion power reactors, namely water coolant, liquid lithium and lithium-lead eutectic ($Li_{17}Pb_{83}$) coolants and/or tritium breeders, solid ceramic tritium breeding materials, and beryllium neutron multiplier.

The use of helium as a coolant is unlikely to present any oxidation and corrosion problems at the maximum operating temperatures (≤550°C) currently envisaged for a steel first wall and breeding blanket structure in a DEMO fusion reactor. The experience with helium-cooled fission reactors [high-temperature gas-cooled reactors (HTGCRs)] and in associated laboratory experiments has demonstrated that the inert gas can be maintained sufficiently pure (total impurity content <10 ppm) to suppress oxidation even in large and complex circuits, although carbon transport could still be a problem even at this low impurity level [1,2].

Extensive data on the compatibility of the high-chromium martensitic steels with liquid sodium, including waterside corrosion and erosion-corrosion effects ("wastage") resulting from sodium-water reactions in the vicinity of cracks in tube welds, have also been obtained in programs carried out in support of steam generator and core component materials development for fast breeder reactors [3–7]. However, sodium is no longer considered a potential coolant in fusion reactor systems, and the compatibility of the steels with this liquid metal will not therefore be addressed here.

WATER COOLANT

Aqueous Corrosion

The experience with plant components and the data obtained in supporting laboratory studies of the waterside corrosion and steam oxidation behavior of the Cr-Mo steels in the boilers of fossil-fired power stations [8–12] and in the steam generators of CO_2-cooled nuclear power stations [advanced gas cooled reactors (AGRs)] in the U.K. [13,14] and fast breeder reactors [4,15,16] have been described and reviewed previously. The 9 and 12% chromium martensitic steels generally exhibit good waterside corrosion resistance in the steam generators in both conventional coal- and oil-fired and nuclear fission power stations. The general corrosion resistance of the high-chromium martensitic steels in aqueous solutions is superior to that of carbon and low-alloy steels but inferior to that of the austenitic steels [10,12,16]. However, the integrity of the protective oxide films formed on these steels can be impaired by, for example, the concentration of dissolved salt species at the surface scales under heat flux conditions. This problem can be prevented by the use of a zero solids water chemistry treatment in which hydrazine is employed instead of sodium sulfate as an oxygen scavenger and ammonia or amines rather than phosphates and sodium hydroxide for pH control.

The fully tempered steels with low concentrations of the austenite-stabilizing elements Ni, Cu, and Co are also virtually immune to transgranular stress corrosion cracking (SCC) in aggressive environments [17,18] and are thus better than the Fe-Cr-Ni austenitic steels in this respect. However, there are some aqueous media (high oxygen, chloride, and caustic) that can cause rapid pitting, intergranular attack (IGA), and even SCC in these steels at stresses equal to or in excess of the tensile yield strength [4,19–22]. The steels are most susceptible to pitting, IGA, and SCC when they are in the hardened condition or not correctly heat treated after welding and when there are chromium-rich $M_{23}C_6$ precipitate particles and associated localized chromium-depleted zones at the prior austenite grain boundaries and other interfaces. It has also been demonstrated that the 12Cr (Type 410) and 12Cr-1MoVW (Type 422 or HT9) martensitic steels in several normalized-and-tempered conditions are resistant to environmental cracking when exposed for prolonged periods at 288°C in simulated boiling water reactor (BWR) environments of high (6.0 to 9.5 ppm) dissolved oxygen and hydrogen water chemistry control (6 to 14 ppb oxygen, 170 to 190 ppb dissolved hydrogen) [23].

Much of this aqueous corrosion experience is very relevant to the conditions in the first wall and breeder structure of a water-cooled fusion system. However, more recent studies have been directed towards establishing the high-temperature, high-pressure water corrosion behavior of the commercial and reduced-activation high-chromium martensitic steels specifically considered for fusion reactor applications. Thus, samples of the 12Cr-1MoVW (HT9) and 8Cr-2WVTa (F82H) steels have been exposed for 250 h in recirculating water containing 0.2 ppm dissolved oxygen at 250°C and 2.5 MPa pressure and the weight losses measured after descaling [24]; the quoted corrosion (weight loss) rates for the F82H (≈17 $\mu g\ m^{-2}\ s^{-1}$) and HT9 (12 to 13 $\mu g\ m^{-2}\ s^{-1}$) steels, assumed to have been derived using linear extrapolation, are comparable and considerably greater than that for a reduced-activation 18% Cr-4% W steel specifically developed to resist corrosion in high-temperature, high-pressure water.

Corrosion tests have also been conducted on the 12Cr-1MoVNb [FV448 and/or 1.4914 (plate, electron beam, and

laser welds)] and 9 and 11Cr-WVTa reduced-activation steels in high-temperature, high-pressure water as follows:

- In static stainless steel autoclaves at 300°C and 16 MPa (160 bar) for times of 500 and 1000 h and with water chemistry conditions typical of pressurized water reactor (PWR) primary circuit coolant [25].
- In an austenitic stainless steel loop in the Studsvik (Sweden) R2 reactor at 275 ± 10°C and 9 MPa (90 bar) [26]. The hydrogen and oxygen contents of the inlet water were 1.5 to 3.0 ppm and < 20 ppb, respectively, with a pH (at 25°C) of 6.8 to 8.0. The steel specimens were located in the reactor core, above-core, and out-of-core regions of the loop and exposed for times of 300, 1460, and 4947 h at a reactor power ≥30 MW. Thermal and fission neutron fluxes for the samples at the core center region were approximately 1.2×10^{18} and 1×10^{18} $n.m^{-2} s^{-1}$ at an average reactor power of 46 MW, and the computed displacement doses for the three exposure times were 0.12, 0.6, and 2.3 dpa, respectively.

The weight changes measured after the exposures result from two processes [12,27]: (a) loss of iron into the water by corrosion and formation of an Fe-Cr spinel oxide (inner layer), the thickness of which corresponds to the thickness of metal consumed, and (b) deposition of magnetite on the surface (outer oxide layer). The depths of the corrosion and the corrosion rates were therefore determined from the weight losses after removal of the outer and inner oxide layers by ultrasonic cleaning and/or descaling.

The high-temperature aqueous corrosion of steels generally follows a parabolic rate law, the thickness of the metal consumed being proportional to time to the power 0.5. The weight gains for the steels in the static tests and the depths of the corrosion are shown in Fig. 5.1(a) and (b) as a function of $t^{0.5}$, where t is the exposure time. These data, although limited to 1000 h, indicate that the high-chromium martensitic steels are not unduly sensitive to aqueous corrosion.

The data for the steels exposed in the loop in the R2 reactor were fitted to the relation $\Delta W = Ct^{0.4}$, where ΔW is the weight loss in mg/cm^2 and t is in hours; the values of the rate constant C for the ultrasonically cleaned and descaled commercial and reduced activation steels are listed in Table 5.1.

The corrosion rates are higher for the steels exposed in the core region, intermediate in the above-core samples and least

TABLE 5.1—Corrosion of the 12Cr-1MoVNb and 9-11Cr-WVTa steels in the high-temperature water loop in the Studsvik R2 reactor [26].

Steel	Loop Region	C ($\Delta W = C.t^{0.4}$)#	Valid for Exposure Time (h) of:
12Cr-1MoVNb	Out-of-core (1)(2)	0.08*	4,947
	Above core (1)	0.18-0.33"	4,947
	Core (1)	0.69-0.90"	300
	Core (2)	0.44"	300
9-11Cr-WVTa	Out-of-core	0.06*	4,947
	Above core	0.19 –0.49"	300
	Core	0.52 - 0.84"	1,460

* Ultrasonically cleaned
" Descaled
Experimental data fitted to this equation with ΔW in $mg \cdot cm^{-2}$ and t in h.
(1) 1.4914 steel. (2) FV448 steel.

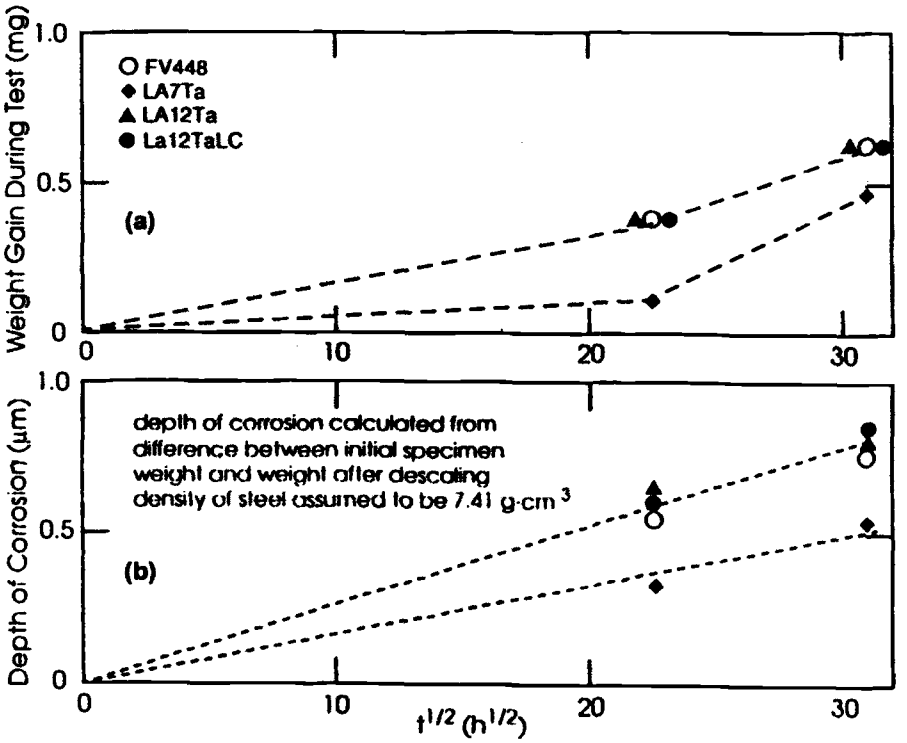

FIG. 5.1—Corrosion of 12Cr-1MoVNb (FV448) and reduced-activation martensitic steels in high-temperature (300°C), high-pressure (16 MPa) water in static autoclaves: (a) weight gain and (b) depth of corrosion [25].

for the coupons tested in the out-of-core region of the loop. The differences may be due to the different times for which the corrosion rates are quoted. Alternatively, the differences in behavior may be attributed to the increased radiolytic decomposition of the water in the core compared to that in the above-core region and the virtual negligible dissociation in the out-of-core position. The corrosion resistance of the steel coupons exposed in the core may also have been impaired as a result of radiation-induced segregation (RIS) of chromium, leading to the precipitation of chromium-rich α′-ferrite and the associated local reduction in the chromium concentration in solution in the steel matrix (see Chapter 10). The scatter in the data is such that a clear distinction cannot be made between the corrosion of the commercial and reduced-activation martensitic steels exposed in the static autoclaves and the respective regions of the reactor loop.

The 12Cr-1MoVNb and 9Cr-WVTa samples exposed for 1460 and 4947 h in the core, above-core and out-of-core regions of the reactor loop did not exhibit SCC or irradiation-assisted stress corrosion cracking (IASCC) when subsequently stressed to 95% of the yield strength in three point bend and autoclave tested for times of ≤1500 h at 250°C in air-saturated high-purity water [28]. The SCC and IASCC might again have arisen as a consequence of the depletion of chromium at interfaces due to thermal sensitization or RIS. However, these observations suffice to confirm that the 9–12% Cr martensitic steels are more resistant to SCC and IASCC in both the unirradiated and irradiated conditions than austenitic steels.

Steam Oxidation

The scales formed on the 9% Cr steels when oxidized in air at temperatures of ≤650°C are adherent and protective and consist of $(Fe,Cr)_2O_3$ and $(Fe,Cr,Mn)_3O_4$ [29]. However, the scales produced during exposure to steam-containing atmospheres are much thicker and spall more easily; they consist of an external Fe_3O_4 scale and an internal duplex scale of Fe_3O_4 and $(Fe,Cr,Mn)_3O_4$. In addition, internal oxidation of the chromium to form $(Fe,Cr,Mn)_3O_4$ at the martensite lath boundaries occurs below the oxide scale [29]. These effects can lead to significant reductions in the component thicknesses and, hence, in the load-bearing cross-sections.

Spalling of the oxide from the high-chromium ferritic/martensitic steels results in complete removal of the scales and the exposure of fresh metal surfaces to the environment such that re-oxidation occurs at an initially faster rate [10]; this can lead to an almost linear rate of metal loss instead of the normal parabolic behavior. Furthermore, the spallation of the oxide scale can result in blockage of the boiler tubes and particles entering the turbine may cause erosion damage, particularly to the blades.

The 9 and 12% chromium steels are generally resistant to oxidation in steam at temperatures up to about 600°C [15,30]. However, 12% Cr steels, such as the 12Cr-MoV (X20CrMoV 12 1), have better oxidation resistance than the 9% Cr [9Cr-MoVNb (T91) and 9Cr-MoVNbW (T92 and E911)] steels at higher temperatures in air (4000 h at 630° and 680°C) and in steam [tube sections exposed in coal-fired power plants for 11 000 h at steam and initial metal temperatures of 600 to 605°C and 630°C, respectively, and in static autoclave tests for about 4000 h at 500°C and 6 bar (0.6 MPa) pressure] [31]. The scales produced on the 12% Cr steel are homogeneous and protective, whereas those on the 9% Cr steels are porous. It has therefore been concluded [31] that none of the 9% Cr steels are suitable for long-term operation as superheater and reheater tubing in boilers at temperatures above about 600°C. In addition to metal loss, the reduction in heat transfer produced by the steamside scale and the consequent increase in tube wall temperature imply that the increased creep-rupture strengths of the newly developed 9% Cr steels cannot be fully exploited in the more advanced power units [10]. It is considered [10,29] that a minimum chromium content of 11% is required to form a protective spinel oxide and thereby provide adequate oxidation resistance in steam-containing atmospheres at 600 and 650°C. Thus, steels such as the 12Cr-MoVNbW (HCM12), 12Cr-MoVNbWCu (HCM12A) and, possibly, 12Cr-MoVNbWCo (NF12) that combine high strength and greater scaling resistance are likely to be the main contenders for future conditions of service (steam temperatures and pressures of 585 to 602°C and 305 bar (30.5 MPa) in the near-term and 620 to 640°C and 320 bar (32 MPa) in the mid-term [10]). However, the restriction of 600°C on the 9% Cr steels does not apply when heat transfer is not involved, and the higher creep-rupture strength potentials of the newer steels can be utilized for headers and pipework in an advanced power plant.

Several approaches for improving the air and steam oxidation resistances of the 9% Cr steels have been advocated. The addition of 3% Pd dramatically enhances the steam oxidation resistance of a 9% Cr-3.3% W steel at 650, 700, and 750°C, decreasing the oxidation in tests of 500 h duration by factors of ten or more [32,33]. The addition of other oxygen-active elements such as Si (up to 1%) and combinations of Si (0.5%) + Ti (0.1%) and Si (0.5%) + Y (0.1%) are also effective in increasing the oxidation resistances of the 9Cr-MoVNbW (T92) steel in both air and steam by reducing the porosity of the surface scales and increasing the compactness [32,34]. Other approaches, such as chromizing, surface deformation treatments and the formation of fine grains, have been successful in increasing the oxidation resistance of austenitic steels [10,30]. However, chromizing the bores of boiler tubes may prove impractical, while the results of exploratory investigations have indicated that surface cold work treatments, which promote an increase in the diffusion rate of chromium to the surface and thereby ensure long-term protection by rapidly replenishing the matrix below the growing scale, are not effective in the case of the 9% Cr martensitic steels [30].

LIQUID METALS (Li AND $Li_{17}Pb_{83}$)

Corrosion tests on the high-chromium martensitic steels in liquid lithium [35–44] and lithium-lead eutectic ($Li_{17}Pb_{83}$) [41,45–52] have been conducted for many thousands of hours in the range 370 to 650°C in thermal convection and pumped loops under semi-stagnant (low-velocity) and turbulent (high-velocity) conditions. The results of these studies have enabled the effects of material variables and system parameters to be identified. The earlier data on the corrosion of iron-base alloys in lithium have been surveyed [53], and the fusion-relevant corrosion behavior of the high-chromium

martensitic steels in lithium and lithium-lead periodically reviewed [40,54–56].

The analysis of the data and observations has shown that the corrosion of the martensitic steels in both liquid metal media is often determined by the uniform dissolution of iron and chromium, followed by the precipitation of the dissolved material in the low-temperature branches of the loops. This contrasts with the liquid metal corrosion behavior of Fe-Cr-Ni austenitic steels, in which the dominant processes are the dissolution of the nickel at a rate significantly faster than that of iron and chromium above about 500°C [57] and the formation of a porous ferrite surface layer.

The corrosion rates of the high-chromium martensitic steels in lithium in the range 350 to 600°C increase with increasing nitrogen content of the liquid metal [36,38, 41–43,58]. The carbon concentrations in the liquid metal and the stabilities of the carbides in the steels also influence the compatibility with the lithium [43] and determine whether carburization or decarburization occurs. However, the nitrogen and carbon appear to have little or no effect on the compatibility of the steels with lithium-lead [35,37,55,59].

The principal factors which determine the corrosion in the lithium-lead are the velocity, temperature, and time; the following expression has been derived [55] for the corrosion rate based on published data in the range 400 to 550°C [45–47,50]:

$$\overline{\Delta W} = 8 \times 10^9 \, e^{-25{,}690/1.98T} \, v^{0.875} \, d^{-0.125} \qquad (5.1)$$

where $\overline{\Delta W}$ is the metal loss ($\mu m \, y^{-1}$), T is the temperature (K), v is the velocity ($m \, s^{-1}$), and d is the hydraulic diameter (m).

Most of the available data show that the lithium-lead corrosion rates are linear with time up to about 10 000 h in the 450 to 500°C temperature range [46,49,60]. However, increases in the corrosion rates of the 12Cr-MoVNb (MANET) steel have been observed after an initial period of 2500 to 3000 h at 500 to 550°C [47,51], but the subsequent corrosion rates appear to be comparable to those reported for other steels if corrections are made for the flow velocity.

The liquid metal corrosion is not significantly dependent on the chromium content (9–12% Cr) of the martensitic steels, very similar rates having been measured for modified 9Cr-1Mo (T91) and 12Cr-1MoVW (HT9) steels exposed in flowing lithium and lithium-lead at 370 to 550°C [41] and for the T91, 12Cr-1MoVNb (1.4914) and HT9 steels in lithium-lead at 450°C and a velocity of 0.1 $m \, s^{-1}$ [48]. The data for the modified 9Cr-1Mo and HT9 steels in the lithium-lead are reproduced in Fig. 5.2 [41]. The initial heat treatments and surface condition are also reported to have little influence on the corrosion rates [49,60].

The weight losses and steady-state dissolution rates of the high-chromium martensitic steels are considerably greater in the lithium-lead than in lithium [41,44,45]; the steady state dissolution rates may be expressed by Arrhenius plots (Fig. 5.3) with activation energies of 68.2 and 92.5 kJ/mol in the lithium and lithium-lead, respectively [41].

A 10 μm thick insulating layer of alumina (Al_2O_3) produced by hot dipping the MANET steel in molten aluminum at 800°C and oxidizing at 950°C is highly stable in flowing (0.3 $m \, s^{-1}$) $Li_{17}Pb_{83}$ at 450°C for times up to 10 000 h, and it reduces the corrosion rate of the bare steel from 0.013 $mm \, y^{-1}$ to virtually zero [61]. The application of a magnetic field of 1.4 tesla increases the corrosion rate of the 1.4914 steel in semi-stagnant lithium-lead at 420 to 475°C by about 30% and also affects the corrosion product precipitation in the cold part of the circuit, the deposition being enhanced in the direction parallel to the magnetic field [62]. It has been suggested, however, that the high-velocity liquid metal corrosion rates of the high-chromium martensitic steels will be reduced as a result of suppression of turbulent flow by a strong magnetic field [56].

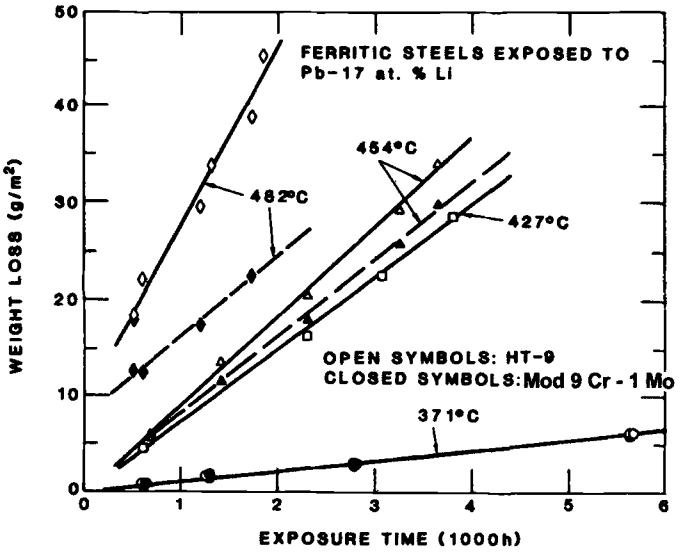

FIG. 5.2—Weight loss versus exposure time for 12Cr-1MoVW (HT9) and modified 9Cr-1Mo steels in flowing lithium-lead [41].

There are no published data on the effects of irradiation on the liquid metal corrosion of the high-chromium martensitic steels. However, it has been postulated [56] that the corrosion will not be significantly affected by high-energy neutron bombardment, since the behavior is normally determined by elemental dissolution at the steel-liquid alloy interface; nevertheless, the activated corrosion products deposited in the cooler parts of the circuit may give rise to shielding problems. Furthermore, the effects of thermal- and irradiation-induced interfacial segregation on the liquid metal corrosion and intergranular attack of the steels need to be established.

Liquid metal embrittlement (LME) of metals and alloys, manifested as reductions in ductility when tested in tension in contact with liquid metals at temperatures just above their melting points, can occur in some systems. The MANET steel, water quenched from 1075°C, exhibits LME when tensile tested in lithium-lead at 250 and 300°C, but the ductility reduction is minimal if the steel is tempered after water quenching [63,64]. Similar behavior has been observed with HT9 [65] and a series of reduced-activation martensitic steels [66,67]. Furthermore, MANET II steel plates, TIG welded using filler wire of the same composition and post-weld heat treated at 750°C for 4 h, show no evidence of LME in tensile tests carried out in lithium-lead at 250 and 450°C [68]. It is conceivable that SCC of the steels could be induced in the liquid metal as a result

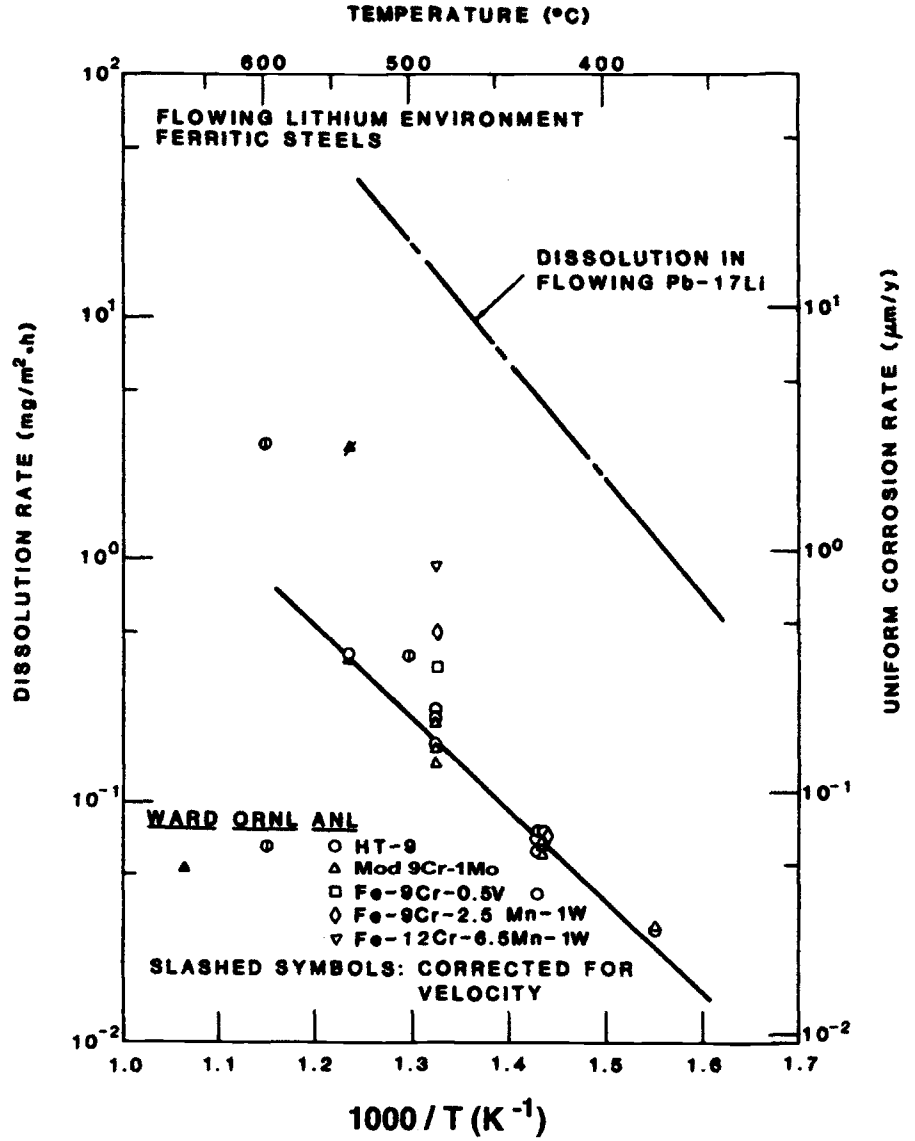

FIG. 5.3—Arrhenius plots of dissolution rate data for HT9 and modified 9Cr-1Mo and three experimental high-chromium martensitic steels exposed to flowing lithium and lithium lead (ANL is Argonne National Laboratory, ORNL is Oak Ridge National Laboratory, and WARD is Westinghouse Advanced Reactor Division) [41].

of thermal sensitization and RIS at temperatures above those at which LME occurs; however, the limited evidence shows that the application of a constant load has no significant effect on either the corrosion rate or susceptibility to SCC of the MANET steel during exposure to lithium-lead [64].

The fatigue lives of the 12Cr-1MoVW (HT9) steel at 482°C in flowing lithium containing ≤100 ppm nitrogen are superior to those in air [40]; however, the endurances are reduced by factors of 2 to 5 as a result of intergranular attack with a nitrogen concentration of ≥1000 ppm in the lithium. The creep-rupture properties and the low-cycle fatigue endurance of the MANET steel are not significantly affected when the tests are performed in stagnant lithium-lead at temperatures up to 600°C [69,70]; nevertheless, the influence of the material loss by corrosion on the properties would have to be taken into consideration in the formulation of design rules. The tensile properties of the 1.4914 and HT9 steels are hardly affected in short duration tests conducted in lithium-lead at 250 to 450°C [40,71].

It has been concluded [56] that the material losses for the 12Cr-MoVNb (MANET-type) steel in flowing $Li_{17}Pb_{83}$ restrict the maximum operating temperature of a self-cooled liquid metal blanket to about 450°C, while the temperature limit for Type 316 austenitic steel is about 50°C lower. In general, the high-chromium martensitic steels are more resistant to corrosion in both lithium and lithium-lead than the austenitic steels.

SOLID CERAMIC BREEDING MATERIALS

There are relatively few published data on the compatibilities of the high-chromium martensitic steels with solid breeder materials.

External scale formation and internal penetration occurs when the 9Cr-1MoVNb and 12Cr-1MoVW steels are exposed to Li_2O in flowing helium containing 1 ppm hydrogen and 1 or 93 ppm water for times up to 4000 h, the attack being more extensive in the helium containing 93 ppm water [72]. Measurements of the reaction rates of powder-compacted lithium-based oxide ceramics Li_2O, Li_2SiO_3, Li_4SiO_4, and Li_2ZrO_3 with the MANET-type steel in argon in the range 500 to 900°C and times of up to 1000 h have confirmed that the magnitudes of the interactions depend on the partial pressure of the water in the atmosphere (1 to 100 Pa) as well as the temperature and time [73–75]. The compatibility of the Li_2O with the MANET-type steel is superior to that of the other ceramics; furthermore, the martensitic steel is more compatible with all the solid breeding materials below 800°C than Type 316 austenitic steel.

BERYLLIUM NEUTRON MULTIPLIER

The results of capsule tests in which corrosion couples are maintained under dynamic vacuum have shown that noticeable interaction between beryllium with low (50 to 100 ppm) and high (1000 to 5000 ppm) oxygen concentrations and 12Cr-1MoVNb (1.4914) martensitic steel only occurs above 600°C, whereas there is greater interaction with Type 316L austenitic steel at temperatures above 580°C [76]. The superior compatibility of the martensitic steel is tentatively attributed to its lower nickel content, as the diffusion of beryllium in nickel is faster than in iron [77]. The interaction leads to the formation of discontinuous brittle intermetallic layers that adhere to the steel and to pores in the beryllium, the thickness of the diffusion zone being dependent on the square root of the exposure time. However, the interaction is not always reproducible due to the protective nature of the oxide layer on the beryllium.

The effects of neutron irradiation [maximum neutron fluxes: 1.1×10^{18} (thermal), 1.0×10^{18} (>1 MeV) n m^{-2} s^{-1}] on the compatibility of beryllium (arc cast, < 300 ppm BeO) with the 1.4914 martensitic steel at 550°C has been investigated as part of the SIBELIUS experiment in the SILOE reactor [78]. Only slight reaction is observed after exposure for 1690 h. However, the beryllium surface is covered with a 5 μm thick gray oxide layer, while a discontinuous oxide layer of the same thickness is present on the surfaces of the steel specimens; it was concluded that the oxidation arose from species (T_2O and/or H_2O) present in the irradiation rig atmosphere.

REFERENCES

[1] High Temperature Gas Cooled Reactors, Nucl. Technol. 1984, Vol. 66.

[2] L. W. Graham, J. Nucl. Mater. 171 (1990) 76.

[3] C. Tyzack and A. W. Thorley, in: Ferritic Steels for Fast Reactor Steam Generators, Eds. S. F. Pugh and E. A. Little (British Nuclear Energy Society, London, 1978) 241.

[4] A. M. Pritchard, C. F. Knights, G. P. Marsh, K. A. Peakall, R. Perkins, B. L. Myatt and J. E. Antill, in: Ferritic Steels for Fast Reactor Steam Generators, Eds. S. F. Pugh and E. A. Little (British Nuclear Energy Society, London, 1978) 360.

[5] A. W. Thorley, in: Liquid Metal Engineering and Technology 84 (British Nuclear Energy Society, London, 1984) 31.

[6] H. U. Borgstedt and C. K. Matthews, Applied Chemistry of the Alkali Metals (Plenum Press, London, 1987).

[7] A. W. Thorley, in: Liquid Metal Engineering and Technology 88 (Société Française d'Energie Nucléarie, Paris, 1988) 532.

[8] L. M. Wyatt, in: Ferritic Steels for Fast Reactor Steam Generators, Eds. S. F. Pugh and E. A. Little (British Nuclear Energy Society, London, 1978) 27.

[9] H. Fricker and B. Walser, in: Ferritic Steels for Fast Reactor Steam Generators, Eds. S. F. Pugh and E. A. Little (British Nuclear Energy Society, London, 1978) 35.

[10] A. Fleming, R. V. Maskell, L. W. Buchanan, and T. Wilson, in: Materials for High Temperature Power Generation and Process Plant Applications, Ed. A. Strang (The Institute of Materials, London, Book 728, 2000) 33.

[11] G. J. Bignold, in: Ferritic Steels for Fast Reactor Steam Generators, Eds. S. F. Pugh and E. A. Little (British Nuclear Energy Society, London, 1978) 342.

[12] J. P. Broomfield, J. E. Forrest, D. R. Holmes, and M. I. Manning, in: Topical Conference on Ferritic Alloys for Use in Nuclear Energy Technologies, Eds. J. W. Davis and D. J. Michel (Met. Soc. AIME, New York, 1984) 77.

[13] Proc. Int. Confs. on Gas Cooled Reactors Today (British Nuclear Energy Society, London, 1974 and 1982).

[14] P. C. Rowlands, J. C. P. Garrett, L. A. Popple, A. Whittaker, and A. Hoaksey, Nucl. Energy, 25 (1986) 267.

[15] P. Hurst and H. C. Cowen, in: Ferritic Steels for Fast Reactor Steam Generators, Eds. S. F. Pugh and E. A. Little, (British Nuclear Energy Society, London, 1978) 371.

[16] M. Aubert, B. Mathieu, and P. Petrequin, in: Topical Conference on Ferritic Alloys for Use in Nuclear Energy Technologies, Eds. J. W. Davis and D. J. Michel (Met. Soc. AIME, New York, 1984) 245.

[17] L. Colombier, Molybdenum in Stainless Steels and Alloys (Climax Molybdenum Co., Ann Arbor, MI, 1968).

[18] A. P. Bond, J. D. Marshall, and H. J. Dundas, in: Stress Corrosion Testing, ASTM STP 425 (American Society for Testing and Materials, Philadelphia, 1967) 116.

[19] G. J. Bignold, in: Ferritic Steels for Fast Reactor Steam Generators, Eds. S. F. Pugh and E. A. Little (British Nuclear Energy Society, London, 1978) 346.

[20] B. S. Poulson, in: Ferritic Steels for Fast Reactor Steam Generators, Eds. S. F. Pugh and E. A. Little (British Nuclear Energy Society, London, 1978) 413.

[21] J. Vrijen, J. K. van Westenbrugge, L. van der Wiel, P. L. F. Rademakers, C. P. Scheepens, and J. W. Schinkel, Nucl. Technol. 55 (1981) 250.

[22] G. P. Kalwa, K. Haarmann, and K. Janssen, in: Ferritic Alloys for Use in Nuclear Energy Technologies, Eds. J. W. Davis and D. J. Michel (Met. Soc. AIME, New York, 1984) 235.

[23] B. M. Gordon, C. W. Jewett, A. E. Pickett, and M. E. Indig, in: Ferritic Alloys for Use in Nuclear Energy Technologies, Eds. J. W. Davis and D. J. Michel (Met. Soc. AIME, New York, 1984) 65.

[24] N. Yamanouchi, M. Tamura, H. Hayakawa, A. Hishinuma, and T. Kondo, J. Nucl. Mater. 191-194 (1992) 822.

[25] C. B. Ashmore and N. R. Large, Corrosion of Low Activation Martensitic Stainless Steels Developed for Reactor Applications, UKAEA, Culham Report, AEA Fusion 102, 1991.

[26] R. Källström, The Effects of Irradiation and Radiolysis on the Aqueous Corrosion of High Chromium Martensitic Steels, Studsvik Material AB, Sweden, Report STUDSVIK/M-93/106, March 1994.

[27] L. Tomlinson, M. H. Hurdus, C. B. Ashmore, and P. J. Silver, Corrosion 41 (1985) 257.
[28] A-C. Nystrand, (i) The Effect of Irradiation on Tensile Properties and Stress Corrosion Cracking Sensitivity of Martensitic Steels, Studsvik Material AB, Sweden, Report STUDSVIK/M-94/18, February 1994, (ii) The Effect of Irradiation on Stress Corrosion Cracking Sensitivity of a Martensitic Steel Type 1.4914, MANET 4-Complementary Studies, Part 2, Studsvik Material AB, Report STUDSVIK/M-94/117, November 1994.
[29] P. J. Ennis and W. J. Quadakkers, in: PARSONS 2000, Advanced Materials for 21st Century Turbines and Power Plant, Eds. A. Strang, W. M. Banks, R. D. Conroy, G. M. McColvin, J. C. Neal and S. Simpson, (The Institute of Materials, London, Book 736, 2000) 265.
[30] M. I. Manning and E. Metcalfe, in: Ferritic Steels for Fast Reactor Steam Generators, Eds. S. F. Pugh and E. A. Little (British Nuclear Energy Society, London, 1978) 378.
[31] K. Sabelt, O. Wachter and B. Melzer, VGB Kraftwerkstechnik, 76 (1996) 936.
[32] F. Abe, M. Igarashi, S. Wanikawa, M. Tabuchi, T. Itagaki, K. Kimura and K. Yamaguchi, in: PARSONS 2000, Advanced Materials for 21st Century Turbines and Power Plant, Eds. A. Strang, W. M. Banks, R. D. Conroy, G. M. McColvin, J. C. Neal and S. Simpson (The Institute of Materials, London, Book 736, 2000) 129.
[33] M. Igarashi, S. Muneki, H. Kutsumi, T. Igataki, N. Fujitsuna and F. Abe, in: PARSONS 2000, Advanced Materials for 21st Century Turbines and Power Plant, Eds. A. Strang, W. M. Banks, R. D. Conroy, G. M. McColvin, J. C. Neal and S. Simpson, (The Institute of Materials, London, Book 736, 2000) 334.
[34] F. Abe, M. Igarashi, N. Fujitsuna, K. Kimura and S. Muneki, in: Materials for Advanced Power Engineering, Eds. J. Lecomte-Beckers, F. Schubert and P. J. Ennis, Forschungszentrum Jülich, Energy Technology Series 5 (1998) 259.
[35] P. F. Tortorelli, J. H. DeVan, and R. M. Yonco, J. Mater. Energy Sys., 2 (1981) 5.
[36] M. G. Baker and S. A. Frankham, J. Nucl. Mater. 107 (1982) 218.
[37] E. Ruedl, V. Coen, T. Sasaki, and H. Kolbe, J. Nucl. Mater. 110 (1982) 28.
[38] M. G. Baker, P. Hubberstey, A. T. Dadd, and S. A. Frankham, J. Nucl. Mater. 114 (1983) 43.
[39] P. F. Tortorelli and J. H. DeVan, in: Topical Conference on Ferritic Alloys for Use in Nuclear Energy Technologies, Eds. J. W. Davis and D. J. Michel (Met. Soc. AIME, New York, 1984) 215.
[40] O. K. Chopra and P. F. Tortorelli, J. Nucl. Mater. 122 & 123 (1984) 1201.
[41] O. K. Chopra and D. L. Smith, J. Nucl. Mater. 155-157 (1988) 715.
[42] P. F Tortorelli, J. Nucl. Mater. 155-157 (1988) 722.
[43] G. E. Bell and M. A. Abdou, Fusion Technol. 15 (1989) 315.
[44] P. F. Tortorelli, J. Nucl. Mater. 191-194 (1992) 965.
[45] O. K. Chopra and D. L. Smith, J. Nucl. Mater. 122 & 123 (1984) 566.
[46] P. F. Tortorelli and J. H. DeVan, J. Nucl. Mater. 141-143 (1986) 592.
[47] H. U. Borgstedt, D. Drechsler, G. Frees, and Z. Peric, J. Nucl. Mater. 154 (1988) 728.
[48] M. Broc, T. Flament, P. Fauvet, and J. Sannier, J. Nucl. Mater. 155-157 (1988) 710.
[49] T. Flament, P. Fauvet, B. Hocde, and J. Sannier, Fusion Technology 1988, Vol. 2, Eds. A. M. van Ingen, A. Nijsen-Vis, and H. T. Klippel (Pergamon Press, Oxford, 1989) 1184.
[50] J. Sannier, T. Flament, and A. Terlain, in: Fusion Technology, 1990, Vol. 1, Eds. B. E. Keen, M. Huguet, and R. Hemsworth (North Holland, Amsterdam, 1991) 901.
[51] H. U. Borgstedt and H. D. Röhrig, J. Nucl. Mater. 179-181 (1991) 596.
[52] J. Sannier, T. Dufrenoy, T. Flament, and A. Terlain, J. Nucl. Mater. 191-194 (1992) 975.
[53] J. H. DeVan, J. E. Selle, and A. E. Morris, Review of Lithium Iron-Base Alloy Corrosion Studies, Oak Ridge National Laboratory, ORNL Report TM-4927, January 1976.
[54] O. K. Chopra and A. B. Hull, Fusion Technol. 15 (1989) 309.
[55] T. Flament, P. Tortorelli, V. Coen, and H. U. Borgstedt, J. Nucl. Mater. 191-194 (1992) 132.
[56] H. U Borgstedt, in: Characterization and Assessment of Ferritic/Martensitic Steels, Eds. K. Ehrlich, D. R. Harries, and A. Möslang, Forschungszentrum Karlsruhe FZKA Report 5626, February 1997, p. 55.
[57] H. U. Borgstedt and H. Feuerstein, J. Nucl. Mater. 191-194 (1992) 988.
[58] J. H. DeVan and C. Bagnall, in: Liquid Metal Engineering and Technology, Vol. 3 (British Nuclear Energy Society, London, 1985) 65.
[59] T. L. Edwards and G. R. Edwards, J. Mater. Energy Sys. 2 (1981) 16.
[60] T. Flament, A. Terlain, J. Sannier, and P. Labbe, in: Fusion Technology, 1990, Vol. 1, Eds. B. E. Keen, M. Huguet, and R. Hemsworth (North Holland, Amsterdam, 1991) 911.
[61] H. U. Borgstedt, H. Glasbrenner, and Z. Peric, J. Nucl. Mater. 212-215 (1994) 1501.
[62] A. Terlain and T. Dufrenoy, J. Nucl. Mater. 212-215 (1994) 1504.
[63] V. Coen, H. Kolbe, and L. Orecchia, J. Nucl. Mater. 155-157 (1988) 740.
[64] V. Coen, H. Kolbe, L. Orecchia, and T. Sasaki, in: Liquid Metal Engineering and Technology, Vol. 3 (Société Francaise d'Energie Nucléaire, Paris, 1988) 526-1.
[65] G. R. Edwards, K. A. Jones, and S. F. Halvorson, Fusion Technol. 10 (1986) 243.
[66] T. Sample, H. Kolbe, and L. Orecchia, in: Fusion Technology 1992, Vol. 2, Eds. C. Ferro, M. Gasparotto, and H. Knoepfel (North Holland, Amsterdam, 1993) 1469.
[67] O. K. Chopra and D. L. Smith, in: Liquid Metal Engineering and Technology, Vol. 3 (Société Francaise d'Energie Nucléaire, Paris, 1988) 529-1.
[68] T. Sample, P. Fenici, and H. Kolbe, J. Nucl. Mater. 233-237 (1996) 244.
[69] H. U. Borgstedt, G. Frees, M. Grundmann, and Z. Peric, Fusion Eng. Design 14 (1991) 329.
[70] M. Grundmann, Strukturmechanische Untersuchungen am 12% Cr-Stahl X18CrMoVNb 12 1 (1.4914) im flüssigen Pb-17Li - Eutektikum, Kernforschungszentrum Karlsruhe KfK Report 4703, February 1990.
[71] T. Sample, V. Coen, H. Kolbe, and L. Orecchia, J. Nucl. Mater. 191-194 (1992) 960.
[72] O. K. Chopra, T. Kurasawa, and D. L. Smith, in: Topical Conference on Ferritic Alloys for Use in Nuclear Energy Technologies, Eds. J. W. Davis and D. J. Michel (Met. Soc. AIME, New York, 1984) 209.
[73] P. Hofmann and W. Dienst, J. Nucl. Mater. 141-143 (1986) 289.
[74] P. Hofmann and W. Dienst, J. Nucl. Mater. 155-157 (1988) 485.
[75] P. Hofmann and W. Dienst, in: Fusion Technology 1992, Vol. 2, Eds. C. Ferro, M. Gasparotto, and H. Knoepfel (North Holland, Amsterdam, 1993) 1374.
[76] T. Flament, D. Herpin, L. Feve, and J. Sannier, J. Nucl. Mater. 191-194 (1992) 163.
[77] A. G. Knapton and K. B. C. West, J. Nucl. Mater. 3 (1961) 239.
[78] N. Roux, J. J. Abassin, M. Briec, D. Cruz, T. Flament, and I. Schuster, J. Nucl. Mater. 191-194 (1992) 168.

6

Hydrogen Isotope Effects

It is well established that small amounts of internal hydrogen produce embrittlement and cracking of ferritic and high-strength martensitic steels. Hydrogen has a large solubility in molten steel, and copious quantities of the gas can be absorbed in the liquid during the steel-making process and retained over and above the equilibrium solubility during subsequent solidification. The hydrogen exerts a high internal pressure and, aided by transformation and thermal contraction stresses, produces defects in ingots and castings and hairline cracking in large forgings and heavy-section steel plates. These deleterious effects have long been recognized, and it is now the practice to remove the hydrogen by vacuum melting and pouring, cooling very slowly, and/or holding of semi-finished or finished products for prolonged periods at high temperatures to allow the hydrogen to diffuse out of the steel. However, embrittlement and cracking may also be produced as a result of hydrogen pick-up during secondary fabrication (acid pickling, welding, cadmium and zinc plating operations, cathodic protection procedures, etc.) and service [electrolytic reactions, corrosion in acids and aqueous solutions, and exposure to high-pressure hydrogen gas at ambient and elevated temperatures and to sour (H_2S-containing) gases and liquids].

The problems of hydrogen-induced embrittlement and failures of low- and high-alloy ferritic and martensitic steels and the mechanisms involved have been extensively documented and reviewed [1–7].

Physical hydrogen embrittlement is manifested as a decrease in ductility (elongation and reduction of area) and notched strength in tensile tests and delayed failure by fracture under high static loading (termed static fatigue or hydrogen-induced delayed cracking), the degree of embrittlement generally increasing with increasing strength of the steel [1]. The hydrogen introduced electrolytically and by exposure to the high-pressure gas is in the uncombined state, but recombination to form molecules may occur at sub-surface discontinuities, particularly sulfide particles, resulting in the development of high pressures and surface blistering, principally in the lower-strength steels.

Carbon and low-alloy steels are also susceptible to chemical attack and embrittlement when exposed to high-pressure hydrogen at temperatures above about 200°C. The hydrogen reacts with the carbon in solution in the steels to form methane gas, which collects at the grain boundaries and leads to brittle intergranular (IG) cracking. However, ferritic and martensitic steels containing ≥6% Cr are not susceptible to decarburization and methane formation at temperatures below about 600°C irrespective of the hydrogen partial pressure and, hence, are resistant to this form of hydrogen attack and embrittlement [8–10].

SOLUBILITY, DIFFUSION, AND PERMEATION

The hydrogen inventory and effects on the steel properties are determined by the permeability (P), diffusivity (D), and solubility (S), which are interrelated (P = SD). The experimentally determined solubilities, diffusivities, and permeabilities of hydrogen in a high-chromium martensitic steel (MANET) in the range 250 to 600°C are as follows [11,12]:

Solubility (mol m^{-3} $Pa^{-1/2}$):

$$S = 1.29 \exp(-29620/RT) \quad (6.1)$$

Diffusivity (m^2 s^{-1}):

$$D = 7.17 \times 10^{-8} \exp(-13490/RT) \quad (6.2)$$

Permeability (mol m^{-1} s^{-1} $Pa^{-1/2}$):

$$P = 2.92 \times 10^{-8} \exp(-43100/RT) \quad (6.3)$$

where T is in K and R is the molar gas constant (8.314 J mol^{-1} K^{-1}).

Hydrogen (atomic) has low solubility in the high-chromium martensitic steel and diffuses much more rapidly than in austenitic steel at ambient and elevated temperatures (Fig. 6.1). Furthermore, the apparent diffusivity (Fig. 6.2) and permeation of hydrogen in the 9 to 12% Cr steels appears to decrease with increasing alloying element (chromium) content, primarily due to an increase in the activation energy [13,14]. The diffusivities at temperatures below 250 or 300°C have a pronounced dependence on pressure and deviate from the Arrhenius-type behavior [that is, $D = D_0 \exp(-E_m/RT)$] [11,12,15–18], due to trapping of the hydrogen at various lattice sites where the misfit energy is reduced and there is strong binding. The behavior can be described by a trapping model in which the effective diffusion coefficient is given by [19]:

$$D_{eff} = D/[1 + N_t/N_L \exp(E_b/RT)] \quad (6.4)$$

where N_L is the density of normal lattice diffusion sites.

The data for the high-chromium martensitic steels can be fitted with estimated trap densities (N_t) and average binding energies (E_b), respectively, of 1.5×10^{25} sites m^{-3} and 39.5 kJmol^{-1} for MANET II, 3.4×10^{25} sites m^{-3} and 38.4 kJmol^{-1} for T91 and 6.3×10^{24} sites m^{-3} and 39.0 kJmol^{-1} for modified F82H [20,21]. These values are consistent with the data derived from electrochemical hydrogen permeation measurements on other steels of this type [22]. The traps may be interfaces (martensite lath and prior austenite grain boundaries and particle/matrix interfaces) or dislocations [23]. The

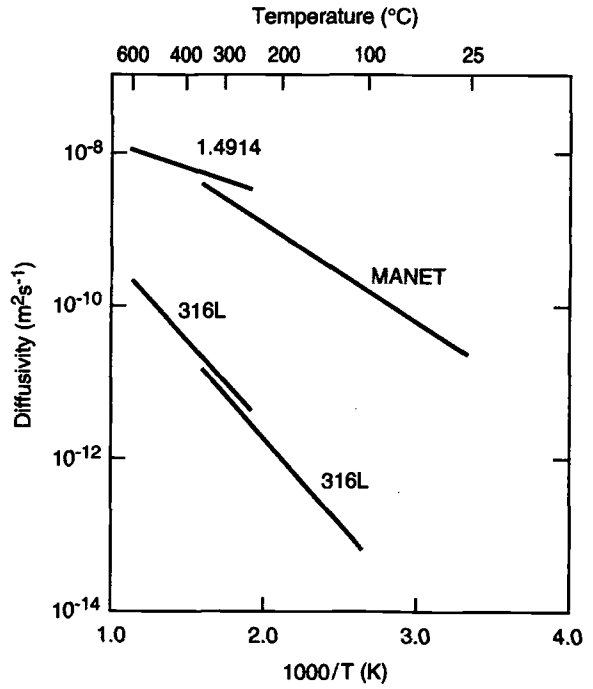

FIG. 6.1—Arrhenius plots of the diffusivities of hydrogen in martensitic (1.4914) and austenitic (316L) steels [11,12,15].

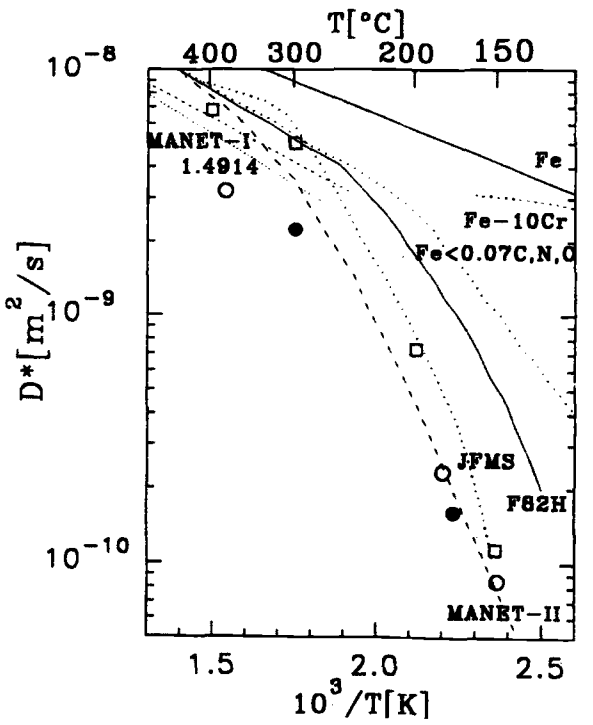

FIG. 6.2—Temperature dependence of the apparent diffusion coefficients for hydrogen in pure iron (Fe), iron with <0.07 C, N, O, Fe-10% Cr alloy, F82H (8% Cr), JFMS (9.6% Cr), 1.4914 (10.5% Cr), MANET I (10.6% Cr), and MANET II (10% Cr) steels [14]. Filled circles: MANET II steel pre-irradiated with 12.3 MeV protons at ≤80°C to 1.5 × 10^{-3} dpa.

dislocation traps are considered to be weaker than interfacial traps [6], and hydrogen may be channeled from dislocations to lath and grain boundaries during plastic deformation [24], thereby becoming enriched at these interfaces.

The data on the high-chromium martensitic steels may also be described by a model of saturable trapping of the hydrogen at vacancies with N_t/N_L and E_b values of $\approx 2 \times 10^{-6}$ and 65 kJmol^{-1}, respectively (MANET II) [17], and 7×10^{-8} and ≈60 kJmol^{-1}, respectively (F82H steel) [18]. These data yield a virtually constant value of the hydrogen solubility at temperatures below 300°C of $\approx 10^{-3}$ mol m^{-3} Pa$^{-1/2}$, that is ≈0.08 wppm at 1 bar [14].

There are only limited data on the effects of irradiation on the permeation and diffusivity of hydrogen in the high-chromium martensitic steels. Pre-irradiation with 12.3 MeV protons to a displacement dose of 1.5×10^{-3} dpa at ≤80°C has no significant effect on the permeability of hydrogen in the MANET II steel at temperatures in the range 150 to 400°C [17]. The pre-irradiation reduces the diffusivity slightly (Fig. 6.2), corresponding to an increase in the trap concentration by a factor of about two and with no significant change in the binding energy. However, the permeability is enhanced under simultaneous proton irradiation at temperatures below about 300°C, possibly due to dissociation/ionization of the gas [17].

PHYSICAL HYDROGEN EMBRITTLEMENT

The 9–12% Cr martensitic steels are only briefly considered in the earlier reviews of hydrogen embrittlement. However, while the information now available on hydrogen effects in the 12Cr (Type 410, HT9, and MANET), 9Cr-1Mo, and reduced activation steels is still relatively limited, it suffices to show that these high-chromium steels, in common with α-iron and plain carbon, low- and other high-alloy steels, are prone to hydrogen-induced changes in mechanical properties and fracture behavior [5,25–27]. Thus, atomic hydrogen, introduced internally by cathodic charging or exposure to the high-pressure gas, results in physical embrittlement, the principal characteristics and observations being as follows [28–38]:

1. The magnitudes of the reduction in tensile ductility, true fracture stress, and notched strength increase with increasing current density, hydrogen partial pressure and concentration and decrease with increasing deformation rate; the effects are reversible and are normally restricted to temperatures below 200°C. The strength reductions are particularly important as they can lead to failure at low operating stresses; decreases in ductility are of lesser concern, but they signify a reduction in fracture toughness and a lower resistance to fatigue and fatigue crack growth.

2. *HT9 steel*—Cathodic charging to a concentration of about 6 wppm (1 wppm = 55 appm = 11.1 ml.kg^{-1}) hydrogen reduces the ambient temperature tensile ductility (reduction of area) of this steel (containing 0.016 to 0.018% P and 0.003 to 0.007% S and initially austenitized at 1050°C for 0.5 h, air cooled, and tempered at 750°C for 1 h) from about 60 to 15% (Fig. 6.3) [28–30]; the effects are associated with a change in the failure mode from ductile microvoid coalescence (MVC) with some secondary cracking along the prior austenite grain boundaries to one with a high (≈28%) com-

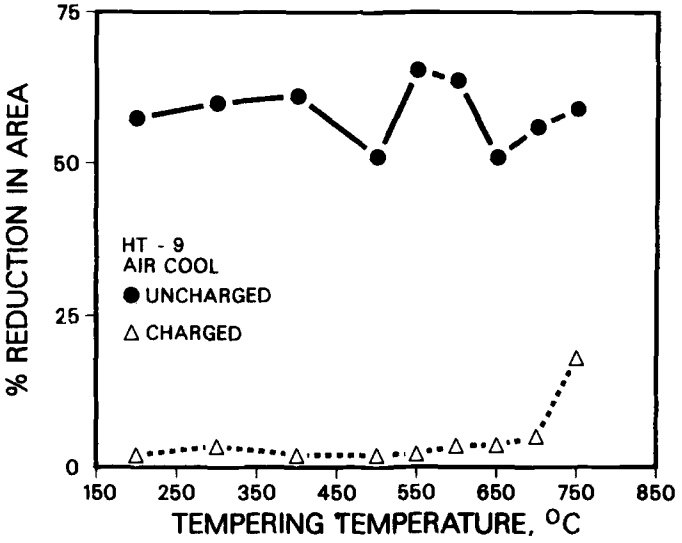

FIG. 6.3—Tensile ductility (reduction of area) of HT9 steel austenitized at 1050°C for 0.5 h, air cooled and heated (tempered) at temperatures of 200 to 750°C before and after cathodic charging of ≈6 wppm hydrogen [29].

ponent of IG fracture [21–23]. Similar reductions in ductility and a change in the type of fracture from MVC to mixed IG and quasi-cleavage (QC) are produced following exposure to an external pressure (≥10 MPa) of the gas to induce concentrations of 5 to 10 wppm hydrogen [31] and when the cathodic hydrogen charging and tensile testing are carried out simultaneously [32,33].

The ductilities of the hydrogen-charged steel are improved by cold swaging and re-tempering after the initial quenching and tempering treatment [30], but tempering of the steel at 200 to 700°C after austenitization at 1050°C results in substantially greater hydrogen embrittlement than in the 750°C tempered condition, the tensile ductility (reduction of area) being reduced to values as low as ≈2% (Fig. 6.3) [29]. The hydrogen embrittlement in the steel tempered at ≥550°C is associated with an increased tendency to IG fracture. This is attributed to the presence of a continuous network of grain boundary $M_{23}C_6$ and MC carbides, formed as a result of the transformation of retained austenite during tempering, and significant interfacial segregation of phosphorus [29,30] and sulfur [32]. However, there is no additional influence of temper embrittlement in the hydrogen-charged steel. Thus, aging of the air-cooled and 750°C-tempered steel for 1000 h at 550°C has little or no effect on the tensile ductility after hydrogen charging, but it reduces the amount of IG fracture from ≈28 to 8% and encourages fracture along the martensite lath boundaries [28].

The hydrogen embrittlement of this steel is also manifested as an increase in the ambient temperature fatigue crack growth rate and a decrease in the threshold stress [34].

3. *9Cr-1Mo steel*—The extent of the hydrogen embrittlement, again evidenced as reductions in tensile ductility at ambient temperature after cathodic charging, is dependent on the initial heat treatment and microstructure of the steel [35] and increases with increasing hydrogen concentration [36]. Thus, heating to 1350, 1100, or 850°C followed by rapid cooling to produce respectively duplex martensite plus δ-ferrite, fully martensitic, and martensite plus δ-ferrite plus carbide structures, simulating those of the HAZs of weldments, results in severe embrittlement (reduction of area values ≤5%) of the steel (containing 0.025% P and 0.012% S) after cathodic charging of 2 to 3 wppm hydrogen [35]. However, tempering of the martensite for 1 h at 750°C considerably improves the resistance to hydrogen embrittlement, the quenched and tempered fully martensitic steel showing the maximum susceptibility with the reduction of area values decreasing from about 68 to 42% after the hydrogen charging. This ductility reduction is associated with a partial change in failure mode from ductile MVC to a ductile QC type fracture produced by the linking up of cracks across individual martensite laths after lath splitting and possessing a "chisel-tip" appearance. IG fracture was not evident in any of the microstructural conditions examined in this study.

There is a strong synergistic effect of hydrogen charging and temper embrittlement (induced by prior aging for 5000 h at 500 or 550°C), which results in major losses in ductility (reduction of area values as low as ≈2%) (Fig. 6.4) [36] and is associated with the formation of progressively increasing amounts of brittle IG and transgranular cleavage (TG) fractures of the steel (Fig. 6.5) [36]. The dominant factor controlling this embrittlement is the interaction of the hydrogen with precipitates of the brittle intermetallic Laves phase (Fe_2Mo type) formed at the martensite lath and prior austenite grain boundaries during aging and containing phosphorus in solution [36,39,40]. Tests on model 9Cr-Mo alloys with variations in silicon and phosphorus contents show that silicon enhances the susceptibility to hydrogen embrittlement by promoting interfacial phosphorus segregation in the unaged (non-temper embrittled) material and Laves phase formation in the aged (temper embrittled) steel, the silicon effect being enhanced by phosphorus segregation in each case [40].

The threshold stress for fatigue crack growth of 9Cr-1Mo steel at ambient temperature is halved by loading to 3 wppm hydrogen [41]; however, the threshold stress at 100°C is unaffected by the introduction of 4 wppm hydrogen.

4. *MANET and reduced-activation steels*—The critical hydrogen concentrations required to induce cracking in the steel matrix, with and without the application of an external biaxial stress, have been determined using the disc pressure test (DPT) [42] and an electrochemical method (CCR) [43], respectively. The results for various high-chromium martensitic steels, presented in Table 6.1 [15,20,44,45], demonstrate that the critical hydrogen concentrations for cracking are reduced by the applied biaxial stress in the DPT test and with increasing prior austenite grain size.

Reductions in the tensile ductility (total elongation and reduction of area) of notched specimens of the MANET II and F82H steels are also observed in slow strain-rate tests at ambient temperature after electrolytic charging to ≤5 wppm (MANET) and ≤3 wppm (F82H), the embrittlement being evident at hydrogen concentrations as low as 1 to 2 wppm [38]; however, the yield and ultimate tensile stresses are not significantly affected. The decreases in the reduction of area values are greater in these tests with the triaxial stress system at the base of the notch than in the corresponding biaxial DPT tests [45] referred to above. Globular alumina inclusions are the observed nucleation sites for the hydrogen-induced brittle type (IG) fractures in the F82H steel in both the biaxial and triaxial tests.

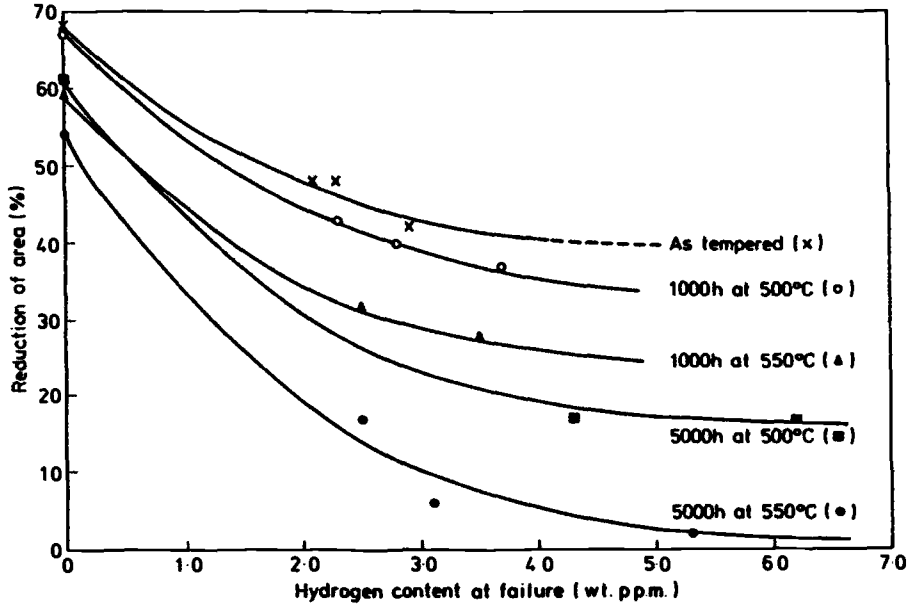

FIG. 6.4—Effects of hydrogen charging and aging at 500 and 550°C on the tensile ductility (reduction of area) of 9Cr-1Mo steel initially austenitized at 1100°C for 1 h, air cooled and tempered at 750°C for 1 h [36].

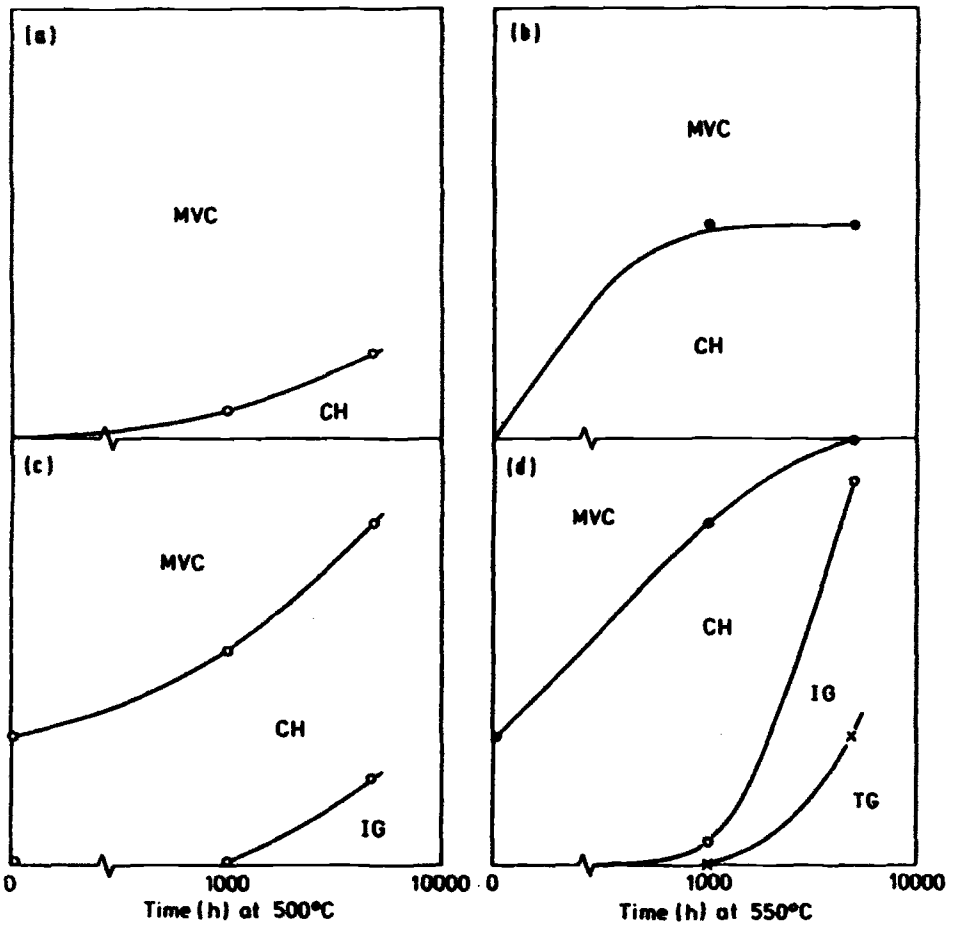

FIG. 6.5—Influence of electrolytic hydrogen charging (2.9 to 6.2 wppm) and aging at 500 and 550°C on the fracture mode of 9Cr-1Mo steel initially austenitized at 1100°C for 1 h, air cooled and tempered at 750°C for 1 h [36]; full vertical scale represents 100% of the fracture surface. (a) and (b): no hydrogen; (c) and (d): hydrogen charged. MVC: microvoid coalescence, CH: chisel fracture, IG: intergranular fracture, TG: transgranular fracture.

TABLE 6.1—Critical hydrogen concentrations for cracking [15,20,44,45].

Steel	Prior Austenite Grain Size, (μm)	Critical (Threshold) Hydrogen Concentrations for Cracking, wppm	
		CCR Test	DPT Test
MANET II (A)	70–100	3–4	2–3
MANET II (B)	15–20	14–15	8–9
Grade 91 (T91)	12–18	14–15	11–12
Mod. F82H	55	5–6	3–4

Hydrogenation to ≤0.5 wppm has no detectable influence on the tensile and sub-size Charpy V-notch impact properties of the F82H steel [46], but small concentrations of hydrogen introduced cathodically are reported to decrease the room temperature tensile fracture strains from 19 to 5% and promote intergranular failure of a 9Cr-2W reduced-activation steel [47].

The crack initiation and propagation resistance are dependent on the hydrogen content of the steel and the crack angle relative to the loading direction as well as on the test temperature [48,49]. Thus, mixed-mode I/III (tensile/shear) loading reduces the mixed-mode J-integral fracture toughness (J_{TQ} - the energy for crack initiation)* and tearing modulus (dJ_T/da which reflects the resistance to stable crack growth) relative to the mode I (tensile) values (J_{1Q} and dJ_1/da) for both uncharged and hydrogen-charged (4 wppm) F82H steel in tests at ambient temperature, as shown in Figs. 6.6(a) and (b). Hydrogen decreases the overall fracture toughness and resistance to crack growth; however, the minimum values of J_{TQ} and dJ_T/da occur between $P_{iii}/(P_{iii} + P_i) = 0.4$ and 0.6, corresponding to crack angles of 35 and 55° for both the hydrogenated and hydrogen-free steel. The minimum mixed-mode J_{TQ} is about half that of J_{1Q} for the uncharged steel and approximately 35% of J_{1Q} after hydrogen charging.

SEM examinations showed a microvoid coalescence type of fracture (MVC) in all the samples, with no evidence of intergranular or cleavage failures. The reduction in J_{TQ} with increasing mode III (shear) component (P_{iii}) with no hydrogen present is associated with an increased density of small voids nucleated on non-metallic particles by shear and, hence, a reduced void spacing . However, the fracture surfaces of the hydrogen-charged specimens are more planar and less tortuous as a result of enhanced void formation, growth, and coalescence, thereby further degrading the toughness.

The authors concluded [48,49] that mixed-mode loading is the most severe stress condition for tough steels such as F82H, both with and without hydrogen, and that the minimum J-integral values are the most conservative for use in the design of complex engineering structures.

Reductions in the fatigue endurance of the MANET steel are produced in load-controlled, low-cycle fatigue tests at room temperature in hydrogen at a pressure of 1.5 bar (Fig. 6.7) [50,51]. The deleterious effect of the external hydrogen increases at low frequencies, and the introduction of hold times during the fatigue cycles results in further reductions in the endurance; the associated metallographic evidence confirms that the hydrogen influences both crack initiation and propagation.

* The subscript Q denotes that the tests do not satisfy plane strain conditions.

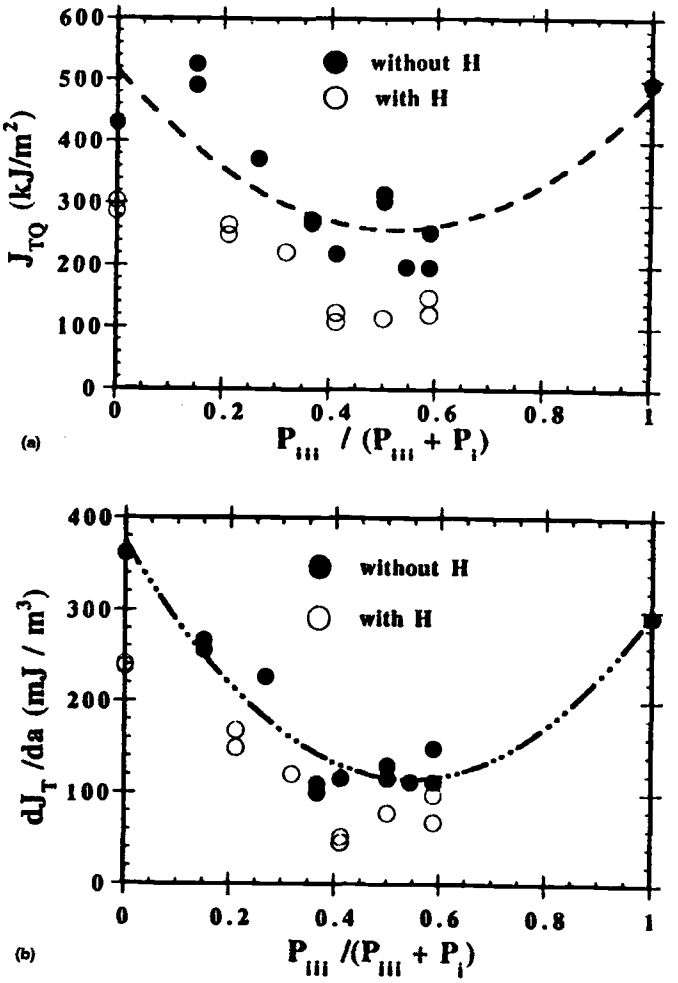

FIG. 6.6—The dependence of the fracture toughness J_{TQ} (a) and tearing modulus dJ_T/da (b) on the mode III load component for uncharged and hydrogen-charged F82H steel [49].

5. *Mechanisms*—It has been concluded from discussions of the mechanisms responsible for the hydrogen embrittlement in the high-chromium martensitic steels [35,36,39] that hydrogen is transported to microstructural features and regions of triaxiality during tensile testing by lattice diffusion and mobile dislocation sweeping and is eventually trapped at interfaces and dislocations [6]. The embrittlement then results from either one or a combination of the following processes:

a. Interaction of the hydrogen with dislocations such that plastic flow is localized on specific slip planes, with cross slip possibly being inhibited, and leading to shear modes of failure.

b. Lowering of the cohesive strength of the interfaces on which the hydrogen has accumulated, thereby promoting brittle modes of fracture.

The hydrogen-induced flow localization and decohesion are considered to be responsible for the observed changes in failure modes and embrittlement of the HT9 and 9Cr-1Mo steels as follows:

Ductile MVC Decohesion of the martensite lath precipitate/matrix interfaces facilitating void nucleation and coalescence across the laths, aided by flow localization.

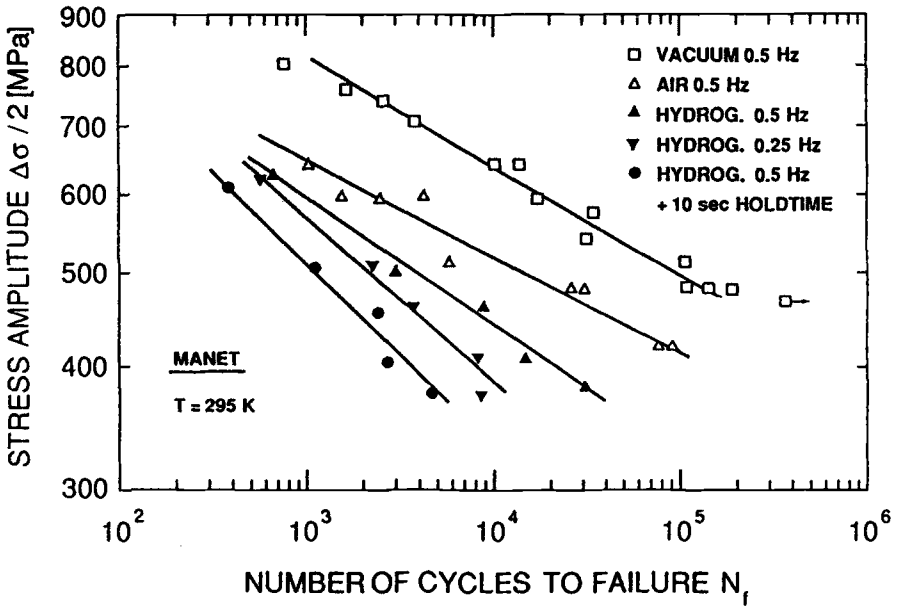

FIG. 6.7—Fatigue endurance of 1.4914 (MANET) steel at ambient temperature in load-controlled tests in vacuum, air, and hydrogen at a pressure of 1.5 bar [50,51].

Ductile QC Decohesion of martensite lath boundaries and subsequent shear failure of lath ligaments as a result of flow localization.

Brittle IG Reduction of the fracture strength of the Laves Fe_2Mo phase and hence the grain boundary cohesive strength plus crack nucleation at intergranular carbides due to flow localization, aided by segregation of phosphorus and/or sulfur.

Brittle TG Lowering of the cohesion of lath boundaries on which Laves phase has precipitated and phosphorus has segregated to such an extent that fully brittle inter- and trans-lath cleavage fractures are produced.

6. *Effects of irradiation*—There is considerable uncertainty regarding the combined influences of hydrogen and irradiation on the embrittlement of the 9–12% Cr steels. The results of initial studies suggest that the critical concentration of hydrogen for embrittlement may either be marginally reduced or increased after low-dose irradiation [47,52]. The effect of 12.5 MeV proton irradiation at ≤70°C to 14 dpa per implanted hydrogen atom on the tensile properties of the reduced-activation F82H steel at 30, 200, and 350°C and strain rates of 7×10^{-5} to 9×10^{-4} s^{-1} have recently been investigated [14]. The yield and ultimate tensile strengths are increased in the ambient temperature tests and reduced slightly at 200°C for homogeneously implanted hydrogen concentrations of ≤7 wppm; the uniform and total elongations are marginally decreased at both test temperatures. However, there is little or no effect of the implantation in the 350°C tests, probably due to the complete release of the hydrogen at this temperature. The tensile strengths and ductilities show large variability in the tests at ambient temperature and 200°C with hydrogen levels ≥10 wppm, possibly as a result of microcrack formation when a critical hydrogen concentration (see Table 6.1) is exceeded [18]. These observations are in general agreement with those on MANET I steel [53], in which implantation with ≤500 appm hydrogen and 0.3 dpa by proton irradiation at 80°C increases the tensile strengths at ambient temperature but has little or no effect in tests above 100°C, again due to rapid loss of the hydrogen from the small section specimens employed.

HYDROGEN ISOTOPE EFFECTS IN FUSION REACTOR SYSTEMS

The main sources of hydrogen and hydrogen isotopes in D-T and breeder structural component materials are [14,18, 25,54]:

a. Neutral and charged tritium and deuterium atoms with energies ranging from about 0.2 eV to ≤10 keV injected into the plasma facing components.
b. Hydrogen formed by (n,p) transmutation reactions in isotopes of the base material and alloying elements.
c. Tritium generated in the breeding blanket.
d. Hydrogen produced by corrosion at the steel-water coolant interfaces, radiolysis of the water coolant, and hydrogen added to the water to inhibit radiolytic decomposition.
e. Hydrogen added to helium coolant to prevent oxidation and aqueous corrosion.

The problem of tritium permeation and control in water- and helium-cooled solid breeder and self- or water-cooled liquid metal ($Li_{17}Pb_{83}$) blankets for a DEMO fusion reactor has been discussed with respect to ensuring safe operation, minimizing the cost of coolant detritiation, and reducing the overall tritium inventory in the system [55,56]. It is evident that surface barrier layers, which can be applied to the first wall, coolant tubes, and/or breeder structural components,

have to be developed to restrict the permeation and thereby retain the tritium in locations where it can be easily extracted.

A thin alumina (Al_2O_3) coating reduces the hydrogen isotope permeability through steel [57], the reduction being as much as four orders of magnitude at temperatures in the range 250 to 600°C and a pressure of 1 bar for the MANET steel [11,12, 58,59]. The results of initial investigations also demonstrate that an effective coating can be produced by a commercial pack aluminizing process in which the high-chromium steel is exposed to $AlCl_3$ vapor at elevated temperatures [11,12]. Iron aluminides are produced on the surfaces, and an adherent layer of the Al_2O_3 is formed by subsequent exposure to oxygen at a high temperature. The coating is resistant to thermal cycling and is self-healing in an oxidizing atmosphere in the event of the surface being damaged by abrasion.

Other chemical vapor deposition (CVD) methods and additional developmental approaches, such as hot isostatic pressing (HIP), hot-dip aluminizing, and vacuum plasma spraying (VPS), are being pursued as part of the European Fusion Program to produce and qualify alumina coatings for the MANET and reduced-activation F82H steels [60]. A characteristic feature of the coatings produced by some of these techniques, particularly hot-dip aluminizing in which the steel samples are immersed for 10 to 30 s in an aluminum melt at 700°C under a protective inert cover gas, is the formation of a layer of Al_5Fe_2 intermetallic phase between the aluminum coating and the steel substrate [60,61]. This brittle phase is transformed completely to a dense, ductile layer of AlFe and/or α-Fe(Al) solid solution phase free of porosity and cracks by heat treatment at 1075°C for 0.5 h after dipping [61].

The tritium permeation barrier developmental approaches mentioned above are applicable for the helium-cooled, solid breeder outside tube (BOT) and self- and water-cooled lithium-lead ($Li_{17}Pb_{83}$) concepts but may not be appropriate for the helium-cooled solid breeder inside tube (BIT) blanket design (see Chapter 2), and other methods may have to be developed [62].

The equilibrium concentration of hydrogen isotopes produced in a high-chromium martensitic steel first wall in a D-T tokamak fusion reactor from the potential sources listed above [a, c, d, and e] have been estimated and compared with the threshold levels judged to be required for blistering (2.5 wppm), embrittlement (1.5 wppm) and slow crack growth (2 wppm) in these types of steels [54]. This analysis assumes a water- or helium-cooled, 10 mm thick first wall operating at temperatures ranging from 250 to 550°C and with a neutron wall loading of 4.15 MW m^{-2} corresponding to the EEF reactor design [63]. It is concluded that deuterium and tritium ion implantation from the plasma is the only potentially significant source of hydrogen isotopes in the first wall, but the concentration is dependent on the assumed ion flux (0.04 and 40 wppm at 250°C for fluxes of 1×10^{17} and 1×10^{20} ions m^{-2} s^{-1}, respectively). Even so, ion implantation from the plasma is unlikely to be a problem under normal operating conditions with a first wall protected against particle erosion and plasma disruptions by bonded coatings or mechanically attached tiles; however, it could become significant in the event of local failure of the coating or the detachment of the tiles.

The stationary hydrogen concentration produced by (n,p) transmutation reactions [source b above] in a 9 to 12% Cr ferritic/martensitic steel fusion reactor blanket structure relative to the critical value required for embrittlement of the unirradiated steel has also been assessed [18]. The assumptions made in this analysis are: a neutron wall loading of 2 MW m^{-2}, a blanket structure thickness of ≈0.5 m, and a hydrogen generation rate of 6×10^{-7} wppm s^{-1}. The results of the computations indicate that the critical hydrogen concentration for embrittlement (a value of ≈10 wppm, based on the results of tensile and disc pressure tests on fine-grained steel, was adopted in this instance [18]) is not achieved if the temperature of the structure is maintained at ≥215°C; allowance is made in this case for the reduction in neutron flux through the blanket, and only one of the blanket surfaces is assumed to be fully permeable to the hydrogen. Furthermore, the effusion time for the hydrogen concentration to decrease to one tenth of its original value during reactor shutdown is estimated to be 1–2 years at 300°C [18].

Additional computations of this type need to be carried out for realistic blanket structure designs and allowance made for the possibility of irradiation-induced point defects and/or helium gas bubbles acting as traps for the hydrogen, thereby reducing the diffusivity and permeability. The use of barriers to reduce the tritium permeation through the structure further complicates the issues and needs to be taken into account in more detailed assessments. In addition, the radiolysis of the coolant water and the production of H_2, O_2, and H_2O_2 radicals may not be so effectively suppressed by an overpressure of hydrogen in a fusion reactor as in a pressurized water fission reactor (PWR). The decomposition of the water is enhanced as a consequence of the high-energy (14 MeV) neutron dose rate and the recombination is less favorable with the low γ flux in the fusion system. Finally, the cross sections for some O (n,p) transmutation reactions are relatively small for neutrons with energies between 1 and 5 MeV but are significantly higher for 14 MeV neutrons; such reactions may therefore provide an additional source of hydrogen in the water coolant under fusion conditions.

Computer codes (TIRP and TIRP2D) have recently been developed to assess and quantify all aspects of the behavior of the hydrogen isotopes in the high-chromium martensitic steels being considered for first wall and breeder blanket structural applications in fusion power reactors [20].

REFERENCES

[1] A. R. Troiano, Trans. ASM 52 (1960) 54.
[2] H. H. Johnson, in: Fundamental Aspects of Stress Corrosion Cracking (Nat. Assoc. Corrosion Engngs., Houston, TX, 1969) 439.
[3] I. M. Bernstein and A. W. Thompson, Int. Met. Rev. 21 (1976) 269.
[4] ASM Metals Handbook, 8th Edition, Vol. 10 (1975) 230; 9th Edition, Vol. 1 (1978) 687.
[5] A. W. Thompson, in: Handbook of Stainless Steel, Eds. D. Peckner and I. M. Bernstein (McGraw-Hill, New York, 1977) Chapter 46.
[6] J. P. Hirth, Metall. Trans. 11A (1980) 961.
[7] A. Turnbull (Ed.), Hydrogen Transport and Cracking in Metals (The Inst. of Materials, London, Book 605, 1995).

[8] G. A. Nelson and R. T. Effinger, Welding J. 34 (1955) 12s.
[9] G. A. Nelson, J. Eng. Ind. 81 (1959) 92.
[10] G. A. Nelson, Amer. Pet. Inst., Publ. 941, 2nd Edition (American Petroleum Institute, Washington, DC 1977) 389.
[11] K. S. Forcey, D. K. Ross, J. C. B. Simpson, and D. S. Evans, J. Nucl. Mater. 160 (1988) 117.
[12] K. S. Forcey, D. K. Ross, J. C. B. Simpson, D. S. Evans, and A. G. Whitaker, J. Nucl. Mater. 161 (1989) 108.
[13] P. Jung, J. Nucl. Mater. 238 (1996) 189.
[14] P. Jung, J. Nucl. Mater. 258-263 (1998) 124.
[15] G. Benamati, A. Donato, A. Solina, R. Valentini, and S. Lanza, J. Nucl. Mater. 212-215 (1994) 1401.
[16] E. Serra, A. Perujo and G. Benamati, J. Nucl. Mater. 245 (1997) 108.
[17] F. Wedig and P. Jung, J. Nucl. Mater. 245 (1997) 138.
[18] P. Jung, Fusion Technology 33 (1998) 63.
[19] R. Kircheim, Acta Metall. 30 (1982) 1069.
[20] G. Benamati, Compiler, Hydrogen Permeation and Embrittlement Studies, ENEA Fusion Division Report ERF FUS ISP MAT 62, January 1996.
[21] R. Valentini, A. Solina, L. Tonelli, S. Lanza, G. Benamati, and A. Donato, J. Nucl. Mater. 233-237 (1996) 1123.
[22] A. Turnbull, M. W. Carroll, and D. H. Ferriss, Acta Metall. 37 (1989) 2039.
[23] J. P. Laurent, G. Lapasset, M. Aucouturier, and P. Lacombe, in: Hydrogen in Metals, Eds. I. M. Bernstein and A. W. Thompson (American Society for Metals, Metals Park, OH, 1974) 559.
[24] G. M. Pressourye, in: Hydrogen Effects in Metals, Eds. I. M. Bernstein and A. W. Thompson, (AIME, New York, 1981) 27.
[25] D. R. Harries, Radiation Effects 101 (1986) 3.
[26] D. R. Harries, in: Topical Conference on Ferritic Alloys for Use in Nuclear Energy Technologies, Eds. J. W. Davis and D. J. Michel (Met. Soc. AIME, Warrendale, PA, 1984) 141.
[27] P. Jung, Literature Survey on Hydrogen Effects in 9-12% Cr Steels, Sub Task MAN-801-D, KFA, Jülich, December 1992.
[28] T. Lechtenberg, W. M. Garrison and J. M. Hyzack, in: Topical Conference on Ferritic Alloys for Use in Nuclear Energy Technologies, Eds. J. W. Davis and D. J. Michel (Met. Soc. AIME, Warrendale, PA, 1984) 365.
[29] W. M. Garrison, J. M. Hyzack, and T. A. Lechtenberg, in: Topical Conference on Ferritic Alloys for Use in Nuclear Energy Technologies, Eds. J. W. Davis and D. J. Michel (Met. Soc. AIME, Warrendale, PA, 1984) 379.
[30] J. M. Hyzack and W. M. Garrison, in: Topical Conference on Ferritic Alloys for Use in Nuclear Energy Technologies, Eds. J. W. Davis and D. J. Michel (Met. Soc. AIME, Warrendale, PA, 1984) 385.
[31] J. M. Hyzack and R. E. Stoltz, J. Nucl. Mater. 103 & 104 (1981) 877.
[32] R. H. Jones and M. T. Thomas, in: Topical Conference on Ferritic Alloys for Use in Nuclear Energy Technologies, Eds. J. W. Davis and D. J. Michel (Met. Soc. AIME, Warrendale, PA, 1984) 395.
[33] R. H. Jones, Metall. Trans. 17A (1986) 1229.
[34] G. F. Rodkey and R. H. Jones, J. Nucl. Mater. 155-157 (1988) 760.
[35] N. P. Haworth and C. A. Hippsley, The Influence of HAZ Microstructures on the Ductility and Hydrogen Embrittlement of 9% Cr 1% Mo Steel, UKAEA Harwell Report AERE R 11473, June 1985.
[36] C. A. Hippsley and N. P. Haworth, Mater. Sci. & Tech. 4 (1988) 791.
[37] G. Krauss and C. J. Manon, in: Martensite, Eds. G. R. Olsen and W. S. Owen, (American Society for Metals, Metals Park OH, 1992) 297.
[38] M. Beghini, G. Benamati, L. Bertini and R. Valentini, J. Nucl. Mater. 258-263 (1998) 1295.
[39] M. Wall, C. E. Lane and C. A. Hippsley, Acta Metall. and Mater. 42 (1994) 1295.
[40] G. J. Jordan, S. J. Andrews and C. A. Hippsley, Mat. Sci. and Tech. 9 (1993) 1115.
[41] L. Coudreuse, R. Blondeau, and A. Cheviet, Mém. Etudes Sci. Rev. de Métallurgie 86 (1989) 35.
[42] J. P. Fidelle, in: Hydrogen Embrittlement: Prevention and Control, ASTM STP 962, Ed. L. Raymond (American Society for Testing and Materials, Philadelphia, PA, 1988) 153.
[43] G. M. Pressourye and F. M. Faure, in: Hydrogen Embrittlement: Prevention and Control, ASTM STP 962, Ed. L. Raymond (American Society for Testing and Materials, Philadelphia, PA, 1988) 353.
[44] G. Benamati, A. Donato, A. Solina, and R. Valentini, in: Fusion Technology 1994, Eds. K. Herschbach, W. Maurer, and J. E. Vetter (North Holland, Amsterdam, 1995) 407.
[45] M. Beghini, G. Benamati, and L. Bertini, J. Eng. Mater. Tech. 118 (1996) 179.
[46] S. Hara, T. Abe, M. Enoeda and H. Takatsu, J. Nucl. Mater. 258-263 (1998) 1280.
[47] A. Kimura, H. Kayano, and M. Narui, J. Nucl. Mater. 179-181 (1991) 737.
[48] H. Li, R. H. Jones, J. P. Hirth, and D. S. Gelles, J. Nucl. Mater. 212-215 (1994) 741.
[49] H-X. Li, R. H. Jones, J. P. Hirth, and D. S. Gelles, J. Nucl. Mater. 233-237 (1996) 258.
[50] H. Ullmaier and W. Schmitz, J. Nucl. Mater. 169 (1989) 233.
[51] J. I. Shakib, H. Ullmaier, E. A. Little, R. G. Faulkner, W. Schmitz, and T. E. Chung, J. Nucl. Mater. 212-215 (1994) 579.
[52] J. Koutsky and K. Spichal, Int. J. Pressure Vessel Piping 24 (1986) 13.
[53] K. Bae, K. Ehrlich, and A. Möslang, J. Nucl. Mater. 191-194 (1992) 905.
[54] R. Boler, C. A. B. Forty, and G. J. Butterworth, An Initial Examination of the Likely Effect of Hydrogen on Low Activation Martensitic Steels, AEA Technology Report AEA FUS 164, February 1992.
[55] E. Proust, L. Anzidei, G. Casini, M. Dalle Donne, L. Giancarli, and S. Malang, Fus. Eng. Des. 22 (1993) 19.
[56] M. Dalle Donne, D. R. Harries, G. Kalinin, R. Mattas, and S. Mori, J. Nucl. Mater. 212-215 (1994) 69.
[57] J. D. Fowler, D. Chandra, T. S. Elleman, A. W. Payne and K. Verguese, J. Amer. Ceramic Soc. 60 (1977) 155.
[58] K. S. Forcey, D. K. Ross and C. H. Wu, J. Nucl. Mater. 182 (1991) 36.
[59] A. Perujo, K. S. Forcey and T. Sample, J. Nucl. Mater. 207 (1993) 86.
[60] G. Benamati, C. Chabrol, A. Perujo, E. Regal and H. Glassbrenner, J. Nucl. Mater. 271 & 272 (1999) 391.
[61] H. Glassbrenner, J. Konys, K. Stein-Fechner, and O. Wedemeyer, J. Nucl. Mater. 258-263 (1998) 1173.
[62] X. Raepsaet, E. Proust, and V. Violante, Fus. Eng. Des. 17 (1991) 367.
[63] M. G. Sowerby and R. A. Forrest, Eds., A Study of the Environmental Impact of Fusion, AEA Technology Report AERE R-13708, March 1990.

7

Joining

The use of a high-chromium martensitic steel for first wall and blanket structural component applications in a fusion reactor will require joining by welding or brazing. It is also envisaged that the construction and heat treatment of such large and complex structures cannot be carried out entirely in the fabrication shop and that some field erection will be necessary.

FUSION WELDING

Welding Processes

The high-chromium martensitic steels are generally regarded as being more difficult to weld than, for example, austenitic steels, because it is often necessary to pre-heat before welding to avoid cracking, and it is essential to carry out a post-weld heat treat treatment (PWHT) to temper the brittle martensitic structures formed in the fusion zone (FZ) and heat affected zones (HAZ). However, experience has shown that the standard steels can be satisfactorily joined by several arc-welding processes using filler wire or in the autogenous mode and by manual and automatic techniques [1–10]. The more conventional processes include shielded metal arc welding (SMAW), gas (helium or argon) tungsten arc welding (GTAW), gas metal arc welding (GMAW), submerged arc welding (SAW), and electroslag welding (ESW), the custom being to use electrodes of the same or similar compositions to those of the base steels. The GMAW process is particularly applicable for narrow gap welding of thick (≥300 mm) section components, while SAW and ESW are favored for automated welds with high deposition rates using single, double, or multiple passes.

Advanced, low-heat input and high-speed processes such as electron beam [11,12] and laser [13] welding are also being developed and/or utilized on an increasing scale for joining the 9 to 12% chromium steels. The heating and cooling rates and the temperature gradients achieved in these processes are much higher compared to arc welding, so that narrower weld zones are produced and thermal damage to the material adjacent to the welds is therefore minimized.

Plates of the quenched-and-tempered (Q & T) MANET I steel, 8, 15, and 20 mm thick, have been electron beam welded without filler wire, and nondestructive and metallographic (transmission and extraction replica electron microscopy) examinations and mechanical property (tensile, creep, fatigue, notched impact, and fracture toughness) tests were carried out on the weldments after tempering for 2 h at 750°C [12,14–17]. The electron beam welds exhibited a fine microstructure and comparable or only marginally inferior mechanical properties to those of the wrought steel.

Autogenous bead-on-plate welds have been made without preheat on 6.4 mm thick plates of HT9 steel [13] and 4–6 mm thick plates of the quenched-and-tempered 9Cr-1Mo, 1.4914, MANET I, and MANET II steels [18,19] using 5 or 6 kW CO_2 lasers and the welding parameters optimized. Characterization of the MANET steel welds by radiography and metallography and hardness, tensile, and notched-impact testing [18,20] showed that the welds were free from defects; the hardness of the MANET II steel welds were comparable, while the tensile strengths at room temperature and 400°C were lower and the toughness superior to those of the base steel after tempering at 760°C for 1 h. In addition, 4 and 6 mm thick plates of the MANET steel have been welded using a pulsed 1.2 kW YAG laser [21]; the FZs and HAZs were slightly wider than those produced by the CO_2 laser welding, but the hardness, tensile and impact properties of the respective FZs were similar.

Weldments have also been made by the SMA, SAW, and GTA processes in thin and thick sections of the advanced, highly alloyed Japanese 9 and 11% Cr steels containing 1.8 to 2.0% W (NF616, HCM12A and TB12M) and the results of weldability tests reported [22]. However, only limited studies have been conducted on the weldability of the reduced-activation martensitic steels. Sound, autogenous bead-on-plate welds have been made in 2¼ to 12Cr-2W-0.25V steels by the GTA process [23]. The as-welded steels containing ≤5% Cr showed no cracking, while the 9% Cr (fully martensitic) and 12% Cr (martensite plus 12 to 17% δ-ferrite) steels developed cracks on subsequent three-point bend testing, but none of the 9 and 12% Cr steel welds cracked after PWHT to restore the toughness. In addition, mechanical property tests have been carried out on GTA welds of the F82H steel made using seven filler wires differing in C, Ta, and B contents [24]. It was concluded from the results of tensile and Charpy V-notch impact tests that the optimum filler metal contained 0.08% C, 0.02% Ta, and with B as low as possible; welds made with such a filler wire had equivalent strengths and toughness to the base steel containing 0.10% C, 0.04% Ta, and 0.0034% B.

Microstructural Characteristics

The microstructures of the FZ and HAZ in weldments of all metallic alloys are usually complex, but they are further complicated in air-hardenable steels of the type considered here due to the phase transformations that occur during the heat-

ing and cooling cycles of the fusion welding process [25]. The various zones in a high-chromium martensitic steel fusion-welded joint are shown schematically in Fig. 7.1; the microstructures of these respective zones in "as-welded" 0.1–0.2% C steels can be interpreted on the basis of the temperatures (defined in Fig. 7.1) achieved during welding and consideration of the phase fields in the equilibrium diagram for high-chromium alloys with low and high net Cr-equivalents (Fig. 7.2) [7] as follows:

FZ ($T>T_m$)—The first phase to form during solidification of the molten weld is δ-ferrite; the ferrite-to-austenite transformation occurs on further cooling, and the austenite transforms to martensite on cooling below the M_s temperature. Some δ-ferrite is usually retained in the FZ at ambient temperature, even when there is no ferrite present in the base and filler wire materials, as complete transformation to austenite does not occur during cooling at the fast rates typical of the welding process [26,27]. Since the δ-ferrite can have detrimental effects on the mechanical properties, particularly strength and fracture toughness, of the high-chromium martensitic steels [28] and welds, the content should be controlled at ≤3% by balancing the concentrations of the austenite- and ferrite-forming elements in the base steels and filler wires. As noted previously, the formation of δ-ferrite can be inhibited in the high-chromium steels by maintaining the Cr-equivalent, calculated using Eq 3.15 in Chapter 3, below approximately 9% [29]; however, experimental data suggest the net Cr-equivalent concentration calculated using Eqs 3.13 and 3.14 in Chapter 3 has to be reduced to ≤7.3 to avoid the presence of δ-ferrite in the FZ of autogenous TIG welds of the MANET-type steel made with a heat input of 1.1 MJ m^{-1} [9].

HAZ—Region 1 ($T_m>T>T_{\gamma\delta}$)—This region (see Fig. 7.1) consists of martensite and δ-ferrite. The ferrite is formed along the prior austenite grain boundaries as the region is heated into the two-phase (γ+δ) field during welding; some of the δ-ferrite is again retained at ambient temperature in a band typically 0.3 to 0.5 mm wide adjacent to the fusion line as a result of the rapid cooling after welding [27]. The δ-ferrite content and width of this region increase with increasing weld heat input and cooling rate; low heat input welding processes such as narrow gap, electron beam, and laser are consequently advantageous in minimizing the extent of the ferrite formation in this part of the HAZ.

HAZ—Region 2 ($T_{\gamma\delta}>T>A_{C3}$)—The microstructure is fully martensitic. This region is heated into the higher temperature part of the γ-phase field during welding, and the original carbide particles are dissolved, resulting in coarse prior austenite grain and martensite lath structures.

HAZ—Region 3 ($T_{\gamma\delta}>T>A_{C3}$)—The structure of this region, which is heated into the lower temperature part of the γ-phase field, is again martensitic, but it is finer grained than Region 2, as some of the original carbides are not dissolved and inhibit grain growth.

HAZ—Region 4 ($A_{C3}>T>A_{C1}$)—The structure consists of untempered and overtempered martensite. Incomplete transformation to austenite and additional tempering of the original tempered martensite structure of the base steel occur during heating in this intercritical zone, with the austenite again transforming to martensite on cooling.

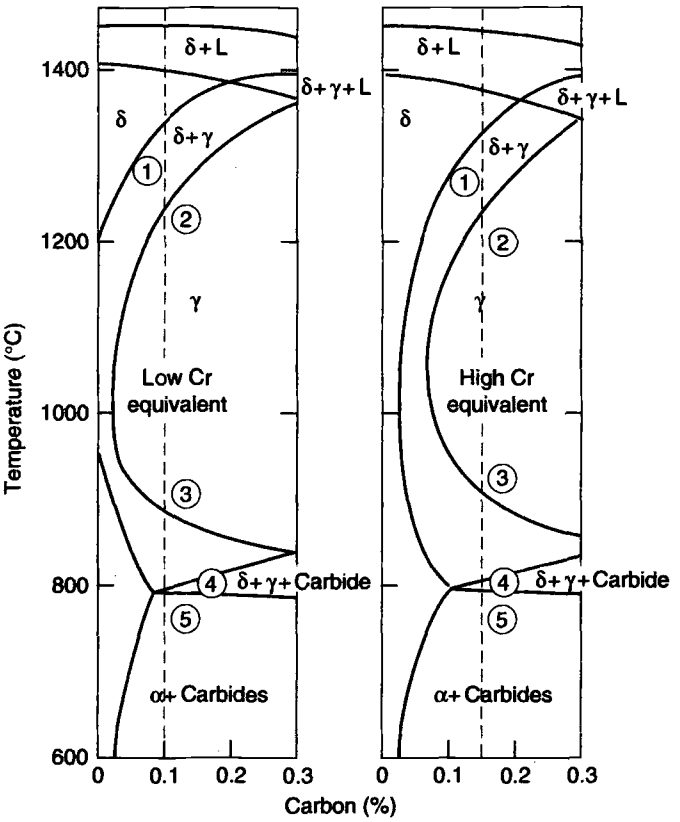

FIG. 7.2—Phase diagram for high-chromium steels illustrating the effect of net Cr-equivalent and the relationship with the HAZ regions observed in fusion welds of 0.1% C low Cr-equivalent and 0.15% C high Cr-equivalent martensitic steels [7].

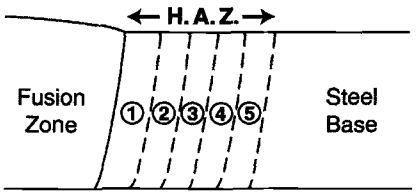

Fusion Zone (FZ): $T > T_m$

Heat - Affected - Zone (HAZ) [as-welded]:

Region 1	$T_m > T > T_{\gamma\delta}$	γ+ δ → Martensite + δ
Region 2	$T_{\gamma\delta} > T > A_{c3}$	Coarse grained γ → Martensite
Region 3	$T_{\gamma\delta} > T > A_{c3}$	Fine grained γ → Martensite
Region 4	$A_{c3} > T > A_{c1}$	γ → Martensite + Overtempered Martensite
Region 5	$A_{c1} > T > T_T$	Overtempered Martensite

where
- T = temperature achieved during welding
- T_m = melting point of steel
- $T_{\gamma\delta}$ = temperature at which γ → δ transformation is complete on heating
- T_T = original tempering temperature of steel
- A_{c1} = temperature at which α → γ transformation starts on heating
- A_{c3} = temperature at which α → γ transformation is complete on heating

FIG. 7.1—Schematic diagram of the heat-affected zone regions in a fusion weld of high-chromium martensitic steel.

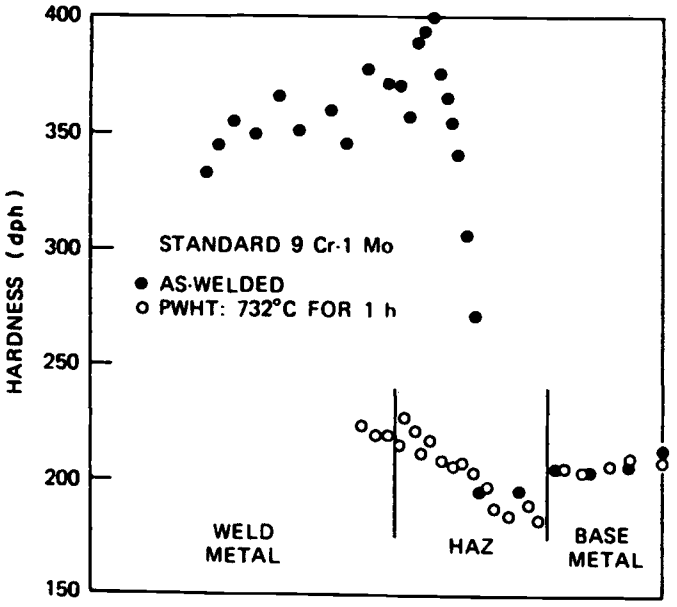

FIG. 7.3—Microhardness traverse across a GTA weld before and after PWHT at 732°C for 1 h; standard 9Cr-1Mo steel base and filler wire [30].

HAZ—Region 5 ($A_{C1}>T>T_T$)—The original tempered martensite in this narrow zone is further tempered during welding, but the microstructure is otherwise similar to that of the base steel.

The micro-hardness profiles across GTA welds in modified 9Cr-1Mo [30] and HT9 [25] steels are reproduced in Figs. 7.3 and 7.4, respectively. The data in Fig. 7.4 show that the various regions of the HAZ can be differentiated by their hardness. The presence of the softer δ-ferrite phase in the untempered martensite matrix is responsible for the reduction of hardness in Region 1. Since the hardness of the martensite increases with increasing carbon content, the dissolution of the carbide particles in the austenite in Region 2 has resulted in the formation of high carbon martensite with maximum hardness. The carbon content of the martensite in Region 3 is reduced relative to Region 2 due to the incomplete dissolution of the carbides at the lower austenitizing temperature and hence the hardness is lower. The hardness reduction in Regions 4 and 5 result from overtempering of the original microstructure at temperatures between A_{C3} and A_{C1} and below A_{C1}, respectively. The hardness of the FZ and HAZ are reduced after PWHT at 732°C for 1 h and, as shown in Fig. 7.5 for a 9Cr-1MoVNb steel weld [3], the hardness of the weld and HAZ approach that of the base steel after PWHT for times up to 80 h at 732°C. The low hardness of the HAZ adjacent to the base steel, clearly evident in Figs. 7.3, 7.4, and 7.5, is characteristic of all Cr-Mo steels, and it has a significant effect on the mechanical properties of the weldment, as discussed below.

A typical microstructure of a 9Cr-1MoVNb steel weld is illustrated in Fig. 7.6 [3]. Four regions are delineated—the weld metal (W) corresponds to the fusion zone (FZ) of Fig. 7.1, the transformed zone (TZ) corresponds to Regions 1, 2, 3, and 4, the tempered zone (TMPZ) corresponds to Region 5, and the base metal (BM) is the steel base which was unaffected during the welding process. Thin foil transmission and extraction replica electron microscopy of a welded and PWHT 12Cr-1MoV steel [8] has shown larger sub-grains, lower dislocation densities, and larger and more spherical undissolved carbide particles in the intercritical Region 4 than in the base steel, indicating lower strength of the former. The carbide structure in the coarse-grained transformed Region 2 was similar to that in the original base steel, the carbides having been dissolved during welding and reprecipi-

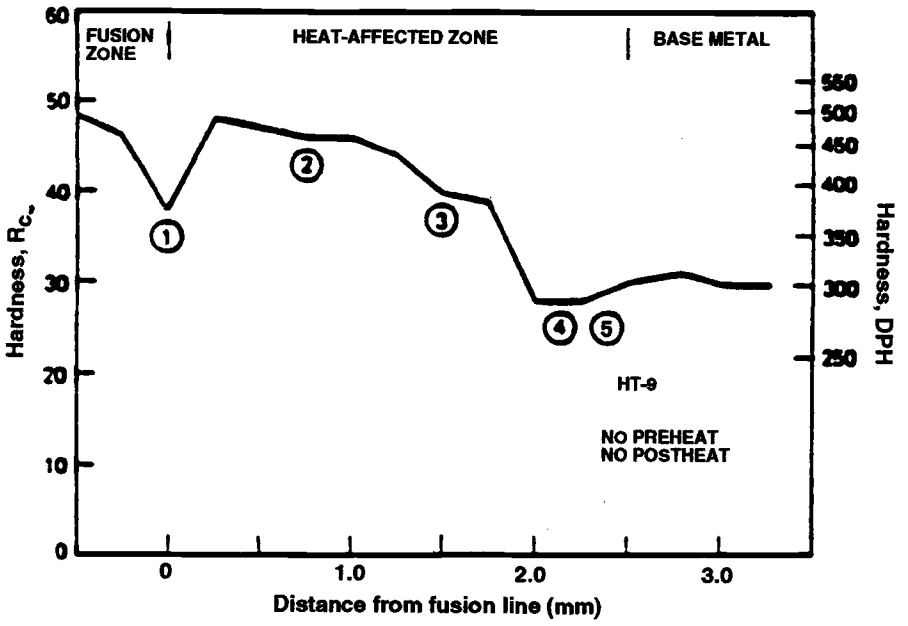

FIG. 7.4—Microhardness traverse across a GTA weld in HT9 steel [25]; the numbers 1–5 correspond to the HAZ regions in Fig. 7.1.

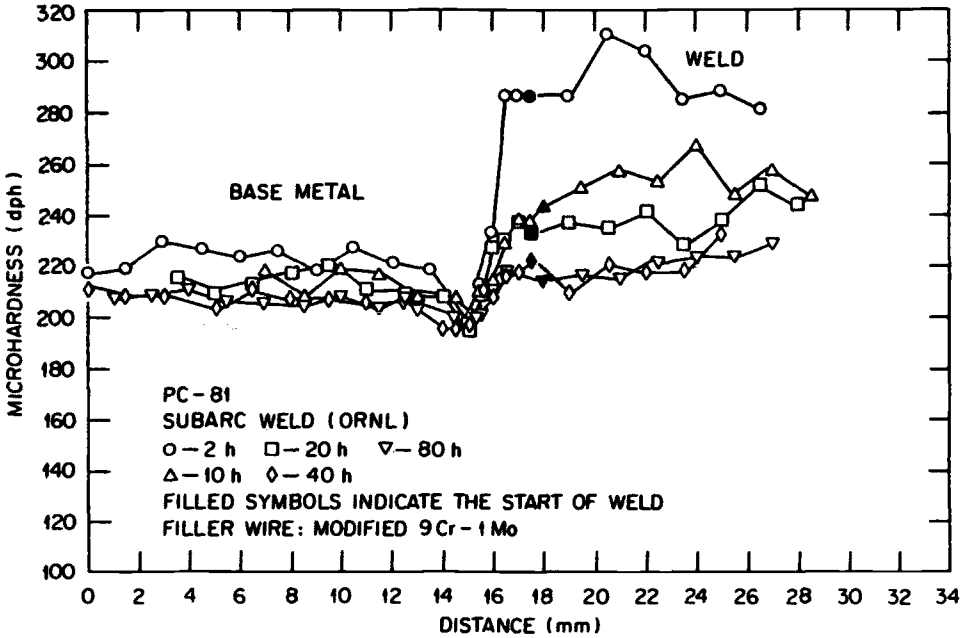

FIG. 7.5—Microhardness traverse across an SA weld after PWHT for various times at 732°C; modified 9Cr-1Mo steel base and filler wire [3].

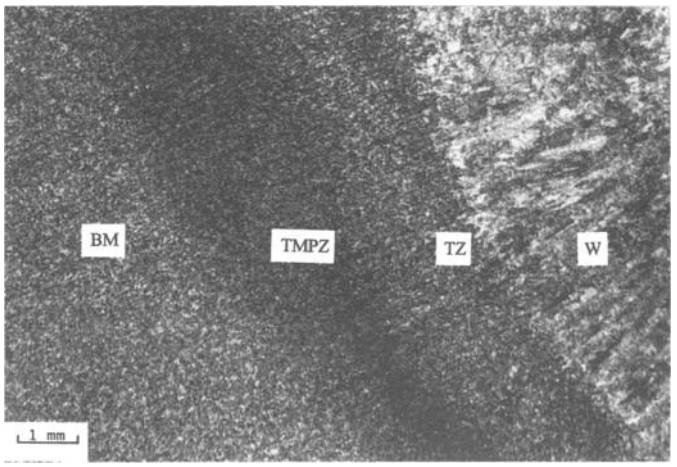

FIG. 7.6—Typical microstructure of a modified 9Cr-1Mo steel weld illustrating the weld (W) and two regions of the HAZ [transformed zone (TZ) and tempered zone (TMPZ)] [3].

tated during PWHT. There were fairly large carbide particles on the prior austenite grain boundaries, and smaller carbides precipitated on the sub-grain boundaries within the relatively fine prior austenite grains in Region 3.

Weld Defects

The welding of the 9–12% chromium steels requires a high degree of preparation and control to avoid cracking during the welding, PWHT, or service. Cracking processes include:

Solidification cracking—The steels may become susceptible to solidification or hot cracking as the weld pool solidifies due to elemental segregation to the inter-dendritic regions, producing local reductions in melting point and the liquation of discrete second phases. Cracking is induced by the thermal contraction and restraint stresses set up during solidification and in underlying weld runs reheated by subsequent passes.

The elements that promote the cracking by interfacial segregation include sulfur, phosphorus, and boron [7,9]; sulfur appears to be particularly detrimental as it can form a low-melting eutectic [(FeMn)S] [31]. A high concentration of niobium is also harmful due to the formation of an NbC/γ eutectic [32–35] and other low melting point compounds with phosphorus (Nb_8P_5) and silicon (NbSi) [36]. It has also been reported that vanadium in combination with niobium is harmful, although the former is not particularly detrimental by itself [33].

The results of an extensive program using the Tigamajig test [37] on many experimental heats of the modified 9Cr-1Mo steel have indicated little or no susceptibility to solidification cracking. This is consistent with observations on a large number of actual welds made in the laboratory and the experience of commercial fabricators, where no solidification cracking has been observed [38]. However, it has been shown that TIG welds of the MANET II steel are more prone to solidification cracking than martensitic steels containing $\approx$9% Cr [39]. The cracks were associated with regions of high chromium and other elemental segregation, which can act as sites for the formation of the embrittling α' (Cr-rich ferrite) and carbide phases during service. Nevertheless, cracking of this type can be avoided by reducing the concentrations of the liquation-promoting elements in the steel and consumables and decreasing the thermal shrinkage stresses by lowering the weld heat input.

HAZ liquation cracking—The high-chromium martensitic steels may also be prone to liquation cracking in the HAZ immediately adjacent to the FZ. For example, the susceptibility of the 9Cr-2MoVNb (EM12) steel to this type of cracking has been investigated in Gleeble machine tests in which samples

are heated at high rates and fractured at various temperatures during heating [35]. While complete fusion of the steel occurred at 1450°C, grain boundary liquation, as evidenced by the results of reduction of area measurements, was produced at 1350°C.

Hydrogen or cold cracking—Cold cracking of the brittle martensitic phase can occur during cooling after welding of low- and high-alloy martensitic steels, particularly in thick sections, as a result of the stresses induced by thermal contraction and the volume expansion associated with the austenite-to-martensite transformation. This type of cracking is exacerbated by the introduction of hydrogen into the weld pool, the principal source of hydrogen being moisture in the electrode coatings and fluxes; the solubility of hydrogen is high at elevated temperatures but decreases at lower temperatures, with the result that high-pressure stresses are generated at lattice discontinuities, such as dislocations, microvoids, precipitate-matrix and other interfaces, leading to cracking of the hard and brittle martensite phase in the FZ and HAZ.

The incidence of this type of cracking is minimized by the use of covered electrodes with low hydrogen contents and protection of the wires and electrodes by storage at elevated temperatures prior to welding. However, an effective way of preventing cold and hydrogen-assisted cracking is by controlling the preheat, interpass, and PWHT temperatures.

It is essential that a fully martensitic structure is produced in the weld zone prior to PWHT to achieve the optimum combination of strength and toughness in the tempered structure. Preheating is normally carried out at about 200°C, which corresponds to the M_f temperatures of the simple 9Cr and 9Cr-1Mo steels and thereby ensures maximum transformation to martensite during welding as well as allowing hydrogen to diffuse out of the weld zone. However, the M_f temperatures for the more highly alloyed martensitic steels (9Cr-1MoVNb, 12Cr-1MoV and 12Cr-1MoVNb) can be significantly below 200°C, so that there is a possibility of incomplete transformation to martensite on cooling to ambient temperature after welding. This has led to various options for welding these steels [6,8,40], the procedure initially developed for the 12Cr-1MoV steel (X20) being illustrated in Fig. 7.7. The "austenitic welding" is carried out with an interpass temperature above the M_s temperature so that the deposited weld metal remains austenitic until intercooled to or below the M_f temperature (80 to 120°C) to ensure full martensite transformation before PWHT (Fig. 7.8). There is a danger that intercooling at a temperature above 120°C would result in significant amounts of the weld metal remaining austenitic during PWHT and in transformation of the residual austenite to the brittle martensite after this treatment. It may be necessary, however, to maintain the interpass temperature at 200 to 300°C for very thick sections or for very constrained welds so as to achieve partial martensitic transformation of each weld bead and tempering of the martensite by subsequent beads. A more ductile weld is produced by this "martensitic welding" procedure and cracking thereby avoided during intercooling.

The susceptibilities of various 9–12% Cr martensitic steels to hydrogen cracking have been established using the Tekken Y groove restraint [39] and Implant [41] tests in investigations carried out in support of the fast breeder and fusion reactor and non-nuclear alloy development programs [29]. Cracking of the 9Cr-1MoVNb steel was observed when no preheat was applied or preheating was carried out at 93°C, whereas preheating to 204°C prevented cracking [3]. Furthermore, it has been demonstrated that the sensitivity of the MANET steel to HAZ hydrogen cracking was comparable to that of other high-chromium martensitic steels and could be minimized by preheating to about 200°C [37]. Preheating to lower temperatures of 150 or 175°C appeared to suffice for other types of steel [39,42].

Reheat cracking—Reheat or stress-relief cracking may occur in the HAZ and sometimes in the weld of alloy steels during PWHT or service at elevated temperatures. The cracking results from increased solution of alloy carbides in those parts of the HAZ and weld metal heated to temperatures of $\leq$1320°C (Region 2 of Fig. 7.1), followed by strain-induced precipitation of fine particles on the dislocations and stacking faults within the coarse prior austenite grains when the residual stresses relax by creep at temperatures in the range 400 to 750°C. This leads to marked strengthening of the grains such that the deformation is concentrated at or near the grain boundaries and can result in low-ductility, intergranular failures. This type of cracking is facilitated by segregation of surface-active elements such as P, S, Sn, and Sb at the prior austenite grain boundaries, the phosphorus being particularly detrimental in the absence of molybdenum in the steels [43]. However, the presence of up to $\approx$5% δ-ferrite makes the steels less sensitive to the reheat cracking [35,43,44], probably as a consequence of the ferrite having a higher solubility for the harmful impurity elements and being more ductile than the tempered martensite matrix.

The susceptibility of the MANET II steel to reheat cracking has been investigated by subjecting parent material samples to a coarse-grained HAZ thermal simulation treatment, followed by three-point notched bend relaxation testing at 745°C [39]; the steel proved to have a high resistance to the intergranular reheat cracking in these tests and is probably immune to this type of failure during commercial fabrication and heat treatment. The 9Cr-1MoVNb steel is also resistant to the reheat cracking [38]. These observations are somewhat surprising in view of the presence in these steels of niobium and vanadium, which promote stress-relief cracking in other alloys due to the intragranular precipitation of niobium and vanadium carbides. However, undissolved niobium carbide particles inhibit austenite grain growth by pinning the grain boundaries and the fine-grained structure has superior resistance to the intergranular cracking.

Type IV cracking—This type of failure, also known as mid-life weldment cracking, has become a major inspection and maintenance problem in power generation plants worldwide [45,46]. Although the phenomenon is not fully understood, circumstantial evidence suggests that the cracking results from high stresses across the weldment and the accumulation of creep cavitational damage in the intercritically transformed zone (ICZ)—Region 4 of Fig. 7.1—of the weld HAZ, which has a low rupture ductility [46–49]. It has occurred in low-alloy Cr-Mo steels used for steam pipework and header systems after long periods of operation in the temperature range 500 to 565°C. Type IV cracking has not been detected hitherto in the higher-chromium (X20) martensitic steels exposed for $\geq$150 000 h in fossil-fired

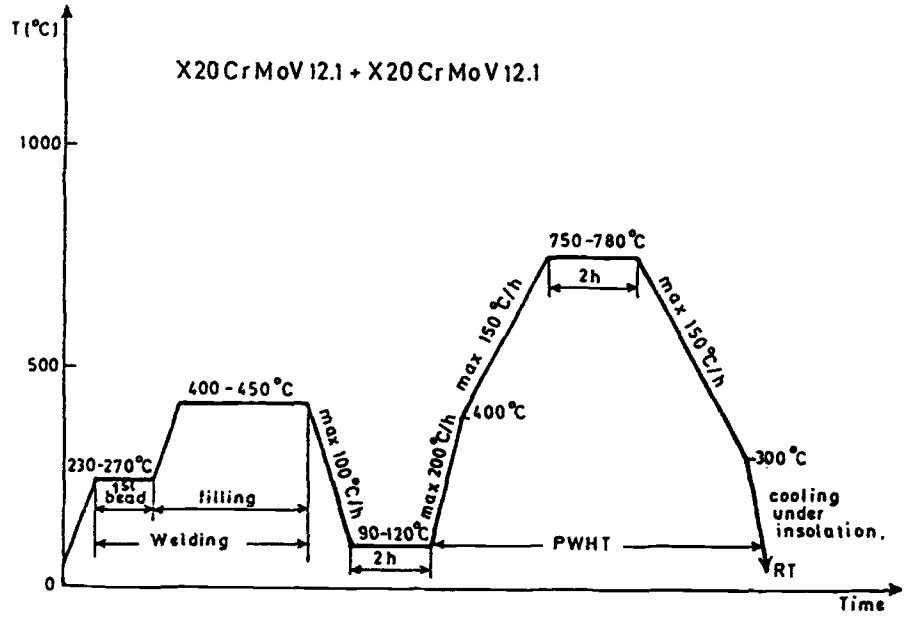

(a) austenitic welding

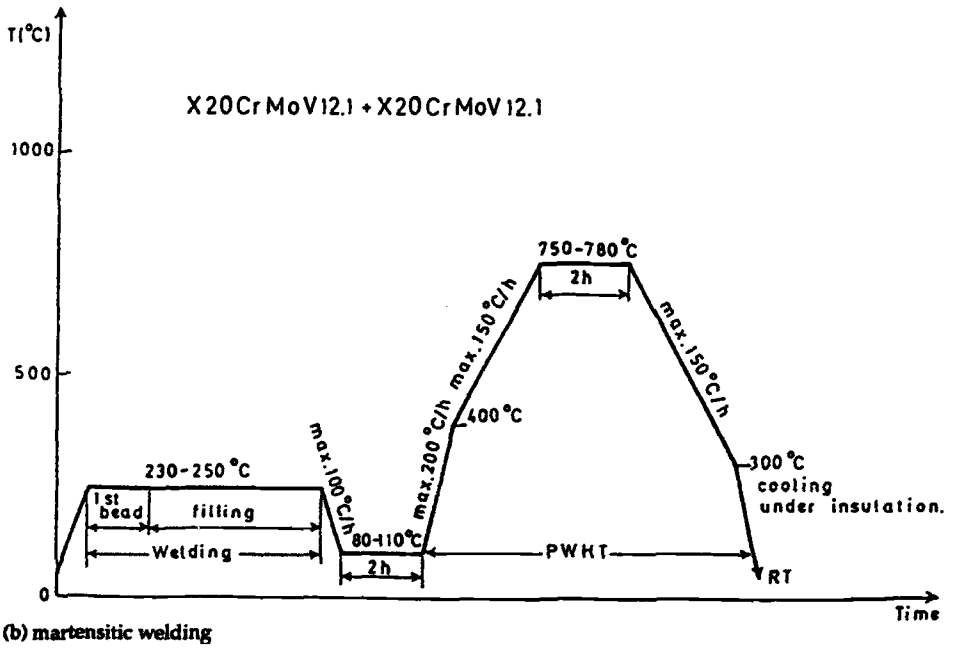

(b) martensitic welding

FIG. 7.7—Preheat, interpass and post-weld heat treatment temperatures for austenitic and martensitic welding of a 12Cr-1MoV steel [8].

power plants [8], but the results of laboratory investigations, in which the failure mode was simulated by accelerated creep-rupture tests on cross-weld specimens at elevated temperatures, suggest that it may also be a problem at moderate to low stresses in the 9Cr-1Mo, 9Cr-1MoVNb, and 12Cr-MoV steels [7,8,46,50–52] and in the newly developed Japanese 9 and 11% Cr steels (NF616, HCM12A, and TB12M) [22]. It has been recommended that the modified 9Cr-1Mo steel should be partially tempered at 600 to 700°C before welding to remove the soft zone [2], and the effectiveness of this approach in preventing premature cracking has been demonstrated [53,54]. Test results have also indicated that Type IV cracking is suppressed by the presence of δ-ferrite in the steel [55].

There is a need to generate long-term creep-rupture data on cross-welded, high-chromium reduced-activation martensitic steels being developed for fusion system applications, produced by both conventional and advanced electron-beam and laser welding techniques, to establish whether or not they are susceptible to Type IV cracking and, if so, there is a minimum temperature below which this problem does not occur [46].

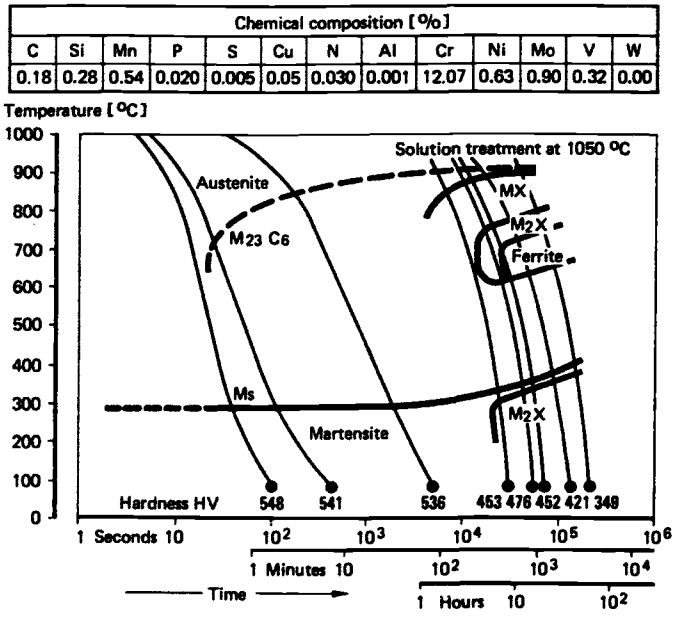

FIG. 7.8—Continuous-cooling-transformation diagram for a 12Cr-1MoV steel and filler metal [6].

SOLID STATE WELDING

There are several solid state welding processes which have been applied or are being developed for joining the high-chromium martensitic steels:

High-frequency induction welding has been utilized for producing longitudinal seams in the manufacture of 9–12% Cr steel pipe and tubing, the edges to be joined being forged together by pressure rolls at the high temperatures induced by high-frequency AC heating [9]. The process does not require high heat input, but its application is generally restricted to thin sections, and tempering of the martensite in the welded joints is again essential.

Diffusion welding essentially involves pressing together components with parallel faces in vacuum at high temperatures so as to facilitate inter-diffusion and thereby produce strong bonding. Earlier investigations had shown that AISI 410 (11.5 to 13.5% Cr) steel joints possessing reasonable strengths at ambient temperature could be produced using Ni-Be alloy interlayers and the application of 1 psi (6.895 kPa) pressure at 1150 to 1200°C for 5 min [9].

More recently, the feasibility of diffusion bonding MANET II steel plates, with and without an intermediate electrodeposited layer of nickel, for the highly loaded breeder blanket structure in a fusion reactor has been evaluated [56]. The results of tests on small (80 mm diameter) disks showed that leak tight bonds with bend strengths almost equivalent to those of the base steel could be produced under the following conditions:

1. Plates with finely ground surfaces (≤3 μm roughness) - 980°C, initial pressurization at 30 MPa for 1 h, and then 7 MPa for 1 h.
2. Plates with 20 μm thick nickel surface layers—1050°C, initial pressurization at 18 MPa for 1 h, and then 7 MPa for 1 h.

Helium leak tight joints in 320 mm diameter MANET II steel disks with typical fusion reactor first wall geometries have subsequently been made under these optimized conditions.

Sound diffusion-bonded F82H reduced-activation steel joints have also been produced without an intermediate layer, with the proviso that the initial surface roughness was $\leq 1\mu$ R_{max}, by heating in vacuum (7×10^{-3} Pa) for 10 or 60 min at temperatures of 950 and 1050°C with a compressive stress of 3 to 12 MPa [57]. However, a post-bonding normalizing-and-tempering treatment was essential to eliminate the martensite formed in the joint. While adequate tensile strengths of the diffusion bonds can thus be attained, the ductilities and toughness tend to be inferior to those of the base steel [58].

Explosive welding is a well-established process in which high pressures are produced and mutual deformation of the mating surfaces obtained as a result of applying a high-velocity impact between the components to be joined [59]. It is an attractive joining technique as precise control of the composition, prior heat treatment, and metallurgical structure of the base materials is not required. The method has been developed commercially for producing clad plates, tube-tube plate joints, and plugging repairs in steam generators [60–62]. Furthermore, almost 3000 leaking tube-tube plate welds in the evaporator units in the Dounreay Prototype Fast Reactor (PFR) were repaired by a combination of explosive welding and brazing [63]. The defective welds were bridged by internal sleeves of 9Cr-1Mo steel explosively welded to the top of the tube plate (2¼Cr-1Mo steel) and brazed into the leaking tube (2¼Cr-1MoNb steel) about 100 mm below the defective weld. Earlier experience of explosive welding the 9Cr-2¼Cr steel combination had been obtained in the development and manufacturing work undertaken on the replacement superheater tube bundles for PFR [64]; helium leak, dye penetrant, ultrasonic, and peel tests, together with metallographic examinations, have demonstrated that sound joints can be consistently produced by this process.

DISSIMILAR METAL WELDING

The superheater sections of conventionally powered boilers and pipe runs often contain welded transition joints or dissimilar metal joints between low-alloy (usually 2¼Cr-1Mo) ferritic and austenitic steel components [7,45]. The joints have to accommodate significant differences in physical, chemical, and mechanical properties and may operate at temperatures well within the creep range of the ferritic steel. Experience has shown that the service lives of these transition joints can be much shorter than those of joints between similar materials, the failures being due to low ductility cracking in the HAZ of the ferritic steel close to the fusion line [45].

It is probable that the use of a high-chromium martensitic steel for structural component applications in a fusion reactor will also involve welding to a different material such as an austenitic stainless steel (e.g., Type 316). Observations on transition joints between X20 or 9Cr-1Mo and Type 316 steels have revealed that the interstitial carbon diffuses

from the martensitic to the austenitic steel during welding, heat treatment, and high-temperature service, resulting in the formation of a band of ferrite adjacent to the fusion zone. The carbon migration and the incidence of the thermal stress cracking in the transition joint can be inhibited by incorporating a nickel-base alloy insert between the martensitic and austenitic steels to act as a diffusion barrier and minimize the thermal expansion differences [65]. Thus, tube-to-tube butt welds have been produced between 9Cr-1Mo and 316 steels using a transition piece of Alloy 600 (0.04% C, 16% Cr, 72% Ni, 0.3% Ti, 0.2% Al, Fe-balance), the 9Cr-1Mo steel being joined to the Alloy 600 by a two-pass TIG weld with synchronous Inconel 82 (0.025% C, 20% Cr, 1% Mo, 0.28% Fe, Ni-balance) filler wire feed [66,67]. Failures of re-normalized-and-tempered specimens occurred along the fusion line between the martensitic steel and the Inconel 82 weld metal in uniaxial and biaxial creep tests at temperatures in the range 525 to 640°C and testing times of $\leq$ 25 000 h.

Joints between 9Cr-1Mo and 2¼Cr-1Mo and 9Cr-1Mo and Type 316 austenitic steels have also been successfully made by explosive welding [60]; the welds were free from porosity and HAZs, although some isolated melted regions were evident along the weld interfaces.

In addition, transition joints between dissimilar materials may be produced using inserts of graded compositions manufactured by the powder metallurgy (PM)-hot isostatic pressing (HIPping) process [7,68]. The chemical composition gradient is effected by mixing powders of the two materials (such as 10Cr-1Mo martensitic and Type 316 austenitic steels) powders in various ratios along the transition piece, thereby enabling one dissimilar weld to be replaced by two similar ones [68].

BRAZING

Brazing was initially adopted as the joining technique for the manufacture of the 9Cr-1Mo steel replacement tube bundles for the PFR reheaters and superheaters. The process was subsequently developed further and, as mentioned above, applied successfully as part of the repair technique for defective welds between the steam tubes (2¼Cr-1MoNb steel) and tube plate (2¼Cr-1Mo steel) in the PFR evaporator units [63]. The required cleanliness of the surfaces to be joined, which influences the wetting angle, and, hence, the flow of the braze filler, was achieved by degreasing and grit blasting. Brazing was then effected using a high-nickel alloy filler (BNi4—1.7% B, 3.5% Si, 0.9% Fe, 0.06% max C, Ni-balance; liquidus temperature 1060°C) with a capillary gap of $\leq$50 μm by induction heating in an argon atmosphere at 1180°C for a total cycle time of 5 min, the martensite formed in the brazed zone being finally tempered at 750°C to reduce the hardness (Fig. 7.9).

Brazing has also been considered and evaluated for joining materials, principally austenitic steels, for fusion reactor first wall and breeding blanket structural components [69–71]. However, preliminary brazing tests using BNi6 (0.10% C, 11% P, 0.02% S, 0.05% Al, 0.05% Ti, 0.05% Zr, Ni-balance) and BNi7 (0.08% C, 0.10% Si, 0.2% Fe, 0.01% B, 14% Cr, 10% P, 0.04% Mn, S, Al, Ti and Zr as for BNi6, Ni-balance) filler materials have been carried out on modified 9Cr-1Mo steel in vacuum at 1200°C followed by tempering at 740°C to demonstrate the feasibility of the approach and the quality of the brazed joints [72]. There is a significant advantage if the brazing can be carried out with the whole component located within an evacuated or controlled-atmosphere furnace, as the entire structure is subjected to the same temperature-

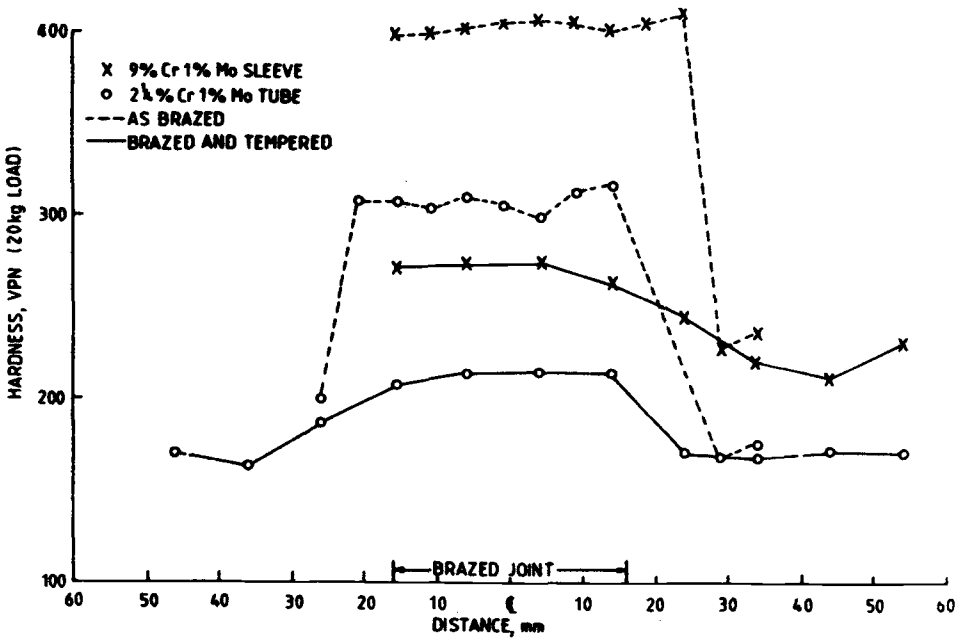

FIG. 7.9—Hardness profile across a brazed repair joint between the 9Cr-1Mo steel sleeve and 2¼Cr-1Mo steel steam tube in the PFR evaporator units [63].

time cycle as the brazed joint; this ensures uniformity of the microstructure and mechanical properties and obviates the formation of the HAZ characteristic of welding. However, the fusion reactor components may be too large for the brazing to be carried out in a furnace so that resort may have to be made to local inert gas purging and induction heating of the joint area as in the case of the PFR evaporator repair brazements referred to above.

WELDING OF IRRADIATED STEELS

It is anticipated that repair by conventional welding techniques and replacement of irradiated fusion reactor components will be necessary during the plant life. In addition to radioactivity considerations, the rewelding may pose significant problems because the insoluble helium produced by (n,α) reactions during service precipitates as bubbles at grain boundaries. These bubbles grow by the absorption of vacancies at high temperatures under the action of the internal tensile stresses produced during welding and eventually coalesce, resulting in premature intergranular fracture (see Chapter 13).

There are only limited data on the welding of irradiated materials, although some studies have been performed on austenitic steels [73–75], and a preliminary investigation has been carried out on the 12Cr-MoVW (HT9) steel [74]. Helium concentrations of 0.3 and 1.0 appm were produced in normalized-and-tempered samples of the martensitic steel by the "tritium trick" technique [dissolution of tritium in the steel by heating at 300°C with various gas pressures, followed by decay of the tritium to helium ($^3H \rightarrow {}^3He + {}^0\beta$) and removal of residual tritium by holding in vacuum (10^{-3} Pa) at 400°C] and autogenous bead-on-plate welds then made by the GTAW process.

While no weld defects were observed in control samples and specimens with 0.3 appm helium, the welds containing 1.0 appm helium showed discontinuous micro-cracking at the prior austenite grain boundaries in that part of the HAZ located within several grain diameters of the fusion boundary. It was concluded [74] that the cracking occurred at high temperatures as a result of the shrinkage stresses induced in the constrained plates during cooling after welding and originated from the growth and coalescence of the grain boundary helium bubbles as observed by SEM and TEM examinations. The behavior of the martensitic steel, whose structure is austenitic in the approximate temperature range 850 to 1350°C, closely paralleled that of Type 316 austenitic steel.

It has been established that the application of a compressive stress during welding suppresses helium bubble growth parallel to the weld direction and thereby inhibits the HAZ cracking in the 316 austenitic steel [75], but this approach has not yet been investigated in the case of the martensitic steel.

REFERENCES

[1] C. H. Kreischer, J. Cothren and A. E. Near, Welding J. 40 (1961) 489s.

[2] J. R. DiStefano, V. K. Sikka, J. J. Blass C. R. Brinkman, J. M. Corum, J. A. Horak, R. L. Huddleston, J. F. King, R. W. McClung, and W. K. Sartory, Summary of Modified 9Cr-1Mo Steel Development Program: 1975-1985, Oak Ridge National Laboratory, Report ORNL-6303, October 1986.

[3] J. F. King, V. K. Sikka, M. L. Santella, J. F. Turner, and E. W. Pickering, Weldability of Modified 9Cr-1Mo Steel, Oak Ridge National Laboratory, ORNL-6299, September 1986.

[4] T. Lechtenberg, in: Ferritic Steels for High Temperature Applications, Ed. A. K. Khare, (ASM, Metals Park, OH, 1983) 163.

[5] G. P. Kalwa, K. Haarmann and K. J. Janssen, in: Topical Conference on Ferritic Steels for Use in Nuclear Energy Technologies, Eds. J. W. Davis and D. J. Michel (Met. Soc. AIME, Warrendale, PA, 1984) 235.

[6] F. Brühl and H. Müsch, in: Topical Conference on Ferritic Steels for Use in Nuclear Energy Technologies, Eds. J. W. Davis and D. J. Michel (Met. Soc. AIME, Warrendale, PA, 1984) 253.

[7] A. T. Price, in: Rupture Ductility of Creep Resistant Steels, Ed. A. Strang (The Instit. of Metals, London, Book No. 522, 1991) 246.

[8] J. Hald, in: Rupture Ductility of Creep Resistant Steels, Ed. A. Strang (The Inst. of Metals, London, Book No. 522, 1991) 268.

[9] P. Buttol, G. Carboni, E. Filippini, B. Mussini, and C. Cappabianca, Review of the Fabrication of the MANET Steel, ENEA, Dipartimento Reattori Innovativi, Report CT. WCH. 00017, February 1993.

[10] B. Mussini, Microstructural and Mechanical Properties of Welded Joints Performed by Fusion Welding Processes on 9-12% Cr Martensitic Steels, ENEA, Report N. DRI CT. WCB. 00012, March 1993.

[11] Y. Arata, F. Matsuda, and K. Nakata, in: Plasma, Electron and Laser Beam Technology (ASM, Metals Park, OH, 1986) 319.

[12] B. van der Schaaf and M. I. de Vries, in: Fusion Technology, 1990, Vol. 1, Eds. B. E. Keen, M. Huguet, and R. Hemsworth (North Holland, Amsterdam, 1991) 954.

[13] J. C. Lippold, J. Nucl. Mater. 103-104 (1981) 1127.

[14] P. Groot and F. A. van der Berg, TEM Study of Martensitic Stainless Steel (MANET), ECN Petten, Report 1-90-045, November 1990.

[15] P. Groot and F. A. van der Berg, Transmission Electron Microscopy of Electron Beam Welded Ferritic 12% Cr Steel by Extraction Replica Technique, ECN Petten, Report 1-91-066, October 1991.

[16] H. Th. Klippel (Ed.), Progress Report 1990 on Fusion Technology Tasks, ECN Petten, Report C-91-035, June 1991.

[17] H. Th. Klippel, (Ed.), Progress Report 1991 on Fusion Technology Tasks, ECN Petten, Report C-92-049, July 1992.

[18] C. Charissoux and A. Richard, Laser Welding of 1.4914 and T91 Steels, Determination of Parameters, CEA, CEN de Saclay Report STA/LMS/89-NT620, November 1989.

[19] C. Charissoux and A. Richard, Soudage par Laser CO_2 de 6 kW des Aciers T91 et 1.4914, CEA, CEN de Saclay, Report STA/LMS/92-NT658, May 1992.

[20] A. Richard, Soudage par Laser CO_2 de L'Acier MANET en Epaisseurs 4 et 6 mm, CEA, CEREM Report STA/LMS/93-NT730, December 1993.

[21] A. Richard and J. Schildknecht, Soudage par Laser YAG de L'Acier MANET en Epaisseurs 4 et 6 mm et Comparaison avec Les Resultant Obtenus en Laser CO_2, CEA, CEREM Report STA/LMS/94-NT753, November 1994.

[22] B. Nath, E. Metcalfe, and J. Hald, in: Microstructural Development and Stability in High Chromium Ferritic Power Plant Steels, Eds. A. Strang and D. J. Gooch (The Inst. of Materials, London, Book 667, 1997) 123.

[23] C. A. Wang, R. L. Klueh, and B. A. Chin, J. Nucl. Mater. 191-194 (1992) 831.

[24] H. Hayakawa, J. Nucl. Mater. 179-181 (1991) 693.

[25] J. C. Lippold, in: Topical Conference on Ferritic Steels for Use in Nuclear Energy Technologies, Eds. J. W. Davis and D. J. Michel (Met. Soc. AIME, Warrendale, PA., 1984) 497.
[26] R. S. Fidler and D. J. Gooch, in: Ferritic Steels for Fast Reactor Steam Generators, Eds. S. F. Pugh and E. A. Little (British Nuclear Energy Society, London, 1978) 128.
[27] P. Fenn and M. F. Jordan, Metals Tech. 9 (1982) 327.
[28] L. Schäfer, J. Nucl. Mater. 258-263 (1998) 1336.
[29] A. Iseda, Y. Sawaragi, S. Kato, and F. Masuyama, in: Proc. 5th. Int. Conf. on Creep of Materials, (ASM Int., Materials Park, OH, 1992) 389.
[30] V. K. Sikka and P. Patriarca, Data Package for Modified 9Cr-1Mo Alloy for ASME Code Section III and N-47 Design Allowables, Submitted to American Society of Mechanical Engineers, November 1984.
[31] P. Hartnell and R. D. Howard, in: Welding and Fabrication in the Nuclear Industry (British Nuclear Energy Society, London, 1979) 117.
[32] P. Berge, 2ème Colloque Aciers Spéciaux et Energie Nucléaire, (EDF, Paris, 1976).
[33] T. Yukitoshi, K. Yoshikawa, K. Tokimasa, Y. Shida, and Y. Inaba, Sumitomo Search No. 23 (1980) 45.
[34] D. R. Harries, in Mechanical Behaviour and Nuclear Applications of Stainless Steel at Elevated Temperatures (The Metals Soc., London, Book 280, 1982) 1.
[35] G. Colombe, S. Debiez, J. R. Donati, P. Petrequin, and G. Zacharie, in: Ferritic Steels for Fast Reactor Steam Generators, Eds. S. F. Pugh and E. A. Little (British Nuclear Energy Society, London, 1978) 447.
[36] S. Abe et al. in: Countermeasures for Pipe Cracking in BWRs, EPRI Report WS-79-174, Vol. 3, May 1980.
[37] G. M. Goodwin, W. F. Savage, and E. F. Nippes, Welding Journal 56 (1977) 238s.
[38] D. P. Edmonds and P. L. Sturgill, Weldability of Modified 9Cr-1Mo Steels, Oak Ridge National Laboratory, ORNL/TM-6890, August 1979.
[39] R. Boler, D. Ko, P. Upe, I. H. Craig, and G. Graham, Crack Susceptibility of MANET II Steel During Welding, NNC, Engineering Development Centre Report 92, Issue A, September 1992.
[40] P. J. Alberry, B. Chew, and J. M. Hamilton, The Welding Procedure Metallurgy of 12CrMoV Weld Metal, CEGB Report RD/M/1686/RR88, 1989.
[41] H. Cranjon, Welding in the World 17 (1979) 81.
[42] P. J. Grobner and T. Wada, Climax Molybdenum Co., Ann Arbor, Michigan, Report J-4617, 1981.
[43] C. A. Hippsley, C. L. Briant, and B. C. Edwards, Mat. Sci. and Tech. 2 (1986) 386.
[44] P. J. Grobner and W. C. Hagel, Met. Trans. 11A (1980) 633.
[45] R. D. Townsend, in: Rupture Ductility of Creep Resistant Steels, Ed. A. Strang (The Inst. of Metals, London, Book 522, 1991) 1.
[46] C. K. Bullough, An Investigation of Critical Issues for Type IV Cracking of Low Activation Steels, UKAEA, Culham Report AEA FUS 145, September 1991.
[47] P. Auerkari and J. Salonen, in: Creep and Fracture of Engineering Materials and Structures, Vol. 2, Eds. B. Wilshire and D. R. J. Owen (Pineridge Press, Swansea, 1984) 1227.
[48] C. R. Brinkman, P. J. Maziasz, B. L. P. Keys, and H. D. Upton, Development of Stress-Rupture Reduction Factors for Weldments and the Influence of Pretest Thermal Aging to 50,000 h on the Stress-Rupture and Microstructural Properties of Modified 9Cr-1Mo Steel, Oak Ridge National Laboratory, ORNL/9Cr/90-1, February 1990.
[49] J. A. Williams, in: Seminar on Life of Welds at High Temperatures (Inst. Mech. Engrs., London 1990).
[50] C. Coussement, M. De Witte, and A. Dhooge, Rev. de la Soudure 45 (1989) 41.
[51] P. F. Aplin and C. J. Middleton, in: Steam Plant for the 1990s (Inst. Mech. Engrs., London 1990) 149.
[52] C. J. Middleton, in: Steam Plant for the 1990s (Inst. Mech. Engrs., London, 1990) 251.
[53] C. R. Brinkman, V. K. Sikka, J. A. Horak, and M. L. Santella, Long-Term Creep-Rupture Behavior of Modified 9Cr-1Mo Steel Base and Weldment Behavior, Oak Ridge National Laboratory, ORNL/TM-10504, November 1987.
[54] R. Viswanathan, M. Berasi, J. Tanzosh, and T. Thaxton, in: New Alloys for Pressure Vessels and Piping (American Society of Mechanical Engineers, New York, 1990) 97.
[55] A. Iseda, Y. Sawaragi, and F. Masuyama, in: Heat Resistant Materials, Eds. K. Natesan and D. J. Tillack (ASM Int., Materials Park, OH, 1991) 577.
[56] K. Ehrlich, D. R. Harries and A. Möslang, Eds., Characterization and Assessment of Ferritic/Martensitic Steels, Forschungszentrum Karlsruhe, FZKA Report 5626, February 1997.
[57] T. Kurasawa, H. Takatsu, S. Sato, T. Kuroda, S. Sugimoto, and M. Tamura, J. Nucl. Mater. 233-237 (1996) 313.
[58] L. Schäfer, Jahrestagung Kerntechnik 99, (Tagungberichte Inforum, Bonn, 1999) 569.
[59] G. R. Cowan, O. R. Bergman, and A. H. Holtzman, Metall. Trans. 2 (1971) 3145.
[60] P. W. Jackson, M. D. Chadwick, and B. L. Graham, in: Ferritic Steels for Fast Reactor Steam Generators, Eds. S. F. Pugh and E. A. Little (British Nuclear Energy Society, London, 1977) 488.
[61] M. D. Chadwick and P. W. Jackson, in: Developments in Pressure Vessel Technology, Vol. 3, Ed. R. W. Nichols (Applied Science Publishers., Essex, UK, 1980) 217.
[62] P. W. Jackson, in: Explosive Welding, (The Welding Inst., London, 1975) 24.
[63] F. S. Dickinson, A. F. Taylor, P. W. Jackson, and R. W. Smith, in: Topical Conference on Ferritic Steels for Use in Nuclear Energy Technologies, Eds. J. W. Davis and D. J. Michel (Met. Soc. AIME, Warrendale, PA., 1984) 269.
[64] P. W. Jackson and M. D. Chadwick, in: Welding and Fabrication in the Nuclear Industry (British Nuclear Energy Society, London, 1979) Paper No. 41.
[65] C. Dueren, Stahl und Eisen 102 (1982) 479.
[66] J. N. Soo, in: Rupture Ductility of Creep Resistant Steels, Ed. A. Strang, (The Inst. of Metals, London, Book No. 522, 1991) 282.
[67] J. N. Soo, in: Rupture Ductility of Creep Resistant Steels, Ed. A. Strang, (The Inst. of Metals, London, Book No. 522, 1991) 294.
[68] J. Petersheim, 1st Bodycote Int. HIP Conf., Vasteras, Sweden, May 1995.
[69] U. Guerreschi, A. Cardella, and R. Matera, in: Fusion Technology 1984, Vol 1 (Pergamon Press, Oxford, 1984) 285.
[70] U. Guerreschi, F. Farfaletti-Casali, U. Guerreschi, O. Iop, R. Matera, F. Munch, A. Cardella, and M. Turri, in: Fusion Technology 1986, Vol 1 (Pergamon Press, Oxford, 1986) 453.
[71] J. L. Boutard, J. Nucl. Mater. 174 (1990) 240.
[72] M. Brossa and U. Guerreschi, J. Nucl. Mater. 155-157 (1988) 626.
[73] B. A. Chin, R. J. Neuhold, and J. L. Straalsund, Nucl. Technol. 57 (1982) 426.
[74] H. T. Lin and B. A. Chin, J. Mater. Sci. 26 (1991) 2063.
[75] C. A. Wang, H. T. Lin, M. L. Grossbeck, and B. A. Chin, J. Nucl. Mater. 191-194 (1992) 696.

8

Irradiation Damage, Irradiation Facilities, Irradiation Testing

Since the subject of this book concerns the use of the high-chromium ferritic/martensitic steels in radiation environments, this chapter will provide a brief introduction to irradiation damage of metals and alloys, along with a discussion of irradiation facilities and testing of irradiated materials. Irradiation damage is a complicated process, and the literature contains numerous reviews on various aspects of the subject.

IRRADIATION EFFECTS ON FERRITIC/MARTENSITIC STEELS—GENERAL

Irradiation damage caused by high-energy particles—electrons, ions, protons, or neutrons—occurs when the particles displace atoms from their normal lattice positions to form Frenkel defects (vacancies and interstitials) [1]. A transfer of only several tens of electron volts is required to displace the atom. Since neutrons in a fission or fusion environment will have energies in excess of 10^4 eV, considerable damage will occur in the fuel cladding of a fission reactor or the first wall of a fusion power plant.

The atom displaced by the high-energy particle (termed the "primary recoil atom" or "knock-on atom") transfers energy to surrounding atoms, often displacing some of them, which, in turn, may also cause displacements, resulting in a "displacement cascade." The cascade consists of a region around the path of the primary recoil atom with a core consisting of the vacant lattice sites (vacancies) surrounded by the displaced atoms (interstitials). The size and shape of the cascade depends on the energy of the knock-on atom and the atomic number of the atoms being displaced. The range of the knock-on atom in low atomic-number materials is large, and the cascades are diffuse; they will be more compact in high atomic-number materials. The extent of the displacement damage is expressed in terms of how often an atom is displaced from its normal lattice position during the irradiation as displacements per atom, or dpa. The calculation of dpa depends on the secondary displacement model assumed for the calculation. Different models have been used. The standard industry model used today [see ASTM Practice for Characterizing Neutron Exposures in Iron and Low Alloy Steels in Terms of Displacements per Atom (DPA), E706, ID)(E 693)] is referred to as the NRT dpa (for Norgett, Robinson, and Torrens, the originators of the model used in the calculation). The NRT dpa is designated simply as dpa; most of the data presented in this book will have that designation. Another designation that will be used occasionally when some older data are presented is dpa F (for French, because it originated in France): 1 dpa F = 0.77 dpa.

In addition to displacement damage, neutrons in both fission and fusion reactors cause transmutation reactions with atoms of the irradiated steel that produce solid and gaseous reaction products. The solid products, which are usually another metal atom, are, with a few exceptions, not expected to produce detrimental effects to properties [2], but since they are generally radioactive, they can give the long-lived radioactive isotopes that provide the impetus to develop the reduced-activation steels (introduced in Chapter 2). The gases produced are helium and hydrogen. Helium is produced primarily by an (n,α) reaction (a reaction between a neutron and the nucleus of a lattice atom to form the nucleus of a new atom and an α-particle—helium ion) and hydrogen by a (n,p) reaction [similar to the (n,α) reaction but with a proton—a hydrogen ion— formed instead of helium]. From fission reactor studies, it is known that small amounts of transmutation helium produced within the lattice by (n,α) reactions can have pronounced effects on properties.

As discussed above, the outcome of each displacement event is the production of a vacancy (a vacant lattice site left by the displacement) and an interstitial (a displaced atom that came to rest in an interstitial position). It is the disposition of the vacancies and interstitials that is the primary cause of the irradiation effects on properties. At reactor temperatures, interstitials and vacancies are mobile, and most are eliminated by a one-to-one recombination and have no effect on properties. Those that do not recombine migrate to "sinks," where they are absorbed. Sinks include surfaces, grain boundaries, precipitate-matrix interfaces, dislocations, and existing cavities. If vacancies and interstitials are accepted equally at the sinks, they also annihilate. It is when the vacancies or interstitials are accepted preferentially at sinks that damage accumulates and properties are affected. Mechanical and physical properties are affected by the defect clusters that can form. Clusters consisting of interstitials can evolve into dislocation loops, and vacancy clusters can develop into vacancy loops, microvoids, or cavities. Solute clusters and precipitates can also form under certain conditions.

The type of defect cluster that forms depends on irradiation temperature [1,3,4]. Below $\approx 0.3T_m$, where T_m is the absolute melting point of the irradiated material, interstitials are mobile relative to vacancies, and the interstitials combine to form dislocation loops that increase strength and decrease ductility. Dislocation loops with two Burgers vector orientations are possible in ferritic/martensitic steels: a cube-edge loop with **a**<100> Burgers vectors on {100} planes and glis-

sile edge loops with **a**/2<111> Burgers vectors on {111} planes [5]. They can form by shear from a common **a**/2 <110> faulted nucleus. The interaction of such loops eventually leads to a complex dislocation network. Such defects have been observed, primarily on pure iron [6] and Fe-Cr binary alloys [7–10], but also in commercial steels [11].

Vacancies become increasingly mobile for irradiation above $\approx 0.3T_m$, and a dislocation and cavity structure results [1,3]. In the absence of dissolved gases in the irradiated steel, vacancies can collapse into loops. Cavities form in the presence of dissolved gases and cause an increase in volume (swelling), which occurs because certain sinks have a bias and do not accept vacancies and interstitials equally [1]. Two types of cavities can form: bubbles and voids. Bubbles contain gas atoms at a pressure in equilibrium with the surface tension. Voids can contain gas atoms, but the pressure is less than the equilibrium pressure. Swelling is explained by assuming dislocations act as biased sinks for the interstitials, meaning that excess vacancies must be absorbed by neutral sinks. The latter sinks are envisioned as gas-atom clusters that act as void nuclei, which above a critical size allow bias-driven void growth [1,4]. For void swelling to occur, the temperature must be high enough for the vacancies to be mobile and low enough for vacancy supersaturation (above the thermal equilibrium value) to occur.

Finally, at high irradiation temperatures (greater than about 0.35 to 0.4 T_m), defect clusters are unstable. That is, the high equilibrium vacancy concentration and rapid diffusion lead to vacancy-interstitial annihilation, and displacement damage has little effect on properties [3]. However, as discussed in later chapters, any transmutation helium produced at elevated temperatures can lead to problems in embrittlement and a loss in tensile ductility.

IRRADIATION DAMAGE IN A FUSION NEUTRON ENVIRONMENT

In the extensive testing programs that preceded the development of thermal and fast fission power reactors, prototypic test reactors were available well in advance of the construction of the first demonstration power reactors. No such prototype fusion reactor is available for the development of materials for fusion, and none will be available in the near future. International discussions are in progress to build a 14 MeV neutron source to test materials for fusion, but if such a facility is built, it will not be available for at least ten years [12].

It is the exposure of the first wall and blanket structures of a fusion power plant to unique irradiation conditions that has caused materials specialists the most concern. The challenge in developing materials for operation under these conditions is to use existing irradiation facilities to qualify materials for a fusion demonstration (DEMO) reactor and the first reactors built to produce power. To do this, irradiation effects expected to be produced by the intense high-energy neutron flux generated in an operating fusion reactor must be "simulated." Simulations must be performed by irradiating with neutrons in existing fission facilities or by the use of ion irradiation that generates irradiation damage processes similar to those expected in a fusion reactor. Because all available irradiation facilities but an actual fusion reactor have significant shortcomings, it is necessary to have an understanding of radiation-damage mechanisms that occur during high-energy neutron irradiation so that the effects developed during simulation can be correlated with those that are expected to occur in a fusion environment.

Energy in a fusion reactor will be derived from the deuterium-tritium (D-T) fuel cycle through the reaction

$$D + T \rightarrow \alpha + n + \text{energy} \qquad (8.1)$$

Approximately 17.6 MeV of energy results, 3.5 MeV as kinetic energy of the α-particle (a helium ion) and 14.1 MeV as kinetic energy of the neutron (n). Most of the energy of the α-particle is deposited in the plasma and transferred by electromagnetic and charged-particle radiation to surfaces facing the plasma. Although materials problems arise from this energy transfer, it will probably have little effect on a ferritic steel first wall, because the first wall material will be protected from the plasma by graphite (or some other material) tiles or some other type of protective shield. It is the 80% of the energy carried by the 14.1 MeV neutrons that will have the major effect on the ferritic steel first wall and blanket structure.

The primary difference between the fusion reactor irradiation environment and that in the core of a fission reactor is the high-energy component of the neutron spectrum. Neutrons at energies of up to the 14.1 MeV are present in the neutron spectrum of a fusion plant compared with the average creation energy of neutrons in a fast reactor of about 2 MeV (Fig. 8.1). The high-energy (14.1 MeV) neutrons from the fusion reaction have a high cross section for (n,α) reactions with some typical elements (e.g., Fe, Cr etc.) present in the steels of interest (Fig. 8.2), which means considerably more helium will form in steels exposed to a fusion environment than a fission reactor environment (Fig. 8.1). More hydrogen will also form in the fusion neutron environment, and the solid transmutant elements will also differ to some extent from those formed in a fission plant.

NEUTRON IRRADIATION

Fission reactors are the only facilities available currently that provide the large volume of test space required to develop improved radiation-resistant materials or to qualify materials for fusion reactor service. Figure 8.1 compares the neutron spectra of a fusion system with two types of fission reactors that have been used to study irradiation damage of fusion materials: a fast fission reactor (EBR-II) and a mixed-spectrum reactor (HFIR and ORR). Before existing fission reactors can be used to simulate the radiation damage, however, the equivalence of the lattice damage caused by 14 MeV neutrons and neutrons of lower energy generated in a fission reactor needed to be established [1,2]. Such studies were conducted in accelerator-based high-energy neutron sources, such as the Rotating Target Neutron Source (RTNS-II) [13,14] and deuteron-beryllium (d-Be) sources [15–17]; these facilities are no longer in existence.

The RTNS-II produced 14 MeV neutrons by accelerating deuterons to 400 kV, and a 150-ma beam of these deuterons then struck a rotating, water-cooled copper target that was coated with titanium tritide. The neutron spectrum produced was due to the D-T fusion reaction. The d-Be source generated

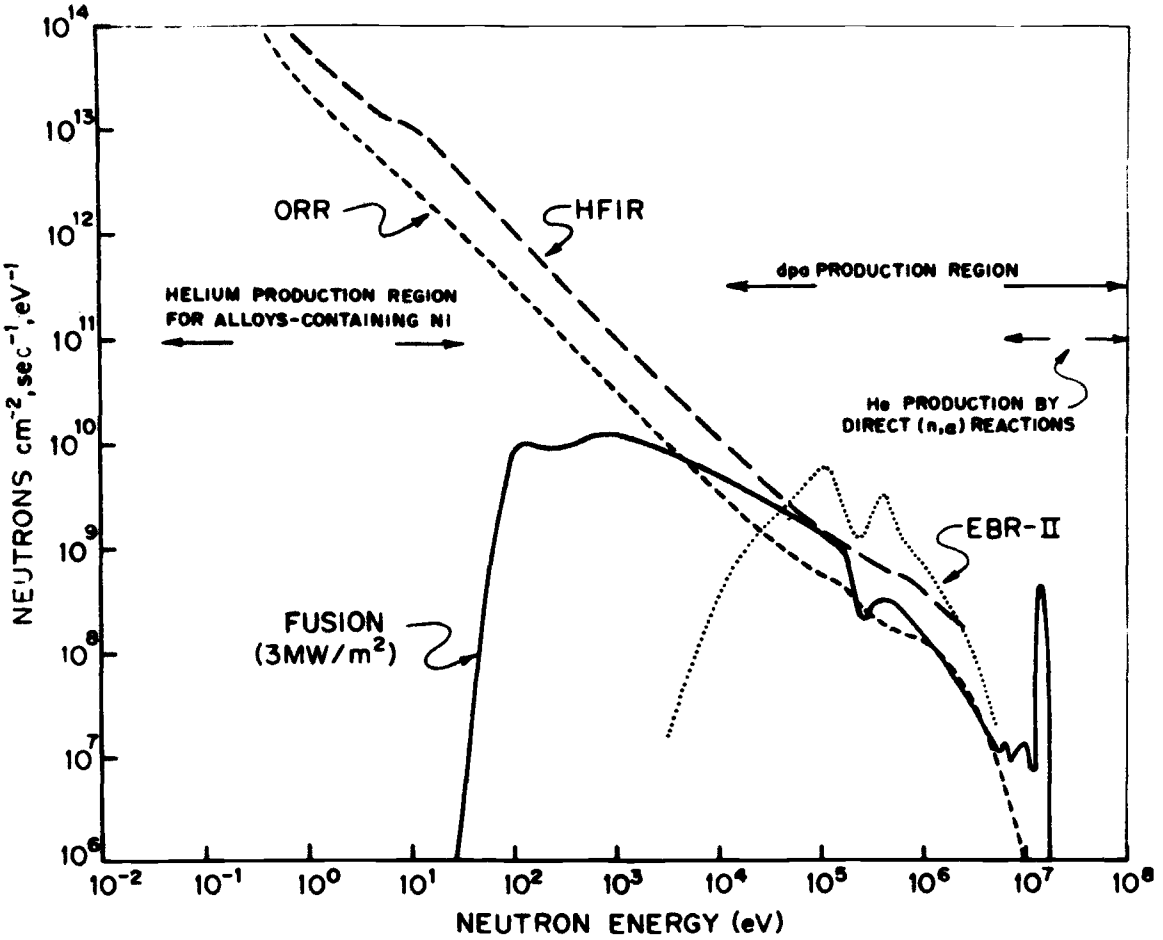

FIG. 8-1—Neutron-energy spectra for various fission reactors and the spectrum at the first wall of a lithium-cooled fusion reactor. The primary difference between the spectra of the fission and fusion reactors occurs above 10^7 eV.

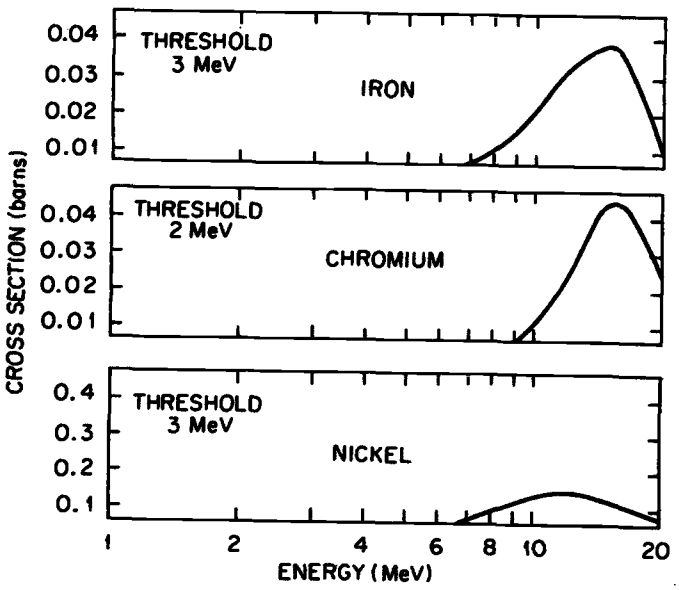

FIG. 8.2—Cross section for (n,α) reactions for iron, chromium, and nickel as a function of neutron energy. Note the high cross section in the vicinity of the 14 MeV energy of neutrons from the fusion reaction.

neutrons by directing a beam of 15 to 40 MeV deuterons onto a beryllium target. A neutron spectrum with energies from thermal to 30 MeV is produced from the deuteron breakup reaction—Be(d,n). Because of the small irradiation volumes and the low flux of these facilities, only a limited number of small specimens could be irradiated. Further, the low flux of the accelerator-based high-energy neutron sources precluded high doses and the formation of significant amounts of helium. The experiments in those facilities sought to establish equivalence in fission and high-energy neutron irradiation, and they demonstrated excellent correlation between the type of displacement damage produced by 14 MeV neutrons and from other sources, thus providing confidence that at low dpa levels the data derived from fission reactor studies are meaningful for fusion systems. This work has been reviewed [2], and some of it will be discussed in later chapters.

IRRADIATION STUDIES AND SIMULATION TECHNIQUES

Once the damage equivalence for fission and fusion systems was established, the larger test specimens needed to carry out various mechanical properties studies could be irradiated in

fission reactors to simulate fusion displacement damage. In the past, fast-spectrum reactors were used to study the effects of the displacement damage expected in a fusion reactor during its lifetime, and the irradiation effects produced in these reactors will be the subject of much of the discussion in later chapters.

In a fast reactor where the average neutron energy is less than 1 MeV, displacement damage occurs with little helium formation (Fig. 8.1). Therefore, other techniques must be used to simulate the simultaneous formation of displacement damage and helium formation. One technique is to irradiate nickel-containing materials in a mixed-spectrum reactor, such as the High Flux Isotope Reactor (HFIR) (Fig. 8.1). Both fast and thermal neutrons are present in a mixed-spectrum reactor. Displacement damage is produced by the fast neutrons, and transmutation helium is produced from an (n,α) reaction when the ^{58}Ni (68% of natural nickel is ^{58}Ni) in the material undergoes the following two-step reaction with thermal neutrons to produce an α-particle—a helium atom:

$$^{58}\text{Ni} + \text{n} \rightarrow {}^{59}\text{Ni} + \gamma \qquad (8.2)$$

$$^{59}\text{Ni} + \text{n} \rightarrow {}^{56}\text{Fe} + {}^{4}\text{He} \qquad (8.3)$$

For austenitic stainless steels with high-nickel contents, "spectral tailoring" techniques were required to produce the proper He (in appm) per atom displacement (He/dpa ratio) similar to that expected in a Tokamak fusion plant. However, by simply adding 2% Ni to a ferritic steel, it is possible to irradiate in the HFIR and simulate the appropriate He/dpa production (Fig. 8.3). For this method there is a dpa production due to the recoil of the ^{56} Fe when the (n,α) reaction occurs; this is a small contribution that can be taken into account [18]. This simulation technique has been used to study the effects of helium on martensitic steels [20], and results from such studies will be discussed in later chapters. It should be noted that helium production from ^{59}Ni is not strictly simultaneous with the formation of displacement damage. Damage begins to form immediately when neutron irradiation begins. Helium does not begin to form until sufficient ^{59}Ni has been transmuted from ^{58}Ni. Therefore, some time is required before the proper He/dpa production rate is reached, as indicated in Fig. 8.3.

Because the nickel doping of the steel could possibly affect the microstructure and/or properties of the steel being studied, an alternative isotopic tailoring technique has been proposed, in which various isotopes of nickel are used [20]. The

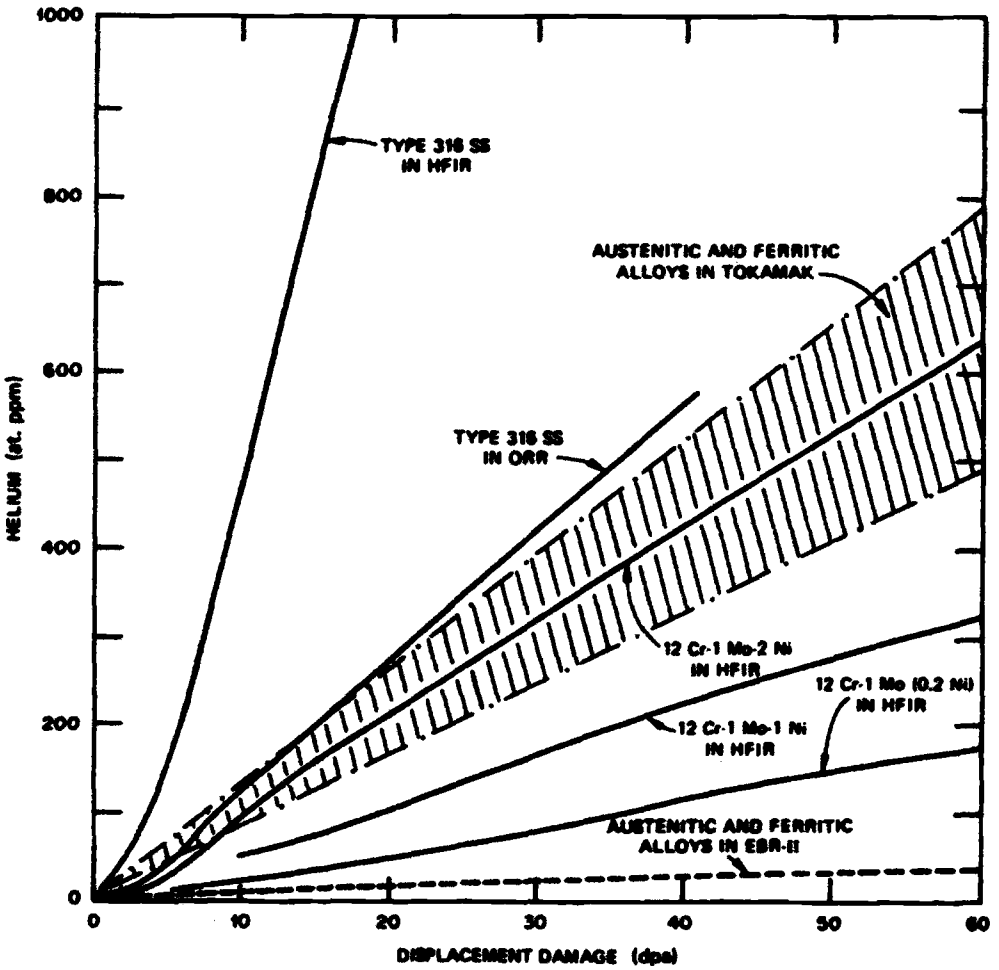

FIG. 8.3—Relationship between helium concentration and displacements per atom for austenitic and ferritic steels irradiated in HFIR, EBR-II, and the first wall of a fusion reactor. Curves for 12Cr-1MoVW steel containing various nickel concentrations are also shown.

^{59}Ni isotope could be added to the steel directly, thus eliminating the need for Eq 8.2, and helium forms directly.

The effect of nickel in the absence of helium can be determined by comparing the results of the ^{59}Ni alloy with one that contains an equal amount of ^{60}Ni isotope, from which no helium is produced, or with natural nickel, from which helium is produced by Eqs 8.2 and 8.3. Also, it has been proposed that by mixing ^{59}Ni and ^{60}Ni while keeping the nickel concentration constant, a single variable experiment in the He/dpa ratio is possible [20]. The major problems with the isotopic tailoring technique are the expense of the nickel isotopes and the radioactivity of the ^{59}Ni.

Another (n,α) reaction used to produce helium during irradiation involves the use of ^{10}B (natural boron contains about 20% ^{10}B) [21],

$$^{10}B + n \rightarrow {}^{7}Li + {}^{4}He \qquad (8.4)$$

Because the cross section for this reaction is greatest for low-energy neutrons, irradiation in a relatively high thermal flux, such as that in the mixed-spectrum of HFIR, will result in all of the ^{10}B being reacted within 1 to 2 dpa. Complete burn up of the ^{10}B in a fast reactor will take much longer, depending on the neutron spectrum (e.g., in FFTF, burn up would be completed after about 1 year, ≈30 dpa).

The energies of the lithium ion and the α-particle (He) produced by the transmutation of the ^{10}B are about 0.87 and 1.53 MeV, respectively. These energetic particles create atomic displacements as they slow down to thermal energies. Estimates have been made that as many as 680 and 85 displaced atoms are produced by the lithium and the α-particle, respectively. The additional displacements could cause an increase in the local defect concentration, as evidenced by defect haloes often observed around boron-containing precipitate particles after irradiation. Another problem is the high reactivity of the boron, so that it segregates to interfaces and may be present in precipitate particles such as B_4C and $M_{23}(CB)_6$ [20,21].

The effect of helium can also be determined by injecting α-particles directly into a specimen with an accelerator. Because of the light weight of the α-particle, only small amounts of displacement damage will accompany the injection. Alternatively, the pre-injected specimen can be inserted in a fission reactor and irradiated with neutrons to produce further displacement damage [22]. Dual-beam accelerator irradiations are also possible, where the specimen is simultaneously irradiated with α-particles to inject the helium and a heavier ion to produce the displacement damage [22,23]. Triple-beam accelerator irradiations are also carried out with a proton beam added to determine the effect of the hydrogen and helium in conjunction with the displacement damage from the heavy-ion bombardment. Displacement damage studies at high displacement rates are also possible with high-energy electrons. Both accelerator and electron irradiations present problems for correlating the resulting structures and properties with those produced in a fusion reactor (Table 8.1). More importantly, it is difficult and expensive to irradiate mechanical property specimens because of their relatively large size, and most of the irradiations are used for electron microscopy studies.

IRRADIATION FACILITIES

Since the fusion materials programs in the various countries of the world began in the 1970s, a large number of reactors have been used to irradiate candidate materials, many of them having previously been used in the development of materials for fast reactor applications. Tables 8.2, 8.3, and 8.4 list nuclear fission reactors, accelerators, etc., that have been used in Europe, the United States, and Japan, respectively, for studying fusion materials. Irradiation studies for fusion and fast reactors are also being carried out in the Russian Federation, but details on their facilities are not readily available. Several of the reactors in the table have now been shut down, including the Fast Flux Test Facility (FFTF) and the Experimental Breeder Reactor (EBR-II) in the United States, and the Prototype Fast Reactor (PFR) in the UK, all three of which were fast reactors, and the Oak Ridge Research Reactor (ORR), a mixed-spectrum reactor in the United States. Today, neutron irradiations for fusion are still being carried out in the High Flux Isotopes Reactor (HFIR) in the United States, the High Flux Reactor (HFR) in The Netherlands, and the Phénix Fast Reactor in France. Irradiations are also carried out in the Japan Materials Test Reactor (JMTR) and the

TABLE 8.1—Some characteristic features of different simulation techniques for fusion materials research.

Particles Energy Range Source	Advantages	Disadvantages	Main Field of Application
Heavy ions (self ions) 2–5 MeV Van de Graaffs	Extremely high displacement rates (100 dpa in a few hours). Many accelerators available almost everywhere. Variable He/dpa ratio in dual-beam facilities.	Very small ranges (<1 μm). No mechanical tests. Surface effects, injected interstitials, inhomogenous damage. Unknown distribution of high stresses.	TEM investigation of: microstructural and microchemical changes and swelling by void formation. Screening of candidate materials.
Light ions (p, d, α) 5–50 MeV Cyclotrons	Somewhat higher displacement rates than reactors. Homogeneous damage in 50–200 μm thick specimens. In situ mechanical tests. Low to very high He/dpa ratios.	Limited to a few dpa. Recoil spectrum different from neutron damage. Limited specimen thickness. Studies of weld and fracture mechanics samples hardly possible.	Basic studies of "in pile" mechanical property changes such as irradiation creep, embrittlement under static (creep) and cyclic stresses (fatigue).
Electrons 0.2–3 MeV HVEM, Van de Graaffs	Very high displacement rates. Simultaneous production and observation of defect structure. Variable He/dpa ratios in dual beam facilities.	Very small irradiated thicknesses and areas. Surface effects. Unknown distribution of high stresses, temperature gradients. Recoil spectrum very different.	In situ observation of the evolution of microstructure (dislocations, voids, clusters, precipitates, segregation).

TABLE 8.2—European irradiation facilities used for fusion materials.

Type	Site	Facility	Particle	Displacement dose rate		Gas generation rate	
				dpa, s^{-1}	dpa, y^{-1}	He[1] appm, s^{-1}	H appm, s^{-1}
Mixed spectrum fission reactor	Mol, Belgium	BR2	Neutron	4×10^{-7} [core center]	6	4×10^{-6}	
	Petten, Holland	HFR	Neutron	$2.3\text{-}2.8 \times 10^{-7}$ [high flux]	5.9 - 6.7		
				$1.6\ 10^{-7}$	3.8	3.2×10^{-6}	
	Studsvik, Sweden	R2	Neutron	2.5×10^{-7} [core center]	4	5.9×10^{-6}	8.1×10^{-7}
				8×10^{-8} [core edge]	1.2	2.4×10^{-6}	3.3×10^{-7}
Fast Fission reactor	France	PHENIX	Neutron	1.8×10^{-6} [core center]		5.4×10^{-7}	
	Dounreay, UK	PFR[2]	Neutron	1.3×10^{-6} [DMSA[2] position]		3.9×10^{-7}	3×10^{-6}
Accelerator/ Cyclotron	FZK, Germany	Dual beam	104 MeV α-particle	$2\text{-}3 \times 10^{-6}$		2.5×10^{-5} 3×10^{-3}	
			30 MeV proton	5×10^{-6}			
	PSI, Switzerland	PIREX	590 MeV proton	5×10^{-7}		5×10^{-5}	4×10^{-4}

Type	Site	Facility	Particle	Displacement dose rate		Gas generation rate	
				dpa, s^{-1}	dpa, y^{-1}	He appm, s^{-1}	H appm, s^{-1}
Accelerator/ Cyclotron (cont'd)	CEA, Cadarache, France	Dual beam	500 KeV Fe^{+} and 20 KeV He^{+}	2×10^{-3}		2×10^{-2}	
	FZJ, Germany	Cyclotron	5-20 MeV proton, 5-14 MeV Deuterium, 5-28 Mev α-particle	10^{-5} - 10^{-6}	5.9 - 6.7	2.8×10^{-2} - 5.6×10^{-4}	
	HMI, Germany	Single beam	M^{+}, α-particle and proton 10-20 MeV	10^{-4}		10^{-2}	
		Dual beam	300 KeV metal ions and 60 KeV α-particle				
	Harwell, U.K.	Variable energy cyclotron[2]	52 MeV $Cr\ 6^{+}$ 46 MeV $Ni6^{+}$ α-particle	1.7×10^{-3}		2.2×10^{-2}	
High Voltage Electron Microscope	U.K.,[3] Belgium, and France	HVEM	1-1.2 MeV electron	$1\text{-}5 \times 10^{-3}$			

(1) 0.0075 - 0.0085 wt.% boron. (2) Facility now shut down. (3) Demountable subassembly.

TABLE 8.3—Japanese irradiation facilities used for fusion materials.

Type	Site	Facility	Particle	Damage Rate		Gas Generation Rate	
				dpa, s^{-1}	dpa, y^{-1}	Appm He, s^{-1}	appm H, s^{-1}
Mixed Spectrum Fission Reactor	JAERI, Oarai	JMTR	Neutron	Fuel position			
				3×10^{-7}	2.7	$1 \times 10^{-5(1)}$	
				Reflector position			
				8×10^{-8}	0.7	$1 \times 10^{-5(1)}$	
	JAERI, Tokai	JRR-3	Neutron	2×10^{-7}	1.4	$7 \times 10^{-6(1)}$	
Fast Fission Reactor	PNC, Oarai	JOYO	Neutron	Mark II Core 1st Grid			
				3×10^{-6}	21	5×10^{-7}	
Accelerator Cyclotron	JAERI, Takasaki	TIARA (triple beam)	Typical 11 MeV Fe^{3+} 1 MeV He^{+} 400 KeV proton	3×10^{-6}		3×10^{-2}	5.6×10^{-2}
	JAERI, Takasaki	Cylotron	Typical 50 MeV He^{2+}			4×10^{-4}	

(1) At linearly increasing region (≈20 dpa).

TABLE 8.4—U.S. irradiation facilities used for fusion materials.

Type	Site	Facility[1]	Particle	Displacement Dose		Gas Generation Rate	
				dpa, s^{-1}	dpa, y^{-1}	He appm, s^{-1}	H appm, s^{-1}
Mixed Spectrum Fission Reactor	Oak Ridge, Tennessee	ORR[2]	Neutron	3.5×10^{-7}	11	1.1×10^{-7}	5.6×10^{-7}
	Oak Ridge, Tennessee	HFIR[3]	Neutron	1.1×10^{-7}	35	3.7×10^{-7}	6.8×10^{-6}
Fast Fission Reactor	Idaho Falls, Idaho	EBR-II[2]	Neutron	1.2×10^{-6}	37	1.8×10^{-7}	2.8×10^{-6}
	Hanford, Washington	FFTF[2]	Neutron	1.3×10^{-7}	41	2.2×10^{-7}	

(1) A high-flux position has been chosen for each reactor.
(2) Reactor is no longer operating.
(3) Values for HFIR are for 100 MW operation; reactor is now operated at 85 MW.

Japan Research Reactor (JRR-2) in Japan, the Studsvik Reactor R2 in Sweden, and the SM-2 and BOR-60 reactors in Russia. Irradiations also continue in a limited number of ion sources, although most of these irradiations are restricted to irradiating small transmission electron microscopy specimens. In general, the pace of irradiation studies on candidate fusion materials has decreased considerably from the effort in the 1970s to 1980s period.

IRRADIATION EXPERIMENTS

Conducting irradiation experiments involves many difficulties, for example, temperature measurement and control (i.e., heating and/or cooling specimens in the reactor) to obtain the desired conditions. Different capsules have been designed for different reactors to obtain the experimental objectives. These will not be discussed. One of the prime challenges in this work is caused by the space limitations in test reactors. To increase the amount of data that can be generated given the limited irradiation space, miniature specimens have been developed to measure the properties of irradiated specimens.

Miniature specimens that are reductions of typical full-size specimens are in general use for irradiation-damage studies [24]. Various rod and sheet tension specimens have been used by various test programs over the years. Typical for sheet specimens is an overall length of 25 to 30 mm with thicknesses ranging from 0.25 to 0.8 mm with a gage length

of 7 to 8 mm. One of the smallest tension specimens being used is 16 mm long, 0.25 mm thick, with a 5 mm gage length.

Rod or round-bar tensile-type specimens are also used, but primarily for fatigue tests. Longer specimens are generally used in this case: length 50 to 80 mm, gage length 7 to 30 mm, with diameters in the gage section of 2 to 6 mm [24]. A still smaller size specimen is being investigated: the specimen is a 25.4 mm long hour-glass specimen that has a 1.25 mm diameter at the minimum cross section [25].

Various types of miniature Charpy specimens have been used. Instead of irradiating full-size (10 by 10 by 55 mm) specimens, half-size (5 by 5 by 25.4 mm) and one-third-size specimens (3.3 by 3.3 by 25.4 mm) are used in the United States, while in Europe and Japan, a subsize specimen (3 by 4 by 27 mm) specified under the term of KLST is most often used. The Japanese have used a still smaller specimen with dimensions 1.5 by 1.5 by 20 mm. Since a Charpy test measures the fracture energy, the results will depend on the size of the specimen. Therefore, for the miniature Charpy specimens, much smaller energies are measured and reported for these specimens than for full-size specimens.

Irradiation creep is now generally determined with small pressurized tubes [26], typically about 24 mm long with a 4.6 mm diameter. Toughness measurements are conducted on miniature compact tension specimens: a 15.625 by 15 by 6.25 mm specimen has been used in Europe; in the U.S. and Japan, a 12.5 mm diameter cylindrical specimen 4.6 mm thick is in use.

Several conferences have been held on specimen miniaturization, testing, and correlation of data from these small specimens, and the proceedings of these conferences can be consulted for more detail on the subject [27–30].

REFERENCES

[1] L. K. Mansur, Kinetics of Nonhomogeneous Processes, Ed. G. R. Freeman (John Wiley & Sons, Inc., New York, 1987) 377.

[2] F. W. Wiffen and J. O. Stiegler, in: The Technology of Controlled Nuclear Fusion, Eds. G. L. Kulcinski and N. M. Burleigh (U.S. Energy Research and Development Administration, Washington, D.C., 1976) 135.

[3] E. E. Bloom, in: Radiation Damage in Metals, Eds. S. D. Harkness and N. L. Peterson (American Society for Metals, Metals Park, OH, 1976) 295.

[4] E. A. Little, J. Nucl. Mater. 206 (1993) 324.

[5] B. L. Eyre and R. Bullough, Phil. Mag. (1965) 31.

[6] A. E. Ward and S. B. Fisher, J. Nucl. Mater. 166 (1989) 227.

[7] L. Horton, J. Bentley, and K. Farrell, J. Nucl. Mater. 108 & 109 (1982) 222.

[8] D. S. Gelles, J. Nucl. Mater. 108 & 109 (1982) 515.

[9] D. S. Gelles, in: Effects of Radiation on Materials: Fourteenth International Symposium, ASTM STP 1046, Vol. 1, Eds. N. H. Packan, R. E. Stoller, and A. S. Kumar (American Society for Testing and Materials, 1990) 73.

[10] D. S. Gelles, S. Ohnuki, H. Takahashi, H. Matsui, and Y. Kohno, J. Nucl. Mater. 191-194 (1992) 1336.

[11] D. S. Gelles, J. Nucl. Mater. 233-237 (1996) 293.

[12] T. Kondo, T. E. Shannon, and K. Ehrlich, J. Nucl. Mater. 233-237 (1996) 82

[13] Rotating Target Neutron Source II Facility, Lawrence Livermore Laboratory Report M-094 (1978).

[14] J. J. Holmes and J. L. Straalsund, J. Nucl. Mater. 85 & 86 (1979) 447.

[15] C. M. Logan, R. Booth, and R. A. Nickerson, Nucl. Instru. & Methods 145 (1977) 77.

[16] M. J. Saltmarsh, C. A. Ludemann, C. B. Fulmer, and R. C. Styles, Nucl. Instru. & Methods 145 (1977) 81.

[17] J. Narayan and S. M. Ohr, J. Nucl. Mater. 63 (1976) 454.

[18] L. R. Greenwood, D. W. Kneff, R. P. Skowronski, and F. M. Mann, J. Nucl. Mater. 122 & 123 (1984) 1002.

[19] R. L. Klueh and D. J. Alexander, J. Nucl. Mater. 218 (1995), 151.

[20] G. R. Odette, J. Nucl. Mater. 141-143 (1986) 1011.

[21] D. S. Gelles and F. A. Garner, J. Nucl. Mater. 85 & 86 (1979) 689.

[22] K. Farrell, Rad. Effects 53 (1980) 175.

[23] A. Möslang, S. Cierjacks, and R. Lindau, in: Twelfth International Conference on Cyclotrons and Their Applications, Eds. B. Martin and K. Ziegler (World Scientific, London, 1999) 545.

[24] R. L. Klueh, Ed., Proceedings of the IEA Working Group Meeting on Ferritic/ Martensitic Steels, ORNL/M-4939, September 1995.

[25] Y. Miwa, S. Jitsukawa, and A. Hishinuma, J. Nucl. Mater. 258-263 (1998) 457.

[26] E. R. Gilbert and B. A. Chin, Nucl. Tech. 52 (1981) 273.

[27] W. R. Corwin and G. E. Lucas, Eds., in: The Use of Small-Scale Specimens for Testing Irradiated Material, ASTM STP 888 (American Society for Testing and Materials, Philadelphia, 1986).

[28] W. R. Corwin, F. M. Haggag, and W. L. Server (Eds.), in: Small Specimen Test Techniques Applied to Nuclear Reactor Vessel Thermal Annealing and Plant Life Extension, ASTM STP 1204 (American Society for Testing and Materials, Philadelphia, 1993).

[29] P. Jung and H. Ullmaier (Eds.) in: Miniaturized Specimens for Testing of Irradiated Materials (Forschungszentrum Jülich, Jülich, Germany, 1995).

[30] W. R. Corwin, S. T. Rosinski, and E. van Walle (Eds.), in: Small Specimen Test Techniques, ASTM STP 1329 (American Society for Testing and Materials, Philadelphia, 1998).

9

Dimensional Stability—Swelling

SWELLING BEHAVIOR

Irradiations at temperatures in the approximate range 0.3 to $0.5T_m$ to intermediate and high neutron doses, typical of those encountered in the cores of fast breeder reactors and projected for the first wall and breeder structural components in a DEMO D-T tokamak fusion system, produce significant density decreases and volume swelling of some austenitic steels [1] and other non-fissile metals and alloys. The swelling is associated with the formation of intragranular voids and dislocation loops.

There is general agreement as to why the voids nucleate and grow within a fairly narrow temperature range in the unstressed materials. The void swelling results from the production of equal numbers of vacancies and interstitial atoms; the dislocations in the structure have a slightly higher preference for the interstitials, and the excess vacancies migrate and form clusters, which are stabilized as three-dimensional voids by the innate gases in the material and/or transmuted gas, such as helium produced by (n,α) reactions. Voids are not formed below about $0.3T_m$ because of dominant mutual recombination of the interstitials and slow diffusing vacancies and above about $0.5T_m$ because the thermal vacancy concentration exceeds that induced by irradiation.

Extensive data on void swelling have been obtained by:

- Dimensional and immersion density measurements and/or TEM of specimens obtained from the irradiated cladding and wrappers of fast reactor fuel element sub-assemblies and small specimens exposed in un-instrumented or instrumented rigs in fast and mixed-spectrum fission reactors.
- Simulation experiments in accelerators/cyclotrons and high-voltage microscopes in which the void formation and swelling are rapidly simulated (approximately one thousand times faster) by charged particle and 1 MeV electron bombardments, respectively, with and without prior or simultaneous helium implantation.

The void swelling-fluence relation has been represented in terms of an incubation dose, below which the swelling is negligible (<0.1%), followed by a linear swelling rate regime thus:

$$S \leq 0.1\% \text{ for } D \leq D_0 \quad (9\text{-}1)$$

$$S = A(D - D_0) \text{ for } D > D_0 \quad (9\text{-}2)$$

where S is the total swelling, A is the swelling rate, and D and D_0 are the total and incubation doses, respectively.

The extensive experimental data for the austenitic stainless steels have shown that the magnitude of the swelling depends on the major and minor elemental composition and initial thermomechanical treatment. However, it has been shown [2] that these factors only affect the incubation or transient dose before the swelling in the austenitic steels accelerates to a constant rate of about 1% per dpa, independent of the irradiation temperature (Fig. 9.1) for temperatures in the peak swelling range. The length of the transient can vary over a wide range, from <1 dpa to tens of dpa.

Extensive data are also available on pure iron and iron alloys, low, intermediate, and high chromium ferritic, bainitic, and martensitic steels that have demonstrated that these body-centered-cubic (bcc) materials have considerably greater resistance to irradiation-induced void swelling than the face-centered-cubic (fcc) austenitic steels (Fig. 9.1). The void swelling observations and data on these irradiated bcc steels have been reviewed periodically [3–7] and the microstructural evolution and origins of the void swelling resistance discussed [6,7].

SWELLING OF FERRITIC AND MARTENSITIC STEELS

The collected swelling data on the electron- and ion-irradiated high chromium commercial ferritic and martensitic steels are plotted in Fig. 9.2 [8–19], while the data for neutron-irradiated commercial and reduced activation steels are reproduced in Figs. 9.3 and 9.4 [20–47], respectively. The swelling rates are typically 0.1% per dpa (compared to the typically 1%/dpa for austenitic stainless steels) and decrease to less than linear at high displacement doses. It is also noted that the δ-ferrite regions in the duplex steels such as EM12 generally exhibit greater void formation and swelling than the adjacent tempered martensite structure [22].

In an effort to understand the swelling resistance of ferritic/martensitic steels, research has been carried out on the swelling of pure iron [5,20,21,48–52], dilute iron binary alloys [48], Fe-Cr binary alloys with up to 18% Cr [20,21,25,53], and Fe-Cr ternary alloys containing Si, Mn, V, W, Ta, and Zr [53] after neutron [20,21,25,53] and ion [48–52] irradiation. Although these results are only peripherally relevant to the swelling of the more complicated steels, the results established the low-swelling nature of ferritic alloys relative to austenitic alloys and demonstrate the effect of solutes and the overall microstructure on suppressing void swelling by interacting with irradiation-produced vacancies or the dislocation structure (theories developed to explain swelling resistance will be discussed below).

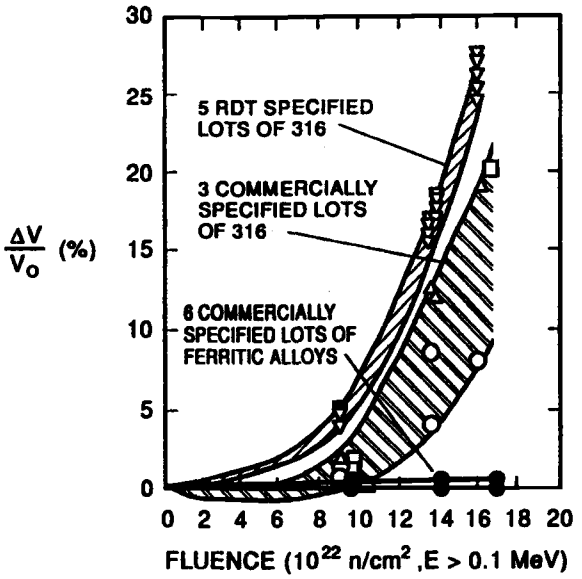

FIG. 9.1—Swelling behavior of six commercial heats of ferritic/martensitic steels compared to type 316 stainless steel after irradiation in EBR-II at 420°C to ≈80 dpa (from D. S. Gelles, unpublished research).

These are also important processes for the high-chromium ferritic and martensitic steels, the swelling behavior of which will now be presented in some detail.

SWELLING DURING NEUTRON IRRADIATION

Little and Stowe [20,21] irradiated the three 12% Cr martensitic steels FI, CRM-12, and FV448, the bainitic steel 2¼Cr-1Mo, and the fully ferritic Fe-14Cr-4Al (Fecralloy) at 380 to 615°C to 30 dpa in DFR. At all irradiation temperatures, swelling was below the detection limit of 0.1% for immersion density measurements. The only changes noted were at 595°C for Fecralloy and at 615°C for FI and FV448, where densification near the detection limit was observed. TEM observations verified the lack of swelling, finding only small isolated regions that contained a low density of cavities in the FI and FV448 steels irradiated at 380°C [21].

Gelles and co-workers [25–29,53,54] studied several commercial steels after irradiation in EBR-II. For 2¼Cr-1Mo, H-11 (5Cr-1.0Mo-0.9Si-0.5V-0.4C), modified 9Cr-1Mo (9Cr-1MoVNb), Sandvik HT9 (12Cr-1MoVW), AISI 416 (13Cr-0.25Mo-0.4Mn-0.3Ni-0.5Si-0.1C), AISI 430F (18Cr-0.4Mn-0.5Si-0.04C), and EM12 (9Cr-2MoVNb) irradiated to 70 dpa at 400 to 650°C, cavities were observed only in the 2¼Cr-1Mo and the duplex EM12 at 400 to 450°C (a few helium bubbles were observed in the EM12 at 650°C). The EM12 was the only steel that showed significant swelling by densitometry, but its swelling rate was one-twentieth that of austenitic steels [53]. Figure 9.1 summarizes the work of Gelles and co-workers and shows the marked contrast in the swelling behavior of AISI type 316 stainless steel and several commercial ferritic steels irradiated to ≈70 dpa in EBR-II [54].

Gelles also irradiated the above-mentioned commercial steels (2¼Cr-1Mo, H-11, 9Cr-1MoVNb, Sandvik HT9, AISI 416, AISI 430F, and EM12) plus FeCrAlY (22.5Cr-5Al-0.68Y-0.009C) and Carpenter Custom 455 (12Cr-8.4Ni-0.24Nb-1.2Ti-2.1Cu-0.008C) to 125 dpa at 400 to 650°C [25]. Peak swelling occurred for most steels at 400 to 420°C with <0.2% swelling, except for the EM12 (0.6% at 400 to 420°C) and Carpenter Custom 455 (1.78% at 540°C). The latter steel contains 10% Ni, which was concluded to promote austenite formation, and the higher swelling at the higher temperature was attributed to austenite that formed during irradiation as a result of radiation-induced segregation [25].

Although no voids were observed in the Sandvik HT9 irradiated to 70 dpa in EBR-II [28], a few scattered voids formed in another heat irradiated in the Fast Flux Test Facility (FFTF) at 420°C [27,34] in two different heat treatment conditions. After irradiation to 114 dpa at 420°C, voids were nonuniformly distributed, and swelling varied from 0.24 to 0.7% for one heat-treatment condition and from 0.78 to 0.9% for the other condition. Heat treatment was considered a possible cause for the variation, although the precipitate distribu-

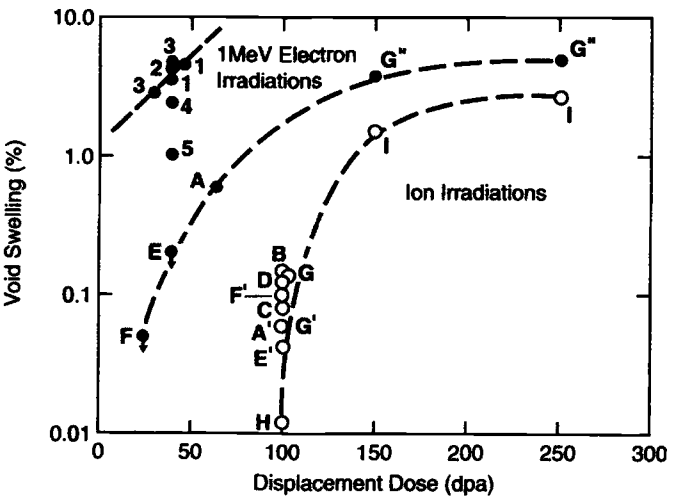

1MeV Electron ● Irradiated

Designation	Steel	Peak Swelling Temperature (°C)	Reference
1	FV607	425-450	8
2	FV448	400	9
3	EM12	450-500	10
4	EM10	450	10
5	ODS	450	11,12

Ion Irradiated ○

Designation	Steel	Ion/Energy	Peak Swelling Temperature (°C)	Reference
A	FI	52 MeV Cr^{6+}	425-450	14
A'	"	20 MeV Cr	475	14
B	FV607	"	"	"
C	CRM12	"	"	"
D	FV448	"	"	"
E	1.4914	46.5 MeV Ni^{6+}	"	15
E'	"	500 keV Fe^{+}	500	10
F	9Cr-1MoVNb	3 MeV Ni	450	16
F'	"	4 MeV Fe	500, 550	17
G	HT9	3 MeV Ni^{+} & 4 MeV Ni^{3+}	450	18
G'	"	500 keV Fe^{+}	500	10
G"	"	2.8 MeV Fe^{+}	"	19
H	EM10	500 keV Fe^{+}	"	10
I	EM12	2.8 MeV Fe^{+}	550	19

FIG. 9.2—Void swelling of electron- and ion-irradiated ferritic/martensitic steels.

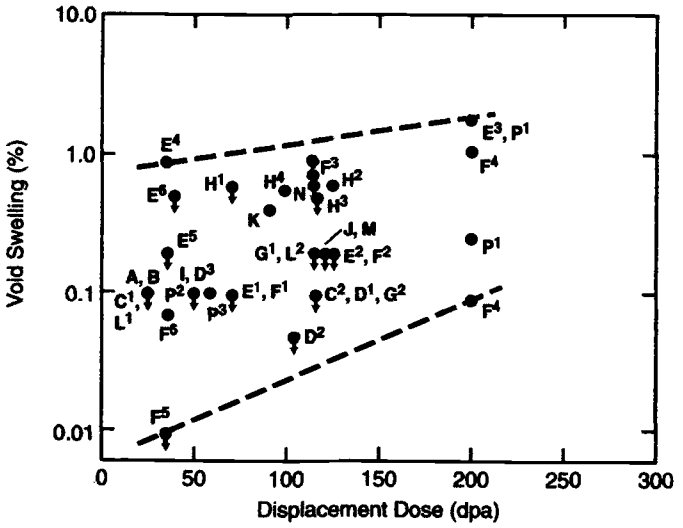

Designation	Steel	Irradiation Temperature (°C)	Reference
A	FI	380-61	20, 21
B	CRM12	"	"
C^1	FV448	"	"
C^2	"	400-500	22
D^1	1.4914	"	"
D^2	"	400-480	23
D^3	"	400-580	24
E^1	9Cr-1MoVNb	400-650	25-28
E^2	"	"	25
E^3	"	~420	29
E^4	"	"	30
E^5	"	300-600	31, 21
E^6	"	"	33
F^1	HT9	400-650	25-28
F^2	"	"	25
F^3	"	~420	27, 34
F^4	"	"	29
F^5	"	"	30
F^6	"	300-600	25, 26
G^1	EM10	400-600	35
G^2	"	400-550	22
H^1	EM12	400-650	25-28, 36
H^2	"	"	25
H^3	"	400-550	22
H^4	"	400-500	10
I	1.4923	400-580	24
J	H11	400-540	25, 28
K	EP450	280-520	37-39
L^1	FeCrAl	380-615	20, 21
L^2	"	425, 540	25, 28
M	430F	400-650	25, 28
N	17Cr	400-600	35, 40, 41
P^1	ODS	420	29
P^2		427-710	42
P^3		420-460	12

FIG. 9.3—Void swelling of neutron-irradiated commercial ferritic/martensitic steels.

tion and dislocation structures appeared similar for the two conditions. A swelling rate of 0.015%/dpa was estimated between 50 and 114 dpa for the 0.9% change, a much lower rate than the ≈1%/dpa typically found in austenitic stainless steels [34].

Gelles extended the irradiations to 200 dpa in FFTF at 420°C for the 9Cr-1MoVNb and 12Cr-1MoVW steels [29] and found the continued low swelling. The 9Cr-1MoVNb showed a larger swelling (1.76%) than the 12Cr-1MoVW (0.09 and 1.02% for steel tempered at 700 and 750°C, respectively), in agreement with a maximum in swelling around 9% Cr observed for Fe-Cr binary alloys [21,53].

In addition to irradiating the 9Cr-1MoVNb and 12Cr-1MoVW steels, Gelles also irradiated two ODS (oxide dispersion-strengthened) alloys to 200 dpa in FFTF: a commercial heat of MA 956 (Fe-19.1Cr-0.02C-0.2Ni-0.26Y_2O_3-0.9Ti) and two batches of an experimental steel designated MA957 (Fe-13.5Cr-0.25Mo-0.26Y_2O_3-0.95Ti) [29]. Immersion density measurements showed swelling of 1.17% for the MA 956 and 1.75 and 0.25% for the two batches of MA 957. Swelling in the MA956 was described as uniform, while a non-uniform distribution of voids was observed in the MA 957. Voids in the MA 957 were found in regions that recrystallized before irradiation. The difference in the swelling amounts of the two MA 957 batches was attributed to differences in the amount of recrystallization that occurred during processing [29].

Dubuisson et al. [22] examined the microstructure of the 17% Cr non-transformable ferritic steel F17, the duplex steel EM12, and the martensitic steels FV448, HT9, DIN 1.4914, and EM10 after irradiation in the Phénix reactor from 400 to 550°C up to 110 dpa. Few voids were observed in any of the steels. The most swelling was observed in the δ-ferrite regions of the duplex EM12 and in the ferrite of the F17 steel. No cavities were observed in the lath martensite microstructure of the HT9, and although cavities were observed in the FV448, 1.4914, and EM10, the voids were widely scattered, giving essentially zero swelling [22].

DIN 1.4914 steel was found to be low swelling in other studies [12,23,24,42]. A fuel wrapper of DIN 1.4914 irradiated to 105 dpa in the range 400 to 480°C in Phénix showed a maximum swelling of only 0.05% [23]. TEM indicated the presence of α′ particles at a number density of 2×10^{15} cm^{-3}

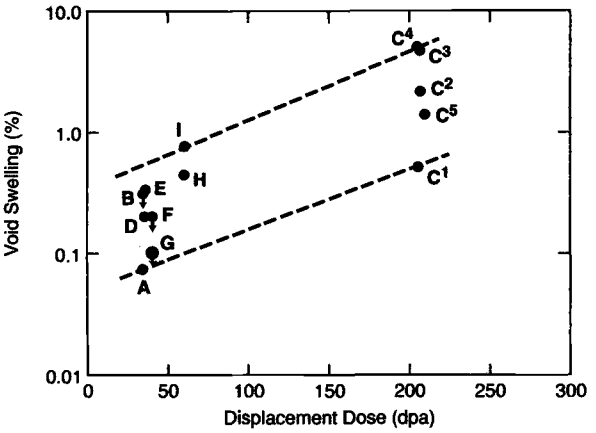

Designation	Steel	Irradiation Temperature (°C)	Reference
A	9Cr-WV	426	43
B	11Cr-WV	"	"
C^1	9Cr-0.5V	420	43-45
C^2	9Cr-1V-1Mn	"	"
C^3	9Cr-0.5V-3Mn	"	"
C^4	9Cr-1W-2Mn	"	"
C^5	12Cr-1V-6.5Mn	"	"
D	9Cr-2WV	"	30
E	9Cr-2WVTa	"	"
F	9Cr-2WVTaB	"	46
G	9Cr-2WVTa	"	"
H	9Cr-2WVTaTiB	"	47
I	9Cr-2WVTaTi	"	"

FIG. 9.4—Void swelling of neutron-irradiated reduced activation ferritic/martensitic steels.

that also formed during irradiation in this temperature range. The swelling behavior of the DIN 1.4914 and EM12 was compared to the swelling of several oxide dispersion-strengthened (ODS) alloys after 55 dpa in the Rapsodie fast reactor in France [12,42]. The ODS steels tested were Fe-13Cr-1.5Mo-3.5Ti with <0.08% C that contained either titanium oxide (TiO_2) or yttrium oxide (Y_2O_3) for dispersion strengthening. The DIN 1.4914 and EM12 had greater irradiation resistance than the ODS alloys. Over the range 410 to 490°C and 30 to 55 dpaF, the TiO_2-strengthened steel showed the greatest amount of swelling (≈1.2% max), followed by the Y_2O_3-strengthened steel (≈0.8% max), and the EM12 and DIN 1.4914 with swelling of ≈0.4% max [12,24,42].

Russian investigators [37,55] have compared ferritic/martensitic steel wrapper materials for fast reactors with austenitic stainless steel wrapper materials irradiated to a maximum of 144 dpa. The chosen Russian ferritic/martensitic steels were EP-450 (Fe-12Cr-1.5Mo-0.2V-0.4Nb-0.5Si-0.8Mn-0.004B-0.12C) [37,55], 05X12H2M (Fe-13.5Cr-0.3Ni-0.55Nb-0.5Si-0.02P-0.15C) [36], and EP823 (12Cr-0.8Ni-0.4 Nb-1.3Si-0.06B-0.18C) [55]. Dose dependence of the swelling of EP-450 was described in a summary report as just 0.004%/dpa [37]. It was stated that swelling for the three ferritic/martensitic steels would not limit the attainment of damage doses of 140 dpa, compared with a limit of 50 to 70 dpa for the austenitic steels [55].

Gelles examined the swelling of Cr-V, Cr-W, and Cr-W-V-Mn reduced-activation steels with ≈2.5, 9, and 12% Cr irradiated in FFTF to 9.8, 43.3, and 114.2 dpa at 420°C, 14.4 dpa at 520°C, and 33.8 dpa at 600°C [29,43–45]. Void formation occurred at 420°C, but not at 520 and 600°C [44]. Specimens of these steels were also irradiated to 200 dpa at 420°C [45] in the experiment discussed above where the 9Cr-1MoVNb and 12Cr-1MoVW steels were irradiated (Table 9.1) [43]. Qualitatively, the swelling of the reduced-activation steels was similar to that for the two Cr-Mo steels, with the 9Cr steels again showing the most swelling. The peak in swelling at 9% Cr agrees with results obtained by Gelles from irradiation studies on Fe-Cr binary alloys with chromium concentrations between 2 and 18% [53]. The 9Cr-0.5V-0.1C, 9Cr-1.2V-1.1Mn-0.2C, 9Cr-0.5V-2.7Mn-0.1C, and 9Cr-1W-0.25V-2.5Mn-0.1C reduced-activation steels had swelling values of 0.54, 2.20, 4.66, and 5.04%, respectively. This variation in swelling and the observation that all but one of the reduced-activation steels showed larger swelling than the commercial 9Cr-1MoVNb and 12Cr-1MoVW steels indicates that swelling depends on more than just the chromium composition. The 2.5 and 12% Cr steels showed swelling values similar to the 9Cr-1MoVNb and 12Cr-1MoVW (Table 9.1) [45]. The 12Cr-1W-6.5Mn-0.1C steel showed a negative swelling, indicating that the change in density due to precipitation more than offset any void swelling. Figure 9.5 shows the void microstructures of the reduced-activation steels [45].

TABLE 9.1—Swelling of a Series of Reduced-activation Ferritic/Martensitic Steels and Conventional 9Cr-1MoVNb and 12Cr-1MoVW Steels.

Alloy	Fluence, dpa	Swelling
2Cr-0.5V	203.2	1.11
2Cr-1V	203.5	1.3
2Cr-1.5V	204	1.52
9Cr-0.5V	204.8	0.54
9Cr-1V-1Mn	205.7	2.2
9Cr-0.5V-3Mn	206	4.66
12Cr-1V-6.5Mn	208.8	1.43
9Cr-1W-2Mn	204.4	5.04
12Cr-1W-6.5Mn	206.9	−0.77
9Cr-1MoVNb	204.5	1.76
12Cr-1MoVW[a]	204.5	0.09
12Cr-1MoVW[b]	204.5	1.02

[a]Tempered at 700°C.
[b]Tempered at 750°C.

The observation that some reduced-activation steels showed higher swelling than the commercial steels does not necessarily mean that reduced-activation steels in general swell more than the conventional steels. It is probably a reflection that these are experimental steels and not optimized compositions. After irradiation in FFTF to 35 dpa at 420°C, swelling of the reduced-activation 9Cr-2WV and 9Cr-2WVTa steels and the conventional 9Cr-1MoVNb and 12Cr-1MoVW steels was estimated by TEM to be 0.2, 0.33, 0.85, and 0.007%, respectively [30]. The results again verify the superior swelling resistance of the 12 Cr steel, but they also show the relatively good resistance of the more optimized 9Cr reduced-activation compositions, even relative to the conventional 9Cr-1MoVNb steel. As stated above, the 9Cr-1MoVNb steel, which was the highest swelling steel in this experiment, showed less than 2% swelling at 200 dpa in FFTF at 420°C [29].

Garner et al. [56] recently reexamined results from the Fe-Cr binary, ternary, and quaternary alloys irradiated in EBR-II that were earlier studied by Gelles and Thomas [26] and concluded that there had been an error in "dose assignment" for the bcc alloys, and the steady-state swelling rate was not as different from the austenitic stainless steels as usually stated. For the Fe-Cr alloys investigated, a steady-state swelling rate of ≈0.2%/dpa was obtained, which is closer to the ≈1%/dpa typically found for austenitic stainless steels than previous calculations. The reason for the low swelling rates usually observed for ferritic/martensitic steels was attributed to the longer transient stage for the bcc structure relative to the fcc structure of austenitic stainless steels [56]. The transient stage is dominated by void nucleation (formation of critical size cavities), which was taken to indicate that nucleation is more difficult in the bcc structure. These results also indicated that swelling occurred at temperatures as high as 650°C, which is well above the peak swelling temperature [56].

Of course, the compositions of the ferritic/martensitic steels used for fission and fusion applications, as opposed to the Fe-Cr alloys in the work of Garner et al. [56], extend the transient beyond those observed for these simple alloys, thus giving rise to the observations that the ferritic steels show less swelling than austenitic stainless steels. According to this interpretation, the low swelling rates for ferritic steels observed in some experiments (e.g., 0.004%/dpa [37]) are for swelling in the transient stage. Further, by this interpretation, it must be concluded that a quite long incubation period must be possible for these steels, given the observations in some high dpa irradiations, such as: a swelling rate of 0.015%/dpa between 50 and 114 dpa at 420°C for HT9 [34], a maximum swelling of 0.09 and 1.02% in HT9 with different heat treatments after irradiation at 420°C to 200 dpa, and a maximum swelling in DIN 1.4914 of only 0.05% after irradiation at 400

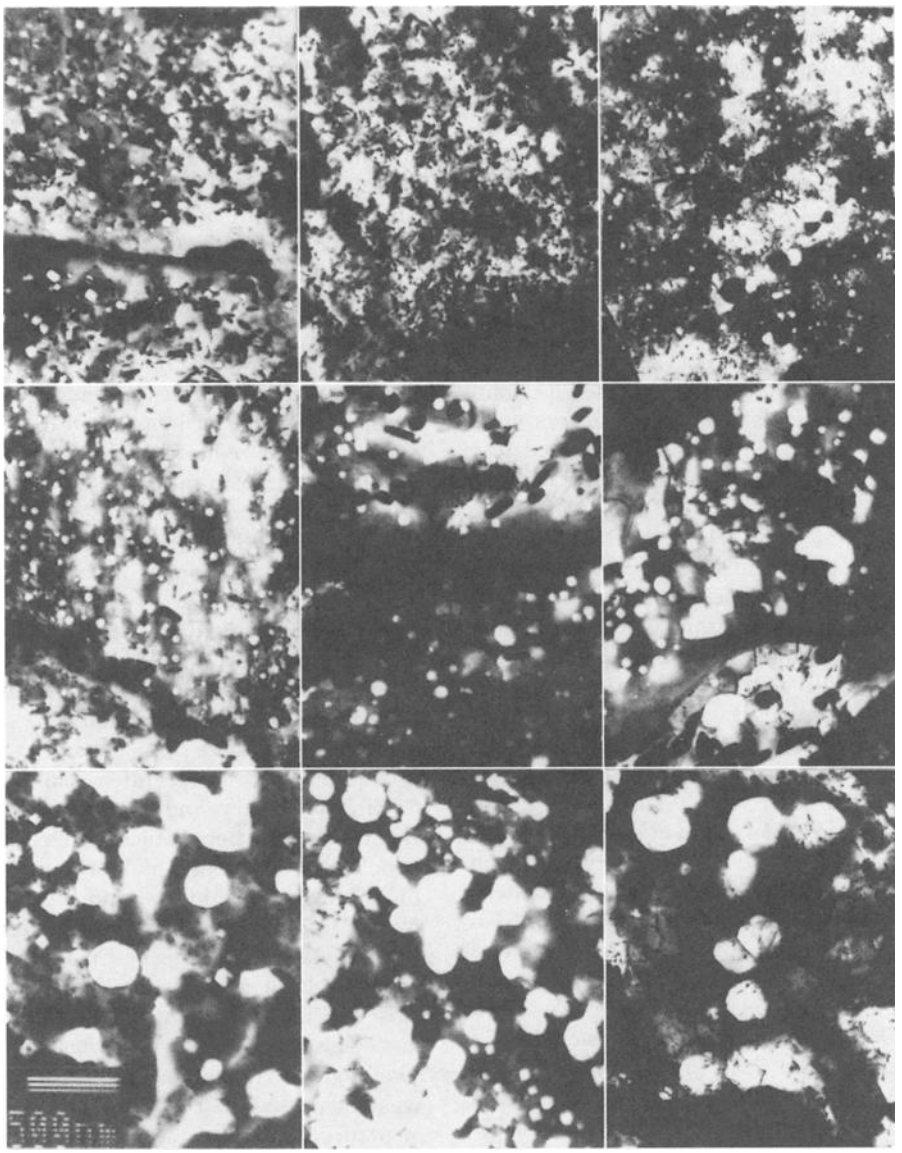

FIG. 9.5—Microstructures of experimental reduced-activation ferritic/martensitic steels following irradiation at 420°C in FFTF to 200 dpa: top row, left to right, 2Cr-0.5V, 2Cr-1V, and 2Cr-1.5V; middle row, left to right, 9Cr-0.5V, 9Cr-1V, and 9Cr-0.5V-3Mn; bottom row, left to right, 12Cr-1V-6.5Mn, 9Cr-1W-2Mn, and 12Cr-1W-6.5Mn [29].

to 480°C to 105 dpa [23]. However, Garner et al. warn that in a fusion reactor where large amounts of helium will form in the first wall, the low-swelling character of the ferritic/martensitic steels might be compromised by the effect of the helium on the nucleation of voids [56].

Basically, the swelling results for commercial Cr-Mo steels and experimental reduced-activation steels irradiated in fast reactors can be summarized as indicating that these steels show relatively low swelling (much less than the austenitic stainless steels), even when irradiated to 200 dpa near the peak swelling temperature. This is true whether the steel is in the martensitic, bainitic, or ferritic condition and whether the steel is transformable or non-transformable. Helium is expected to be important in a fusion reactor, and that will be discussed next.

Helium Effects

Because of the large amount of helium produced in a fusion reactor first wall, the effect of helium on swelling was investigated by irradiating 9Cr-1MoVNb and 12Cr-1MoVW steels and these steels with 2% Ni (9Cr-1MoVNb-2Ni and 12Cr-1MoVW-2Ni) in the HFIR [31–33,57]. The thermal neutrons in this mixed-spectrum reactor react with ^{58}Ni according to Eqs 8.2 and 8.3 to produce transmutation helium. By comparing microstructures (Fig. 9.6) of the undoped and nickel-doped steels irradiated at 400°C in HFIR (≈37 dpa with 30 and 400 appm He in the undoped and doped steels, respectively) with those irradiated at 407°C in FFTF (47 dpa and ≈5 dpa in both the undoped and doped steels), it was concluded that increases in the He/dpa ratio

enhanced the formation of large, bias-driven voids [33]. Furthermore, after irradiation in HFIR, the extent of void formation depended on nickel concentration, an indication that helium affected void formation, since nickel appeared to produce no significant differences in the general microstructure for the steel irradiated in HFIR and FFTF [31–33,57]. The nickel-containing steel irradiated in *both* reactors contained a high density of fine M_6C precipitates (Fig. 9.6) [33].

This conclusion on helium effects was questioned by Gelles and Kohyama [34], based on the observation that no voids formed in HT9 after 70 dpa in EBR-II, but a few did form in a different heat of the steel after 34 dpa [27] and many formed after 114 dpa [34] in FFTF. They concluded that significant helium was not required for void formation, and they argued that the behavior appeared to be different even in different fast reactors (EBR-II versus FFTF). Since different heats of HT9 were irradiated in EBR-II [27] and FFTF [27,34], an alternate explanation might be differences in dissolved gas concentrations (e.g., O or N) in the two heats. Such gases can play a pivotal role similar to transmutation helium in nucleating voids [58,59].

Gelles and Kohyama [34] compared FFTF results for HT9 steel irradiated to 114 dpa with dual ion-beam irradiations to 100 dpa and 15 appm He by Asano et al. [18]. The latter studies showed a density change of only 0.14%, compared to the high of 0.9% in FFTF. With 100 dpa and 5 appm He, only small cavities formed in the high-damage-rate ion-beam experiments [18]. However, no cavities formed without helium, and Asano et al. concluded that helium was required for cavity formation [18]. Despite these observations, Gelles and Kohyama implied that helium might still not be a factor in FFTF by stating [34], ". . . in those materials where precipitation that formed during irradiation plays a role in microstructural development, care must be taken in interpreting the results of high-damage-rate irradiation." As stated above, other gases besides helium (or in addition to helium) can play a role in void formation [58,59].

Kimura et al. [46] examined the microstructure of a 9Cr-2W-0.25V-0.05Ta-0.1C reduced-activation steel with and without 0.003% B irradiated in FFTF. The steels with boron showed as much as 0.2% swelling after irradiation to 40 dpa (≈30 appm He) at 420°C, compared with negligible swelling for the steels without boron. The authors attributed the higher swelling rate in the boron-containing steel [46] "to be due to the helium transmuted from ^{10}B included in the natural boron."

Shibayama et al. [47] irradiated two 9Cr-2WVTa steels similar to the ones irradiated by Kimura et al. [46] but with 0.02% Ti, one steel with a 0.003% B addition and one without. After irradiation to 60 dpa at 420°C in FFTF, microvoids formed in both steels. The mean size of the voids in the boron-containing steel with ≈30 appm He was much smaller than for the voids in the steel without boron, but the void number density in the steel with boron was about twice that of the steel without boron. Less swelling occurred in the steel with boron (0.45% versus 0.77%) because the high density of smaller bubbles in this steel acted as neutral sinks (no bias

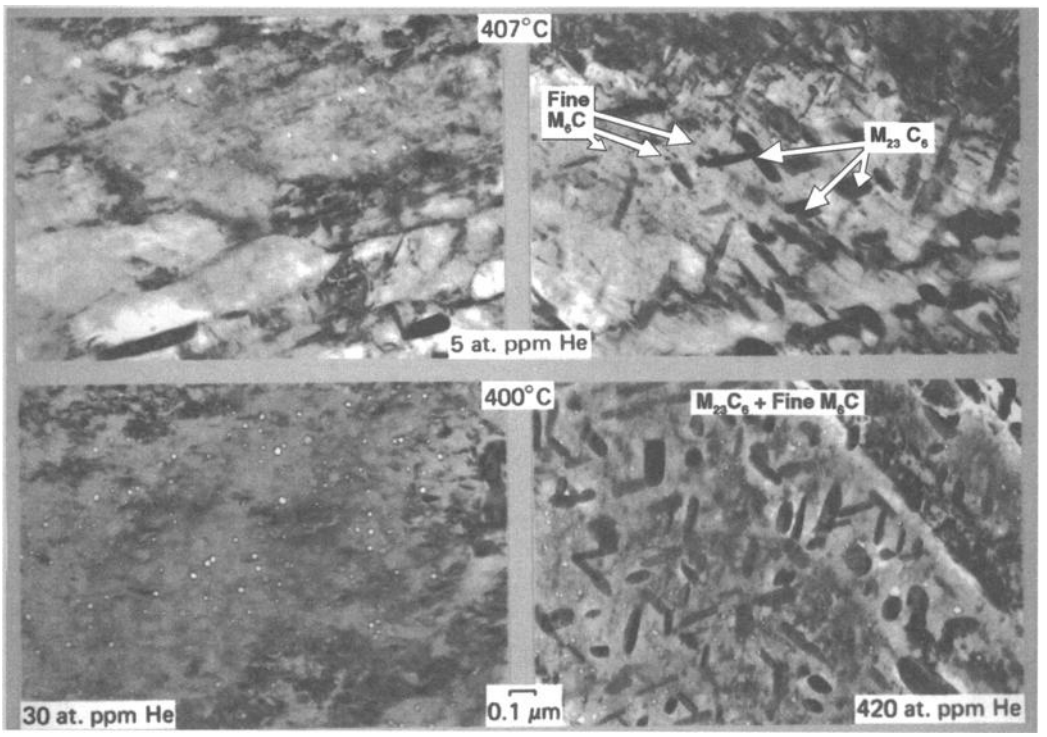

FIG. 9.6—Microstructures of 9Cr-1MoVNb (left) and 9Cr-1MoVNb-2Ni (right) steels irradiated in FFTF at 420°C to 47 dpa (top) and in HFIR at 400°C to 37 dpa (bottom) showing increased void formation after HFIR irradiation; the micrographs on the right indicate little difference in the precipitate microstructures formed in the 9Cr-1MoVNb-2Ni steel during irradiation in FFTF (top) and HFIR (bottom) [33].

for either vacancies or interstitials), which is how helium often affects swelling [58,59].

Gelles used the nickel doping technique in Fe-12Cr-1.5Ni ternary alloys to study the effect of the nickel by irradiating alloys containing 1.5% of natural nickel, ^{59}Ni, and ^{60}Ni to ≈7 dpa in HFIR at 300 and 400°C [60]. About 45 appm He was produced from the natural nickel, 80 appm He from ^{59}Ni, and no helium from ^{60}Ni. An Fe-12Cr alloy was also irradiated. A high density of helium bubbles formed in the alloys with natural nickel and ^{59}Ni irradiated at 300°C. Lower densities were observed in the alloys with ^{60}Ni additions and no added nickel. At 400°C, precipitate formation in the nickel-containing alloys hindered the observations of bubbles, while the alloy without nickel contained some cavities. In addition to the α' that is usually found in such 12% Cr alloys, it was concluded that the nickel promoted additional precipitate formation. The new precipitates were not identified. It was concluded that because of the precipitates, caution must be exercised when using nickel doping to study helium effects [60]. It should be pointed out, however, that these alloys are quite different from typical 12 Cr steels. For example, in addition to iron and chromium, HT9 also contains Mo, V, Nb, W, Si, Mn, and C.

The question of the effect of nickel additions on the microstructure of the steels was also addressed in the work on 9Cr-1MoVNb and 12Cr-1MoVW steels with up to 2% Ni [31–33,57]. No difference in the precipitate microstructure of the steels with and without the 2% Ni was observed before irradiation [31–33]. However, irradiation of the nickel-doped steels in both HFIR and FFTF at 400 and 500°C resulted in the production of a fine distribution of M_6C (Fig. 9.6), which was rich in Cr, Ni, and Si [33]. Since the precipitate microstructures in HFIR and FFTF at ≈400°C were similar, the precipitate was not thought to invalidate the conclusion that helium enhanced the formation of voids (bias-driven cavities) and bubble formation at 300 to 600°C [33].

Ion and Electron Irradiation

Ion and electron irradiations are carried out to simulate neutron irradiation. However, peak swelling temperatures for electron and heavy-ion irradiations occur at 100 to 150°C higher than for neutron irradiation due to the higher displacement rate (dpa s^{-1}) for ion and electron irradiation. For a higher defect production rate during ion or electron irradiation, a higher temperature must be reached before the thermal vacancy emission rate exceeds the net influx of irradiation-produced vacancies, the net result being a shift in the peak swelling temperature. Electron irradiation has been used primarily to study microstructural changes, often with tests conducted in situ. Much ion-irradiation work on ferritic/martensitic steels has involved the study of helium effects, either by dual-beam (heavy ion/helium) irradiations [14–18,52,61–63] or by pre-injecting helium before the heavy-ion bombardment [62,64]. Triple-beam irradiations with hydrogen ions as the third beam have also been used [17].

Dual-beam experiments by Mazey et al. [15] demonstrated the low-swelling character of ferritic/martensitic steels by irradiating several austenitic stainless steels and nickel-base alloys along with the FV448, FV607, CRM 12, and FI ferritic/martensitic steels. The authors concluded that the ferritic/martensitic steels are low swelling relative to the other materials, and that "gas concentrations appropriate to fusion-reactor conditions do not induce an enhancement in swelling relative to fission neutron irradiation." Similar results were obtained in an ion-bombardment experiment of an Fe-10Cr binary alloy following helium injection. A high density of voids developed during ion irradiation, and Mazey et al. used this observation to explain the low swelling in terms of the ultra-high dislocation densities generated in the martensite transformation, which are then stabilized by carbide precipitates and helium gas bubbles [15].

Gilbon and Rivera [10] compared ion, electron, and neutron irradiation. They used TEM to examine the five commercial ferritic steels, EM10, HT9, DIN 1.4914, EM12, and F17 after dual-beam (He^+/Fe^+) irradiation at 450, 500, and 550°C, EM10 and EM12 after 1 MeV electron irradiation at 400, 450, and 500°C, and EM12 and F17 after irradiation in the Phénix fast reactor at 400 to 500°C. The dual-beam irradiations to 100 dpa and 20 appm He/dpa produced microstructures with small helium bubbles after irradiation to 500°C, with the size (2.2 to 3.1 nm) and number density (≈1 × 10^{17} cm^{-3}) of the bubbles only weakly sensitive to the type of steel, even though the chromium concentration ranged from 9 to 17% and the microstructures ranged from ≈100% tempered martensite (HT9, EM10, and DIN 1.4914) to the duplex structure of tempered martensite and δ-ferrite (EM10) to 100% ferrite (F17). Bubble size increased slightly and number density decreased slightly with temperature, but the bubble volume fraction was relatively independent of temperature. Voids were only observed at ~500°C. The highest swelling resistance of the three tempered martensitic steels was observed for EM10, with the HT9 showing the highest swelling, although it was still very low at 0.06%. The F17 showed no indication of cavity formation [10].

Results for the electron irradiation of the EM10 and EM12 were similar to the dual-beam tests in that the swelling rate was <0.1%/dpa, with the EM10 having the best swelling resistance [10]. One difference between ion and electron irradiations of the EM10 was that voids appeared after electron irradiation to 5 dpa with a saturation value of $10^{16}/cm^3$, compared to no voids in the ion irradiations even after 100 dpa. Swelling resistance in the δ-ferrite and tempered martensite constituents of the EM12 were similar [10].

Irradiations of the F17 in Phénix at 407°C to 80 dpa resulted in a homogeneous distribution of voids (2.5 × 10^{14} cm^{-3}, 35 nm) to give a swelling of ≈0.5% along with the production of a high density of α' precipitate [10]. Swelling became negligible at 493°C. Void swelling in the EM12 after 100 dpa at 413°C was ≈0.55%, with little difference in the voids in the ferrite or the tempered martensite. No voids were observed after irradiation at 459°C, but chi-phase was observed [10].

The authors [10] concluded that their dual-beam results were in agreement with previous dual- and triple-beam irradiations [16,17,63] and mixed-spectrum reactor irradiations [31–33] in that they observed "a high density of small bubbles over a wide range of temperatures (300 to 600°C) and their preferential distribution at dislocations and lath boundaries for temperatures above 500°C." In the dual-beam experiments, the authors also compared tempered and untempered DIN 1.4914 and found precipitate formation in the untem-

pered steel but no void formation [10]. This was the only precipitation that was found for the ion irradiations, and the authors observed that whereas dual-beam irradiations allow for the simulation of helium effects, the reactor irradiations are irreplaceable to determine possible degradation effects caused by precipitation during irradiation [10].

Differences were observed between neutron irradiation and electron irradiation by Little, who irradiated FV448 with 1 MeV electrons at 300 to 500°C to 2, 10, and 40 dpa [9]. Whereas **a**<100> loops formed during fast reactor irradiation, a uniform dislocation network formed after electron irradiation to 40 dpa. Rapid void nucleation was found in the electron-irradiated steel; this high density of voids constituted a distribution of neutral sinks that affected the subsequent swelling behavior [9].

Ion irradiation was also used to examine the effect of steel purity on swelling. Reduced-activation steels will need to be produced from pure components to eliminate the small concentrations of deleterious elements such as Nb, Mo, Ag, etc. Nagaszki et al. [65] investigated the effect of purity on helium bubble formation in Fe-9Cr-0.1C steel produced with iron purified by floating zone (FZ) refining and commercial high-purity chromium. They compared the results with commercial-grade (C-grade) Fe-9Cr-0.06C and Fe-9Cr-0.15C steels. Results after 1000 appm He implantation at 0.2 dpa showed that a higher density of smaller bubbles formed in the FZ-Fe-9Cr-0.1C steel than the C-Fe-9Cr-0.06C and C-Fe-9Cr-0.15C, with much larger denuded zones at prior austenite grain boundaries for the latter two steels. The C-Fe-9Cr-0.15C had a more uniform distribution of somewhat smaller cavities than the C-Fe-9Cr-0.06C steel.

Based on previous work in which sulfur was added to high-purity Fe-Cr alloys [66], the authors attributed the differences in the three steels to vacancy segregation to strain fields of sulfide clusters or complexes (FeS, CrS, and MnS) that then act as cavity nucleation sites. They cite carbon or nitrogen interstitials as nucleation sites in the high-purity steel and for the lesser amount of large cavities in the C-grade Fe-9Cr-0.15C steel. The larger denuded zones are related to the sulfur-containing clusters that may be present in the C-grade steels [65,66].

Swelling Mechanisms

Several explanations have been put forward for the superior swelling resistance of ferritic steels relative to the austenitic steels [6,7,14,21,26,33,62,67–72]. They include mechanisms that depend on solute trapping [21,26,63], the character of the dislocation loop structure [67,68], the lower relaxation volumes of the body-centered cubic structure [69], and the tempered martensite microstructure [33,62,72]. The model based on the assumption of a lower dislocation bias for interstitials in bcc alloys than fcc alloys because of a lower relaxation volume [69] has been questioned based on observed growth rates [70] and computer simulation studies [73].

Little and Stow [20] studied the swelling of Fe-Cr (0, 1, 5, 10, and 15% Cr) binary alloys and observed a decrease in swelling for chromium up to 5% followed by a gradual increase from 5% to 15%. They explained their results by solute trapping; they envisioned the suppression of the void nucleation rate by the enhanced recombination of vacancies and interstitials due to the trapping effects caused by the weak interactions between chromium atoms and vacancies. The swelling increase above 5% was attributed to depletion of chromium caused by α' precipitation [20]. A similar explanation was used for commercial steels [20]. Solute-atom trapping involves both interstitial and substitutional elements that bind preferentially to irradiation-produced point defects (see Chapter 10 on radiation-induced segregation); it retards the migration of the defects to sinks, thus enhancing vacancy-interstitial recombination. Solute-trapping effects were also cited in other work on commercial steels [26].

Observations on ferritic/martensitic steels irradiated in a fast reactor indicate that **a**<100> dislocation loops form within a network that consists predominantly of **a**/2<111> loops [67]. It has been suggested that the **a**<100> loops have a strong interstitial bias that results in the **a**/2<111> loops becoming sinks for the vacancies [67,68]. Electron irradiation studies verified that the **a**<100> loops have a strong bias for interstitials, while the **a**/2<111> loops are essentially neutral sinks [68]. These latter loops therefore become sinks for the vacancies as well [74,75], thereby reducing the vacancies available to cause cavity growth. Solute segregation was also found to be stronger to the **a**<100> loops in an Fe-10Cr-1Ni alloy [74].

For Fe-Cr binary alloys with 3, 6, 9, 12, 15, and 18% Cr irradiated in fast reactors up to 19 dpa at 400 to 540°C, Gelles and Thomas found that the maximum swelling occurred for the 9% Cr alloy, and the minimum occurred for the 3% Cr alloy [26,52]. Peak swelling corresponded with a network dislocation structure of equivalent parts of **a**<100> and **a**/2<111> Burgers vectors, compared with predominantly **a**<100> dislocation loops and some large **a**/2<111> loops and dislocations present in the alloys with 6, 12, 15, and 18% Cr, which showed less swelling. Twelve ternary alloys with Fe-10Cr to which respectively 0.1 and 1% Si, Mn, V, W, Ta, and Zr were individually added to the binary composition were irradiated to 30.5 dpa at 430°C [53]. With the exception of the zirconium, the results indicated that swelling varied linearly with solute atom size misfit between the solute and the iron lattice for the 1% alloys. Dislocation loop evolution for these alloys generally favored equal components of **a**<100> and **a**/2<111> Burgers vectors, but the 1% V alloy promoted **a**<100> and Zr promoted **a**/2<111> vectors. The general conclusion was that radiation-induced solute segregation controls the microstructural development, and it was suggested that the solutes that segregated to dislocations and cavities affected the dislocation bias and/or surface energies [53].

For the 9Cr-1MoVNb and 12Cr-1MoVW martensitic steels and the MA 956 and MA957 irradiated to 200 dpa in FFTF, Gelles found regions in the steels with comparable void development but with different dislocation structures [29]. The general dislocation structure consisted of **a**<100> loops and a network of **a**/2<111> dislocation segments. However, in some areas, the structure was primarily **a**/2<111>, which may have been caused by nearby subgrain boundaries. From the observation of similar void structures in both regions, it was concluded that the void swelling was [29] "unaffected by whether the dislocation structure contains a significant **a**<100> component," and the results were taken to [29] "indicate that either the Burgers vector distribution has little ef-

fect on swelling, or the magnitude of swelling is independent of differences in dislocation response in isolated regions."

The normalized-and-tempered microstructure of the steels or the microstructure that evolves during irradiation has also been cited for the swelling resistance [13,33,71]. The extensive subgrain and lath boundary surfaces in martensitic steels can act as neutral point defect sinks to reduce point-defect supersaturation. Likewise, in the 12Cr steels, small irradiation-induced α' precipitates that form during irradiation could act as recombination sites for vacancies and interstitials [20]. That is, α' is thought to form as a coherent particle, so that vacancies and/or interstitials could be trapped there and become annihilated by recombination. An incoherent particle is required for the precipitate to act as a sink. The size and number density of precipitates and the dislocation structure formed during tempering was used to explain the observation that indicated 0.09 and 1.02% swelling for HT9 steel tempered at 700 and 750°C, respectively [29]. A higher density of finer precipitates and a higher dislocation density will be present after tempering at 700°C than after tempering at 750°C. Further, if precipitation is incomplete after the 700°C temper, further precipitation during irradiation can lead to densification that can offset swelling due to void growth [29].

Lee and Mansur [72] described bias-driven swelling behavior in terms of the critical radius or the critical number of gas atoms required to stabilize a cavity and allow it to continue to grow by vacancy accumulation and a parameter Q that measures the relative importance of the dislocation structure and cavities as sinks for the irradiation-produced defects.

$$Q = \frac{L}{4\pi \bar{r}_c N_c} \tag{9.3}$$

where L is the dislocation density, $\bar{r}_c$ is the average cavity radius, and N_c is the cavity density.

Swelling resistance is greatest for microstructures with an imbalance in Q (i.e., $Q << 1$ or $Q >> 1$) and for any Q with a very large N_c. A $Q << 1$ occurs for a high density of cavities and a low dislocation density and vice versa for $Q >> 1$.

According to Lee and Mansur [72], the more open structure of the bcc lattice allows for a higher helium mobility, which results in low rates of formation of helium-stabilized cavities. Lower helium generation rates in both fast and mixed-spectrum reactors is also important. With the resulting low N_c (large Q), recombination is favored within the lattice or at dislocations. The authors cited experimental evidence that indicates cavity growth rates for ferritic/martensitic steels are similar to those of austenitic steels, indicating that swelling of the ferritic/martensitic steels might be expected to increase under conditions where more cavities form to give $Q \approx 1$.

Equation 9.3 shows that if one type of sink dominates the microstructure—either dislocations or cavities—then that sink can act as a recombination center to inhibit swelling. A high density of cavities generated early in the electron irradiation process was used to explain a lower swelling rate for FV448 [9]. A high concentration of helium can lead to the nucleation of a high number density of bubbles that act as neutral sinks. This occurred in dual-beam irradiations of DIN 1.4914 that contained 1 and 10 appm He; the steel containing the 1 appm He showed the most swelling [52]. Likewise, a high density of helium bubbles acting as neutral sinks was used to explain the reduced swelling in boron-doped 9Cr-2WVTaTi steels [47] irradiated in FFTF. A cavity-dominated structure in the ion-bombarded, helium-injected Fe-10Cr alloy was used to explain the low swelling of this alloy [14]. Another demonstration of this effect was observed in an ODS Fe-13Cr steel containing a high density of yttria particles simultaneously irradiated to 50 dpa by 52 MeV Cr^{6+} ions and 4 MeV α-particles to 600 appm He [73]. Swelling in the ODS steel was less than half (0.24 versus 0.49%) the swelling that occurred in a steel without the yttria particles. The cavities were consistently associated with the yttria particles, which probably trapped the helium that then acted as nuclei for the cavities [73].

Kim et al. [76] demonstrated the effect of microstructure on swelling during dual-beam (3.2 MeV Fe^+, 330 keV He^+) irradiations to 50 dpa and 260 appm He at 650°C. They irradiated solution-annealed type 316LN stainless steel (SS), normalized-and-tempered 9Cr-2WVTa steel, and three ferritic ODS steels; the ODS steels were: Fe-17Cr-0.25Y_2O_3 (17Y3), Fe-12Cr-0.25Y_2O_3 (12Y1), and Fe-12Cr-3W-0.4Ti-0.25Y_2O_3 (12YWT). The microstructures of these steels were quite varied. The 316LN SS had clean grains with a dislocation density estimated at $\rho << 10^{13} m/m^3$, compared to $\rho \lesssim 10^{15}$ m/m^3 for the 9Cr-2WVTa, which contained the typical large $M_{23}C_6$ precipitates. The dislocation densities of 17Y3, 12Y1, and 12YWT ODS steels were estimated at 10^{15}, 10^{15}, and 10^{15} to 10^{16} m/m^{-3}, respectively. Average diameters of the oxide particles in the 12Y1 were estimated to be 10 to 40 nm at a number density of 10^{20} to 10^{21} m^{-3}. The particles in 17Y3 were said to be larger and fewer than in 12Y1. Finally, in 12YWT, the particles were small and numerous: 3 to 5 nm at a number density $1–2 \times 10^{23}$ m^{-3} [76].

Irradiation produced cavities (Figs. 9.7 and 9.8) and a modification of the dislocation microstructures. The 316LN SS contained a bimodal distribution of bubbles ($r < 0.5$ nm) and voids ($0.5 \text{ nm} \lesssim r < 100$ nm), where bubble denotes gas-filled cavities at or below the critical size, and void (cavity with a helium pressure below equilibrium) denotes a cavity above critical size that is growing by bias-driven vacancy absorption [Figs. 9.7(a) and (c)]. Bubbles ($r < 0.5$ nm) and voids ($0.5 \lesssim r < 10$ nm) were also detected in the 9Cr-2WVTa, but they were mainly in recovered areas and smaller than in the 316LN SS [Figs. 9.7(b) and (d)]. Still smaller voids ($r < 5$ nm) were observed in the 17Y3 [Figs. 9.8(a) and (d)] and 12Y1 [Figs. 9.8(b) and (e)] ODS steels, along with small bubbles. It was concluded that the bimodal distribution developed (in time) in the order of 316LN SS, 9Cr-2WVTa, 17Y3, and 12Y1. Finally, bubbles with $r < 1$ nm (no bimodal distribution) "too fine to count precisely" were detected in the 12YWT [Fig. 9.8(c) and (f)]; they were associated with the fine distribution of particles and high density of dislocations at a number density of $\approx 10^{23}$ to 10^{24} m^{-3} [76].

These results indicated that the more complicated microstructures showed the least swelling. Most swelling occurred in the relatively clean 316LN SS, followed by the 9Cr-2WVTa on through the 12YWT with its high number density of dislocations and particles. Furthermore, most of the void or cavity growth (swelling) in the 9Cr-2WVTa occurred in the highly recovered areas.

Therefore, it follows that the difference in void formation between the austenitic and ferritic steels did not originate from differences in crystal structure, point defect diffusivity, migration energy, etc., but rather, it was caused by the dif-

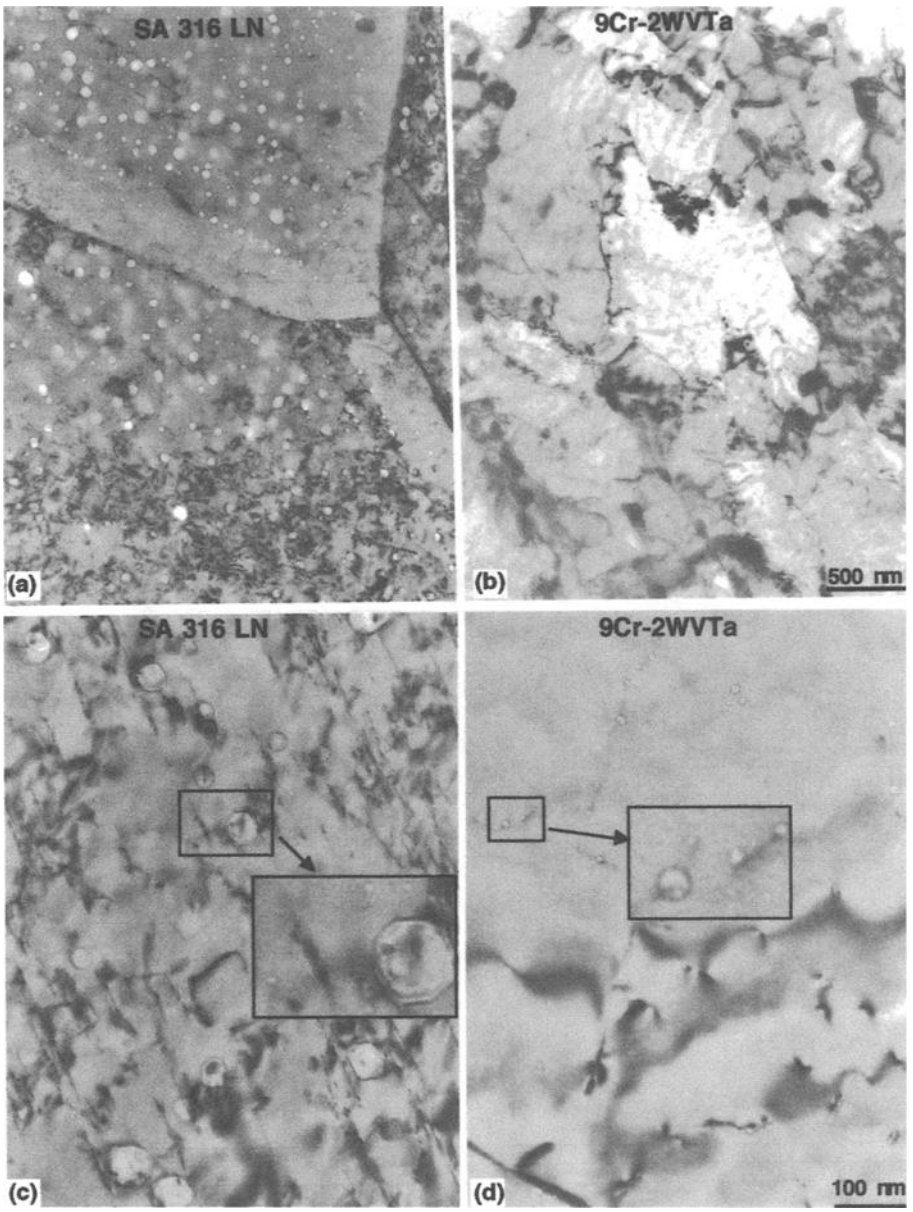

FIG. 9.7—Microstructure of (a) and (c) 316LN austenitic stainless steel and (b) and (d) 9Cr-2WVTa martensitic steel at two magnifications after irradiation with 3.2 MeV Fe^+ and 330 keV He^+ ions to 50 dpa and 260 appm He at 650°C [77].

ferent microstructures [76]. Based on the rate-theory model (Eq. 9.3), it was suggested that the sink density (dislocations, bubbles, precipitates, etc.) of the steel determines point defect recombination and void formation and that the change in bias due to change in microstructure could also be important. Therefore, microstructure affects the length of the transient stage, and once sufficient bias-driven voids are nucleated, the ferritic steels will swell [76].

This agrees with Garner et al. that the ferritic/martensitic steels will swell at steady-state rates closer to those of austenitic steels than previously thought, although the typical steady-state rates found by Garner et al. for the austenitic steels (1%/dpa) was still four to five times greater than that of ferritic steels (≈0.2%/dpa) [56]. Garner et al. observed that the steady-state rates of ≈0.2%/dpa and ≈1%/dpa for ferritic and austenitic steels, respectively, are in good agreement with those predicted by the assumption of a lower dislocation bias for interstitials in bcc alloys than fcc alloys because of a lower relaxation volume [69].

It is generally agreed that none of the proposed mechanisms completely explains the low-swelling observations [6,7,77]. Odette [6] used a critical bubble-rate theory of swelling to assess the possible mechanisms for the ferritic/martensitic steels and concluded that "low bias, high self-diffusion, and low helium generation rates, possibly coupled with high subgrain boundary sink strengths, explain most swelling trends observed to date." He pointed out that incubation periods could be reduced and swelling rates increased under fusion conditions where the He/dpa ratios produced are much higher than in a fast reactor [6].

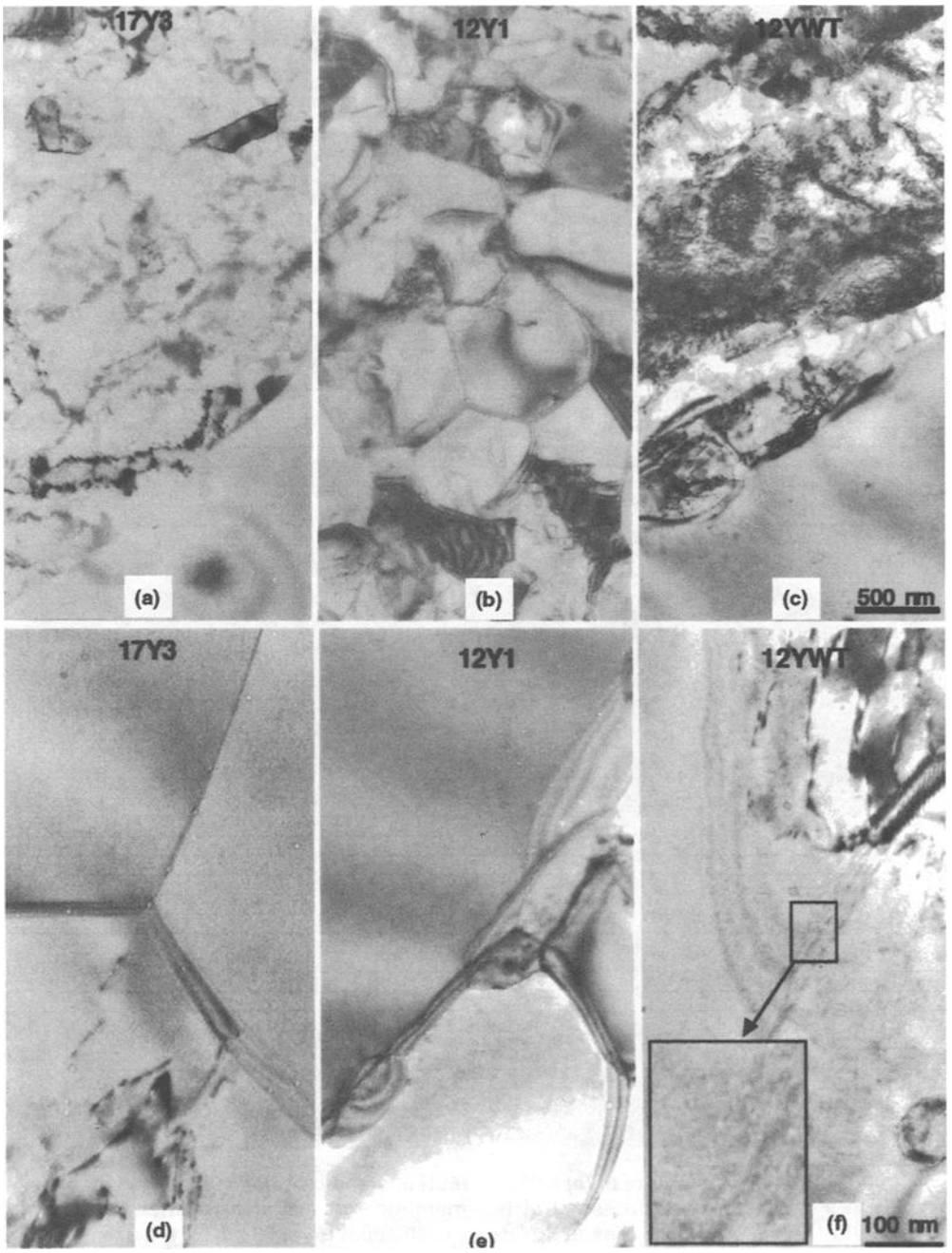

FIG. 9.8—Microstructure of the ODS steels (a) and (d) Fe-17Cr-0.25Y_2O_3 (17Y3), (b) and (e) Fe-12Cr-0.25Y_2O_3 (12Y1), and (c) and (f) Fe-12Cr-3W-0.4Ti-0.25Y_2O_3. (12YWT) at two magnifications after irradiation with 3.2 MeV Fe^+ and 330 keV He^+ ions to 50 dpa and 260 appm He at 650EC [77].

REFERENCES

[1] C. Cawthorne and E. J. Fulton, Nature 216 (1966) 575.
[2] F. A. Garner, J. F. Bates, and M. A. Mitchell, J. Nucl. Mater. 189 (1992) 201.
[3] K. Anderko, J. Nucl. Mater. 95 (1980) 31.
[4] D. R. Harries, in: Ferritic Steels for Use in Nuclear Energy Technologies, Eds. J. W. Davis and D. J. Michel (The Metallurgical Society of AIME, Warrendale, PA, 1984) p. 141.
[5] E. A. Little, Materials for Nuclear Reactor Core Applications, Vol. 2 (British Nuclear Energy Society, London, 1988) 47.
[6] G. R. Odette, J. Nucl. Mater. 155-157 (1988) 921.
[7] E. A. Little, J. Nucl. Mater. 206 (1993) 324.
[8] D. R. Arkell and T. M. Williams, J. Nucl. Mater. 74 (1978) 144.
[9] E. A. Little, Phys. Stat. Sol. (a) 87 (1985) 441.
[10] D. Gilbon and C. Rivera, J. Nucl. Mater. 155-157 (1988) 1268.
[11] M. Snykers, J. Nucl. Mater. 89 (1980) 80.
[12] M. Snykers and W. Vandermeulen, in: Dimensional Stability and Mechanical Behavior of Irradiated Metals and Alloys, Vol. 1 (British Nuclear Energy Society, London, 1983) 91.
[13] E. A. Little, D. R. Arkell, D. R. Harries, G. R. Lewthwaite, and T. M. Willams, Irradiation Behaviour of Metallic Materials for Fast

Reactor Core Components, Vol. 1, Eds. J. Poirier and J. M. Dupouy (CEA, Gif-Sur-Yvette, France, 1979) 31.
[14] D. J. Mazey, G. P. Walters, S. N. Buckley, S. M. Murphy, W. Hanks, and D. E. J. Bolster, J. Nucl. Mater. 155-157 (1988) 891.
[15] D. J. Mazey, S. M. Murphy, G. P. Walters, W. Hanks, and D. E. J. Bolster, in: Effects of Radiation on Materials: 14th International Symposium, Vol. I, ASTM STP 1046, Eds. N. H. Packan, R. E. Stoller, and A. S. Kumar (American Society for Testing and Materials, Philadelphia, 1989) 203.
[16] G. Ayrault, J. Nucl. Mater. 114 (1983) 34.
[17] K. Farrell and E. A. Lee, in: Effects of Radiation on Materials: Twelfth International Symposium, ASTM STP 870, Eds. F. A. Garner and S. J. Perrin (American Society for Testing and Materials, Philadelphia, 1985) 383.
[18] K. Asano, Y. Kohno, and A. Kohyama, J. Nucl. Mater. 155-157 (1988) 912.
[19] F. A. Smidt, P. R. Malmberg, J. A. Sprague, and J. E. Westmoreland, in: Irradiation Effects on the Microstructure and Properties of Metals, ASTM STP 611 (American Society for Testing and Materials, Philadelphia, 1976) 227.
[20] E. A. Little and D. A. Stow, J. Nucl. Mater. 87 (1979) 25.
[21] E. A. Little and D. A. Stow, Metal Sci. 14 (1980) 89.
[22] P. Dubuisson, D. Gilbon, and J. L. Séran, J. Nucl. Mater. 205 (1993) 178.
[23] E. Materna-Morris, C. Petersen, M. Rieth, O. Romer, M. Schirra, and K. Ehrlich, in: EuroMat 96: Conference on Materials and Nuclear Power (The Institute of Materials, London, 1996) 273.
[24] J.-J. Huet, A. De Bremaecker, M. Snykers, and Ph. Van Asbroeck, in: Irradiation Behavior of Metallic Materials for Fast Reactor Core Components, Vol. 1., Eds. J. Poirier and J. M. Dupouy (CEA, Gif-Sur-Yvette, France, 1979) 5.
[25] D. S. Gelles, J. Nucl. Mater. 122 & 123 (1984) 207.
[26] D. S. Gelles and L. E. Thomas, in: Topical Conference on Steels for Use in Nuclear Energy Technologies, Eds. J. W. Davis and D. J. Michel (The Metallurgical Society of AIME, Warrendale, PA, 1984) 559.
[27] C. Y. Hsu, D. S. Gelles, and T. A. Lechtenberg, in: Radiation-Induced Changes in Microstructure, ASTM STP 955, Eds. F. A. Garner, N. H. Packan, and A. S. Kumar (American Society for Testing and Materials, Philadelphia, 1987) 545.
[28] D. S. Gelles, J. Nucl. Mater. 148 (1987) 136.
[29] D. S. Gelles, J. Nucl. Mater. 233-237 (1996) 293.
[30] J. J. Kai and R. L. Klueh, J. Nucl. Mater. 230 (1996) 116.
[31] J. M. Vitek and R. L. Klueh, in: Topical Conference on Ferritic Steels for Use in Nuclear Energy Technologies, Eds. J. W. Davis and D. J. Michel (The Metallurgical Society of AIME, Warrendale, PA, 1984) 551.
[32] J. M. Vitek and R. L. Klueh, J. Nucl. Mater. 122 & 123 (1984) 254.
[33] P. J. Maziasz, R. L. Klueh, and J. M. Vitek, J. Nucl. Mater. 141-143 (1986) 929.
[34] D. S. Gelles and A. Kohyama, in: Fusion Reactor Materials Semiannual Progress Report for Period Ending March 31, 1989, Department of Energy Report DOE/ER-031316, p. 193.
[35] J. Erler, A. Maillard, G. Brun, J. Lehmann, and J. M. Dupouy, in: Irradiation Behaviour of Metallic Materials for Fast Reactor Core Components, Vol. 1, Eds. J. Poirier and J. M. Dupouy (CEA, Gif-Sur-Yvette, France, 1979) 11.
[36] R. W. Powell, D. T. Peterson, M. K. Zimmerschied, and J. F. Bates, J. Nucl. Mater. 103 & 104 (1981) 969.
[37] V. M. Poplavsky and L. M. Zadbudko, in: Proc. IAEA Technical Committee Meeting on The Influence of High Dose Irradiation on Advanced Reactor Core Structural and Fuel Materials, IAEA-TECDOC-1039 (IAEA, Vienna, 1998) 7.
[38] V. S. Khabarov, A. M. Dvoriashin, and S. I. Porollo, in: Proc. IAEA Technical Committee Meeting on the Influence of High Dose Irradiation on Advanced Reactor Core Structural and Fuel Materials, IAEA-TECDOC-1039 (IAEA, Vienna, 1998) 139.
[39] V. S. Agueev, E. A. Medvedeva, N. M. Mitrofanova, V. V. Romanueev, and A. V. Tselishev, Nucl. Energy 31 (1992) 277.
[40] K. Q. Bagley, E. A. Little, V. Levy, A. Alamo, K. Ehrlich, K. Anderko, and A. Calza Bini, Nuclear Energy 27 (1988) 295.
[41] D. Gilbon, J. L. Séran, R. Cauvin, A. Fissolo, A. Alamo, F. Le Naour, and V. Lévy, in: Effects of Radiation on Materials: 14th International Symposium, Vol. I, ASTM STP 1046, Eds. N. H. Packan, R. E. Stoller, and A. S. Kumar (American Society for Testing and Materials, Philadelphia, 1989) 5.
[42] A. De Bremaecker and J. -J. Huet, in: Dimensional Stability and Mechanical Behavior of Irradiated Metals and Alloys, Vol. 1 (British Nuclear Energy Society, London, 1983) 117.
[43] D. S. Gelles, C. Y. Hsu, and T. A. Lechtenberg, J. Nucl. Mater. 155-157 (1988) 902.
[44] D. S. Gelles, in: Reduced Activation Materials for Fusion, ASTM STP 1047, Eds. R. L. Klueh, D. S. Gelles, M. Okada, and N. H. Packan (American Society for Testing and Materials, Philadelphia, 1990) 113.
[45] D. S. Gelles, J. Nucl. Mater. 212-215 (1994) 714.
[46] A. Kimura, M. Narui, and H. Kayano, J. Nucl. Mater. 191-194 (1992) 879.
[47] T. Shibayama, A. Kimura, and H. Kayano, J. Nucl. Mater. 233-237 (1996) 271.
[48] F. A. Smidt, Jr., A. Sprague, J. E. Westmoreland, and P. R. Malmberg, Nuclear Metallurgy, 18 (1973) 341.
[49] L. L. Horton, J. Bentley, and W. A. Jesser, J. Nucl. Mater. 103 & 104 (1981) 1085.
[50] S. Ohnuki, H. Takahashi, and T. Takeyama, J. Nucl. Mater. 103 & 104 (1981) 1121.
[51] S. Ohnuki, H. Takahashi, and T. Takeyama, J. Nucl. Mater. 122 & 123 (1984) 317.
[52] K. Exel, Simulationsbestrahlungen mit 200 keV Ni-Ionen zur Untersuchung des Schwellverhaltens von Eisen und Nickel sowie der technischen Legierungen 1.4914 und 1.4970, KfK 4083, Kernforschungszentrum Karlsruhe, Karlsruhe, Germany, May 1986.
[53] D. S. Gelles, in: Effects of Radiation on Materials: 14th International Symposium, Vol. I, ASTM STP 1046, Eds. N. H. Packan, R. E. Stoller, and A. S. Kumar (American Society for Testing and Materials, Philadelphia, 1989) 73.
[54] D. S. Gelles, Private Communication, November 1996.
[55] V. V. Chuev, A. N. Ogorodov, and V. V. Maltsev, Irradiation Performance of BN-600 Fast Reactor Core Fuel Sub-Assemblies Structural Materials, Preprint for IAEA Technical Committee Meeting on The Influence of High Dose Irradiation on Advanced Reactor Core Structural and Fuel Materials, Obninsk, Russia, June 1997.
[56] F. A. Garner, M. B. Toloczko, and B. H. Sencer, J. Nucl. Mater. 276 (2000) 123.
[57] P. J. Maziasz and R. L. Klueh in: Effects of Radiation on Materials: 14th International Symposium, Vol. I, ASTM STP 1046, Eds. N. H. Packan, R. E. Stoller, and A. S. Kumar (ASTM, Philadelphia, 1989) 35.
[58] K. Farrell, Radiation Effects 53 (1980) 175.
[59] K. Farrell, P. J. Maziasz, E. H. Lee, and L. K. Mansur, Radiation Effects 78 (1983) 277.
[60] D. S. Gelles, Effects of Radiation on Materials: in: 18th International Symposium, ASTM STP 1325, Eds. R. K. Nanstad, M. L. Hamilton, G. A. Garner, and A. S. Kumar (American Society for Testing and Materials, Philadelphia, 1999) p. 899.
[61] M. R. Hayns and T. M. Williams, J. Nucl. Mater. 74 (1978) 151.
[62] L. L. Horton and L. K. Mansur, in: Effects of Radiation on Materials: Twelfth International Symposium, ASTM STP 870, Eds. F. A. Garner and S. J. Perrin (American Society for Testing and Materials, Philadelphia, 1985) 344.
[63] J. J. Kai, G. L. Kulcinski, and R. A. Dodd, J. Nucl. Mater. 141-143 (1986) 731.

[64] P. Dauben, R. P. Wahi, and H. Wollenberger, J. Nucl. Mater. 133 & 134 (1985) 619
[65] T. Nagasaka, T. Shibayama, H. Kayano, A. Hasegawa, and K. Abe, Phys. Stat. Sol. 167 (1998) 335.
[66] T. Nagasaka, T. Shibayama, H. Kayano, A. Hasegawa, and K. Abe, Sci. Rep. RITU A45 (1997) 121.
[67] E. A. Little, R. Bullough, and M. H. Wood, Proc. Roy. Soc. (London) A372 (1980) 565.
[68] R. Bullough, M. H. Wood, and E. A. Little, in: Effects of Radiation on Materials: Tenth Conference, ASTM STP 725, Eds. D. Kramer, H. R. Brager, and J. S. Perrin (American Society for Testing and Materials, Philadelphia, 1981) 593.
[69] J. J. Sniegowski and W. G. Wolfer, in: Topical Conference on Ferritic Alloys for Use in Nuclear Energy Technologies, Eds. J. W. Davis and D. J. Michel (The Metallurgical Society of AIME, Warrendale, PA, 1984) 579.
[70] T. S. Morgan, E. A. Little, R. G. Faulkner, and J. M. Ticthmarsh, Effects of Radiation on Materials: Fifteenth International Symposium, ASTM STP 1125, Eds. R. E. Stoller, A. S. Kumar, and D. S. Gelles (American Society for Testing and Materials, Philadelphia, 1985) 633.
[71] L. K. Mansur and E. H. Lee, J. Nucl. Mater. 179-181 (1991) 105.
[72] E. H. Lee and L. K. Mansur, Metal. Trans. A, 21A (1990) 1021.
[73] E. Kuramoto, J. Nucl. Mater. 191-194 (1992) 1279.
[74] T. Muroga, A. Yamaguchi, and N. Yoshida, in: Effects of Radiation on Materials: 14th International Symposium, Vol. I, ASTM STP 1046, Eds. N. H. Packan, R. E. Stoller, and A. S. Kumar (American Society for Testing Materials, Philadelphia, 1989) 396.
[75] D. S. Gelles, S. Ohnuki, H. Takahashi, H. Matsui, and Y. Kohno, J. Nucl. Mater. 191-194 (1992) 1336.
[76] I.-S. Kim, J. D. Hunn, N. Hashimoto, D. L. Larson, P. J. Maziasz, K. Miyahara, and E. H. Lee, *Journal of Nuclear Materials*, 280 (2000) 264.
[77] L. K. Mansur, Kinetics of Nonhomogeneous Processes, Ed. G. R. Freeman (John Wiley & Sons, Inc., New York, 1987) 377.

10

Interfacial Segregation and Precipitation During Irradiation

RADIATION-INDUCED SEGREGATION

The microstructural evolution in alloy systems during irradiation at elevated temperatures is determined by, among other factors, a non-equilibrium segregation process termed radiation-induced segregation (RIS), which can occur as a consequence of:

1. The strong interaction between solutes and the point defects (vacancies and interstitial atoms) generated during irradiation, resulting in coupled transport of the solute atoms by the point-defect fluxes to and away from sinks, such as grain boundaries, free surfaces, dislocations loops, void surfaces, etc. The magnitude of the solute-point defect binding energy determines whether the solute flow is towards or away from the sinks. In general, undersize solutes such as silicon and phosphorus in α-iron bind strongly to the interstitials in a mixed dumbbell configuration, resulting in a marked enrichment at sinks. Conversely, the oversize solutes (Cr and Mo in α-iron) are weakly bound to vacancies and are depleted at sinks. These processes have been modeled [1–3] using a simplified analytical method similar to that for thermally induced non-equilibrium segregation [4,5]; however, these approaches apply essentially to dilute alloys containing <1 at% solute, and their accuracy is limited in many cases by the lack of precise knowledge of the binding and migration energies of the solute-point defect complexes.
2. The Inverse Kirkendall Effect, whereby the faster-diffusing species exchange more often with the irradiation-induced vacancies migrating to sinks than slow-diffusing species. The fast-diffusing solutes are therefore depleted at sinks while the concentrations of the slow-diffusing species increase. This Inverse Kirkendall Effect due to vacancies has been modeled with some success for both dilute and concentrated alloys using rate theory in which the elemental distribution is obtained by the simultaneous solution of a series of partial differential equations defining the fluxes of all atomic species [6–12]. An Inverse Kirkendall Effect due to interstitials, analogous to the effect of vacancies, may also be expected [13]; the atom fluxes are in the same direction as the defect fluxes in this case, but the contribution of this effect to the RIS process is uncertain at present.

The theoretical modeling and experimental observations on RIS have been reviewed in several publications [8,12,14–16]. The early work on RIS was carried out almost exclusively on face-centered-cubic (fcc) alloy systems, such as the Fe-Cr-Ni austenitic stainless steels [17–20]. It was established, using analytical electron microscope techniques, that extensive local changes in chemical composition could occur, leading to microstructural instability and precipitation; thus, the sensitization and intergranular corrosion during post-irradiation storage of the 20Cr-25Ni-Nb austenitic steel used for fuel element cladding in the U.K. civil advanced gas cooled reactors (CAGRs) have been attributed to RIS and, in particular, the observed chromium depletion near grain boundaries [21]. Increasing attention has subsequently been devoted to the investigations of RIS in the body-centered-cubic (bcc) iron and steels. For example, intergranular segregation of phosphorus following irradiation has been observed in Fe-P and Fe-Cu-P alloys [22], resulting in grain boundary fracture, as well as in a nuclear reactor pressure vessel steel weld metal [23] and in a 9Cr-1Mo martensitic steel [17].

The predicted RIS of silicon in a ferritic steel matrix is illustrated in Figs. 10.1 and 10.2 [3] in terms of C/C_g, where C is the interfacial (grain boundary) solute concentration and C_g is the concentration within the grains. The data demonstrate that the magnitude and temperature dependence of the RIS of silicon are dependent on the initial dislocation density (Fig. 10.1) and grain size (Fig. 10.2) as well as the displacement dose and dose rate [3]. The model also predicts significant RIS of phosphorus and nickel in ferritic steels [1,2], but the predictions in terms of the temperature dependence are not strictly in accord with the experimental observations, possibly as a result of concurrent thermally induced segregation.

Experimental observations and quantitative analyses of the RIS at ferrite and prior austenite grain boundaries, martensite lath boundaries, precipitate/matrix interfaces, dislocation loops and void surfaces in pure iron alloys and commercial high-chromium martensitic steels have been made using Auger Electron Spectroscopy (AES), Scanning Transmission Electron Microscopy (STEM), and high spatial resolution Field Emission Gun Scanning Transmission Electron Microscopy (FEGSTEM) coupled with Energy Dispersive X-Ray Analysis (EDX) and Electron Energy Loss Spectroscopy (EELS). The irradiation sources employed and the alloys and steels studied include: high energy electron [24–27] and heavy ion irradiation of pure Fe-X [24,26,28,29], Fe-12Cr-Y [25–27] and multicomponent Fe alloys [25], electron irradiation of JFMS steel [27], heavy ion irradiation of 1.4914 steel [30], heavy ion [28,29] and neutron [31] irradiation of HT9 steel, neutron irradiation of FV448 steel [1,32–34], heavy ion and neutron irradiation of 9Cr-2Mo and 12Cr-2MoVNbB steels [35], and neutron irradiation of 9Cr-1W-2Mn and 12Cr-1W-6Mn reduced-activation steels [36,37]. The RIS, as evidenced by the results of FEGSTEM examinations, is exemplified in Fig. 10.3, which shows the concentration gradients

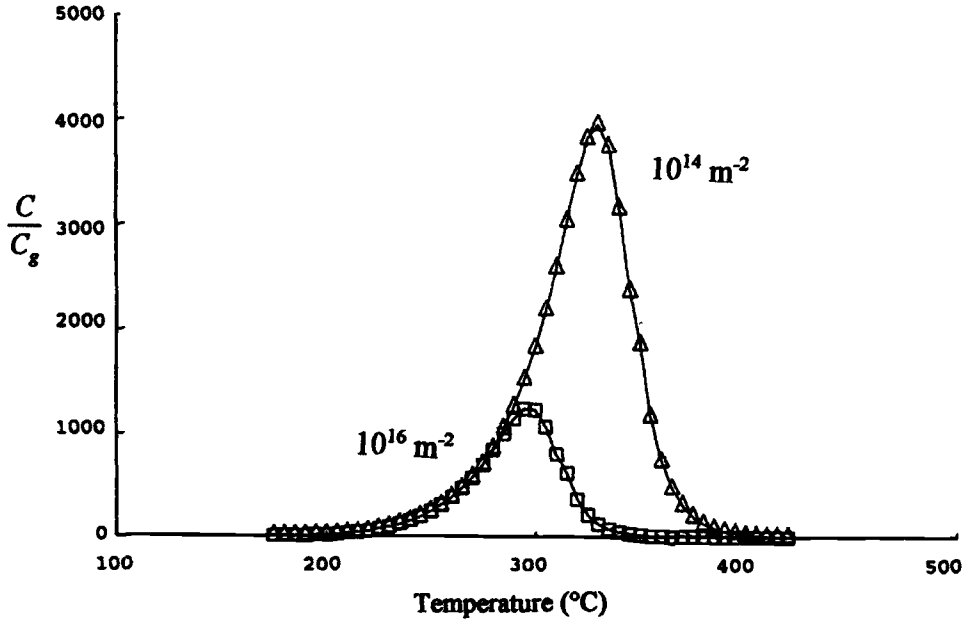

FIG. 10.1—Effect of initial dislocation density on the RIS of Si at the grain boundaries in ferritic steel irradiated to 1 dpa at a dose rate of 1×10^{-5} dpa s^{-1} [3].

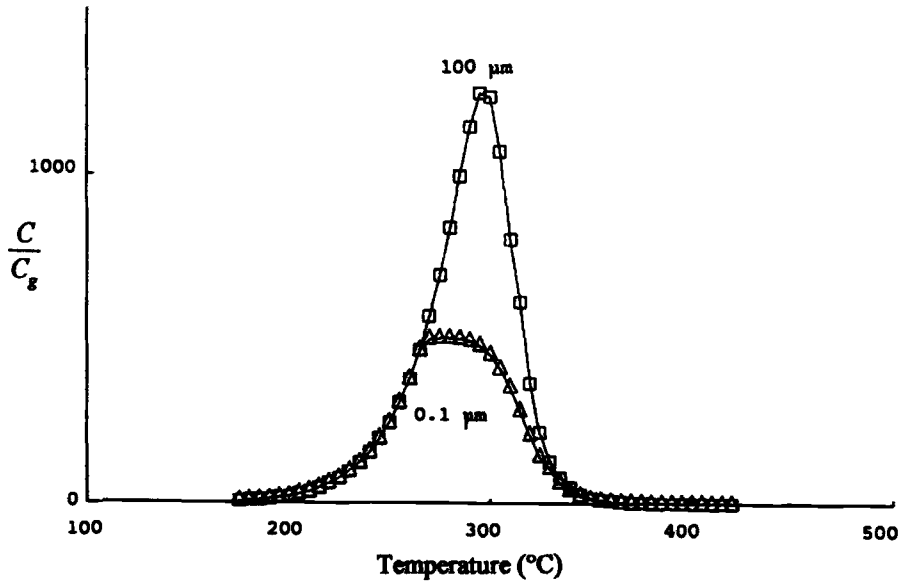

FIG. 10.2—Effect of grain size on the RIS of Si at the grain boundaries in ferritic steel irradiated to 1 dpa at a dose rate of 1×10^{-5} dpa s^{-1}. Initial dislocation density was 1×10^{16} lines m^{-2} [3].

for Cr, Ni, Si and Fe at the martensite lath boundaries in neutron-irradiated FV448 steel [32].

Although some of the observations of RIS in the ferritic and high-chromium martensitic steels are ambiguous, it has been concluded [16] that the segregation is markedly dependent on the displacement dose and the irradiation temperature in the approximate range 300 to 625°C and that (a) chromium is generally depleted at the interfaces, (b) nickel, silicon, and phosphorus are enriched at sinks, and (c) molybdenum and manganese may either be enriched or depleted at the sinks. It is believed that silicon segregates according to the first of the two mechanisms referred to above, while nickel is enriched and chromium and iron are depleted at interfaces as a result of the Inverse Kirkendall Effect.

PRECIPITATE PHASES

The fundamental processes which affect phase formation and stability in alloys during irradiation include:

1. Displacement cascade-induced dissolution, disordering and mixing, leading to phase decomposition and transformation.
2. Irradiation-enhanced diffusion.

3. Radiation-induced segregation (RIS) of trace impurities and alloying elements, as discussed in the preceding section.

These processes have been considered and are briefly reviewed elsewhere [38,39].

The evolution of the precipitates in the high-chromium ferritic and martensitic steels during irradiation is determined by:

(a) The irradiation stability of the thermal phases produced during the initial normalizing (or quenching) and tempering treatments.
(b) Irradiation-induced modification of the phases which are normally precipitated during thermal aging after the initial heat treatment.
(c) Irradiation-induced formation of new, non-equilibrium precipitate phases.

The effects of energetic neutron and charged particle irradiations on the precipitate phase evolution in pure iron-based alloys and the high-chromium ferritic/martensitic steels have been documented in the many publications referenced later in this section. In addition, the experimental observations and their interpretations have been periodically reviewed [16,40].

The phases formed in the high-chromium martensitic steels during initial heat treatment have been listed previously in Chapter 4 and include $M_{23}C_6$, MX [(CrV)C, NbC, etc.], M_2X (usually Cr_2N), and, in some steels, η-carbide (M_6C); Laves [$Fe_2(Mo,W)$] and chi (χ) phases may also be precipitated during prolonged thermal aging at elevated temperatures. The changes produced in these phases by irradiation have been investigated by AEM examinations of 12Cr (FI), 12Cr-1MoV (CRM12) and 12Cr-1MoVNb (FV448) martensitic steels following exposure to 26 dpa at temperatures in the range 380 to 615°C in DFR [41] and 9Cr-1MoVNb (T91) and 12Cr-1MoVW (HT9) steels with and without additions of 1 and 2% Ni, after irradiation to 36 to 47 dpa in the range 300 to 600°C in HFIR and FFTF [42–44]. The irradiation produces coarsening and/or partial dissolution and modification of the composition of the $M_{23}C_6$ particles in the FI and T91 steels at 420 to 460°C and at 300 and 400°C, respectively, and at 600°C in the 12% Cr steels. Partial or complete dissolution of the M_2X and MX phases also occurs in the latter steels during the irradiation at 420 to 460°C. However, the size and distribution of the MC precipitates appear to be unaffected by the irradiation but, as described later, the Laves phase is not always formed during irradiation. The nature and magnitude of these irradiation-induced changes depend on the steel composition and structure (fully martensitic or duplex martensite plus δ-ferrite) and the irradiation temperature and displacement dose.

The phases formed in the various high-chromium ferrous alloys and ferritic and martensitic steels during irradiation are listed in Table 10.1 [33,41–43,45–69]. It has been concluded, based on comparisons of the microstructural observations on the 9 and 12% Cr steels doped with ≤2% Ni and irradiated in the mixed-spectrum (HFIR) and fast (FFTF) reactors, that the He to dpa ratio has little influence on the radiation-induced precipitation in these steels [40,42,43]. The principal observations on the precipitate phases are summarized as follows:

Chromium-rich ferrite (α′)—High densities of fine (2 to 30 nm diameter) particles of this bcc phase are usually produced in tempered martensite (Fig. 10.4) [52] and duplex tempered martensite plus δ-ferrite steels containing ≥11 or 12% Cr during neutron irradiation [41,47, 52–61]. This phase also forms profusely in the ferritic 17% Cr steels [47,62,63] and binary Fe-Cr alloys containing ≥10% Cr [41,45,46] or ≥6% Cr [46,47] during neutron irradiation. In addition, α′ is precipitated in binary Fe-Cr alloys with much lower chromium con-

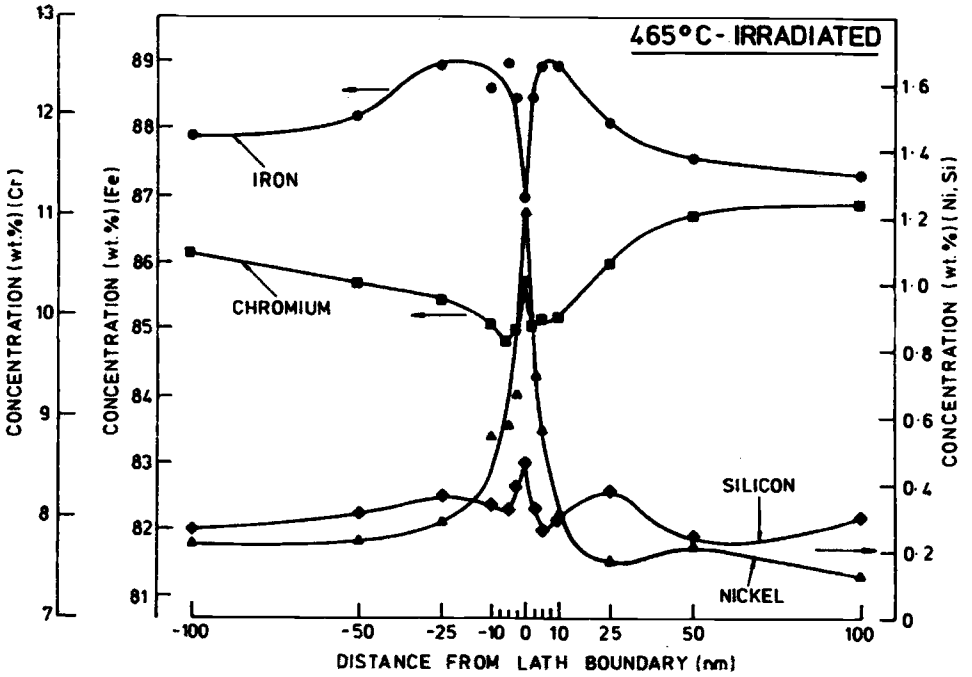

FIG. 10.3—Typical concentration gradients for Cr, Ni, Si, and Fe adjacent to a martensite lath boundary in a 12Cr-MoVNb (FV448) steel irradiated to 46 dpa at 465°C [32].

TABLE 10.1—Irradiation-induced phases in Fe-Cr Alloys and high-chromium ferritic/martensitic steels.

Precipitate Phase	Alloy/Steel (Alloying element in wt.%)	Reactor/ Facility	Irradiation Temperature (°C)	Dose (dpa)	Ref.
Cr-rich Ferrite (α′)	Fe-10 and 15Cr	DFR	420	30	45
	Fe-10 and 13Cr	DFR	380-420	30	41
	Fe-(6-18)Cr	EBR II	400-450	25-60	46, 47
	Fe-12, 15 and 18Cr	FFTF	430	15	48
	Fe-10Cr-(0.1-1.0) X (where X is Si, Mn, V, W, Ta and Zr)	FFTF	426	33.5	48
	Fe-12Cr-1V Fe-12Cr-1VW	FFTF	≈420	10-115	49
	Fe->7.4Cr	16 MeV Protons	25	0.2-0.4	50
	Fe-2.8(at)Cr	HVEM (2MVe$^-$)	500 and 600	12.5×10^{26} e m^{-2}	51
	12Cr-1MoV (CRM-12) 12Cr-1MoVNb (FV448)	DFR	380-615	30	41
	12Cr-1MoVW (HT-9)	EBR II FFTF 14 MEV Ni ions PHÉNIX	400, 425 420 300-600 400-530	25-60 35 200 30-116	47 52 53 54
	13Cr-2MoVNbB	BOR 60	450 330	4.5×10^{26} nm^{-2} (>0.1 MeV)	55 56
	12Cr-2.0-6.6Mn-1MoVNb	FFTF	420-600	9.8-48.2	57
	12Cr-6.5MnV 12Cr-6.5MnVW	FFTF	≈420	15-209	49, 58 59
	12Cr-2WVTaN (JLF-5) 12Cr-2WVTaTiN (JLF-6)	FFTF	425 390-600 425	36 35 36	60 61 60
	17.6Cr (430F)	EBR II	425 and 510	25-60	47, 62
	17Cr (F-17)	PHÉNIX	400-540	78-100	54, 63
M_6X (η)	12Cr-1MoV (CRM-12) 12Cr-1MoVNb (FV448)	DFR	380-460	30	41
	12Cr-1MoVNb (FV448)	PFR	465	28-46	33
	9Cr-1MoVNb+2Ni	HFIR	400	37	42,43
	12Cr-1MoVW (HT9)	FFTF	407	47	64
	12Cr-1MoVW+2Ni	HFIR	400	37	42,43
	7Cr-2WVTaN (JLF-3) 9Cr-2WVTaN (JLF-1) 9Cr-2WVTaTiN (JLF-2)	FFTF	425	36	60
	12Cr-1MoVNb (FV448) 12Cr-1MoVW (HT9) 11Cr-0.8MoNiVNb (1.4914)	PHÉNIX	419 419 429, 459	79 79 68, 50	54

tents and at low temperatures during irradiation at high damage displacement rates with high-energy electrons [51] and protons [50]. The α′ is enriched mainly in chromium and molybdenum, but with smaller levels of silicon and iron, the composition (wt%) for the phase in irradiated 12Cr-1MoVW (HT9) steel being reported as Cr, 13Mo, 8Fe, 3Si [47].

As noted previously in Chapter 4, the precipitation of coherent particles of α′ during thermal aging at temperatures of ≈475°C induces severe embrittlement of steels containing ≥14% Cr [70,71].

M_6X (η)—This diamond cubic phase is found in some unirradiated thermally aged high-chromium steels and is often detected in the form of fine and coarse precipitates in irradiated martensitic steels containing ≥0.3% Ni (Fig. 10.5) [40,43]. It appears that the η precipitates replace some of the coarse "as-tempered" $M_{23}C_6$ or M_2X particles, which are partially dissolved during irradiation [41]. The phase is reported to be enriched in Si, Cr, Ni, and P [16,42], the analyzed compositions (wt%) in the irradiated steels being 17Si, 32-39Cr, 15Fe, 16-27.5Ni, 6Mo, 5V, 2.5Mn [12Cr-1MoV (CRM12) and 12Cr-1MoVNb (FV448)] [41] and (at%) 18.4-25Si, 48-64.2Cr, 7.0-7.3Fe, 1.0-2.1Ni, 2.4-2.9Mo, 0.7-6.2V, 0.8-1.1Ti, 0.7-1.2 W, 0.2-4.6Nb [12Cr-1MoVW (HT9)] [42,43,64].

The η phase has not been observed in the 9Cr-1Mo (EM10) and 9Cr-2MoVNb (EM12) steels after irradiation in PHÈNIX to 47 dpa [63]; however, it has been detected as a fine (≈10

TABLE 10.1—Continued.

Precipitate Phase	Alloy/Steel (Alloying element in wt.%)	Reactor/ Facility	Irradiation Temperature (°C)	Dose (dpa)	Ref.
Chi (χ)	12Cr-1MoV (CRM-12) 12Cr-1MoVNb (FV448)	DFR	420-460	30	41
	9Cr-2Mo (EM12) 12Cr-1MoVW (HT9)	EBR II	425 and 510 450-540	25-60	47, 62
	9Cr-1MoVNb (T91) 12Cr-1MoVW (HT9)	FFTF	≈420	≈35	52
	9Cr-1MoVNb+2Ni 12Cr-1MoVW+Ni	HFIR	400 and 500	36-39	42
	9Cr-2Mo (EM12)	PHÉNIX	430-460	50-100	54, 63
	9.76Cr-2.4MoNiVNb	HFIR	500	34-57	65, 66
	12Cr-4.7Mn-1MoVNb 12Cr-6.6Mn-1MoVNb	FFTF	≈420	14.4-48.2	57
	12Cr-6.6MnV 12Cr-6.6MnVW	FFTF	≈420	203-209	59
	12Cr-1MoVW (HT9)	14 MeV Ni ions	500	200	53
G	12Cr-1MoVW (HT9) .. 13.4Cr-0.26Mo (416)	EBR II HFIR EBR II	400 and 425 300 and 400 425	25-60 10-12 25-60	47
	12Cr-1MoVW (HT9)	HFIR	500	38	42, 64
	12Cr-1MoVNb (FV448) Plate and Weld HAZ	PFR	465	28-46	33
	12Cr-1MoVNb (FV448)	VEC (52 MeV Cr^{6+})	425-625	100	67
Laves	9Cr-2Mo (EM12)	EBR II	650	25-60	62
	8Cr-2WVTa (F82H)	FFTF	750	37	68
	9Cr-2WVTaTiN (JLF-2)	FFTF	600	33	69
	7Cr-2WVTaN (JLF-3) 9Cr-2WVTaN (JLF-1) 9Cr-2WVTaTiN (JLF-2)	FFTF	425	36	60
	12Cr-2WVTaN (JLF-5)	FFTF	520	35	61
Sigma (σ)	12Cr-1MoV (CRM-12) 12Cr-1MoVNb (FV448)	DFR	420 and 460	30	41
M_3P	Fe-13 Cr 12Cr-1MoVNb (FV448)	DFR	420 and 460	30	41
MP	12Cr-1MoVNb (FV448)	DFR	460-615	30	41

nm) Ta- and W-rich matrix precipitate in 7Cr-2WVTaN (JLF-3), 9Cr-2WVTaN (JLF-1) and 9Cr-2WVTaTiN (JLF-3) steels irradiated in FFTF at 425°C to 36 dpa [60].

Chi (χ)—Fine and coarse dispersions of this bcc intermetallic phase are formed heterogeneously in many high-chromium martensitic steels during irradiation in mixed-spectrum or fast reactors (Fig. 10.4) [41,42,47,52,57,59, 62,63,65,66]. However, the phase has not been detected in the 9Cr-1Mo (EM10) steel irradiated in PHÈNIX at 460°C to 83 dpa [63] and the F82H and other reduced-activation 9 and 12Cr-2WVTa steels irradiated in FFTF at temperatures in the range 365 to 750°C to doses up to 40 dpa [52,60,61,68,69]. Furthermore, while this phase was not found in earlier investigations on 9Cr-1MoVNb (T91) and 12Cr-1MoVW (HT9) steels exposed in HFIR [42], more recent work using STEM/EDX techniques has shown that very high number densities of fine (13 nm) coherent particles of the chi phase are produced in these steels during FFTF irradiation at 420°C to ≈35 dpa [52].

The absence of the chi phase formation in the irradiated reduced-activation steels has been tentatively ascribed to the lower diffusivity of tungsten compared to molybdenum in ferritic steels and/or the greater stability of the $M_{23}C_6$ (possible source of molybdenum in the chi-phase) in the tungsten-containing steels [52]; these observations are in agreement with experimental evidence and the results of thermodynamic calculations on the Fe-Cr-Mo [72] and Fe-Cr-W [73] ternary alloy systems.

The possible effect of molybdenum can also be seen in the comparative amounts of chi phase found in the tempered martensite of the 9Cr-1MoVNb (T91) and in the duplex (tempered martensite and δ-ferrite) structure of 9Cr-2MoVNb

(EM12). Small (13 nm) particles were seen in the 9Cr-1MoVNb, compared with more massive amounts in the EM12, where it was observed in both martensite and δ-ferrite (Fig. 10.6) [63].

The chi phase is enriched in iron, silicon, and nickel and contains significant amounts of molybdenum and phosphorus [Fig. 10.7(a)]. The following compositions (wt.%) of the chi phase in irradiated steels have been reported: 16Si, 24Cr, 43Fe, 7Ni, 4Mn, 3Mo, 3P [12Cr-1MoV (CRM12) and 12Cr-1MoVNb (FV448)] [41], 6Si, 26Cr, 7Ni, 5Mo, 3.15Nb, bal Fe (HT9) [47] and 16Si, 24Cr, 51Fe, 1.35Ni, 13Mo, 0.8 V (EM12) [63].

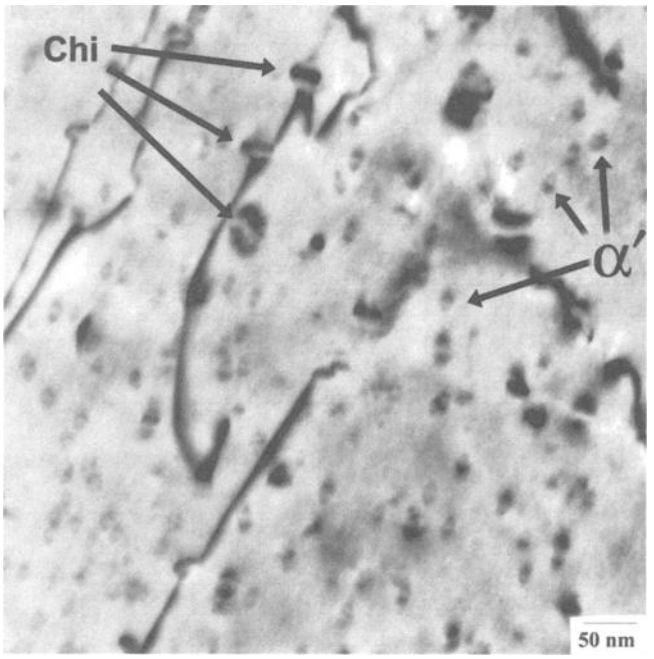

FIG. 10.4—Photomicrograph showing the α′ and chi phase in 12Cr-1MoVW steel irradiated in FFTF at 420°C to ≈35 dpa [52].

G phase—Earlier investigations showed extensive precipitation of this complex fcc silicide phase in the 12Cr-1MoVW (HT9) steel irradiated to 25 to 60 dpa at 400 to 425°C in EBR II and 10 dpa at 300 and 400°C in HFIR [47]. However, particles of this phase were only found infrequently or not at all in AEM studies on the HT9 steel irradiated at 400 and 500°C to 36 to 38 dpa in HFIR [42,43], 9Cr-1MoVNb (T91) steel irradiated in the range 300 to 600°C to ≤39 dpa in HFIR [44] and at ≈400°C to 47 dpa in FFTF [43], and in 12Cr-MoVNb (FV448) steel plate samples exposed in DFR [41].

In more recent observations on FV448 steel plate and weldment specimens irradiated in DFR to 28 to 46 dpa at 465°C, the precipitation of G phase has subsequently been detected in the parent plate and nucleated on dislocation networks in the large δ-ferrite grains in the HAZ of FV448 steel weldments irradiated to 28 to 46 dpa at 465°C in DFR [33]. The G phase was reported to have an almost ideal $Mn_7Ni_{16}Si_{17}$ composition [42,64], somewhat different from that found in the earlier work (Ni, 24.1Fe, 12.7Si, 8.7Mn, 3.8Mo, 1.9Cr) [47].

Laves phase—The Laves (Fe_2Mo type) phase is not always found in the high-chromium martensitic steels after irradiation although, as described in Chapter 4, it forms extensively during thermal aging. Thus, the formation of this phase is suppressed in the 9 and 12Cr-1MoVNb (T91 and FV448) and 12Cr-1MoVW (HT9) steels during irradiation at temperatures in the range 300 to 615°C [41,43,44]. Nevertheless, it has been observed in the 12Cr-1MoV (CRM12) [41] and 9Cr-2MoVNb (EM12) [63] steels following irradiation at 615 and 650°C, respectively, but the composition (wt%), 6Si, 4P, 20Cr, 46Fe, 17Mo, 2.5Mn, 1.5V, 1Ni, is modified relative to that produced thermally [41]. There is only one recorded in-

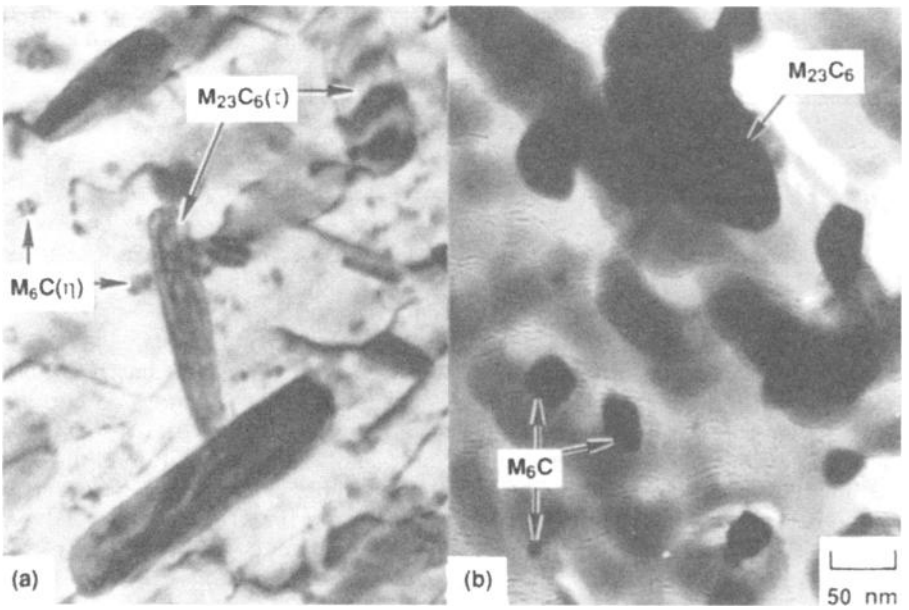

FIG. 10.5—Transmission electron microscope photomicrographs showing fine M_6C (η) formed in 9Cr-1MoVNb-2Ni steel irradiated in FFTF at 407°C to ≈47 dpa, (a) in-foil and (b) on a carbon film extraction replica [43].

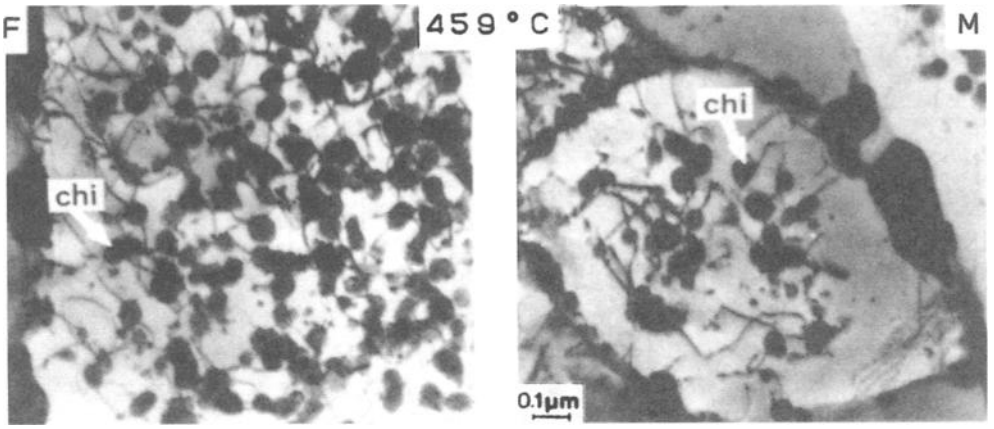

FIG. 10.6—Transmission electron microscope photomicrographs showing massive amounts of chi phase formed in the δ-ferrite (left) and tempered martensite (right) of 9Cr-2MoVNb (EM12) steel cladding irradiated to ≈40 dpa at 459°C in PHÉNIX [63].

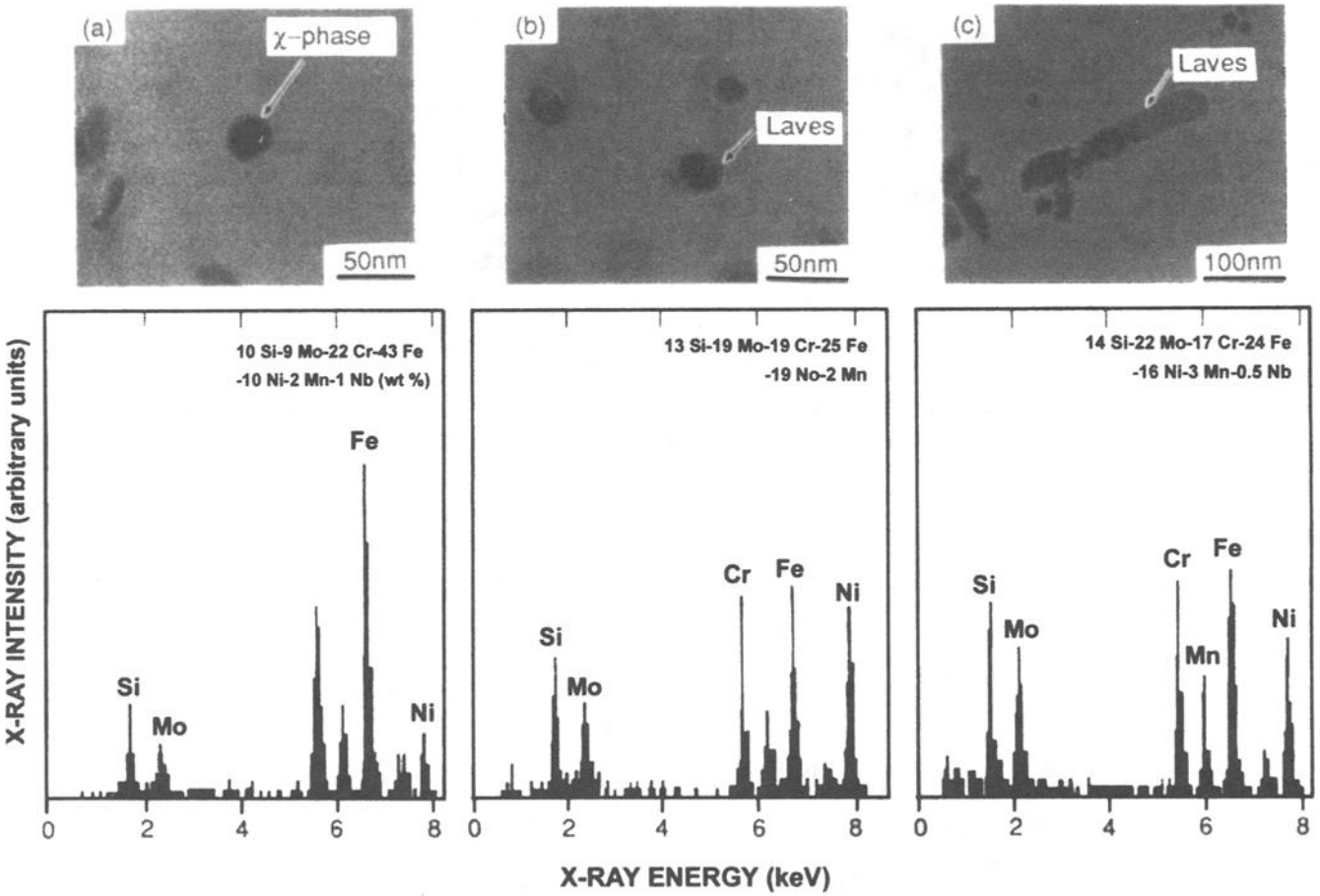

FIG. 10.7—Micrographs of replicas and XEDS spectra of chi and Laves phases from 10Cr-2MoVNb steel irradiated in HFIR to 34 dpa at 500°C: (a) chi phase and (b) and (c) Laves phase [45].

stance of Laves (Fe_2Mo) phase precipitation at temperatures below 600°C, namely in 10Cr-2MoVNb (JFMS) steel irradiated in HFIR at 500°C to 34 and 57 dpa [65]; the composition of the phase is again significantly different from that of the thermally induced phase as seen in the comparison of the spectra in Fig. 10.7(b) and (c) for the irradiated steel with Fig. 10.8 for the aged steel [65].

However, grain boundary and matrix precipitation of the Laves phase (Fe_2W type) occurs in the reduced-activation 7Cr-2WVTaN (JLF-3), 9Cr-2WVTaN (JLF-1), 9Cr-2WVTaTiN (JLF-2), and 12Cr-2WVTaN (JLF-5) steels during FFTF irradiations to 33 to 36 dpa at 425 to 600°C [60,61,69] and in the 8Cr-2WVTaB (F82H) steel to 37 dpa at 750°C [68]. It has been suggested that the TTP curve for the Laves phase precipita-

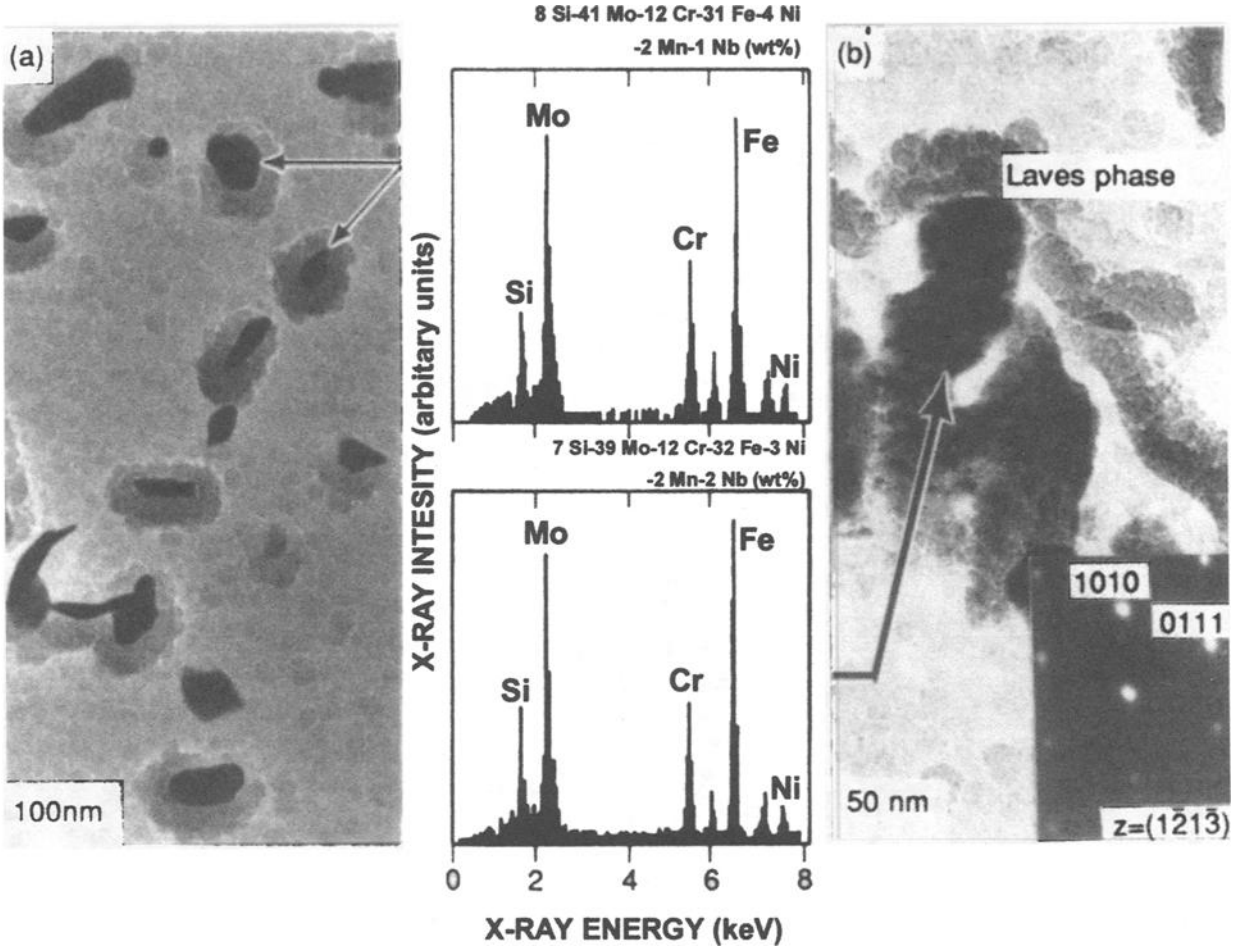

FIG. 10.8—Micrographs of XEDS spectra of (a) smaller and (b) larger particles of Laves phase on extraction replica from 10Cr-2MoVNb steel thermally aged for 5000 h at 500°C [65].

tion in the F82H steel (Fig. 10.9) is shifted to higher temperatures by the irradiation [68].

Minor phases—Sigma (σ) phase (Fe-Cr enriched in Si, Ni and P) has been observed to form as large sheets and thin ribbons surrounding $M_{23}C_6$ particles in 9–13% Cr martensitic steels after irradiation at 420 to 460°C in DFR [41]. In addition, Cr_3P needles and MP (where M is Fe, Cr and Mo) particles have been detected in the 13Cr (FI) and 12Cr-1MoVNb (FV448) steels after the DFR irradiations at 420 to 460°C and 460 to 615°C, respectively [41].

While trace amounts of M_2X produced in the steels during tempering may persist after irradiation [42], there is evidence that this phase forms within the δ-ferrite grains, on dislocations in the tempered martensite laths and at the prior austenite grain boundaries of the duplex 13Cr-2MoVNbB steel during irradiation at 330 to 550°C [55,56].

The formation of these phases during irradiation may be rationalized in terms of the strong RIS of alloying and impurity elements to point defect sinks in the steels [16,40]. The M_6X (η), chi (χ), G, and sigma (σ) phases are all enriched in silicon and nickel, elements which are known to segregate to interfaces during irradiation. With the possible exception of G-phase, these irradiation-induced phases, as well as the chromium-rich ferrite (α′), are also chromium rich. Since

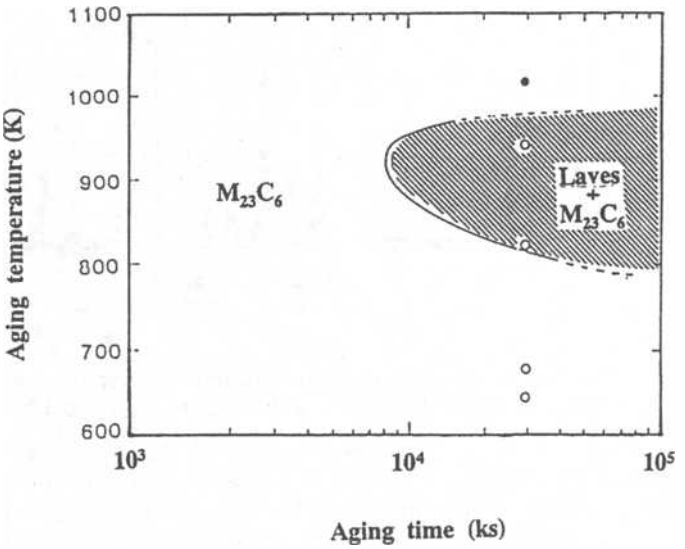

FIG. 10.9—TTP diagram for Laves phase formation in unirradiated thermally aged and FFTF-irradiated 8Cr-2WVTaB (F82H) reduced-activation steel [68]. ○ $M_{23}C_6$ and • Laves phase identified after irradiation.

chromium is invariably depleted near voids and at other interfaces which act as point-defect sinks [74], it follows that in steels containing ≥11 or 12% Cr, the chromium enrichment within the matrix may lead to local concentrations exceeding those (≥14%) at which α′ forms thermally. Furthermore, enrichment of the chromium may also result from the partial dissolution of chromium-rich precipitates such as $M_{23}C_6$ during irradiation, leading to an increase in the local chromium supersaturation and thus, for example, the observed nucleation of M_6C on the $M_{23}C_6$ particles [41]. In addition, it is evident that RIS of phosphorus leads to the formation of phosphides in some of the irradiated steels. The irradiation-induced point defect clusters and dislocation loops may also facilitate and enhance the nucleation of these new phases.

REFERENCES

[1] R. G. Faulkner, E. A. Little, and T. S. Morgan, J. Nucl. Mater. 191-194 (1992) 858.

[2] R. G. Faulkner, N. C. Waite, E. A. Little, and T. S. Morgan, Mater. Sci. Eng. 171 (1993) 241.

[3] R. G. Faulkner, S. Song, and P. E. J. Flewitt, J. Nucl. Mater. 212-215 (1994) 608.

[4] R. G. Faulkner, J. Mater. Sci. 16 (1981) 373.

[5] R. G. Faulkner, Acta Metall. 35 (1987) 2905.

[6] R. A. Johnson and N. Q. Lam, Phys. Rev. 13 (1976) 4364.

[7] A. D. Marwick, J. Phys. F. 8 (1978) 1849.

[8] H. Wiedersich and N. Q. Lam, in: Phase Transformations During Irradiation, Ed. F.V. Nolfi (Applied Sci. Publishers, London, 1983) 1.

[9] A. D. Marwick, R. C. Piller, and M. E. Horton, in: Dimensional Stability and Mechanical Behaviour of Irradiated Metals and Alloys, Vol. 2 (British Nuclear Energy Society, London, 1984) 11.

[10] S. M. Murphy, in: Proc. Symp. on Radiation-Induced Sensitisation of Stainless Steels, Ed, D.I.R. Norris (CEGB, Berkeley Nuclear Laboratories, 1987) 35.

[11] E. P. Simonen, E. R. Bradley, and R. H. Jones, in: Effects of Irradiation on Materials: 14th International Symposium, ASTM STP 1046, Vol. II, Eds. N. H. Packan, R. E. Stoller and A. S. Kumar (American Society for Testing and Materials, Philadelphia, 1990) 411.

[12] C. A. English, S. M. Murphy, and J. M. Perks, J. Chem. Soc. Faraday Trans. 86 (1990) 1263.

[13] H. Wiedersich, P. R. Okamoto, and N. Q. Lam, J. Nucl. Mater. 83 (1979) 98.

[14] D. R. Harries and A. D. Marwick, Phil. Trans. Roy. Soc. A295 (1980) 197.

[15] J. M. Perks, A. D. Marwick, and C. A. English, in: Proc. Symp. on Radiation-Induced Sensitisation of Stainless Steels, Ed. D.I.R. Norris (CEGB, Berkeley Nuclear Laboratories, 1987) 15.

[16] E. A. Little, J. Nucl. Mater. 206 (1993) 324.

[17] J. M. Titchmarsh and I. A. Vatter, in: Proc. Symp. on Radiation-Induced Sensitisation of Stainless Steels, Ed. D. I. R. Norris (CEGB, Berkeley Nuclear Laboratories, 1987) 74.

[18] D. I. R. Norris, C. Baker, and J. M. Titchmarsh, in: Proc. Symp. on Radiation-Induced Sensitisation of Stainless Steels, Ed., D. I. R. Norris (CEGB, Berkeley Nuclear Laboratories, 1987) 86.

[19] D. I. R. Norris, C. Baker, and J. M. Titchmarsh, in: Materials for Nuclear Reactor Core Applications, Vol. 1 (British Nuclear Energy Society, London, 1987) 277.

[20] T. M. Williams, R. M. Boothby, and J. M. Titchmarsh, in: Materials for Nuclear Reactor Core Applications, Vol. 1 (British Nuclear Energy Society, London, 1987) 293.

[21] C. Taylor, in: Proc. Symp. on Radiation-Induced Sensitisation of Stainless Steels, Ed. D. I. R. Norris (CEGB, Berkeley Nuclear Laboratories, 1987) 60.

[22] J. Kameda, X. Mao and A. J. Bevolo, J. Nucl. Mater. 179-181 (1991) 1034.

[23] J. T. Buswell and R. B. Jones, in: Effects of Radiation on Materials: 15th International Symposium, ASTM STP 1175, Eds. A. S. Kumar, D. S. Gelles, R. K. Nanstad and E. A. Little (American Society for Testing and Materials, Philadelphia, 1994) 424.

[24] H. Takahashi, S. Ohnuki, and T. Takeyama, J. Nucl. Mater. 103 & 104 (1981) 1415.

[25] G. J. Mahon, A. W. Nichols, I. P. Jones, C. A. English, and T. M. Williams, in: Proc. Symp. on Radiation-Induced Sensitisation of Stainless Steels, Ed. D. I. R. Norris (CEGB, Berkeley Nuclear Laboratories, 1987) 99.

[26] H. Takahashi, H. Kinoshita, S. Ohnuki, R. Nagasaki, F. A. Garner, and D. S. Gelles, J. Nucl. Mater. 155-157 (1988) 908.

[27] T. Muroga, A. Yamaguchi, and N. Yoshida, in: Effects of Irradiation on Materials: 14th International Symposium, ASTM STP 1046, Vol. II, Eds. N. H. Packan, R. E. Stoller, and A. S. Kumar (American Society for Testing and Materials, Philadelphia, 1990) 396.

[28] J. L. Brimhall, D. R. Baer, and R. H. Jones, J. Nucl. Mater. 117 (1983) 218.

[29] J. L. Brimhall, D. R. Baer, and R. H. Jones, J. Nucl. Mater. 122 & 123 (1984) 196.

[30] P. Jung and H. Klein, J. Nucl. Mater. 182 (1991) 1.

[31] R. E. Clausing, L. Heatherly, R. G. Faulkner, A. F. Rowcliffe, and K. Farrell, J. Nucl. Mater. 141-143 (1988) 978.

[32] T. S. Morgan, E. A. Little, R. G. Faulkner, and J. M. Titchmarsh, in: Effects of Radiation on Materials: 15th International Symposium, ASTM STP 1125, Eds. R. E. Stoller, A. S. Kumar, and D. S. Gelles (American Society for Testing and Materials, Philadelphia, 1992) 633.

[33] T. S. Morgan, E. A. Little, and R. G. Faulkner, in: Effects of Radiation on Materials: 16th International Symposium, ASTM STP 1175, Eds. A. S. Kumar, D. S. Gelles, R. K. Nanstad and E. A. Little (American Society for Testing and Materials, Philadelphia, 1994) 607.

[34] E. A. Little, unpublished data (see Ref 16).

[35] I. M. Neklyudev and V. N. Voyevodin, J. Nucl. Mater. 212-215 (1994) 39.

[36] A. Kimura, L. A. Charlot, D. S. Gelles, D. R. Baer, and R. H. Jones, J. Nucl. Mater. 191-194 (1992) 885.

[37] A. Kimura, L. A. Charlot, D. S. Gelles, and R. H. Jones, J. Nucl. Mater. 212-215 (1994) 725.

[38] H. Wiedersich, J. Nucl. Mater. 206 (1993) 121.

[39] K. C. Russell, J. Nucl. Mater. 206 (1993) 129.

[40] P. J. Maziasz, J. Nucl. Mater. 169 (1989) 95.

[41] E. A. Little and L. P. Stoter, in: Effects of Irradiation on Materials: Eleventh Conference, ASTM STP 782, Eds. H. R. Brager and J. S. Perrin (American Society for Testing and Materials, Philadelphia, 1982) 207.

[42] P. J. Maziasz, R. L. Klueh, and J. M. Vitek, J. Nucl. Mater. 141-143 (1986) 929.

[43] P. J. Maziasz and R. L. Klueh, in: Effects of Irradiation on Materials: 14th International Symposium, ASTM STP 1046, Vol. II, Eds. N. H. Packan, R. E. Stoller, and A. S. Kumar (American Society for Testing and Materials, Philadelphia, 1990) 35.

[44] P. J. Maziasz and R. L. Klueh, in: Effects of Radiation on Materials: 15th International Symposium, ASTM STP 1125, Eds. R. E. Stoller, A. S. Kumar, and D. S. Gelles (American Society for Testing and Materials, Philadelphia, 1992) 1135.

[45] E. A. Little and D. A. Stow, J. Nucl. Mater. 87 (1979) 25.

[46] D. S. Gelles, J. Nucl. Mater. 108 & 109 (1982) 515.

[47] D. S. Gelles and L. E. Thomas, in: Ferritic Alloys for Use in Nuclear Energy Technologies, Eds., J. W. Davis and D. J. Michel (Met. Soc. AIME, Warrendale, PA, 1984) 559.

[48] D. S. Gelles, in: Effects of Irradiation on Materials: 14th International Symposium, ASTM STP 1046, Vol. II, Eds. N. H. Packan, R. E. Stoller, and A. S. Kumar (American Society for Testing and Materials, Philadelphia, 1990) 73.
[49] D. S. Gelles, in: Reduced Activation Materials for Fusion Reactors, ASTM STP 1047, Eds., R. L. Klueh, D. S. Gelles, M. Okada, and N. H. Packan (American Society for Testing and Materials, Philadelphia, 1990) 113.
[50] K. Kuwano and Y. Hamaguchi, J. Nucl. Mater. 155-157 (1988) 1071.
[51] T. Ezawa, T. Akashi, and R. Oshima, J. Nucl. Mater. 212-215 (1994) 252.
[52] J. J. Kai and R. L. Klueh, J. Nucl. Mater. 230 (1996) 116.
[53] J. J. Kai and G. L. Kulcinski, J. Nucl. Mater. 175 (1990) 227.
[54] P. Dubuisson, D. Gilbon, and J. L. Séran, J. Nucl. Mater. 205 (1993) 178.
[55] V. S. Agueev, V. N. Bykov, A. M. Dvoryashin, V. N. Golovanov, E. A. Medvendeva, V. V. Romaneev, V. K. Sharmardin and A. N. Vorobiev, in: Effects of Radiation on Materials: 14th International Symposium, ASTM STP 1046, Vol. I, Eds. N. H. Packan, R. E. Stoller, and A. S. Kumar (American Society for Testing and Materials, Philadelphia, 1989) 98.
[56] Yu. I. Zvezdin, O. M. Vishkarev, G. A. Tulyakov, Yu. G. Magerya, V. A. Smirnov, and I. A. Shenkova, J. Nucl. Mater. 191-194 (1992) 855.
[57] Y. Kohno, A. Kohyama, and D. S. Gelles, J. Nucl. Mater. 179-181 (1991) 725.
[58] D. S. Gelles and M. L. Hamilton, J. Nucl. Mater. 148 (1987) 272.
[59] D. S. Gelles, J. Nucl. Mater. 212-215 (1994) 714.
[60] A. Kimura and H. Matsui, J. Nucl. Mater. 212-215 (1994) 701.
[61] Y. Kohno, A. Kohyama, M. Yoshino and K. Asakura, J. Nucl. Mater. 212-215 (1994) 707.
[62] D. S. Gelles, J. Nucl. Mater. 103 & 104 (1981) 975.
[63] D. Gilbon, J. L. Séran, R. Cauvin, A. Fissolo, A. Alamo, F. Le Naour, and V. Lévy, in: Effects of Radiation on Materials: 14th International Symposium, ASTM STP 1046, Vol. I, Eds., N. H. Packan, R. E. Stoller and A. S. Kumar (American Society for Testing and Materials, Philadelphia, 1989) 5.
[64] P. J. Maziasz, in: Materials for Nuclear Reactor Core Applications, Vol. 2 (British Nuclear Energy Society, London, 1988) 61.
[65] M. Suzuki, A. Hishinuma, P. J. Masiasz, and T. Sawai, J. Nucl. Mater. 170 (1990) 270.
[66] M. Suzuki, T. Sawai, P. J. Maziaz, and A. Hishinuma, J. Nucl. Mater. 179-181 (1991) 718.
[67] D. J. Mazey, W. Hanks, and T. M. Williams, J. Nucl. Mater. 168 (1989) 228.
[68] Y. Kohno, D. S. Gelles, A. Kohyama, M. Tamura, and A. Hishinuma, J. Nucl. Mater. 191-194 (1992) 868.
[69] A. Kimura, M. Narui, and H. Kayano, J. Nucl. Mater. 191-194 (1992) 879.
[70] R. Lagneborg, Trans. ASM 60 (1967) 67.
[71] P. J. Grobner, Metall. Trans. 4 (1973) 251.
[72] J. O. Andersson and N. Lange, Metall. Trans. 19A (1988) 1385.
[73] P. Gustafson, Metall. Trans. 19A (1988) 2531.
[74] E. A. Little and D. A. Stow, Metal Sci. 14 (1980) 89.

11

Irradiation Creep

Creep is defined as the time-dependent plastic deformation that occurs under the influence of a constant applied stress (although most tests are conducted with a constant load). At elevated temperatures, it is referred to as thermal creep. Deformation processes that operate during thermal creep include (1) dislocation climb in combination with dislocation glide that leads to slip, (2) dislocation climb that leads to subgrain formation, (3) grain boundary sliding, and (4) grain shape change by diffusional processes. The first two processes are the most important for the thermal creep of the high-chromium ferritic/martensitic steels at normal operating temperatures (≤600°C).

Time-dependent plastic deformation can also occur under the influence of the simultaneous application of stress and irradiation. Thermal creep becomes significant for irradiation at temperatures ≥0.5 T_m (T_m is the absolute melting temperature), but irradiation creep can be significant at much lower temperatures. However, as noted by Harries [1], "the strain rate measured during irradiation, relative to that determined in an unirradiated specimen in a laboratory test, is a function of the true (flux dependent) irradiation creep and the (fluence dependent) hardening (reduced creep rate) or softening (increased creep rate) resulting from accumulated irradiation-induced defect damage and/or microstructural changes." As is the case for thermal creep, dislocation climb and glide play a prominent role in the deformation processes that occur during irradiation creep.

THEORY

Irradiation creep involves stress-induced processes that enhance the annihilation of irradiation-produced point defects [1–6]. In general, the deformation processes involve the stress-induced absorption of irradiation-produced point defects on dislocations that cause the dislocations to climb, which can subsequently lead to glide of the dislocations. For irradiation creep to occur, the absorption of point defects at dislocations must be asymmetric, for if vacancies and interstitials were partitioned equally, annihilation would occur without climb, and there would be no creep. Proposed mechanisms for irradiation creep include swelling-driven creep (I-creep) [2], Stress Induced Preferential Absorption (SIPA) creep [3–5], and Preferred Absorption Glide (PAG) creep [6].

I-creep involves climb-enabled glide that occurs because dislocations have a slight bias for interstitials, and these interstitials induce dislocation climb; the excess vacancies are incorporated in voids [2]. Under the influence of a stress, pinned dislocations can bow out to give an increment of elastic strain. The bias-driven interstitials at dislocations can cause them to climb around the pinning obstacles and glide until they encounter another obstacle and are again pinned. Each time this process is repeated, an increment of creep strain occurs, with the creep rate depending on the climb velocity. The creep rate for I-creep, $\dot{\varepsilon}_I$, can be written as [7]

$$\dot{\varepsilon}_I = b\left(\frac{\pi}{L}\right)^{1/2} \varepsilon \dot{s} \tag{11.1}$$

where b is the Burgers vector, L is the dislocation line density, $\dot{s}$ is the swelling rate, and ε is the creep strain. Since $\varepsilon = \sigma/E$, where σ is stress and E is Young's modulus, it follows that there is a linear relationship between strain rate and stress [2].

In SIPA creep, dislocations are assumed to be sinks for both vacancies and interstitials, but there is a slight bias for interstitials to be absorbed by dislocations with their Burgers vectors aligned with the stress axis. This preferential absorption due to the stress-induced higher capture efficiency of the dislocations with properly aligned Burgers vectors causes dislocation climb and deformation in the stressed direction. The creep rate for SIPA creep, $\dot{\varepsilon}_{SIPA}$, can be written as [7]

$$\dot{\varepsilon}_{SIPA} = \frac{2}{9}\Omega L D_i C_i \Delta Z_i^d \tag{11.2}$$

where Ω is the atomic volume, D_i is the diffusion coefficient for interstitials, C_i is the concentration of interstitials, and ΔZ_i^d is the difference in capture efficiencies for interstitials with aligned and nonaligned dislocations; ΔZ_i^d is proportional to stress, making $\dot{\varepsilon}_{SIPA}$ linear in stress [7].

PAG creep is due to climb-enabled glide; that is, first, the dislocations climb around obstacles by the SIPA process, after which the dislocations can glide under the influence of the applied stress until they are again stopped by an obstacle. For this mechanism, the creep rate, $\dot{\varepsilon}_{PAG}$, is given by [7]

$$\dot{\varepsilon}_{PAG} = \frac{4\varepsilon}{9b}(\pi L)^{1/2}\,\Omega D_i C_i \Delta Z_i^d \tag{11.3}$$

where again $\varepsilon = \sigma/E$ and ΔZ_i^d is proportional to σ, thus producing a quadratic dependence on stress for PAG creep. Because of this higher-order dependence on stress, PAG creep becomes more important as the stress increases [6]. For details on these mechanisms, the reader is referred to the original literature [2–6] and a recent review [8].

MEASUREMENT TECHNIQUES

Several techniques have been used to measure irradiation creep in a neutron-irradiation environment, including uniaxial tension, pressurized tubes, helical springs, and stress-relaxation techniques [1,9,10]. Creep strains can also be estimated on reactor components (e.g., reactor pressure tubes and sub-assembly wrappers) [1].

Instrumented uniaxial tension test machines have been used, similar to those used for thermal creep. However, these present difficulties (i.e., instrumentation within the reactor, space required to accommodate the test rig in the reactor, etc.) and have generally given way to more compact systems.

Helical tension springs are dead-weight loaded, and the extensions are periodically measured after removal from the reactor. In experiments in DFR, the coiled wire springs were measured by x-radiography after irradiation [1,11].

Stress relaxation tests involve springs that are elastically loaded and measured during periodic reactor shutdowns. The change in stress is determined, and from this the creep rate is calculated [1,10].

The most popular measurement technique is the use of small, thin-wall pressurized tubes (20 to 40 mm long and 4 to 6 mm outer diameter) that are internally pressurized with an inert gas to various hoop stresses [1,9,10]. Creep strain is determined by removing the specimens from the reactor at intervals and measuring the tube diameter. An unstressed tube is irradiated to determine the amount of swelling that occurs, and the diameter of the unstressed tube is subtracted from that of the stressed tubes to determine the creep strain. This ignores any stress-induced swelling or swelling-induced creep that may have occurred, a good assumption in most cases for ferritic/martensitic steels, since they are low swelling.

Because of the different techniques used to apply a stress to determine irradiation creep, a formalism is required to relate the data thus acquired. The following relationship is used to relate an effective strain, ε_{eff}, to an effective stress, σ_{eff}, to the stresses and strains measured in a test using the uniaxial, helical spring, or pressurized tube techniques [1,12]:

$$\frac{\varepsilon_{eff}}{\sigma_{eff}} = \frac{\varepsilon}{6\sigma} = \frac{\gamma}{3\tau} = \frac{4\varepsilon_h}{33\sigma_h} \tag{11.4}$$

where ε is the tensile strain and σ the tensile stress in a uniaxial test, γ the surface shear strain and τ the surface shear stress in a helical-spring test, and ε_h the hoop strain and σ_h the hoop stress in a pressurized-tube test.

IRRADIATION CREEP OF FERRITIC/MARTENSITIC STEELS

In-reactor creep has been investigated for FV448, modified 9Cr-1Mo, Sandvik HT9, EM10, EM12, DIN 1.4914, and several experimental reduced-activation ferritic steels over the range 60 to 600°C, with some data on the HT9 obtained for radiation doses >200 dpa. Most of the experiments have been carried out in fast reactors at temperatures from 400 to 650°C, although, as discussed below, irradiation in HFIR has demonstrated that creep can occur at temperatures as low as 60°C.

The initial irradiation creep tests on the ferritic/martensitic steels were begun in various fast reactor materials programs in the late 1970s. An early study was on FV448 using helical springs irradiated in DFR at 280°C (5.3×10^{-7} dpa/s, 36.6 MPa) and 330 to 360°C (0.34×10^{-7} dpa/s, 22.6 MPa) [11]. Thermal creep was negligible, and at 280°C, the irradiation creep rate exceeded that for thermal creep at 410°C. This is seen in Fig. 11.1, which shows the normalized creep strain

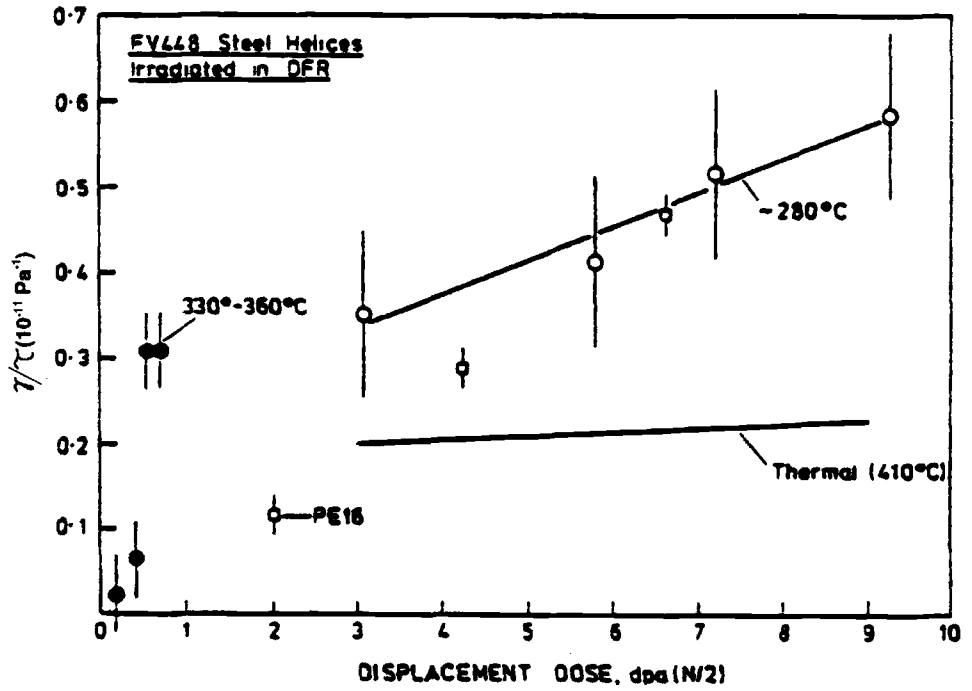

FIG. 11.1—Normalized creep strain (creep/unit stress) for FV448 and PE-16 [11].

(γ/τ) as a function of dose and indicates that the creep rate at 280°C reached a steady state that was linear with dose. The steady-state rate (0.4×10^{-12} Pa^{-1} dpa^{-1}) for the FV448 was nearly an order of magnitude less than for cold-worked (2.2 to 4.3×10^{-12} Pa^{-1} dpa^{-1}) or annealed ($2.8–4.0 \times 10^{-12}$ Pa^{-1} dpa^{-1}) austenitic stainless steels. The creep rate was also less than that for Nimonic PE16 at 280°C, which up until then had the best creep resistance of any alloys that had been tested [11].

In-reactor creep data are usually analyzed according to a semi-empirical relationship between stress, σ, and strain, ε, as [13]

$$\varepsilon = B\sigma^n\varphi t \tag{11.5}$$

where the temperature effects are contained in B, the creep coefficient or creep compliance with

$$B = Ae^{-Q/RT} \tag{11.6}$$

where n and A are constants, φ is the irradiation flux, t is time, Q is the activation energy, R the gas constant, and T the absolute temperature. Alternatively, a relationship between the steady-state creep rate and stress is often used:

$$\dot{\varepsilon} = B'\sigma^n\varphi \tag{11.7}$$

where B′ contains the temperature effect. A linear relationship (n = 1) is often found, as was the case in Fig. 11.1.

Sandvik HT9 (12Cr-1MoVW) was the first ferritic steel considered in the U.S. fast reactor program [9,14–17]. Early studies at nominal temperatures of 540 and 595°C compared the creep resistance of normalized-and-tempered HT9 with various austenitic stainless steels and various precipitation-hardened alloys after different thermomechanical treatments [9]. Irradiation was in EBR-II to nominal fluences of 2 and 4 $\times 10^{22}$ n/cm^2 (≈10 and 20 dpa). The precipitation-hardened alloys (A-286, M-813, Nimonic PE16, Inconel 706, and Inconel 718) were the most creep resistant, followed by HT9, and then the solid-solution alloys (AISI 310, AISI 330, AISI 316, and Ti-modified 316 stainless steel). A linear relationship was found between creep rate and stress for the precipitation-hardened steels, but the HT9 and the solid solution alloys displayed some nonlinearity [9]. As discussed below, this nonlinearity was probably caused by thermal creep, which will occur at 540°C and above.

Chin [17] extended the studies on Sandvik HT9 irradiations in EBR-II by irradiating pressurized tubes over the range 400 to 650°C to 1×10^{23} n/cm^2 (≈50 dpa). Figure 11.2 from Chin's paper shows the equivalence of creep curves (ε_{eff} versus t and φt) for a control test and an irradiated test at 540°C and 50 MPa. Steady-state creep rates for the two specimens were similar, with the only difference being a typical primary stage for the uniaxial specimen and no primary (transient) stage for the irradiated specimen [17]. To explain the lack of a transient stage for the in-reactor creep, it was suggested that "the appearance of an ultra-fine precipitate within the martensitic laths" may be responsible [17].

All of Chin's in-reactor tests displayed the linear behavior without a transient creep stage as shown in Fig. 11.2 [17]. However, Wassilew et al. [18] found a transient stage in uniaxial irradiation-creep tests on DIN 1.4914 steel, in which deformation was measured continuously during irradiation. The latter tests did not measure a steady state. However, as

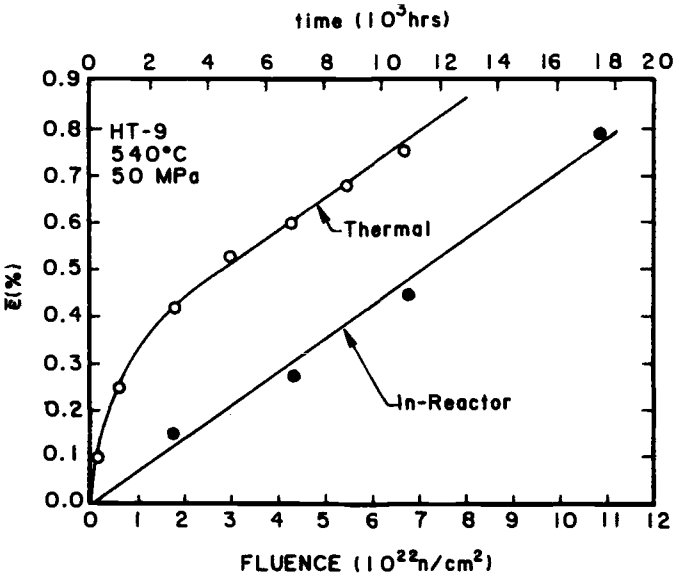

FIG. 11.2—Comparison of thermal and in-reactor creep of Sandvik HT9 [17].

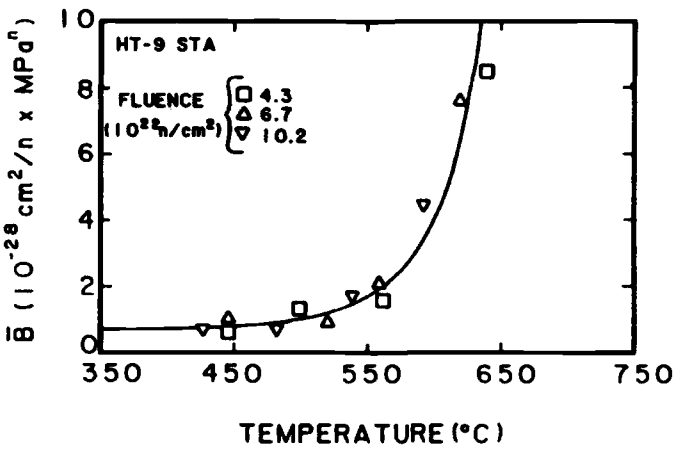

FIG. 11.3—Temperature dependence of creep coefficient for in-reactor creep of Sandvik HT9 [17].

pointed out by Chin, the tests of Wassilew et al. were made in a fluence range that is below that of the first measurements by Chin. Most pressurized-tube studies, such a Chin's, do not find a transient, probably because the first measurements are made after the transient stage is complete.

Under conditions at low temperatures where there is little effect of thermal creep, irradiation creep is relatively insensitive to temperature. This is demonstrated in Fig. 11.3 for the creep coefficient B [Eq 5] [17]: B is little changed below ≈500°C, after which it increases rapidly with increasing temperature as thermal creep begins to dominate. The large increase at elevated temperatures occurs because thermal creep dominates in this regime.

A similar effect of temperature was observed by Puigh and Wire, who irradiated pressurized tubes of Sandvik HT9, EM10 (9Cr-2Mo), and 2-1/4Cr-1Mo steel in EBR-II at 443, 505, and 572°C to ≈20 dpa [19]. At the two lowest temperatures, creep deformation of the three steels was similar, and the steels de-

formed less than type 316 stainless steel. However, at the highest temperature (572°C) where thermal creep dominated, the less creep-resistant 2¼Cr-1Mo steel showed much more deformation than the two higher-chromium steels, which were more creep resistant than the 316 stainless steel.

Irradiation creep behavior of EM10 and EM12 was determined after irradiation in Phénix [20,21]. A creep coefficient of 6.1×10^{-7} MPa^{-1} dpa^{-1} was obtained on EM12 tubes with a hoop stress of 70 MPa and irradiated to ≈50 and 100 dpaF (1 dpaF = 0.77 dpa) [20]. A similar coefficient (4.4×10^{-7} MPa^{-1} dpa^{-1}) was obtained in further experiments at 400 to 490°C in Phénix for both EM10 and EM12 [21]. This compares with a value $3–6 \times 10^{-6}$ MPa^{-1} dpa^{-1} for a cold-worked 15-15Ti austenitic stainless steel irradiated in the same experiment (the 15-15Ti is more swelling resistant than type 316 stainless steel) [21].

Puigh and Garner irradiated HT9 and modified 9Cr-1Mo steels to ≈50 dpa in FFTF at 400 to 540°C [22]. They found no evidence of swelling, and the steels exhibited superior creep resistance to that of 316 SS. Garner and Puigh [23] later extended the FFTF studies on the HT9 and modified 9Cr-1Mo steels by irradiating in FFTF to ≈155 dpa at 403 to 426°C and to about half that value at 520 and 590°C. Figure 11.4 shows the diametral strains at 403 to 426°C as a function of fluence [Fig. 11.4(a)] and hoop stress [Fig. 11.4(b)]. In Fig. 11.4(a), the stress-free curve indicates that swelling begins after a relatively long incubation period, with the 9Cr-1MoVNb steel showing a little more swelling than the HT9. After the highest fluence, however, the HT9 shows a little more creep than the 9Cr-1MoVNb. The authors stated that [22], "both alloys exhibit a linear stress dependence for hoop stress levels ≥50 MPa and exposures ≈50 dpa, but there is a nonlinearity at <50 MPa, suggesting that some stress-initiated process is involved." A linear dependence with stress was also observed for creep at 520°C, but at 590 to 605°C, a stress exponent greater than unity was observed. The latter tests are in the temperature regime where thermal creep would be expected to dominate for these steels.

Toloczko et al. [24] irradiated Sandvik HT9 and modified 9Cr-1Mo steels to ≈208 dpa at 400°C in FFTF (Fig. 11.5). For a given stress, the HT9 displayed a higher deformation than the 9Cr-1MoVNb steel. Although the 9Cr-1MoVNb showed the highest swelling after 208 dpa (≈2.4% compared to 1.1% for the HT9), stress affected the swelling of the HT9 more than the 9Cr-1MoVNb [22]. The authors calculated a creep coefficient for 9Cr-1MoVNb steel as 6×10^{-7} MPa^{-1} dpa^{-1} [24], which agrees quite well with the value obtained for EM10 and EM12 [20,21]. Toloczko and Garner [25] examined the creep behavior of two heats of Sandvik HT9 irradiated to 60 to 174 dpa and found some heat-to-heat variation. In this case they found values for the creep coefficient of ≈1×10^{-6} MPa^{-1} dpa^{-1}, which they concluded was similar to that of a variety of austenitic stainless steels irradiated in different reactors [25].

Herschbach and co-workers used a uniaxial creep test rig in the BR2 reactor to study DIN 1.4914 at 450 to 600°C [19,26,27]. The steady-state creep rate in units of dpa^{-1} was expressed according to

$$\dot{\varepsilon} = 2.0 \times 10^{6} \sigma^{5} \exp\left(\frac{-3.0}{kT}\right) \qquad (11.8)$$

where k is the Boltzman constant. The high stress exponent was taken to mean that neither SIPA nor I-creep was oper-

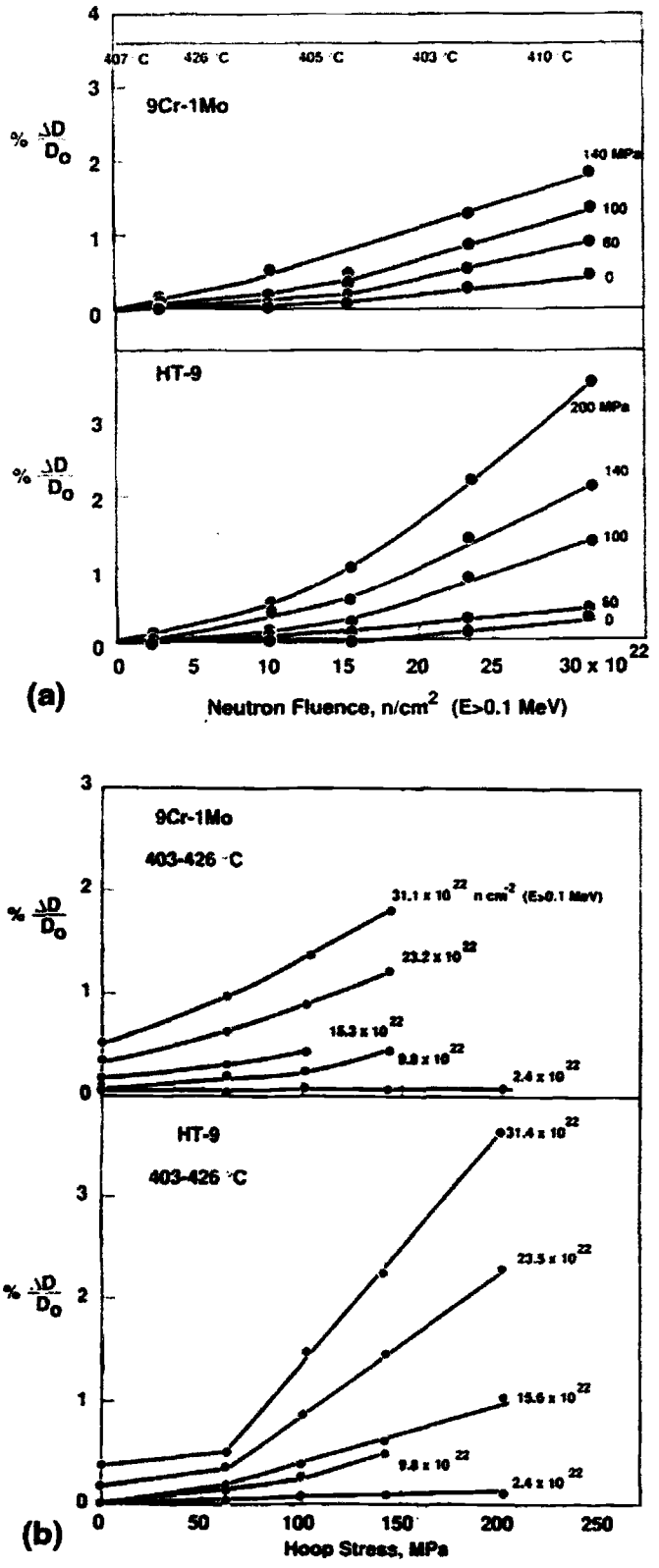

FIG. 11.4—Diametral strains as a function of (a) fluence and (b) hoop stress for modified 9Cr-1Mo and Sandvik HT9 steels irradiated at 403 to 426°C in FFTF/MOTA [23].

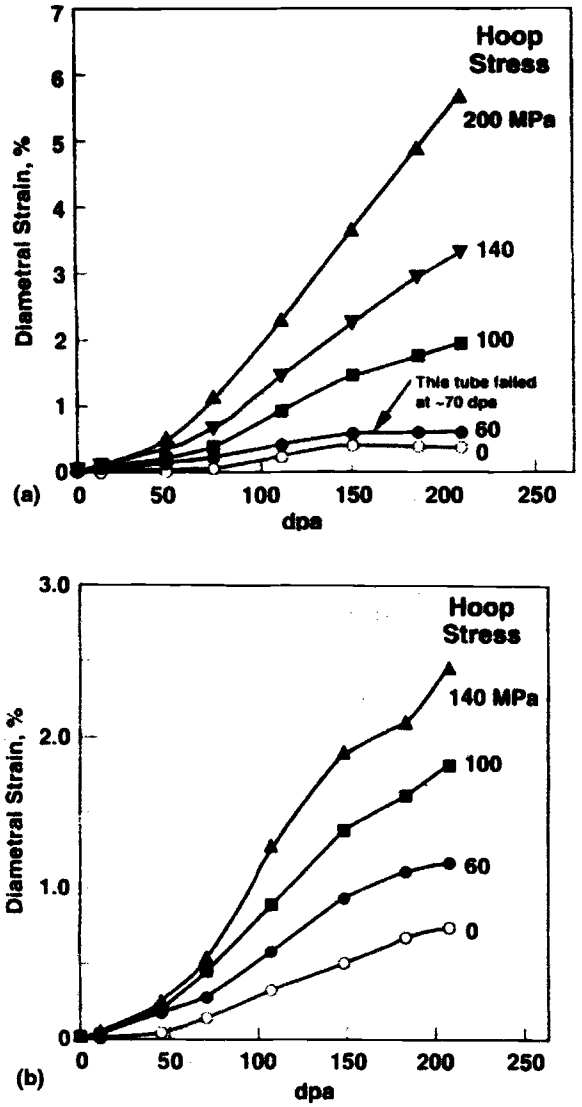

FIG. 11.5—Total diametral strain as a function of fluence for (a) Sandvik HT9 and (b) modified 9Cr-1Mo steels [24].

ating. Creep rates were one to two orders of magnitude higher than for thermal creep, which had a stress exponent of six. The high activation energy was unexpected, because it was as high as for thermal creep. That result and the high stress exponent was taken to mean that the irradiation creep was just thermal creep accelerated by irradiation [26,27].

Jung and Afify [28] conducted in-beam uniaxial tensile creep tests on 50 μm foil specimens of two heats of DIN 1.4914 at 400 to 537°C under the irradiation of 6.2 MeV protons. The primary creep stage in these tests extended beyond the 0.56 to 0.76 dpa used in the tests. By continuing the tests during beam-off periods, it was concluded that there was no significant difference between the creep rate with and without irradiation, which is different from Herschbach's observations [26,27], but similar to Chin's on HT9 [17]. However, the authors [28] state that Chin's observations were made at strain rates not observable in their experiments. By comparison with other tests [27], the stress dependence for these variable-stress tests was concluded to be lower than for constant-stress tests. The results for the two heats of DIN 1.4914 used in these tests and heats used in other experiments [27] indicated that a slight change in composition can affect the results. Nitrogen, which ranged from 0.003 to 0.048, was suggested as a possibility for this observation. Finally, in agreement with Herschbach [27] and the high-stress data of Chin [17], the activation energy dependence of the creep rate was found to be 3.0 eV [28], which was below the value for thermal creep of 4.6 eV [29].

In Table 11.1, irradiation creep coefficients are presented for Cr-Mo steels irradiated with neutrons under conditions where irradiation creep appears to be the dominant deformation process. Where values in the original references were presented in graphical form, coefficients were estimated for the temperature range where irradiation creep was clearly dominant (a constant coefficient). Given the different steels, the different reactors, and different investigators, the variation in coefficients of 1.25 to 10×10^{-7} MPa^{-1} dpa^{-1} would appear to indicate that there is not much difference in the creep behavior of the different steels. An average value near 5×10^{-7} MPa^{-1} dpa^{-1} is probably a good estimate for such ferritic/martensitic steels, which include both tempered martensite and duplex tempered martensite and δ-ferrite microstructures. The data for the ferritic/bainitic steel (2¼Cr-1Mo) also fell in this range of coefficients.

Kohyama et al. [30] determined the irradiation creep of a series of experimental reduced-activation Fe-Cr-2W-0.2V-0.07Ta steels with 2.25–12% Cr irradiated in FFTF at ≈410, 520, and 600°C to ≈36 and 60 dpa. F82H (8Cr-2WVTa) was also irradiated. The 2.25Cr steel exhibited the best creep resistance, with the resistance decreasing up to about 7% Cr, after which it again increased as the chromium increased to 12%. This is shown in Fig. 11.6(a) for a comparison of the 2.25Cr (JLF-4), 7Cr (JLF-3), 9Cr (JLF-1), 12Cr (JLF-5), and F82H steels irradiated at 520°C. Figure 11.6(b) compares the F82H (8Cr-2WVTaB) and the JLF-1 (9Cr-2WVTaN) after irradiation at 460°C and indicates that F82H has less creep resistance than JLF-1, although the JLF-1 was not irradiated at 120 MPa, the highest stress used for F82H.

Despite having limited data, an attempt was made to determine an average creep coefficient for JLF-1 and F82H as a

TABLE 11.1—Irradiation creep coefficient for neutron-irradiated steels.

Steel	Reactor	Temperature Maximum Dose	Coefficient MPa^{-1} dpa^{-1}	Reference
HT9[a]	EBR-II	425–500°C 50 dpa	2×10^{-7}	[17]
HT9[a]	EBR-II	440, 500°C	5×10^{-7}	[19]
9Cr-2Mo[a]		14 dpa	1.3×10^{-7}	
2¼Cr-1Mo[a]			2.5×10^{-7}	
EM-12	Phénix	400–440°C 100 dpaF	6.1×10^{-7}	[20]
EM-10	Phénix	400–490°C	4.4×10^{-7}	[21]
EM-12		100 dpaF		
HT9	FFTF	390–500°C	3.6×10^{-7}	[22]
Mod 9Cr-1Mo		50 dpa	2.4×10^{-7}	
Mod 9Cr-1Mo	FFTF	400°C, 208 dpa	5×10^{-7}	[23]
HT9 (2 heats)	FFTF	400°C, 165 dpa	1×10^{-6}	[24]
JLF-1[a]	FFTF	390, 410,	1.5×10^{-7}	[30]
F82H[a]		460°C		

[a]Data were estimated from graphical data presented in the respective references.

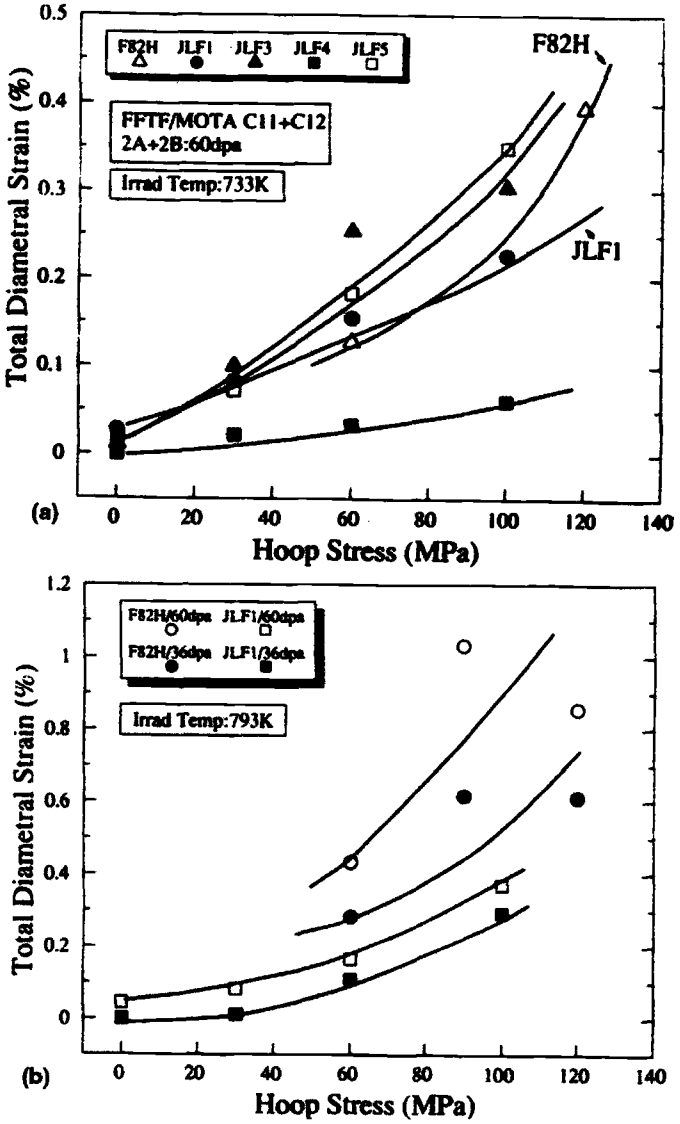

FIG. 11.6—Diametral strain as a function of hoop stress for (a) several reduced-activation steels irradiated at 460°C and (b) a comparison of JLF-1 and F82H steels irradiated at 520°C in FFTF. JLF-1 is a 9Cr-2WVTaN steel, JLF-3 is a 7Cr-2WVTa steel, JLF-4 is a 2.25Cr-2WVTa steel, JLF-5 is a 12Cr-2WVTa steel, and F82H is a 8Cr-2WVTaB steel [30].

function of irradiation temperature (Fig. 11.7) [30]. For the analysis, it was assumed that n = 1.5 [Eq 5]. The peak near 700 K (430°C) in Fig. 11.7 reflects the swelling in this temperature range [30]. The difference between F82H and JLF-1 at 520°C was concluded to be due to the lower tantalum and nitrogen in F82H compared to JLF-1. The higher coefficient for F82H at 600°C is due to the dominance of thermal creep under these conditions, and a similar large increase would be expected for JLF-1 under the same conditions. The creep coefficients for the 8 to 9% Cr steels were compared to that for the 2.25 Cr steel and the coefficient for 2.25% Cr steel was an order of magnitude lower, a result that was attributed to the effect of tungsten on the stability of the carbides developed in the low-chromium steel [30]. If the peak near 430°C is disregarded (high value was attributed to higher swelling at this temperature), then the average creep coefficient estimated from Fig. 11.7 is $\approx 1.5 \times 10^{-7}$ MPa^{-1} dpa^{-1}. This is at the lower end of the range of values obtained from the Cr-Mo steels (Table 11.1).

In these studies on the reduced-activation steels [30], a TIG weld of an F82H tube pressurized to a hoop stress of 240 MPa was irradiated to 25 dpa at 390°C. A 34% greater deformation was observed for the weld than for the base metal (0.63% strain for the weld versus 0.47% for the base metal).

Irradiation creep of steels irradiated in fast reactors shows no large temperature effect (Fig. 11.3) in a temperature regime where the creep is primarily irradiation creep (≈370 to 500°C) [17]. Grossbeck and Mansur, on the other hand, found a temperature effect for the creep of Sandvik HT9 and an Fe-15Cr binary alloy irradiated to 8 dpa at 60, 330, and 400°C in the ORR (a mixed-spectrum reactor where it is possible to irradiate at lower temperatures than are possible in a fast reactor) [31]. In agreement with previous work, they found little difference in the creep coefficient of the specimens irradiated at 330 and 400°C. However, for specimens irradiated at 60°C, the creep rates were 6 to 18 times higher than at the two higher temperatures (Fig. 11.8). Although contrary to the behavior expected from thermal creep, such an inverse temperature relationship caused by low-temperature irradiation has also been observed in uranium at 220°C [32,33] and nickel and Zircaloy at −195°C [34].

Since the low-temperature observations of Grossbeck and Mansur [31] were not consistent with the SIPA and PAG mechanisms, a mechanism was proposed [31,35] based on

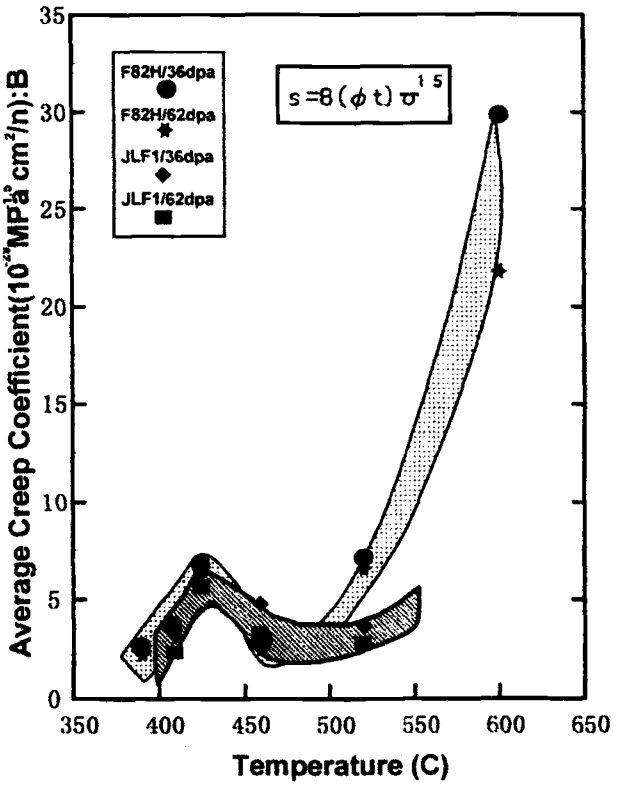

FIG. 11.7—Temperature dependence of the average creep coefficient for JLF-1 and F82H steels [30].

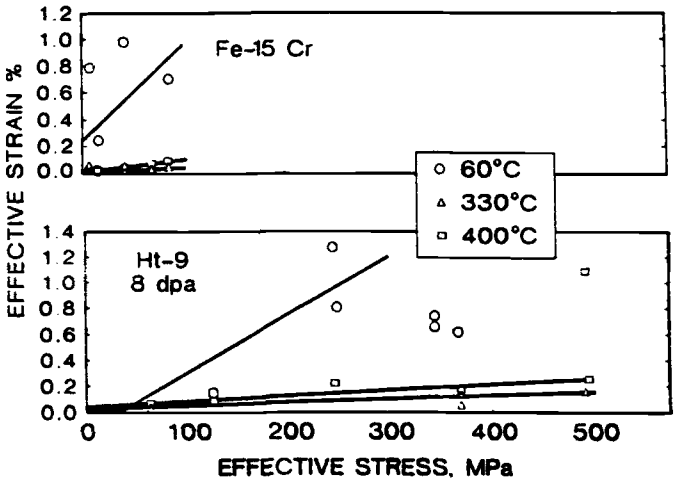

FIG. 11.8—Irradiation creep deformation in an Fe-15% Cr binary alloy and Sandvik HT9 after irradiation in the Oak Ridge Research Reactor to 8 dpa at 60, 330, and 400°C [31].

the difference in diffusion rates of vacancies and interstitials. SIPA and PAG are based on steady-state concentrations of point defects and predict a decrease in creep with increasing temperature. At low temperatures, however, the time for vacancies to diffuse to sinks and reach steady state is longer than the time of the experiment. The interstitials diffuse more rapidly and can reach their sinks (dislocations). Therefore, steady state is never reached. In contrast to elevated temperatures where both vacancies and interstitials are absorbed at dislocations and cancel each other out except for the small bias for interstitials at favorably oriented dislocations, at low temperatures only the faster-diffusing interstitials reach dislocations. The interstitials reaching dislocations cause climb and thus cause an increased creep rate over that at higher temperatures [31].

When Grossbeck et al. [36] irradiated HT9 in HFIR at 200, 330, and 400°C, they found that the enhanced creep found in the 60°C experiments did not occur (Fig. 11.9), indicating that the low-temperature phenomenon occurs somewhere below 200°C. A linear dependence on stress was apparent at 330°C, but difficult to discern at 200°C because of limited data and small strains [36]. At 400°C, the strain as a function of stress shows an abrupt increase at the highest stress. The authors state that the stress is higher than any used in previous investigations at this temperature, so the results could not be compared to previous studies. It was concluded that the observation is in agreement with a quadratic dependence of irradiation creep deformation with stress predicted by the PAG mechanism. It is envisioned that the SIPA mechanism is dominant at low stresses, and PAG becomes dominant at high stresses [36].

The above discussion involved conventional ferritic/martensitic steels. In some early studies in Europe, Vandermeulen et al. [37] irradiated pressurized tubes of two developmental ODS ferritic steels that were of interest for fuel cladding for fast reactors. One steel was strengthened by TiO_2 (designated DT) and one by Y_2O_3 (designated DY), and they were irradiated with the commercial steels EM12 and DIN 1.4914 in the Rapsodie Reactor at 400 to 500°C to a maximum dose of 3.7×10^{22} n/cm^2. These experiments were later extended to 80 dpaF [38,39]. Since ODS alloys are designed for creep strength, differences between them and conventional ferritic/martensitic steels might be expected. Parallel out-of-pile tests were conducted to determine thermal creep strains that could then be subtracted from the in-pile strains to eliminate the thermal creep component.

Although swelling in the ODS steels (<0.67%) was greater than in the two commercial steels [38], the creep resistance of the ODS steels was superior, being a factor of 2 to 5 lower for a given stress and temperature. The creep of type 316 SS

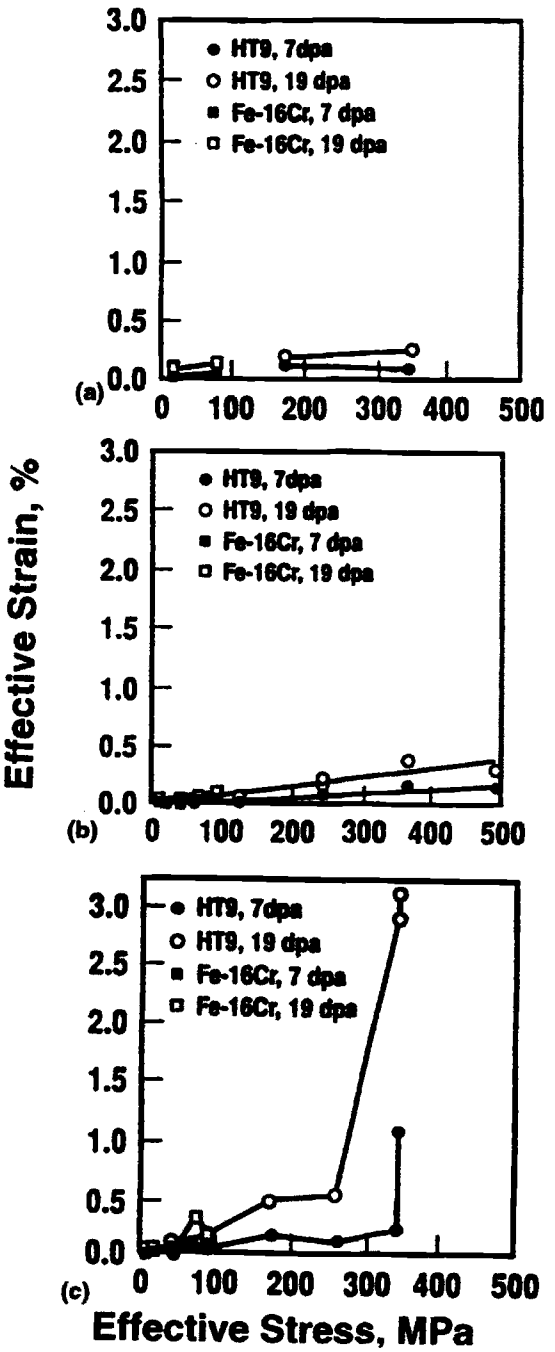

FIG. 11.9—Irradiation creep strain of an Fe-15%Cr binary alloy and Sandvik HT9 steel irradiated at (a) 200°C, (b) 330°C, and (c) 400°C in HFIR [35].

irradiated in the same experiment was three-to-four times greater. Creep resistance for the ferritic steels decreased in the order DY, DT, EM12, and 1.4914 [38]. As seen in Fig. 11.10, where the average creep coefficients (labeled K in the figure) for the in-pile results are plotted against 1/T, the coefficients for the conventional steels increased with increasing temperature, as observed by other investigators, while those for DT and DY decreased.

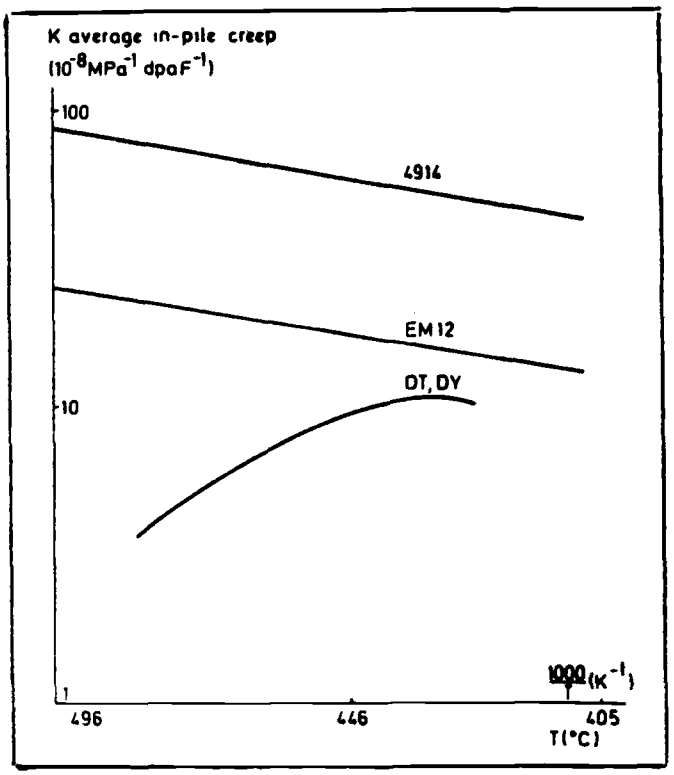

FIG. 11.10—A comparison of the average creep coefficient for in-pile creep as a function of 1/T for ODS alloys with TiO_2 (DT) and Y_2O_3 (DY) with EM12 and DIN 1.4914 after irradiation in the Rapsodie reactor [37].

After the out-of-pile creep component was subtracted from the in-pile component, a coefficient for irradiation creep was determined. This value turned out to be negative under various conditions and increased slightly with dose (Fig. 11.11). For the conventional steels, the irradiation-creep coefficient increased slightly, but for the ODS steels, it increased up to ≈450°C, above which it decreased, and above 475°C, it became negative [38].

According to the authors [38], the increase in creep coefficient with temperature in the low-temperature regime is in accordance with the literature. Above 450°C, thermal creep dominates for the conventional steels, and the total creep increases continuously with increasing temperature. For the ODS steels, however, irradiation creep rate decreases above 450°C, and since the thermal creep in these dispersion-strengthened steels remains low in this temperature regime, the total in-pile creep rate actually decreases with increasing temperature above 450°C. The authors summarized the behavior between 400 and 500°C as follows: "... the irradiation creep of the DT, DY and even EM12 steels is always quite low: their coefficient is comprised between -25 and $+20 \times 10^{-8}$ MPa^{-1} $dpaF^{-1}$ whatever the dose, the temperature, and the internal pressure."

The qualitative behavior of the ODS steels—decreasing irradiation creep with increasing temperature—appears analogous to the observations of Grossbeck and co-workers [31,36], who noted a decrease in the irradiation creep of HT9 above 200°C. The explanation for the HT9 results involved the movement of the interstitials relative to the vacancies, an explanation that does not apply for the ODS materials. One difference with the ODS steels is the high number density of fine Y_2O_3 and TiO_2 particles. The particle interfaces must act as sinks and alter the portion of defects going to the dislocations to cause irradiation creep.

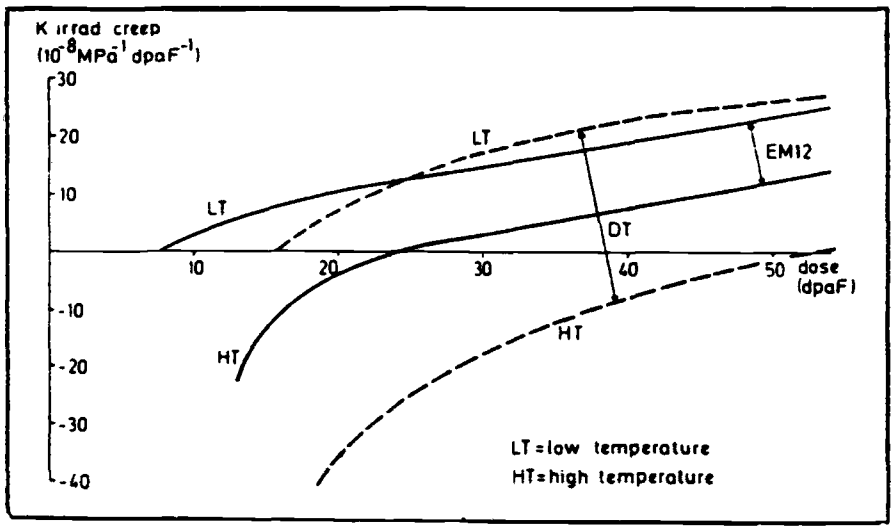

FIG. 11.11—Irradiation-creep coefficient for an ODS steel (DT) and EM12 as a function of dose irradiated in the Rapsodie reactor at high (HT) and low (LT) temperatures [37].

REFERENCES

[1] D. R. Harries, J. Nucl. Mater. 65 (1977) 157.
[2] J. H. Gittus, Philos. Mag. 25 (1972) 345.
[3] P. T. Heald and M. V. Speight, Philos. Mag. 29 (1974) 1075.
[4] R. Bullough and J. R. Willis, Philos. Mag. 31 (1975) 855.
[5] W. G. Wolfer and M. Ashkin, J. Appl. Phys. 47 (1976) 791.
[6] L. K. Mansur, Philos. Mag. A 39 (1979) 497.
[7] J. O. Stiegler and L. K. Mansur, Ann. Rev. Mater. Sci. 9 (1979) 405.
[8] L. K. Mansur, J. Nucl. Mater. 216 (1994) 97.
[9] E. R. Gilbert and B. A. Chin, Nucl. Tech. 52 (1981) 273.
[10] W. A. Coghlan, International Metals Review 31 (1986) 245.
[11] E. A. Little, D. R. Arkell, D. R. Harries, G. R. Lewthwaite, and T. M. Williams, in: Irradiation Behaviour of Metallic Materials for Fast Reactor Core Components, Eds. J. Poirer and J. -M Dupouy (CEA, Gif-Sur-Yvette, France, 1979) Vol. 1, 31.
[12] E. R. Gilbert and L. D. Blackburn, Nucl. Eng. Design 12 (1970) 421.
[13] G. D. Johnson, J. L. Straalsund, and G. L. Wire, Matls. Sci. Eng. 28 (1977) 69.
[14] M. M. Paxton, E. R. Gilbert B. A. Chin, and R. E. Nygren, J. Nucl. Mater. 80 (1979) 144.
[15] M. M. Paxton, E. R. Gilbert and B. A. Chin, J. Nucl. Mater. 95 (1980) 185.
[16] J. L. Straalsund, R. W. Powell, and B. A. Chin, J. Nucl. Mater. 108 & 109 (1982) 299.
[17] B. A. Chin, in: Topical Conference on Ferritic Steels for Use in Nuclear Energy Technologies, Eds. J. W. Davis and D. J. Michel (The Metallurgical Society of AIME, Warrendale, PA, 1984) 593.
[18] C. Wassilew, K. Herschbach, E. Materna-Morris, and K. Ehrlich, in: Topical Conference on Ferritic Steels for Use in Nuclear Energy Technologies, Eds. J. W. Davis and D. J. Michel (The Metallurgical Society of AIME, Warrendale, PA, 1984) 607.
[19] R. J. Puigh and G. L. Wire, in: Topical Conference on Ferritic Steels for Use in Nuclear Energy Technologies, Eds. J. W. Davis and D. J. Michel (The Metallurgical Society of AIME, Warrendale, PA, 1984) 601.
[20] J. M. Dupouy, Y. Carteret, H. Aubert, and J. L. Boutard, in: Topical Conference on Ferritic Steels for Use in Nuclear Energy Technologies, Eds. J. W. Davis and D. J. Michel (The Metallurgical Society of AIME, Warrendale, PA, 1984) 125.
[21] J. L. Séran, V. Lévy, P. Dubuisson, D. Gilbon, A. Maillard, A. Fissolo, H. Touron, R. Cauvin, A. Chalony, and E. Le Boulbin, in: Effects of Radiation on Materials: 15th International Symposium, ASTM STP 1125, Eds. R. E. Stoller, A. S. Kumar, and D. S. Gelles (American Society for Testing and Materials, Philadelphia, 1992) 1209.
[22] R. J. Puigh and F. A. Garner, in: Radiation-Induced Changes in Microstructure, ASTM STP 1046, Vol. II, Eds. N. H. Packan, R. E. Stoller, and A. S. Kumar, American Society for Testing and Materials, Philadelphia, 1990) 527.
[23] F. A. Garner and R. J. Puigh, J. Nucl. Mater. 179-181 (1991) 577.
[24] M. B. Toloczko, F. A. Garner, and C. R. Eiholzer, J. Nucl. Mater. 212-215 (1994) 604.
[25] M. B. Toloczko and F. A. Garner, J. Nucl. Mater. 233-237 (1996) 289.
[26] K. Herschbach and W. Doser, in: Dimensional Stability and Mechanical Behaviour of Irradiated Metals and Alloys (British Nuclear Energy Society, London, 1983) Vol. 1, 121.
[27] K. Herschbach, J. Nucl. Mater. 65 (1985) 239.
[28] P. Jung and N. M. Afify, J. Nucl. Mater. 155-157 (1988) 1019.
[29] U. Stamm and H. Schröder, J. Nucl. Mater. 155-157 (1988) 1059.
[30] A. Kohyama, Y. Kohno, K. Asakura, M. Yoshino, C. Namba, C. R. Eiholzer, J. Nucl. Mater. 212-215 (1994) 751.
[31] M. L. Grossbeck and L. K. Mansur, J. Nucl. Mater. 179-181 (1991) 130.
[32] S. T. Konobeevsky, N. F. Pravdyuk, and V. I. Kutaitsev, in: Proc. Peaceful Uses of Atomic Energy (United Nations, Geneva, 1955) 433.
[33] A. S. Zaimovsky et al., in: Proc. 2nd Conf. On Peaceful Uses of Atomic Energy (United Nations, Geneva, 1958) 566.
[34] R. V. Hesketh, in: Proc. On Solid State Physics Research with Accelerators (Brookhaven National Laboratory, Upton, New York, 1967) 389.
[35] R. E. Stoller, M. L. Grossbeck, and L. K. Mansur, in: Effects of Radiation on Materials: 15th International Symposium, ASTM STP 1125 Eds. R. E. Stoller, A. S. Kumer, and D. S. Gelles (American Society for Testing and Materials, Philadelphia, 1999) 517.
[36] M. L. Grossbeck, L. T. Gibson, S. Jitsukawa, L. K. Mansur, and L. J. Turner, in: Effects of Radiation on Materials: 18th International Symposium, ASTM STP 1325 Eds. R. K. Nanstad, M. L. Hamilton, F. A. Garner, and A. S. Kumar (American Society for Testing and Materials, Philadelphia, 1999) 725.
[37] W. Vandermulen, A. de Bremaecker, S. de Burbure, J. J. Huet, P. van Asbroeck, in: Irradiation Behaviour of Metallic Materials for Fast Reactor Core Components, Vol. 1, Eds. J. Poirer and J.-M Dupouy (CEA, Gif-Sur-Yvette, France, 1979) 1.
[38] A. De Bremaecker and J.-J.Huet, in: Dimensional Stability and Mechanical Behavior of Irradiated Metals and Alloys, Vol. 1 (British Nuclear Energy Society, London, 1983) 117.
[39] M. Snykers and W. Vandermeulen, Dimensional Stability and Mechanical Behavior of Irradiated Metals and Alloys, Vol. 1 (British Nuclear Energy Society, London, 1983) 91.

12

Irradiation Effects on Tensile Behavior

The effect of neutron irradiation on the strength of ferritic/martensitic steels depends on the irradiation temperature. Below 400 to 500°C (depending on the steel), irradiation-induced microstructural changes lead to lattice hardening, which causes an increase in the yield stress and ultimate tensile strength and a decrease in the uniform and total elongation (Fig. 12.1). The magnitude of the hardening (increase in strength) decreases with increasing temperature until it disappears between 400 to 500°C.

Limited data exist on the radiation-damage microstructures that develop during neutron irradiation below ≈400°C [1,2]. Below $\approx 0.35T_m$, where T_m is the absolute melting temperature of the steel ($T_m \approx 1800$ K), hardening is caused by small interstitial and vacancy loops produced by irradiation. Between ≈0.35 to $0.4T_m$, hardening is due to the loops and the dislocation structure that develops from the loops as the temperature is raised, along with any irradiation-induced or irradiation-accelerated precipitation that occurs. At temperatures above $\approx 0.4T_m$, diffusion is such that the irradiation-induced defects anneal out and precipitates that form can coarsen rapidly (i.e., normal thermal processes are enhanced by irradiation). The temperatures at which these various processes occur vary somewhat depending on the composition of the steel (e.g., as discussed below, F17 steel continues to show hardening up to 500°C, whereas steels like modified 9Cr-1Mo and HT9 show no hardening at 450°C).

Most of the work carried out to determine irradiation effects on strength have been on steels irradiated in fast and mixed-spectrum reactors, with some other studies in test reactors where only low-fluence irradiations are possible. A few tests have been made on steels irradiated in a 14 MeV neutron source in an attempt to determine if there are differences in the damage caused by fusion and fission neutrons.

IRRADIATION HARDENING BY FISSION NEUTRONS

Conventional Cr-Mo and Reduced-Activation Steels

Irradiation hardening of the high-chromium steels can occur for even low irradiation doses, as demonstrated on normalized-and-tempered MANET II and normalized CETA steels irradiated in the Saphir test reactor in Switzerland to 0.042 dpa at 250°C [3]. Tests at room temperature, 250, and 400°C indicated increases in the yield stress and ultimate tensile strength. For the room temperature tests, the yield stress increased 14 and 23% for the MANET II and CETA, respectively ($\Delta\sigma_y$ = 243 MPa for CETA and 93 MPa for MANET II, where $\Delta\sigma_y$ is the change in yield stress). The steels were also irradiated to 0.13 dpa at 405°C. The tempered martensite microstructure of the normalized-and-tempered MANET II steel again showed hardening. In the case of the quenched CETA, however, softening occurred, because exposure was for 1700 h, which provided time at the higher temperature for irradiation-enhanced diffusion to accelerate the tempering processes in the untempered martensite [3].

As an example of the effect of fast reactor irradiation for doses more typical for irradiation studies for nuclear applications, the tensile properties for 9Cr-1MoVNb steel are shown in Figs. 12.2 and 12.3 for irradiation in EBR-II at 390, 450, 500, and 550°C to ≈9 dpa with tension testing at the irradiation temperature (the specimens irradiated at 390°C were tested at 400°C) [4]. Also shown are data for the unirradiated (normalized-and-tempered) steel and for steel thermally aged at the irradiation temperature for 5000 h—the approximate time in the reactor.

At 390°C, irradiation caused an increase in both the 0.2% yield stress and the ultimate tensile strength (Fig. 12.2). At 450, 500, and 550°C, there was little difference in strength among the different specimens, indicating little effect of irradiation or thermal aging. The effect of irradiation on ductility reflected the effect on strength (Fig. 12.3). Uniform and total elongations of specimens irradiated at 390°C were slightly less than those of the unaged and aged controls. At the three highest temperatures, no effect of irradiation was observed [4].

Specimens of 12Cr-1MoVW (Sandvik HT9) steel were irradiated to 13 dpa in EBR-II in the same experiment as the 9Cr-1MoVNb steel [5]. Similar irradiation effects were observed: hardening occurred at 390°C, and essentially no change occurred at 450, 500, and 550°C.

Both the 9Cr-1MoVNb and 12Cr-1MoVW steels were further irradiated in EBR-II to 23 to 25 dpa at the same temperatures [6]. At 390°C there was little change relative to the steels irradiated to 9 to 13 dpa, an indication that the hardening saturated by around 10 dpa or less. After irradiation at 450, 500, and 550°C, there was also little difference in the tensile properties of the steels irradiated to the two different doses [6], although there was an indication of irradiation-enhanced thermal aging occurring at 550°C.

The effect of irradiation temperature and fluence is further demonstrated in Fig. 12.4 for MANET I steel irradiated to 5 and 10 dpa at 300, 400, and 475°C in HFR [7,8]. Hardening, as measured by an increase in yield stress and ultimate tensile strength, is greatest for the steel irradiated at 300°C, is

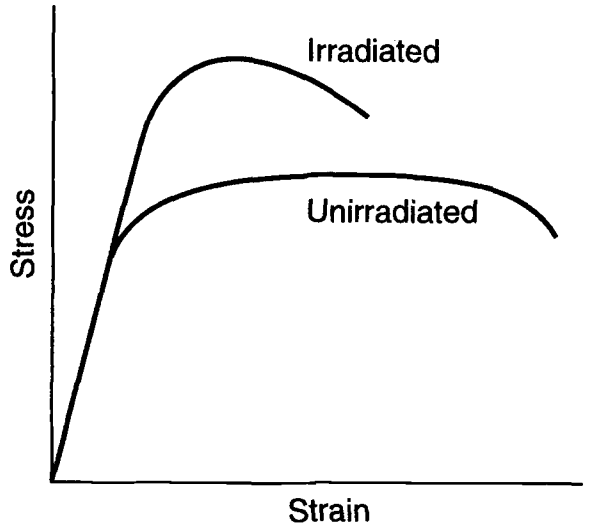

FIG. 12.1—Schematic diagram of stress-strain curves for ferritic steel in an unirradiated condition and after irradiation in the temperature regime where irradiation hardening occurs.

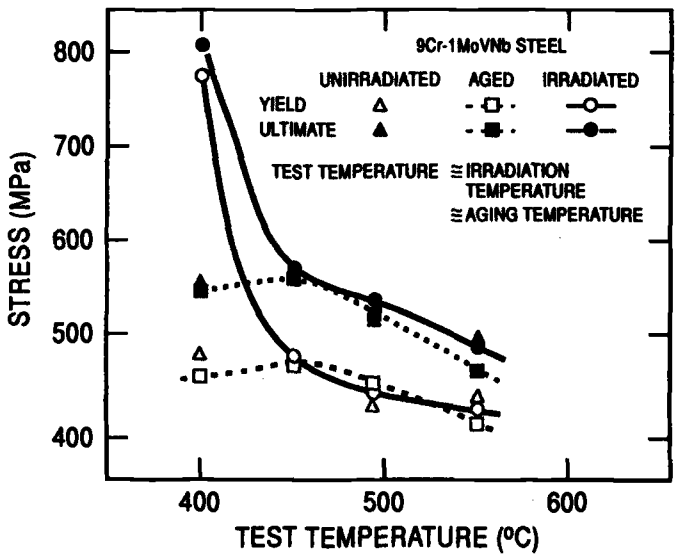

FIG. 12.2—Yield stress and ultimate tensile strength of normalized-and-tempered, thermally aged, and irradiated 9Cr-1MoVNb steel. Irradiation was in EBR-II to 0.9 dpa [4].

somewhat less for irradiation at 400°C, and shows no change occurred for irradiation at 475°C. Note also that there was little difference in the strength after irradiation to 5 and 10 dpa, indicating the saturation of hardening with fluence. Tension tests on the MANET steel irradiated in HFR at 250 and 350°C to about 0.5 to 10 dpa indicated that rapid hardening occurred up to ≈1.5 dpa, after which it leveled off; saturation was concluded to occur by ≤5 dpa [7,9]. Uniform and total elongation were reduced after 10 dpa at 350°C, but some work hardening capability was still maintained. Exposure to 5 dpa at 250°C had relatively little effect on ductility [9].

Gelles and Thomas [10] used transmission electron microscopy (TEM) to examine specimens of the same 9Cr-1MoVNb and 12Cr-1MoVW steels that were tested by Klueh and Vitek after irradiation to 9 to 13 and 23 to 25 dpa (Figs. 12.2 and 12.3) [4–6]. In the normalized-and-tempered (unirradiated) condition, the 9Cr-1MoVNb steel had a tempered martensite structure that contained large blocky $M_{23}C_6$ precipitate particles along with a higher density of small, mainly MC precipitates. After irradiation at 390°C, a high density of dislocation loops and tangles formed [10]. Small, rod-shaped precipitates identified as Cr_2C and a small number density of faceted voids were also found. For specimens irradiated at 500 and 550°C (none were examined after irradiation at 450°C), there was very little change in microstructure compared to the unirradiated condition [10].

The TEM observations fit quite well with the observations on tensile properties. Hardening is caused by irradiation-induced dislocation loops and precipitation. Irradiation-produced dislocation loops have their greatest effect for low-temperature irradiation, and the irradiation-induced precipitation has its largest effect at irradiation temperatures of 350 to 400°C. The lack of a significant change in microstructure at 500 and 550°C is in conformity with the unchanged tensile properties after irradiation or thermal aging at these temperatures. The strength decreases that occurred at the elevated temperatures at higher doses [6] occurred by the same thermal aging processes that occur in the absence of irradiation, although irradiation-accelerated diffusion accelerates

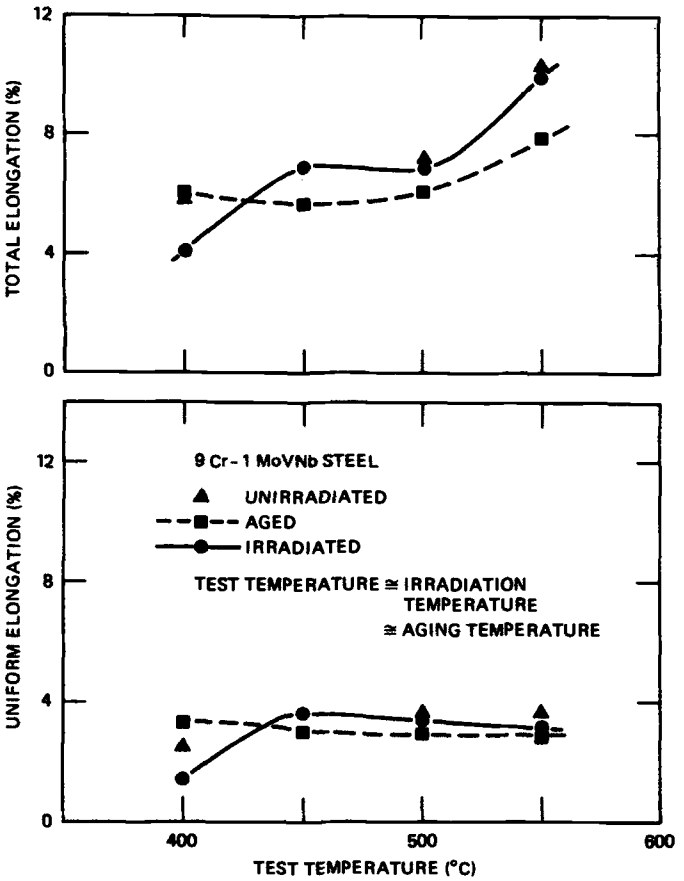

FIG. 12.3—Uniform and total elongation of normalized-and-tempered, thermally aged, and irradiated 9Cr-1MoVNb steel. Irradiation was in EBR-II to 0.9 dpa [4].

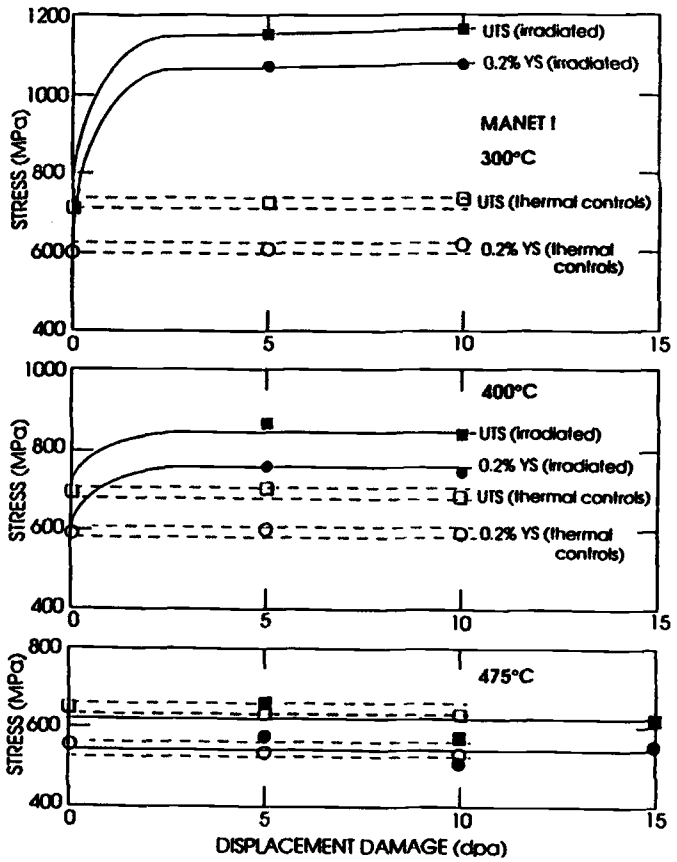

FIG. 12.4—Effect of fluence on the yield stress and ultimate tensile strength of MANET I steel irradiated at 300, 400, and 475°C [7].

the processes (i.e., dislocation recovery, precipitate coarsening, etc.). Irradiation accelerates thermal aging because the irradiation-produced vacancies enhance diffusion.

Yukitoshi et al. [11] irradiated a duplex (martensite and δ-ferrite) low-carbon (0.06% C) 9Cr-2Mo steel in EBR-II to 3×10^{26} n/m^2 (≈15 dpa) at 400, 450, 550, and 650°C and observed a similar behavior to that of HT9 and modified 9Cr-1Mo steel. Irradiation hardening occurred at 400 and 450°C, with a slight decrease in strength at 550 and 650°C. Even when the steel hardened, the failures were ductile, and the elongation at the lowest irradiation temperature remained above 3% and the reduction of area above 58%. Before irradiation, there was only a minor amount of precipitation (unidentified) present. Microstructural changes included some recovery at the lowest temperatures, with more recovery, precipitation of Laves phase, and growth of the Laves phase at the highest temperatures. Significant Laves precipitation occurred in the δ-ferrite. No voids were observed [11].

Similar observations on hardening have been made on these and other conventional Cr-Mo steels [12–18]. Little and Stoter [12] measured the Vickers hardness of FV448, CRM-12, and FI steels before and after irradiation at 380, 420, 460, and 615°C and found hardening after irradiation at 380 and 420°C and softening at the two highest temperatures. They attributed the softening to reduction of the dislocation density and the increase in subgrain size (recovery processes). Hu and Gelles [13] found a similar effect for hardness measurements on 9Cr-1MoVNb and 12Cr-1MoVW steels irradiated to 13 and 26 dpa at 390, 450, 500, and 550°C in EBR-II. Hardening occurred at 390°C, no change at 450°C, and some softening at 500 and 550°C. These results were in agreement with the tensile results for the same steels irradiated in EBR-II under similar conditions (Fig. 12.2) [4–6].

Wassilew et al. [14] irradiated DIN 1.4923 at room temperature in BR2 to 1.9×10^{26} n/m^2 (up to 1 dpa). Specimens were tested at room temperature, 400, 500, 600, 750, 820, 860, and 900°C. Considerable hardening occurred for the room temperature tests and then decreased as the test temperature increased. No hardening occurred for tests at 600°C and above. Total elongation was slightly lower for the room temperature test, but there was little difference at the higher temperatures (the unirradiated specimens had slightly more ductility), except at 860 and 900°C, where the irradiated specimens had a considerably lower elongation than the unirradiated specimens because these test temperatures were above the A_{C1} temperature and austenite formed during the test. Wassilew et al. [14] concluded that the loss of ductility at these high temperatures "can be attributed to the well known helium embrittlement," which has a larger effect on fcc steels than bcc steels (helium embrittlement will be discussed in the next chapter). Uniform elongation went through a minimum between 500 and 750°C in both the unirradiated and irradiated condition. At room temperature the uniform elongation of the unirradiated and irradiated specimens was similar, while at the higher temperatures, the uniform elongation of the irradiated specimens was higher than the unirradiated specimens. This must be an effect of the irradiation temperature and the steel, because as discussed below, quite large reductions in uniform elongation can occur for certain steels and irradiation conditions.

Wassilew et al. [14] also irradiated DIN 1.4914 up to 9 dpa at 590°C in BR2 and tested in the same temperature range as the tests on the DIN 1.4923; the yield stress and ultimate tensile strength were reduced independent of the test temperature. The authors agreed with Little and Stoter [12] that the softening was due to recovery processes. They verified this by thermal aging similar specimens and found a similar effect, indicating that the observed softening during irradiation is "mainly caused by thermal effects and to a lesser extent by the irradiation." The uniform elongation again went through a minimum after irradiation, but not in the unirradiated condition as for the DIN 1.4923.

Several French investigators published results for EM10, EM12, and F17 irradiated in the Phénix fast reactor [15–18]. Dupouy et al. [15] presented results for room temperature tensile tests on EM12 irradiated at 600°C to 75 dpa and found little effect of the irradiation.

Allegraud et al. [16] and Gilbon et al. [17] tested specimens of F17 cut from wrapper tubes irradiated at 370 to 550°C to 62.5 and ≈100 dpa. In the second study, tension specimens of EM10 irradiated to ≈40 dpa over the same temperature range were also tested [17]. For tests at the irradiation temperature, the ferritic stainless steel F17 (100% ferrite) showed considerably more hardening than the EM10 (100% tempered martensite). For example, at ≈420°C, the yield stress of F17 more than doubled compared to an approximate 20% increase for the EM10. The F17 hardened at 500°C and below, and the EM10 hardened at 450°C and below. The reason for

the greater hardening of the F17 and hardening at a higher temperature is that F17 is subject to 475°C embrittlement, and the hardening was traced to the precipitation of α′ in this high-chromium (17% Cr) steel; α′ precipitation was also observed when the steel was thermally aged at 450 and 500°C. It was concluded that for the F-17, "the main effect of irradiation is to shift the maximum in tensile strength and the minimum in elongation by 50 to 100°C towards lower temperature and to reduce the total elongation to less than 2% at about 400°C" [17].

Sèran et al. [18] tested material taken from two EM10 (100% tempered martensite) wrappers irradiated to about 2 and 5 dpa at 386°C, 90 dpa at 490°C, and 24 dpa at 525°C; tests were at 25°C, 180°C, and the irradiation temperatures. Hardening occurred for the two lowest irradiation temperatures, and no change occurred in the 525°C irradiation. Dislocation densities decreased with increasing irradiation temperature in accordance with the strength changes that were observed [18].

De Vries tested the MANET steel (modified DIN 1.4941) after irradiation to 5 dpa at 250°C and 10 dpa at 350 and 450°C in HFR [9]. Tests at the irradiation temperature revealed that all of the specimens hardened, with the amount of hardening decreasing with increasing irradiation temperature; relatively little hardening occurred at the higher temperature. The MANET II steel behaved similarly to the MANET I.

Materna-Morris et al. [19] studied a DIN 1.4914 fuel wrapper following irradiation for two years in Phénix to a maximum dose of 105 dpa at about 380 to 630°C. Tests at 400°C revealed that the steels irradiated at 380 to 430°C hardened moderately after irradiation to 10 to 105 dpa, indicating a small temperature and fluence dependence. Total elongation decreased from ≈12 to 7% after irradiation at 380°C. For specimens irradiated at 480°C and above, there was no effect on strength and ductility, as expected from previous work [14]. Electron microscopy revealed irradiation-induced α′ precipitates in the materials irradiated at 380 to 410°C at a number density of $10^{15}/cm^3$, which can account for some of the observed hardening.

These results on the effects of irradiation on tensile properties of the ferritic/martensitic steel base metals are all quite similar for the different Cr-Mo steels: hardening occurs below ≈425 to 500°C, while at higher temperatures there was little change in properties or irradiation-enhanced softening for higher doses. Although ductility decreases when the steels harden, fractures occur in a ductile mode, with no indication of intergranular or other types of brittle failure.

Sèran et al. [20] compared the behavior of EM10 base metal with EM10/EM10 welds made by the TIG and EB weld processes after irradiation at ≈460°C to 65 dpa in Phénix. They found little difference between the weldments and base metal for the EB welds in the as-welded and PWHT condition. A similar observation was made on the annealed TIG weld, but in the as-welded condition, the TIG weld showed considerably more hardening.

A similar irradiation hardening behavior with temperature to that observed on the conventional Cr-Mo steels was observed for experimental heats of reduced-activation steel [21–30], including a series of Fe-Cr-V [21,23,30], Fe-Cr-V-Mn [21], Fe-Cr-W-Mn [21], and Fe-Cr-W-V-X (X included Ta and Ti) steels with chromium ranging between 2.2 and 12% [22–30]. After irradiation below 450°C, the results indicated that there was an effect of chromium concentration on the hardening behavior [22–24]. Steels with concentrations of ≈2.2 and 12% Cr hardened significantly more than those with 5 to 9% Cr [22–24]. In one study on Cr-W-V steels, there was an indication that hardening was related to microstructure: the 2.2 Cr steels containing a duplex structure of bainite and polygonal ferrite and a 12% Cr steel containing a duplex structure of martensite and δ-ferrite showed more hardening than 5 and 9% Cr steels that were 100% martensite and a 2.25% Cr steel that was 100% bainite [23].

The similarity of the hardening of a reduced-activation steel and a conventional Cr-Mo steel is seen by comparing Fig. 12.5 for F82H (8Cr-2WVTa) irradiated over the range 200 to 600°C in HFIR [27] with the data for modified 9Cr-1Mo (9Cr-1MoVNb) in Figs. 12.2 and 12.3 irradiated in EBR-II at 390 to 550°C [4]. One major difference is that hardening apparently disappeared by 400°C for the F82H but not for 9Cr-1MoVNb.

As stated above, it appears that hardening saturates with increasing fluence. For the 9Cr-1MoVNb and 12Cr-1MoVW

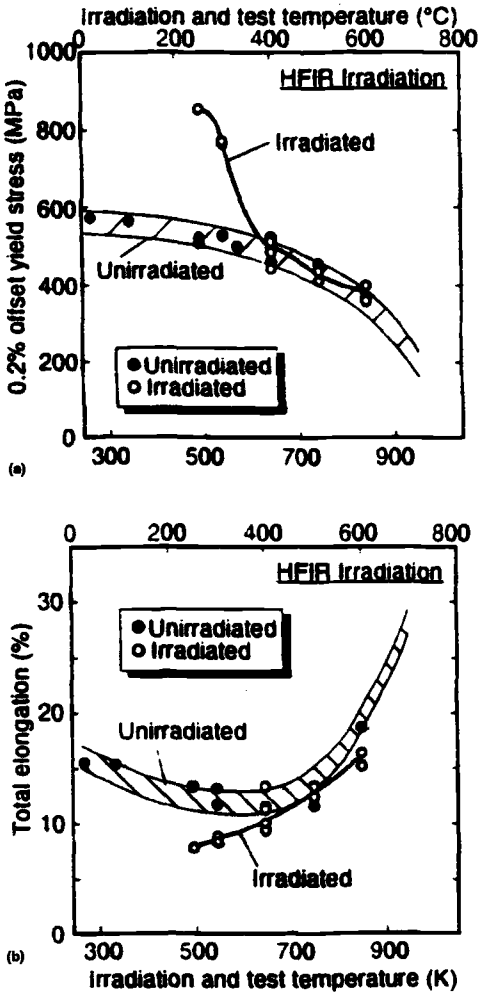

FIG. 12.5—(a) Yield stress and (b) total elongation as a function of irradiation temperature for F82H irradiated at 200 to 600°C in HFIR [26].

steels, saturation at 390°C occurred by 9 to 13 dpa, because there was little or no change between 9 to 13 dpa and 23 to 25 dpa [4–6]. The Cr-W-V steels with 2.25–12% Cr irradiated in FFTF over the range 7 to 30 dpa at 365°C saturated by 7 dpa (the lowest dose tested) [23]. However, for a series of Cr-W-V-Ta steels with 2.25, 7, 9, and 12% Cr irradiated to 25, 35, and 60 dpa at 400°C in FFTF, the hardening went through a maximum [Fig.12.6(a)] [24]. The 2.25, 9, and 12 Cr steels softened by 60 dpa, and the strength of the 7 Cr steel was similar to the unirradiated steel. A similar observation of a maximum in strength was made on F82H irradiated at 400°C to 12, 21, and 34 dpa in HFIR [Fig. 12.6(a)]; there was also an indication of a minimum in elongation [Fig. 12.6(b)] [25].

Khabarov et al. [31] studied the Russian steel 13Cr2Mo-NbVB (a nominally 12Cr-1.5Mo-0.5Nb-0.2V-0.1C steel) after specimens were removed from eight wrappers of driver subassemblies and six fuel pin claddings of experimental subassemblies irradiated in the BN-350 and BN-600 fast reactors to 4 to 85 dpa at 350 to 365°C. For tests at the irradiation temperature, a maximum occurred in the yield stress and ultimate tensile strength at 30 to 40 dpa. The elongation decreased with dose up to 30 to 40 dpa, but whereas the yield stress went through a maximum, the elongation remained at the lowest level at higher doses [31].

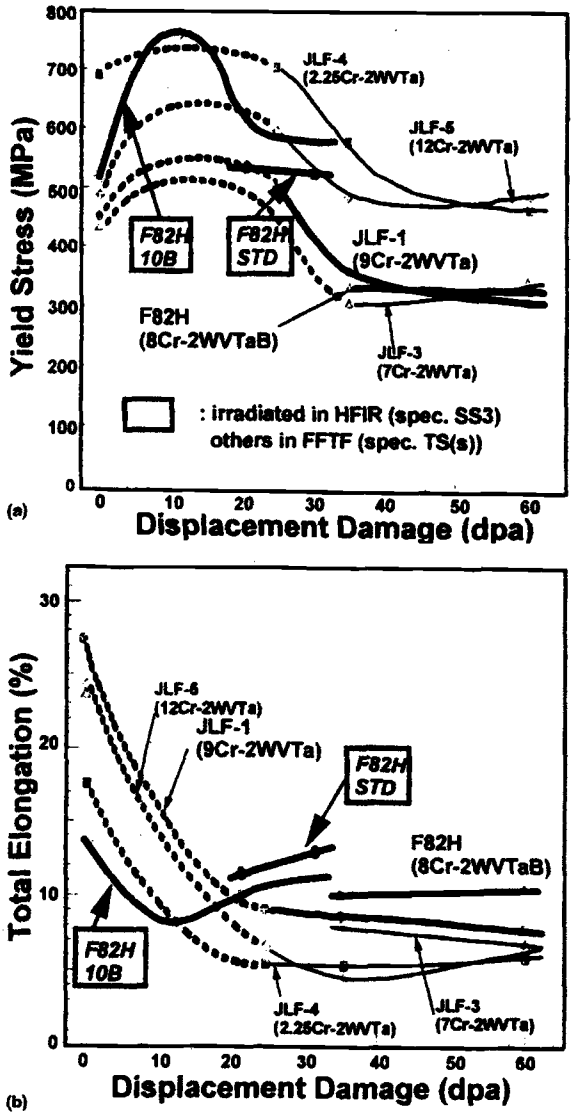

FIG. 12.6—(a) Yield stress and (b) total elongation of several reduced-activation steels as a function of fluence for irradiation at 400°C in FFTF and HFIR [24].

One explanation for the maximum in strength with fluence is that beyond the fluence for peak strength irradiation-enhanced softening (recovery) has proceeded to the point where it offsets the hardening due to irradiation. This would not be completely unexpected, since thermal aging will cause a reduction of strength due to carbide coarsening and dislocation recovery [31]. However, in the absence of irradiation, such softening would occur only after extremely long thermal aging times below 400°C [32]. Thus, irradiation-enhanced diffusion must accelerate the process for the maximum in strength to occur.

The effect of irradiation in HFR on the hardening of the MANET I steel was discussed above. The same steel was also irradiated to 5 and 10 dpa at 250 and 400°C in the BR2 reactor, after which the steel was tested at the irradiation temperatures at initial strain rates of 2.8×10^{-3} and 2.8×10^{-2} s^{-1} [7,33]. An approximate linear increase in strength with dose occurred at 250°C. At 400°C, saturation occurred at 5 dpa for the 2.8×10^{-3} s^{-1}, but saturation did not occur by 10 dpa for the higher strain rate. Also, the strength increases at 400°C were greater than at 250°C, especially for the higher strain rate.

These observations were not in accord with other results for MANET in HFR and with most of the results observed for other steels. When the results for the different reactors (and different investigators) were examined in detail, it was found that the strengths of the normalized-and-tempered steel irradiated in HFR were higher than for those irradiated to comparable fluences in BR2, and the irradiation hardening at 250°C was less in BR2 than in HFR [7]. Likewise, the hardening measured after irradiation in the BR2 at 400°C was greater than that observed after irradiation in HFR, because irradiation hardening apparently increased with temperature for the irradiation in BR2 but decreased for irradiation in HFR. It was concluded [7] that the differences "may be associated with the differences in the prior history of the steel products tested, minor compositional variations, and differences in the heat treatments of the steels, in the initial tensile strain rates, or a combination of these."

An effect of heat treatment was observed on two sets of Sandvik HT9 tension specimens irradiated to 9 to 13 dpa at 390, 450, 500, and 550°C in EBR-II [5]. One set of specimens, referred to as HT1, was austenitized 0.08 h at 1038°C, air cooled, and then tempered 0.5 h at 760°C, while the other, referred to as HT2, was austenitized 0.5 h at 1038°C and tempered 2.5 h at 760°C. Because of the shorter tempering time and smaller grain size of the HT1 specimens, they were substantially stronger than the HT2 specimens before irradiation. Furthermore, the increase in strength caused by irradiation at 390°C was greater for HT1 than HT2. The only explanation advanced for the observations was that since precipitation during irradiation of the HT1 occurs from a different starting point (the steel is under tempered), the hardening caused by the irradiation could be quite different, and any irradiation-enhanced precipitate that forms in the HT1 causes more hardening [5].

Most of the above irradiation-hardening data were obtained from irradiation in fast reactors, where irradiation temperatures are restricted to ≳360°C. At lower irradiation and test temperatures (20 to 360°C), a deformation behavior occurs that exhibits a reduced work-hardening capacity. This behavior is illustrated by the tensile curves in Fig. 12.7 for HT9 and F82H specimens irradiated in HFIR at 90 to 400°C [34]. The curves at 400°C for HT9 [Fig. 12.7(a)] and F82H [Fig. 12.7(b)] are fairly typical of tensile curves for these steels when irradiated at 400 to 600°C and tested at the irradiation temperature. With increasing irradiation temperature, the uniform and total elongation for tests at these temperatures increased (Fig. 12.2). Similarly shaped curves to that at 400°C were found for the ferritic/martensitic steels in the unirradiated condition at 400 to 600°C, the primary difference being that at 400°C, the unirradiated specimens had a higher uniform and total elongation than after irradiation.

As seen in Fig. 12.7, specimens irradiated at <400°C can show a different deformation behavior. In particular, these low-temperature deformation curves show very little uniform elongation (<0.5% and sometimes as little as 0.1%) and essentially no capacity to work harden (i.e., the rapid drop in stress after the ultimate tensile strength is indicative of a greatly reduced strain-hardening coefficient). The HT9 [Fig. 12.7(a)] displays this behavior after irradiation at 90 and 200°C, but not at 250°C and above. The F82H [Fig. 12.7(b)] displayed the behavior from 200 to 400°C; at 400°C, the uniform elongation is still quite low, but it appears that the curves are approaching the expected behavior for higher temperature tests. Such behavior was also observed before on HT9 [35,36] and modified 9Cr-1Mo [36,37] steels irradiated in HFIR at 50°C and tested at 25°C.

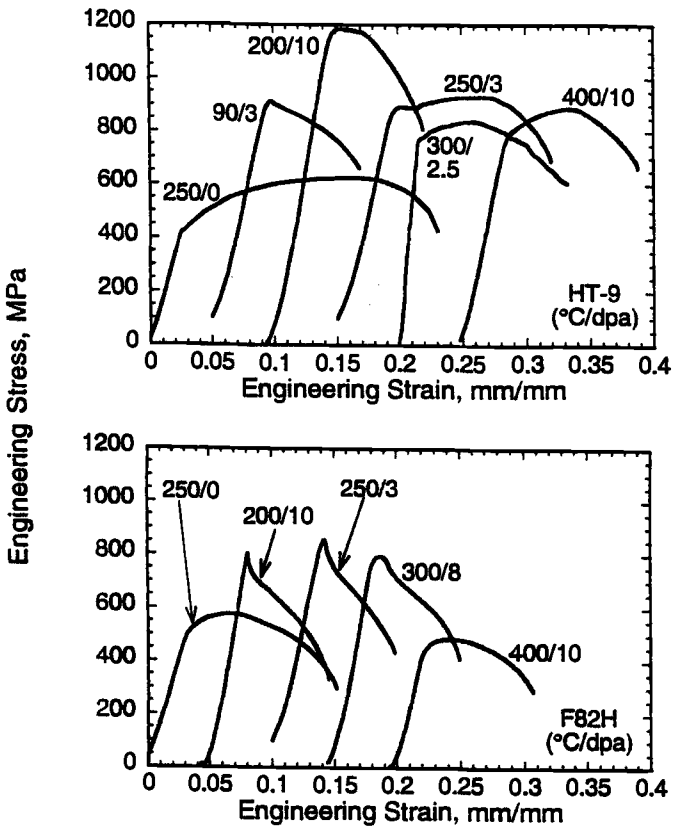

FIG. 12.7—Engineering stress-strain curves for Sandvik HT9 (12Cr-1MoVW) (top) and F82H (8Cr-2WVTa) (bottom) steels irradiated in HFIR [34].

This type of tensile curve has been attributed to a highly localized deformation process termed dislocation channel deformation, because dislocation-free channels are often observed by TEM in the deformed specimen [38–40]. The explanation for dislocation channel deformation is that dislocations sweep across slip planes and somehow "clear out" irradiation-produced obstacles to dislocation motion. As deformation continues, other dislocations can move through these "cleared channels" under a much lower stress than would be required to move through material outside the channels that still contain obstacles [39,40]. Dislocation channel deformation has been observed in neutron-irradiated Au, Cu, Ni, Fe, V, Nb, Ta, Mo, Re, and alloys of some of these metals, as well as Zircaloy and austenitic stainless steels [39–45].

The obstacles swept away by dislocations to clear the channels are defects created during irradiation [45]. In Nb-1Zr, Mo-0.5Ti, and unalloyed molybdenum where this behavior was observed, the microstructure was dominated by high concentrations of small dislocation loops and black dots believed to be unresolved loops [39]. Note that the reappearance of the strain hardening capacity for the HT9 [Fig. 12.7(a)] occurs by 250°C and 3 dpa, while for the F82H the effect remains at 300°C [Fig. 12.7(b)]. Farrell and Mahmood [41] have demonstrated how the shape of the tensile curve changes with fluence for pressure vessel steels. With increasing fluence, tensile curves evolve from the normal curve (Fig. 12.1) that has a higher strength and a slightly lower ductility, into one displaying a yield point with lower work-hardening capacity. As fluence increases, the deformation at the lower yield stress increases and the work-hardening capacity decreases, until eventually, a curve displaying a low uniform elongation and essentially no strain hardening of the type shown in Fig. 12.7 is found. For the pressure vessel steels, this evolution of curve shape occurred between 3.6×10^{21} and 3.5×10^{23} n/m^2 (<<1 dpa) [41]. Since much higher fluences were achieved for the specimens of Fig.12.7, these types of curves should be expected.

An explanation given by Farrell and Mahmood [41] for the evolution of the curves for the observations was based on the observations of Okada et al. [44,45], and it involves the localized channel deformation and subsequent halt of that mode of deformation when dislocation tangles form at channel intersections and grain boundaries. With increasing fluence, channel deformation is believed to be more persistent, leading to [41], "a sharp yield drop followed by a barely perceptible shoulder that merges into necking."

Fracture surfaces of specimens that undergo channel deformation reveal a highly dimpled ductile failure [36,42] with slip confined to very narrow bands of slip planes [43]. Although the channel deformation is accompanied by a greatly reduced uniform elongation, the total elongation for the ferritic/martensitic steels remains quite high (see Fig. 12.7) [34,36]; for the refractory metals, reduction of area also remained high [39]. Thus, the problem is not the loss of overall ductility but the early onset of unstable deformation—low uniform elongation.

Oxide Dispersion-Strengthened Steels

A detailed investigation of the microstructure and tensile properties was recently published on the DT2203Y05 (Fe-13Cr-1.5Mo-2Ti-0.45Y-0.3O) ODS steel irradiated as fuel-pin cladding in PHÉNIX up to 81 dpa at 400 to 580°C [46]. Severe embrittlement was observed. During the cutting of the tube to obtain tensile specimens, a piece of the tube broke off. Also, cracks were observed over portions of the cladding tube, and because of such cracks [46], "about 50% of the tensile specimens broke off during the fitting of samples on the tensile machine in the hot cell."

Tension tests at the irradiation temperature indicated an increase in the yield stress and ultimate tensile strength, with the increase being greatest at the lowest irradiation temperature. A large reduction in ductility accompanied the strength increase, with essentially no necking (equal uniform and total elongation) for specimens irradiated from 30 to 81 dpa. Elongations were less than 1% and as low as 0.2% at the maximum fluence. Only at the higher temperatures and lower doses did the ductilities exceed 1% [46].

Fractography indicated transgranular failures. For material highly irradiated below 520°C, failures had "starlike structure zones with planar surfaces akin to cleavage facets." Cleavage-type failures were also observed for the material that failed during cutting. Specimens irradiated at high temperatures or low doses displayed ductile failures with small dimples, even for specimens that failed when being fitted to the tensile machine [46].

Examination by TEM indicated the complicated microstructure of these materials. Before irradiation [46]:

1. The general microstructure consisted of two types of elongated fine grains, one recrystallized with a low dislocation density and the other unrecrystallized with a high dislocation density. Grain boundaries were decorated by chi-phase.
2. The oxide particles were titania and two types of yttria (differing in composition), the sizes ranging from 5 to 200 nm, with no difference between recrystallized and unrecrystallized grains. There were variations in the oxide distribution with scattered bands that were denuded of oxide particles.

After irradiation [46]:

1. The general microstructure (two types of elongated grains) appeared unchanged. The chromium concentration of the matrix decreased (originally 12.9%) with increasing irradiation temperature: chromium concentrations of 12.3 to 12.7% were measured at 400 to 480°C, 11.4% at 508°C, 10.1% at 532°C, and 10.7% at 580°C. Molybdenum concentration also varied, from 2% at 400°C to 0.3% at 580°C. The morphology of the chi-phase at the grain boundaries appeared unaffected, although it showed an increase of molybdenum and chromium and a decrease in titanium, the amount of the change increasing with increasing temperature.
2. Irradiation did not affect grains with the high dislocation density before irradiation. For irradiation at <500°C, dislocation loops and lines formed in the recrystallized grains with low dislocation density before irradiation. By 55 dpa, these loops evolved into a dislocation network. Above 500°C, no loops formed, and the dislocation density of the grains decreased to values lower than before irradiation. Distribution of the dislocations was non-uniform, showing bands of high and low dislocation density that appeared correlated with oxide denuded zones observed before irradiation.
3. Few voids were observed, indicating no swelling, in agreement with profilometry measurements.
4. Below 480°C, a uniform distribution of small particles formed and were tentatively identified as α'-phase formed at a number density higher than the original oxide particles. They did not form at the higher temperatures because of the reduction in chromium concentration.
5. Above 500°C, a uniform distribution of chi-phase nucleated and grew on titania particles throughout all grains with narrow denuded zones near grain boundaries. At high temperatures and low doses above the fissile column, where there was little or no fluence, Laves phase formed instead of the chi-phase.
6. Throughout the matrix, fine oxide particles <20 nm in size dissolved during irradiation. This was confirmed on steel irradiated to 55 dpa at 435°C, 75.6 dpa at 484°C, and 78 dpa at 508 and 532°C. The interface of larger oxide particles became [46] "cluttered with tiny precipitates," that were "spherically distributed around the larger oxides." It was concluded that "These tiny particles are probably oxides which have reprecipitated during irradiation or more probably when irradiation stopped." Oxide evolution was considered to be correlated with dose rather than temperature and was attributed to recoil dissolution (i.e., oxide atoms are ballistically ejected by impinging neutrons).

IRRADIATION HARDENING BY 14 MeV NEUTRONS

Because fusion neutrons have a higher energy than fission neutrons, it is of interest to determine whether there is a difference in the hardening caused by the different energies. When the RTNS-II 14 MeV neutron source was available (see Chapter 8), a few tests were carried out with this objective [47,48].

High purity iron was irradiated in RTNS-II at ≈75°C at 9.8×10^{20} to 2.7×10^{22} n m^{-2} (≪1 dpa), and the results were compared with the same material irradiated to 3.6×10^{22} n m^{-2} in a university test reactor [47]. There was little difference in the yield stress of the steel irradiated in RTNS-II and in the fission reactor. When compared with results from a previous unpublished study where iron with a higher interstitial content was irradiated, the latter showed more hardening. There were also differences in hardening with increasing fluence, which were attributed to the interaction of point defects with the interstitial impurities. The steel with the higher interstitial content showed a strength plateau with increasing fluence, which was not observed for the higher purity iron.

Kohyama et al. [48] irradiated TEM disks of four 9Cr-1-2MoVNb steels and one 11.5Cr-1MoV steel to 5×10^{22} n m^{-2} (≪1 dpa) in RTNS-II at 200 and 400°C. A "microbulge" test indicated that in contrast to high purity iron, the steels showed a softening, although two of the steels began to harden after 5×10^{22} n/m^2. Softening was attributed to [48]

"the scavenging of interstitial impurities from the dislocations with the production of fresh dislocations and also the scavenging of interstitial-impurity clusters and free interstitial impurities in the matrix." These results from RTNS-II are interesting because of the use of the 14 MeV neutrons—the maximum energy of neutrons in a fusion reactor neutron spectrum. However, because of the low fluences in RTNS-II, the results are probably of little significance for the high fluences in an operating fusion reactor. The subtle hardening and softening effects noted at these very low fluences will probably be swamped by the hardening produced by doses of 1 dpa and higher. For irradiation-damage studies at the higher fluences of interest, fission reactor irradiation studies are necessary, since they are essentially the only neutron sources available.

One of the consequences of the high-energy neutrons in a fusion neutron spectrum is the production of large amounts of helium by (n,α) reactions. Because of the low neutron flux of RTNS-II, no information on helium effects produced by 14 MeV neutrons could be obtained. Until a 14 MeV neutron source with an adequate flux and irradiation volume becomes available, such information must come from studies using available irradiation facilities.

IRRADIATION HARDENING—HELIUM EFFECTS

Mechanisms by which transmutation helium can affect mechanical properties of irradiated materials have been postulated to involve the interaction of helium with point defects [49–52]. Mansur and Grossbeck [49] identified possible species causing an effect as small helium-vacancy and helium-interstitial clusters, helium-stabilized matrix cavities, helium-assisted interstitial loops, and helium-stabilized grain boundary cavities. All but the grain boundary cavities were thought to produce hardening, either by pinning dislocations or inhibiting the operation of dislocation sources. Helium-assisted interstitial loops were concluded to be important at low doses [49].

Helium effectively stabilizes vacancy clusters, which, in turn, means that less vacancies are available to recombine with interstitials, (i.e., helium ties up vacancies and reduces interstitial-vacancy recombination). Interstitial clusters can then grow into dislocation loops and increase the strength [52]. In addition, the helium stabilizes the clusters to a higher temperature than in the absence of helium [49,52], thus extending the hardening temperature range.

Migration of helium to grain boundaries during irradiation to form bubbles can lead to intergranular fracture and embrittlement. This effect can be exacerbated by hardening within the grain interiors and the formation of a zone adjacent to the grain boundary that is denuded of defect clusters [49,51].

Several attempts have been made to examine the effect of helium on hardening using the nickel-doping technique described in Chapter 8 to produce the simultaneous formation of displacement damage and helium according to Eqs 8.2 and 8.3 [35,37,53–56]. The 9Cr-1MoVNb steel, this steel with 2% Ni (9Cr-1MoVNb-2Ni), 12Cr-1MoVW steel, and this steel with 1% Ni (12Cr-1MoVW-1Ni) and 2% Ni (12Cr-1MoVW-2Ni) were irradiated in HFIR [54–56] and EBR-II [52]. The standard 9Cr-1MoVNb contains ≈0.1% Ni, and the standard 12Cr-1MoVW contains ≈0.5% Ni. The objective of the experiments was to determine the effect of helium by comparing results for the steels with different nickel contents irradiated in HFIR and by comparing results from HFIR with those from EBR-II, where little helium forms.

The nickel-doped steels were irradiated in HFIR at ≈50°C (the HFIR coolant temperature) up to a fluence of ≈25 dpa and helium concentrations up to 327 appm [35,37,53]. Tension tests were conducted at room temperature. Results for the 12Cr-1MoVW, 12Cr-1MoVW-1Ni, and 12Cr-1MoVW-2Ni steels indicated that the YS increased with increasing displacement damage (Fig. 12.8) [53]. Based on the similar yield stress for the 12Cr-1MoVW and 12Cr-1MoVW-1Ni steels in the unirradiated condition, the results were interpreted to mean there was a helium effect on hardening. If the difference in unirradiated properties of the steels with 1 and 2% Ni is taken into consideration (Fig. 12.8), there does not appear to be any additional hardening for the steel with 2% Ni over the one with 1% Ni. One of the difficulties with these tests involved the starting conditions for the steels. Since nickel lowers the A_{C1} temperature, the steels with 2% Ni had to be tempered at a lower temperature (700°C) than the conventional steels and the 12Cr-1MoVW-1Ni steel (780°C). The attempt to vary time at temperature to temper to similar strengths was

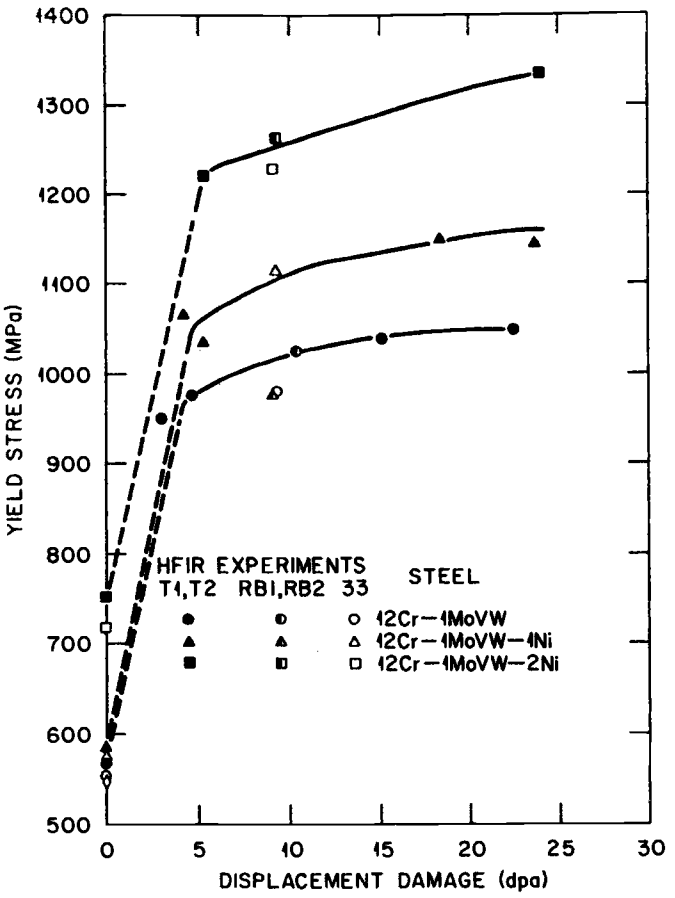

FIG. 12.8—The 0.2% yield stress of 12Cr-1MoVW, 12Cr-1MoVW-1Ni, and 12Cr-1MoVW-2Ni steels as a function of fluence for irradiation at 50°C in HFIR [52].

not successful, and the different strengths in the unirradiated condition caused difficulty in interpreting the results [37]. Further uncertainty involved the fact that the results are from three different irradiation capsules and two types of specimens—rod and sheet specimens—with somewhat different properties in the unirradiated condition [53].

More uncertainty on the effect of helium for these low-temperature irradiations is seen from results on a 9Cr-2W reduced-activation steel with and without 1% Ni irradiated in JMTR to 0.15 dpa at 170 and 220°C [57]. After irradiation at 170°C, an increase in the room temperature yield stress of up to 350 MPa was observed for the nickel-containing steel, compared to a 120 MPa increase for the steel without 1% Ni. No difference in the strength increases was observed for the steels with and without nickel when the steels were irradiated at 220°C. Post-irradiation annealing experiments showed that the anomalous hardening of the nickel-containing steel irradiated at 170°C started to recover at 190°C and was eliminated after annealing at 250°C [57]. Thus, although there was an indication of a helium effect on tensile behavior for low-temperature irradiations of nickel-doped HT9 and modified 9Cr-1Mo in HFIR [35,37,53], hardening of the type observed below 250°C in the 1% Ni steel [57] could have played a role.

Nickel-doped and undoped rod-tensile specimens of 9Cr-1MoVNb, 9Cr-1MoVNb-2Ni, 12Cr-1MoVW, 12Cr-1MoVW-1Ni, and 12Cr-1MoVW-2Ni were irradiated in HFIR at 300, 400, and 500°C (above 220°C where no hardening was observed in the 1% Ni steel [57]) up to ≈11 dpa and up to 103 appm He [54].

The results were compared with sheet specimens irradiated in EBR-II at 390, 450, 500, and 550°C up to ≈16 dpa and little helium [55]. No effect of helium on hardening was evident for irradiation at 500°C (no hardening was observed) in HFIR, similar to the results above 400°C for fast reactors where little helium was produced [4]. Because of the experimental uncertainties discussed above, the results from the nickel-doped specimens were inconclusive concerning the effect of helium on tensile behavior at 300 and 400°C, where hardening was observed [54,55]. Any helium contribution from these tests, if it exists, constitutes only a small amount of the total hardening at 300 and 400°C, and it saturates with fluence. There was no evidence of any change in fracture mode for the specimens with high-helium concentrations.

Similar conclusions were reached when these same 9 and 12% Cr steels with nickel additions were irradiated in HFIR up to 72 dpa at 400 and 600°C [56]. The strength of all the steels increased after irradiation at 400°C, but there was little difference in the strength of the steels with and without nickel. At 600°C, there was a loss in strength, which was larger than the loss observed for steels thermally aged 27 000 h at 600°C [56].

Gelles et al. [58] used the Fe-12Cr-1.5Ni ternary alloys, which were also used to study swelling [59] (see Chapter 9) to study strengthening effects by doing shear-punch tests on irradiated and unirradiated TEM disks. The shear-punch test is described as [58] "essentially a blanking operation that is common to sheet metal forming. A 1 mm diameter punch is driven at a constant rate . . . through a TEM-sized disk . . . . The load on the punch is measured as a function of punch travel, which is taken to be equivalent to the cross head displacement." The load-displacement curve is similar to a tensile curve that can be analyzed to obtain "an effective shear yield strength" and "an effective maximum shear strength." The shear-punch test was used on the Fe-12Cr-1.5Ni alloys with ^{59}Ni, ^{60}Ni, and natural nickel irradiated to ≈7 dpa in HFIR at 300, 400, 500, and 600°C. About 45 appm He was produced from the natural nickel, 80 appm He from ^{59}Ni, and no helium from ^{60}Ni. An Fe-12Cr alloy without nickel was also irradiated [58].

No effect of helium on the effective shear yield and maximum shear strengths was observed, but there was an increase in strength due to irradiation, which decreased with increasing temperature [58]. In the unirradiated condition, a strengthening effect due to nickel was reported. This strengthening effect was attributed to the unidentified precipitate that was observed (see Chapter 9) [59]. It might be noted that the microstructures of these alloys, which contained 0.004% C, were reported to be martensitic [58]. The steels were normalized 1 h at 1040°C and tempered 1 h at 760°C. Nickel lowers the A_{C1} temperature, and for a 12Cr-1MoVW steel with 2% Ni, the A_{C1} is below 760°C (near 700°C) [37]. No mention was made of this [58,59]. If the A_{C1} for a 1.5% Ni alloy is below 760°C, then some or all of the hardening in the unirradiated condition could be due to untempered martensite produced when the specimens were cooled from the tempering temperature.

Several investigators have used ^{10}B doping to produce helium [25–27,60,61]. Shiba et al. [25–27] added ^{10}B and natural boron to F82H and irradiated the steels in: (1) the JMTR to 0.9 dpa (510 appm He) at 390, 470, 530, and 590°C, (2) the JRR-2 to 0.07 dpa (50 appm He) at 530 to 570°C, and (3) the HFIR at 400 and 500°C to 12 to 34 dpa (65 to 320 appm He). They were unable to discern any effect of helium on tensile properties for these conditions [25–27]. Likewise, little difference in the hardening (yield stress) behavior of F82H and F82H with 100 ppm ^{10}B was found after irradiation at 260°C in JMTR to 0.7 dpa (500 appm He) when tensile tested at room temperature to 400°C, including the irradiation temperature (Fig. 12.9) [60]. If anything, the steel with the ^{10}B

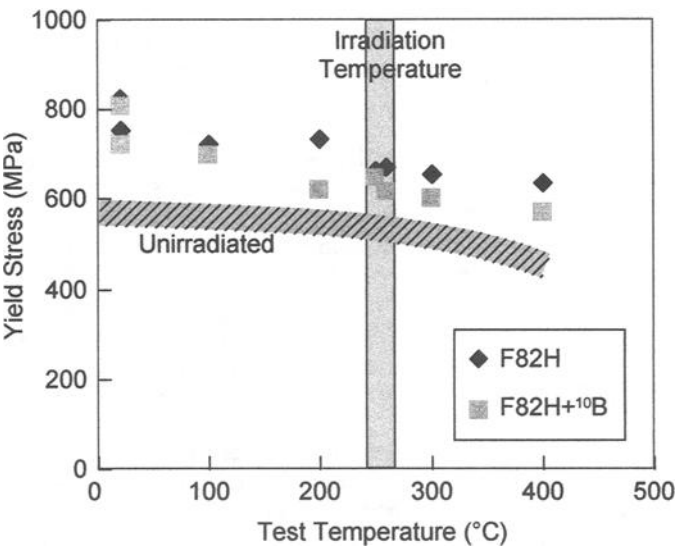

FIG. 12.9—Yield stress of F82H and F82H containing ^{10}B that was irradiated in the JMTR to 0.7 dpa at 260°C, after which it was tested at room temperature, 100, 200, 300, and 400°C [59].

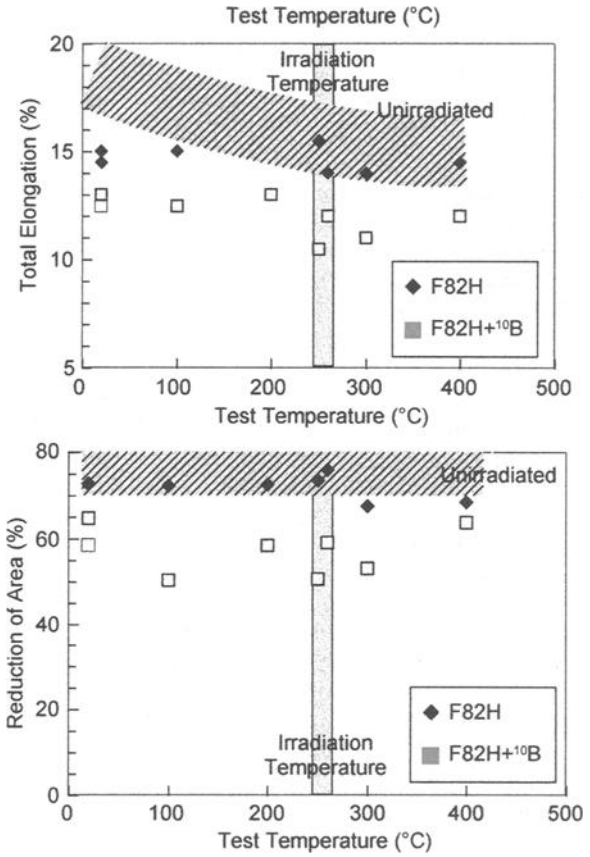

FIG. 12.10—The (a) total elongation and (b) reduction of area of F82H and F82H containing ^{10}B that was irradiated in the JMTR to 0.7 dpa at 260°C, after which it was tested at room temperature, 100, 200, 300, and 400°C [59].

addition showed slightly less hardening. However, there were reductions in the total elongation [Fig. 12.10(a)] and reduction in area [Fig. 12.10(b)] for the steel with the ^{10}B addition. The only difference in the two materials of these tests was the ^{10}B in the one steel, which produced the helium [60].

Kimura et al. irradiated a 9Cr-2WVTa steel (Fig. 12.11) without boron (JLM-0 in Fig. 12.11) and with a 32 ppm boron addition (JLM-1 in Fig. 12.11) in FFTF to 10 to 15 dpa at ≈370, 390, 430, 520, and 600°C [61]. They concluded that boron caused an increase in the irradiation hardening that occurred at the three lowest temperatures. It also caused a reduction of the amount of softening that occurred at the two highest temperatures. The authors [61] stated that the results can be understood "in terms of thermal stabilization of micro voids by helium transmuted from ^{10}B in the natural boron added to the steel." Another explanation is that small helium bubbles pinned dislocations and retarded the reorganization of the dislocation structure.

European Union investigators used ion irradiations to study helium effects on tensile properties [7,62–64]. Bombardment with 28 MeV α-particles was used to inject 100 appm helium into DIN 1.4914 at 20 to 700°C, after which the specimens were tested at the bombardment temperature [62,63]. Little change in the tensile properties was observed. In dual-beam irradiations of quenched-and-tempered DIN 1.4914 with degraded 104 MeV α-particles and 30 MeV proton beams at 300 to 720°C, injection of 100 appm He (at the rate of 1850 appm He/dpa) also produced no significant change in the strength or ductility [64]. Long-time irradiations above 440°C did reduce the strength by dislocation recovery. Ductile-transgranular failures were always observed. Helium bubbles were observed by TEM [64].

To study possible interactive effects of displacement damage, helium, and hydrogen on MANET I, dual-beam irradiations were used to implant specimens with up to 500 appm He and/or 500 appm hydrogen at 80 to 500°C [65]. Tension tests indicated significant hardening below 400°C, but little or no effect was observed above that temperature [Fig. 12.12(a)]. Results for the yield stress and ultimate tensile strength were similar to those produced by neutron irradiation in HFR [8] at comparable irradiation temperatures [7]. Since relatively small helium concentrations were produced in HFR, it was concluded that the results for the ion irradiations were due to displacement damage. Reductions in ductility were relatively small, except at 250 to 350°C, where serrations in the tensile curves indicated dynamic strain aging

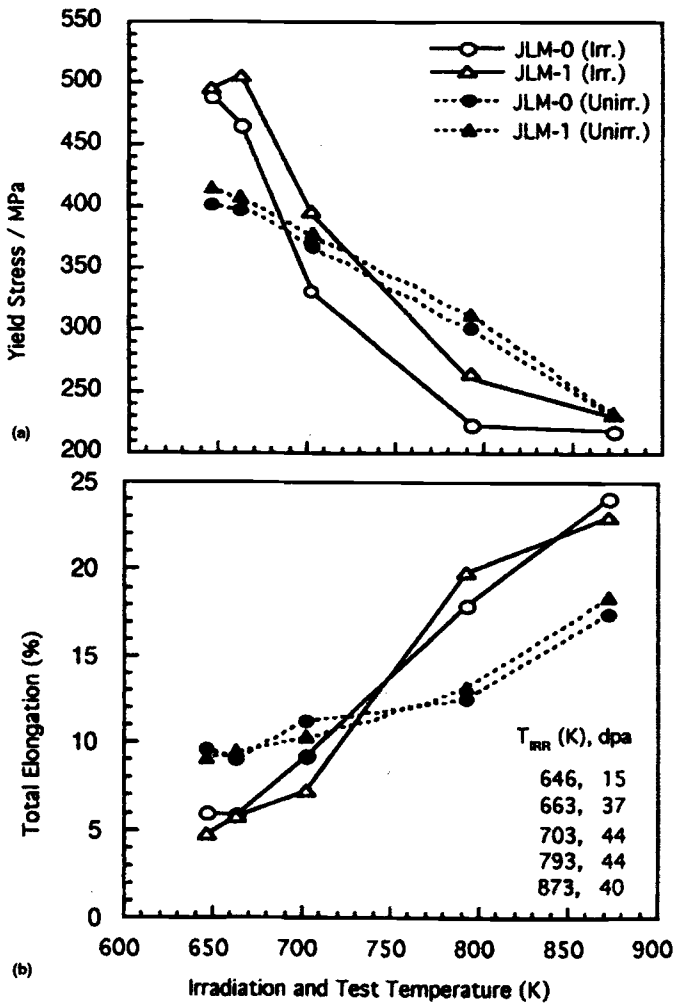

FIG. 12.11—The (a) yield stress and (b) total elongation of 9Cr-2WVTa steel without (JLM-0) and with (JLM-1) 32 ppm boron irradiated in FFTF to 10 to 15 dpa. Tests were at the irradiation temperature [60].

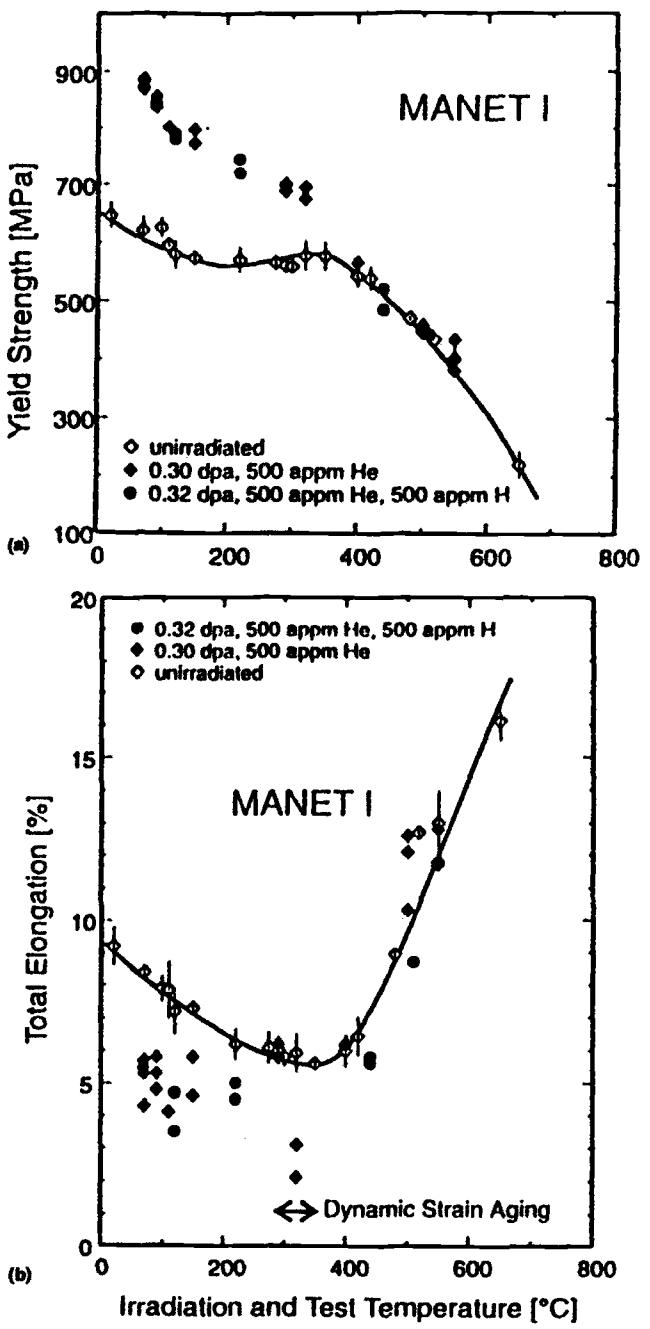

FIG. 12.12—Effect of single- and dual-beam (helium and hydrogen) irradiation on (a) yield stress and (b) total elongation of MANET I steel [64].

occurred [Fig. 12.12(b)]. Furthermore, the uniform and total elongations were reduced to ≤0.3 and 2 to 3%, respectively, in this regime, although the fractures remained ductile and transgranular. By comparison with specimens from HFR irradiated to similar doses, it was concluded that the ductilities were at least partially dependent on the implanted helium [7]. Above 100°C, up to 500 appm hydrogen did not have an effect on the tensile behavior, probably because hydrogen rapidly diffuses from the steel [65].

MANET I also hardened when irradiated with protons up to 1 dpa and 130 appm He (130 appm He/dpa formed by spallation reactions with displacement damage formed by high-energy recoiling ions after the nuclear reaction) in PIREX at 170 to 420°C, with the magnitude of the hardening decreasing with irradiation temperature; tests were at room temperature and the irradiation temperature [66,67]. Yield stresses were consistent with those after the dual-beam experiments when compared for similar displacement doses—0.3 to 0.4 dpa [7]. They were also comparable to reactor-irradiated specimens for comparable doses. The results were concluded to corroborate conclusions from the dual-beam experiments, namely, that [7] "displacement damage determined the strength properties whilst the helium appeared to be effective in reducing the ductilities at temperatures of 400°C." Dynamic strain aging was observed near 300°C, which coincides with a minimum in ductility, but the serrated yielding was less pronounced after irradiation, with the strain rate sensitivity being negative before and after irradiation [66,67]. Indications were that irradiation did not modify the mechanism of dynamic strain aging.

Similar experiments were performed in PIREX on F82H irradiated from 0.2 to 1.75 dpa at 37, 250, 350, and 400°C [68]. Irradiation hardening for the room temperature tests decreased with irradiation temperature, with essentially no hardening for the specimens irradiated at 400°C. No detectable effect of helium was found for up to 175 appm He. From activation volume determinations, it was concluded that neither helium nor helium bubbles caused a change in the rate-controlling process for dislocation motion. Any helium bubbles present in the steel were below the limit of detection [68].

Chen and Jung [69] irradiated DIN 1.4914 (MANET) with α-particles to implant helium, and then, for comparison, other specimens were irradiated with the α-particles being allowed to pass through the specimens, thus producing only displacement damage. Doses ranged from $\approx 10^{-3}$ to 10^{-1} dpa with helium concentrations of 7.9, 36, and 185 appm. Microhardness measurements were made with a computerized depth-sensing indentation tester over the range −180 to +160°C at different loads, penetration rates, and indenter geometry. The hardness increased with increasing dose and helium concentration. Results were interpreted as a shift in hardness due to irradiation, and the hardness shifts were related to a shift in DBTT. It was claimed that the results showed that for equal displacement doses, the hardness changes translate to significantly larger shifts in DBTT for helium-implanted specimens, indicating that helium had caused hardening and had an effect on the DBTT shift, in addition to the shift caused by displacement damage [69].

As opposed to the 12Cr steel implanted with helium in the EU program [7,63–65], Hasegawa and co-workers examined the effect on 9Cr steels [70,71]. Two reduced-activation steels—9Cr-0.5V and 9Cr-2W—and the 9Cr-1MoVNb steel were implanted with up to 500 appm He with a 26 MeV ^{3}He beam at 400 to 600°C; the specimens were tensile tested at the implantation temperature [70]. Implantation of 100 appm He at 400 and 500°C had no effect on properties. Softening occurred for specimens implanted with 100 and 500 appm He at 600°C (softening would be expected to occur by thermal aging at 600°C). The fracture mode always remained ductile, but after the 500 appm He implantation, the total elongation of the 9Cr-0.5V decreased, while that for the other two steels

increased slightly. Helium bubbles formed at all implantation temperatures, mainly at lath and sub-boundaries. There was no preferential bubble growth on the boundaries that would promote intergranular fracture [70].

In a second experiment, Hasegawa et al. [71] tensile tested at 25 to 700°C the 9Cr-2W and 9Cr-1MoVNb steel after implanting with 300 appm He at a lower temperature (260 to 300°C). In this case, the strength increased at all temperatures. There was no change in total elongation for tests below 500°C, but it decreased above 500°C; the fracture mode remained ductile. No defect clusters were observed for specimens tested up to 500°C, but at ≥600°C, bubbles were observed on lath boundaries and dislocations were in a more uniform distribution than for the hot implantation [71]. The increase in strength was attributed to these bubbles. In general, the behavior of the reduced-activation 9Cr-2W and the conventional 9Cr-1MoVNb steel were taken to be similar in terms of bubble formation and fracture mode [71].

The results for helium effects on strength and ductility of the ferritic/martensitic steels over the temperature regime where irradiation hardening occurs (<400 to 500°C, depending on the steel) can probably be best summarized as inconclusive. All indications are that, if there is an effect, it is probably small and of minor significance, at least for the conditions that have been examined.

REFERENCES

[1] V. S. Agueev, V. N. Bykov, A. M. Dvoryashin, V. N. Golovanov, E. A. Medvedeva, V. V. Romaneev, V. K. Shamardin, and A. N. Vorobiev, in: Effects of Radiation on Materials: 14th International Symposium, ASTM STP 1046, Vol. I, Eds., N. H. Packan, R. E. Stoller, and A. S. Kumar (American Society for Testing and Materials, Philadelphia, 1989) 98.

[2] P. J. Maziasz, R. L. Klueh, and J. M. Vitek, J. Nucl. Mater. 141-143 (1986) 929.

[3] I. Belianov and P. Marmy, J. Nucl. Mater. 258-263 (1998) 1259.

[4] R. L. Klueh and J. M. Vitek, J. Nucl. Mater. 132 (1985) 27.

[5] R. L. Klueh and J. M. Vitek, J. Nucl. Mater. 137 (1985) 44.

[6] R. L. Klueh and J. M. Vitek, J. Nucl. Mater. 182 (1991) 230.

[7] K. Ehrlich, D. R. Harries, and A. Möslang, Characterisation and Assessment of Ferritic/Martensitic Steels, Forschungszentrum Karlsruhe, FZKA Report 5626, February 1997.

[8] E. Materna-Morris and O. Romer, in: Fusion Technology, Vol. II, Eds. K. Herschbach, W. Maurer, and J. E. Vetteer (North Holland, Amsterdam, 1995) 1281.

[9] M. I. deVries, in: Effects of Radiation on Materials: 16th International Symposium, ASTM STP 1175 Eds. A. S. Kumar, D. S. Gelles, R. K. Nanstad, and E. A. Little (American Society for Testing and Materials, Philadelphia, 1993) 558.

[10] D. S. Gelles and L. E. Thomas, in: Topical Conference on Ferritic Steels for use in Nuclear Energy Technologies, Eds. J. W. Davis and D. J. Michel (The Metallurgical Society of AIME, Warrendale, PA, 1984) 559.

[11] T. Yukitoshi, K. Yoshikawa, H. Teranishi, T. Lauritzen, W. L. Bell, and S. Vaidyanathan, J. Nucl. Mater. 133 & 134 (1985) 644.

[12] E. A. Little and L. P. Stoter, in: Effects of Irradiation on Materials: Eleventh Conference, ASTM STP 782, Eds. H. R. Brager and J. S. Perrin (American Society for Testing and Materials, Philadelphia, 1982) 207.

[13] W. L. Hu and D. S. Gelles, in: Influence of Radiation on Material Properties: 13th International Symposium, ASTM STP 956, Part II, Eds. F. A. Garner, C. H. Henager, Jr., and N. Igata, (American Society for Testing Materials, Philadelphia, 1987) 83.

[14] C. Wassilew, K. Herschbach, E. Materna-Morris, and K. Ehrlich, in: Topical Conference on Ferritic Steels for Use in Nuclear Energy Technologies, Eds. J. W. Davis and D. J. Michel (The Metallurgical Society of AIME, Warrendale, PA, 1984) 607.

[15] J. M. Dupouy, Y. Carteret, H. Aubert, and J. L. Boutard, in: Topical Conference on Ferritic Steels for Use in Nuclear Energy Technologies, Eds. J. W. Davis and D. J. Michel (The Metallurgical Society of AIME, Warrendale, PA, 1984) 125.

[16] G. Allegraud, J. M. Boyer, R. Cauvin, A. Daniel, and A. Grivaud, in: Materials for Nuclear Reactor Core Applications, Vol 1 (British Nuclear Energy Society, London, 1987) 249.

[17] D. Gilbon, J. L. Seran, R. Cauvin, A. Fissolo, A. Alamo, F. Le Naour, and V. Levy, in: Effects of Radiation on Materials: 14th International Symposium, ASTM STP 1046, Vol. 1, Eds. N. H. Packan, R. E. Stoller, and A. S. Kumar (American Society for Testing and Materials, Philadelphia, 1989) 5.

[18] J. L. Séran, V. Lévy, P. Dubuisson, D. Gilbon, A. Maillard, A. Fissolo, H. Touron, R. Cauvin, A. Chalony, and E. Le Boulbin, in: Effects of Radiation on Materials: 15th International Symposium, ASTM STP 1125, Eds. R. E. Stoller, A. S. Kumar, and D. S. Gelles (American Society for Testing and Materials, Philadelphia, 1992) 1209.

[19] E. I. Materna-Morris, C. Petersen, M. Rieth, O. Romer, M. Schirra, and K. Ehrlich, in: Proceedings, Conference on Materials and Nuclear Power (The Institute of Materials, London, 1996) 273.

[20] J. L. Seran, A. Alamo, A. Maillard, H. Touron, J. C. Brachet, P. Dubussion, and O. Rabouille, J. Nucl. Mater. 212-215 (1994) 588.

[21] D. S. Gelles, in: Reduced Activation Materials for Fusion Reactors, ASTM STP 1047, Eds. R. L. Klueh, D. S. Gelles, and M. Okada, and N. H. Packan (American Society for Testing and Materials, Philadelphia, 1990) 113.

[22] R. L. Klueh, J. Nucl. Mater. 179-181 (1991) 728.

[23] R. L. Klueh and D. J. Alexander, in: Effects of Radiation on Materials: 18th International Symposium, ASTM STP 1325, Eds. R. K. Nanstad, M. L. Hamilton, F. A. Garner, and A. S. Kumar (American Society for Testing and Materials, Philadelphia, 1997) 911.

[24] A. Kohyama, A. Hishinuma, D. S. Gelles, R. L. Klueh, W. Dietz, and K. Ehrlich, J. Nucl. Mater. 233-237 (1996) 138.

[25] K. Shiba, M. Suzuki, A. Hishinuma, and J. E. Pawel, in: Effects of Radiation on Materials: 17th International Symposium, ASTM STP 1270, Eds. D. S. Gelles, R. K. Nanstad, A. S. Kumar, and E. A. Little (American Society for Testing and Materials, Philadelphia, 1996) 753.

[26] K. Shiba, I. Ioka, J. E. Robertson, M. Suzuki, and A. Hishinuma, in: Proceedings, Conference on Materials and Nuclear Power (The Institute of Materials, London, 1996) 265.

[27] K. Shiba, M. Suzuki, and A. Hishinuma, J. Nucl. Mater. 233-237(1996) 309.

[28] E. I. Materna-Morris, M. Rieth, and K. Ehrlich, in: Effects of Radiation on Materials: 19th International Symposium, ASTM STP 1366, Eds. M. L. Hamilton, A. S. Kumar, S. T. Rosinski, and M. L. Grossbeck (American Society for Testing and Materials, West Conshohocken, PA, 2000) 597.

[29] F. Abe, M. Narui, and H. Kayano, Mater. Trans. JIM 34 (2993) 1053.

[30] F. Abe, T. Noda, H. Araki, M. Narui, and H. Kayano, J. Nucl. Mater. 166 (1980) 265.

[31] V. S. Khabarov, A. M. Dvoriashin, and S. I. Porollo, J. Nucl. Mater. 233-237 (1996) 236.

[32] P. J. Maziasz and R. L. Klueh, in: Effects of Radiation on Materials: 16th International Symposium, ASTM STP 1125, Eds. A. S. Kumar, D. S. Gelles, R. K. Nanstad, and E. A. Little (American Society for Testing and Materials, Philadelphia, 1992) 1135.

[33] W. Vandermeulen, W. Hendrix, V. Massaut, J. Van de Velde, and Ch. De Raedt, MASTER. Test Results, SCK/CEN, Mol Report FT/Mol/92-05, December 1992.

[34] A. F. Rowcliffe, J. P. Robertson, R. L. Klueh, K. Shiba, D. J. Alexander, M. L. Grossbeck, and S. Jitsukawa, J. Nucl. Mater. 258-263 (1998) 1275.
[35] R. L. Klueh, J. M. Vitek, and M. L. Grossbeck, J. Nucl. Mater. 103&104 (1981) 887.
[36] R. L. Klueh and J. M. Vitek, in: Topical Conference on Ferritic Steels for Use in Nuclear Energy Technologies, Eds. J. W. Davis and D. J. Michel (The Metallurgical Society of AIME, Warrendale, PA, 1984) 615.
[37] R. L. Klueh, J. M. Vitek, and M. L. Grossbeck, in: Effects of Irradiation on Materials: Eleventh Conference, ASTM STP 782, Eds. H. R. Brager and J. S. Perrin (American Society for Testing and Materials, Philadelphia, 1982) 648.
[38] F. A. Smidt Jr., Dislocation Channeling in Irradiated Metals, NRL Report 7078, Naval Research Laboratory, 1970.
[39] F. W. Wiffen, in: Defects and Defect Clusters in B.C.C. Metals and Their Alloys, Ed. R. J. Arsenault (National Bureau of Standards, Gaithersburg, Maryland, 1973) 176.
[40] M. S. Wechsler, in: Inhomogeneity of Plastic Deformation (American Society for Metals, Metals Park, Ohio, 1973) 19.
[41] K. Farrell and S. T. Mahmood, to be published.
[42] R. L. Fish, J. L. Straalsund, C. W. Hunter, and J. J. Holmes, in: Effects of Radiation on Substructure and Mechanical Properties of Metals and Alloys, ASTM STP 529 (American Society for Testing and Materials, Philadelphia, 1973) 149.
[43] F. W. Wiffen and P. J. Maziasz, J. Nucl. Mater. 103 & 104 (1981) 821.
[44] A. Okada, K. Kanao, and T. Yoshiie, Bull. Faculty of Engineering, Hokkaido University, 141 (1988) 93.
[45] A. Okada, T. Yoshiie, S. Kojima, and M. Kiritani, J. Nucl. Mater. 141-143 (1986) 907.
[46] P. Dubuisson, R. Schill, M. P. Hugon, I. Grislin, and J. L. Séran, in: Effects of Radiation on Materials: 18th International Symposium, ASTM STP 1325, Eds. R. K. Nanstad, M. L. Hamilton, F. A. Garner, and A. S. Kumar (American Society for Testing and Materials, West Conshohocken, PA, 1999) 882.
[47] H. Matsui, K. Abe, S. Hirano, O. Yoshinari, and M. Koiwa, J. Nucl. Mater. 133&134 (1985) 615.
[48] A. Kohyama, K. Asakura, Y. Kohno, K. Komamura, K. Suziki, M. Kiritani, T. Fujita, and N. Igata, J. Nucl. Mater. 133 & 134 (1985) 628.
[49] L. K. Mansur and M. L. Grossbeck, J. Nucl. Mater. 155-157 (1988) 130.
[50] K. Ehrlich, J. Nucl. Mater. 133 & 134 (1985) 119.
[51] K. Farrell, P. J. Maziasz, E. H. Lee, and L. K. Mansur, Radiation Effects 78 (1983) 277.
[52] K. Farrell, Radiation Effects 53 (1980) 175.
[53] R. L. Klueh and J. M. Vitek, J. Nucl. Mater. 161 (1989) 13.
[54] R. L. Klueh and J. M. Vitek, J. Nucl. Mater. 150 (1987) 272.
[55] R. L. Klueh, P. J. Maziasz, and J. M. Vitek, J. Nucl. Mater. 151-143 (1986) 960.
[56] R. L. Klueh and P. J. Maziasz, J. Nucl. Mater. 187 (1992) 43.
[57] R. Kasada, A. Kimura, H. Matsui, and M. Narui, J. Nucl. Mater. 258-263 (1998) 1199.
[58] D. S. Gelles, G. L. Hankin, and M. L. Hamilton, J. Nucl. Mater. 251 (1997) 188.
[59] D. S. Gelles, in: Effects of Radiation on Materials: 18th International Symposium, ASTM STP 1325, Eds. R. K. Nanstad, M. L. Hamilton, F. A. Garner, and A. S. Kumar (American Society for Testing and Materials, Philadelphia, 1999) 899.
[60] K. Shiba and A. Hishinuma, J. Nucl. Mater., 283-287 (2000) 474.
[61] A. Kimura, T. Morimura, M. Narui, and H. Matsui, J. Nucl. Mater. 233-237(1996) 319.
[62] U. Stamm and H. Schoroeder, J. Nucl. Mater. 155-157 (1988) 1059.
[63] H. Schroeder and H. Ullmaier, J. Nucl. Mater. 179-181 (1991) 118.
[64] A. Möslang and D. Preininger, J. Nucl. Mater. 155-157 (1988) 1064.
[65] K. K. Bae, K. Ehrlich, and A. Möslang, J. Nucl. Mater. 191-194 (1992) 905.
[66] P. Marmy and M. Victoria, J. Nucl. Mater. 191-194 (1992) 905.
[67] P. Marmy, Y. Ruan, and M. Victoria, J. Nucl. Mater. 179-181 (1991) 697.
[68] P. Spätig, R. Schäublin, S. Gyger, and M. Victoria, J. Nucl. Mater. 258-263 (1998) 1345.
[69] J. Chen and P. Jung, J. Nucl. Mater. 212-215 (1994) 45.
[70] A. Hasegawa and H. Shiraishi, J. Nucl. Mater. 191-194 (1992) 910.
[71] A. Hasegawa, N. Yamamoto, and H. Shiraishi, J. Nucl. Mater. 202 (1993) 266.

13

Elevated-Temperature Helium Embrittlement

At irradiation temperatures $T_i \geq 0.5T_m$, where T_m is the absolute melting temperature, irradiation-induced atom displacement damage in steels is unstable, and the flow properties are generally unaffected by irradiation [1,2]. However, austenitic steels and other face-centered-cubic alloys are embrittled at elevated temperatures following or during neutron irradiation in thermal or fast reactors and helium implantation. This embrittlement is manifested as a reduction in tensile ductility [1–4], as shown in Fig. 13.1 for type 316 stainless steel [5]. Creep-rupture life and ductility [4,6–14] and fatigue endurance at low frequencies [12,14–16] are also affected in austenitic steels alloys. The irradiation does not significantly influence the deformation behavior but modifies the fracture process at high temperatures. Thus, the irradiation embrittlement is primarily associated with an increased tendency to intergranular fracture above about $0.5T_m$.

It is now well established that helium gas is primarily responsible for this high-temperature irradiation embrittlement. The helium is generated in the austenitic steels and alloys by the ^{10}B (n,α) ^{7}Li and the ^{58}Ni (n,γ) ^{59}Ni (n,α) ^{56}Fe reactions (see Chapter 8) during irradiation in thermal and mixed-spectrum fission reactors, while threshold (n,α) reactions in Ni, Cr, and Fe are major sources of helium in fast fission and D-T fusion reactors. The embrittlement is manifested in austenitic steels containing ≤1 to a few appm He depending on the steel composition, initial thermomechanical treatment, irradiation, and test conditions [1,2].

The most widely accepted model of the embrittlement is based on the stress-induced growth of cavities nucleated from helium bubbles at the grain boundaries [1,3,14,17]. The helium bubbles of radius r_0 are initially in equilibrium with the internal gas pressure (P_0) being balanced by the surface tension (γ):

$$P_0 = \frac{2\gamma}{r_0} \tag{13.1}$$

The bubbles on the grain boundaries orthogonal to the applied tensile stress become unstable and grow by grain boundary vacancy condensation if the stress exceeds a critical value σ_c. Assuming ideal gas behavior, σ_c is given by [17]*:

$$\sigma_c = \frac{0.76\gamma}{r_0} \tag{13.2}$$

* The critical stress is higher than indicated by the ideal gas approximation if Van der Waal's equation of state for helium is used and only approaches the result for the former at low gas pressures (small values of γ/r_0) [18].

Taking $\gamma = 1$ J m^{-2}, it follows that helium bubbles with radii ≥7.6 nm lying on boundaries perpendicular to the applied tensile stress will grow by this process at stresses ≥100 MPa. Intergranular helium bubbles of these dimensions have been observed to nucleate cavities that enlarge and coalesce to form cracks on the transverse grain boundaries in irradiated austenitic steels and alloys [1,7,19] in a manner analogous to the growth of cavities during thermal creep [20].

The stress-induced growth of the intergranular helium bubbles by grain boundary vacancy diffusion is accompanied by plating of atoms along the transverse boundaries. If all other deformation processes are neglected, this atom plating process produces a strain (ε) given by [21]:

$$\varepsilon = \frac{2a}{3d} \tag{13.3}$$

where a is the mean spacing of the grain boundary bubbles and d is the average grain size.

Thus, the ductility due solely to this process is low in coarse-grained steels with closely spaced grain boundary bubbles larger than the critical size.

The "in-reactor" creep-rupture lives of austenitic steels at stresses ≤100 MPa and temperatures of 700 to 750°C [9,10] and the high-temperature creep-rupture lives after irradiation or helium implantation at ambient temperature [22] are dependent on the inverse square or cube root of the tensile stress. These observations are consistent with the model of gas-driven growth of the intergranular helium bubbles [22,23], with the time required to grow the bubbles to the critical size constituting most of the time to rupture. However, the "in-reactor" times to failure at stresses of ≥100 MPa and those in post high-temperature irradiation tests are inversely proportional to the stress to a much higher power, indicating that the deformation is controlled by thermal dislocation creep processes.

Several approaches have been considered theoretically or shown experimentally to be beneficial in improving the post-irradiation high-temperature ductility of austenitic steels. These include grain refinement [24,25], trapping of the helium at particles within the grains [26,27], and the formation of precipitates at the grain boundaries to reduce their effectiveness as sources of vacancies [28], but a complete and practical solution to the problem of elevated-temperature intergranular helium embrittlement of austenitic alloys has not yet been realized.

The body-centered-cubic iron-based alloys, including the high-chromium ferritic and martensitic steels, are generally

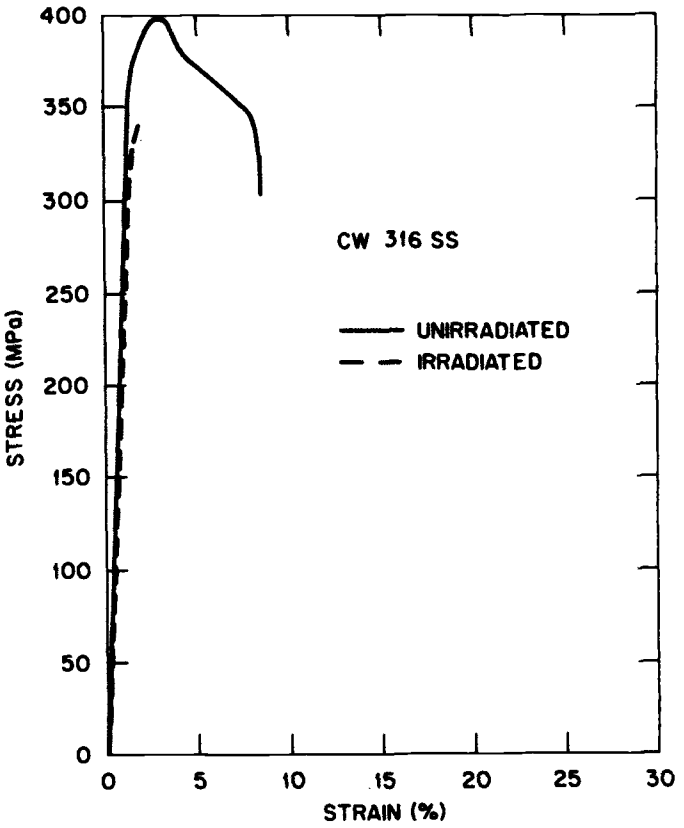

FIG. 13.1—Engineering stress-strain curves for 20% cold-worked type 316 stainless steel tensile tested at 700°C in the unirradiated condition and after irradiation in HFIR at 60°C to about 9 dpa and 230 appm He [5].

more resistant to intergranular helium embrittlement than the austenitic steels and alloys. Thus, the elevated-temperature tensile ductilities of the quenched-and-tempered fully martensitic 12Cr-MoVNb (1.4914) steel were not significantly affected in tests below the A_{C1} (ferrite-to-austenite) transformation temperature following thermal reactor irradiation, the samples failing in a ductile-transgranular manner in both the unirradiated and irradiated conditions [29,30]. However, there was a sharp reduction in the total elongation and a change to intergranular fracture when the tests were conducted above the A_{C1} temperature when some austenite was present. Similar observations were made on a quenched-and-tempered 12Cr-MoV (1.4923) steel after irradiation in the mixed-spectrum BR2 reactor at <100°C to 1 dpa and <1 appm He [31].

The tensile ductilities of modified 9Cr-1Mo and 12Cr-1MoVW (HT9) steels with and without additions of 2% Ni tested at 700°C and the low initial strain rate of 4×10^{-5} s^{-1} were not reduced after irradiation in HFIR at 50°C to ≈6 dpa and ≤49 appm He. The total elongation exceeded 20% for all the specimens [5]. In addition, while the 700°C tensile ductilities of duplex (martensite plus δ-ferrite) 13Cr-2Mo-1W steels, with and without a dispersion-strengthening addition of 4% TiO_2, was reduced after irradiation in the BR2 reactor at 60 or 700°C to induce a helium concentration of 10 appm (max), the total elongation remained above 10% in all cases [32].

The ambient and elevated-temperature tensile properties of the quenched-and-tempered 1.4914 steel have been determined following homogeneous implantation of 100 appm helium in 0.09-mm-thick specimens at temperatures in the range 20 to 750°C and of 100 to 340 appm helium in 0.2-mm-thick samples at 320 to 720°C by bombardment with degraded 28 MeV [33] and 104 MeV [34] α-particle beams, respectively. Furthermore, 0.15-mm-thick specimens of the reduced-activation 9Cr-0.5V and 9Cr-2W steels and the modified 9Cr-1Mo alloy have been implanted with up to 500 appm He at 400, 500, and 600°C using a 26 MeV ^3He beam [35]. Although small bubbles 4 to 22 nm diameter, nucleated at the prior austenite grain boundaries, lath boundaries, subboundaries within the laths, and precipitates, were readily observable by TEM [33–35], there was no evidence of elevated-temperature helium embrittlement in tension tests conducted at the implantation temperatures. The fractures remained ductile and transgranular.

Post-irradiation creep-rupture properties of normalized-and-tempered 1.4923 (12Cr-MoV) and 1.4914 (12Cr-MoVN6) steels were determined at 600°C after irradiation in the mixed-spectrum BR2 reactor at 590°C [37,38]. The 1.4923 is a 12Cr-1MoV-type steel, and the 1.4914 is similar to 1.4923, but it also contains Nb, B, and N in its composition along with less C. After irradiation, the 1.4923 contained ≈1 appm He compared to ≈90 appm He for 1.4914. There was little difference in the rupture lives of the irradiated and unirradiated 1.4923, but the rupture elongations diverged with increasing rupture times (decreasing stress). The irradiated 1.4914 had a shorter rupture life than the unirradiated material for high-stress tests and a longer rupture life for low-stress tests. Rupture elongation of the irradiated 1.4914 was less than for the unirradiated steel, but at long test times, the irradiated and unirradiated results appeared to converge, with values for the irradiated steel remaining above 5% for all tests. The rupture strength of the 1.4914 was greater than that of the 1.4923, but the rupture elongations of the two steels were similar. This occurred despite the larger amount of helium in the 1.4914 steel, and the results were taken as further evidence for the excellent elevated-temperature helium embrittlement resistance of these steels [37,38].

In addition to the tensile tests conducted on DIN 1.4914 specimens implanted to 100 appm He using a 28 MeV α-particle beam discussed above, post-implantation creep tests at 600 and 700°C were also conducted on such specimens [13,33,39]. Just as there was no effect in the tension tests, there was no effect of 100 appm He on creep-rupture properties. However, higher helium concentrations (≥1000 appm) markedly reduced the creep rates and the rupture elongations, indicative of radiation hardening by the implantation, particularly at 700°C. Nevertheless, the rupture times were increased relative to those of the unirradiated controls. Broadly similar behavior was exhibited in "in-beam" tests on the same steel at 600 and 700°C [13,33,39]. Ductilities were not significantly reduced with maximum helium concentrations of 3000 and 2700 appm He at 600 and 700°C, respectively, although some intergranular fracture was evident in the specimens with 3000 appm He tested at 700°C. TEM observations (Fig. 13.2) on the in-beam specimens indicated that the mean bubble radius in the matrix was larger than that at prior austenite grain boundaries and increased with

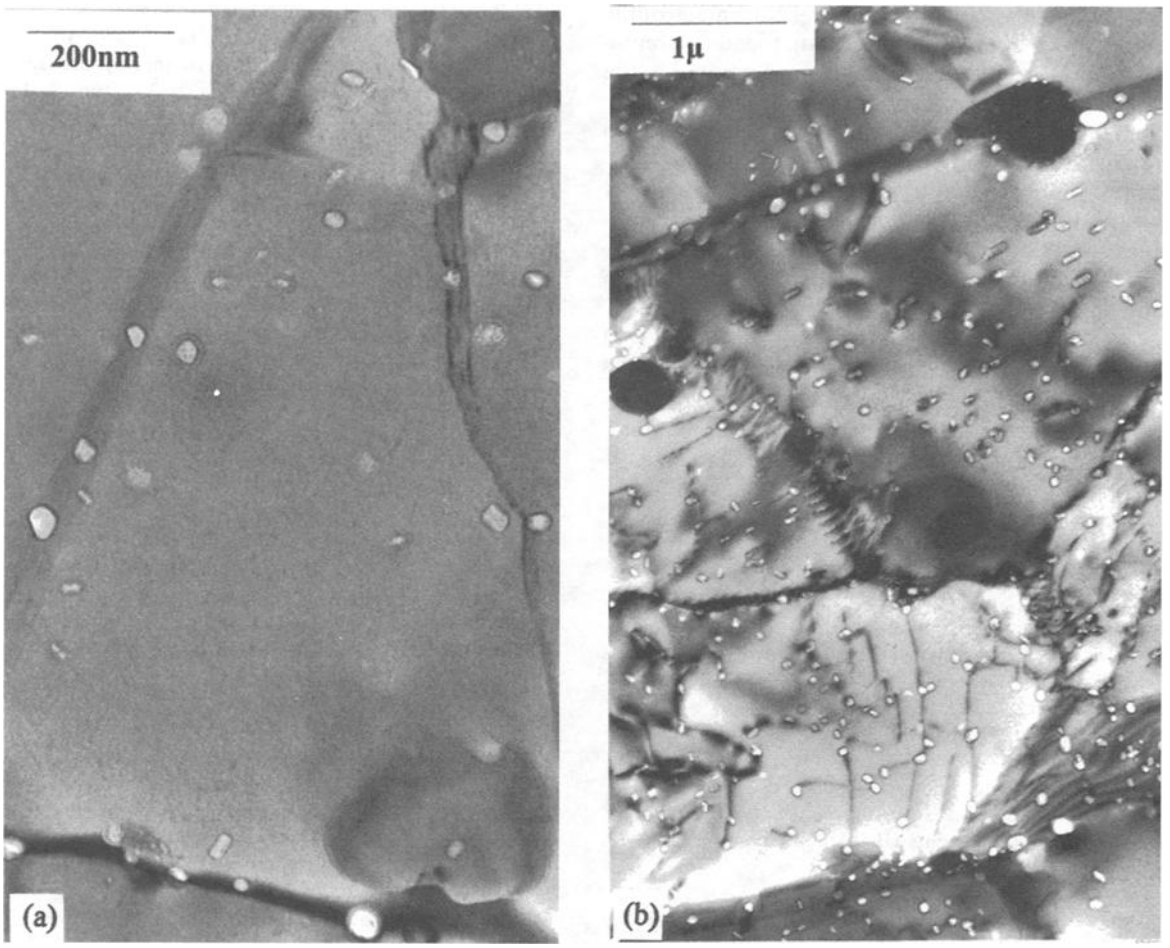

FIG. 13.2—TEM micrographs of DIN 1.4914 steel creep tested in a cyclotron γ-particle beam showing helium bubbles on prior austenite grain boundaries, lath boundaries, precipitates, and in the matrix after the following test conditions: (a) irradiated at 600°C, tested at 230 MPa, with 3000 appm He and (b) irradiated at 700°C, tested at 70 MPa, with 2700 appm He [33].

helium content and temperature; however, the number densities did not vary significantly. Thus, the bubble microstructures did not differ substantially from those observed under similar conditions for austenitic stainless steels that exhibit extensive elevated-temperature helium embrittlement [33].

Low-alloy ferritic/pearlitic and non-transformable ferritic steels appear to be less resistant to the elevated-temperature helium embrittlement than the transformable high-chromium martensitic steels. Thus, a low-alloy 0.13% C-0.24% Mo steel, which tends to fail intergranularly in the unirradiated condition, exhibited reductions in total elongation in tension tests at temperatures below the A_{C1} after thermal reactor irradiation, and no enhancement of the embrittlement was observed in tests above the transformation temperature [30]. In addition, large reductions in the tensile ductilities of a coarse-grained ferritic Fe-14% Cr-4% Al alloy have been recorded on testing in the range 700 to 950°C after thermal reactor irradiation at 50 or 650°C [40]. Furthermore, the non-transformable Types 405 (0.1% C:12% Cr) and 430 (17% Cr) ferritic steels showed decreases in total elongation from 52 to 33% and 89 to 48%, respectively, in tension tests at 700°C following α-particle bombardment to a helium concentration of about 40 appm [41].

Several possible reasons have been advanced to explain the greater resistance to high-temperature helium embrittlement of the bcc ferritic/martensitic steels compared to the austenitic steels. These include:

1. The high diffusion rate and grain boundary mobility in the bcc structures lead to stress relaxation at the boundaries, thereby delaying or preventing the development of intergranular cracks [29].
2. The high stacking fault energy coupled with a large effective energy for grain boundary fracture ($2\gamma = 2\gamma_S - \gamma_{GB}$, where γ_S and γ_{GB} are the surface and grain boundary energies, respectively) and a finer effective grain size combine to render the high-chromium martensitic steels more resistant to intergranular fracture [42].
3. The helium and helium clusters are trapped at the martensite lath boundaries and dislocations, thereby inhibiting the migration of helium and the development of large bubbles at the prior austenite grain boundaries [5,36].
4. Although numerous but small helium bubbles are generally observed in the irradiated or helium-implanted martensitic steels [31,33–35], the low strengths of these steels at elevated temperatures do not allow high tensile stresses to be developed at the orthogonal prior austenite grain

boundaries [14]. The critical radius (r_c) for catastrophic growth of the grain boundary bubbles that lead to premature intergranular fracture is inversely proportional to the applied tensile stress (σ_c of Eq 13.2) and is large in these steels; consequently, a very high helium concentration and/or long irradiation time are required to reach it.

5. The precipitates observed at the grain boundaries are very effective in preventing the boundaries from acting as efficient sources and sinks for vacancies and thus limit the growth of the helium bubbles and their coalescence to form cracks.

Additional experimental work and supporting theoretical studies are required to isolate the factors that determine the resistance of the high-chromium martensitic steels to elevated-temperature irradiation (helium) embrittlement and to further the understanding of the underlying mechanisms.

REFERENCES

[1] D. R. Harries, J. Brit. Nucl. Energy Soc. 5 (1966) 74.
[2] E. E. Bloom, in: Radiation Damage in Metals, Eds. S. D. Hackneys and N. L. Petersen (American Society for Metals, Metals Park, OH, 1976) 295.
[3] D. R. Harries, J. Nucl. Mater. 82 (1979) 2.
[4] L. K. Mansur and M. L. Grossbeck, J. Nucl. Mater. 155-157 (1988) 130.
[5] R. L. Klueh and J. M. Vitek, J. Nucl. Mater. 117 (1983) 295.
[6] E. E. Bloom, in: Irradiation Embrittlement and Creep in Fuel Cladding and Core Components (British Nuclear Energy Society, London, 1972) 93.
[7] H. Ullmaier, Nuclear Fusion 24 (1984) 1039.
[8] H. Schroeder, W. Kesternich, and H. Ullmaier, Nucl. Eng. Design/Fusion 2 (1985) 65.
[9] C. Wassilew, W. Schneider, and K. Ehrlich, Rad. Effects 101 (1987) 201.
[10] C. Wassilew, Irreversible Thermodynamic Models and Constitutive Equations of the Irradiation Induced Deformation and Damage Accumulating Processes, Kernforschungszentrum Karlsruhe, KfK Report 4668, November 1989 (in German).
[11] H. Schroeder, J. Nucl. Mater. 155-157 (1988) 1032.
[12] M. L. Grossbeck, K. Ehrlich, and C. Wassilew, J. Nucl. Mater. 174 (1990) 264.
[13] H. Schroeder and H. Ullmaier, J. Nucl. Mater. 179-181 (1991) 118.
[14] H. Ullmaier and H. Trinkhaus, Matls. Sci. Forum 97-99 (1992) 451.
[15] M. I. de Vries, in: Effects of Radiation on Materials: Eleventh International Symposium, ASTM STP 782, Eds. H. R. Brager and J. S. Perrin (American Society for Testing and Materials, Philadelphia, 1982) 665 and 720.
[16] H. Trinkhaus and H. Ullmaier, J. Nucl. Mater. 155 (1988) 148.
[17] E. D. Hyam and G. Sumner, in: Radiation Damage in Solids, Vol. 1 (International Atomic Energy Agency, Vienna, 1962) 323.
[18] R. M. Boothby, J. Nucl. Mater. 168 (1989) 343.
[19] R. M. Boothby, J. Nucl. Mater. 171 (1990) 215.
[20] D. R. Harries and C. M. Shepherd, in: Rupture Ductility of Creep Resistant Steels, Ed. A. Strang (The Institute of Metals, London, Book No. 522, 1991) 132.
[21] J. E. Harris, in: Vacancies '76 (The Metals Society, London, 1977) 170.
[22] H. Trinkhaus and H. Ullmaier, J. Nucl. Mater. 212-215 (1994) 303.
[23] R. Bullough, D. R. Harries, and M. R. Hayns, J. Nucl. Mater. 88 (1980) 312.
[24] W. R. Martin and J. R. Weir, J. Nucl. Mater. 18 (1966) 108.
[25] E. Hellstrand, R. Lagneborg, P. Lindhagen, R. Westin, and G. Ostberg, J. Nucl. Mater. 48 (1973) 1.
[26] W. Kesternich, M. K. Matta and J. Rothaut, J. Nucl. Mater. 122 and 123 (1984) 146.
[27] P. J. Maziasz, in: MiCon 86: Optimization of Processing, Properties, and Service Performance Through Microstructural Control, ASTM STP-979, Eds. B. L. Bramfitt, R. C. Benn, C. R. Brinkman, and G. F. Vander Voort (American Society for Testing and Materials, Philadelphia, 1988) 116.
[28] J. E. Harris, J. Nucl. Mater. 59 (1975) 303.
[29] H. Böhm and H. Hauck, J. Nucl. Mater. 21 (1967) 112.
[30] H. Böhm and H. Hauck, J. Nucl. Mater. 29 (1969) 184.
[31] C. Wassilew, K. Herschbach, E. Materna-Morris, and K. Ehrlich, in: Topical Conference on Ferritic Alloys for Use in Nuclear Energy Technologies, Eds. J. W. Davis and D. J. Michel (The Metallurgical Society of AIME, Warrendale, PA, 1984) 607.
[32] J.-J. Huet, A. Delbrassine, Ph. Van Asbroeck and W. Vandermeulen, in: Radiation Effects in Breeder Reactor Structural Materials, Eds. M. L. Bleiberg and J. W. Bennett (The Metallurgical Society of AIME, New York, 1977) 357.
[33] U. Stamm and H. Schroeder, J. Nucl. Mater. 155-157 (1988) 1059.
[34] A. Möslang and D. Preininger, J. Nucl. Mater. 155-157 (1988) 1064.
[35] A. Hasegawa and H. Shiraishi, J. Nucl. Mater. 191-194 (1992) 910.
[36] A. Hasegawa, H. Shiraishi, H. Matsui, and K. Abe, J. Nucl. Mater. 212-215 (1994) 720.
[37] C. Wassilew, in: Mechanical Behaviour and Nuclear Applications of Stainless Steel at Elevated Temperatures (The Metals Society, London, Book 280, 1982) 172.
[38] C. Wassilew, K. Ehrlich, and K. Anderko, in: Dimensional Stability and Mechanical Behaviour of Irradiated Metals and Alloys, Vol. I (British Nuclear Energy Society, London, 1983) 161.
[39] U. Stamm, Kernforschungsanlage Julich, Report Jul. 2225, August 1988.
[40] A. C. Roberts, D. R. Harries, D. R. Arkell, M. A. P. Dewey, and J. D. H. Hughes, in: Irradiation Effects in Structural Alloys for Thermal and Fast Reactors, ASTM STP 457 (American Society for Testing and Materials, Philadelphia, 1969) 312.
[41] D. Kramer, A. G. Pard, and C. G. Rhodes, in: Irradiation Embrittlement and Creep in Fuel Cladding and Core Components (British Nuclear Energy Society, London, 1972) 109.
[42] R. G. Faulkner and K. Anderko, J. Nucl. Mater. 113 (1983) 168.

14

Irradiation Effects on Impact Properties

A major concern for ferritic/martensitic steels in light-water reactors, fast reactors, and future fusion reactors is the effect of irradiation on fracture [1,2], as exhibited in a Charpy V-notch (CVN) test as an increase in the ductile-brittle transition temperature (DBTT) and a decrease in the upper-shelf energy (USE) (see Fig. 14.1) [3]. (Note that values for the Charpy energy in Fig. 14.1 and other figures in this chapter appear low relative to values normally reported for such steels; this is due to the use of the subsize Charpy specimens discussed in Chapter 8.) Such a change in properties is referred to as irradiation embrittlement [1,2] or low-temperature irradiation embrittlement to distinguish it from elevated-temperature helium embrittlement discussed in Chapter 13.

Although Charpy data are important to demonstrate the effect of irradiation on fracture during impact loading and they serve as a method for rating the relative irradiation resistance of different steels, they cannot be used by the reactor designer. Rather, fracture toughness data are used for that purpose. The limited fracture toughness data available at present for irradiated ferritic/martensitic steels will be discussed in the next chapter. Because the Charpy test is easier to conduct and the specimens can be more easily miniaturized for irradiation experiments, much of the information on the possible effect of irradiation on toughness comes from such tests.

Even if a steel has good Charpy properties before irradiation with a DBTT well below room temperature, it can be well above room temperature after irradiation. Irradiation embrittlement of ferritic steels is related to the hardening (see Chapter 12) caused by the production of dislocation loops, dislocation lines, and precipitates during irradiation below $\approx 0.4T_m$ [1,2]. Hardening causes an increase in flow stress, and, under the assumptions that the fracture stress is unaffected by irradiation and that the intersection of the fracture stress curve and the flow-stress curve (represented schematically in Fig. 14.2) defines the ductile-to-brittle transition temperature, the increase in flow stress causes a shift in the DBTT* [1].

In a fusion reactor, large amounts of transmutation helium will form in the first wall of the structure (see Chapter 8). Indications are that in addition to displacement-damage effects, the presence of helium in the irradiated steel can exacerbate the shift in DBTT. Both the effects of displacement damage and the effects of transmutation helium will be discussed in this chapter.

* Note that Fig. 14.2 is a schematic diagram to be used for this discussion. The intersection of flow stress and fracture stress does not strictly define the DBTT of a CVN test.

IRRADIATION EMBRITTLEMENT: DISPLACEMENT DAMAGE EFFECTS

Effect of Fluence and Temperature

Tension tests demonstrated that hardening occurred in normalized-and-tempered MANET II and quenched CETA steels irradiated in the Saphir reactor to 0.042 dpa at 250°C and 0.13 dpa at 405°C (see Chapter 12) [4]. Miniature Charpy specimens of these steels were irradiated in the same experiment to the same fluences. Even at these low doses, there was a significant shift in the DBTT (Fig. 14.3), with the largest shift occurring for the higher fluence at 400°C [4]. For the CETA with its untempered martensite microstructure, a shift of 145°C was observed [Fig. 14.3(b)], which compared with a shift of about 40°C for the MANET II [Fig. 14.3(a)] with a tempered martensite microstructure. Smaller shifts were noted for the low-dose irradiations at 250°C. Although the CETA steel showed a large ΔDBTT, it needs to be emphasized that this was for an untempered martensite, and throughout this chapter and other chapters, the martensitic steels being discussed are in the tempered condition unless otherwise indicated. The tempered martensite of the MANET II showed a significantly smaller shift for the same irradiation conditions (Fig. 14.3) [4].

Figure 14.1 shows results for a more typical irradiation experiment. Here a shift in DBTT (ΔDBTT) of ≈160°C was observed on one-half-size Charpy specimens of 12Cr-1MoVW steel (HT9) irradiated to 10 dpa at 365°C in FFTF [3]. Irradiation to 17 dpa gave a similar shift to the one for 10 dpa, indicating that there was a saturation in the shift with increasing fluence (Fig. 14.1). This agrees with the saturation observed for hardening in a tensile test of the same steel irradiated similarly (see Chapter 12) [5]. Although the Charpy curves are shifted by irradiation hardening, the fracture mode is generally unaltered between the unirradiated and irradiated steels: cleavage or quasi-cleavage is the dominant fracture mode on the lower shelf (occasional, scattered indications of intergranular fracture are observed), and ductile void coalescence (dimpled fracture surface) occurs on the upper shelf.

Below 400 to 450°C, the magnitude of the shift caused by displacement damage varies inversely with irradiation temperature, as shown in Fig. 14.4 for MANET I steel irradiated to 5 dpa in the HFR at 300, 400, and 475°C [6]. To demonstrate the origin of the shift, a specimen irradiated at 300°C was annealed 0.5 h at 535°C and impact tested at 500°C, and part of the loss in USE was recovered [6] (annealing to restore prop-

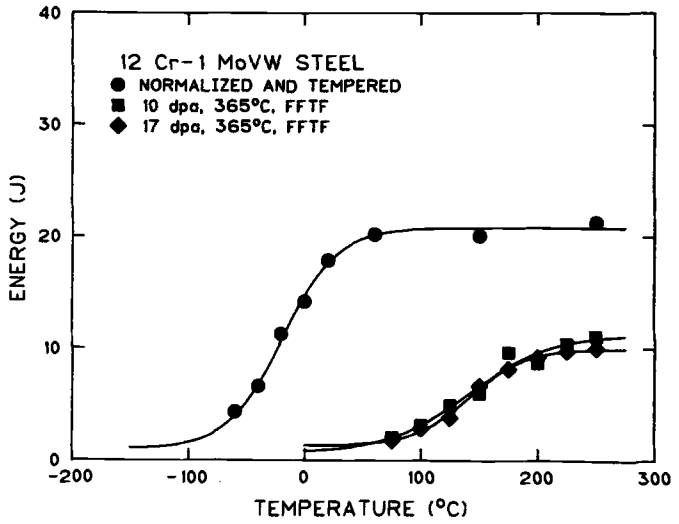

FIG. 14.1—Charpy curves for half-size specimens of 12Cr-1MoVW steel before and after irradiation to 10 and 17 dpa at 365°C in FFTF [3].

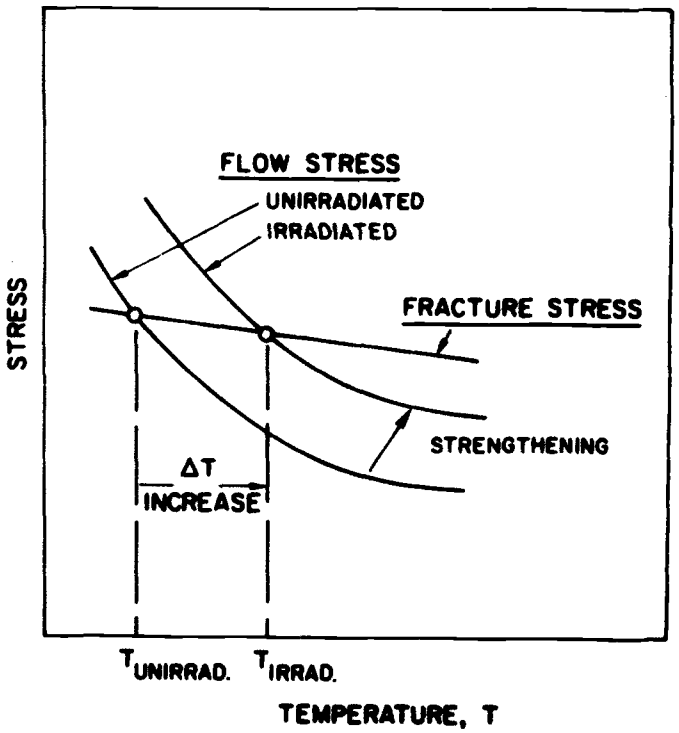

FIG. 14.2—Schematic diagram that illustrates how strength increase due to irradiation causes a shift in the ductile-brittle-transition temperature [1].

erties will be discussed in Chapter 17). Such an anneal "dissolves" the irradiation-induced defect structures (particularly tiny interstitial clusters) and coarsens the dislocation structure that causes hardening and embrittlement [7].

Most irradiation studies of Charpy behavior have involved specimens irradiated in fast reactors between ≈360 to 600°C (lower temperatures are generally not possible in fast reactors) [3,8,9–11]. Hu and Gelles [8] irradiated 9Cr-1MoVNb

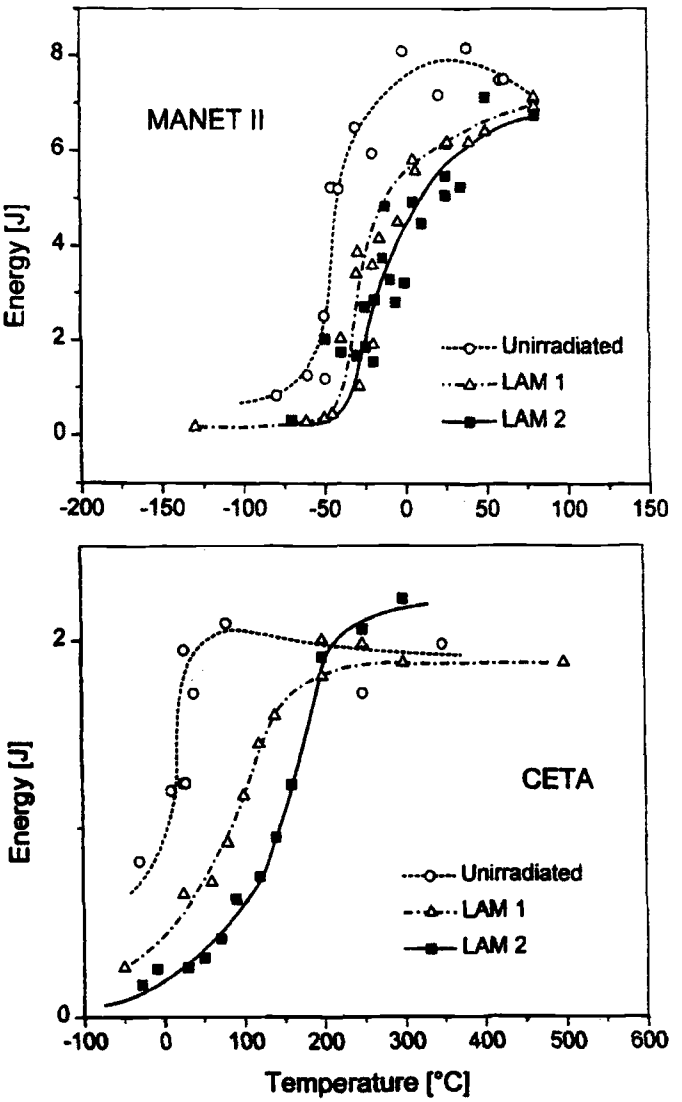

FIG. 14.3—Charpy curves for MANET II and CETA irradiated to 0.042 dpa at 250°C (LAM 1) and to 0.13 dpa at 400°C (LAM-2) in the Saphir reactor [4].

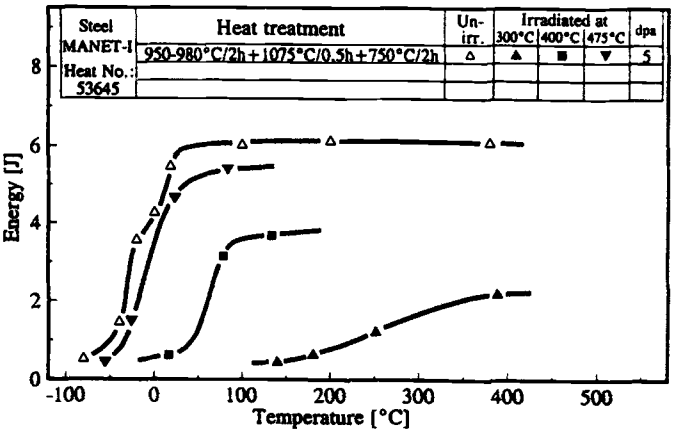

FIG. 14.4—Effect of irradiation temperature on the impact properties of MANET I steel [6].

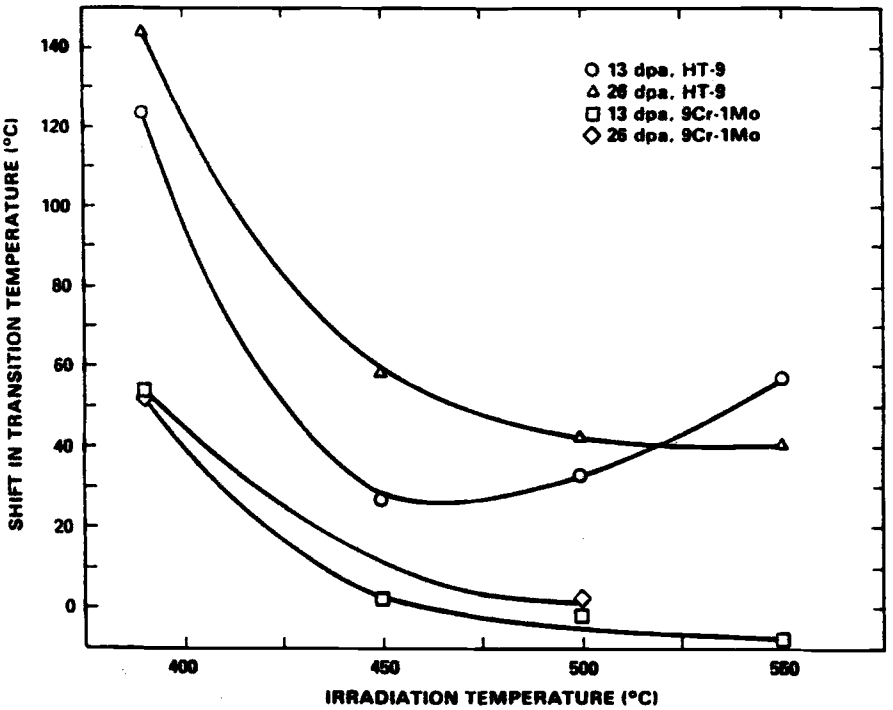

FIG. 14.5—Irradiation temperature and fluence effect on the shift in transition temperatures for 9Cr-1MoVNb (modified 9Cr-1Mo) and 12Cr-1MoVW (Sandvik HT9) steels [8].

(modified 9Cr-1Mo) and 12Cr-1MoVW steels at 390, 450, 500, and 550°C in EBR-II to 13 and 26 dpa (Fig. 14.5). For the 9Cr-1MoVNb irradiated at 390°C, the ΔDBTT saturated by 13 dpa (values of 52 and 54°C were obtained after 13 and 26 dpa, respectively). Irradiation of the 9Cr-1MoVNb steel at 450, 500, and 550°C caused little change in the DBTT, in agreement with observations on this steel that hardening vanishes in a tensile test above 425 to 450°C (see Fig. 12.2) [5]. This was verified by Hu and Gelles with Rockwell hardness measurements on their Charpy specimens that showed hardening occurred only for the specimens irradiated at 390°C [8].

It was concluded that saturation also occurred for the 12Cr-1MoVW steel irradiated at 390°C [10], although the values of 124 and 144°C obtained after 13 and 26 dpa, respectively, showed a somewhat larger difference than for the 9Cr-1MoVNb steel [8]. As seen in Fig. 14.5, the ΔDBTT for the 12Cr-1MoVW steel did not go to zero at 450, 500, and 550°C, as observed for the 9Cr-1MoVNb and as observed for the change in yield stress [5] and change in hardness [8] for both of 9Cr-1MoVNb and 12Cr-1MoVW steels irradiated at the same temperatures. The difference in the observations on the two steels is caused by the difference in the microstructures of the two steels (Fig. 14.6) [12]. The 12Cr-1MoVW steel contains twice as much carbon as the 9Cr-1MoVNb steel, and in the normalized-and-tempered condition, the 12Cr-1MoVW contains over twice as much precipitate (3.8 wt% precipitate in the 12Cr-1MoVW compared to 1.5 wt% in 9Cr-1MoVNb). The majority of the precipitate in both steels is $M_{23}C_6$, with a small amount of MC. A larger amount of larger precipitate particles is relatively uniformly distributed in the 12Cr-1MoVW steel [12]. Fracture in steels is generally initiated at carbide particles or inclusions [13,14].

The precipitate structure of the 12Cr-1MoVW steel can be used to explain the observation that ΔDBTT did not go to zero. The critical stress to propagate a crack is inversely proportional to the crack length [13]. If it is assumed that fracture initiation occurs at an $M_{23}C_6$ particle (the dominant precipitate) and the crack length at initiation equals the diameter of a carbide particle, then the fracture stress (see Fig. 14.2) will decrease with increasing precipitate size. (A more recent micromechanical description of the fracture process in tempered martensite will be discussed later in this chapter.) The precipitate particles coarsen during irradiation at 400 to 500°C [15–17], thus causing a decrease in fracture stress and an increase in DBTT (Fig. 14.2), even in the absence of further hardening. At 500°C, considerably more coarsening was observed for the 12Cr-1MoVW than the 9Cr-1MoVNb [17]. Therefore, the fact that the ΔDBTT for 12Cr-1MoVW steel increased between 13 and 26 dpa at 390°C and did not go to zero at 450 to 550°C even though hardening disappeared at these temperatures [18] can be attributed to coarsening of the large precipitates during irradiation at the higher temperatures.

The 9Cr-1MoVNb and 12Cr-1MoVW steels were also irradiated in HFIR at ≈50°C up to ≈10 dpa [19,20]. Contrary to what occurred at 390°C in EBR-II, the ΔDBTT for the 9Cr-1MoVNb steel (≈135°C) was larger than that for the 12Cr-1MoVW steel (≈55°C). The most logical explanation for this observation is that the change in irradiation temperature caused a change in fracture behavior for one of the steels. Support for this is found in work by Gelles et al. [21,22], who observed δ-ferrite stringers on the cleavage fracture surface of 12Cr-1MoVW steel irradiated in EBR-II at 390°C [22] but not after irradiation at 50°C in HFIR [21]. They concluded

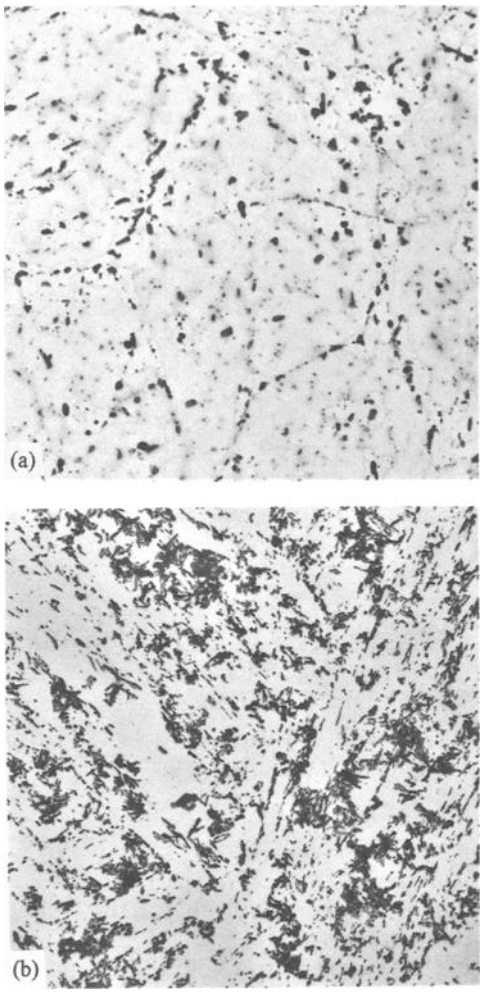

FIG. 14.6—Extraction replicas of normalized-and-tempered (a) 9Cr-1MoVNb and (b) 12Cr-1MoVW steels [12].

that the large ΔDBTT for 12Cr-1MoVW at 390°C was due to "precipitation at δ-ferrite stringers" in the 12Cr-1MoVW steel [22], although they concluded further that the reason for the difference between 9Cr-1MoVNb and 12Cr-1MoVW steels at 50°C was due to an irradiation effect on the 9Cr-1MoVNb. Carbide crystal structure alteration due to recoil dissolution was suggested as a possibility [21].

An alternate suggestion was that the explanation for the observations need only involve the change in fracture behavior of the 12Cr-1MoVW steel [23]. That is, neutron irradiation at 50°C has an inherently greater relative hardening effect on 9Cr-1MoVNb than 12Cr-1MoVW, and then the magnitude of the effect reverses at higher temperatures because of the precipitation and precipitate coarsening that occurs in the 12Cr-1MoVW steel [23]. This is consistent with the above explanation for the difference between the impact behavior of the 9Cr-1MoVNb and 12Cr-1MoVW steels at 390 to 550°C. Because of the irradiation-enhanced diffusion at 390°C in EBR-II, precipitates can form at δ-ferrite/martensite interfaces of the 12Cr-1MoVW steel (no δ-ferrite is present in the 9Cr-1MoVNb) during irradiation, and these precipitates can cause a change in fracture behavior. No such diffusion-assisted precipitates would be expected after 10 dpa at 50°C. Thus, although the ΔDBTT of 12Cr-1MoVW at 50°C is about half as large as the ΔDBTT of 9Cr-1MoVNb, the change in fracture process for the 12Cr-1MoVW makes the ΔDBTT of the latter steel over twice that of the former at the higher temperatures [23].

In addition to the growth of $M_{23}C_6$ precipitates, chromium-rich α′ precipitates form during irradiation in the 12Cr steel, but not in the 9Cr steel [16]. Because the δ-ferrite is enriched in chromium, more α′ would be expected to form in this phase, and since α′ can harden the lattice, this could further embrittle the steel.

The explanation involving δ-ferrite for the different relative behavior of 9Cr-1MoVNb and 12Cr-1MoVW at 50 and 390°C is supported by work [24,25] that indicates the δ-ferrite in 12Cr steels does not by itself cause early cleavage, as suggested by other investigators [26]. In fact, the relatively soft δ-ferrite can improve the ductility and toughness [25]. Rather, it was concluded [24,25] that fracture initiated at $M_{23}C_6$ precipitates on the δ-ferrite/martensite interface.** Therefore, the fact that δ-ferrite stringers were not observed by Hu and Gelles on the 12Cr-1MoVW fracture surface after the 50°C irradiation suggests that the absence of interface precipitation at 50°C may be responsible for the inherently better behavior of 12Cr-1MoVW than 9Cr-1MoVNb at 50°C. At higher temperatures where precipitation occurs, including α′ precipitation in the 12Cr-1MoVW steel but not the 9Cr-1MoVNb steel, the carbides on the δ-ferrite/martensite interface cause a larger ΔDBTT for 12Cr-1MoVW than 9Cr-1MoVNb [23]. Detailed TEM and SEM are required to determine the actual mechanism.

It should be pointed out that no δ-ferrite was detected in some of the heats of 12Cr-1MoVW studied [12,16,17], compared to a few percent found by Hu and Gelles [22]. This may mean that there was a very small amount present but not detected, or the more extensive precipitation and radiation-induced growth of $M_{23}C_6$ precipitates and formation of the α′ in 12Cr-1MoVW (compared to the 9Cr-1MoVNb) in the temperature range 300 to 500°C discussed above is responsible for the relative change in impact behavior of 9Cr-1MoVNb and 12Cr-1MoVW between 50 and 400°C.

French investigators studied the Charpy properties of F17 (ferritic) steel cut from two wrapper tubes irradiated in Phénix up to ≈63 and 100 dpa in the range ≈390 to 540°C [27–29]. There was no difference in the Charpy properties after irradiation to 63 and 100 dpa. The DBTT decreased with increasing irradiation temperature, but even at 548°C, the irradiated steel had a ΔDBTT of 100°C. Hardening of the 17% Cr steel at the higher temperatures was associated with irradiation-enhanced nucleation and growth of α′ relative to that formed by thermal aging alone, where α′ causes 475°C embrittlement (see Chapter 4). The increased effect of irradiation on Charpy behavior with decreasing irradiation temperature was ascribed to the high density of irradiation-induced dislocations that are immediately locked by the α′ precipitate. Contrary to the tensile behavior, where it takes up to 40

** Although it is assumed that the $M_{23}C_6$ interface precipitates discussed here grew during irradiation, these precipitates can grow also from the chromium-enriched δ-ferrite under other conditions. For example, $M_{23}C_6$ precipitate with a dendritic morphology can form at the interface when the cooling rate from the melt is too slow [25].

dpa for the loss in total elongation to saturate with fluence at temperatures below 420°C, the saturation in the shift in DBTT and reduction in USE occurred at low fluence (<5 dpa) [28].

For comparison with the F17, EM10 (100% tempered martensite) steel and EM12 (70% martensite, 30% δ-ferrite) steel wrappers along with Charpy specimens were irradiated to 90 dpa at 390 to 580°C in the Phénix reactor. The Charpy properties of EM10 and EM12 were nearly unchanged over the range 390 and 580°C (Fig. 14.7). The slightly smaller DBTT for EM10 at the lowest irradiation temperatures shown in Fig. 14.7 was for specimens taken from the bottom of the wrapper, where the dose was described as negligible (at the other irradiation temperatures, irradiation was to 90 dpa) [29]. As was true for the F17 results, the EM10 and EM12 steels also showed a shift in DBTT after irradiation above 400°C. The shift for EM12 at 400°C was ≈60°C, compared to ≈45°C for the EM10 and about 330°C for F17. This means that the DBTT of the EM12—the duplex steel—falls between the values for the fully martensitic EM10 and the fully ferritic F17. Above 500°C, the DBTT values of EM12 and F17 were similar (Fig. 14.7).

The microstructures of the three steels were examined after irradiation to 70 to 90 dpa at 420 to 440°C. The EM10 had the most stable microstructure. Scattered voids were observed, with the major precipitate phase being the $M_{23}C_6$, most of which was present before irradiation. The only irradiation-induced precipitate observed was Laves phase. The EM12 showed more void formation, a higher density of voids being observed in the δ-ferrite than the tempered martensite; this steel also showed a dense precipitation of chi-phase,

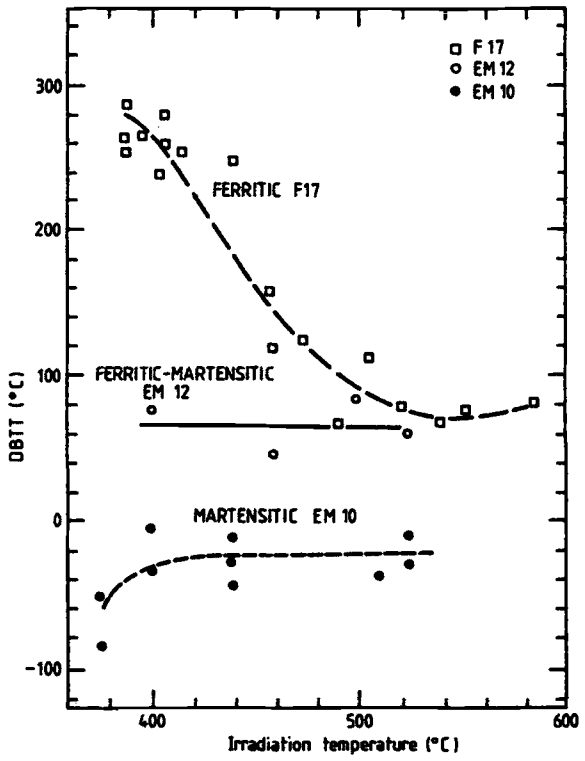

FIG. 14.7—A comparison of the DBTT of F17, EM 12, and EM-10 steels irradiated in the Phénix reactor [29].

which was blamed for the deterioration of properties in this steel. Finally, the F17 steel had the highest void density, and the voids were associated with the high number density of α'.

Like modified 9Cr-1Mo steel, the EM10 is a 9Cr-1Mo tempered martensite steel, but it differs from the modified 9Cr-1Mo steel in that it is not stabilized with niobium and vanadium (it contains no niobium and only 0.03% V compared to 0.06% Nb and 0.25% V for the modified 9Cr-1Mo steel). The shift in DBTT observed for the EM10 above 450°C and not for modified 9Cr-1Mo may be caused by this compositional difference, which may allow the formation of Laves in the EM10 during irradiation. Laves phase is generally suppressed by irradiation in the range 300 to 600°C for these steels, and it has not been observed in modified 9Cr-1Mo steel after irradiation (see Chapter 10).

Kimura et al. [30] examined the effect of irradiation temperature on the impact properties of reduced-activation 9Cr-2WVTa steels irradiated in FFTF up to 22 dpa at 390 and 460°C and in JMTR to 0.0063 dpa at 60°C. At 390°C where hardening occurred, a ΔDBTT of ≈40°C was observed, compared to a value of ≈54°C for modified 9Cr-1Mo irradiated in EBR-II [8]. Although irradiation at 460°C produced a softening, a shift in DBTT of ≈15°C was observed for the 9Cr-2WVTa. Despite a displacement damage of only 0.0063 dpa in the JMTR irradiations at 60°C, the shift in DBTT was 35 to 40°C [30].

Microstructural examination of the FFTF-irradiated steels indicated the presence of dislocation loops and small $M_{23}C_6$ precipitates for the specimens irradiated at 390°C [30]. No loops or small $M_{23}C_6$ precipitates were observed for the specimens irradiated at 460°C, but tantalum-rich M_6C and tungsten-rich Fe_2W Laves phase were observed. It was concluded that M_6C and Laves phase are detrimental to the cleavage fracture toughness, and they account for the increase in DBTT at 460°C in the absence of hardening [30]. (The possible effect of tantalum on the shift in DBTT will be discussed later in this chapter.) A linear relationship between the shift in DBTT and hardening for these steels was developed and compared with data for modified 9Cr-1Mo steel (Fig. 14.8). Such a linear relationship has also been developed for the light-water reactor pressure-vessel steels [31,32].

The ΔDBTT is related to irradiation hardening (increase in yield stress, $\Delta\sigma_y$), and hardening, like ΔDBTT, is generally observed to saturate with fluence. As described in Chapter 12 on tensile behavior, there have been several observations of a maximum in hardening with fluence [33–35]. Until recently, no evidence was found of a maximum in the DBTT or ΔDBTT with fluence. For example, in the experiment where Khabarov et al. [35] found a maximum in yield stress with dose for the 13Cr-2MoNbVB steel irradiated to 4 to 85 dpa at 350 to 365°C in a fast reactor (see Chapter 12), no maximum was observed for the DBTT. They did show data that indicated the USE went through a minimum at 30 to 40 dpa. Embrittlement of the steel irradiated at 280 to 420°C was attributed to the voids, dislocation loops, and α' precipitates that formed during irradiation [35].

Recently, Kohno et al. [36] found a maximum in DBTT for JLF-1 steel irradiated in FFTF to 60 dpa at 410°C. Evidence of a possible maximum in DBTT was also observed for 12Cr-1MoVW steel irradiated to 35 and 100 dpa in FFTF (this experiment will be discussed in more detail in the following

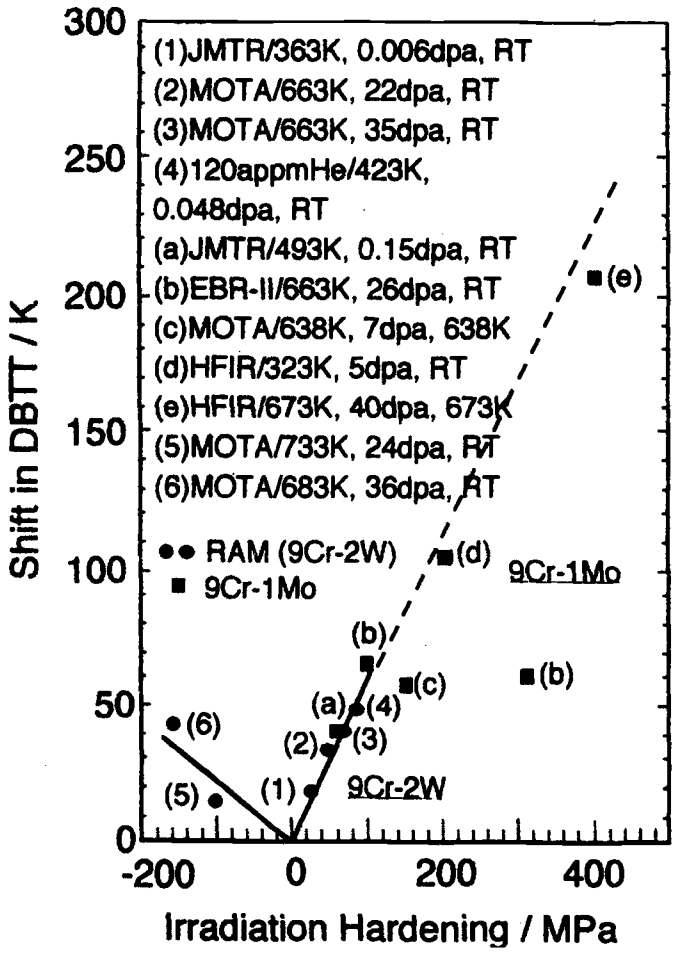

FIG. 14.8—Relationship between the shift in DBTT and irradiation hardening (change in yield stress) for 9Cr-2WVTa and 9Cr-1MoVNb steels. Legend of data refers to: reactor/irradiation temperature, dose, tension test temperature [30].

section) [37]. It would appear that a high fluence and/or high irradiation temperature are required before a maximum is observed. This observation implies that the strength and impact properties are a balance between the point defect production and irradiation-induced precipitation hardening, which harden the steel, and irradiation-accelerated recovery and aging, which soften the steel, the latter processes becoming more important at high fluences and/or higher irradiation temperatures. As mentioned earlier, hardening in most of these steels ceases above 425 to 450°C because of recovery and thermal aging processes.

Effect of Heat Treatment

To study the effect of heat treatment on the irradiation effects on the Charpy impact toughness of 9Cr-1MoVNb and 12Cr-1MoVW steels [37,38], four plates of each steel were given different normalizing-and-tempering treatments: normalization with austenitization at 1040 or 1100°C was followed by tempering 1 h at 760 or 2.5 h at 780°C. One-third size Charpy specimens were tested in each heat-treated condition, as well as after thermal aging and after irradiation in FFTF at 365°C to 4–5 [37] and 20 dpa [38]. Specimens normalized at 1040°C and tempered at 760 and 780°C were also irradiated at 420°C to 35–36 [37] and 100 dpa [38]. The different austenitizing treatments caused a small difference in average prior-austenite grain size for the 9Cr-1MoVNb steel (≈20 and 32 mm for the 1040 and 1100°C treatments, respectively) and a larger difference for 12Cr-1MoVW steel (≈32 to 45 and 90 to 125 mm for the 1040 and 1100°C treatments, respectively). The smaller change for the 9Cr-1MoVNb was attributed to the niobium in this steel, as niobium carbide inhibits austenite grain growth during the austenitization [39].

If the effect of austenitizing temperature on properties is taken to imply an effect of prior austenite grain size, then for the 9Cr-1MoVNb steel, prior austenite grain size had an effect on DBTT, with the steel austenitized at 1040°C having the lowest value [Fig. 14.9(a)] [38]. There was less difference in the USE [Fig. 14.9(b)]. The normalized-and-tempered 12Cr-1MoVW steel showed a different behavior. Although a change in austenitization temperature for this steel produced a larger

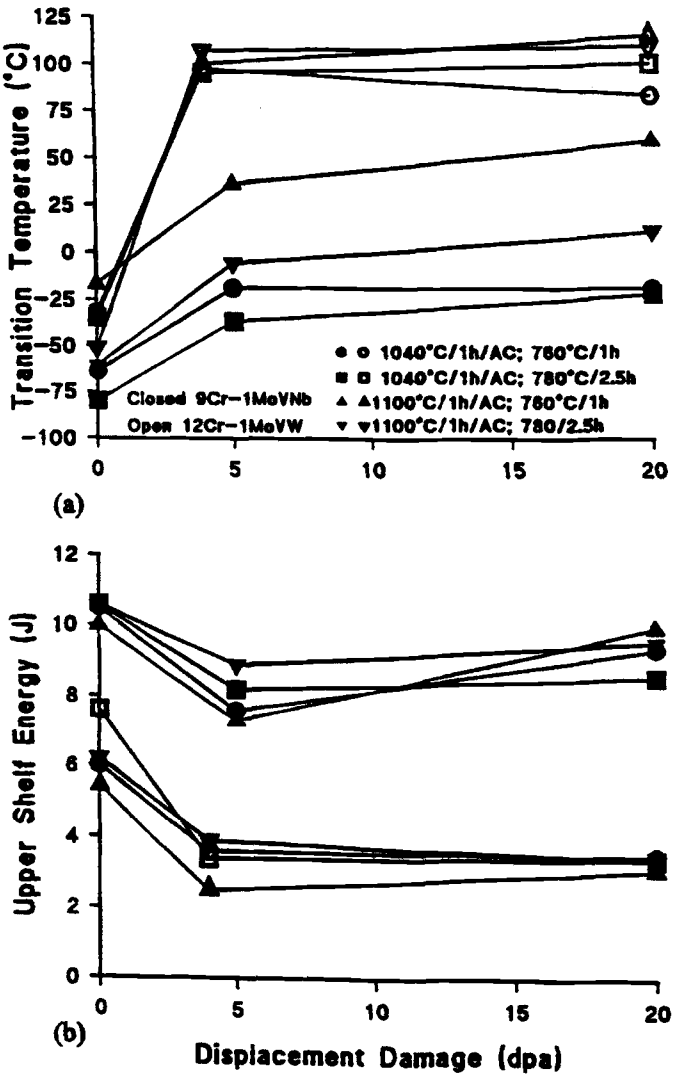

FIG. 14.9—The (a) ductile-brittle transition temperature and (b) upper-shelf energy as a function of displacement damage for 9Cr-1MoVNb and 12Cr-1MoVW steels with four different heat treatments after irradiation at 365°C in FFTF [38].

difference in prior austenite grain size than for 9Cr-1MoVNb, there was very little effect of prior austenite grain size on DBTT [Fig. 14.9(a)]. Tempering (for the two normalization treatments used) also had only a small effect. The USE of the 12Cr-1MoVW in the normalized-and-tempered condition appeared to be affected by tempering, because for each austenitizing treatment, the steel tempered at 780°C had a higher USE than that tempered at 760°C [Fig. 14.9(b)] [37]. Thermal aging for up to 20 000 h at 400°C had little effect on the Charpy behavior of the 9Cr-1MoVNb and 12Cr-1MoVW steels [37].

The lack of a prior austenite grain size effect in 12Cr-1MoVW steel compared to 9Cr-1MoVNb steel in the unirradiated condition probably indicates that the precipitate in the microstructure of the 12Cr-1MoVW rather than the prior austenite grain size controls the fracture behavior [37]. As seen in Fig. 14.6, the larger amount of larger precipitates relatively uniformly distributed in the 12Cr-1MoVW steel could dictate the fracture behavior, as discussed in the previous section.

The results on the unirradiated 9Cr-1MoVNb and 12Cr-1MoVW agreed with results of Little et al. [40], who studied a 12Cr-0.9Mo-0.3V-0.14C steel. They observed an increase in DBTT from −90 to −60°C when austenitized at 950 and 1050°C, respectively. The change was attributed to a change in prior austenite grain size [40]. There was no change in the USE. The main difference between this steel and the 12Cr-1MoVW steel involves the carbon content. Based on the microstructural studies of Little et al., it was concluded [37] that the reason their steel showed a prior austenite grain size effect and the 12Cr-1MoVW steel did not was probably due to the lower carbon content, which caused a much finer precipitate distribution to form in the steel of Little et al., who noted an increase in USE with increasing tempering temperature and time. Little et al. also examined a 12Cr-0.6Mo-0.15V-0.25Nb-0.1C steel, a steel more similar to the 9Cr-1MoVNb steel than the 12Cr-1MoVW steel because of the niobium and lower carbon, although it had considerably more niobium than the 9Cr-1MoVNb steel. They found that the niobium stabilized the prior austenite grain size, similar to the observations on the 9Cr-1MoVNb steel [37]. Because of the larger amount of niobium in the steel of Little et al., it was not possible to change the prior-austenite grain size by the austenitizing treatments used [40].

An effect of austenitization temperature on DBTT was also observed for MANET II [41] and F82H [42] steels austenitized between 900 and 1050°C, which was attributed to the change in prior austenite grain size. A change of DBTT (°C)/change in austenitization temperature (°C) of ≈0.25°C/°C can be determined for the steels for austenitization at 900 to 1050°C and then tempered at 750°C for 1 h. After tempering at 700°C, the changes were ≈0.40 and 0.18°C/°C for MANET II and F82H, respectively. This difference reflects the differences in tempering behavior of the two steels. The value after the 750°C temper should be closer to reflecting the effect of the austenitization treatment, since the higher temperature should fully temper both steels. More work would be required to determine whether the 0.25°C/°C for the two different steels after the 750°C temper can be taken as a value for any steel of this type.

Irradiation of the 9Cr-1MoVNb and 12Cr-1MoVW steels with the different heat treatment conditions at 365 (Fig. 14.9) and 420°C (Fig. 14.10) in FFTF caused an increase in DBTT and a decrease in USE for all conditions [37,38], with the shift in DBTT for the 12Cr-1MoVW steel being over twice that for 9Cr-1MoVNb. The relative differences in DBTT of the 9Cr-1MoVNb steel with the different normalizing-and-tempering treatments was the same after 5 dpa at 365°C as it was unirradiated [Fig. 14.9(a)]. After 20 dpa, the difference for the plates austenitized at 1100°C and tempered at 700 and 750°C remained, but there was a convergence in the DBTT for the two 9Cr plates austenitized at 1040°C [Fig. 14.9(a)]. These results indicate that, at least for the 9Cr-1MoVNb and steels like it, it may be possible to improve the irradiation resistance of the impact properties by the heat treatment used.

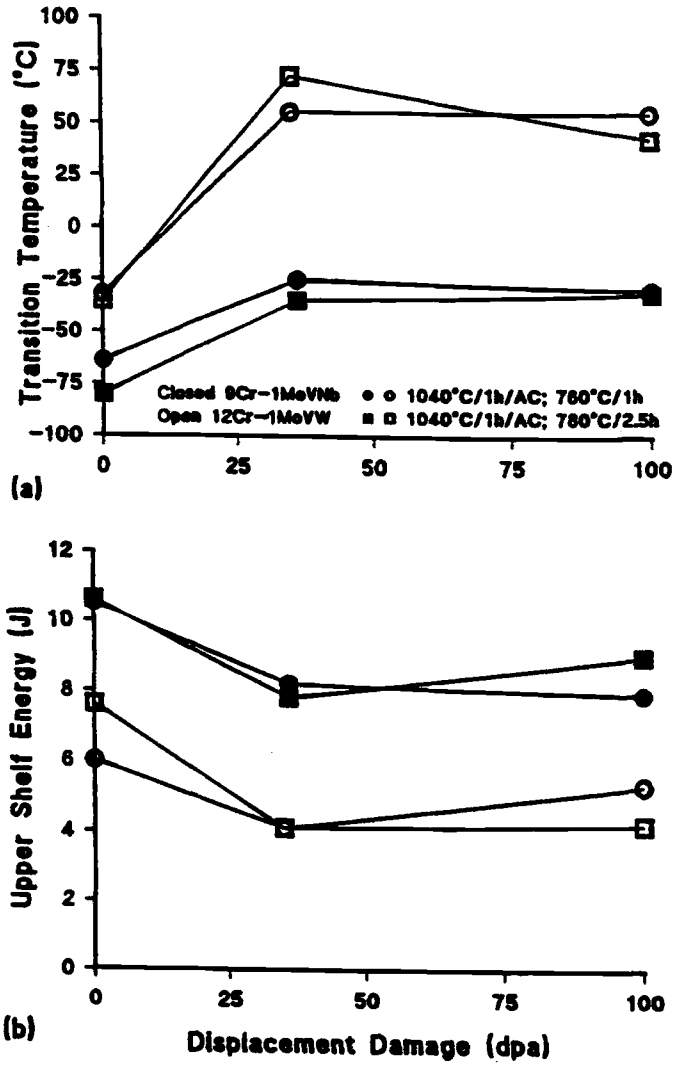

FIG. 14.10—The (a) ductile-brittle transition temperature and (b) upper-shelf energy as a function of displacement damage for 9Cr-1MoVNb and 12Cr-1MoVW steels with two different heat treatments after irradiation at 420°C in FFTF [38].

Although the 12Cr-1MoVW steel showed a somewhat larger variation in prior-austenite grain size than the 9Cr-1MoVNb steel, it showed a smaller variation in transition temperature for the four heat-treated conditions in both the normalized-and-tempered condition and after irradiation at 365°C (Fig. 14.9). The most variation occurred after 20 dpa,

where the specimens with the smallest prior-austenite grain size had the lowest transition temperature [Fig. 14.9(a)]. Larger precipitates were postulated to minimize the role of the prior austenite grain size for the higher-carbon 12Cr-1MoVW steel [37,38].

Possible confirmation that carbide particles are a source of cracks is the relative behavior of the DBTT [Fig. 14.9(a)] with different heat treatments after irradiation at 365°C. The 12Cr-1MoVW steel with the smallest grain size had the lowest DBTT after 20 dpa, but the effect of tempering temperature was different from what was expected: the 12Cr-1MoVW steel tempered at 780°C had the higher DBTT. The opposite is expected, because under most conditions, a higher tempering temperature reduces the strength, which improves Charpy properties [39]. However, the higher tempering temperature will also produce larger precipitate particles, thus enhancing fracture. Note that the opposite occurs for the 9Cr-1MoVNb steel [Fig. 14.9(a)], which contains the smaller particles. The results indicate that the 2.5 h temper at 780°C that is often used for the 12Cr-1MoVW steel could be replaced by shorter times at a lower temperature, thus providing an improved strength without a reduction in toughness.

Observations on DBTT after irradiation at 420°C indicate that for the 9Cr-1MoVNb steel the saturation with fluence that occurs is independent of the tempering conditions [Fig. 14.10(a)]. A similar conclusion follows for the 12Cr-1MoVW steel, except specimens tempered at 780°C may go through a maximum, although there is a limited amount of data to make such a conclusion. Indications are that the precipitates in the steel grow during irradiation [16,17]. This probably means that precipitate particles in the 12Cr-1MoVW steel plates tempered at 760°C reached a size during the 100 dpa irradiation where further irradiation-enhanced growth does not affect fracture properties, thus giving the steels tempered at 760 and 780°C a similar DBTT.

The change in the USE with heat treatment and irradiation appeared more random than for the DBTT [37,38]. In most cases, USE values after 20 dpa at 365°C [Fig. 14.9(b)] or 100 dpa at 420°C [Fig. 14.10(b)] were equal to or greater than those after the previous irradiations. The relatively small change in USE for the 9Cr-1MoVNb steel up to 100 dpa at 420°C and 20 dpa at 365°C shows the superior behavior of this steel. In the normalized-and-tempered condition, the 9Cr-1MoVNb steel has a higher USE than the 12Cr-1MoVW steel, thus making the relative change for the 9Cr-1MoVNb steel considerably less.

For the above discussion on the effect of austenitization temperature, it was assumed that the observed effect was caused by a change in prior-austenite grain size. In reality, lath packet size can also be affected by the austenitization temperature, and it may affect fracture behavior. Odette, Lucas, and co-workers [43–45] looked at the effect of heat treatment on the mechanical properties of Sandvik HT9 (12Cr-1MoVW) by examining 25 different conditions. Austenitization temperatures, T_γ, of 950, 1000, 1050, 1100, and 1200°C were selected, and five different tempering conditions were selected for each T_γ. Austenitizing times were 1 h at each temperature. Tempering temperatures were 650, 715, 735, and 780°C, and tempering times were selected to get a range of tempering parameters, defined as $P_T = T(\log t + 20) \times 10^{-3}$, with the temperature T in kelvin and the time t in h [43]. Prior-austenite grain sizes increased with T_γ from 25 μm at 950°C to 330 μm at 1200°C. Lath packet sizes were estimated to change from 10 μm at 950°C to 95 μm at 1200°C. Significant amounts of δ-ferrite formed above a T_γ of 1050°C. The amount of carbide precipitated depended on the tempering conditions, increasing with increasing P_T. Precipitate analysis indicated the presence of five different morphological types, depending on where they formed. Positive identification was made of $M_{23}C_6$; M_6C was tentatively identified, and the possibility of small M_2X was cited. At $T_\gamma < 1050$°C, massive (perhaps undissolved during austenitization) $M_{23}C_6$ precipitates were observed on prior-austenite grain boundaries. At higher temperatures, the $M_{23}C_6$ particles were smaller [44].

Hardness measurements showed little effect of the austenitization temperature (perhaps a slight peak at 1050°C) but a large effect of tempering, with the hardness decreasing with increasing P_T [45]. The room-temperature yield stress and ultimate tensile strength (for a given tempering condition) showed an increase with T_γ up to 1050°C, then a decrease at 1100 and 1200°C, with little difference for the latter two temperatures. The ductility also showed a peak at 1050°C, with a continuous decrease in going from 1050 to 1100 and then 1200°C. Dynamic yield strengths were also determined from instrumented Charpy specimens tested at −101 and −112°C, and the static and dynamic yield strengths showed decreases with increasing P_T similar to the hardness changes. The dynamic lower-shelf fracture toughness showed a slight minimum at 1050°C that coincided with the strength peak; it also increased with P_T. The microcleavage fracture stress, σ_f^*, was determined as a function of T_γ and P_T. For $P_T = 18.5$, there was a peak at 1050°C, whereas at $P_T = 20$, σ_f^* decreased with T_γ. The σ_f^* was roughly inversely proportional to the square root of the lath packet size.

Fracture surfaces of the Charpy specimens were examined by SEM and indicated cleavage fracture over most of the surface [45]. However, in some instances, the fractures were de-

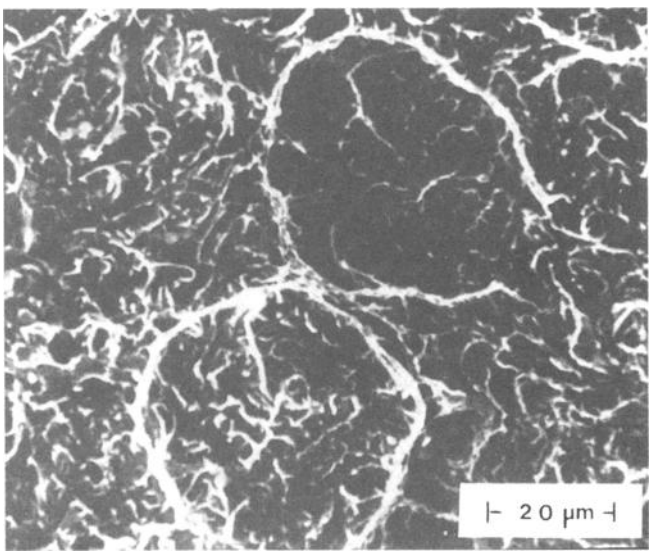

FIG. 14.11—SEM micrograph of a HT9 Charpy V-notch specimen broken at −101°C that illustrates quasi-cleavage fracture, which consists of ductile-tear ridges caused by tearing at the prior austenite grain boundaries and lath boundaries; the ridges outline areas of cleavage [45].

scribed as "quasi-cleavage," because in addition to the cleavage on the fracture surface, the surface contained narrow regions of ductile tearing. Closer examination indicated that the ductile tearing often outlined prior-austenite grain boundaries or lath packet boundaries (Fig. 14.11). Measurement of the regions coincided with the previous measurements of prior-austenite grain size and lath packet boundary size [45]. Subsurface microcracks and secondary surface cracks were often found associated with large boundary carbides. It was suggested that cleavage fracture initiated in the HT9 by the propagation of a microcrack from such a carbide into the matrix. Propagation was inhibited by the intercepted boundaries—lath or grain—and ductile tearing was required to continue propagation. The amount of tearing increased with increasing T_γ.

The fracture process was evaluated in terms of the Ritchie-Knott-Rice (RKR) model [46], which postulates that a cleavage fracture occurs when the stress ahead of the crack exceeds the critical stress σ_f^* over a critical distance l*. There appeared to be a weak dependence of lower-shelf dynamic toughness on the prior-austenite grain size. No direct relationship was determined between l* of the RKR model [46] and the prior-austenite grain size. Therefore, the model could not be applied, leading to the conclusion that statistical models would have to be applied [45].

In a later paper, Odette [47] proposed that the single event models for crack propagation were not sufficient to describe quasi-cleavage failure. It was shown that "quasi-cleavage involved small clusters of planar cleavage facets [emanating from a carbide or inclusion] separated from other co-planar facets or clusters of facets by the ductile tear ridges." Thus, quasi-cleavage involves frequent microcrack nucleation and propagation events that are arrested at misoriented boundaries. Confocal microscopy studies demonstrated that several such regions form before the final unstable cleavage event occurs by the coalescence of the regions [47].

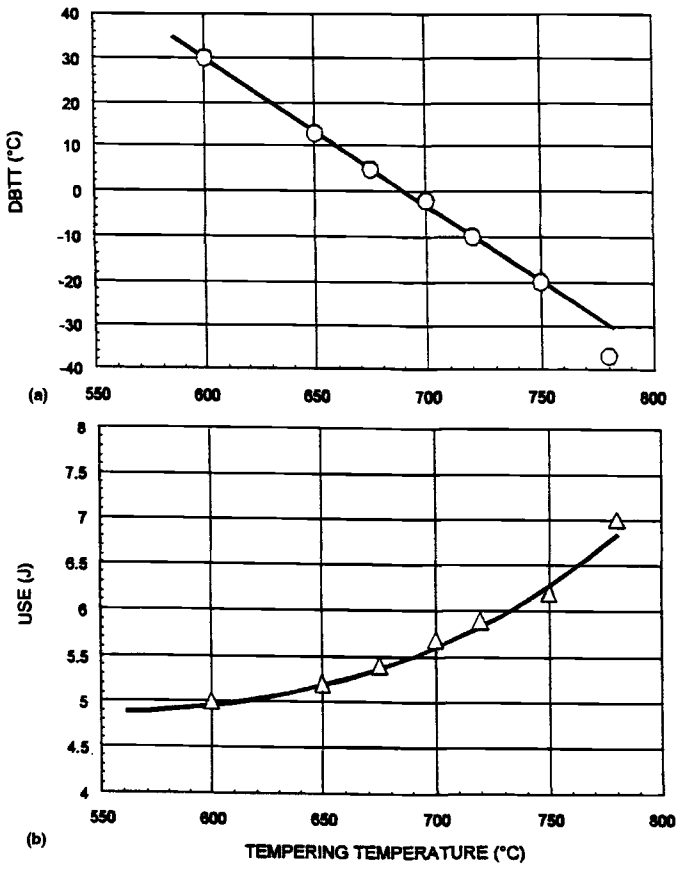

FIG. 14.12—The influence of the tempering temperature on (a) the DBTT and (b) the USE of MANET I steel [48].

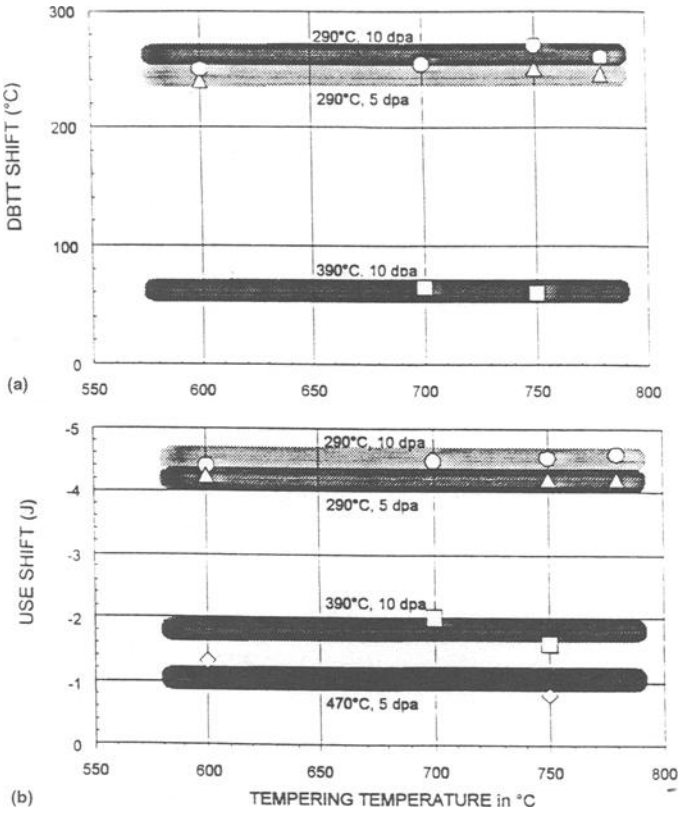

FIG. 14.13—The irradiation-induced (a) increase in DBTT and (b) decrease in USE of MANET I steel irradiated in HFR [48].

Wassilew and Ehrlich [6] and Reith et al. [48] reported on the effect of heat treatment on the Charpy behavior of miniature specimens of the MANET I steel in the unirradiated and irradiated condition. For these studies, the austenitization temperature was 950 to 980°C, and when austenitized at 950 and 980°C, respectively, there was little difference in properties [48]. Tempering over the range 600 to 780°C had a marked effect (Fig. 14.12). For a 2 h temper at each temperature, there was a linear decrease in DBTT with tempering temperature between 600 and 750°C, with a slight deviation from linear occurring for the 780°C temper [Fig. 14.12(a)]. The USE increased with tempering temperature [Fig. 14.12(b)] in a "quasi-exponential relationship" [48].

After irradiation in the HFR over the nominal range of 290 to 470°C at nominal doses of 5, 10, and 15 dpa [6,48], the effect of the 950 and 980°C austenitization treatments was concluded to fall within the scatter of the data, indicating a minor effect. No effect of tempering temperature was observed for the shift in DBTT [Fig. 14.13(a)] and shift in USE [Fig. 14.13(b)] within the limits of the scatter of the data (±20°C). These results agree with those on the 9Cr-1MoVNb steel that

showed an effect of tempering in the unirradiated condition and after irradiation showed relatively little change in ΔDBTT due to different tempering conditions out to 4–5 dpa at 365°C (Fig. 14.9).

The effect of dose on the ΔDBTT of MANET I at ≈290, 390, and 470°C is shown in Fig. 14.14, and in all cases there appeared to be a saturation with fluence [48].

The effect of irradiation temperature on the ΔDBTT of MANET I is shown in Fig. 14.15, and it shows the same character as the curves for 9Cr-1MoVNb and 12Cr-1MoVW steels irradiated in EBR-II (Fig. 14.5). At temperatures above ≈500°C, the ΔDBTT is essentially zero, similar to what was observed for the 9Cr-1MoVNb steel, which is probably closer in composition to the MANET I than the 12Cr-1MoVW steel.

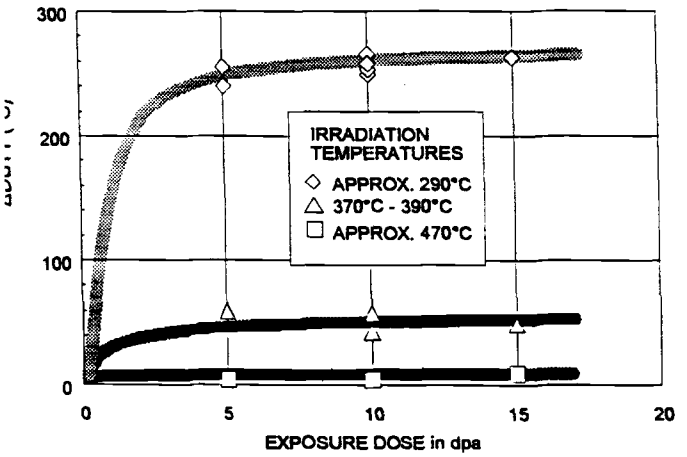

FIG. 14.14—Shift in DBTT as a function of fluence for MANET I steel irradiated in HFR [48].

However, there is a large increase in the shift between 375 and 290°C, where a shift of ≈280°C was observed, based on the curve in Fig. 14.15.

For the low-alloy pressure-vessel steels used for light-water reactors, the data indicate a correlation between ΔDBTT and hardening—the increase in yield stress, $\Delta\sigma_y$ [31,32]. For the MANET I data of Fig. 14.15, the following correlation was obtained for irradiation at about 300°C [49]:

$$\Delta DBTT = (0.50-0.55)\Delta\sigma_y \quad (14.1)$$

However, at 400°C, this correlation did not apply; instead:

$$\Delta DBTT = (0.35-0.42)\Delta\sigma_y \quad (14.2)$$

was observed. These data will be discussed further later in this chapter.

Effect of Melting Practice

Shamardin et al. [50] investigated the effect of processing on the irradiated properties of the Russian steels 10Kh13M2FB (nominally 12Cr-1.4Mo-0.3Ni-0.4Nb-0.25V-0.25Cu-0.4Mn-0.3Si-0.1C), 10Kh9MFB (10Cr-0.7Mo-0.3Ni-0.12Nb-0.16V-0.4Mn-0.2Si-0.1C), 10Kh9M2FB (9Cr-1.7Mo-0.3Ni-0.11Nb-0.15V-0.25Cu-0.4Mn-0.25Si-0.1C), and 05Kh14N5M2 (13Cr-2Mo-4.5Ni-0.25Cu-0.3Mn-0.1Si-0.05C); to simplify this discussion, these steels will be designated as 12Cr-1.4Mo, 10Cr-0.7Mo, 9Cr-1.7Mo, and 13Cr-2Mo-4.5Ni, respectively. The steels were smelted in three ways: (1) in an induction furnace (IF) using conventional charge materials, (2) in an open electric-arc furnace (OEAF) using pure charge materials, and (3) OEAF but with an additional electro-slag remelting treatment (OEAF+ESR). Chemical analysis indicated that when the pure charge technique was used the phosphorus and copper (for the steels that contained high copper) were

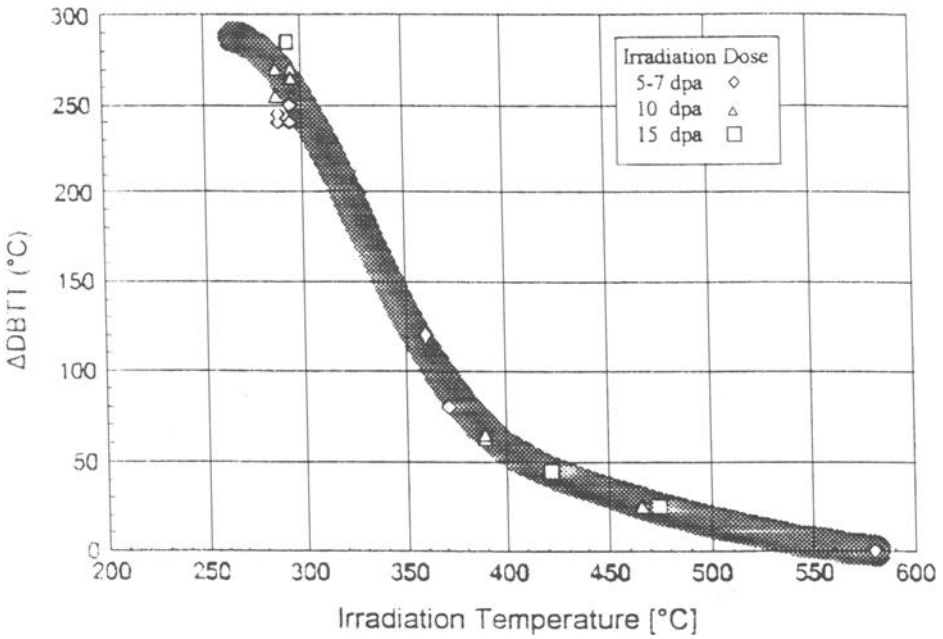

FIG. 14.15—Shift in DBTT as a function of irradiation temperature for MANET I steel irradiated in HFR [48].

reduced up to a factor of ten. Oxygen was removed in the ESR process.

The normalized-and-tempered steels were irradiated to 5 to 8 $\times 10^{25}$ n/m^2 at 330 to 360°C in the BOR-60 fast reactor. The shift in DBTT for the 10Cr-0.7Mo steel given the ESR process was reduced by ≈170°C compared to the steel with a pure charge but no ESR. The difference in the shift in DBTT for the OEAF and OEAF+ESR for the 9Cr-1.7Mo was much less (≈25°C), which the authors attributed to the higher molybdenum in this steel. There was essentially no effect of the ESR process for the 12Cr-1.4Mo steel. The results indicated an enhanced irradiation resistance of the 9Cr steels relative to the 12Cr steels following irradiation at 330 to 360°C as well as at 450 to 550°C. The 13Cr-2Mo-4.5Ni steel was irradiated in all three melting conditions at 330 to 360°C and 470 to 515°C. A decided advantage was observed for the OEAF over the IF and for the OEAF+ESR over the OEAF, both before and after irradiation, indicating that an improvement in irradiation resistance can be achieved by the choice of the smelting practice [50].

The most probable cause of the enhanced irradiation resistance caused by the different smelting practices was attributed to, "the hindrance of radiation-stimulated α'-phase segregation." The authors [50] based this conclusion on the work of Little and Stoter [51] and proposed that the OEAF and OEAF+ESR processes along with the use of pure charge materials lowered the phosphorus and copper contents and increased the homogeneity of the solid solution, thus affecting the "kinetics of α'-phase segregation." The removal of molybdenum was postulated to have a similar effect (decrease), and the improved behavior of the 9Cr steels over the 12Cr steels was attributed to the fact that α' does not form in 9Cr steels. No microstructures were presented, and although δ-ferrite was mentioned, no indication was given on how much of the phase was present or in which steels [50].

In a subsequent paper by Zvezdin et al. [52] on three of the steels discussed by Shamardin et al. [50] (10Kh9MFB, 10Kh9M2FB, and 10Kh13M2FB, although in this paper the Kh in the designation was replaced by X), it was revealed that the 12Cr-1.4Mo steel contained 30 to 50% δ-ferrite, which, the authors stated, "unfavorably affects the impact properties of the steel." Electron microscopy revealed that the steels contained globular α' particles (primarily in the δ-ferrite) with an average size of 7 nm and a number density of 8 to 20 $\times 10^{16}$ cm^{-2}. They also found a phase that precipitated "during the solid solution disintegration" which they concluded to be M_2X; it formed in tempered martensite, δ-ferrite, and on grain boundaries [52].

As stated above, the ESR process removes oxygen from the melt, but no mention was made of the effect of the oxygen on the properties [50,52]. Schirra et al. showed that an increase in oxygen concentration caused a rather strong increase in the notch impact toughness of the OPTIMAR [53] and OPTIFER [54,55] steels (unirradiated) from Germany, thus again demonstrating how complicated the effect of composition on properties is. For the OPTIMAR steel (a variation of DIN 1.4914, Fe-10.5Cr-0.6Mo-0.7Ni-0.2Nb-0.03N-0.1C), an increase in oxygen from 36 to 161 ppm caused the DBTT of the higher-oxygen material to be 28°C higher [53]. A heat of the OPTIFER steel containing 320 ppm oxygen had a DBTT that was ≈60°C higher than a heat of the steel with only 90 ppm oxygen [55]. The oxygen effect can be attributed to deoxidation products in the steel that act as crack initiation sites [56].

Effect of Chemical Composition

The effect of carbon on the unirradiated and irradiated Charpy impact properties of the 9Cr-1MoVNb and 12Cr-1MoVW steels was discussed in a preceding section. That the difference between the 9Cr and 12Cr steels may not be strictly a carbon effect can be seen from a recent irradiation of the 9Cr-1MoVNb and two new "improved" commercial steels, N616, nominally 9Cr-2W-0.5Mo-0.2V-0.07Nb-0.004B-0.045N-0.1C, and HCM12A, nominally 11Cr-1Mo-0.5W-0.3Ni-0.2V-0.05Nb-0.002B-0.06N-0.1C [57]. These steels have many similarities with the 9Cr-1MoVNb including carbon. The major differences appear to be the W and B in both steels and the Cr and Ni in the HCM12A. Nevertheless, the Charpy properties were quite different before and after irradiation in HFR at 300°C, with the properties of the 9Cr-1MoVNb being superior both before and after irradiation (Table 14.1) [57]. The DBTT of the NF616 and HCM12A were similar before and after irradiation; the USE of the NF616 was less than that of HCM12A before irradiation, but similar after irradiation. The 50 to 74°C larger increase in DBTT for the two new steels relative to the 9Cr-1MoVNb steel with all steels having similar carbon concentrations indicates that the effect of chemical composition is probably quite complicated.

During the development of the reduced-activation steels, more systematic investigations of compositional effects of elements other than carbon were made. These will be discussed here, along with some general observations on the irradiation effects on the impact properties of the reduced-activation steels relative to the commercial Cr-Mo steels after which they were patterned.

Charpy specimens for a range of reduced-activation steels have been irradiated [58–68]. Kayano et al. [58] used miniature Charpy specimens to study several compositions of reduced-activation Cr-W steels and compare them with Cr-Mo steels before and after irradiation in JMTR to 2.2 $\times 10^{23}$ n/m^2 (<<1 dpa) to determine the effect of different alloying elements (Table 14.2). For steels with 0, 3, 5, and 9% Cr [Group (1) in Table 14.2], there was little difference in the DBTT between 3 and 9% Cr in the unirradiated and irradiated conditions. The highest DBTT values occurred for the steel with 0% Cr, followed by the one with 15% Cr (below ≈5% Cr, the steels will be bainitic compared to martensitic at 5–12% Cr, and ferritic at 15% Cr). The 9Cr steel was slightly better than the other steels, especially when the ΔDBTTs were compared. A comparison of 0 and 15% Cr steels [Group (2) of Table 14.2] with steels containing 7 and 9% Cr and 1.1, 1.7, and 2.0% Mo, respectively [Group (3) of Table 14.2], showed that the

TABLE 14.1—Charpy impact properties of Cr-Mo dteels irradiated 2.5 dpa at 300°C [57].

	Unirradiated		Irradiated		Property Changes	
Steel	DBTT, °C	USE, J	DBTT, °C	USE, J	ΔDBTT	ΔUSE
Mod 9Cr-1Mo	−78	8.9	97	6.6	175	2.2
NF616	−41	7.3	209	4.5	249	2.8
HCM12A	−36	8.3	189	4.3	225	4.0

TABLE 14.2—Chemical compositions of Cr-Mo and Cr-W steels [58].

Alloy Group	C	Si	V	Cr	W	Mn	Ta	Ti	B	Zr	Y	Mo	Nb
(1)	0.03	0.03	0	0									
				3		0.03							
				5									
				9									
(2)	0.10	0.05	0.25	7	1	0.5	0	0.02	0	0.017	0.05		
						1	0.05						
				9	2	2	0.10	0.05	0.003				
				15									
(3)	0.01	0.05	0.15	5								1.1	
				7								1.7	0.06
				9								2.0	

Fe-Cr-Mo steels had the better properties, with a beneficial effect of molybdenum. There did not appear to be much effect of niobium. The effect of tantalum, tungsten, and chromium, was examined in 7 and 9% Cr steels containing 0.1% C and different amounts of B, Ti, and Mn [Group (2) of Table 14.2] [58]. It was concluded that an 0.05% Ta steel had the lowest DBTT, 2% W was better than 1% W, and 9% Cr was better than 7% Cr. In these same 7 and 9% Cr steels, it was concluded that 0.003% B improved the properties, 0.02% Ti was an improvement over 0.05% Ti, and that 0.6% Mn was an improvement over 1% Mn, but there was little difference between the 0.6 and 2.0% Mn. The main conclusion of the work was that the best toughness was obtained in the range 3–9% Cr, and that [58], "the 9Cr-2W-Ti-Ta-B ferritic steels showed the highest toughness caused presumably by the refinement of the crystal grains and the improvement of quenching characteristics by the complex effect of Ti and B." It is not immediately obvious how some of these conclusions follow, given the varying compositions for the different alloys being compared in Table 14.2.

In another reduced-activation steel development program, the effect of tungsten and vanadium on the behavior of 9Cr-W and 9Cr-V steels, respectively, were determined [59,60]. The DBTT increased with increasing (0 to 4%) tungsten concentration, with the duplex (δ-ferrite and martensite) microstructure of the 9Cr-4W steel having the worst toughness. The DBTT for the 9Cr-V steels with 0 to 1% V went through a minimum at 0.25% V. Thermal aging at 550 and 650°C had the greatest effect on the DBTT of the 9Cr-4W steel, which contained extensive amounts of Laves phase. When the tungsten and vanadium were combined with tantalum to produce 9Cr-1WVTa and 9Cr-3WVTa steels, the 1% W steel showed excellent toughness compared to 9Cr-1MoVNb with creep strength equivalent to 9Cr-1MoVNb, whereas the 3% W steel had higher creep strength than 9Cr-1MoVNb with impact toughness equivalent to that for 9Cr-1MoVNb. It was suggested that the 9Cr-1WVTa was most promising for temperatures below 500°C, and the 9Cr-3WVTa was best for temperatures above 500°C, where it had the superior creep strength [60].

Rybin et al. [61] irradiated reduced-activation steels with the following designations: 7Cr-1.5WV, 7Cr-1.5WVP (0.035% P), 7.5Cr-1.5WVCu (0.15%Cu), 8Cr-1.5WV, 9Cr-V (0.7% V), 9Cr-WV (0.5% W, 0.4% V), 9Cr-1.5WV, 11Cr-1.5WV, and 11Cr-1MoV. Carbon was nominally 0.1% in all steels , and where not otherwise indicated, vanadium was ≈0.25%. Rare earth additions were made to the 8 to 11% Cr steels. Irradiation was in the WWR-M experimental reactor at 70 and 240 to 300°C to 1.2–2 × 10^{24} n/m^2 (E ≥0.5 MeV), a displacement damage level much less than 1 dpa.

For irradiation at 240°C, the smallest ΔDBTT values (15 to 35°C) were for 8Cr-1.5WV, 9Cr-1.5WV, and 11Cr-1.5WV, with the largest shifts (100 to 130°C) occurring for 7Cr-1.5WV, 7Cr-1.5WVP, 7.5Cr-1.5WVCu, the latter two being attributed to the higher phosphorus and copper. The 7Cr-1.5WV had a ΔDBTT of 100°C, considerably larger than the 9Cr-1.5WV (25°C). However, none of these 7Cr steels contained the rare earth additions, which were credited for contributing to the good properties of the steels containing them, although this was not directly demonstrated. Irradiations on the 8Cr-1.5WV, 9Cr-V (0.7V), and 9Cr-WV (0.5W, 0.4V) were made at 240 to 300°C and 70°C, and the ΔDBTT increased from 35 to 110°C, 45 to 105°C, and 50 to 80°C, respectively, when the temperature was decreased. The two 11% Cr steels, one with tungsten and one with molybdenum, contained ≈20% δ-ferrite, with the tungsten-containing steel having the smallest ΔDBTT (15°C versus 60°C), indicating an improvement by substituting this element for molybdenum.

It was concluded [61] that the 8-9Cr steels showed the most promise, and these steels along with a 2.5Cr-1.4WV bainitic steel that was studied were recommended for consideration for "first wall and blanket of fusion reactor as well as to pressure vessels and in-reactor equipment of nuclear power fission reactors."

The improved impact behavior before and after irradiation of 9Cr-WV steels relative to those with greater or lesser chromium concentrations has been demonstrated in other studies [33,58,62–65]. Figure 14.16 shows the effect of chromium composition on the ΔDBTT for Fe-CrWVTa steels of various composition after irradiation in FFTF [33]. It appears that there is a minimum in ΔDBTT in the vicinity of 9% Cr that is more pronounced than the slight minimum seen by Kayano [58] for his low-fluence irradiations. As seen in Fig. 14.16, the steel most resistant to irradiation embrittlement is the U.S. experimental 9Cr-2WVTa steel.

Data for the U.S. 9Cr-2WVTa steel irradiated to 7 dpa (ΔDBTT = 15°C) in FFTF at 365°C are shown in Fig. 14.16. After irradiation to 27 dpa at 365°C in FFTF, a ΔDBTT of only 32°C was observed for the 9Cr-2WVTa, compared to 150 to 160°C for 12Cr-1MoVW (Fig. 14.17) [63]. Not only does the

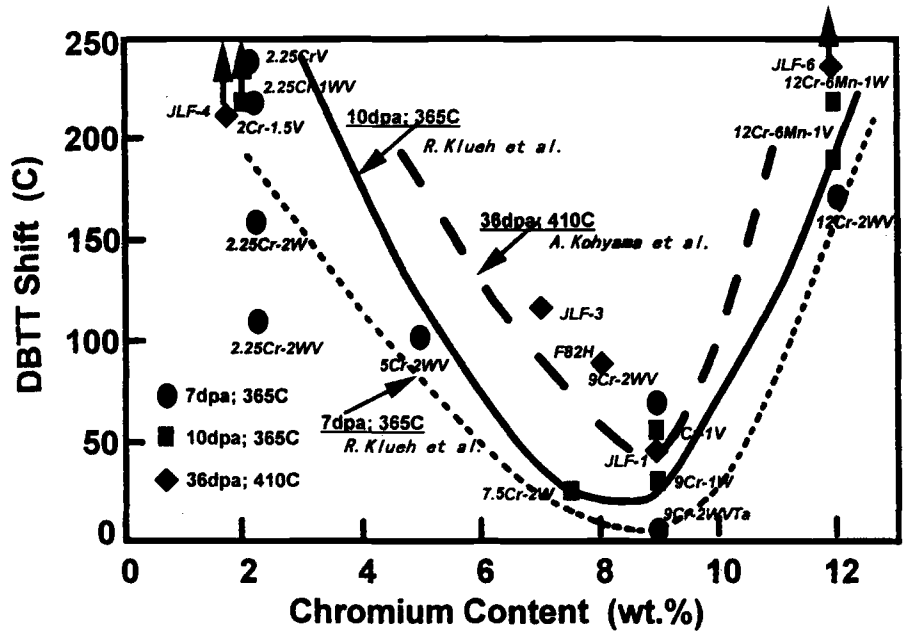

FIG. 14.16—Effect of chromium content on DBTT shift of reduced-activation ferritic/martensitic steels irradiated in the FFTF [33].

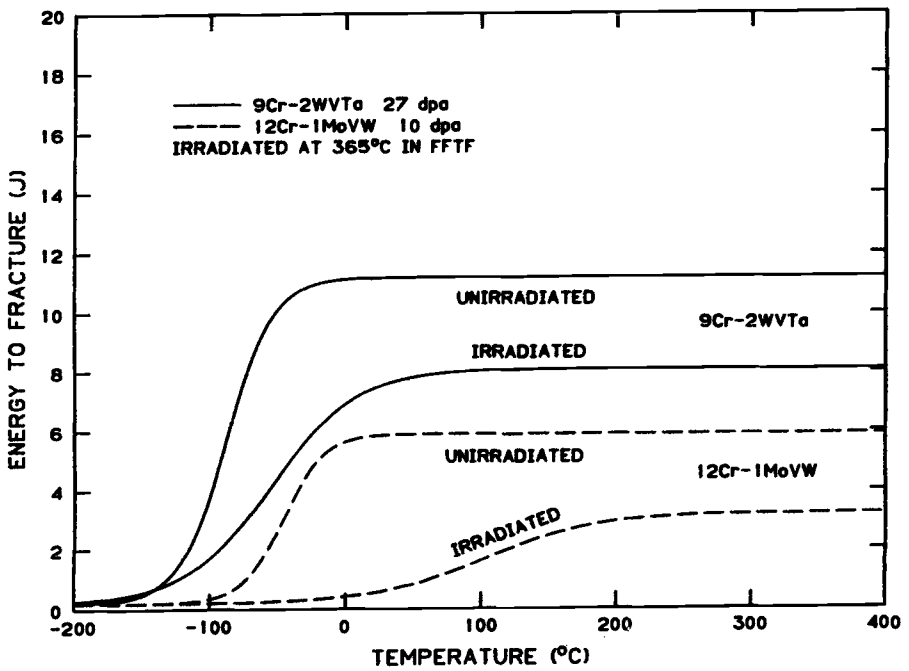

FIG. 14.17—Comparison of the unirradiated and irradiated Charpy curves for one-third-size specimens of 12Cr-1MoVW and 9Cr-2WVTa steels irradiated in FFTF at 365°C [63].

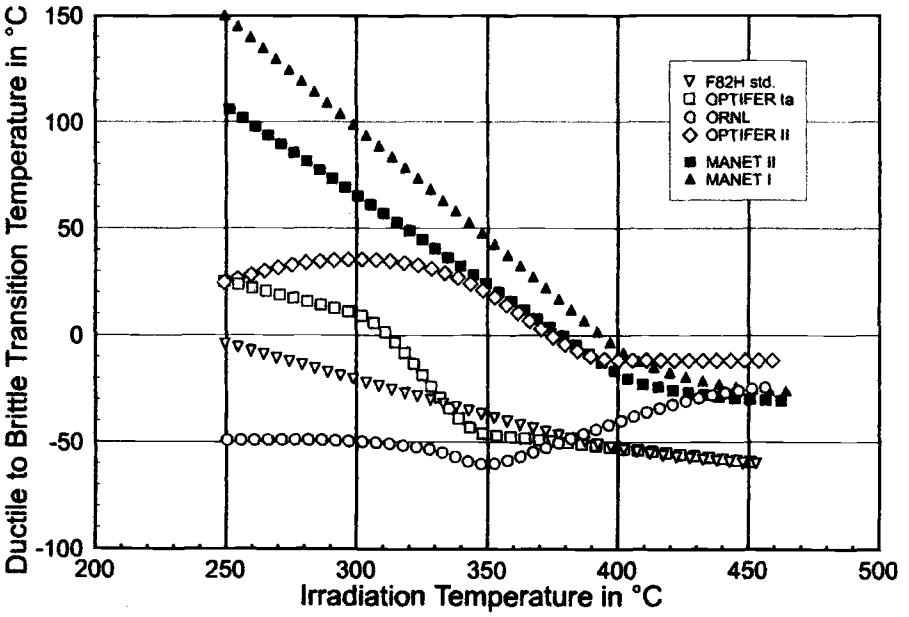

FIG. 14.18—DBTT as a function of temperature for four reduced-activation and two conventional martensitic steels irradiated to 0.8 dpa in the HFR [69].

9Cr-2WVTa show a very small ΔDBTT, but because it has a very low DBTT (1/3-size specimens) in the unirradiated condition (−88°C), the DBTT after irradiation is considerably below that for any other steel after irradiation. The DBTT for the 9Cr-2WVTa *after* irradiation to 27 dpa is −56°C, similar to that for the 9Cr-1MoVNb *before* irradiation (it is considerably lower than the before-irradiation value for the 12Cr-1MoVW and many reduced-activation steels). This is demonstrated in Figure 14.17, where the 12Cr-1MoVW (Sandvik HT9, an early candidate for fast reactor and fusion applications) is compared to the 9Cr-2WVTa after irradiation in FFTF at 365°C.

The excellent behavior of the 9Cr-2WVTa steel and the superiority of some reduced-activation steels to the commercial Cr-Mo steels was further demonstrated when the 9Cr-2WVTa steel was irradiated with reduced-activation steels (F82H, OPTIFER Ia, and OPTIFER II) and conventional Cr-Mo steels (MANET I and II) in the HFR to 0.8 dpa at 250, 300, 350, 400, and 450°C (Fig. 14.18) [69–71]. The nominal compositions for these steels are: F82H, 8Cr-2W-0.2V-0.04Ta-0.1C; OPTIFER Ia, 9Cr-1W-0.25V-0.07Ta-0.1C; OPTIFER II, 9.5Cr-1.1Ge-0.3V-0.018Ta-0.13C***; MANET I, 10.8Cr-0.75 Mo-0.2V-0.9Ni-0.16Nb-0.06Zr-0.009B-0.14C; and MANET II, 10Cr-0.6Mo-0.2V-0.7Ni-0.15Nb-0.03Zr-0.007B-0.1C. The 9Cr-2WVTa steel (labeled by the authors [70] ORNL) in Fig. 14.18 had the lowest DBTT. This superior behavior has now been verified after irradiation to 2.4 dpa in HFR [71]. One unusual aspect of the behavior of the 9Cr-2WVTa steel is that the DBTT appears to increase above 400°C; this is inverse to the expected decrease in the ΔDBTT with increasing temperature, which is shown by the other steels in Fig. 14.18. A similar inverse temperature effect was observed for the 9Cr-2WVTa steel when it was irradiated to 14 dpa at 393°C in FFTF [72] and compared to data from irradiation at 365°C to 15 dpa [63]. For seven other reduced-activation steels irradiated in the same experiments at 365 and 393°C as the 9Cr-2WVTa [72] and for 9Cr-1MoVNb and 12Cr-1MoVW steels irradiated under similar conditions [63], the expected behavior with temperature was observed.

The origin of the improved behavior for the ORNL 9Cr-2WVTa steel was sought by examining the microstructure of this steel, a 9Cr-2WV steel, which is the same as the 9Cr-2WVTa but without the tantalum, and the conventional 9Cr-1MoVNb and the 12Cr-1MoVW steels [16]. The 9Cr-2WV and 9Cr-2WVTa steels were irradiated at 365°C in FFTF, with the 9Cr-2WVTa showing exceptionally small shifts in DBTT: 4, 14, 21, and 32°C after 6.4, 15.4, 22.5, and 27.2 dpa, respectively [63]. There appeared to be a continuous increase in DBTT with fluence, whereas the DBTT for the 9Cr-2WV saturated with fluence by the first irradiation (≈4 dpa) with a saturation ΔDBTT of ≈61°C, which compares with the 9Cr-1MoVNb and 12Cr-1MoVW steels irradiated at 365°C in FFTF for which the ΔDBTT saturated after ≈5 dpa at ≈45 and ≈150°C, respectively.

When the 9Cr-2WV and 9Cr-2WVTa steels were compared, differences in Charpy properties before and after irradiation occurred despite relatively little difference in strength before and after irradiation. A comparison of the optical microstructures of the normalized-and-tempered 9Cr-2WV and 9Cr-2WVTa steels indicated that the 9Cr-2WVTa had a smaller prior-austenite grain size (22 versus 32 μm). Transmission electron microscopy revealed only minor differences prior to irradiation [16,73,74]: they had similar lath sizes (one investigation noted a smaller lath size for the 9Cr-2WVTa [74]) and precipitate type ($M_{23}C_6$ and MC) and number densities. One difference involved a small amount of tantalum-rich MC carbide in addition to vanadium-rich MC in the 9Cr-2WVTa, whereas the 9Cr-2WV steel contained vanadium-rich MC. There was also no marked difference in microstructure after irradiation to 35 dpa at 420°C, the major

*** Although no tantalum was evidently added to OPTIFER II, chemical analysis indicated 0.018% Ta [70].

change caused by irradiation in both steels being the similar number of dislocation loops that formed [16]. Thus, the similarity in strength of these two steels before and after irradiation was not unexpected.

Without any gross differences in the microstructure of the two steels, the only other major difference to account for the difference in Charpy properties is the tantalum in solid solution. Because tantalum is a strong carbide former, it was expected that most of the tantalum would be incorporated in MC precipitates. However, based on the estimated tantalum in the MC carbides of the 9Cr-2WVTa determined by energy dispersive x-ray spectroscopy of the unirradiated steel, it was concluded that most of the tantalum remained in solid solution after the normalizing-and-tempering treatment [16]. An atom probe analysis of the normalized-and-tempered 9Cr-2WVTa steel indicated that ≥90% of the tantalum remained in solution [74]. Since there are no other compositional differences in the two steels, the tantalum in solution in the 9Cr-2WVTa must cause the smaller prior-austenite grain size in that steel [63]. Tantalum is known to refine the prior austenite grain size in F82H. A smaller lath (subgrain) size might also be expected, but no significant difference in lath size was observed in two microstructural studies [16,73].

A smaller grain size can lead to a lower DBTT in the normalized-and-tempered condition, and the smaller prior austenite grain size was originally used to explain the difference between the 9Cr-2WV and 9Cr-2WVTa steels. However, this grain size explanation was subsequently questioned as being the sole reason for the difference in properties of the two steels, because the normalized-and-tempered steels had similar yield stresses at 365°C, similar yield stresses after irradiation at 365°C, and similar microstructures before and after irradiation [76]. These observations lead to the conclusion that tantalum in solution affects the impact behavior.

There has been considerable work to determine the mechanism by which alloying elements affect the DBTT, for example, on why nickel and platinum decrease the transition temperature of α-iron and silicon increases it [77,78]. Based on the schematic diagram of Fig. 14.2, the DBTT can be decreased by either decreasing the flow stress or increasing the fracture stress. An analysis of the fracture stress can begin with the work of Griffith [79,80], who considered the balance between the energy released by elastic relaxation and that required for the creation of new surface area during the growth of a crack in a brittle material. For a through crack, Griffith found that

$$\sigma_f = \left(\frac{2E\gamma_s}{\pi a(1-\nu^2)}\right)^{1/2}, \qquad (14.3)$$

where σ_f is the stress at fracture, E is Young's modulus, γ_s is the true surface energy, ν is Poisson's ratio, and a is the crack half-length. For an embedded penny-shaped crack, as would result from initiation at a carbide particle, at an inclusion, or from a crack forming within an entire grain or other microstructural unit, this equation becomes [75]

$$\sigma_f = \left(\frac{4E\gamma_e}{D(1-\nu^2)}\right)^{1/2} \qquad (14.4)$$

where D is the crack diameter and γ_s from Eq. 14.3 has been replaced by an effective surface energy, γ_e, that takes into account the plastic work.

For a ferritic steel with spherical carbide particles, the diameter of the carbide particle can be used for the crack diameter, D. This equation could not be used to account for the observations on 9Cr-2WVTa and 9Cr-2WV, however, since there appeared to be no difference in the amount or morphology of the precipitates in the two steels.

In the case of a bainitic or martensitic steel, the packet or lath size can determine the crack size that determines fracture behavior. There did not appear to be a significant difference in the lath size of the normalized-and-tempered 9Cr-2WV and 9Cr-2WVTa steels. More importantly, no difference was observed after irradiation to 36 dpa at 420°C in FFTF [16]. If lath size determined fracture behavior, the ΔDBTT for the two steels should have been similar or that for the 9Cr-2WVTa should have been larger (if it had a smaller lath size before irradiation as one study [74] indicated). Therefore, lath size does not offer an explanation. Prior austenite grain size could also be considered as the crack size, but this does not explain the change in DBTT because prior austenite grain size does not change during irradiation.

If the crack length cannot explain the observations, Eq 14.4 indicates that the tantalum effect either involves Young's modulus or the effective surface energy. The small amount of tantalum will have little if any effect on the modulus. Gerberich et al. found effects of nickel and silicon on the effective surface energy for binary iron-based alloys [78], and concluded that a change in fracture stress could explain why nickel caused a decrease and silicon caused an increase in the transition temperature of binary Fe-Ni and Fe-Si alloys.

Besides the suggested explanation that tantalum affects the fracture stress of the 9Cr-2WVTa, the other possible explanation involves a change in flow stress caused by tantalum in solution (Fig. 14.2). The only information on this possibility is that there is little difference in the yield stress at 365°C (the irradiation temperature) and over the range room temperature to 600°C [82]. Tests to determine the effect of strain rate and temperature (at low temperatures) are planned for the steels [72].

The effects of microstructural parameters on the transition temperature are complex, as Gerberich et al. [78] have noted; the ductile-brittle transition model for iron and iron-binary alloys that they derived involved 19 flow and fracture parameters.

The observation that the ΔDBTT of the 9Cr-2WVTa appeared to increase slightly with fluence would follow if tantalum is being removed from solution during irradiation and being incorporated in the existing or new precipitates. This can also explain the increase in DBTT for the 9Cr-2WVTa specimens irradiated above 400°C relative to those irradiated at lower temperatures in HFR (Fig. 14.18) and the higher DBTT after irradiation at 393 than at 365°C in FFTF (inverse temperature effect) [72]. In both cases, the increase occurred at the higher irradiation temperatures, where irradiation-enhanced diffusion can accelerate a reduction of tantalum in solution. With a continued removal of tantalum from solution during irradiation, it might be expected that the ΔDBTT for the 9Cr-2WVTa would approach that for the 9Cr-2WV, and this was observed for the steels irradiated to 14 dpa at 393°C [72]. It was noted that even though the ΔDBTT values for 9Cr-2WVTa and 9Cr-2WV became similar with increasing dose, the 9Cr-2WVTa still had the lowest DBTT after irradia-

tion, as would be expected, because of its lower DBTT before irradiation—probably because of the smaller prior-austenite grain size. If tantalum in solution does improve fracture resistance but this resistance is lost when tantalum precipitates during irradiation, then tantalum should precipitate in the 9Cr-2WVTa until equilibrium is achieved, after which the ΔDBTT should saturate with fluence.

This tantalum effect should also occur for the other tantalum-containing steels shown in Fig. 14.18, namely, F82H (0.04% Ta) and OPTIFER Ia (0.07% Ta). In fact, it does occur for these steels [83]. Figure 14.18 shows data after irradiation to 0.8 dpa, and no increase in DBTT at the highest irradiation

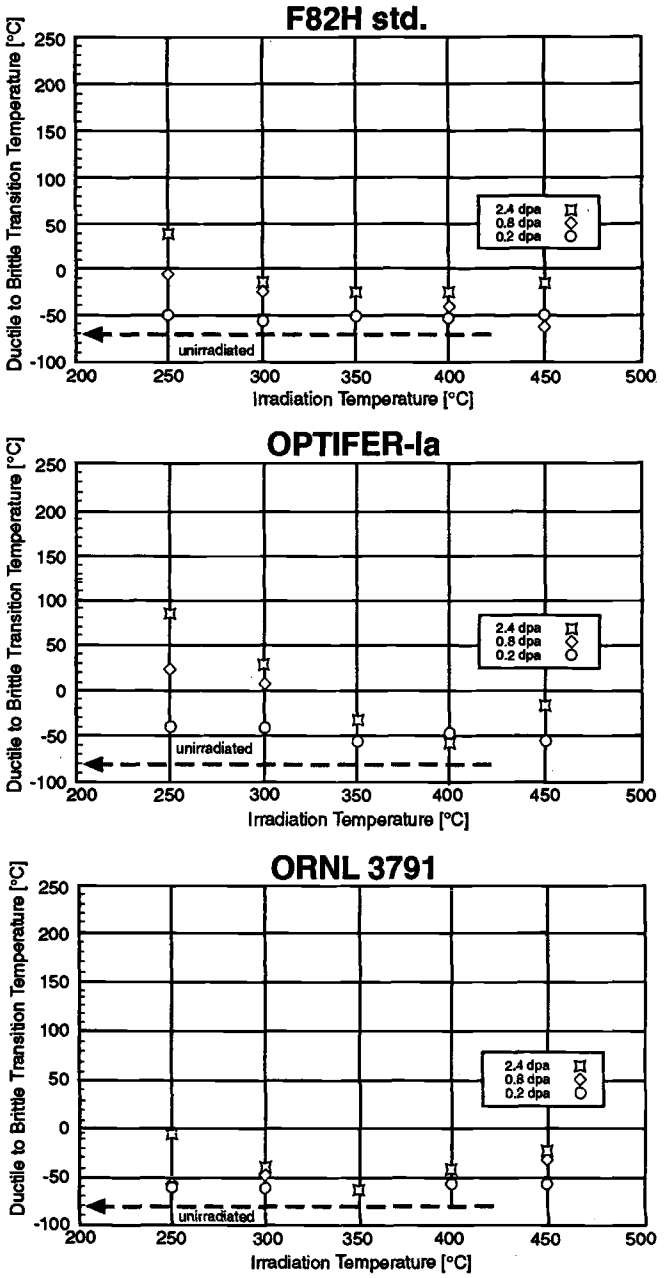

FIG. 14.19—Ductile-brittle transition temperature as a function of irradiation temperature for F82H, OPTIFER-Ia, and 9Cr-2WVTa steels [71].

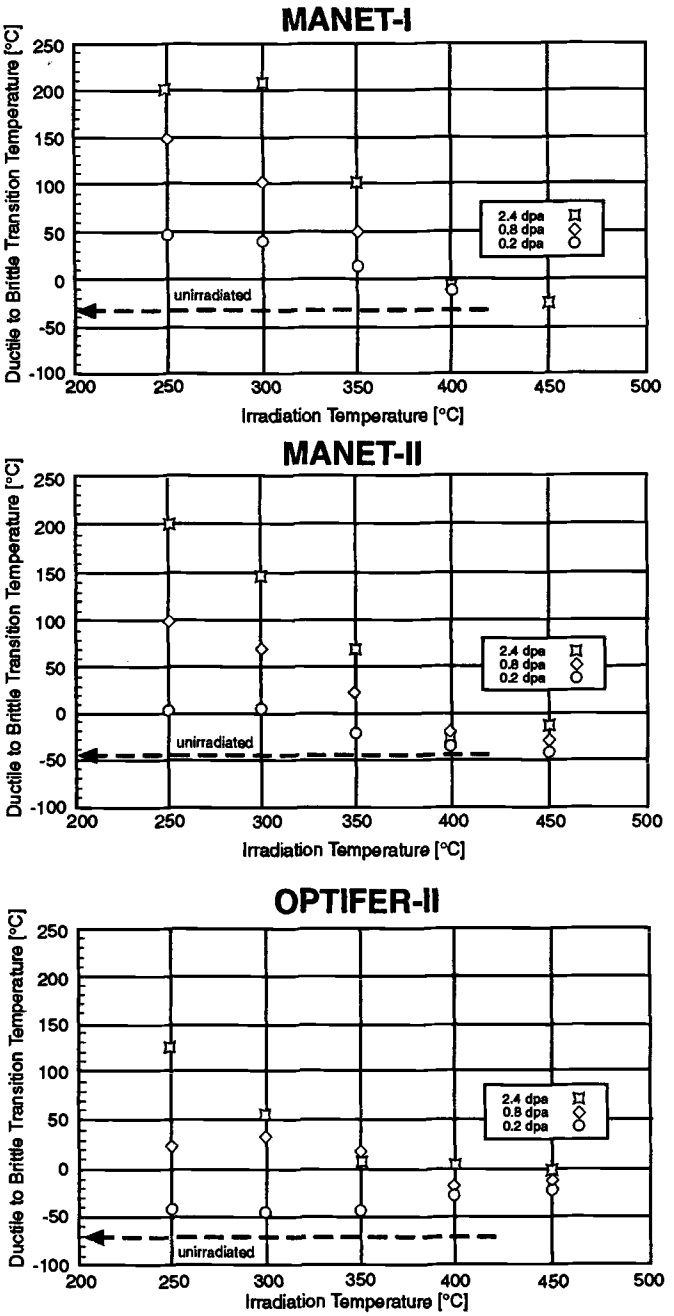

FIG. 14.20—Ductile-brittle transition temperature as a function of irradiation temperature for MANET-I, MANET-II, and OPTIFER-II [71].

temperature is observed for these two steels. The combined DBTT data for the steels after irradiation to 0.2, 0.8, and 2.4 dpa in HFR [73] are shown in Fig. 14.19 for F82H, OPTIFER Ia, and 9Cr-2WVTa—the tantalum-containing steels (actually the steels to which tantalum was added; as explained above, the OPTIFER II was analyzed to have 0.018% Ta). After 2.4 dpa, the DBTT at 450°C for all three steels was higher than it was at 350 and 400°C. The behavior of these three tantalum-containing steels contrasted with that of MANET I [Fig. 14.20(a)], MANET II [Fig. 14.20(b)]—steels with no added tantalum—and OPTIFER II [Fig. 14.20(c)]—the steel with only 0.018% Ta. With one exception, these three steels did

not show a DBTT after 2.4 dpa at 450°C that was above that at 350 and 400°C. The only exception was MANET II [Fig. 14.20(b)], where the DBTT at 450°C was slightly higher than at 400°C, but it was well below that at 350°C. The observation that the OPTIFER II did not show the effect may mean there is a tantalum level below which it does not occur.

It is recognized that Charpy data can contain considerable scatter. Nevertheless, the trend of these data for the tantalum-containing F82H and OPTIFER-Ia are consistent with the suggestion that tantalum causes the increase in DBTT with increasing dose (rather than a saturation) and causes the inverse temperature effect for the DBTT of the 9Cr-2WVTa steel. A loss of tantalum from solution during irradiation can explain these results. The actual loss of tantalum still needs to be correlated with the change in properties for 9Cr-2WVTa steel. Atom probe analysis is probably the best method to study this given the small amount of tantalum in the steels. As discussed in an earlier section, however, Kimura et al. [30] found that tantalum-rich M_6C precipitated in their 9Cr-2WVTa steel irradiated at 460°C in FFTF. No tantalum-rich precipitate was observed in the steel when irradiated at 390°C, indicating that tantalum did precipitate in this experiment in a temperature range similar to that used for the experiments on 9Cr-2WVTa. What is equally important in the Kimura et al. experiments [30] was that despite softening after irradiation at 460°C, an increase in DBTT of ≈15°C was observed, the same inverse temperature effect as observed on the ORNL 9Cr-2WVTa in the HFR experiments [69,70].

Chemical composition can affect the irradiation embrittlement in other ways. Depending on the amounts of other ferrite-stabilizing elements present, δ-ferrite can form. In the 12Cr-1Mo steels (e.g., HT9), nickel and carbon are used to stabilize the austenite during the heat treatment. Since nickel is not a reduced-activation element by some criteria [84], manganese has been used for 12Cr reduced-activation steels [62]. In studies on martensitic 9Cr-1W-2.5Mn, 9Cr-1V-1Mn, 9Cr-0.5V-3Mn, 12Cr-1V-6Mn, and 12Cr-1W-6Mn steels, the 12Cr steels containing 6% Mn developed large increases in DBTT and a change in fracture mode on the lower shelf from transgranular cleavage to intergranular [62,85]. This same change in fracture mode was observed for a 9Cr-1W steel containing about 3% manganese, although this steel did not show as large a shift in DBTT. A similar change in fracture mode was observed when the 0.5% Ni in 12Cr-1MoVW steel was replaced by 3.3 and 6.6% Mn and irradiated at 407°C in FFTF [86,87]. For both types of steel, the change in fracture mode and the large shift in DBTT were attributed to manganese and to the formation of chi-phase on prior-austenite grain boundaries.

TEM studies of thermally aged specimens and neutron irradiated 12Cr-1W-6Mn specimens found chi-phase [88–91]. Auger spectroscopy of grain boundary surfaces on fractured specimens of 12Cr-1W-6Mn and 9Cr-1W-2.5Mn steels indicated that silicon segregated to the surface in the 9Cr steel, and manganese segregated there in the 12Cr steel. Again the possibility of chi-phase was cited to explain the 12Cr results, but for the 9Cr steels the silicon was alluded to, even though only 0.1% silicon was present in the steel [91]. No chi-phase was found after dual-ion irradiation, indicating that chi-phase does not form without long-time anneals [90].

Oxide Dispersion-Strengthened Steels

The only apparent impact properties measurements on an irradiated ODS steel were for an experimental steel developed in Japan and labeled 1DS (nominally Fe-11Cr-2.7W-0.4Ti-0.66Y_2O_3-0.1C) [92]. Miniature (1.5 by 1.5 by 20 mm) Charpy specimens of the 1DS steel were irradiated in JOYO at 373 to 572°C to 0.3 to 3.8 × 10^{26} n/m^2 (E > 0.1 MeV) [93]. Figure 14.21(a) shows the Charpy curves for the unirradiated material tested in the longitudinal (1DS-L) and transverse (1DS-T) orientation. The difference in the values indicates that there is anisotropy that [93], "may be attributed to the elongated bamboo-like grain structure." The interesting thing pointed out by the authors is the high lower-shelf energy—as high as 65% of the upper-shelf energy. In Fig. 14.21(b), the 1DS-L data are compared to Charpy curves for the commercial Y_2O_3-strengthened ODS steel MA 957 and the non-ODS steel 2WFK (11Cr-0.5Mo-2.0W-0.2V). The superiority of the lower shelf energy (LSE) of the 1DS-L is evident. SEM of the 1DS steel indicated fibrous fractures at all temperatures, which was taken to mean there was no ductile-brittle temperature for this steel. This was confirmed in the load-displacement curves obtained on the lower shelf.

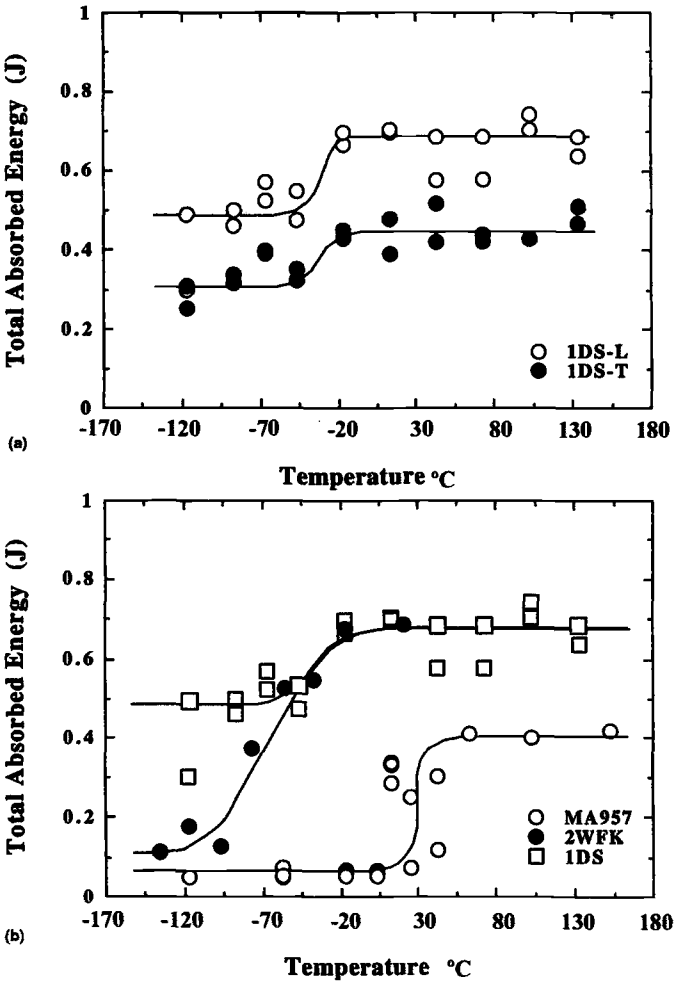

FIG. 14.21—Charpy curves (1.5-mm specimens) for (a) 1DS experimental ODS steel in a longitudinal (1DS-L) and transverse (1DS-T) orientation and (b) 1DS-L, MA957 (a commercial ODS steel), and 2WFK (11Cr-0.5Mo-2.0W-0.2V) steels [93].

Figure 14.22 shows the irradiated properties for 1DS-L [Fig. 14.22(a)] and 1DS-T [Fig. 14.22(b)]. The conclusion from these results was that [93], "irradiation below 775 K [502°C)] does not cause appreciable change in total absorbed energy . . . ." Embrittlement occurred at higher temperatures, especially at 520°C (793 K) for IDS-L and 572°C (845 K) for IDS-T (note that these were the high-dose tests. It was concluded that, "such embrittlement is not significant and the LSE is still fairly high." Load-displacement curves on the lower shelf, which gave no indication of brittle fracture, were used to verify this statement [93]. It should be noted, however, that the use of very small blunt-notch specimens (specimens with a 1.5 by 1.5 mm^2 cross section were used) can be tested at low temperatures without cleavage. This does not necessarily mean there is no DBTT for the steel. Instead, it might just mean the specimen size and geometry does not allow the determination of a DBTT for the steel, and larger specimens with a sharper crack might give different results.

If the results are as presented by the authors [93], they are very encouraging. However, as pointed out [93], anisotropy [see Fig. 14.21(a)], such as that observed for ODS steels previously for biaxial creep also is manifested in the impact behavior of the steels. Missing from the investigation of this steel is any detailed microstructural analysis of the 1DS steel beyond a TEM photomicrograph in the unirradiated condition showing a high density of fine oxide particles [92].

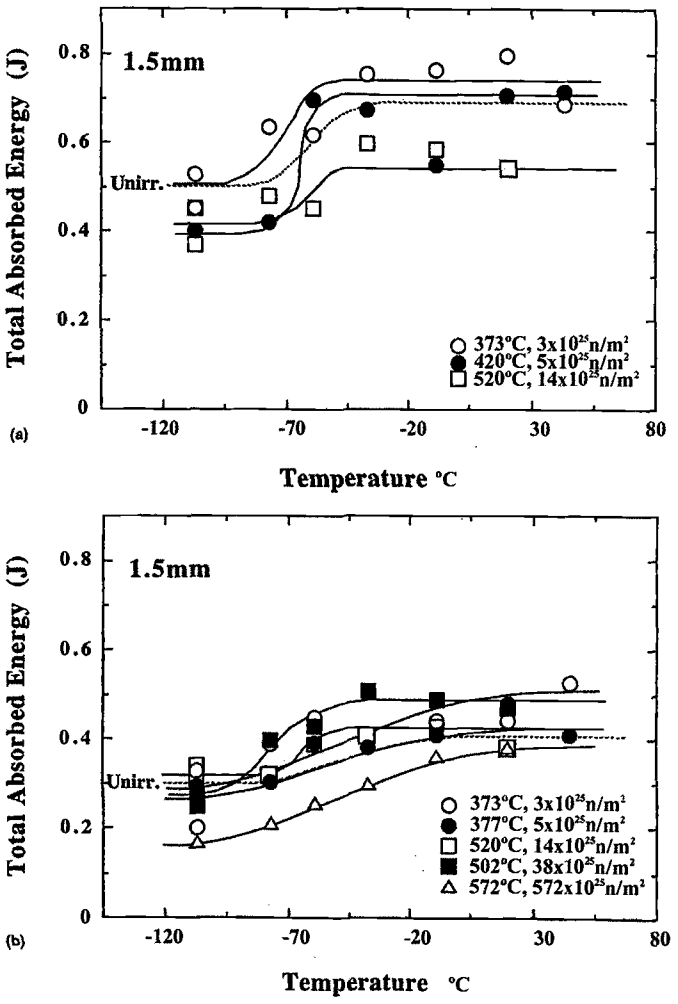

FIG. 14.22—Charpy curves (1.5-mm specimens) of (a) 1DS-L and (b) 1DS-T in the unirradiated and irradiated condition [93].

IRRADIATION EMBRITTLEMENT: HELIUM EFFECTS

Nickel-Doped Steels

The preceding discussion on embrittlement focused on the effects of displacement damage on Charpy impact behavior. Displacement damage leads to changes in the dislocation structure and, in some cases, induces precipitation and changes in precipitates, both of which can lead to hardening and embrittlement. Effects due to transmutation helium, if they occur, will be in addition to those caused by displacement damage.

The experimental technique described in Chapter 8 to produce helium simultaneously with displacement damage by irradiating nickel-doped steels was used to study the effect of helium on the 9Cr-1MoVNb and 12Cr-1MoVW steels. Charpy V-notch impact specimens of the following five steels were irradiated in the HFIR (a mixed-spectrum reactor): 9Cr-1MoVNb, 9Cr-1MoVNb-2Ni (9Cr-1MoVNb with 2% Ni), 12Cr-1MoVW, 12Cr-1MoVW-1Ni, (12Cr-1MoVW with 1% Ni), and 12Cr-1MoVW-2Ni (12Cr-1MoVW with 2% Ni) [20,23,94]. The compositions of standard 9Cr-1MoVNb and 12Cr-1MoVW steels contain ≈0.1 and ≈0.5% Ni, respectively.

Results from the HFIR irradiations were compared with results from irradiations in the EBR-II, a fast reactor where little helium forms. In irradiations in EBR-II to 13 and 26 dpa at 390°C, the ΔDBTT saturated with fluence at ≈54°C for 9Cr-1MoVNb and ≈144°C for 12Cr-1MoVW (Fig. 14.5) [8]. Other fast-reactor irradiations demonstrated that saturation occurred by 10 dpa or less [3]. When the same heats of 12Cr-1MoVW and 12Cr-1MoVW-2Ni steels used in the HFIR experiments were irradiated to 12 dpa in EBR-II at 390°C, shifts in DBTT of 122 and 90°C, respectively, were observed [95], in line with data for 12Cr-1MoVW after 13 and 26 dpa.

The ΔDBTT values for 9Cr-1MoVNb (204°C) and 12Cr-1MoVW (242°C) steels after irradiation in HFIR at 400°C to ≈40 dpa [94] were considerably higher than after irradiation in EBR-II at 390°C to 13 and 26 dpa (Fig. 14.23). After HFIR irradiation, the 9Cr-1MoVNb contained ≈30 appm He, and the 12Cr-1MoVW contained ≈110 appm He. The difference in properties was taken to indicate that the saturation in ΔDBTT observed in the EBR-II at 390°C did not apply to HFIR. Further, when the 12Cr-1MoVW-2Ni and 9Cr-1MoVNb-2Ni were irradiated in HFIR at 400°C to ≈40 dpa and ≈370 appm He, the ΔDBTTs were >325°C, which was considerably above the values for the steels without the nickel additions, and also greater than the value (90°C) obtained for 12Cr-1MoVW-2Ni when irradiated in EBR-II at 390°C. Examination of some fractured specimens of 9Cr-1MoVNb-2Ni and 12Cr-1MoVW-2Ni provided an indication of intergranular fracture, although these observations were not on the Charpy specimens.

Irradiation at 300°C in HFIR indicated there was an effect of helium when the Charpy properties of the steels with 2% Ni were compared to those with no added nickel (no com-

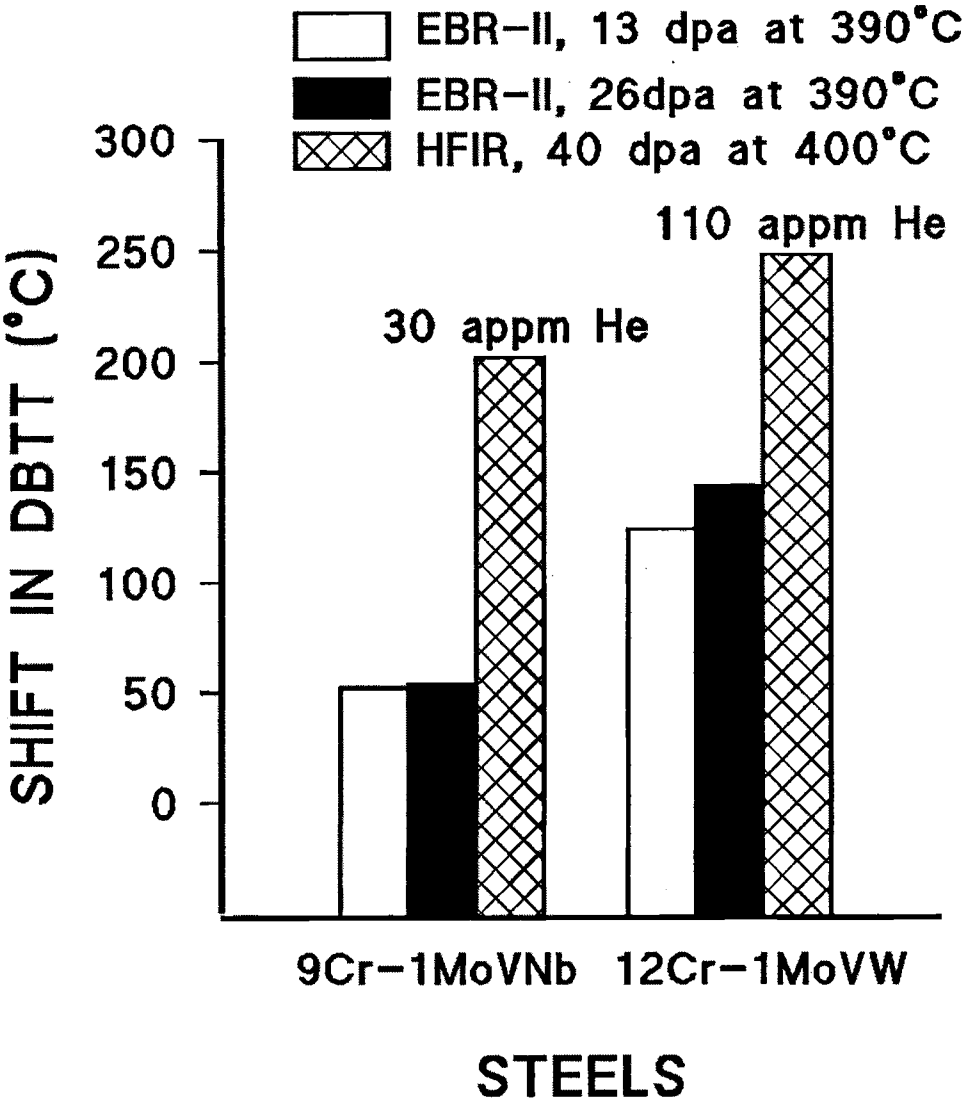

FIG. 14.23—A comparison of the shift in DBTT after irradiation in EBR-II to 13 and 26 dpa and in HFIR to 40 dpa for 9Cr-1MoVNb and 12Cr-1MoVW steels.

parison with fast reactor irradiation was possible because of the low irradiation temperature) [94]. However, the ΔDBTT at 300°C for the respective steels with and without the nickel additions was considerably less than at 400°C, which, as discussed in the previous section of this chapter, is inverse to the temperature effect for these steels and most other steels irradiated in a fast reactor over the range 365 to 550°C (i.e., the ΔDBTT decreases with increasing irradiation temperature for irradiation in a fast reactor).

After considering possible explanations for the difference in ΔDBTT for the same steels irradiated in HFIR and EBR-II and why the steels with 2% Ni were embrittled more than those with less nickel when irradiated in HFIR, it was concluded that helium plays a role in the embrittlement [94]. This helium effect is in addition to the effect caused by the irradiation hardening from dislocation loops and irradiation-enhanced precipitation. Since excess hardening by helium as measured in tensile tests was not sufficient to explain the observations, it was proposed that helium decreases the fracture stress (the third helium effect discussed in Chapter 12 on irradiation effects on tensile behavior) by promoting intergranular fracture (see Fig. 14.2).

To explain the helium effect in the absence of significant hardening caused by helium, it was proposed that when the steels contain sufficient helium, the microcrack source to initiate fracture could be helium bubbles on a prior-austenite grain boundary or a lath boundary [23,94]. Helium was envisioned to collect into small cavities that under stress become nuclei for fracture and/or enhance crack propagation, which explains why fracture surfaces of HFIR-irradiated, helium-containing steels contain intergranular facets. This hypothesis can explain the inverse temperature effect (a larger shift at 400°C than 300°C) relative to fast-reactor irradiations because more rapid diffusion of helium at 400°C than at 300°C means that at 400°C more helium reaches boundaries to produce more and larger bubbles and a larger ΔDBTT. Bubble development at 300°C is slower than at 400°C, but bubble development at the lower temperature will proceed at higher fluences (longer diffusion times) or higher helium generation rates, with a corresponding in-

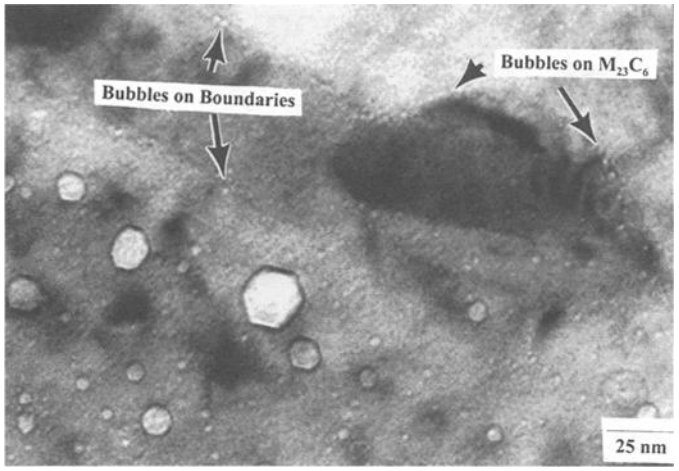

FIG. 14.24—Bubbles on lath boundaries and on precipitates of 12Cr-1MoVW-2Ni steel irradiated to 74 dpa (760 appm He) at 400°C in HFIR [96].

crease in the ΔDBTT. This was observed for the 9Cr-1MoVNb-2Ni and 12Cr-1MoVW-2Ni steels irradiated to 27 dpa at 300°C, where these steels developed a larger ΔDBTT than the steels without any nickel additions.

Bubbles have been observed on prior austenite grain boundaries and lath boundaries of steels containing 2% Ni (Fig. 14.24), and as seen in Fig. 14.24, bubbles also agglomerate on precipitates [96]. Precipitates are generally the source of crack nuclei in steels [13,14], and as an alternative crack-nucleation process, it is suggested that bubbles on a precipitate/matrix interface could enhance crack nucleation. Obviously, more work is required to understand the mechanism.

The nickel-doping technique is not the ideal way to conduct helium-effects studies because of the danger that nickel will change the microstructure. As noted in Chapter 9, some nickel-containing precipitates can form during irradiation of nickel-doped steels that do not form in undoped steels [17,97]. A fairly high number density of such precipitates identified as M_6C were observed in the 9Cr-1MoVNb-2Ni [17]. However, it has also been shown that the same precipitates in similar amounts to those formed in the mixed spectrum of HFIR at 400°C also formed during fast reactor irradiation in FFTF at 407°C [17]. Since the ΔDBTT was much smaller after the fast reactor irradiation than the mixed-spectrum irradiation, the extra embrittlement could not be attributed to the precipitates.

Alternate explanations for the nickel-doping observations were considered [23,94]. They included other transmutation reactions with thermal neutrons in HFIR, thermal aging effects, and nickel-enhanced hardening. None of these provided a satisfactory explanation for the observations. A mechanism for intergranular fracture of irradiated ferritic steels that does not involve helium was proposed by Faulkner and co-workers [98,99], who demonstrated that silicon and phosphorus segregate to lath boundaries in FV448 when irradiated to 46 dpa in the DFR (a fast reactor) at 465°C. The proposed segregation model assumed a linkage between impurities (Si, P, etc.) and irradiation-produced point defects to drive the transfer of impurities to boundaries. Kimura et al. observed intergranular fracture in 9Cr-2Mn-1W and 12Cr-6Mn-1W steels irradiated to 10 and 25 dpa at 365°C in FFTF [91]. They attributed the fracture behavior to radiation-induced segregation of manganese and silicon to grain boundaries, which were detected on fracture surfaces by Auger spectroscopy. Such irradiation-induced segregation models could only explain the nickel-doping observations if helium enhanced segregation, since no similar effect occurred when the steels were irradiated in a fast reactor.

There is also evidence of irradiation-induced nickel segregation to lath boundaries in FV448 irradiated in DFR at 465°C [98] and 12Cr-1MoVW irradiated in EBR-II at 410°C [100]. This segregation could amplify the helium produced at a boundary in nickel-containing ferritic steels over that involving helium diffusion to the boundary alone. Although this could enhance the effect of helium after irradiation to high displacements, it should not affect the relevance of the observations for fusion, since the concentration of helium on grain boundaries in the steels will be well below concentrations relevant for boundaries in a fusion reactor first wall.

The use of the nickel-doping technique to simulate helium effects is not without controversy. Possible explanations other than helium were proposed, including precipitation-hardening reactions due to G-phase and α′ and possible errors in temperatures [101]. In a reply by the investigators, they demonstrated why these suggestions could not explain their observations [102]. In a recent publication, Gelles et al. [103] used the work on the Fe-12Cr-1.5Ni alloys [97,104] discussed in Chapters 9 and 12 to again warn about the use of the nickel-doping technique to study helium effects on Charpy behavior.

If the results of the nickel-doping experiments are examined objectively (note that one of the authors of this book was an investigator in the nickel-doping experiments), several problems are obvious. Tensile and Charpy irradiations were conducted separately, and different product forms were used to make the tensile (rod and sheet) and Charpy (plate) specimens. This resulted in the heat treatment of different product forms. Because nickel lowers the A_{C1} temperature, different tempering temperatures were used for the steels with no nickel and 2% Ni. This procedure was chosen to allow a comparison with previous tensile data for the undoped steels, although it made the interpretation of tensile results more difficult. An effort was made to temper to similar hardnesses, although the steels still had different strengths when they were irradiated (Chapter 12). No direct temperature measurements were made during irradiation; a gas gap between the specimen holder and the specimen was used to achieve the calculated temperature from nuclear heating. All of these difficulties could hinder the interpretation of the results.

Boron-Doped Steels

Until recently, the nickel-doping experiments provided the only indications that helium might affect impact toughness. Results are now available from boron-doping experiments that show similar effects.

Shiba et al. [66] used ^{10}B additions to F82H steel to study the effect of helium on Charpy properties after irradiation in JMTR and JRR-2. Irradiation of ^{10}B-doped specimens and undoped specimens at 355 to 375°C to 0.3 to 0.5 dpa to form 300 appm He in the doped F82H produced a DBTT in the

doped steel ≈15°C higher than in the undoped steel. No shift in transition was observed for these steels when irradiated at 500 to 590°C.

A larger effect using ^{10}B doping was obtained for F82H irradiated at a lower temperature (260 to 360°C) to 0.3 to 0.6 dpa in JMTR [105]. Although a complete Charpy curve was not determined (because of temperature limitations of the Charpy test rig) for the ^{10}B-doped steel with 100 appm He, the ΔDBTT appeared to be well above room temperature (Fig. 14.25) and much larger than for the standard F82H irradiated similarly. Both steels had similar Charpy curves before irradiation. As shown in Chapter 12 on tensile properties, there was no difference in the yield stress of the ^{10}B-containing steel and a steel without the ^{10}B addition. Both hardened by a similar amount, although there was a slight loss of ductility for the ^{10}B-containing steel.

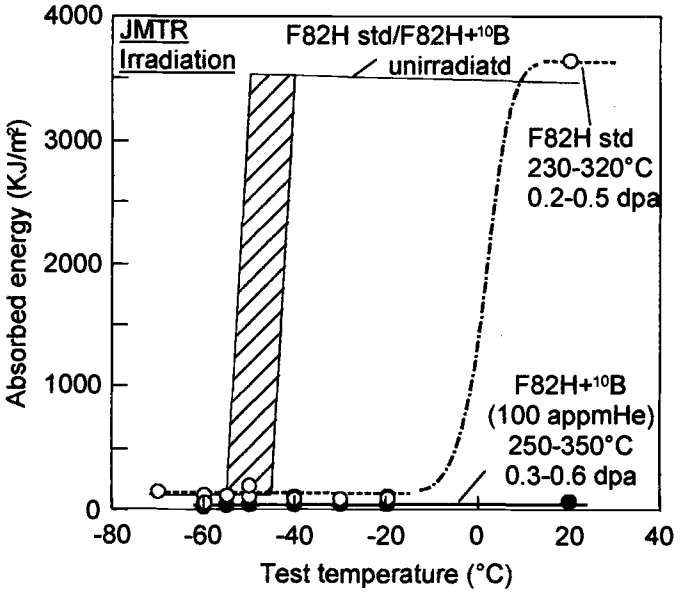

FIG. 14.25—Charpy impact curves for standard F82H and ^{10}B-doped F82H in the unirradiated condition and after irradiation to 0.2 to 0.6 dpa at 250 to 350°C in JMTR [105].

Van Osch et al. [106] irradiated the standard JLF-1 (a 9Cr-2WVTa steel) and this steel with 0.0022% B to 2.5 dpa at 300°C in HFR. Before irradiation, the steels had similar Charpy curves. After irradiation, the DBTT of the boron-containing steel with ≈23 appm He was about 70°C higher than for the steel without the boron addition.

The data obtained from irradiation in HFR that are shown in Fig. 14.18 has also been explained as a possible helium effect [71,107]. Figure 14.18 shows the relative behavior of four reduced-activation steels and two conventional Cr-Mo steels irradiated to 0.8 dpa and, as stated above, relatively similar results were observed after 2.4 dpa. In Fig. 14.26, the ΔDBTT data for these steels are shown as a function of dose for the 300°C irradiation. Also shown is the boron content of each steel. It was observed that the higher the boron content, the steeper the slope of the curve and the higher the ΔDBTT for the individual steels. A curve for the ^{10}B-to-He transformation is also shown, and it has the same characteristics as the embrittlement curves. Over 99% of the ^{10}B has transformed to helium by 1.6 dpa, which is near where saturation in ΔDBTT with fluence occurs for the MANET I steel. Maximum

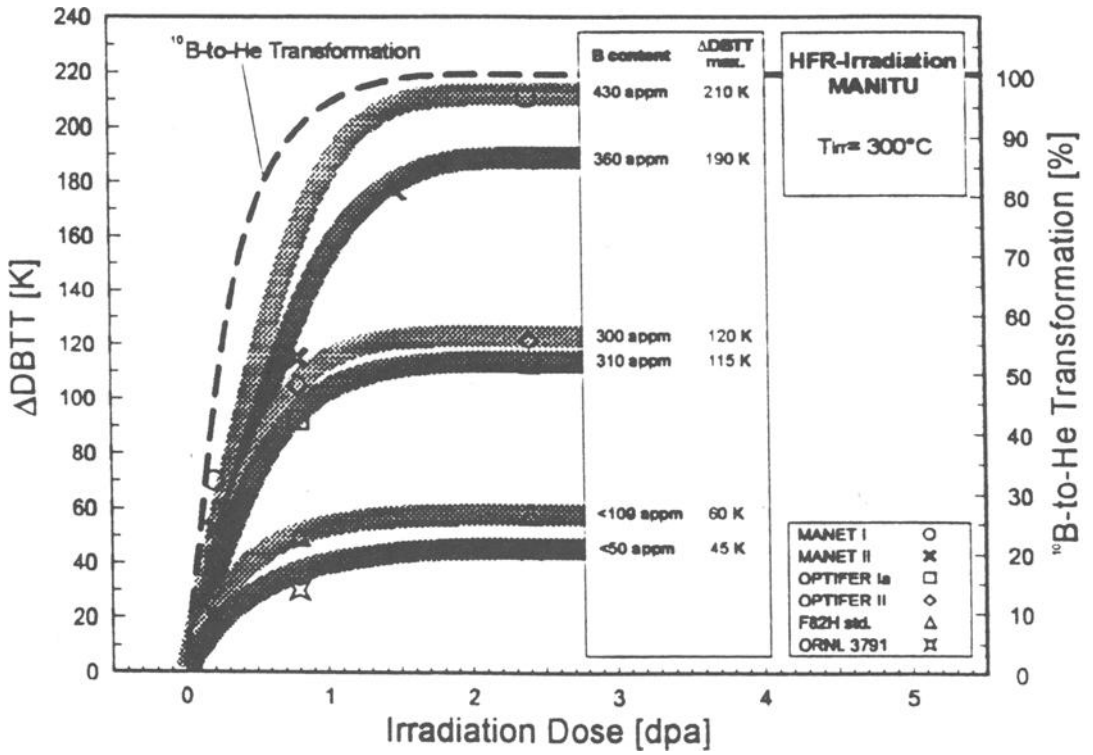

FIG. 14.26—Shift in DBTT versus irradiation dose of six steels irradiated in HFR showing how the shift in DBTT correlates with boron content, and therefore, helium content [71].

helium in the steels was calculated as 85, 70, 60, 60, <20, and <10 appm for MANET I, MANET II, OPTIFER Ia, OPTIFER II, F82H, and ORNL 9Cr-2WVTa, respectively. The ΔDBTTs for the steels scale with the boron content and, therefore, the helium content; the ratio of ΔDBTT to helium was essentially the same for all of the steels at ≈2 to 3°C/appm He [71].

Hardness measurements and SEM and TEM observations were made on the five steels irradiated to 0.8 dpa at 250 and 450°C in HFR [107]. There was a slight increase in hardness of all the steels irradiated at 250°C, with the ORNL 9Cr-2WVTa steel showing the smallest increase and the MANET II showing the largest increase.

Before irradiation, SEM of the fracture surfaces of the OPTIFER IA, OPTIFER II, and MANET II steel displayed the typical fracture modes: cleavage on the lower shelf and ductile tearing on the upper shelf [107]. After irradiation of these steels at 250°C, some indications of intergranular failure appeared. This mixed-mode of intergranular and transgranular fracture became more pronounced after irradiation at 450°C. The F82H, on the other hand, had the typical transgranular cleavage or ductile tearing (dimple fracture) under all conditions. Some areas of intergranular fracture were noted on the brittle-fracture areas of the ORNL 9Cr-2WVTa steel in the unirradiated condition. However, after irradiation, the fracture mode returned to that generally observed: cleavage for the brittle fracture mode and dimples for the ductile mode. These SEM results do not appear to show any correlation with helium content.

The TEM observations before irradiation indicated the typical tempered martensite microstructures with $M_{23}C_6$ and MC precipitates. After irradiation at 250°C, helium bubbles, dislocation loops, and α′ precipitates were observed (Table 14.3). Bubbles were located in the matrix and on dislocation loops. The highest concentration of bubbles and dislocation loops appeared in the OPTIFER II, and the highest concentration of α′ was in OPTIFER Ia. It was reported that the bubbles in F82H and ORNL 9Cr-2WVTa were difficult to detect, and the number densities reported were maximum values found in one or two laths, with large areas appearing to be free of bubbles [107].

After irradiation at 450°C, bubbles were observed, and the largest bubbles were again in the OPTIFER II. However, the bubble number densities were not very different for the different steels. No loops were observed, and α′ was only observed in the F82H. The appearance of α′ in these steels is interesting, because this phase does not generally appear in steels with less than 10 to 12% Cr (only the MANET steels contained over 10% Cr). This irradiation-induced phase appears to depend on irradiation temperature; it was observed in all the steels after irradiation at 250°C but only in F82H after irradiation at 450°C. There have been few previous studies of the microstructures of such steels irradiated at temperatures as low as 250°C.

The results of the studies were interpreted in terms of helium concentrations [107], similar to the interpretation after 2.4 dpa [71] discussed above. The authors presented the results for irradiation at 250°C graphically (Fig. 14.27) to show that the shift in DBTT could be correlated with the helium content of the steels. Based on the complicated microstructures, it may be premature to say that helium is the cause of this behavior. In examining the results at 250°C (Table 14.3 and Fig. 14.27), it is interesting to note that in addition to the ORNL 9Cr-2WVTa steel having the lowest shift in DBTT with the lowest helium concentration, it also had the lowest bubble density, dislocation loop density, and the smallest density of α′ precipitates. Also, F82H had a high density of α′ particles, even though it had the lowest chromium concentration (7.7 % for the F82H versus 9 to 10% for the other steels). Ob-

TABLE 14.3—TEM observations and hardness of steels irradiated in HFR at 250°C [107].

Steel	Helium Bubbles Size, μm	Helium Bubbles Density, cm^{-3}	Helium Bubbles Location	Density of Loops, cm^{-3}	Density of α′, cm^{-3}	Hardness Increase
Irradiated at 250°C						
OPTIFER Ia	2	$1.5x10^{16}$	D, H	$5.9x10^{15}$	$1.0x10^{16}$	31
OPTIFER II	3	$3.8x10^{18}$	D	$2.6x10^{17}$	$2.1x10^{15}$	26
F82H	1.5	$1.4x10^{17}$*	H,S,P	$1.9x10^{16}$	$7.5x10^{15}$	18
9Cr-2WVTa	2	$1.1x10^{16}$*	D,P	$1.0x10^{15}$	$3.5x10^{10}$	15
MANET II	2	$3.6x10^{16}$	D,S,P	$1.4x10^{15}$	$3.8x10^{15}$	53
Irradiated at 450°C						
OPTIFER Ia	2	$5.7x10^{15}$	D,S,P	-	-	-1
OPTIFER II	6	$1.2x10^{15}$	D,S	-	-	-8
F82H	3	$3.7x10^{16}$*	H,D	-	$1.9x10^{16}$	-9
9Cr-2WVTa	3	$4.6x10^{15}$*	D	-	-	-11
MANET II	4	$1.1x10^{15}$	D,P	-	-	-2

D: Dislocations; S: subgrain boundaries; P: Precipitates; H: Homogeneously Distributed
*Maximum concentration (large areas were observed that did not contain bubbles)

viously, more detailed microstructural analysis after irradiation is required before the behavior of these steels is completely understood.

The large ΔDBTT (210°C) for MANET I after 0.8 dpa at 300°C (Fig 14.18) is similar to results obtained for this steel when irradiated to 5 to 15 dpa at 290 to 470°C in HFR (Fig. 14.15), although helium was not cited as a reason for the large ΔDBTT in the earlier work [6,48]. The steel contains ≈85 ppm B and 0.9% Ni, and, thus, >100 appm He is generated in the mixed spectrum of HFR. Figure 14.28 displays the data from Fig. 14.15 along with data for the HFIR-irradiated 9Cr-1MoVNb steel [23,94] and for 9Cr-1MoVNb irradiated in EBR-II at 390 to 550°C [8]. Comparison is made with 9Cr-1MoVNb because MANET I contains 10.5% Cr and, like 9Cr-1MoVNb, it contains the strong carbide former niobium. Shifts of around 280°C were observed for the MANET I at ≈290°C [48]. This even exceeds the shift of 218°C observed for 9Cr-1MoVNb-2Ni steel irradiated in HFIR at 300°C to ≈27 dpa [23].

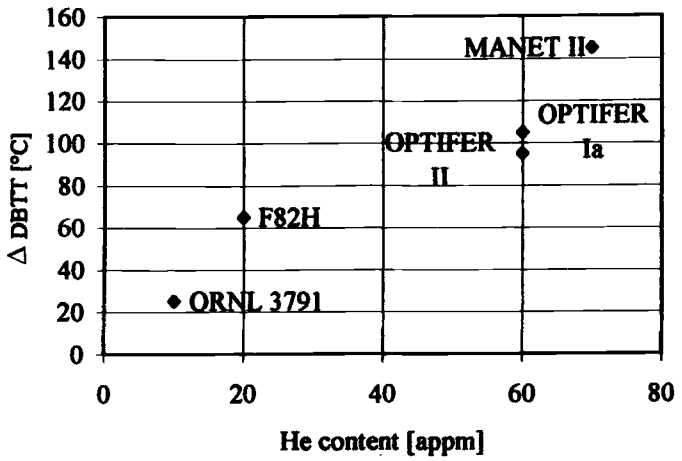

FIG. 14.27—Shift in DBTT as a function helium concentration for various steels irradiated to 0.8 dpa at 250°C in HFR [107].

Although the nickel- and boron-containing steels display similarities that can be attributed to helium (a large increase in DBTT relative to steels containing less helium), there are also differences. Contrary to the behavior of the 9Cr-1MoVNb irradiated in HFIR, which shows the inverse-temperature relationship, MANET I (and the other B-containing steels in Fig. 14.18) displayed the typical decreasing ΔDBTT with increasing temperature (Figs. 14.5, 14.15, 14.18, and 14.28). Near 400°C, where the nickel-containing steels showed the largest effect of helium, the behavior of the boron-containing steels approached that observed in a fast reactor (Fig. 14.28), where little helium is formed. This means that if this is a helium effect, it apparently disappeared at elevated temperatures where hardening no longer occurs.

Boron is a surface-active element and can segregate to austenite grain boundaries depending on the cooling rate from the austenitization temperature (i.e., the boron concentration at the boundaries is enriched over the matrix) [108–110]. All of the ^{10}B in MANET I will be transmuted to produce ≈80 to 90 appm He by the time ≈1.6 dpa is achieved in HFR (Fig. 14.26). Therefore, enhanced amounts of transmutation helium might be expected to form at or near prior austenite grain boundaries. Bubble formation at prior austenite grain boundaries and lath boundaries was observed when boron-containing 9Cr-2WVTa steel was irradiated in FFTF, and the results were interpreted to indicate a propensity for boron to segregate to boundaries [111].

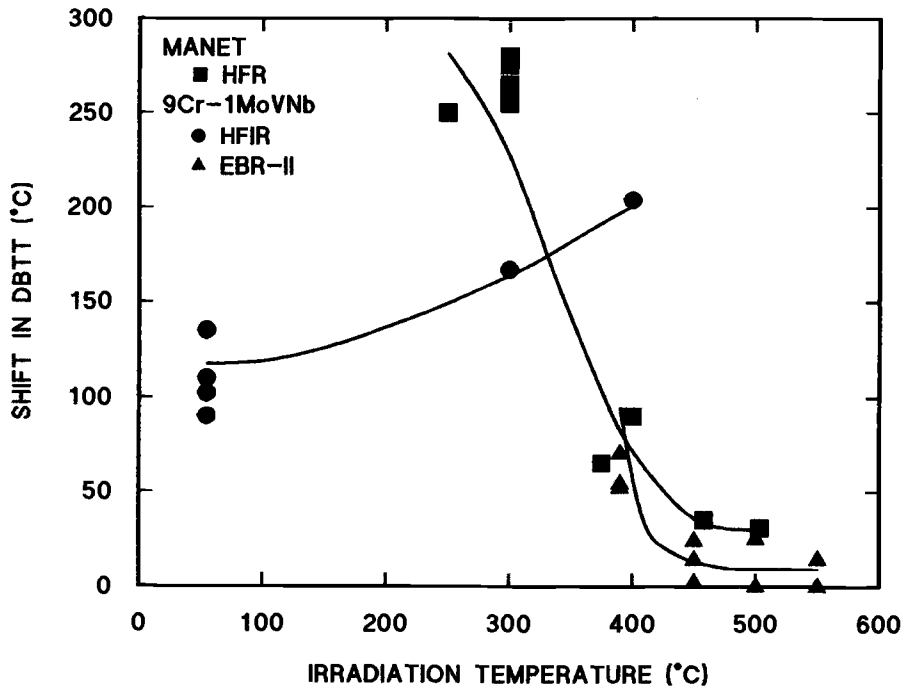

FIG. 14.28—Shift in DBTT as a function of irradiation temperature for MANET I steel and 9Cr-1MoVNb steel. MANET I was irradiated in HFR and 9Cr-1MoVNb was irradiated in HFIR and EBR-II.

In contrast to the boron, nickel does not segregate to grain boundaries prior to irradiation, but there is evidence that segregation can occur during irradiation [98]. If the fracture is assumed to be associated with a boundary, then these differences between how helium reaches grain boundaries can be used to explain the difference between observations on nickel- and boron-doped steels.

If it is assumed that helium causes the initiation of an intergranular fracture, the large shift in DBTT at low temperature (≈250 to 290°C) for the MANET I steel could occur because the helium is formed on or near prior-austenite grain boundaries or martensite lath boundaries. A smaller shift occurs for the nickel-doped 9Cr-1MoVNb steel at 300°C because the helium formed in the matrix during irradiation must first diffuse to the boundary. Alternatively, nickel in the matrix could also diffuse to the boundary and undergo the (n,α) reaction. As discussed above, the required diffusion for nickel-containing steels was used to explain the inverse temperature effect [94]. Likewise, since the assumption is that much less diffusion is required for boron, the largest helium effect for boron-containing steels would be expected at the lowest temperature because hardening is greatest at these temperatures.

Although this might explain the differences in behavior of boron- and nickel-containing steels at around 300°C, a different explanation is required for observations at 400°C, where the 9Cr-1MoVNb steel showed the largest increase in DBTT under conditions where helium forms. However, considerable hardening occurs for the 9Cr-1MoVNb steel irradiated at 390°C in EBR-II (Fig. 12.2) [112] and at 400°C in HFIR [113]. This contrasts to much less hardening at 400°C for MANET I (Fig. 12.12) [114]. Thus, the difference in the steels must reflect the different hardening behavior. (The difference in the embrittlement of MANET I at 300 and 400°C may be reflected in the different correlation factors between ΔDBTT and $\Delta\sigma_y$ in Eqs 14.1 and 14.2 for irradiation at about 300 and 400°C, respectively.) Although the mechanism of embrittlement is unclear, these results show that embrittlement depends on hardening, and there is an upper limit on embrittlement—with or without helium—which is determined by the temperature where hardening ceases.

Cyxloreon-Injected Helium

A more direct effect of helium was observed when subsize Charpy specimens of F82H were implanted with 300 appm He by irradiating at 250°C to 0.2 dpa with a degraded 104 MeV α-particle beam in a cyclotron [115]. The results were compared with results for the steel irradiated to 0.2 dpa (8 appm He) at 250°C in HFR (Fig. 14.29). A significantly higher ΔDBTT was observed for the helium-implanted specimens: a ΔDBTT of 44°C was observed for the cyclotron-irradiated specimen compared to an 18°C shift after the HFR irradia-

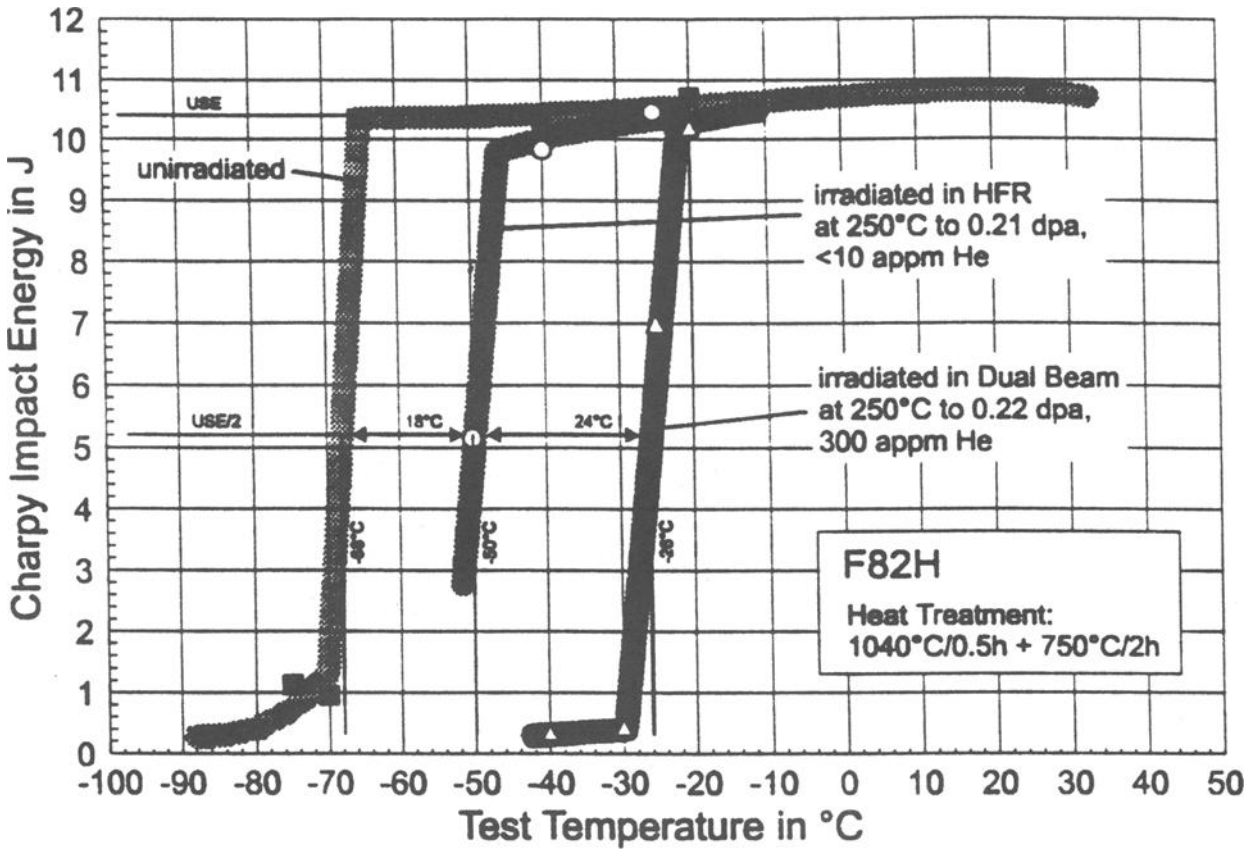

FIG. 14.29—Charpy curves for F82H irradiated in HFR at 250°C to 0.2 dpa (8 appm He) and F82H implanted with helium from a cyclotron to obtain 300 appm He at 0.2 dpa [115].

tion. TEM observations indicated that the helium-injected F82H contained bubbles that were not homogeneously distributed, with the larger bubbles on dislocations, sub-boundaries, and precipitate interfaces. Tension tests of cyclotron-irradiated steel indicated little or no effect of helium on hardening. This agrees with the observations for the nickel-doped and boron-doped steels. Hardening from dislocation loops and precipitates does make a significant contribution to the embrittlement [115]. A phenomenological model to describe the brittle fracture behavior as a stress-induced propagation of microcracks and its dependence on the helium bubble morphology was proposed.

Helium Effects: Past and Future

Indications of a helium effect on the embrittlement of the ferritic/martensitic steels have now been obtained by irradiating nickel- and boron-doped steels and by α-particle injection, and all three techniques produced similar effects on the Charpy properties. These results have led several investigators to conclude that helium exacerbates the embrittlement above that due to displacement damage alone. Results are available from several sources that indicate helium does not contribute to hardening commensurate with the additional shift in DBTT observed when the helium is present in the steel. That leads to the conclusion that helium has somehow reduced the fracture stress (Fig. 14.2).

Much of the above discussion on interpreting the boron- and nickel-doping results relied on speculation. More quantitative information is required before the helium-embrittlement effect is understood. Cyclotron irradiation appears to be the most direct method for such studies. However, such tests are the most difficult and expensive to carry out on even miniature Charpy specimens, because of the difficulty in uniformly injecting the helium and the expense of long injection times. For that reason, much of the work necessary to try to understand the effect will have to rely on the other simulation techniques—namely, boron and nickel doping.

Up until now, the interpretation of the nickel- and boron-doping experiments has suffered because of the difficulty of doing single-variable tests. This produced an uncertainty because of the difficulty associated with not being able to clearly separate the effects of the dopants from the helium. This could be addressed by doping steel with ^{10}B and ^{11}B (from which no transmutation helium forms during irradiation), the ^{11}B being used to determine the effect of boron on the behavior of the steel. Different ratios of ^{10}B:^{11}B could be used to establish the effects of boron and helium.

One problem with boron-doping is the tendency for boron to segregate to grain boundaries and its limited solubility in steels [108,109], which could result in most of the boron being on boundaries and/or in precipitates. However, work on austenitic stainless steel indicated that if the steel was cooled rapidly enough (500°C/s versus 50°C/s) from the solution-treatment temperature, boron was uniformly distributed [110]. Autoradiography could be used to determine if the same thing applies for the ferritic steels during austenitization.

The nickel-doping technique provides a uniform distribution of helium in the steel. However, nickel evidently promotes some precipitation during irradiation [17], although this has not prevented the technique from producing the same kind of results as obtained by cyclotron implantation and boron doping. Similar precipitates were produced in both fast and mixed-spectrum reactor irradiations, and the steel irradiated in the fast reactor containing very little helium was embrittled much less. If nickel is used in the future, the amount of nickel should probably be reduced from 2%, since the objective will be to determine the nature of the helium effect and not necessarily simulate helium effects in a tokamak, as was the original idea behind using 2% Ni for these experiments.

Analogous to the ^{10}B:^{11}B experiment discussed above, another possibility for separating the effects of nickel from helium is by isotopically tailoring the steels with varying ratios of ^{58}Ni:^{59}Ni:^{60}Ni (see Chapter 8) rather than using natural nickel. Unfortunately, the price of nickel isotopes makes this cost prohibitive for Charpy and tension tests, although the technique has been used to study the effect of helium on swelling. On the other hand, the cost of the ^{10}B and ^{11}B isotopes are quite cheap and would not be an impediment to using these isotopes in the ^{10}B:^{11}B experiment.

There are several experiments with boron- and nickel-doped steel that should help reveal helium effects. If the boron distribution can be changed by controlling the cooling rate from the austenitization temperature, then irradiation experiments on specimens from steel cooled at rates that cause most of the ^{10}B to be segregated to boundaries could be compared to those from steel cooled to get a uniform distribution of the ^{10}B. These could be irradiated to 1 dpa or less in a mixed-spectrum reactor to transmute the ^{10}B to helium. The difference (if any) in the embrittlement of the steels should reveal information about the role of boundaries. A comparison of boron- and nickel-doped specimens should provide similar information. Side-by-side irradiation of the two types of specimens over the range 250 to 400°C to various doses (say up to 5 dpa) should reveal whether boundaries are involved in the embrittlement.

All irradiations of Charpy specimens need to be accompanied by tension specimens to determine the hardening that occurs. Transmission electron microscopy is required in all of these experiments to determine the distribution of helium bubbles in the nickel-containing and boron-containing steels. Likewise, detailed scanning electron microscopy of fracture surfaces is required. No such detailed microscopy has been carried out, but with such information in conjunction with the mechanical properties determinations, it should be possible to understand what occurs in the nickel- and boron-containing steels. From that information, assuming the observations on embrittlement are proved to be due to helium, it should be possible to more reliably assess the simulation techniques and extrapolate the results to the effect of helium under fusion conditions. Once an understanding of the effect is available, solutions to the problem can be explored.

Another technique proposed to study helium effects in a single-variable experiment is to replace natural iron in the steel with ^{54}Fe (natural iron contains 5.84% ^{54}Fe) The technique was first suggested for studying hydrogen effects [116], because irradiation of this isotope results in (n,p) reactions in addition to the (n,α) reactions that generate he-

lium. Much more hydrogen than helium is produced [118]. There are two problems with this technique for studying helium effects: only about 2.3 appm He/dpa are produced when irradiated in HFIR [117], and ^{54}Fe is expensive (about $20,000 per gram). Obtaining enough ^{54}Fe to fabricate any kind of mechanical property specimens would be extremely costly. To date, several grams of the ^{54}Fe have been used to produce a few F82H TEM specimens that were irradiated in HFIR [116]. A shear-punch test was used to estimate the hardening that occurred during irradiation. No effect of helium was detected, although an effect of hydrogen was observed [118]. To obtain a higher helium production rate ($\approx$20 appmHe/dpa) than for ^{54}Fe, the use of ^{55}Fe has been suggested [117]. However, ^{55}Fe costs even more than ^{54}Fe. Therefore, the nickel- and boron-doping experiments are the only viable simulation techniques available at present for studying helium effects on mechanical properties.

Obviously, neither the addition of nickel nor boron is the ideal method for studying the effects of helium for fusion applications. A 14 MeV neutron source is required. Until such a neutron source is available, however, simulation techniques must be used with caution to obtain an understanding of possible helium effects.

REFERENCES

[1] J. R. Hawthorn, in: Treatise on Materials Science and Technology Vol. 25 (Academic Press, New York, 1983) 461.

[2] G. E. Lucas and D. S. Gelles, J. Nucl. Mater. 155-157 (1988) 164.

[3] R. L. Klueh and D. J. Alexander, in: Effects of Radiation on Materials: 15th International Symposium, ASTM STP 1125, Eds. R. E. Stoller, A. S. Kumar, and D. S. Gelles (American Society for Testing and Materials, Philadelphia, 1992) 1256-1266.

[4] I. Belianov and P. Marmy, J. Nucl. Mater. 258-263 (1998) 1259.

[5] R. L. Klueh and J. M. Vitek, J. Nucl. Mater. 132 (1985) 27.

[6] C. Wassilew and K. Ehrlich, J. Nucl. Mater. 191-194 (1992) 850.

[7] V. S. Agueev, V. N. Bykov, A. M. Dvoryashin, V. N. Golovanov, E. A. Medvendeva, V. V. Romaneev, V. K. Shamardin, and A. N. Vorobiev, in: Effects of Radiation on Materials: 14th International Symposium, Vol. I, ASTM STP 1046, Eds. N. H. Packan, R. E. Stoller, and A. S. Kumar (ASTM, Philadelphia, 1989) 98.

[8] W. L. Hu and D. S. Gelles, in: Influence of Radiation on Material Properties: 13th International Symposium (Part II), ASTM STP 956, Eds. F. A. Garner, C. H. Henager, Jr., and N. Igata (American Society for Testing Materials, Philadelphia, 1987) 83.

[9] F. A. Smidt, Jr., J. R. Hawthorne, and V. Provenzano, in: Effects of Radiation on Materials: Tenth Conference, STP 725, Eds. D. Kramer, H. R. Brager, and J. S. Perrin (American Society for Testing and Materials, Philadelphia, 1981) 269.

[10] J. M. Vitek, W. R. Corwin, R. L. Klueh, and J. R. Hawthorne, J. Nucl. Mater. 141-143 (1986) 948.

[11] W. R. Corwin, J. M. Vitek, and R. L. Klueh, J. Nucl. Mater. 149 (1987) 312.

[12] J. M. Vitek and R. L. Klueh, Met. Trans. A 14A (1983) 1047.

[13] R. W. Hertzberg, Deformation and Fracture Mechanics of Engineering Materials, 3rd Edition (John Wiley & Sons, New York, 1989) 253.

[14] C. J. McMahon, Jr., in: Fundamental Phenomena in the Materials Sciences, Vol. 4, Eds. L. J. Bonis, J. J. Duga, and J. J. Gilman (Plenum Press, New York, 1967) 247.

[15] D. S. Gelles and L. E. Thomas, in: Topical Conference on Steels for Use in Nuclear Energy Technologies, Eds. J. W. Davis and D. J. Michel (The Metallurgical Society of AIME, Warrendale, PA, 1984) 559.

[16] J. J. Kai and R. L. Klueh, J. Nucl. Mater. 230 (1996) 116.

[17] P. J. Maziasz, R. L. Klueh, and J. M. Vitek, J. Nucl. Mater. 141-143 (1986) 929.

[18] R. L. Klueh and J. M. Vitek, J. Nucl. Mater. 137 (1985) 44.

[19] W. L. Hu and D. S. Gelles, in: Effects of Irradiation on Materials: 14th International Symposium (Volume II) ASTM STP 1046 , Eds. N. H. Packan, R. E. Stoller, and A. S. Kumar (American Society for Testing and Materials, Philadelphia, 1990) 453.

[20] R. L. Klueh, J. M. Vitek, W. R. Corwin, and D. J. Alexander, J. Nucl. Mater. 155-157 (1988) 973.

[21] D. S. Gelles, W. L. Hu, F. H. Huang, and G. D. Johnson, Alloy Development for Irradiation Performance, Semiannual Progress Report for Period Ending September 30, 1983, U. S. Department of Energy, Office of Fusion Energy, DOE/ER-0045/11 (March 1984) 115.

[22] W. L. Hu and D. S. Gelles, in: Topical Conference on Ferritic Alloys for Use in Nuclear Energy Technologies, Eds. J. W. Davis and D. J. Michel (Metallurgical Society of AIME, Warrendale, PA, 1984) 631.

[23] R. L. Klueh and D. J. Alexander, J. Nucl. Mater. 218 (1995) 151.

[24] K. Anderko, L. Schäfer, and E. Materna-Morris, J. Nucl. Mater. 179-181 (1991) 492.

[25] L. Schäfer, J. Nucl. Mater. 258-263 (1998) 1336.

[26] B. A Chin and R. A. Wilcox, in: Technical Conference on Ferritic Alloys for Use in Nuclear Energy Technologies, Eds. J. W. Davis and D. J. Michel (Metallurgical Society of AIME, Warrendale, PA, 1984) 347.

[27] G. Allegraud, J. M. Boyer, R. Cauvin, A. Daniel, and A. Grivaud, in: Materials for Nuclear Reactor Core Applications, Vol. 1 (British Nuclear Energy Society, London, 1987) 249.

[28] D. Gilbon, J. L. Séran, R. Cauvin, A. Fissolo, A. Alamo, F. Le Naour, and V. Lévy, in: Effects of Radiation on Materials: 14th International Symposium, ASTM STP 1046, Eds. N. H. Packan, R. S. Stoller, and A. S. Kumar (American Society for Testing and Materials, Philadelphia, 1989) 5.

[29] J. L. Séran, V. Lévy, P. Dubuisson, D. Gilbon, A. Maillard, A. Fissolo, H. Touron, R. Cauvin, A. Chalony, and E. Le Boulbin, in: Effects of Radiation on Materials: 15th International Symposium, ASTM STP 1125, Eds. R. E. Stoller, A. S. Kumar, and D. S. Gelles (American Society for Testing and Materials, Philadelphia, 1992) 1209.

[30] A. Kimura, M. Narui, T. Misawa, H. Matsui, and A. Kohyama, J. Nucl. Mater. 258-263 (1998) 1340.

[31] G. E. Lucas, G. R. Odette, P. M. Lombrozo, J. W. Sheckherd, in: Effects of Radiation on Materials: Twelfth International Symposium, ASTM 870 (American Society for Testing and Materials, Philadelphia, 1984) 900.

[32] G. R. Odette, P. M. Lombrozo, J. F. Perrin, and R. A. Wullaert, Physically-Based Regression Correlations of Embrittlement Data from Reactor Pressure Vessel Surveillance Programs, Electric Power Research Institute, EPRI NP-3319, 1984.

[33] A. Kohyama, A. Hishinuma, D. S. Gelles, R. L. Klueh, W. Dietz, and K. Ehrlich, J. Nucl. Mater. 233-237 (1996) 138.

[34] K. Shiba, M. Suzuki, A. Hishinuma, and J. E. Pawel, in: Effects of Radiation on Materials: 17th International Symposium, ASTM STP 1270, Eds. D. S. Gelles, R. K. Nanstad, A. S. Kumar, and E. A. Little (American Society for Testing and Materials, Philadelphia, 1996) 753.

[35] V. S. Khabarov, A. M. Dvoriashin, and S. I. Porollo, J. Nucl. Mater. 233-237 (1996) 236.

[36] Y. Kohno, A. Kohyama, M. L. Hamilton, and M. Narui, J. Nucl. Mater. 271 & 272 (1999) 145.

[37] R. L. Klueh and D. J. Alexander, in: Effects of Radiation on Materials: 16th International Symposium, ASTM STP 1175, Eds. A. S. Kumar, D. S. Gelles, and R. K. Nanstad (American Society for Testing and Materials, Philadelphia, 1994) 591.
[38] R. L. Klueh and D. J. Alexander, J. Nucl. Mater. 258-263 (1998) 1269.
[39] Krauss, G., Steels: Heat Treatment and Processing Principles (ASM International, Materials Park, OH, 1989).
[40] E. A. Little, D. R. Harries, F. B. Pickering, and S. R. Keown, Metals Technology 4 (1977) 205.
[41] L. Schäfer, in: Fusion Technology 1996, Eds. C. Varandas and F. Serra (Elsevier Science B. V., Oxford, UK, 1997) 1367.
[42] L. Schäfer, M. Schirra, and R. Lindau, in: Fusion Technology 1996, Eds. C. Varandas and F. Serra (Elsevier Science B. V., Oxford, UK, 1997) 1363.
[43] C. K. Elliot, R. Maiti, G. E. Lucas, and G. R. Odette, J. Nucl. Mater. 141-143 (1986) 439.
[44] R. Maiti, G. E. Lucas, G. R. Odette, and J. W. Sheckherd, J. Nucl. Mater. 141-143 (1986) 527.
[45] G. R. Odette, G. E. Lucas, and R. Maiti, J. Nucl. Mater. 148 (1987) 22.
[46] R. O. Ritchie, J. F. Knott, and J. R. Rice, J. Mech. Phys. Sol. 21 (1973) 395.
[47] G. R. Odette, J. Nucl. Mater. 212-215 (1994) 45.
[48] M. Rieth, B. Dafferner, H. D. Röhrig, C. Wassilew, Fusion Eng. Design 29 (1995) 365.
[49] K. Ehrlich, D. R. Harries, and A. Möslang, Characterisation and Assessment of Ferritic/Martensitic Steels, Forschungszentrum Karlsruhe, FZKA Report 5626, February 1997.
[50] V. K. Shamardin, A. M. Pecherin, O. M. Vishkarev, V. P. Borisov, and G. A. Tulyakov, in: Proc. Int. Conf. on Radiat. Mater. Sci. (Alushta, USSR, May 22-25, 1990) 3.
[51] E. A. Little and L. P. Stoter, in: Effects of Irradiation on Materials: Eleventh Conference, ASTM STP 782, Eds. H. R. Brager and J. S. Perrin (American Society for Testing and Materials, Philadelphia, 1982) 207.
[52] Y. I. Zvezdin, O. M. Vishkarev, G. A. Tulyakov, Y. G. Magerya, V. A. Smirnov, I. A. Shenkova, I. V. Altovski, A. A. Grigoryan, V. K. Shamardin, and U. M. Pecherin, J. Nucl. Mater. 191-194 (1992) 855.
[53] M. Schirra and K. Ehrlich, in: Advanced Heat Resistant Steels for Power Generation, Eds. R. Viswanathan and J. Nutting (The Inst. of Materials, London, Book 708, 1999) 586.
[54] M. Schirra, S. Heger, H. Kempe, M. Klotz, H. Zimmermann, and J. Lapeña, Untersuchungen zu physikalischen und mechanischen Eigenschaften der OPTIFER-Legierungen, FZKA 6167, Forschungszentrum Karlsruhe, April 1999.
[55] M. Schirra, Private Communication, July 2000.
[56] M. Schirra and E. Materna-Morris, Sonderbände der Praktischen Metallografie 29 (1997) 249.
[57] M. G. Horsten, E. V. van Osch, D. S. Gelles, and M. L. Hamilton, in: Effects of Irradiation on Materials: 19th International Symposium, ASTM STP 1366, Eds. M. L. Hamilton, A. S. Kumar, S. T. Rosinski, and M. L. Grossbeck (American Society for Testing and Materials, West Conshohocken, PA, 2000) 579.
[58] H. Kayano, A. Kimura, M. Narui, Y. Sasaki, Y. Suzuki, and S. Ohta, J. Nucl. Mater. 155-157 (1988) 978.
[59] F. Abe, H. Araki, and T. Noda, Mat. Sci. Tech. 6 (1990) 714.
[60] F. Abe, T. Noda, H. Araki, and S. Nakazawa, J. Nucl. Mater. 179-181 (1991) 663.
[61] V. V. Rybin, I. P. Kursevich, and A. N. Lapin, J. Nucl. Mater. 258-263 (1998) 1324.
[62] D. S. Gelles, in: Reduced Activation Materials for Fusion Reactors, ASTM STP 1047, Eds. R. L. Klueh, D. S. Gelles, M. Okada, and N. H. Packan (ASTM, Philadelphia, 1990) 113.
[63] R. L. Klueh and D. J. Alexander, in: Effects of Radiation on Materials: 18th International Symposium, ASTM STP 1325, Eds. R. K. Nanstad, M. L. Hamilton, F. A. Garner, and A. S. Kumar (American Society for Testing and Materials, Philadelphia, 1999) 911.
[64] M. L. Hamilton, L. E. Schubert, and D. S. Gelles, in: Effects of Radiation on Materials: 18th International Symposium, ASTM STP 1325, Eds. R. K. Nanstad, M. L. Hamilton, F. A. Garner, and A. S. Kumar (American Society for Testing and Materials, Philadelphia, 1997) 931.
[65] M. L. Hamilton, L. E. Schubert, and D. S. Gelles, J. Nucl. Mater. 258-263 (1998) 1222.
[66] K. Shiba, I. Ioka, J. E. Robertson, M. Suzuki, and A. Hishinuma, in: Proceedings, Conference on Materials and Nuclear Power (The Institute of Materials, London, 1996) 265.
[67] K. Shiba, M. Suzuki, and A. Hishinuma, J. Nucl. Mater. 233-237(1996) 309.
[68] A. Kohyama, Y. Kohno, K. Asakura, and H. Kayano, J. Nucl. Mater. 212-214 (1994) 684.
[69] M. Rieth and B. Dafferner, J. Nucl. Mater. 233-237 (1996) 138.
[70] M. Rieth, B. Dafferner, and H. D. Röhrig, J. Nucl. Mater. 233-237 (1996) 351.
[71] M. Rieth, B. Dafferner, and H. D. Röhrig, J. Nucl. Mater. 258-263 (1998) 1147.
[72] R. L. Klueh and D. J. Alexander, J. Nucl. Mater. 265 (1999) 262.
[73] R. L. Klueh and P. J. Maziasz, Met. Trans. 20A (1989) 373.
[74] R. Jayaram and R. L. Klueh, Metall. and Matls. Trans. 29A (1998) 1551.
[75] A. Hishinuma, in: Proceedings of the IEA Working Group Meeting on Ferritic/Martensitic Steels, Ed. R. L. Klueh, ORNL/M-5674, October 1996.
[76] R. L. Klueh and D. J. Alexander, J. Nucl. Mater. 212-215 (1994) 736.
[77] W. C. Leslie, The Physical Metallurgy of Steels (McGraw-Hill, New York, 1981) 122.
[78] W. W. Gerberich, Y. T. Chen, D. G. Asteridae, and T. Johnson, Acta Met. 29 (1981) 1187.
[79] A. A. Griffith, Phil. Trans. R. Soc. London 221A (1920) 163.
[80] A. A. Griffith, Proc. 1st Intl. Cong. Appl. Math. (Delft, The Netherlands, 1924) 55.
[81] R. A. Sack, Proc. Phys. Soc. London 58 (1946) 729
[82] R. L. Klueh, Met. Trans. 20A (1989) 463.
[83] R. L. Klueh, D. J. Alexander, and M. Rieth, J. Nucl. Mater. 273 (1999) 146.
[84] R. W. Conn, E. E. Bloom, J. W. Davis, R. E. Gold, R. Little, K. R. Shultz, D. L. Smith, and F. W. Wiffen, Panel Report on Low Activation Materials for Fusion Applications, UCLA Report PPG-728, University of California at Los Angeles, 1983.
[85] D. S. Gelles and N. S. Cannon, Fusion Reactor Materials Semiannual Progress Report for Period Ending March 31, 1988, DOE/ER-0313/4, August 1988, 95.
[86] W. L. Hu and D. S. Gelles, Fusion Reactor Materials Semiannual Progress Report for Period Ending March 31, 1986, DOE/ER-0045/16, September 1986, 140.
[87] D. S. Gelles and W. L. Hu, Fusion Reactor Materials Semiannual Progress Report for Period Ending September 30, 1986, DOE/ER-0313/1, September 1987, 251.
[88] R. D. Griffen, R. A. Dodd, and G. L. Kulcinski, Met. Trans. 21A (1990) 1853.
[89] R. D. Griffen, D. S. Gelles, R. A. Dodd, and G. L. Kulcinski, J. Nucl. Mater. 179-181 (1991) 714.
[90] R. D. Griffen, S. J. Zinkle, R. A. Dodd, G. L. Kulcinski, and D. S. Gelles in: Effects of Radiation on Materials: 15th International Symposium, ASTM STP 1125, Eds, R. E. Stoller, A. S. Kumar, and D. S. Gelles (American Society for Testing and Materials, Philadelphia, 1992) 979.
[91] A. Kimura, L. A. Charlot, D. S. Gelles, D. R. Baer, and R. H. Jones, J. Nucl. Mater. 191-194 (1992) 885.

[92] S. Ukai, M. Harada, H. Okada, M. Inoue, S. Nomura, S. Shikakura, T. Nishida, and M. Fujiwara, K. Asabe, J. Nucl. Mater. 204 (1993) 74.
[93] T. Kuwabara, H. Kurishita, S. Ukai, M. Narui, S. Mizuta, M. Yamazaki, and H. Kayano, J. Nucl. Mater. 258-263 (1998) 1236.
[94] R. L. Klueh and D. J. Alexander, J. Nucl. Mater. 187 (1992) 60.
[95] W. R. Corwin, J. M. Vitek, and R. L. Klueh, J. Nucl. Mater. 149 (1987) 312.
[96] P. J. Maziasz, Unpublished research, 1992.
[97] D. S. Gelles, in: Effects of Radiation on Materials: 18th International Symposium, ASTM STP 1325, Eds. R. K. Nanstad, M. L. Hamilton, G. A. Garner, and A. S. Kumar (American Society for Testing and Materials, Philadelphia, 1997) 899.
[98] R. G. Faulkner, E. A. Little, and T. S. Morgan, J. Nucl. Mater. 191-194 (1992) 858.
[99] R. G. Faulkner, S. Song, and P. J. Flewitt, J. Nucl. Mater. 212-215 (1994) 608.
[100] R. E. Clausing, L. Heatherly, R. G. Faulkner, A. F. Rowcliffe, and K. Farrell, J. Nucl. Mater. 141-143 (1986) 978.
[101] D. S. Gelles, J. Nucl. Mater. 230 (1996) 187.
[102] R. L. Klueh and D. J. Alexander, J. Nucl. Mater. 230 (1996) 191.
[103] D. S. Gelles, G. L. Hankin, and M. L. Hamilton, J. Nucl. Mater. 251 (1997) 188.
[104] D. S. Gelles, G. L. Hankin, and M. L. Hamilton, J. Nucl. Mater. 258-263 (1998) 1216
[105] K. Shiba and A. Hishinuma, J. Nucl. Mater. 283-287.
[106] E. V. van Osch, M. G. Horsten, G. E. Lucas, and G. R. Odette, in: Effects of Irradiation on Materials: 19th International Symposium, ASTM STP 1366, Eds. M. L. Hamilton, A. S. Kumar, S. T. Rosinski, and M. L. Grossbeck (American Society for Testing and Materials, West Conshohocken, PA, 2000) 612.
[107] E. I. Materna-Morris, M. Rieth, and K. Ehrlich, in: Effects of Irradiation on Materials: 19th International Symposium, ASTM STP 1366, Eds. M. L. Hamilton, A. S. Kumar, S. T. Rosinski, and M. L. Grossbeck (American Society for Testing and Materials, West Conshohocken, PA, 2000) 597.
[108] W. C. Leslie, The Physical Metallurgy of Steels (McGraw-Hill Book Company, New York, 1981) 269.
[109] F. B. Pickering, Physical Metallurgy and the Design of Steels (Applied Science Publishers Ltd, London, 1978) 103.
[110] T. M. Williams, A. M. Stoneham, and D. R. Harries, Met. Sci. 10 (1976) 14.
[111] A. Kimura, M. Narui, and H. Kayano, J. Nucl. Mater. 191-194 (1992) 879.
[112] R. L. Klueh and J. M. Vitek, J. Nucl. Mater. 132 (1985) 27.
[113] R. L. Klueh and J. M. Vitek, J. Nucl. Mater. 150 (1987) 272.
[114] K. K. Bae, K. Ehrlich, and A. Möslang, J. Nucl. Mater. 191-194 (1992) 905.
[115] R. Lindau, A. Möslang, D. Preininger, M. Rieth, and H. D. Röhrig, J. Nucl. Mater. 271 & 272 (1999) 450.
[116] M. Suzuki, A. Hishinuma, N. Yamanouchi, M. Tamura, and A. F. Rowcliffe, *J. Nucl. Mater.* 191-194 (1992) 1056.
[117] L. Greenwood, B. M. Oliver, S. Ohnuki, K. Shiba, Y. Kohno, A. Kohyama, J. P. Robertson, J. W. Meadows, and D. S. Gelles, *J. Nucl. Mater.* 283-287 (2000) 1438.
[118] M. L. Hamilton, D. Gelles, S. Ohnuki, K. Shiba, Y. Kohno, and A. Kohyama, Fusion Materials Semiannual Progress Report for Period Ending December 31, 1998, U.S. Department of Energy, Office of Fusion Energy Sciences, DOE/ER-0313/25 (April 1999) 136.
[119] D. Gelles, M. L. Hamilton, B. M. Oliver, and L. R. Greenwood, Fusion Materials Semiannual Progress Report for Period Ending December 31, 1999, U.S. Department of Energy, Office of Fusion Energy Sciences, DOE/ER-0313/27 (March 2000) 149.

15

Fracture Toughness

Charpy impact tests discussed in the preceding chapter are most useful as a screening test to evaluate the relative effect of irradiation on producing embrittlement in different steels. However, Charpy data cannot be used directly for design. Design will probably be based on a defect-tolerant approach, where a plane-strain fracture toughness (thick sections) or a J-integral (thin-walled structure) approach are used [1]. Because of the simpler test procedure for a Charpy test, fewer fracture toughness data, especially of irradiated specimens, are available than are Charpy impact data. There is a qualitative correspondence between changes in Charpy impact properties and fracture toughness of irradiated steels, and the change in USE is often taken as an indication of the change in ductile fracture toughness [1].

Odette [2] has emphasized that "the fracture mode is not sufficient to characterize toughness, which may be appreciable even in the cleavage regime," meaning that DBTT cannot be a measure of toughness. He further pointed out the well-known (often ignored) fact that the DBTT can be influenced by various extrinsic factors, such as notch acuity, specimen geometry, specimen size, the parameter used to index the DBTT, etc., that further complicate the interpretation of such data [2].

As an example of the extrinsic factors that can influence fracture testing, the variation in the DBTT with the choice of index is illustrated in Table 15.1 for HT9 (12Cr-1MoVW) and F82H [3]. The Charpy curves from which the data were taken are shown in Fig. 15.1(a). The authors comment [3] that the most physically meaningful index is the 10 J level, "which has been found to approximately correspond to the maximum temperature of linear elastic fracture." This is the only one of the indices that produced a similar DBTT for HT9 and F82H. All others indicated a higher DBTT for the HT9, as evident from a visual inspection of the data in Fig. 15.1(a). When static fracture toughness data for the two steels were compared [Fig. 15.1(b)], the toughness of the F82H was found to be better than that of HT9, although the difference was not as great as indicated by the Charpy data [3].

Thus, fracture toughness measurements can provide a quantitative measure of the fracture behavior of steels. Whereas a Charpy test measures the total energy to initiate a crack from the notch and propagate the crack across the specimen to produce a complete fracture, fracture toughness tests measure just the critical load to extend a pre-existing crack.

A critical need exists for fracture toughness data on irradiated material. For linear elastic fracture analysis, plane-strain fracture toughness values, K_{IC}, are required; for thin-walled structures, such as those expected for fusion applications, the J-integral approach is most relevant (although for shallow cracks in thin-wall vessels, J-integral methods may not apply).

FRACTURE TOUGHNESS

From the Griffith criterion for fracture, the stress to propagate a crack, σ_F can be written

$$\sigma_F = \left(\frac{EG_C}{\pi a}\right)^{1/2} \tag{15.1}$$

where E is Young's modulus, G_C is the total work of fracture (it accounts for the energy to create a new surface and the plastic energy to form a plastic zone around the crack tip), and a is the flaw (crack) size [4]. Equation 15.1 can be interpreted in terms of the critical values of stress and crack length for an unstable crack to propagate. That is, when $\sigma(\pi a)^{1/2}$ equals $(EG_C)^{1/2}$, the crack will grow. A stress intensity factor, K, is defined as

$$K = \sigma\sqrt{\pi a} \tag{15.2}$$

Fracture is considered to occur when a critical stress intensity factor is reached, that is:

$$K_C = \sqrt{EG_C} \tag{15.3}$$

which is called the fracture toughness.

Plane-strain fracture toughness, K_{IC}, is used for large sections, and it is related to the energy required for the onset of crack propagation according to

$$K_{IC} = \sqrt{\frac{EG_{IC}}{1-\nu^2}} \tag{15.4}$$

where G_{IC} is the critical plane-strain energy release rate for crack extension, and ν is Poisson's ratio (the I in K_{IC} refers to Mode I—tensile—loading of the crack). Although more difficult to determine than a Charpy curve, test techniques using precracked compact tension or three-point bend specimens are well developed and involve the determination of load versus crack-mouth-opening displacement curves, which are similar to load versus displacement curves of a tension test.

TABLE 15.1—DBTT Values for Sandvik HT9 and F82H for Various Indices Obtained from Charpy Tests (full-size specimens) [3].

Index	DBTT (°C)	
	HT9	F82H
41 J absorbed energy	25 + 5	−56 + 5
10 J absorbed energy	−60 + 5	−60 + 5
50% shear fracture appearance	34 + 5	−55 + 5
0.89 mm lateral expansion	119 + 5	−56 + 5
50% upper shelf energy	50 + 5	−50 + 5

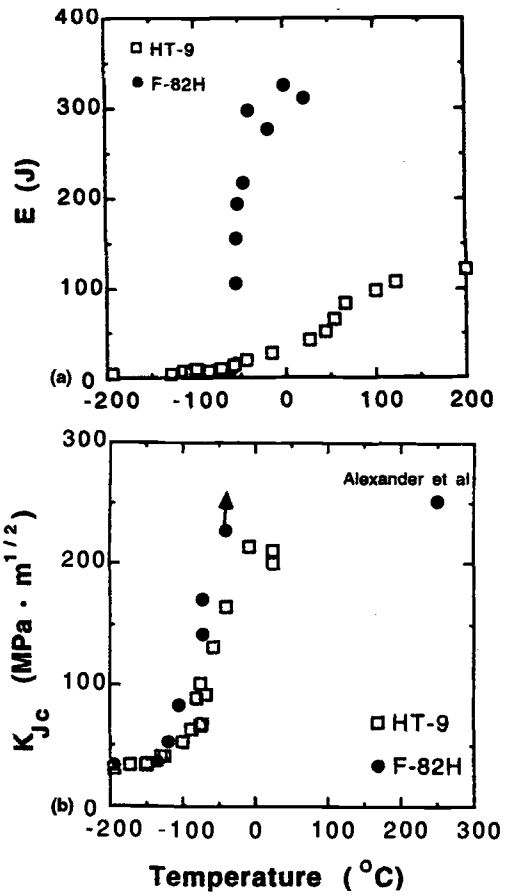

FIG. 15.1—A comparison of (a) the Charpy impact data and (b) the static fracture toughness data of Sandvik HT9 and F82H steels [3].

Miniature compact tension specimens have been developed for use in irradiation experiments.

For thin-walled structures where the size of the plastic zone around the crack tip is significant relative to the section size, the assumption that the elastic stress around the crack controls fracture is no longer valid. The J-integral approach has been developed for this condition. In this approach [4], "J can be thought of as the amount of elastic-plastic strain energy per unit area of crack growth which is applied toward the crack in a specimen under load." Then, J_{IC} is the critical value of J to start a pre-existing crack to grow under these conditions. For a large specimen or for a material with a high yield stress, $J_{IC} = G_{IC}$. Test specimens and procedures used to determine J_{IC} are similar to those used to determine K_{IC}. Values of J_{IC} have been determined on irradiated material and will be discussed below.

Another quantity that has been determined and used for irradiated steels is the tearing modulus, T, defined as

$$T = \frac{dJ}{da}\frac{E}{\sigma_{ys}^2} \tag{15.5}$$

where σ_{ys} is the yield stress. The tearing modulus is a description of a material's resistance to crack extension by ductile tearing [4].

FRACTURE TOUGHNESS—CONVENTIONAL HIGH-CHROMIUM STEELS

Studies have been conducted to determine post-irradiation toughness data for 9Cr-1MoVNb (modified 9Cr-1Mo) [5–9], 12Cr-1MoVW (HT9) [5, 9–11], and MANET steels [12].

Pre-cracked full-size Charpy (PCVN) specimens were used to determine the dynamic fracture toughness, K_{Jd}, of 12Cr-1MoVW steel irradiated to ≈5 dpa in EBR-II at 420°C [10] and 9Cr-1MoVNb and 12Cr-1MoVW steel plates irradiated at 93 to 300°C at ≈0.8 × 10^{20} n/cm^2 (<1 dpa) in the University of Buffalo (UB) reactor (a light-water-moderated test reactor) [5], and the results were compared to full-size, blunt-notch Charpy (C_V) test results (Fig. 15.2).

After the EBR-II irradiation of the 12Cr-1MoVW steel at 420°C, fracture toughness at temperatures corresponding to the upper-shelf region of the C_V curves was ≈170 MPa√m. Below the transition region, fracture toughness was measured as 45 MPa√m, and it was concluded [10] that the use of the steel "will require careful integration of the component design requirements and material properties."

Following irradiation in the UB reactor [5], neither the 9Cr-1MoVNb nor 12Cr-1MoVW steel was "unduly embrittled by 1 × 10^{20} n/cm^2." Specimens from an AOD plate of the 12Cr-1MoVW steel were irradiated at 93, 149, and 288°C, and shifts in the transition temperature at 100 MPa√m corresponded qualitatively to those of the C_V-41J for the steel of ≈67 and 150°C after irradiation at 288 and 93°C, respectively (Fig. 15.2). The K_J lower shelf values of the unirradiated and irradiated steel were ≈40 MPa√m. The K_J upper-shelf values showed a relatively small decrease and had values of ≈180 to 240 MPa√m, depending on the irradiation temperature. There was an overlap of the scatterbands for the unirradiated steel and the steel irradiated at 288°C (Fig. 15.2). Irradiation at 93°C gave a K_J upper-shelf of ≈180 to 200 MPa√m, compared to ≈220 to 240 for the unirradiated steel. An ESR plate of 12Cr-1MoVW steel irradiated to ≈0.8 × 10^{20} n/m^2 at 300°C was found to have similar toughness behavior to that of the AOD plate.

Simulated heat-affected zone (HAZ) microstructures (four positions across the HAZ were produced by a Gleeble simulation) of the 12Cr-1MoVW steel AOD heat were also irradiated at 288°C [5]. The results indicated that the "weldment properties following 288°C irradiation will not be governed primarily by the HAZ properties," since the base metal and HAZ properties were similar.

The 9Cr-1MoVNb steel after irradiation to 0.8 × 10^{20} n/cm^2 at 149°C was slightly more resistant to embrittlement than

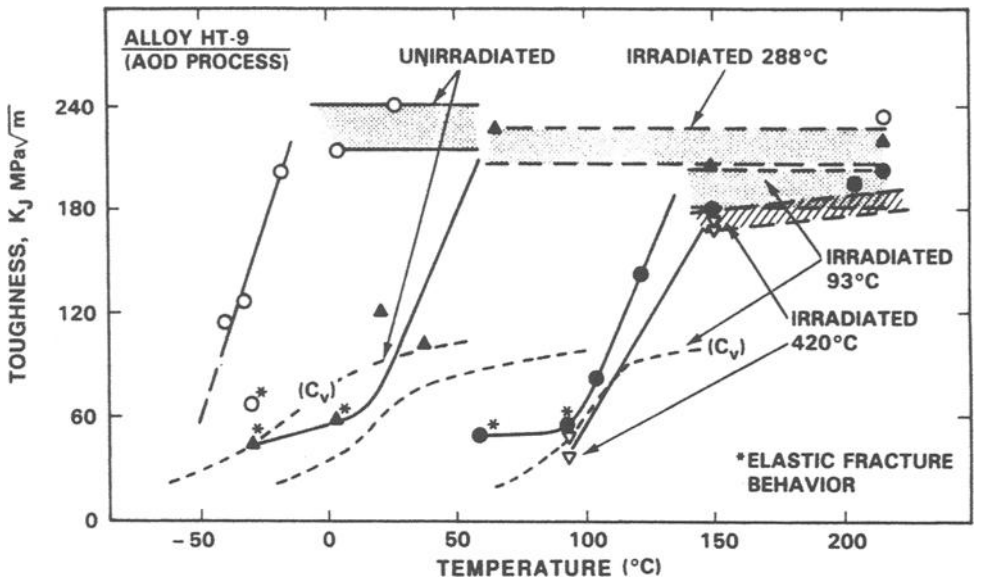

FIG. 15.2—Fracture toughness curves compared to Charpy curves (C_V) for 12Cr-1MoVW (HT9) irradiated in the University of Buffalo Reactor [5].

the 12Cr-1MoVW steel irradiated at that temperature [5]. There was only a small decrease in USE, but a rather large increase in DBTT (83°C), with the increase in the 100 MPa$\sqrt{m}$ temperature about the same as the C_V-41J temperature. However, the K_{Jd} transition was 45°C higher than that of the C_V curve, indicating a high sensitivity of this steel to notch acuity. The PCVN specimens of the 9Cr-1MoVNb [5] "failed predominantly by cleavage at temperatures where C_V specimens failed predominantly by shear."

The most extensive data on irradiated materials is from Huang and co-workers [6–9,11] on 9Cr-1MoVNb (modified 9Cr-1Mo) and 12Cr-1MoVW (HT9) steels studied in the fast-breeder reactor program. The single specimen electric-potential method was used on miniature compact-tension specimens to determine the toughness, J_{IC}, and the tearing modulus, T, for different heats of base metal given different thermomechanical treatments, weldments, and weld metal irradiated in EBR-II and FFTF at 390 to 550°C and exposures of 35 to 100 dpa. Specimens were also tested after irradiation in HFIR at 55°C.

In one series of tests, the effect of the thermomechanical treatment (TMT) on 12Cr-1MoVW steel irradiated in EBR-II to ≈2.9 and 6.0×10^{26} n/m^2 (≈14.5–30 dpa) at 400, 450, and 550°C was investigated by examining a variety of heat treatments and cold-rolled steel [7]. One condition (normalized and tempered) of modified 9Cr-1Mo steel was also investigated.

The heat treatments on the HT9 involved different times (0.08 and 0.5 h) and temperatures (1038 and 1050°C) for the austenitization treatment and a variety of temperatures (700, 760, and 780°C) and times (0.5, 1, 1.5, and 2 h) for the tempering. Given the variety of the TMTs and the limited number of irradiated specimens, it appears difficult to evaluate the meaning of the results, but the author concluded that the initiation fracture toughness, J_C, of the irradiated steels increased with increasing chromium and tempering temperature. The latter effect is expected. It was concluded that cold work did not improve the fracture resistance of the HT9 (not unexpected). For steels irradiated at 400°C to 30 dpa and tested at 205°C, J_C varied from 67.6 kJ/m^2 for the cold worked steel to 114.2 kJ/m^2 for the steel tempered at 760°C, with the other TMT conditions falling within these values. The J_C value for the 9Cr-1MoVNb steel was 65.1, similar to the cold-worked HT9. The J_C values decreased slightly when the irradiation temperature was increased from 400 to 500°C. Neutron fluence was found not to affect the results, which would indicate a saturation.

Tearing modulus measurements for these irradiation and test conditions indicated that the 9Cr-1MoVNb had the highest value (110) and cold-worked HT9 again had the lowest (34) value, with the other HT9 TMT conditions in between. Neutron fluence again had a minor effect, but contrary to toughness, the tearing modulus did show a large increase with increasing irradiation temperature.

The authors' final conclusion was that TMT was a more important factor for toughness properties than strain rate, orientation (relative to the plate the specimens were taken from), or heat-to-heat variation in composition. However, given the limited number of specimens irradiated and the lack of apparent systematic variation in the test variables (i.e., TMT, heat treatment conditions, number of heats, etc.) more work appears to be required to firmly establish such a broad conclusion.

A summary of some of the early irradiation-effects data from irradiations in EBR-II and HFIR for J_{IC} of 12Cr-1MoVW steel as a function of test temperature is shown in Fig 15.3 [8]; later data, discussed below, are in accordance with the trends of this figure. Below room temperature, the unirradiated data on two heats of 12Cr-1MoVW steel indicated an S-shaped curve such as that observed in a Charpy test. The tearing modulus was measured on unirradiated and irradiated specimens from room temperature to 500°C (no tearing modulus can be obtained in the transition and lower-shelf regions because failure is by fast fracture); it was found

to behave opposite to J_{IC}, having a broad maximum around 300°C where the J_{IC} had a minimum [9].

Some of the results used to prepare Fig. 15.3 along with results from irradiations to higher doses will now be presented. These data are mainly from a summary paper by Haung and Hamilton [9].

Irradiation of the 12Cr-1MoVW steel in EBR-II up to 28 dpa at 390, 450, and 550°C (Figs. 15.4 and 15.5) and in FFTF up to 108 dpa at 411 to 420, 520, and 600°C (Fig. 15.5) produced a loss in J_{IC} to a level that, with one exception (73 dpa in FFTF, Fig. 15.5), was essentially no lower than the lowest value observed in the unirradiated condition. The tearing modulus showed a significant decrease [Figs. 15.4(b) and 15.5(b)], especially at the lowest temperatures, where it decreased to about half that in the unirradiated condition. The FFTF J_{IC} data were comparable to the EBR-II data [Fig. 15.4(a)] up to 30 dpa, then fell below those data, indicating a continued drop in J_{IC} with increasing fluence. The change in tearing modulus appeared to saturate by 30 dpa [9].

Irradiation of 12Cr-1MoVW steel in HFIR at 55°C to 5 dpa did not cause a much larger decrease in J_{IC} steel than the fast reactor irradiation to the higher doses at higher temperatures (Fig. 15.6). The values remained above the lowest level observed in the unirradiated condition (Fig. 15.3). HFIR irradiation at 55°C did cause a larger reduction in tearing resistance than fast reactor irradiation: it dropped to values of ≈30 after HFIR irradiation [Fig. 15.6(b)] and to ≈50 after FFTF irradiation [Fig. 15.5(b)]. Since saturation might not be obtained after 5 dpa at 55°C in HFIR, further degradation might be expected.

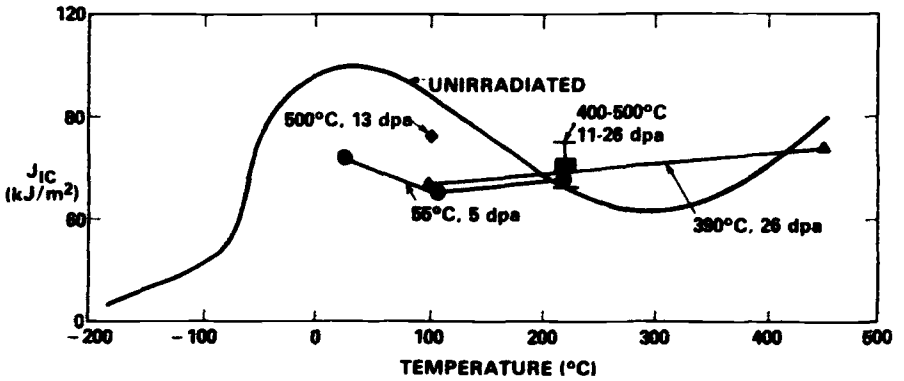

FIG. 15.3—Fracture toughness as a function of temperature for unirradiated and irradiated Sandvik 12Cr-1MoVW (HT9) steel for various irradiated conditions [8].

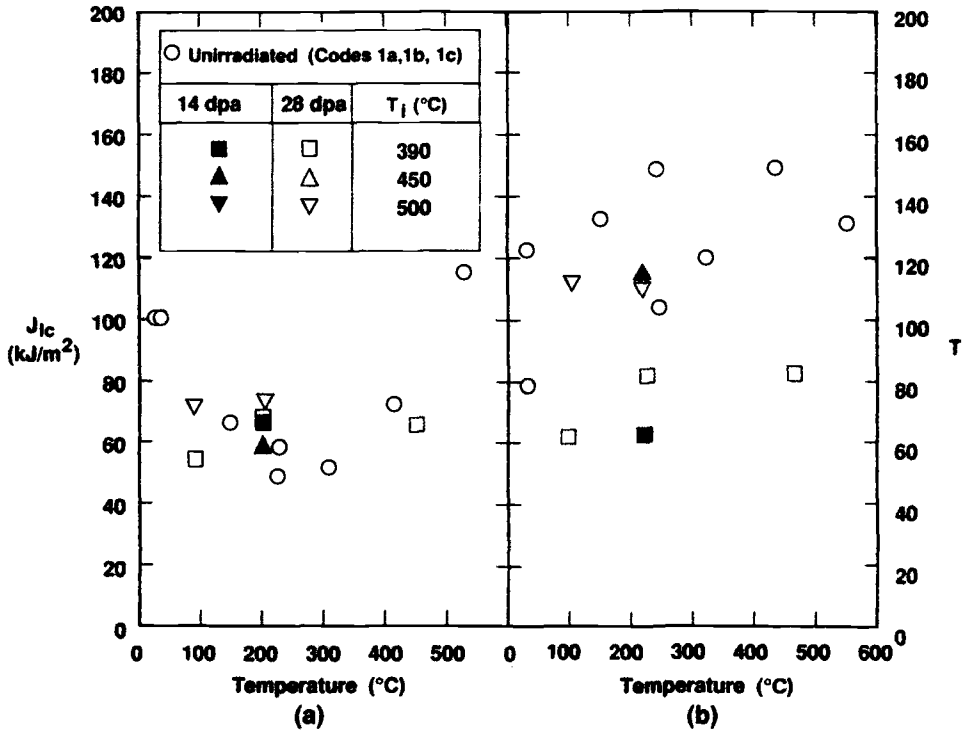

FIG. 15.4—The (a) fracture toughness and (b) tearing modulus of HT9 irradiated in EBR-II [9].

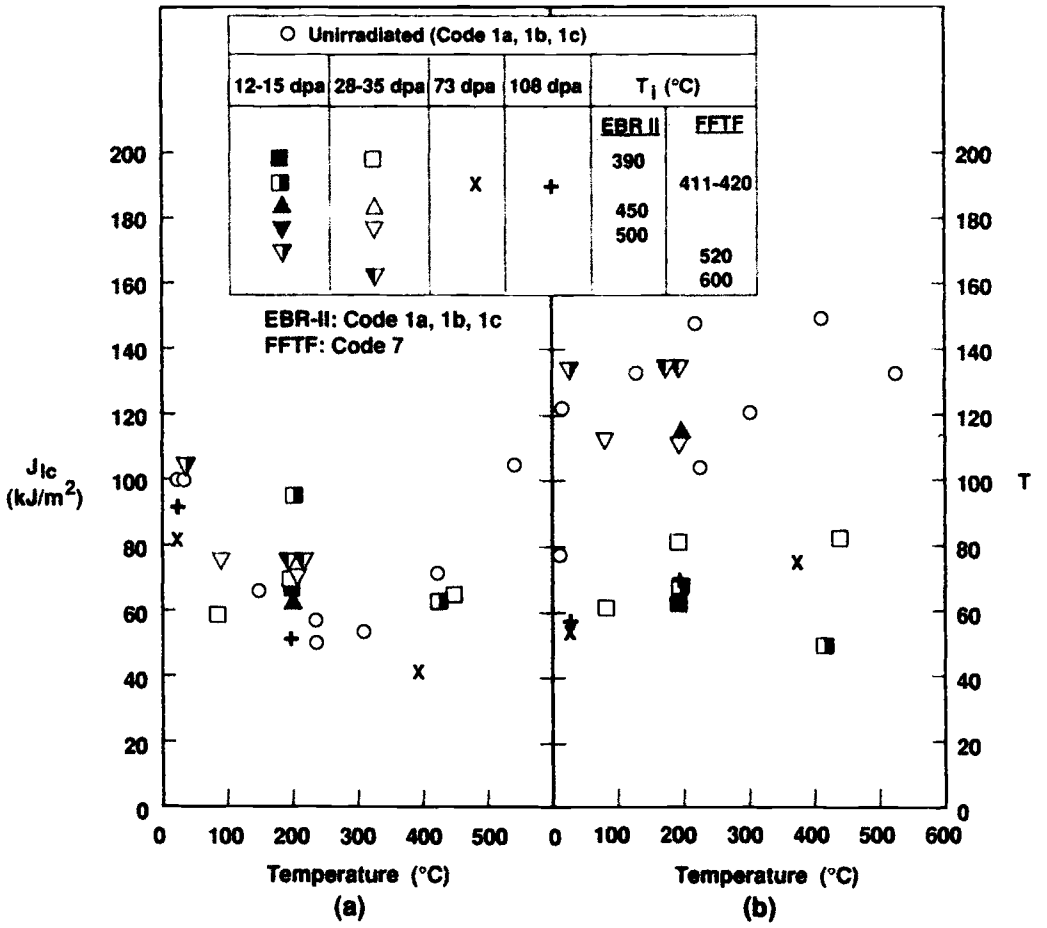

FIG. 15.5—The (a) fracture toughness and (b) tearing modulus of HT9 irradiated in FFTF and EBR-II [9].

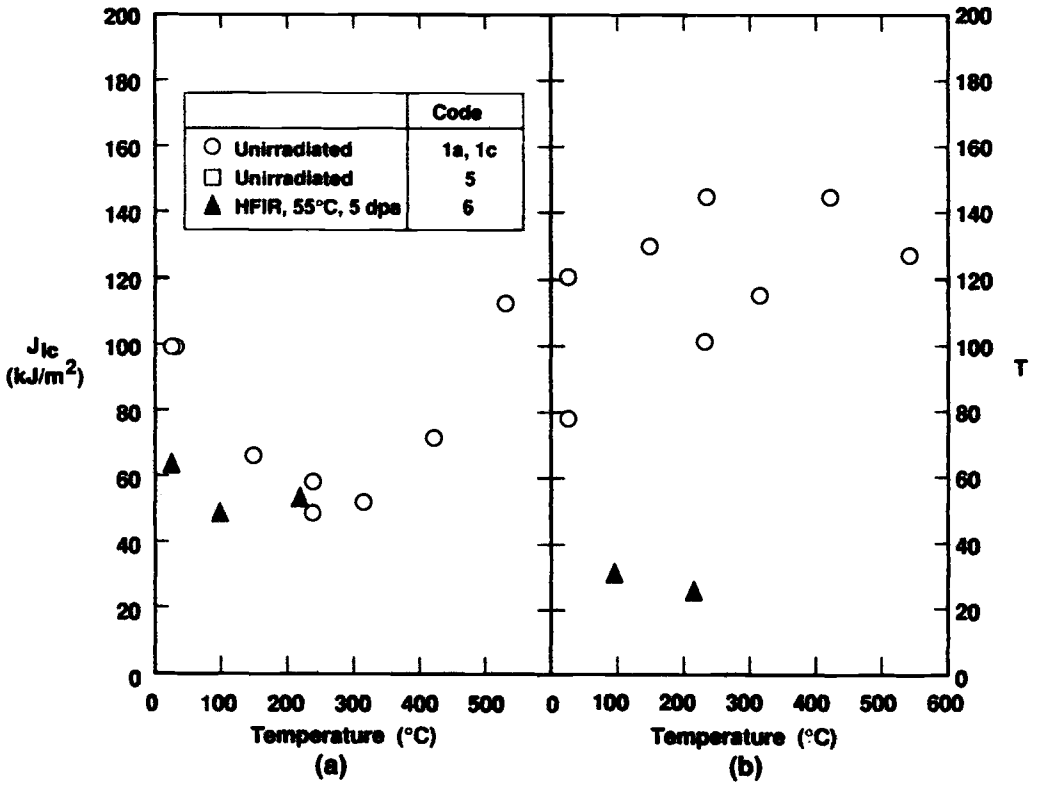

FIG. 15.6—The (a) fracture toughness and (b) tearing modulus of HT9 irradiated in HFIR at 55°C [9].

Regardless of the irradiation temperature, a J_{IC} decrease of ≈35% was observed for 9Cr-1MoVNb steel irradiated in FFTF at 420 and 520°C up to 105 dpa [Fig. 15.7(a)]. An approximate 50% reduction of tearing modulus was observed [Fig. 15.7(b)], which appeared to saturate at a low fluence.

Irradiation of 9Cr-1MoVNb in HFIR to 5 dpa at 55°C (Fig. 15.8) had a much larger effect on the J_{IC} of 9Cr-1MoVNb steel than fast reactor irradiation at the higher temperatures, reducing the J_{IC} and tearing modulus to 35 kJ/m^2 and 20, respectively, compared to a minimum of 45 kJ/m^2 and 80 after

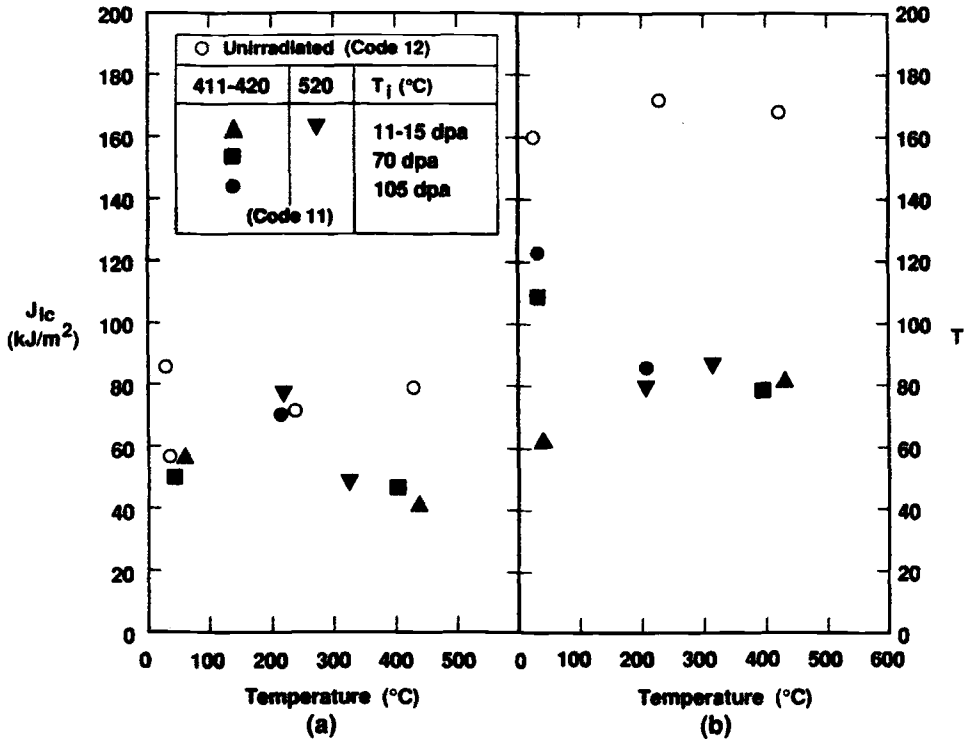

FIG. 15.7—The (a) fracture toughness and (b) tearing modulus of modified 9Cr-1Mo steel irradiated in FFTF [9].

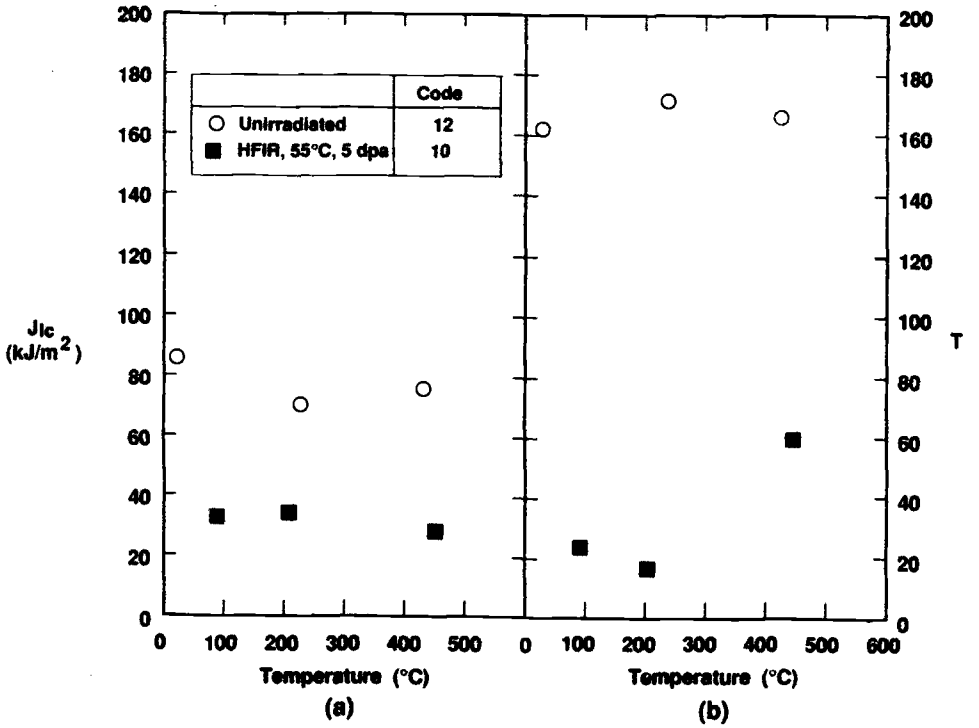

FIG. 15.8—The (a) fracture toughness and (b) tearing modulus of modified 9Cr-1Mo steel irradiated in HFIR at 55°C [9].

up to 105 dpa in FFTF at 420°C. The effect of HFIR irradiation on the 9Cr-1MoVNb steel was much greater than on the 12Cr-1MoVW, which agrees with the Charpy results for low-temperature irradiation in HFIR (see Chapter 14) [13,14].

Contrary to the conclusions drawn from C_V tests, Huang concluded that "the toughness of 9Cr-1Mo is inferior to that of HT9 under neutron exposure at all temperatures." He also indicated that neither steel may have adequate toughness for applications at 55°C [6].

Toughness tests on TIG weldments (unirradiated) of 12Cr-1MoVW tested over the range 93 to 540°C (Fig. 15.9) indicated that the J_{IC} of the fusion zone—weld metal (WM)—and heat-affected zone (HAZ) were somewhat higher than the base metal (BM) when tested at 205°C (the lowest common test temperature). At 400°C, the J_{IC} of the WM and HAZ were similar to the BM, but at 540°C the J_{IC} values of the WM and HAZ were considerably below those of the BM [15.9(a)]. Tearing modulus of the WM and HAZ were less than those of the BM at all test temperatures [Fig. 15.9(b)].

Irradiation had little effect on the J_{IC} of the 12Cr-1MoVW weld metal (fusion zone) specimens irradiated to 12 to 14 dpa in EBR-II at 390, 450, 500, and 550°C, but the tearing modulus dropped to a low value (Fig. 15.10). For one specimen irradiated to 26 dpa at 390°C and tested at 204°C, there was a 40% decrease in J_{IC} relative to the 12 to 14 dpa irradiation, suggesting that [8], "a continued drop in toughness may be observed with increasing neutron exposures, while decreases in the tearing modulus appear to have saturated."

De Vries [12] determined the fracture toughness of MANET I steel irradiated in HFR to 5 dpa at ≈250°C and to 10 dpa at ≈350 and 450°C and reported the engineering toughness parameter, $J_{0.2}$ and $J_{0.5}$ (the J value at 0.2- and 0.5-mm crack extension, Δa). The $J_{0.2}$ was reduced from 120 to 37 kJ/m^2 at 250°C, 109 to 33 kJ/m^2 at 350°C, and 124 to 88 kJ/m^2 at 450°C. Crack growth resistance was characterized by the slope of the resistance curve, dJ/da at 0.2- and 0.5-mm crack extension. The $(dJ/da)_{0.2}$ was reduced by 90, 83, and 32% at 250, 350, and 450°C, respectively, with similar reductions observed for $(dJ/da)_{0.5}$. Values of K_{Ic} were calculated, and using the C_V-41 J criterion for measuring the transition temperature that corresponds closely to the fracture toughness value of 100 MPa$\sqrt{m}$, it was found that [12], "irradiation caused a severe reduction in upper-shelf toughness and a large shift of the ductile-to-brittle transition temperature."

FRACTURE TOUGHNESS—REDUCED-ACTIVATION STEELS

Toughness data for reduced-activation steels in the unirradiated and irradiated condition are limited to a few studies on F82H and JLF-1 steels [3,15–20]. The unirradiated properties are generally similar to those for the conventional Cr-Mo steels [see Fig. 15.1(b)] [3].

Preliminary studies on the effect of loading mode on F82H indicated some unexpected instabilities for mixed-mode loading [15,16]. Figure 15.11 shows the critical J-Integral for Mode I (J_{IC}) at crack angle 0° and Mixed-Mode I/III at 35° (Mode III involves a shear deformation of the crack parallel to the crack tip) for tests at room temperature for two heats of steel. Based on some SEM observations, the lower toughness in the Mixed-Mode I/III was tentatively attributed to inclusions in the steel. From the limited number of tests on the two heats shown in Fig. 15.11 plus tests on another small

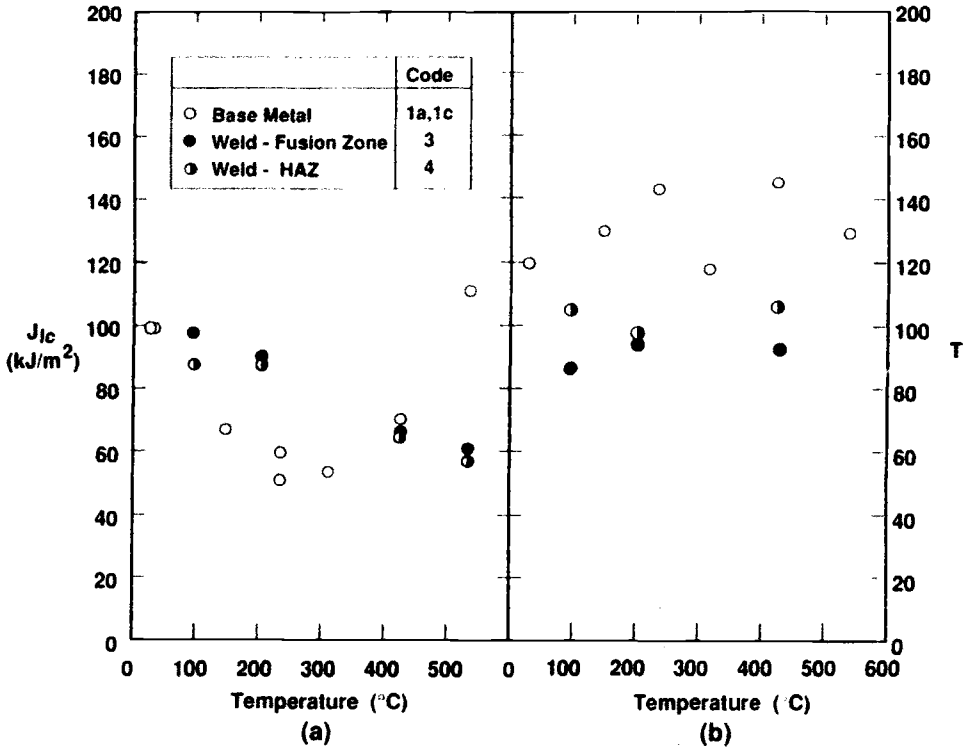

FIG. 15.9—A comparison of the (a) fracture toughness and (b) tearing modulus of HT9 base metal, weld metal (fusion zone) and heat affect zone (HAZ) [9].

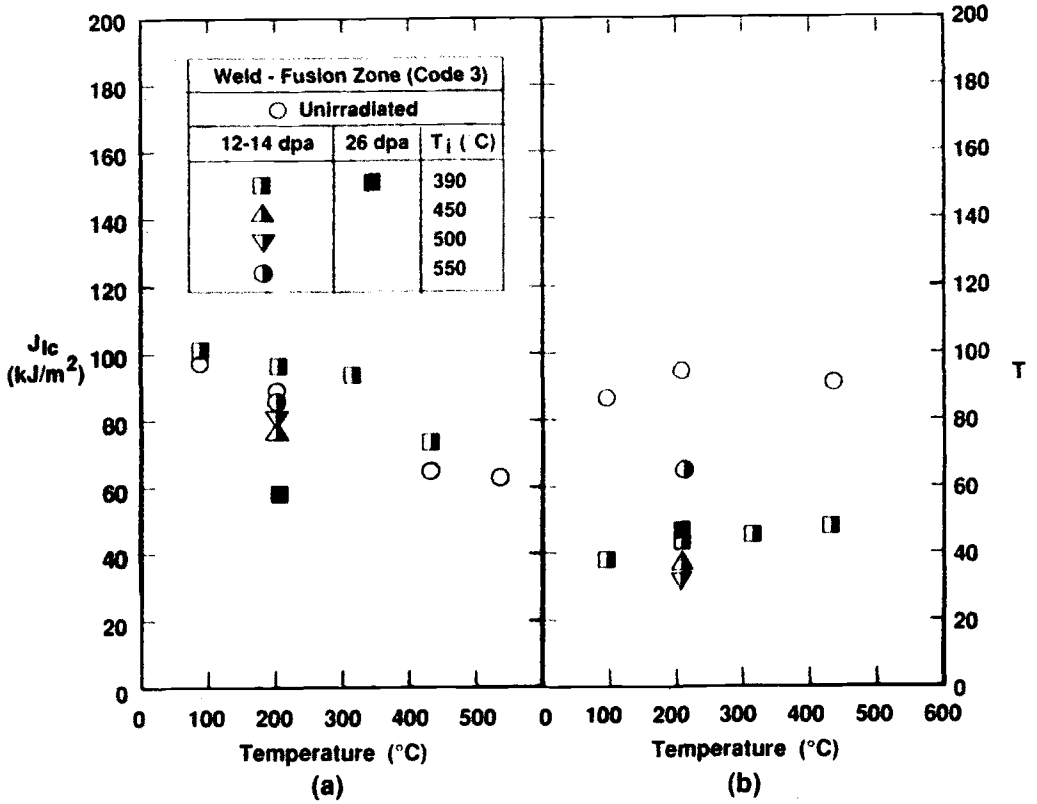

FIG. 15.10—The (a) fracture toughness and (b) tearing modulus of HT9 weld metal irradiated in EBR-II [9].

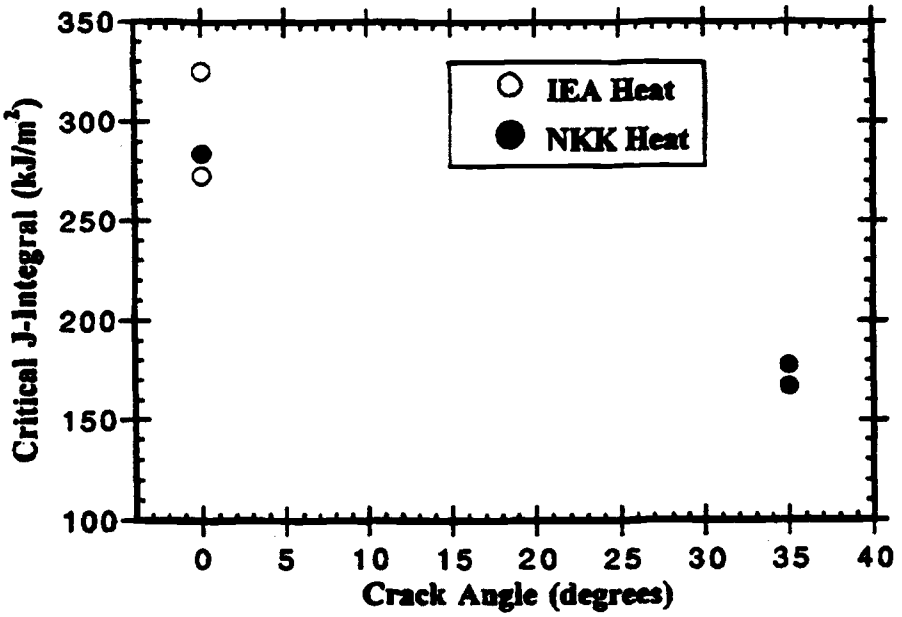

FIG. 15.11—Variation of fracture toughness of F82H as a function of crack angle [16].

heat of F82H, there did not appear to be a heat-to-heat variation in toughness.

Conventional (Mode I) room temperature toughness tests of JLF-1 steel revealed an excellent J_Q of over 400 kJ/m^2 [17]. A slightly lower value (≈350 kJ/m^2) was obtained for one room temperature test of F82H [18]. This was on the IEA Heat shown in Fig. 15.11, where it is seen that values below 350 KJ/m^2 were observed [16]. Toughness tests on a JLF-1 weld joint resulted in a very low J_Q (≈36 kJ/m^2), which without any fractographic evidence was tentatively attributed to "brittle zones or defects" in the deposit. More work was planned [17]. It must be emphasized

that these results are generally from a limited number of tests.

Results from experiments on F82H irradiated to 1.5 to 3 dpa in HFIR [19] and HFR [20] were used to make a comparison of the effect of irradiation on the toughness of HT9 and F82H (Fig. 15.12) [19]. Before irradiation, there were only minor differences in K_J of the two steels, which range from ≈200 to ≈300 MPa√m from room temperature to 300°C [3]. The 100 MPa√m transition temperature for the F82H and HT9 were estimated to be −100 and −75°C, respectively [3]. Irradiation of HT9 to 2.3 to 2.5 dpa at 80 to 90°C caused an increase in transition temperature of ≈100°C, and irradiation at 250 to 300°C caused an increase of about 275°C. Irradiation at the lower temperature did not significantly decrease the upper-shelf fracture toughness of HT9, but there was a large decrease for the higher irradiation temperature. Although the data for F82H are limited, irradiation to 1.6 to 2.5 dpa at 250°C had less effect on this steel than on HT9, and the F82H retained considerable toughness. The effect of irradiation on fracture toughness of the HT9 parallels the observations on the Charpy behavior of this steel in that in the absence of helium formation (displacement damage only), the ΔDBTT is larger after irradiation at 400°C than after irradiation at 55°C [13,14], an observation that was explained (see Chapter 14) as due to irradiation-enhanced precipitation at the higher temperature [21].

The fracture toughness results in Fig. 15.12 were obtained in the temperature range where tensile failure of the F82H and HT9 show limited strain-hardening capacity—low uniform elongation (Fig.12.7) [19]. Despite the low uniform elongation in tension tests in this temperature regime, failure in toughness tests occurred by ductile tearing, indicating that the tensile embrittlement characterized by low uniform strain is not characterized by embrittlement in the fracture toughness tests [19].

FRACTURE TOUGHNESS—OTHER APPROACHES

The micromechanisms of fracture in 9 to 12% Cr ferritic/martensitic steels have been extensively analyzed by Odette, Lucas, and coworkers [2,3,22–27]. As described in the preceding chapter, they showed that low-temperature fracture in Charpy tests of HT9 is not simple cleavage but occurs by a quasi-cleavage mode, in which single or small clusters of planar cleavage facets are separated by ductile tear ridges at misoriented lath packets or prior austenite grain boundaries (Fig. 14.11) [23]. Later work showed that quasi-cleavage fracture also occurred in other tempered martensitic steels such as F82H [27]. Quasi-cleavage occurs when a critical stress level (fracture stress) is reached in a critical area ahead of the crack tip to start the stable-to-unstable growth of a process zone crack. The mixed quasi-cleavage-microvoid coalescence fracture transition occurs when the strains in the process zone exceed a critical value. By using SEM and confocal microscopy, fracture reconstructions can be performed as a function of crack-opening displacement to elucidate fracture mechanisms and allow the determination of fundamental alloy properties, such as critical stress (σ_f^*) and critical area (A^*) for fracture.

Odette and co-workers have proposed that structural integrity in the unirradiated and irradiated conditions can best be assessed using a combination of the macromechanic and micromechanic elements of the fracture process, i.e., the combination of small specimen tests, fracture mechanics, microscopy, fractography, and finite element simulations [2,3,22,27]. This is believed necessary because of the divergent results obtained for fracture using the different test methods presently being applied (i.e., Charpy tests, fracture toughness tests, etc.), which raise the possibility of even greater divergence for actual structures with complicated geometries and loads. To counter these deficiencies, they pro-

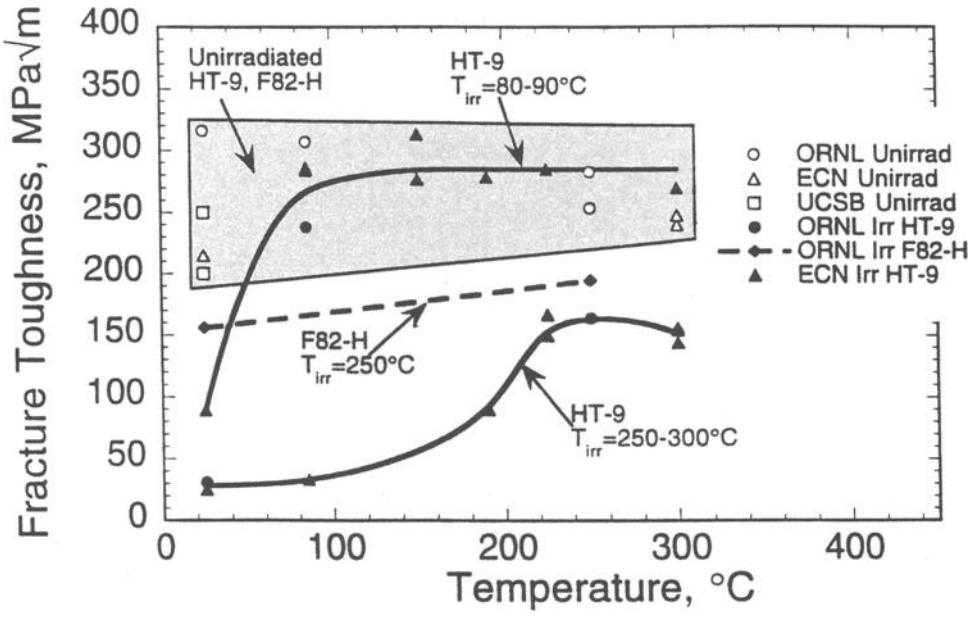

FIG. 15.12—Fracture toughness data for unirradiated and irradiated Sandvik HT9 and F82H taken from various sources [19].

pose to "combine finite element simulations of the evolution of multiaxial crack tip stress and strain fields with local measures of the conditions leading to crack extension (initiation or stable growth)" [3].

The approach to fracture discussed in the preceding sections is based on an experimental determination of a fracture toughness parameter for the steel. A "local approach" has been proposed and used in recent years to study cleavage fracture [28]. In this approach, the objective is to seek to measure the local fracture parameters using one or more specimens and then use this measurement to interpolate and extrapolate to more complicated geometries. For nuclear applications, one procedure is to determine an effective fracture toughness, K_e, that is a function of temperature, irradiation, loading rate (static and dynamic), specimen size, and crack depth-to-width ratio. These toughness-temperature data are then correlated using a master curve method that imposes temperature-indexed shifts (ΔT) to account for irradiation, temperature, loading rate, specimen size, and geometry. Small specimens can be used to measure and correlate the ΔT for irradiation effects. Although the ΔTs can be measured, the ultimate objective is to correlate the toughness under various conditions with tensile behavior to eventually be able to predict the shifts in toughness from changes in yield stress ($\Delta\sigma_{ys}$) [26]. This experimental approach is accompanied by a detailed numerical analysis of the flawed structure to which the method is applied.

A further goal would be a characterization of the microstructure to make it possible to predict microstructural changes as a function of the irradiation and metallurgical variables (including welding). From the microstructural changes, $\Delta\sigma_{ys}$ could be predicted, which could be used to predict shifts in the master curve, that is, $K_e(T)$ would be a function of the irradiation variables, metallurgical variables, and loading rate. With that information, it should be possible to predict $K_e(T)$ curves for actual structures to assess design limits as well as limits to be imposed during service [27]. That is, by sampling the microstructure during service, the change in fracture toughness of the structure can be determined.

REFERENCES

[1] G. E. Lucas and D. S. Gelles, J. Nucl. Mater. 155-157 (1988) 164.

[2] G. R. Odette, J. Nucl. Mater. 212-215 (1994) 45.

[3] G. E. Lucas, and G. R. Odette, K. Edsinger, B. Wirth, and J. W. Sheckherd, in: Effects of Radiation on Materials: 17th International Symposium, ASTM STP 1270, Eds. D. S. Gelles, R. K. Nanstad, A. S. Kumar, and E. A. Little (American Society for Testing and Materials, Philadelphia, 1996) 790.

[4] R. W. Hertzberg, Deformation and Fracture Mechanics of Engineering Materials, 3rd Edition (John Wiley & Sons, New York, 1989) 271.

[5] J. R. Hawthorne, J. R. Reed, and J. A. Sprague, in: Effects of Radiation on Materials: 12th International Symposium, ASTM STP 870, Eds. F. A. Garner, and J. S. Perrin (American Society for Testing and Materials, Philadelphia, 1985) 580.

[6] F. H. Huang, in: Effects of Irradiation on Materials: 14th International Symposium (Volume II) ASTM STP 1046, Eds. N. H. Packan, R. E. Stoller, and A. S. Kumar (American Society for Testing and Materials, Philadelphia, 1990) 459.

[7] F. H. Huang, in: Effects of Radiation on Materials: 16th International Symposium, ASTM STP 1175, Eds. A. S. Kumar, D. S. Gelles, R. K. Nanstad, and E. A. Little (American Society for Testing and Materials, Philadelphia, 1993) 575.

[8] D. S. Gelles, J. Nucl. Mater. 149 (1987) 192.

[9] F. H. Huang and M. L. Hamilton, J. Nucl. Mater. 187 (1992) 278.

[10] F. A. Smidt, Jr., J. R. Hawthorne, and V. Provenzano, in: Effects of Radiation on Materials: Tenth Conference, STP 725, Eds. D. Kramer, H. R. Brager, and J. S. Perrin (American Society for Testing and Materials, Philadelphia, 1981) 269.

[11] F. H. Huang, in: Effects of Radiation on Materials: 15th International Symposium, ASTM STP 1125, Eds. R. E. Stoller, A. S. Kumar, and D. S. Gelles, (American Society for Testing and Materials, Philadelphia, 1992) 1267.

[12] M. I de Vries, in: Effects of Radiation on Materials: 16th International Symposium, ASTM STP 1175, Eds. A. S. Kumar, D. S. Gelles, R. K. Nanstad, and E. A. Little (American Society for Testing and Materials, Philadelphia, 1993) 558.

[13] W. L. Hu and D. S. Gelles, in: Effects of Irradiation on Materials: 14th International Symposium (Volume II) ASTM STP 1046, Eds. N. H. Packan, R. E. Stoller, and A. S. Kumar (American Society for Testing and Materials, Philadelphia, 1990) 453.

[14] R. L. Klueh, J. M. Vitek, W. R. Corwin, and D. J. Alexander, J. Nucl. Mater. 155-157 (1988), 973.

[15] H-X. Li, R. H. Jones, J. P. Hirth, and D. S. Gelles, J. Nucl. Mater. 233-237 (1996) 258.

[16] H-X. Li, D. S. Gelles, J. P. Hirth, and R. H. Jones, Fusion Materials Semiannual Progress Report for Period Ending December 31, 1996, U. S. Department of Energy, DOE/ER-0313/21, April 1997, p. 142.

[17] A. Nishimura, N. Inoue, and T. Muroga, J. Nucl. Mater., 258-263 (1998) 1242.

[18] K. Shiba, Proceedings of the IEA Workshop/Working Group Meeting on Ferritic/Martensitic Steels, Petten, The Netherlands, October 1-2, 1998, Ed. R. L. Klueh, ORNL/M-6627.

[19] A. F. Rowcliffe, J. P. Robertson, R. L. Klueh, K. Shiba, D. J. Alexander, M. L. Grossbeck, and S. Jitsukawa, J. Nucl. Mater. 258-263 (1998) 1275.

[20] M. Horsten, in: Proceedings of the IEA Working Group Meeting on Ferritic/Martensitic Steels, Ed., R. L. Klueh, JET, Culham, U.K., October 24-25, 1996, ORNL/M-5674.

[21] R. L. Klueh and D. J. Alexander, J. Nucl. Mater. 218 (1995) 151.

[22] G. R. Odette, G. E. Lucas, R. Maiti, and J. W. Sheckherd, J. Nucl. Mater. 133/134 (1986) 728.

[23] G. R. Odette, G. E. Lucas, and R. Maiti, J. Nucl. Mater. 148 (1987) 22.

[24] G. R. Odette, B. Chao, an G. E. Lucas, J. Nucl. Mater. 191-194 (1992) 827.

[25] K. Edsinger, G. R. Odette, G. E. Lucas, and J. W. Sheckherd, J. Nucl. Mater. 233-237 (1996) 342.

[26] M. Edmark, K. Edsinger, G. Lucas, and G. R. Odette, J. Nucl. Mater. 233-237 (1996) 347.

[27] G. R. Odette, E. Donahue, G. E. Lucas, and J. W. Sheckherd, in: Effects of Radiation on Materials: 18th International Symposium, ASTM STP 1325, Eds. R. K. Nanstad, M. L. Hamilton, F. A. Garner, and A. S. Kumar (American Society for Testing and Materials, Philadelphia, 1998) 1089.

[28] C. S. Wiesner, The "Local Approach" to Cleavage Fracture: Concepts and Applications (Abington Publishing, Cambridge, England, 1996).

16

Fatigue and Fatigue Crack Growth

High-temperature components in a steam power plant are subject during service to fatigue straining due to thermal cycling or a combination of thermal and mechanical deformation in which the strain cycle includes a hold period. The first wall in a D-T tokamak fusion system will also undergo thermomechanical fatigue (TMF) as a result of the mechanical and electromagnetic loadings and the cyclic strains induced by the temperature changes during the plasma burn and off-burn periods [1,2]. Two approaches may be adopted for estimating the lifetimes of the component materials under combined thermal and mechanical cycling. The first involves the formulation of failure relationships directly from TMF tests; however, the acquisition of TMF data on materials by testing with simultaneously varying temperature and strain is experimentally difficult, time consuming, and expensive, and the procedures have not yet been standardized. Consequently, most of the relevant materials data has been generated by the second approach of isothermal continuous cycling fatigue and creep-fatigue (hold time) testing. However, the service lives extend over many years, and it is not practical to reproduce the conditions in laboratory tests. It has therefore been necessary to develop models of the behavior to enable the long-term service lives of components exposed to TMF to be predicted from the results of the shorter-term laboratory tests.

Fatigue tests may be either stress (or load) or strain (or displacement) controlled. The majority of the early studies of metal fatigue were based on stress-control testing, which is still adopted for design situations in which the applied stress is primarily within the elastic range and the resulting endurance is high [high cycle fatigue (HCF)]; the material strength controls the behavior, and crack initiation is the dominant event under these conditions. However, the strain-controlled method is applied in the design and evaluation of components subjected to secondary stresses, the load is high as in the vicinity of notches, and the total strain range ($\Delta\varepsilon_t$) has a significant plastic component ($\Delta\varepsilon_p$) relative to the elastic strain ($\Delta\varepsilon_e$). In this case, the response of the material is deformation dependent, the ductility being the prime factor governing the fatigue resistance, and the number of cycles to failure is low [low cycle fatigue (LCF)]. Cracks initiate relatively early in life and crack growth is the dominant failure criterion. The point at which the elastic and plastic strain ranges are equivalent, termed the *fatigue transition life*, is usually taken to delineate the LCF and HCF regimes (Fig. 16.1) [3]; it normally occurs in the range 10^2 to 10^4 cycles, depending on the test parameters and environment.

It follows that fatigue is essentially a problem of cracking during cyclic straining or stressing and is generally considered to consist of three stages, namely, crack nucleation and growth on a microscopic scale, propagation through a plastic zone, and propagation through an elastic field. The LCF failure of smooth laboratory specimens can be regarded as being equivalent to the formation of macroscopic cracks in actual components, while the final stage of crack growth through an elastic zone is usually studied by LCF tests on notched specimens. However, the fatigue process may be modified as a result of stress relaxation by thermal creep deformation and cracking during the tension and/or compression hold periods in creep-fatigue tests.

$\Delta\varepsilon_e$ and $\Delta\varepsilon_p$, the peak tensile (σ_{max}) and compressive (σ_{min}) stresses, and the total stress range ($\Delta\sigma_t$) in the strain- or stress-controlled continuous cycling fatigue and creep-fatigue tests are determined from the hysteresis loops (the stress-strain relationship during one cycle) recorded periodically during the tests (Fig. 16.2).

In this chapter, the effects of various test, material, environmental, and irradiation parameters on the LCF and/or HCF behavior are reviewed, and the experimental data on thermal fatigue (TF), TMF, and fatigue crack growth (FCG) of the high-chromium martensitic steels are surveyed. The modeling of the LCF and creep-fatigue data to enable the behavior under TMF loading conditions to be predicted is also summarized.

STRAIN-CONTROLLED LOW-CYCLE FATIGUE

Fairly extensive studies of the fatigue behavior of the high-chromium martensitic steels have been conducted in the United States, Europe, and Asia. Thus, strain-controlled fatigue tests with fully reversed triangular wave forms ($R = \varepsilon_{min}/\varepsilon_{max} = -1$, where ε_{min} and ε_{max} are the minimum and maximum strains, respectively) and with hold periods in the tension and/or compression phases have been carried out on steels of this type in air, vacuum, and other environments at temperatures ranging from ambient to 650 or 700°C, $\Delta\varepsilon_t$ of 0.2 to 2.0%, and a cyclic strain rate ($\dot{\varepsilon}_t$) of 3×10^{-3} to 3×10^{-5} s^{-1}.

Strain Range

The reduction in fatigue endurance with increasing strain range (exemplified in Fig. 16.1) may be described by the

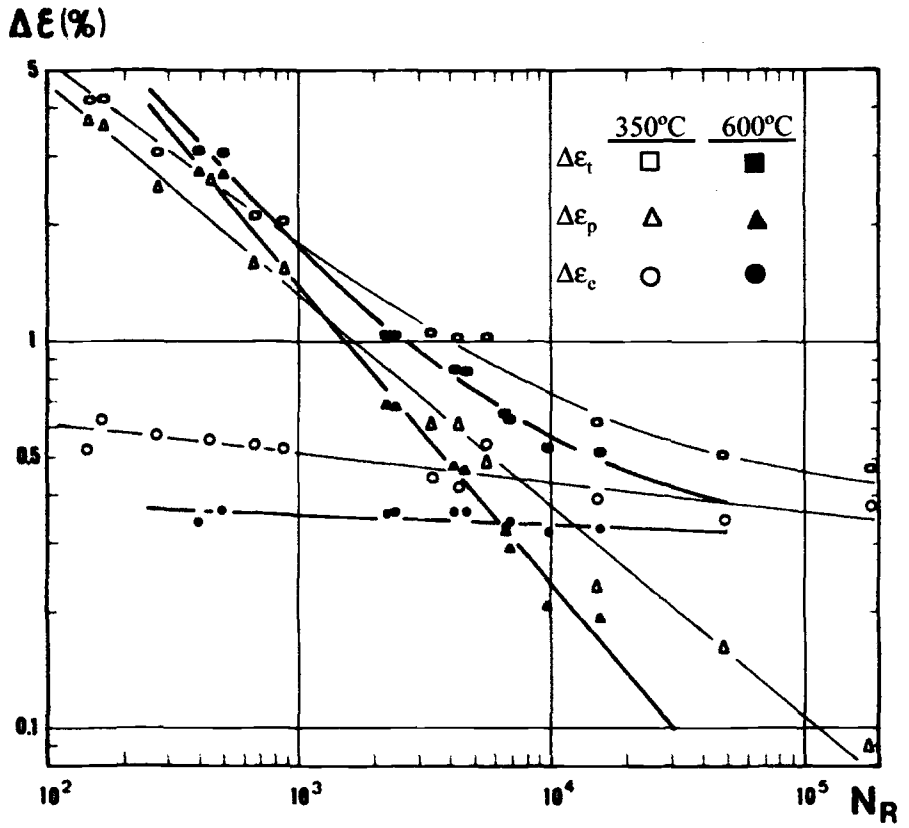

FIG. 16.1—LCF strain-life curves at 350°C and 600°C for 12Cr-1MoV steel [3].

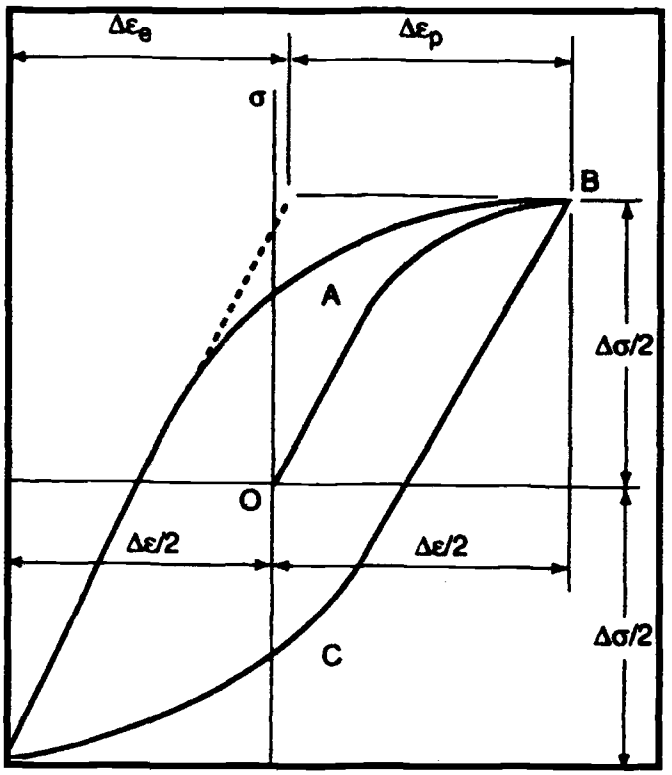

FIG. 16.2—Typical hysteresis loop.

Coffin-Manson relation [4–6]:

$$\Delta\varepsilon_p N_f^{\beta} = C_p \qquad (16.1)$$

where N_f is the number of cycles to failure (fatigue endurance) and β and C_p are material constants.

The values of β (= 0.52) and C_p (=88 with $\Delta\varepsilon_p$ in %) for modified 9Cr-1Mo steel in the normalized-and-tempered (N & T) and N & T plus 5000 h aged conditions are relatively independent of temperature in the range 482 to 704°C when tested in vacuum (Fig. 16.3) [7]; however, the results for the steel tested in air are not independent of temperature and do not fit the Coffin-Manson relation even at a given temperature. The Coffin-Manson plots for the 12Cr-MoV steel (X20) at 350°C (β = 0.546 and C_p = 56.9) and 600°C (β = 0.772 and C_p = 287.1) (see Fig. 16.1) [3] are also reproduced in Fig. 16.3. The material and temperature dependences of the $\Delta\varepsilon_p$-N_f relations correspond with those of the reductions of area in tension tests [8], as proposed in earlier investigations of LCF behavior [4,5]; that is, the larger the reduction of area, the higher the fatigue endurance. Further data on the influences of test temperature and environment are presented in the following sub-sections.

Test Temperature

The effect of temperature on the fatigue endurance of MANET I steel tested in air [9–12] is illustrated in Fig. 16.4 [11]. The endurances at a high total strain range ($\Delta\varepsilon_t$ = 1.5%)

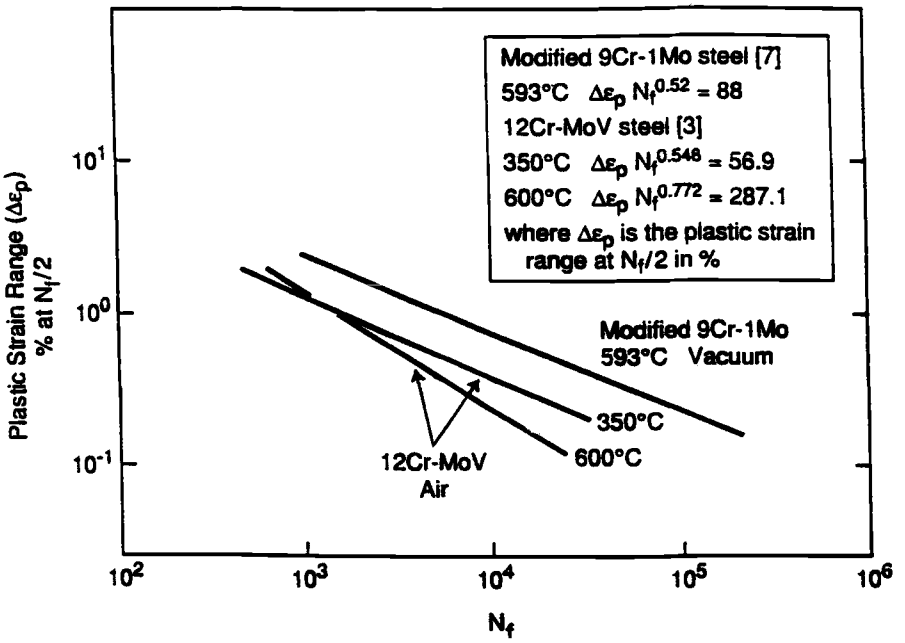

FIG. 16.3—Coffin-Manson plots of the plastic strain range at $N_f/2$ versus numbers of cycles to failure in strain-controlled fatigue tests for modified 9Cr-1Mo steel at 593°C [7] and 12Cr-MoV steel at 350 and 600°C [3].

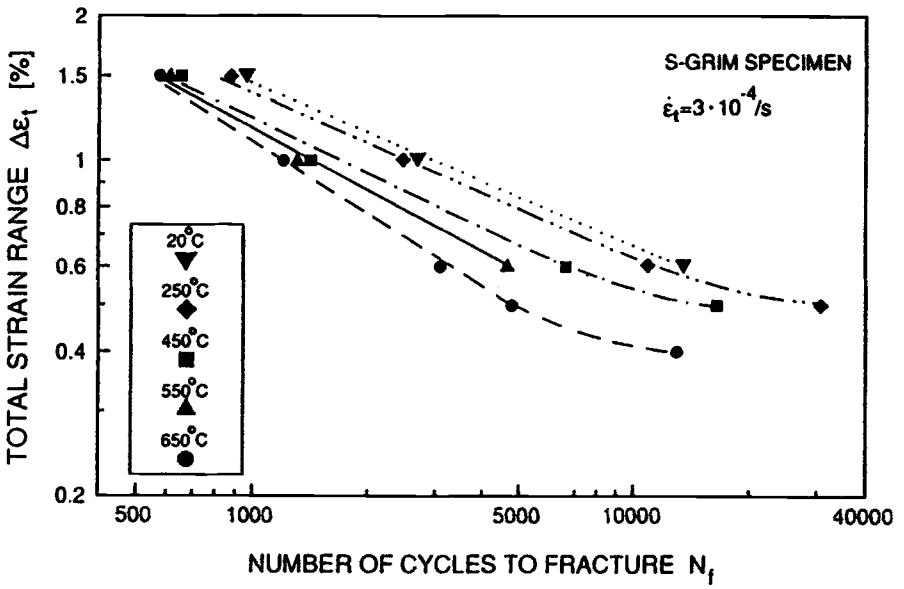

FIG. 16.4—Influence of test temperature on the LCF endurance of the MANET I steel [11].

decrease by a factor of about two on increasing the test temperature from ambient to 650°C, while the endurance for a $\Delta\varepsilon_t$ of 0.6% at 650°C is about a third of that at ambient temperature. However, the results of tests on miniature specimens of the MANET I steel in vacuum show a smaller effect of temperature on the endurance in the range 20 to 450°C [13].

As mentioned above, the LCF endurance of the modified 9Cr-1Mo steel in vacuum is virtually independent of temperature in the range 482 to 704°C [7]; the fatigue lives of this steel are also only weakly dependent on temperature between ambient and about 540°C [14,15]. The fatigue endurance may be represented by the Langer equation relating $\Delta\varepsilon_t$ (in %) to N_f as follows:

$$\Delta\varepsilon_t = x\, N_f^y + \Delta\varepsilon_o \qquad (16.2)$$

where x and y are constants and $\Delta\varepsilon_o$ is the estimated total strain at infinite endurance.

The data for the modified 9Cr-1Mo steel at ambient and elevated temperatures are given by the following Langer equa-

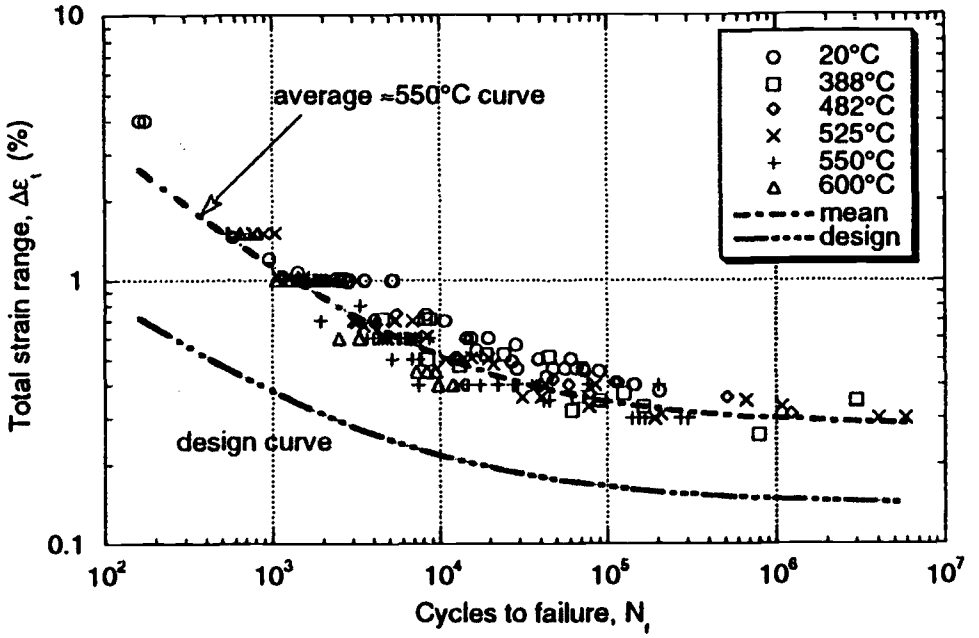

FIG. 16.5—Uniaxial LCF data for modified 9Cr-1Mo steel [16].

tions [14, 15]:

$$\text{RT } \Delta\varepsilon_t = 13.895\ N_f^{-0.382} + 0.25 \quad (16.3)$$

$$371°\text{C } \Delta\varepsilon_t = 33.279\ N_f^{-0.501} + 0.264 \quad (16.4)$$

$$482°\text{C } \Delta\varepsilon_t = 41.235\ N_f^{-0.555} + 0.231 \quad (16.5)$$

$$538°\text{C } \Delta\varepsilon_t = 183.823\ N_f^{-0.750} + 0.322 \quad (16.6)$$

Other studies show that the fatigue endurances of the modified 9Cr-1Mo steel generally decrease with increasing temperature in the range 25 to 600°C (Fig. 16.5) [16]; in this case, the average 550°C data curve is given by:

$$\Delta\varepsilon_t = 39.6068\ N_f^{-0.5562} + 0.28 \quad (16.7)$$

However, the magnitude of the temperature effect is relatively small and equivalent to the heat-to-heat and inter-laboratory data scatter at a given test temperature [16]. This conclusion is supported by fatigue data on EM12 steel at ambient temperature and 500°C [17]. The results of investigations on HT9 [18,19], 9Cr-1Mo [20,21], 9Cr-2Mo [22], X20 [3,23], and other high-chromium martensitic steels [8] have also confirmed that increasing the temperature in the range up to about 600°C results in relatively small reductions in endurance, the effect being more pronounced at the lower $\Delta\varepsilon_t$ values (factor of about six maximum).

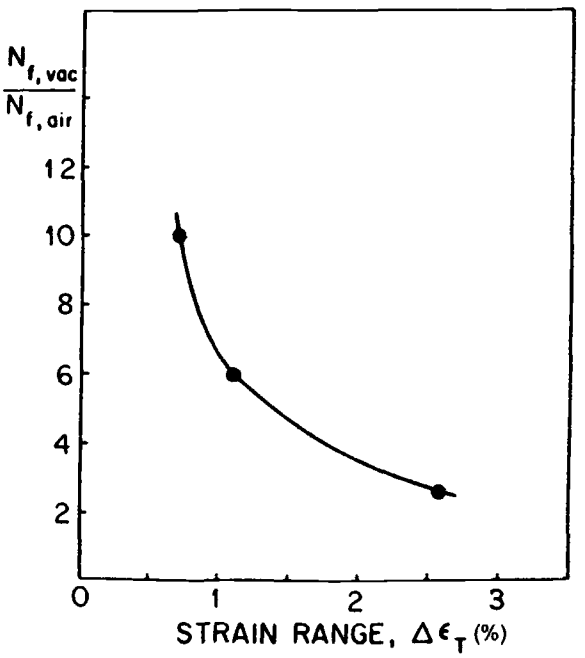

FIG. 16.6—Ratio of cyclic life in vacuum to that in air as a function of total axial strain range for modified 9Cr-1Mo steel in continuous LCF tests at 593°C [7].

Test Atmosphere

Although the majority of the isothermal LCF tests have been conducted in air, the results obtained on the modified 9Cr-1Mo steel in tests at 593 [7,24,25], 538 [26], and 600°C [27] show that the endurances in vacuum (1×10^{-7} to 1×10^{-3} Pa) are significantly greater than in air. The data for the steel tested in air and a vacuum of 1×10^{-3} Pa at 593°C are illustrated in Fig. 16.6 [7]; the ratios of N_f (vacuum): N_f (air) are approximately 10, 6, and 2.5 at $\Delta\varepsilon_t$ of 0.7, 1.1, and 1.4%, respectively.

Also, the endurances of the modified 9Cr-1Mo steel in tests at 593 and 700°C and $\Delta\varepsilon_t = 2.1\%$ in vacuum (1×10^{-3} Pa) are a factor of two to three greater than those in an atmosphere of argon plus 3% hydrogen with some water vapor [28]. Furthermore, the numbers of cycles to failure of the MANET I steel at ambient temperature and $\Delta\varepsilon_t$ of 1% [13] and a 12Cr-1MoV steel at 600°C and $\Delta\varepsilon_t = 0.55$ to 2% [29] in vacuum of $<1 \times 10^{-4}$ and 1×10^{-3} Pa, respectively, are at least twice those of the corresponding specimens tested in air.

Heavy oxidation of the specimen and fracture surfaces and at the crack tips is usually observed after continuous cyclic testing in air at low $\Delta\varepsilon_t$ and elevated temperatures [21,25].

Cracks are produced in the surface oxide and lead to the formation of transgranular cracks in the matrix, which appear as oxide-filled wedges [15]. The oxide in the cracks presumably prevents closure during the compression halves of the cycles, and coalescence of these cracks facilitates propagation, resulting in premature failure relative to the behavior in vacuum.

Intergranular cracking has also been detected in a 12Cr-1MoV steel after continuous cyclic straining at 600°C in air or vacuum, the microcrack densities in air being about an order of magnitude greater than those in vacuum [29]. The cracking occurs primarily at the prior austenite grain boundaries orthogonal to the applied stress direction and is attributed to the formation of precipitate-free zones with large sub-grains adjacent to these boundaries during fatigue. The shear deformation is localized in the zones favorably oriented with respect to the stress direction; this results in stress concentration on the transverse boundaries, which intersect the surface where the oxidation is most pronounced and brittle oxides may form.

Strain Rate and Frequency

The influence of $\dot{\varepsilon}_t$ and frequency (ν) are considered together as they are equivalent parameters related as follows:

$$\dot{\varepsilon}_t = 2\Delta\varepsilon_t \nu \qquad (16.8)$$

The effects of cyclic strain rate within the range 1×10^{-2} to 3.3×10^{-6} s^{-1} on the LCF endurances of a 9Cr-2Mo steel at 550°C [22], a cast 12CrMoV steel at 20 and 530°C [30], MANET I steel at 20 to 650°C [11], and modified 9Cr-1Mo steel at 500 to 650°C [31] have been investigated. The endurances of the 9Cr-2Mo steel are comparable when tested in air at 550°C and $\dot{\varepsilon}_t$ of 1×10^{-3} and 1×10^{-4} s^{-1} [22]. Similarly, the fatigue endurance of the MANET I steel at 450°C is only slightly reduced on decreasing the $\dot{\varepsilon}_t$ from 3×10^{-3} to 3×10^{-5} s^{-1} [11], thereby demonstrating that fatigue and not creep damage controls the failure at this temperature; however, a reduction in the endurance with decreasing strain rate is more evident in tests at 650°C, particularly at low $\Delta\varepsilon_t$.

An analysis of the endurance data for the N & T MANET I and MANET II steels tested in air in the temperature range 20 to 550°C and at average strain rates of 3×10^{-3} to 3×10^{-5} s^{-1} has been conducted [32] based on the premise [3] that the high-temperature LCF process is controlled by two mechanisms, athermal and thermally activated, depending on $\Delta\varepsilon_p$. The following relationship has been derived from the Coffin frequency modified endurance approach [33]:

$$\frac{1}{N_f} = (1/\dot{\varepsilon}_t)^{\alpha} (\Delta\varepsilon_p/C_p)^{1/\beta} [1 + A (\Delta\varepsilon_p)^{b} (1/\dot{\varepsilon}_t)^{\alpha} e^{-Q/RT}] \qquad (16.9)$$

where $\Delta\varepsilon_p$ is in %, $C_p = 165$ and $\beta = 0.753$ are the Coffin-Manson constants, the coefficient $\alpha = 0.055$ and $A = 4203$, $b = -0.64$ and the activation energy $Q = 51.1$ KJ mol^{-1} (12.2 Kcal. mol^{-1}) are material parameters independent of $\Delta\varepsilon_p$ and temperature [T (K)].

The endurances calculated using Eq 16.9 are in good agreement with the experimental values for the MANET I and MANET II steels tested in the range 200 to 550°C [32]. The relatively low value of Q suggests that the contribution from thermally activated mechanisms to the damage per cycle is small even at 550°C, thereby confirming that the temperature dependence of the LCF endurance is moderate.

Steel Composition, Structure, and Fabrication

The LCF (R = −1) endurances as a function of $\Delta\varepsilon_t$ for a series of high-chromium martensitic steels tested in air at ambient temperature and 550°C are shown in Figs. 16.7

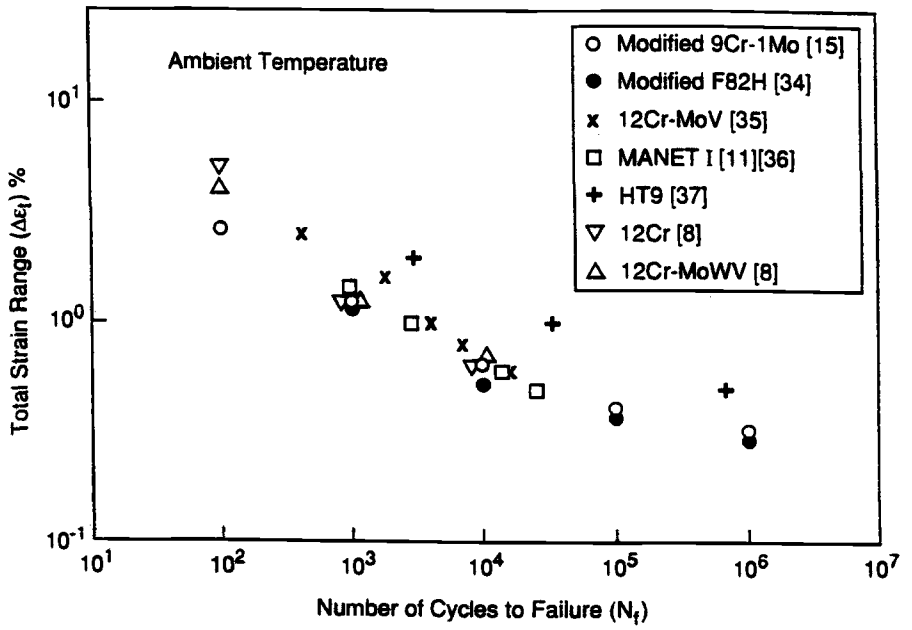

FIG. 16.7—Total strain range versus numbers of cycles to failure for various high-chromium martensitic steels in strain-controlled fatigue tests at ambient temperature [8,11,15,34–37].

[8,11,15,34–37] and 16.8 [3,11,16,17,38,39], respectively. The endurances are relatively independent of the steel composition, apart possibly from the HT9 steel, which shows significantly higher numbers of cycles to failure at a given total strain range in the tests at ambient temperature. The reason for this apparently diverse behavior has not been elucidated but may be associated with the combined influences of the Mo and W in solution in the HT9 steel.

The endurances of the modified F82H reduced activation steel are significantly lower than those of the MANET II steel in LCF tests at 450 and 550°C, particularly at a $\Delta\varepsilon_t$ of 0.6% [40]. The N_f values for the F82H steel are also inferior to those of the MANET I and II steels in LCF tests at 200 to 250°C, $\dot{\varepsilon}_t = 8 \times 10^{-4}\ s^{-1}$ and $\Delta\varepsilon_t \leq 0.7\%$ [41] but are superior at higher total strain ranges. The plastic strains at $N_f/2$ for the modified F82H steel are greater than those for the MANET steels, the failure relationships being given by the following equations [41]:

$$\text{Modified F82H: } \Delta\varepsilon_p^{1.81} N_f = 2.42 \times 10^{-1} \quad (16.10)$$

$$\text{MANET I and II: } \Delta\varepsilon_p^{2.59} N_f = 7.67 \times 10^{-4} \quad (16.11)$$

where $\Delta\varepsilon_p$ is in absolute units.

There has been little systematic study of the effects of initial heat treatment and microstructure on the LCF behavior of these steels. However, some observations have been made on X20 steel heat treated to produce duplex structures consisting of tempered martensite plus δ-ferrite and tested at ambient temperature [35]; the steel with a ferrite content of 17% has superior endurances and lower σ_{max} and σ_{min} values compared to those of the 8% ferrite steel at a $\Delta\varepsilon_t$ of 2.5% but comparable lives to failure at a $\Delta\varepsilon_t$ of 1%. Also, the numbers of cycles to failure of the modified 9Cr-1Mo steel in the form of hot-rolled plate are higher than those for hot-forged plate in continuous-cycling tests in air at 538°C and $\Delta\varepsilon_t$ in the range 0.5 to 1.5% [26]; the $\Delta\varepsilon_e$ components of $\Delta\varepsilon_t$ are larger and the transition life higher for the hot-rolled product. These differences in LCF behavior have been ascribed to the finer prior austenite grain size of the hot rolled plate (19 μm) compared to the forged plate (31 μm). A similar effect of grain size has been inferred in the case of a 1000 mm diameter and 300 mm thick 9Cr-1Mo steel forged tube plate with a prior austenite grain size of 120 μm when tested in a quenched-and-tempered plus 725°C for 3 h simulated post-weld heat treatment (PWHT) condition at 450, 500, and 520°C and $\Delta\varepsilon_t$ of 0.5 to 2.0% [21]; the endurances were claimed to be significantly lower than the published values for finer grain size, thin section hot-rolled steel products.

Prior aging for 5000 h in the range 482 to 704°C has little effect on the endurances, but reduces the $\Delta\sigma_t$ values of the N & T modified 9Cr-1Mo steel when tested in vacuum at $\Delta\varepsilon_t = 1.4\%$ at the respective aging temperatures [7]. However, aging for 50 000 and 75 000 h at 538°C and 50 000 h at 593°C increases the $\Delta\varepsilon_p$ components of the $\Delta\varepsilon_t$ (0.5%) and reduces the $\Delta\sigma_t$ and the endurances in tests in air at 538 and 593°C [25]. The reductions in the fatigue lives range from about 18 to 62% depending on the aging and test conditions.

LCF tests have been conducted at 550°C and $\Delta\varepsilon_t$ of 0.5 to 1.0% on the modified 9Cr-1Mo steel in the form of a forging (550 mm thick), plate (25 mm thick), and TIG-welded plate and 25 mm sections of the forging given a PWHT at 740°C for 8.4 h [27]. The endurances of the forging and plate are superior to those of the weld metal and HAZ by factors of two to five depending on the $\Delta\varepsilon_t$. Other observations on the steel weld and weldments fatigue tested in reverse bending at 550°C show that a weld strength reduction factor of 1.25 in terms of $\Delta\varepsilon_t$ bounds all the data [16]; thus, factoring the proposed design curve for the base steel ($\Delta\varepsilon_t = 6.9971\ N_f^{-0.4891}$

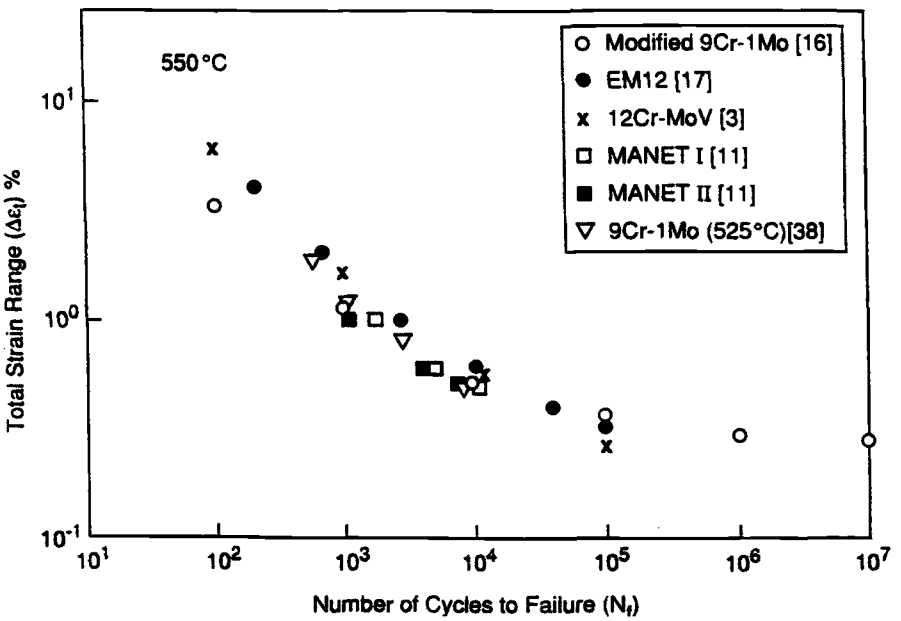

FIG. 16.8—Total strain range versus numbers of cycles to failure for various high-chromium martensitic steels in strain-controlled fatigue tests at 550°C [3,11,16,17,38,39].

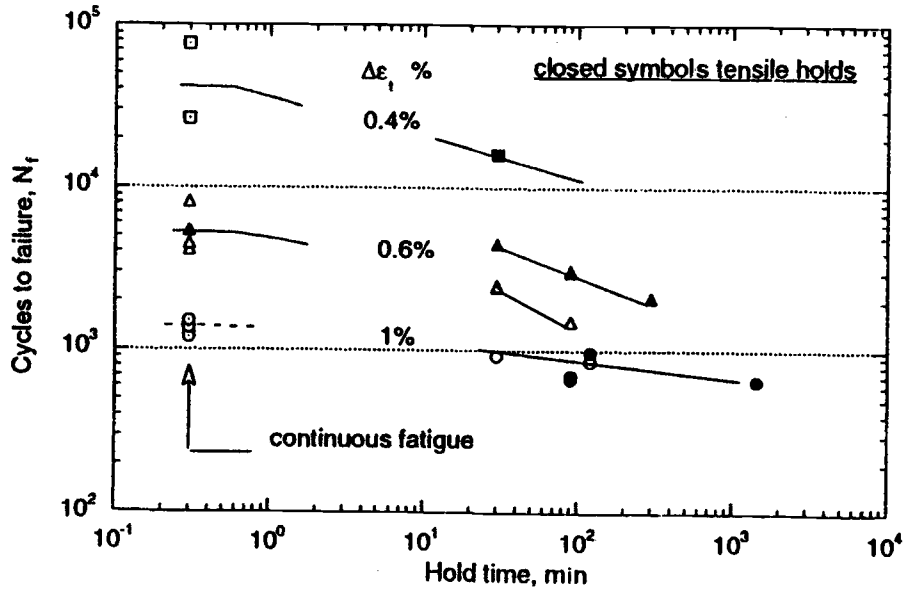

FIG. 16.9—Effects of tensile and compressive hold periods on the number of fatigue cycles to failure of the modified 9Cr-1Mo steel at 550°C [16].

+ 0.14)* results in the following relationship for the weld metal:

$$\Delta\varepsilon_t = 5.5977\ N_f^{-0.4891} + 0.11 \qquad (16.12)$$

LCF tests have also been performed in air at a $\dot{\varepsilon}_t$ of 1×10^{-5} s^{-1} on welded [submerged arc (automatic) and shielded metal arc (manual)] dissimilar steel combinations, namely 2¼Cr-1Mo to modified 9Cr-1Mo at 600°C and 15Cr-11Ni-6Mn-1Mo-1Nb austenitic to modified 9% Cr-1Mo at 650°C [42]. The average cyclic lives are a factor of 2.2 lower with respect to the baseline curve for the 2¼Cr-1Mo steel in the former case, the cracks being initiated in the low-alloy steel close to the HAZ. Likewise, there is a mean cyclic life reduction factor of about 2.4 with respect to the modified 9Cr-1Mo steel reference curve for the latter joints, the failures occurring in the soft regions of the martensitic steel HAZ.

Creep-Fatigue

The test temperature and strain-range dependences of the LCF lives of the steels may be modified by the introduction of hold periods at the peak tension and/or compression strains of the cycles. In general, hold times reduce the high-temperature fatigue endurance compared to that in continuous-cycling tests, the magnitudes of the effects being more pronounced at lower $\Delta\dot{\varepsilon}_t$. The effects are similar to those produced by decreasing the strain rate or frequency in continuous-cycling tests at high temperatures; thus, the influence of hold times has been dealt with as a strain rate or frequency effect in some instances and the correlation with the hold time made by calculating an apparent strain rate ($\dot{\varepsilon}_a$) given by [30,43]:

$$\dot{\varepsilon}_a = \frac{2\Delta\varepsilon_t}{\tau} \qquad (16.13)$$

where τ is the time for one cycle, including hold time.

A reduction in $\dot{\varepsilon}_a$ produces a decrease in N_f for a cast 12% Cr steel in LCF tests with and without hold times at ambient temperature and 530°C [30]. Furthermore, for a given value of $\dot{\varepsilon}_a$, there is no difference between the continuous-cycling and hold-time tests in a log-log plot of $\dot{\varepsilon}_a$ versus time to failure, t_f.

Hold times in tension are more detrimental than in compression in reducing the LCF lives of austenitic steels [44]. Stress relaxation occurs by thermal creep during both tension and compression holds in tests at temperatures ≥500°C. The thermal creep deformation induces the nucleation of grain boundary cavities, which grow and coalesce to form cracks under tension but not in compression; thus, the introduction of tensile holds in the fatigue cycles often produces changes in the fracture mode from transgranular to intergranular in these materials [1]. Furthermore, stress relaxation during a tensile hold may result in a mean compressive stress for the cycle, whereas stress relaxation in compression produces a mean tensile stress. The LCF lives in continuous-cycling tests usually decrease with increasing mean tensile stress, but it appears that the intergranular damage produced by thermal creep during tensile holds overrides any effects of mean stress in the austenitic steels.

In contrast to the behavior of the austenitic steels, the data for the standard [20,21] and modified [7,16,25,27,28,45,46] 9Cr-1Mo and MANET I [35,39,47,48] martensitic steels show negligible or only moderate reductions (factors of two or three maximum) in the continuous-cycling LCF endurances when hold times (1 min to 24 h) are introduced in the tension, compression, or both phases at test temperatures of 450 to 600°C; some of these data are exemplified in Figs. 16.9 [16] and 16.10 [20,21,28,45].

* This suggested design equation was obtained in the traditional manner by reducing the average curve for all data (Eq 16.7) by the greater of times two reduction in $\Delta\varepsilon_t$ (in %) or a times twenty reduction in N_f; the design curve is slightly different from the one proposed in the RCC-MR Design Code as it uses only parallel specimen results and includes additional data [16].

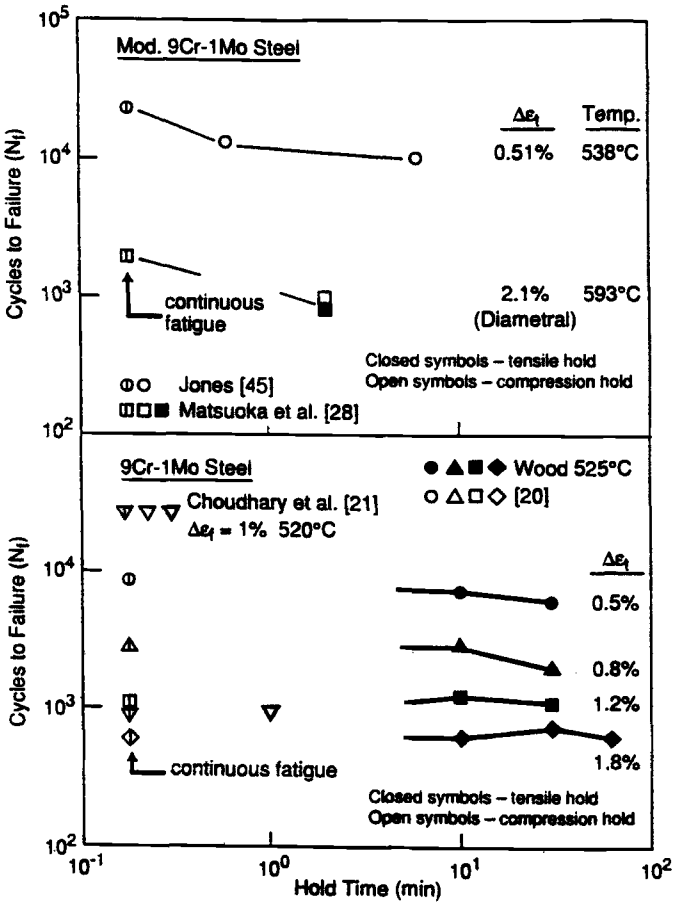

FIG. 16.10—Effects of tensile and compressive hold times on the fatigue endurances of 9Cr-1Mo steels at temperatures in the range 520 to 593°C [20,21,28,45].

In general, compressive hold periods are slightly more damaging than tensile holds for the high-chromium martensitic [27,35,44] and other Cr-Mo steels [49]. Thus, hold times of 1 to 30 min in the tension phase of the cycles in tests on the MANET I steel at 450 and 550°C have little or no effect on the endurances at $\Delta\varepsilon_t$ of 0.6 and 1.0% [39]; larger reductions in N_f, especially at the higher temperature of 550°C and the lower $\Delta\varepsilon_t$ of 0.6%, are produced in the tests with compression and tension plus compression holds. The results of the tests at 450°C are displayed in Fig. 16.11 [39]. Nevertheless, tensile hold periods are reported to be more damaging in tests on the modified 9Cr-1Mo at 593°C in vacuum, whereas compression holds are more detrimental in air [7]; the endurances in air are, however, always inferior to those in vacuum in the continuous-cycling and hold-time tests.

Significant stress relaxation can occur during the hold periods in creep-fatigue tests. Thus, the introduction of hold periods of 1 min in the tension, compression, and both phases in tests on 9Cr-Mo steel in air at 520°C and $\Delta\varepsilon_t$ = 1% [21] and of 15 to 60 min at the peak tensile strain in air tests on the modified 9Cr-1Mo steel at 538 and 593°C and $\Delta\varepsilon_t$ of 0.50 and 0.70% [25] results in the development of increased amounts of inelastic strain relative to that in continuous cycling tests. The stress relaxes rapidly during the initial stages and decreases to about half the original value at the end of hold periods ranging from 1 min to 5 h in tests on the standard and modified 9Cr-1Mo steels at temperatures of 500 to 700°C [20,28]. This observation is in general agreement with that of a factor two to three reduction in residual stress in times of ≤10 h in relaxation tests on the 9Cr-1Mo steel at 475°C [38,50]. However, 2 min hold periods at the peak tensile or compressive strains have no significant effect on the $\Delta\varepsilon_e$ and $\Delta\varepsilon_p$ components in fully reversed fatigue tests on the modified 9Cr-1Mo steel in vacuum at 593°C and $\Delta\varepsilon_t$ of approximately 1.4% [7].

As mentioned previously, the difference in the effects of tensile and compression holds in creep-fatigue tests has often been attributed to the development of an appreciable mean

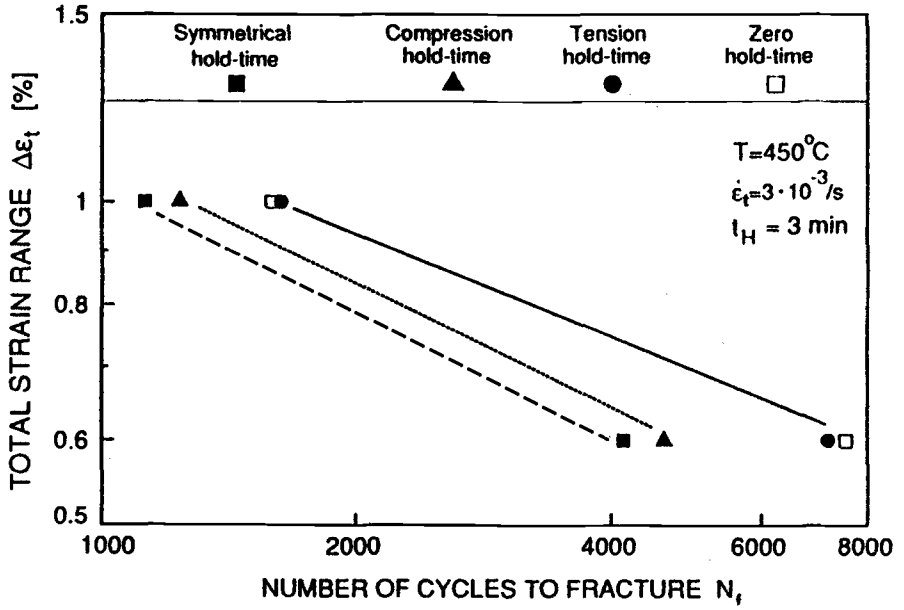

FIG. 16.11—Effect of hold periods on the number of cycles to failure of MANET I steel at 450°C [39].

stress [51]. However, the mean stresses produced as a consequence of the introduction of hold times in the elevated-temperature tests on the high-chromium martensitic steels are usually small (for example, ≤15 MPa over the whole lifetime [7]). This is to be expected since the $\Delta\varepsilon_p$ is a large fraction of $\Delta\varepsilon_t$ in the majority of the continuous cycling tests conducted on these steels. The tendency to develop a significant mean stress effect becomes greater in tests at low $\Delta\varepsilon_t$, in which the strains are mainly elastic.

The high-chromium martensitic steels generally fail during continuous-cycling tests at temperatures of ≤600°C by transgranular fracture [18,38]; also, there are generally few reported instances of intergranular cavitation cracking when tension and/or compression hold periods are introduced in creep-fatigue tests [16,38]. Steels such as 9Cr-1Mo are resistant to grain boundary cavity formation during long-term creep-rupture testing at 475 to 550°C [52–54], the ductility remaining high and failure occurring by ductile tearing as a result of the nucleation and subsequent growth of voids at MnS inclusions [54]. However, there is increasing transmission (TEM) and scanning (SEM) electron microscope evidence of cavity or void formation at the prior austenite grain boundaries in a modified 9Cr-1Mo steel after creep-fatigue testing in vacuum at 593 and 700°C with 2 min tension holds [28] and at low strain rates and 600°C in high vacuum (1×10^{-7} Pa) [55]; the cavities are associated with large intergranular carbide particles in the steel tested at 700°C [28]. While grain boundary fracture has not been detected in this steel following creep-fatigue testing at 538°C, post-test microscopic examinations have shown intergranular cracking and evidence of a true creep-fatigue interaction in tests with tensile hold periods in air at 593°C [25]. In addition, SEM examinations have revealed intergranular microcracks nucleated on the transverse boundaries in a 12Cr-MoV steel in continuous cycling tests in air and

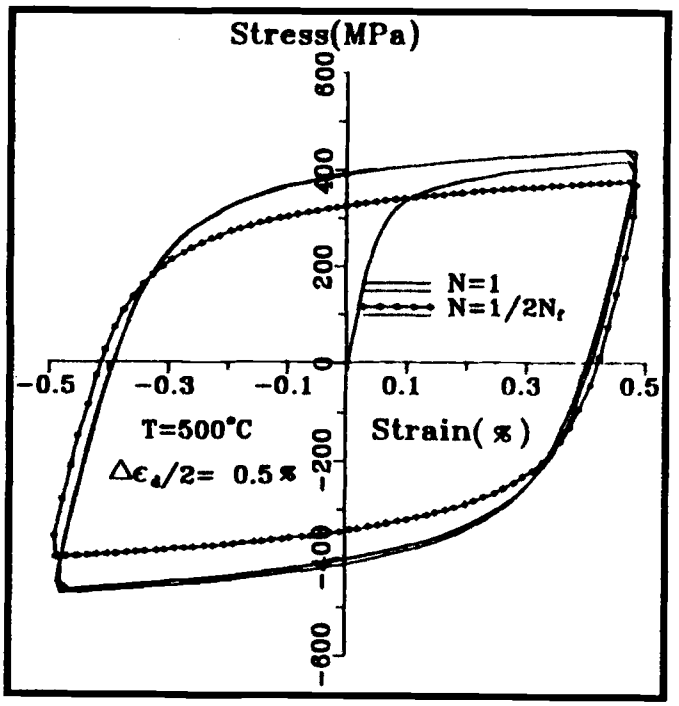

FIG. 16.12—Hysteresis loops at N = 1 and N = N_f/2 for HT9 steel [19].

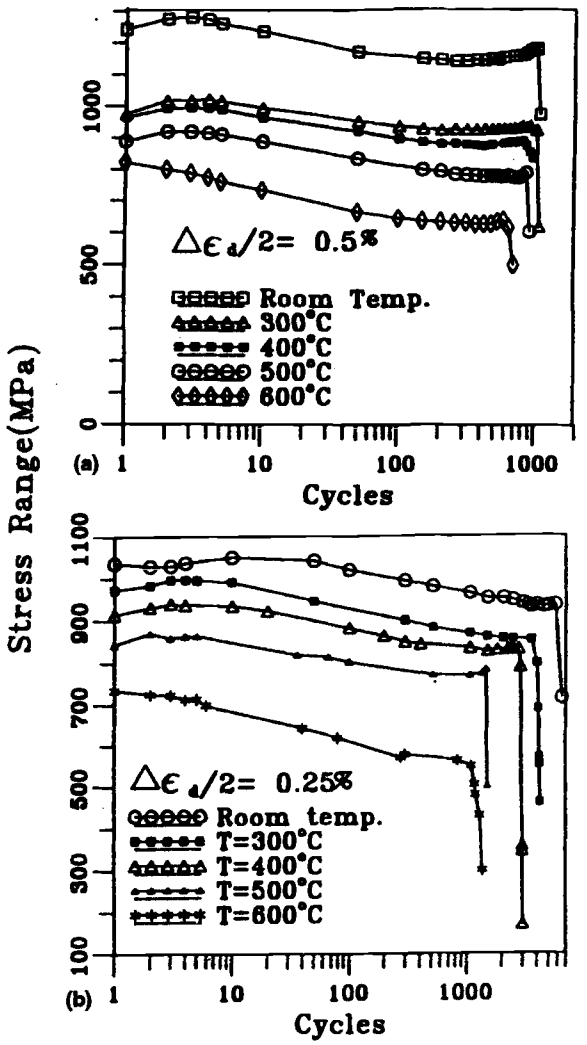

FIG. 16.13—Stress range versus the number of cycles for the HT9 steel tested at (a) $\Delta\varepsilon_d = \pm 0.5\%$ and (b) $\Delta\varepsilon_d = \pm 0.25\%$ [19].

vacuum at 600°C, the microcrack density in air being more than an order of magnitude greater than in vacuum [29].

The observed reductions in endurances in the creep-fatigue tests may also be attributed to enhanced fatigue crack initiation and, possibly, propagation as a result of oxidation during testing in air [16]. An oxide coating forms on the surface cracks and may lead to crack tip blunting during tension holds [7,56]. The cracks are closed and their surfaces are not oxidized during compression holds; they thus remain sharp and result in lower endurances.

Cyclic Strength

The hysteresis loops recorded at N = 1 and N = N_f/2 during LCF tests on the HT9 steel at 500°C and a total diametral strain range ($\Delta\varepsilon_d$) of 1.0% are illustrated in Fig. 16.12 [19]).

A characteristic feature of the behavior of the 8 to 12% Cr martensitic steels is the softening, manifested as a reduction in stress to produce a given strain, which occurs during continuous fatigue cycling at ambient [18,19,34,57–60] and elevated [7,10,11,18–21,28,31,36,45,58–64] temperatures. This is exemplified in Fig. 16.13 where the total stress range ($\Delta\sigma_t$)

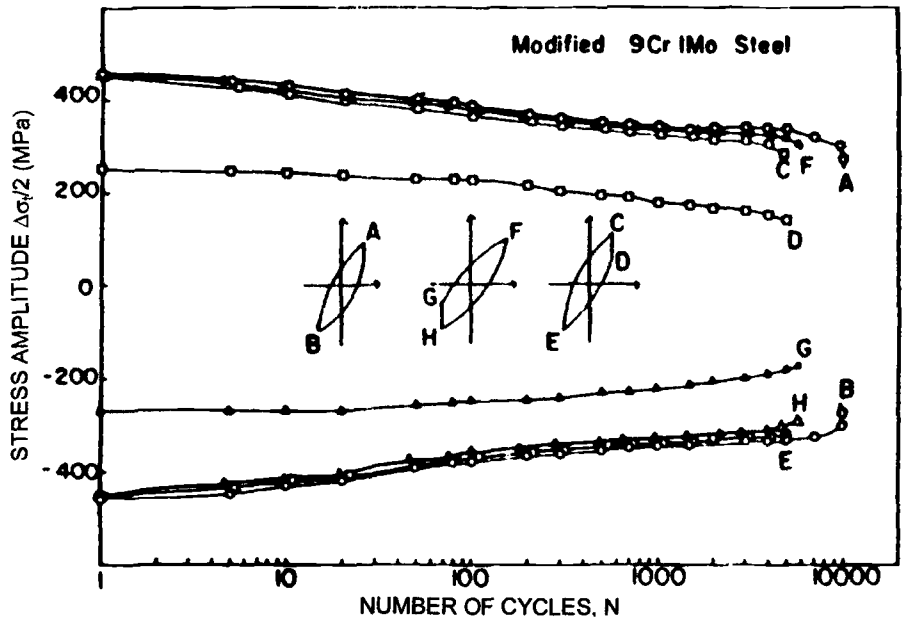

FIG. 16.14—Cyclic softening of modified 9Cr-1Mo steel in vacuum at 593°C and $\Delta\varepsilon_t$ = 1.4%, with and without hold times of 2 min at the peak tensile or compressive strains [7].

is plotted against the number of cycles (N) for the HT9 steel tested at diametral strain amplitudes ($\Delta\varepsilon_d/2$) of 0.5 and 0.25% and temperatures ranging from ambient to 600°C [19]. Cyclic hardening occurs during the first ten cycles or so, except at 600°C, and is followed by softening evident as progressive decreases in the stresses in both the tension and compressive phases of the cycles. The softening occurs in the LCF region where the plastic strain dominates, and it is not so apparent at the lower total strain ranges where the elastic response prevails and $\Delta\varepsilon_p$ is a small fraction of $\Delta\varepsilon_t$ [34].

The magnitudes of the cyclic softening during continuous cycling of the steels at temperatures in the range 450 to 700°C are not significantly affected by the introduction of 1 to 2 min hold periods at the peak tension or compression strains [7,21,28,61]. This is illustrated for the modified 9Cr-1Mo steel tested at 593°C in vacuum in Fig. 16.14 [7]. However, testing of this steel in air at the same temperature results in more softening than in vacuum; this is apparent in the first few cycles, but the rates of softening in air and vacuum are comparable thereafter and proportional to N^{-1} after the first 50 cycles or so [7]. The continuous fatigue and tension and compression hold time stress amplitude ($\Delta\sigma_t/2$) versus log N curves for the modified 9Cr-1Mo steel at 593 and 700°C are nearly linear and have very similar softening slopes [65], with no indication of the development of a mean stress. However, as shown for the modified 9Cr-1Mo steel in Fig. 16.15 [45], the specimens tested at a $\Delta\varepsilon_t$ of 0.51% at 538°C in continuous fatigue and with hold periods of 0.6 and 6 min in compression all exhibit cyclic softening with progressively reduced stress ranges at equivalent cycle numbers with the longer hold duration. The stress amplitude data demonstrate that the peak tensile stress is less dependent on hold periods than the peak compression values, and a small tensile mean stress therefore develops.

Analytical transmission electron microscope (ATEM) examinations of these high-chromium martensitic steels after

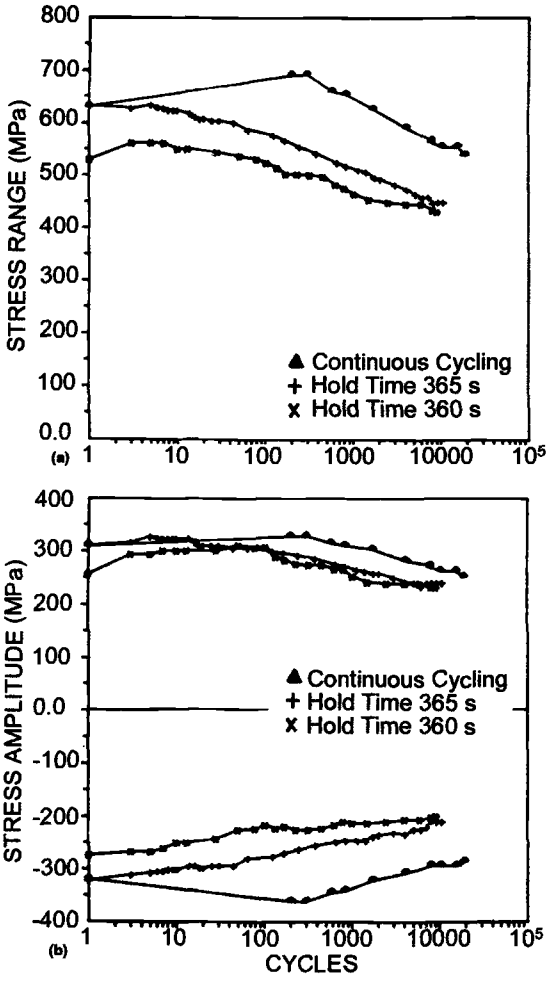

FIG. 16.15—Cyclic softening of modified 9Cr-1Mo steel in LCF tests at 538°C and $\Delta\varepsilon_t$=0.5% with and without compression hold times of 36 and 360 s [45].

TABLE 16.1—Subgrain Size Effects on Cyclic Behavior.

Steel	Test Temperature, °C	Relationship	Reference
Mod 9Cr-1Mo	593	$\sigma_s = 250\ D^{-0.51}$	7
	...	$D = 0.09\ (\Delta\varepsilon_p/2)^{-0.34}$	7
MANET	20–450	$\sigma_s \propto D^{-0.5}$	13
HT9	400–600	$\sigma_s = 460\ D^{-0.65}$	19

LCF testing [7,13,18,19,28,29,61,62,66–68] have established that the softening is due primarily to the cycling-induced rearrangement of the dislocations in the initial highly dislocated tempered martensite lath structure to form tangles and equiaxed cells or sub-grains whose boundaries often coincide with those of the laths and $M_{23}C_6$ precipitates. The sub-grain size is dependent on the martensitic steel composition and the test conditions of temperature, plastic strain amplitude ($\Delta\varepsilon_p/2$), and peak stress [$\sigma_s = (\sigma_{max} + \sigma_{min})/2$] [7]. The reported relationships between the sub-grain size D (μm) and σ_s (MPa) or $\Delta\varepsilon_p/2$ at $N_f/2$ are listed in Table 16.1.

Carbide coarsening and reduced solid solution hardening due to the progressive incorporation of molybdenum in the $(CrFe)_{23}C_6$ matrix precipitates with increasing hold times [45] may also contribute to the cyclic softening.

The cyclic behavior of a 14 to 18% Cr ferritic stainless steel (AISI 430F) when tested at 400 to 500°C in the normalized condition is characterized by a pronounced and extended cyclic hardening stage [69]. This behavior has been attributed to dynamic strain aging (DSA) due to dislocation-solute (carbon and/or nitrogen) atom interactions. There is additional evidence that DSA influences the cyclic behavior of a slowly (furnace) cooled 0.27% C, 12.3% Cr (AISI 420) steel with a ferrite-pearlite structure in fully reversed axial strain-controlled LCF tests conducted at temperatures between ambient and 550°C with $\Delta\varepsilon_t = 1\%$ and $\dot{\varepsilon}_t = 2 \times 10^{-3}\ s^{-1}$ [70]; in this case, the σ_{max} versus N curves exhibit a short initial hardening stage followed by a saturation period that is independent of test temperature between 250 and 450°C and generally extends up to failure. However, as described above, the N & T high chromium martensitic steels generally show a softening tendency after the first few cycles in LCF tests at ambient and elevated temperatures. Nevertheless, the data obtained on the N & T 12%Cr-MoVNb (MANET II) steel in temperature and strain rate change tests exhibit cyclic softening between 150 and 550°C, but the hysteresis loops show high values of σ_{max} at 225 to 425°C, which again can be attributed to DSA [70].

The total cyclic strain range (in %) is given by:

$$\Delta\varepsilon_t = \Delta\varepsilon_e + \Delta\varepsilon_p \qquad (16.14)$$

where $\Delta\varepsilon_e = 100\ (\Delta\sigma_t/E)$ and $\Delta\varepsilon_p$ and the stress range $\Delta\sigma_t$ at $N_f/2$ are related by the following cyclic-hardening relationship at low strain ranges [16]:

$$\Delta\sigma_t/2 = k'(\Delta\varepsilon_p/2)^{n'} \qquad (16.15)$$

and k′ and n′ are temperature-dependent material constants.

Substituting and eliminating $\Delta\varepsilon_e$ and $\Delta\varepsilon_p$ yields the Ramberg-Osgood equation:

$$\Delta\varepsilon_t = 100(\Delta\sigma_t/E) + 2^{1-1/n'}\ (\Delta\sigma_t/k')^{1/n'} \qquad (16.16)$$

Equation 16.16 can be used to describe the LCF data for the modified 9Cr-1Mo steel at ambient temperature (Fig. 16.5). However, analysis of the elevated temperature data for the steel in terms of the fatigue endurance has shown that a temperature dependence exists between about 375 and 600°C such that [16]:

$$\Delta\varepsilon_t = 100(\Delta\sigma_t/E) + 10^F \qquad (16.17)$$

where $\Delta\varepsilon_p = 10^F$ and:

$$F = 1/n'\ [\log \Delta\sigma_t/k' - D'\ (\theta - 371)^{1.5}/1000] \qquad (16.18)$$

where θ is the test temperature and D′ is a constant.

Equations 16.17 and 16.18 may therefore be used to represent the LCF data at 370 and 525°C (Fig.16.5).

The values of n′, k′ and D′ for the modified 9Cr-1Mo steel are given in Table 16.2, and the predicted and observed cyclic stress-strain responses at 20, 370, and 525°C are in reasonable agreement, as illustrated in Fig. 16.16 [16].

The monotonic [$\sigma/2 = k\ (\varepsilon_p/2)^n$ where σ is the stress, ε_p is the plastic strain, and k and n are again temperature-dependent material parameters] and cyclic-hardening behavior of the 12Cr-MoV (X20) steel over a wide temperature range (LCF strain-life curves at 350 and 600°C are shown in Fig. 16.1) have also been modeled [3]; the monotonic (k and n) and cyclic (k′ and n′) constants at ambient and elevated temperatures are listed in Table 16.3 [23,57] and the stress-strain curves are reproduced in Fig. 16.17 [35]. The magnitudes of the cyclic softening at ambient temperature and 350°C are such that the cyclic hardening only approaches the monotonic hardening at $\Delta\varepsilon_t/2 \geq 1\%$. The cyclic softening is excessive at 600°C, and the cyclic stress-strain curve falls well below the monotonic curve at all strain amplitudes.

Irradiation Effects

There are only limited data on the effects of neutron irradiation on the fatigue behavior and endurances of the high-chromium martensitic steels.

Strain-controlled fatigue tests in air at ambient temperature and a strain rate of $4 \times 10^{-3}\ s^{-1}$ have been conducted on HT9, with and without additions of 1 and 2% nickel, and modified 9Cr-1Mo steels before and after irradiation at 55°C in HFIR [37]. Although only a few specimens were tested, irradiation to about 25 dpa and helium concentrations of 210 and 410 appm, respectively, produces cyclic strengthening and reductions in the endurances of the two nickel-doped HT9 steels at a $\Delta\varepsilon_t$ of 1%, these effects being attributed primarily to the helium production by the $^{58}Ni(n,\gamma)\ ^{59}Ni(n,\alpha)\ ^{56}Fe$ reaction. However, cyclic hardening coupled with in-

TABLE 16.2—Cyclic Stress-Strain Constants for the Modified 9Cr-1Mo Steel [16].

Temperature, °C	k′	n′	D′
20	571.10	0.09853	...
375–600	438.7355	0.09022	−0.05197336

TABLE 16.3—Monotonic (k and n) and Cyclic (k^t and n^t) Constants for a 12% Cr-MoV Steel [23,57].

Temperature, °C	k	n	k′	n′
20	628	0.07	568	0.1
350	853	0.104	951	0.138
600	642	0.196	554	0.127

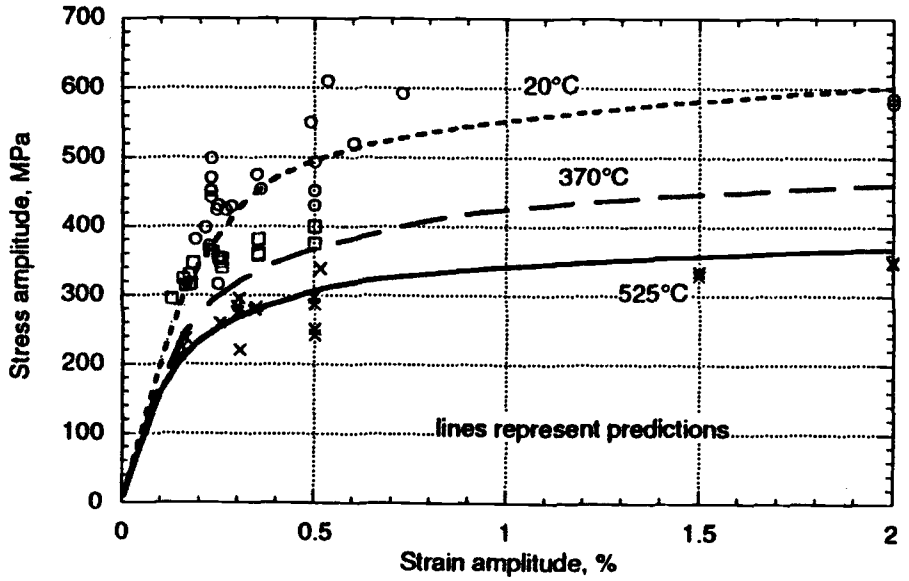

FIG. 16.16—Comparison of predicted and experimental cyclic stress-strain responses for modified 9Cr-1Mo steel [16].

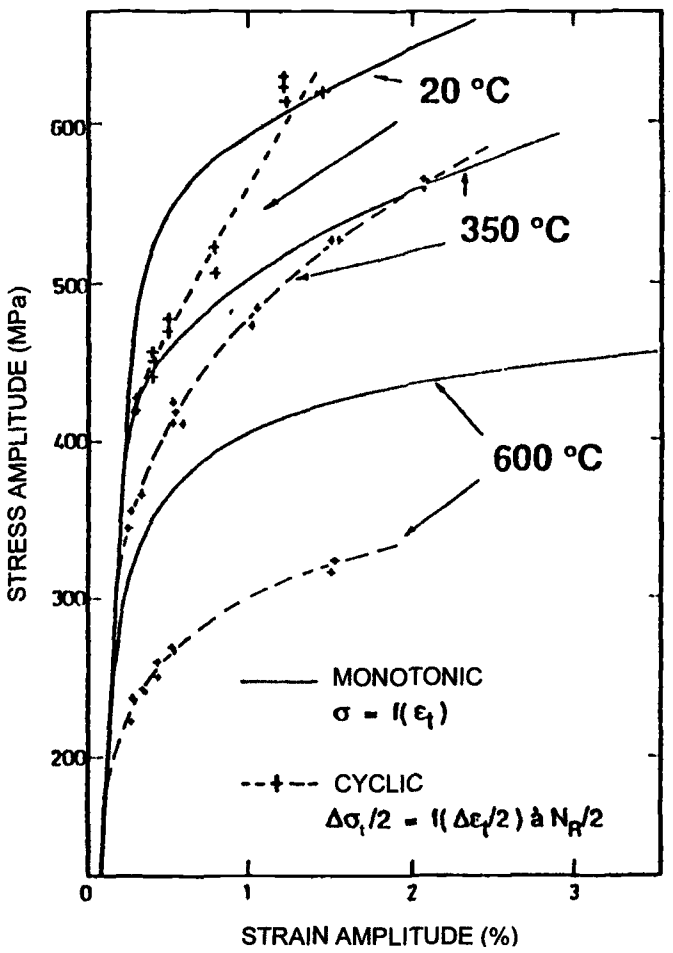

FIG. 16.17—Monotonic and cyclic stress-strain curves for 12Cr-MoV steel at 20, 350, and 600°C [35].

creases in N_f are produced in the HT9 steel (0.5% Ni) under the same test conditions following irradiation to 10 dpa and 34 appm He. The cyclic hardening in tests at $\Delta\varepsilon_t$ of 0.3 and 0.5% is less pronounced in the modified 9Cr-1Mo steel after irradiation to maximum displacement doses and helium concentrations of 3.3 dpa and 4 appm, respectively, but the endurances are again increased, particularly at low $\Delta\varepsilon_t$.

Specimens of the N & T MANET I steel have been irradiated in the BR2 reactor at 250 and 400°C to 10 dpa (max) and 9.2 to 9.7 appm He and subsequently tested in completely reversed strain or load controlled fatigue in air at the same temperature as the irradiation and at strain rates in the range 3.0×10^{-3} to 1.57×10^{-2} s^{-1} [71]. The endurances of the unirradiated and irradiated steels at a given strain amplitude are marginally lower at 400 than 250°C, but there is no detectable effect of irradiation on N_f at $\Delta\varepsilon_t$ of 1.0 and 0.6% at either temperature (Figs. 16.18 and 16.19 [71]. The elastic strains for the unirradiated steel at 250 and 400°C are large fractions of the total strain at a $\Delta\varepsilon_t$ of $\approx$1% and are greater than the plastic strains at a $\Delta\varepsilon_t$ of $\approx$0.6%, as shown in Table 16.4. The plastic strain is reduced significantly after irradiation, particularly in the tests at the lower $\Delta\varepsilon_t$ of $\approx$0.6% ($N \geq 10^4$ cycles) when the imposed strain is almost entirely elastic. The data are insufficient to gage the influence of irradiation on the fatigue limits in the tests at 250 and 400°C.

Irradiation at 250 and 400°C produces considerable hardening, which appears to be more pronounced at the higher strain ranges (Fig. 16.20) [71]. However, the irradiated and, to a lesser extent, the unirradiated steels show cyclic softening at high strains at 250 and 400°C (Fig. 16.21) [71]. Cyclic hardening during the first ten cycles or so is followed by softening at the lower strain range of 0.6%, particularly in the unirradiated steel tested at 400°C; significant reductions in stress are also evident at high N for the irradiated steel tested at the higher strain range of 1% at 250 and 400°C.

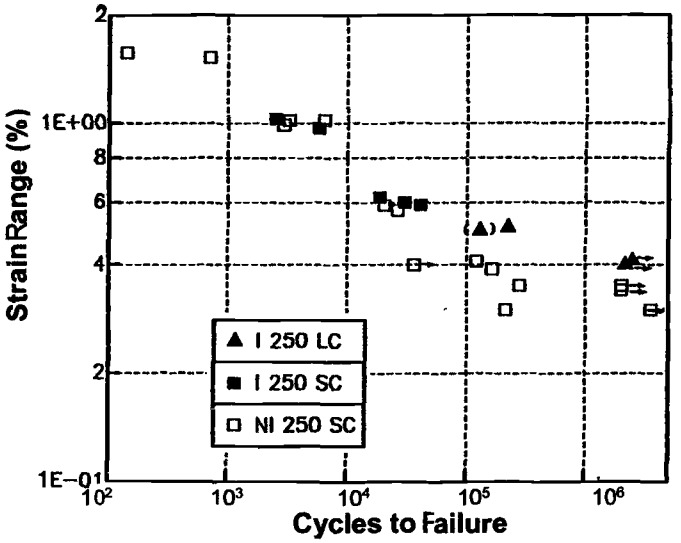

FIG. 16.18—Strain range versus number of cycles to failure for unirradiated (NI) and irradiated (I) MANET I steel in load- (LC) and strain- (SC) controlled tests at 250°C [71].

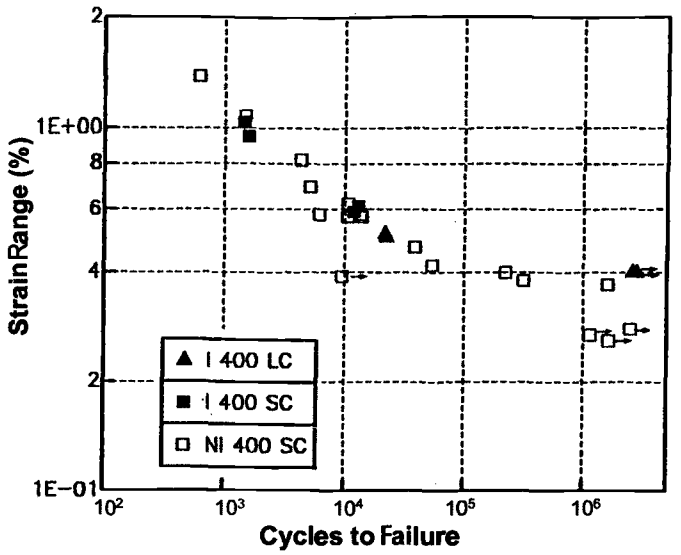

FIG. 16.19—Strain range versus number of cycles to failure for unirradiated (NI) and irradiated (I) MANET I steel in load- (LC) and strain- (SC) controlled tests at 400°C [71].

TABLE 16.4—Elastic and plastic strain ranges for N = 1,000 cycles at 250 and 400°C for the MANET I steel [71].

	Temperature, °C	$\Delta\varepsilon_t$ %	$\Delta\varepsilon_p$ %	$\Delta\varepsilon_e$ %
Unirradiated	250	1.02	0.59	0.43
Irradiated	...	0.97	0.25	0.72
Unirradiated	400	1.08	0.63	0.45
Irradiated	...	1.04	0.38	0.66
Unirradiated	250	0.59	0.18	0.41
Irradiated	...	0.62	0	0.62
Unirradiated	400	0.62	0.21	0.41
Irradiated	...	0.61	0.02	0.59

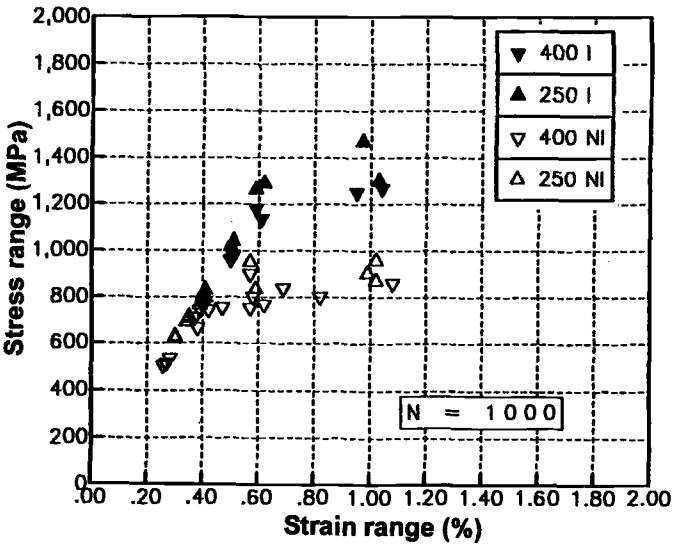

FIG. 16.20—Stress range versus strain range at N = 1000 cycles for unirradiated (NI) and irradiated (I) MANET I steel tested at 250 and 400°C [71].

The fatigue and creep-fatigue behavior of the MANET I and II steels have also been investigated during and after irradiation with light ions in the Dual Beam and PIREX facilities at FzK in Germany [72] and PSI in Switzerland [73], respectively. Specimens were bombarded with degraded 104 MeV α-particles and 30 MeV protons to produce displaced atoms and helium and hydrogen at various generation rates in the Dual Beam facility, while 590 MeV protons were used to produce displacement damage and helium and hydrogen isotopes by spallation reactions in the PIREX facility. These studies were carried out in support of the reactor irradiation experiments, the principal objectives being to establish: (i) the individual and combined effects of displacement damage and implanted helium and hydrogen on the fatigue, and (ii) the effects of stress relaxation by irradiation creep or irradiation-modified thermal creep during hold periods on the cyclic endurance.

The initial Dual Beam irradiations for post-irradiation fatigue tests on the MANET I steel were performed at temperatures in the range 300 to 600°C to displacement damage levels and helium concentrations of ≤1.2 dpa and ≤200 appm, respectively, and with helium to dpa ratios of 10 to 170; the strain-controlled push-pull tests were carried out in air at the same temperature as the irradiation, $\dot{\varepsilon}_t = 5 \times 10^{-4}\ s^{-1}$, $\Delta\varepsilon_t$ = 1.2%, R = −1 and with and without hold times of 120 s in the tension or compression phase [61,67,72]. The stress amplitudes are increased by irradiation/testing at 300°C, are unaffected at 450°C and are reduced slightly at 520 and 600°C (Fig. 16.22) [67,74]. Both the unirradiated and irradiated samples show continuous cyclic softening from the outset or after the first few cycles due to the recovery of the lath dislocations and the formation of distinct cell structures, with the slopes of the stress amplitudes being similar for the unirradiated and irradiated specimens. At 450°C, the introduction of hold times at the peak tensile or compressive strains results in stress relaxation of 70 to 80 MPa and reductions in the endurances of the unirradiated steel by 35 to 40 and 18 to

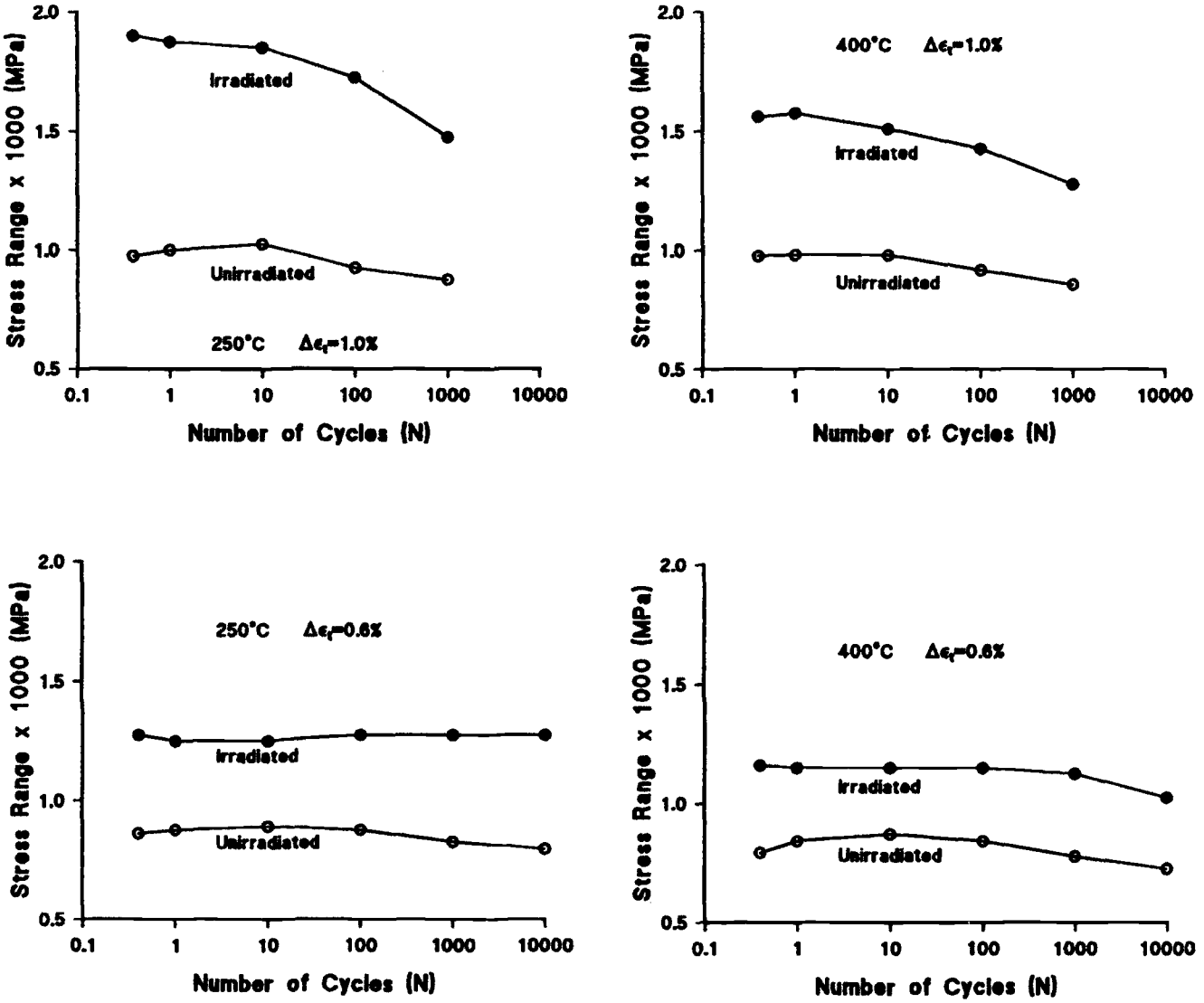

FIG. 16.21—Development of the stress range during fatigue tests on the unirradiated and irradiated MANET I steel at 250 and 400°C [71].

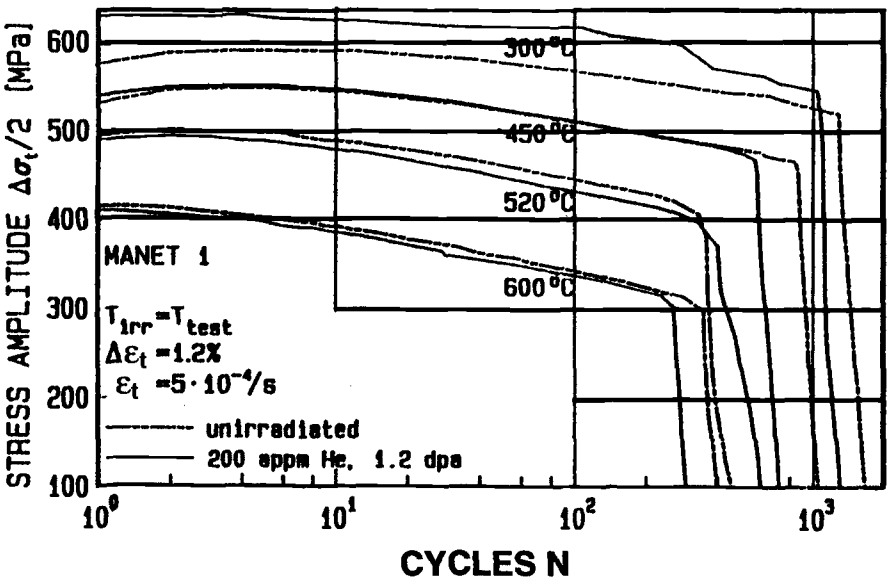

FIG. 16.22—Evolution of stress amplitude during strain controlled fatigue testing of MANET I steel before and after irradiation (200 appm He, 1.2 dpa) in the Dual Beam facility [74].

20%, respectively. The influences of the implanted helium and displacement damage on the fatigue endurances at all temperatures in the range 300 to 600°C are small (≤30%), even when hold times are introduced. The irradiation-induced defects, mainly helium bubbles, are stable during the fatigue lifetimes, and the small reductions in the endurances seem to be more dependent on the helium content than on the He:dpa ratio [67].

In contrast, the endurances of the MANET I steel in vacuum at $\dot{\varepsilon}_t = 3 \times 10^{-3}\ s^{-1}$ and R = −1 are reduced at all test temperatures in the range 90 to 430°C following irradiation in the PIREX facility to 0.01 to 0.7 dpa with a helium to dpa ratio of approximately 130 [58,75]. The decreases in endurance range from a factor of 1.7 to 7.5, depending on the irradiation/test conditions, the reductions being particularly marked in the temperature range 280 to 380°C when DSA occurs [13,76]. Fatigue softening is again observed under all test conditions, the irradiated steel exhibiting a faster softening rate approaching that of the unirradiated steel at the end of life. The TEM microstructures of the unirradiated and irradiated steel are similar after the fatigue testing.

Continuous cycling strain-controlled push-pull fatigue tests on the MANET I steel have also been performed in vacuum ($<1 \times 10^{-5}$ Pa) before and during irradiation at 420 and 450°C and $\Delta\varepsilon_t$ of 0.5 to 1.2% in the Dual Beam facility [62,77]. The data for the unirradiated steel yield the following empirical relationship:

$$\Delta\varepsilon_t = 0.658\ N_f^{-0.04} + 0.036\ N_f^{-0.15} \qquad (16.19)$$

The endurances during irradiation are comparable to those of the unirradiated specimens at high strains but are somewhat lower at low $\Delta\varepsilon_t$; furthermore, the number of cycles to failure of the specimen tested after irradiation to equivalent helium and damage levels is even smaller at $\Delta\varepsilon_t$ = 0.5%. This behavior is exemplified by the Dual Beam facility data in Fig. 16.23 [62]. The continuous cyclic softening of the unirradiated and "in-beam" tested specimens is illustrated in Fig. 16.24 in which $\Delta\sigma_t$ and $\Delta\varepsilon_p$ are plotted as a function of N [62]. The behavior of the unirradiated and "in-beam" specimens is similar at high strains ($\Delta\varepsilon_p \geq 0.6\%$); however, at a low $\Delta\varepsilon_p$ of ≈0.5%, the "in-beam" test is of sufficient duration for significant radiation damage and hardening to be produced, resulting in a reduced rate of cyclic softening, a decrease in $\Delta\varepsilon_p$ towards the end of the test, and a reduction in N_f. The endurances of the post-irradiation tested specimens are even lower due to the irradiation-induced microstructural changes and radiation hardening being well developed before commencing the fatigue testing (Figs. 16.25 [59] and 16.26 [62]). Thus, $\Delta\sigma_t$ is initially higher and, despite decreasing during testing, remains above the values for the unirradiated and "in-beam" tested samples.

Similar patterns of behavior are exhibited by the MANET I and MANET II steels in the unirradiated condition and during and following irradiation/testing at 250°C in the Dual Beam facility [63] and at 35 to 40, 250, and 300°C in PIREX [59,64]. The endurances of the PIREX in-beam specimens decrease on reducing the test temperature from 300°C (4660 cycles) to 250°C (≈1500 cycles) and to 35 to 40°C (≈1100 cycles), with the maximum radiation hardening occurring at the lowest irradiation/test temperature

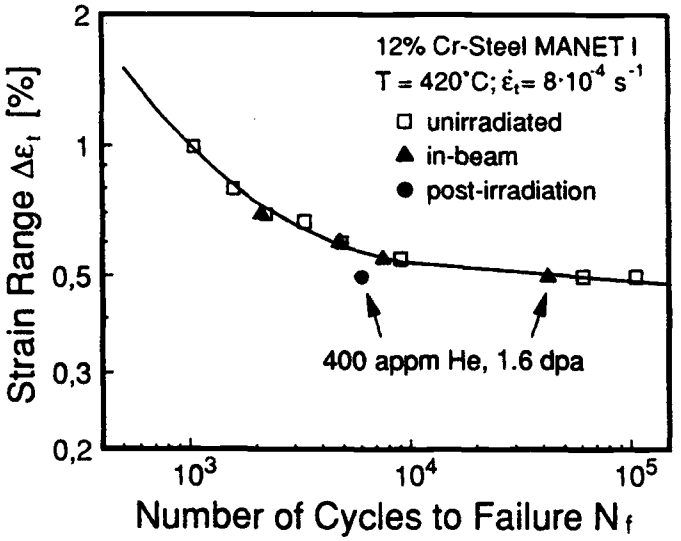

FIG. 16.23—Comparison of the strain-controlled fatigue endurances for the unirradiated, "in-beam" and post-irradiation tested MANET I steel at 420°C in the Dual Beam facility [62].

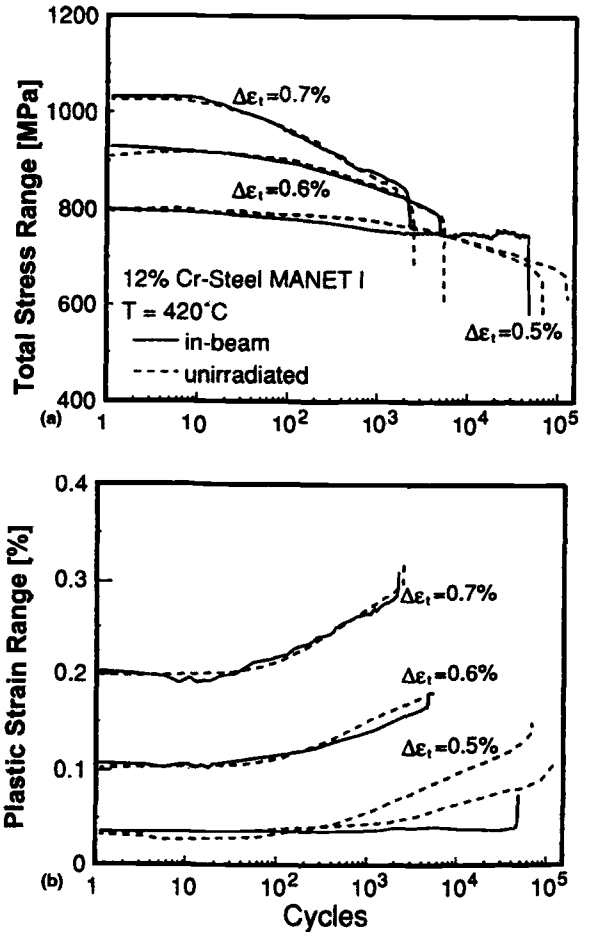

FIG. 16.24—Development of (a) total stress range and (b) total plastic strain range for unirradiated and "in-beam" fatigue-tested MANET I steel at 420°C in the Dual Beam facility [62].

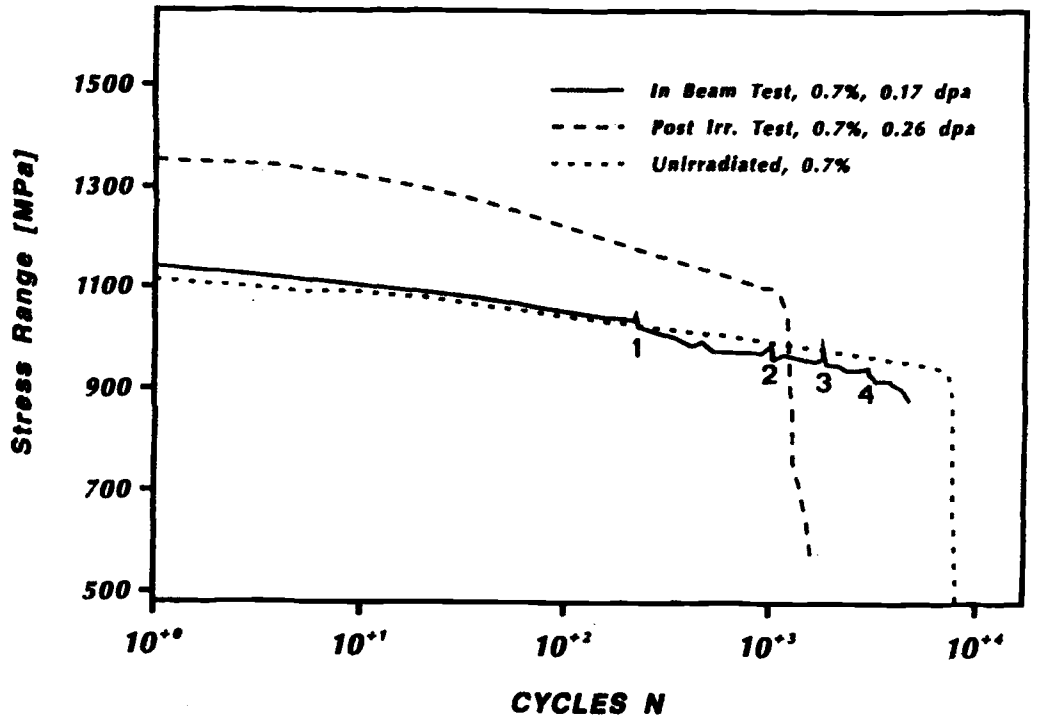

FIG. 16.25—Stress range as a function of the number of fatigue cycles for the "in-beam" (0.17 dpa), post-irradiation (0.26 dpa), and unirradiated MANET II steel in the PIREX facility; irradiation and test temperatures are 300°C [59].

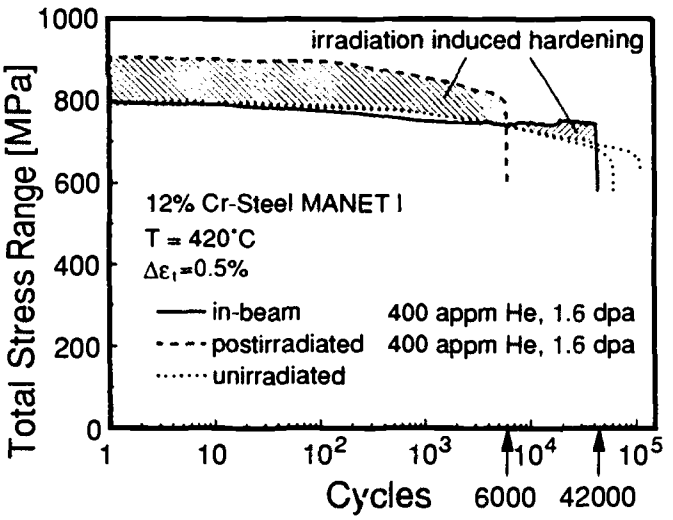

FIG. 16.26—Development of the stress range during strain-controlled "in-beam," post-irradiation and unirradiated fatigue tests on the MANET I steel in the Dual Beam facility; irradiation and test temperatures are 420°C [62].

(Fig. 16.27) [64]. The stress ranges for the unirradiated and in-beam tested specimens are similar in the initial stages of the fatigue and only decrease slightly during the tests; however, after about 10^3 cycles the radiation hardening dominates the softening during the in-beam testing and the stress increases [63]. TEM observations indicate that the helium bubbles are mainly responsible for the strength increase [63], but the stress for the post-irradiation-tested samples is higher from the outset due to the radiation hardening. Stress relaxation tests performed during the post-irradiation fatigue tests at 35 to 40°C show a logarithmic recovery with time, implying that the deformation is controlled by a thermally activated dislocation glide process for which an activation volume can be defined. In addition, the limited available data suggest that the glide mechanism is not modified during the "in-beam" tests [64].

The fracture mode remains ductile and transcrystalline for all the irradiation/test conditions cited above. It can therefore be concluded that the endurances are determined primarily by the time evolution of the irradiation-induced hardening and that the post-irradiation test data provide a conservative approach to *in situ* conditions.

STRESS-CONTROLLED HIGH-CYCLE FATIGUE

High cycle fatigue tests on plain specimens of the 9Cr-1Mo steel have been made in the push-pull stressing mode at a frequency of about 100 Hz and temperatures ranging from 380 to 525°C [20]. The tests were performed under both narrow band random and sinusoidal loading and with a mean stress superimposed. The data obtained in the latter tests showed that increasing the test temperature reduces the fatigue strength, probably as a consequence of the reduction in yield strength.

A comprehensive series of stress controlled fatigue tests have been conducted on the MANET I steel in air and vac-

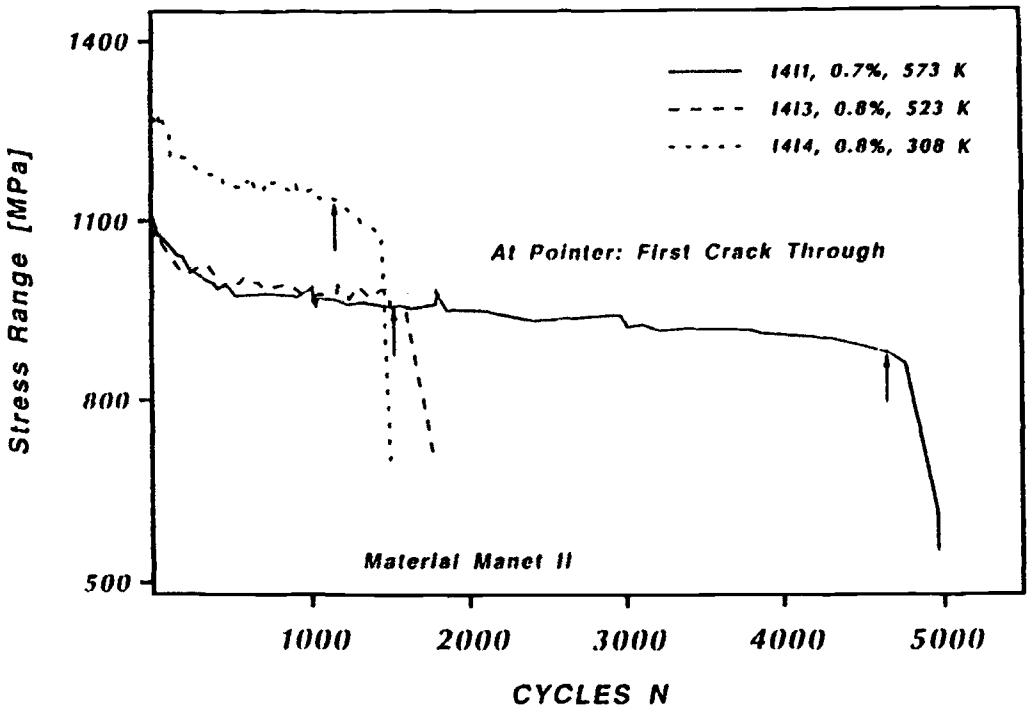

FIG. 16.27—Effect of test temperature on the stress range and fatigue endurances of the "in-beam" tested MANET II steel at 35, 250, and 300°C in the PIREX facility [64].

uum at stress amplitudes ($\Delta\sigma/2$) in the ranges 400 to 800 MPa at ambient temperature and 280 to 450 MPa at 550°C [78]. The results demonstrate that:

(i) The endurances in vacuum are superior to those in air at room temperature, the differences being more pronounced at the higher stress amplitudes.

(ii) The fatigue lives in vacuum at 550°C are about a factor of 40 lower than those at ambient temperature at a given stress amplitude, or the stress amplitude is one and a half times greater at ambient temperature than at 550°C for a given endurance.

(iii) The endurances in vacuum and air at $\Delta\sigma/2$ = 470 MPa at room temperature are independent of the mean stress within the range −100 to +100 MPa and in vacuum at $\Delta\sigma/2$ = 350 MPa at 550°C within the range −100 MPa to zero (Fig. 16.28) [78]; the endurances increase with increasing compressive mean stress in excess of 100 MPa at room temperature and 550°C and decrease with increasing tensile mean stress above 100 MPa and zero at ambient temperature and 550°C, respectively.

(iv) The fatigue lives in vacuum at 550°C decrease markedly with decreasing cyclic frequency in the range 5×10^{-1} to 1×10^{-3} Hz (Fig. 16.29) [78]; there is a reduction by a factor of five in the range 5×10^{-1} to 1×10^{-2} Hz at $\Delta\sigma/2$ of 350 and 450 MPa and by more than two orders of magnitude at lower frequencies.

Surface modifications produced by plasma discharges (about 1500 shots each of approximately 3 s duration at temperatures of 150 to 300°C) in the TEXTOR tokamak have no significant effect on the post-exposure stress-controlled fatigue endurances of the MANET II steel in tests at 250 and

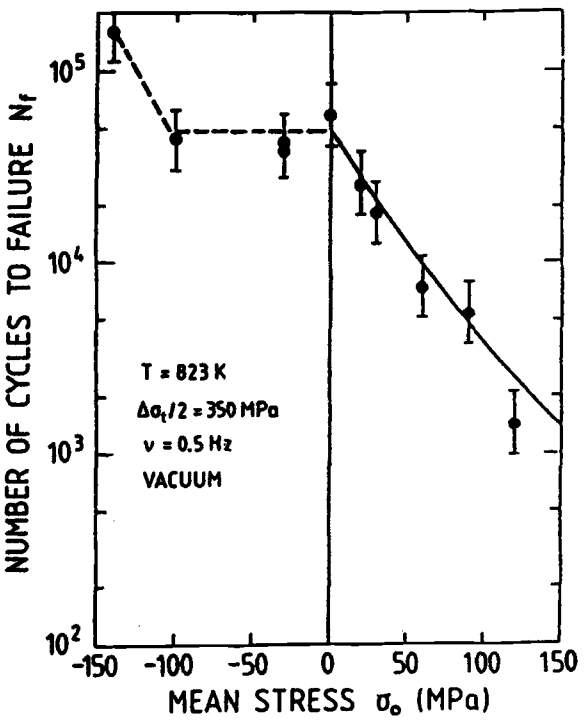

FIG. 16.28—Number of cycles to failure as a function of the mean stress in stress-controlled fatigue tests on the MANET I steel in vacuum at 550°C [78].

450°C [79]. This behavior differs from that of Type 316L austenitic steel, which shows a factor of eight reduction in the number of cycles to failure under the same test conditions [78].

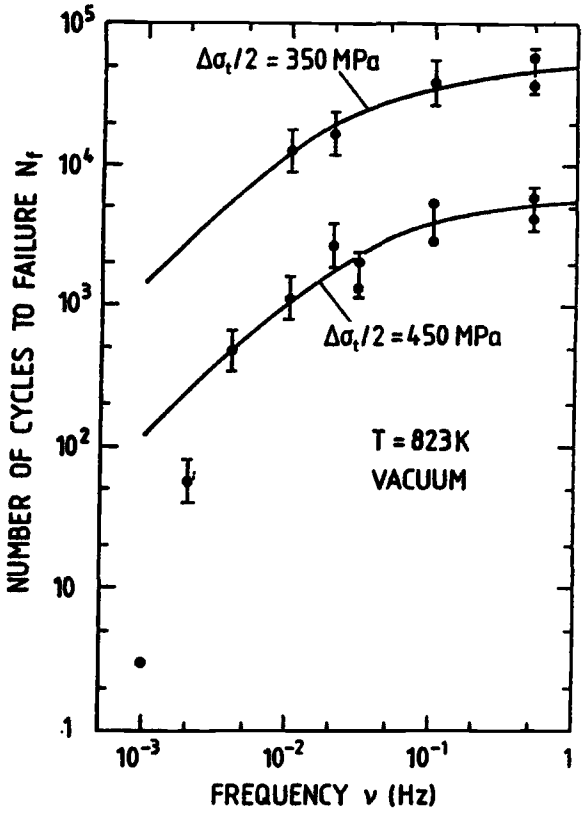

FIG. 16.29—Number of cycles to failure as a function of the frequency at stress amplitudes of 350 and 450 MPa and zero mean stress for the MANET I steel tested in vacuum at 550°C [78].

THERMAL AND THERMOMECHANICAL FATIGUE

Experimental facilities for investigating the thermal fatigue behavior of steels in the unirradiated [80–82] and irradiated [83] conditions have been described. The former consists essentially of a rigidly clamped and ohmically heated hollow specimen in which the axial thermal elongation is converted into elastic and inelastic deformation, and alternating thermal stresses are generated by cycling between low (T_L) and high (T_H) temperatures. The test specimens are initially clamped at the mean temperature of the cycle so that tensile and compressive stresses are developed at T_L and T_H, respectively. Both cyclic thermal (ε_{th}) and mechanical (ε_m) strains are produced, the latter being given by:

$$\varepsilon_m = \varepsilon_{eff} - \varepsilon_{th} \tag{16.20}$$

where ε_{eff} is the strain recorded by the extensometer fitted to the specimen. The total mechanical strain ($\Delta\varepsilon_{t,m}$) and stress ($\Delta\sigma_t$) ranges cannot be controlled in this facility and change with cycling.

The test conditions employed in the majority of the triangular wave form thermal fatigue tests performed on the high-chromium martensitic steels were: T_L = 200°C (constant), T_H = 550 to 700°C, heating and cooling rates = 5.8°C s^{-1} and $\Delta\varepsilon_{t,m}$ = 0.2 to 0.8% [10,11,39,40,47,48, 81,84–87].

The thermal fatigue endurances (N_f) are plotted in Fig. 16.30 as a function of $\Delta\varepsilon_{t,m}$ at $N_f/2$ for the MANET I and MANET II steel specimens tested at T_H = 550, 600, 650, and 700°C [88]. $\Delta\varepsilon_{t,m}$ increases with increasing ΔT (= $T_H - T_L$) and leads to smaller N_f values; this effect is primarily a consequence of the influence of the ΔT on the plastic mechanical

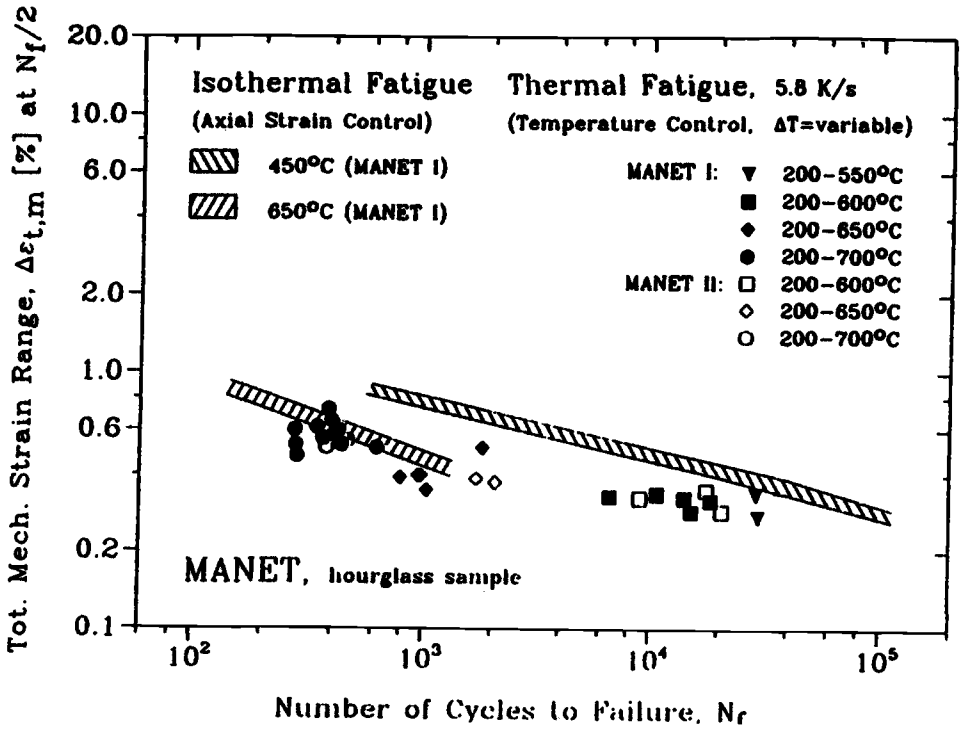

FIG. 16.30—Total mechanical strain range versus number of cycles to failure of the thermal fatigue-tested MANET I and II steels and comparison with isothermal fatigue data [88].

strain ($\Delta\varepsilon_{p,m}$) as illustrated in Fig. 16.31 [87]. The $\Delta\varepsilon_{p,m}$ at $N_f/2$ values range from about 0.02 to 0.5% and increase with increasing ΔT due to the enhanced compressive creep strain at the high temperature end of each cycle. The $\Delta\sigma_t$ at $N_f/2$ values for the MANET I and II steels increase with increasing ΔT and $\Delta\varepsilon_{t,m}$ at $N_f/2$ up to maxima of 670 and 610 MPa, respectively (Fig. 16.32) [87]. The data in Fig. 16.30 also show that the N_f values at the mean thermal fatigue test temperatures (375 to 450°C) are more than an order of magnitude lower than those of the specimens tested in isothermal fatigue at approximately the same temperatures [88]. However, for a given strain range, the numbers of thermal fatigue cycles to failure with T_H = 650 and 700°C are only a factor of about two lower than the LCF endurances at 650°C.

Thermal fatigue tests conducted under similar conditions to those reported above have shown that the endurances of the

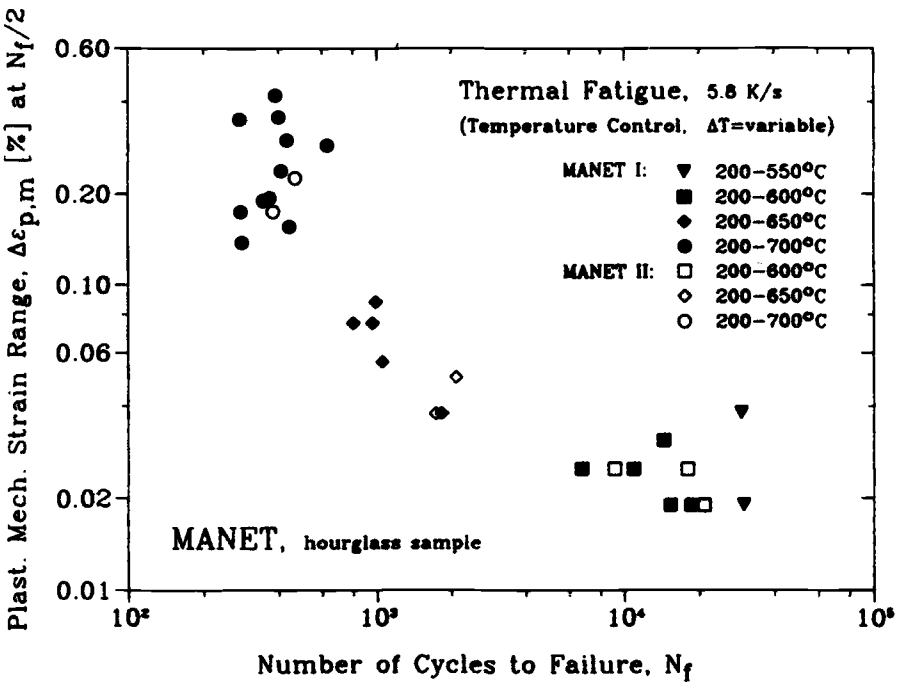

FIG. 16.31—Effects of plastic mechanical strain range at $N_f/2$ on the thermal fatigue endurances of the MANET I and II steels [87].

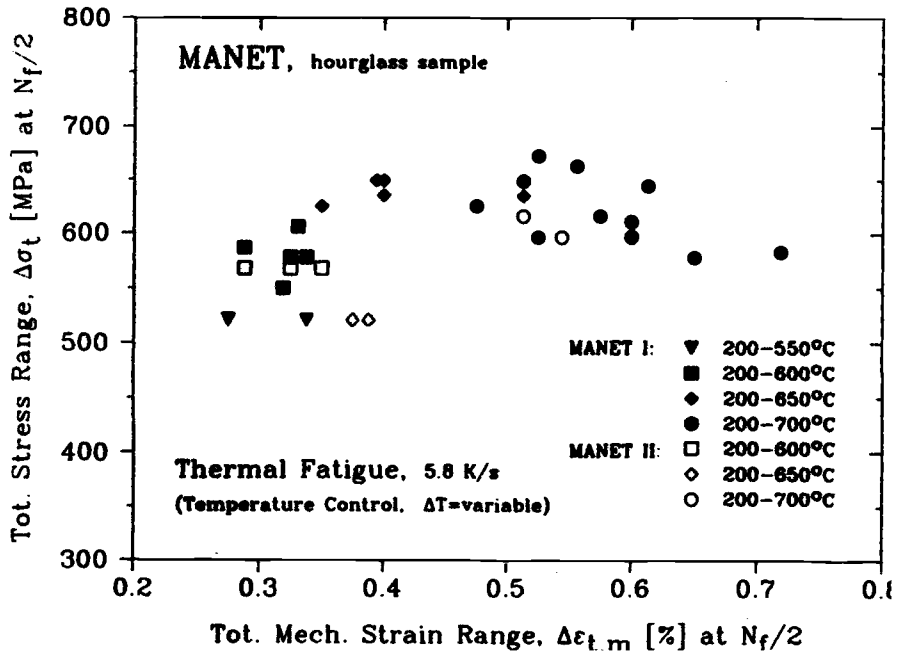

FIG. 16.32—Total stress range versus total mechanical strain range at $N_f/2$ for the thermal fatigue-tested MANET I and II steels [87].

modified F82H steel at a given $\Delta\varepsilon_{t,m}$ at $N_f/2$ are up to an order of magnitude lower than those of the MANET II steel [40,89]. The differences result from the lower $\Delta\sigma_t$ and higher $\Delta\varepsilon_{p,m}$ values for the modified F82H compared to the MANET steel.

The introduction of constant hold periods of 100 s at T_H (HTH), T_L (HTL), or both T_H and T_L (HTHL) during thermal fatigue tests on the MANET I and MANET II steels reduces the endurances [47,81,82,85–87,89], the magnitudes of the reductions increasing in the order HTL, HTH, and HTHL, as exemplified for the MANET II steel in Fig. 16.33 [87].

The thermal fatigue-tested MANET steel exhibits continuous cyclic softening after an initial stable period, the duration of which depends on ΔT and the nature of the hold period imposed [47,48,81,84,86,87]. Accelerated softening, due to enhanced recovery of the martensite lath dislocation structure and leading to lower endurances, is produced by increasing the magnitudes of the thermal cycles (Fig. 16.34) [84] and by the introduction of the hold periods (Fig. 16.35) [81,86].

Thermomechanical fatigue tests (in- and out-of-phase, with and without hold times of 100 and 1000 s) in which specimens are temperature cycled between 200 and 550°C have been performed on the MANET I steel [48,90]. Mechanical strains of ±0.133 to ±0.667% and ±0.533 to ±0.933% without hold times were superimposed on the temperature cycles in the out-of-phase (maximum compressive strain and maximum temperature reached simultaneously) and in-phase (maximum tensile strain and maximum temperature coupled) tests, respectively. In addition, isothermal LCF tests ($R = -1$) with $\Delta\varepsilon_t$ equal to 0.8 and 1.334% were carried out at 200 and 550°C for comparative purposes.

The isothermal and thermomechanical tested specimens show cyclic softening from the beginning of the tests; the magnitudes of the softening in the thermomechanical tests depend on the phase situation, being more rapid under in-than out-of-phase loading conditions with increasing strain ranges. The cyclic softening can be represented by the following function [90,91]:

$$\Delta F = \beta' N^{\alpha'} \tag{16.21}$$

where ΔF is the load range, β' is the starting value of the function, and α' is the "softening coefficient."

The values of β' and α' are 12 793 and −0.0283, respectively, for the steel tested in isothermal fatigue at 200°C and $\Delta\varepsilon_t = 0.8\%$ [86]; the corresponding values are 12 040 and −0.04945 for the out-of-phase tests between 200 and 550°C [91].

The thermal strain (ε_{th}) is additive to the mechanical strain (ε_m) in the out-of-phase thermomechanical fatigue tests, while ε_{th} reduces ε_m in the in-phase tests. The net or effective strain range (ε_{eff}) is plotted as a function of N_f in Fig. 16.36 for the MANET I steel in the isothermal LCF and thermomechanical tests without hold times [90]; the N_f values for the in- and out-of-phase TMF tested specimens fall between those for the LCF samples. Analysis of these data in terms of $\Delta\varepsilon_p$ (%) at N_f yielded the following correlations [90]:

Thermomechanical fatigue (in- and out-of-phase):

$$N_f = 124.7\,\Delta\varepsilon_p^{-1.671} \tag{16.22}$$

Isothermal fatigue:

$$N_f = 2464.6e^{-0.0039T}\,\Delta\varepsilon_p^{-1.404} \tag{16.23}$$

where T is the test temperature in K.

Out-of phase thermomechanical fatigue (OTMF) tests at temperatures of 200 to 700°C, 100 to 600°C and 200 to 600°C have also been performed on the MANET II steel and the data compared with those obtained in LCF tests at 450°C [92]. The degradation in the OTMF endurances, based on $\Delta\varepsilon_{t,m}$, is about an order of magnitude faster compared to LCF. How-

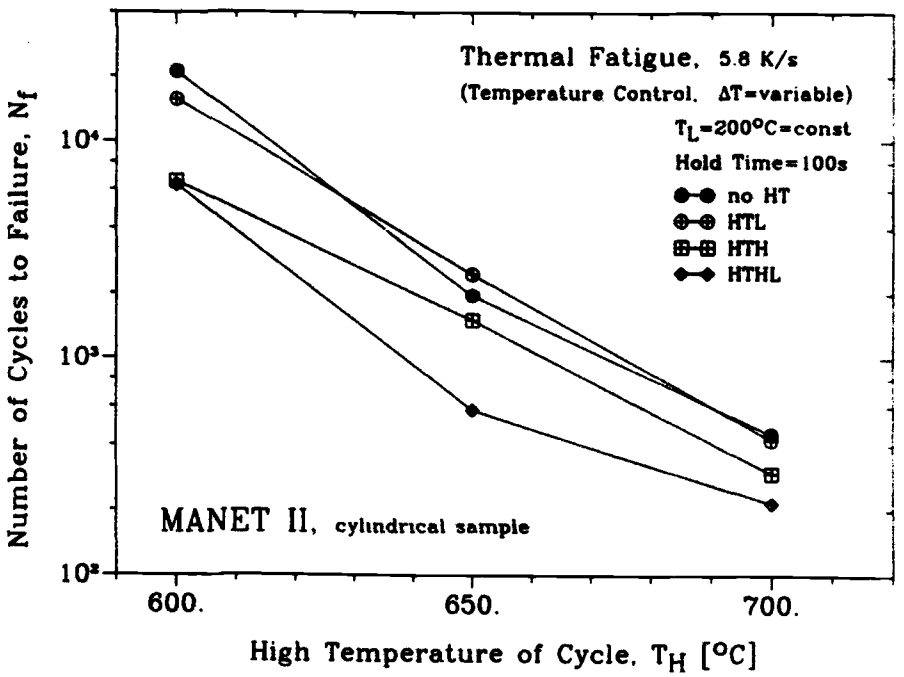

FIG. 16.33—Comparison of thermal fatigue data with and without hold periods of 100 seconds at T_H, T_L and at both T_H and T_L for the MANET II steel [85,87].

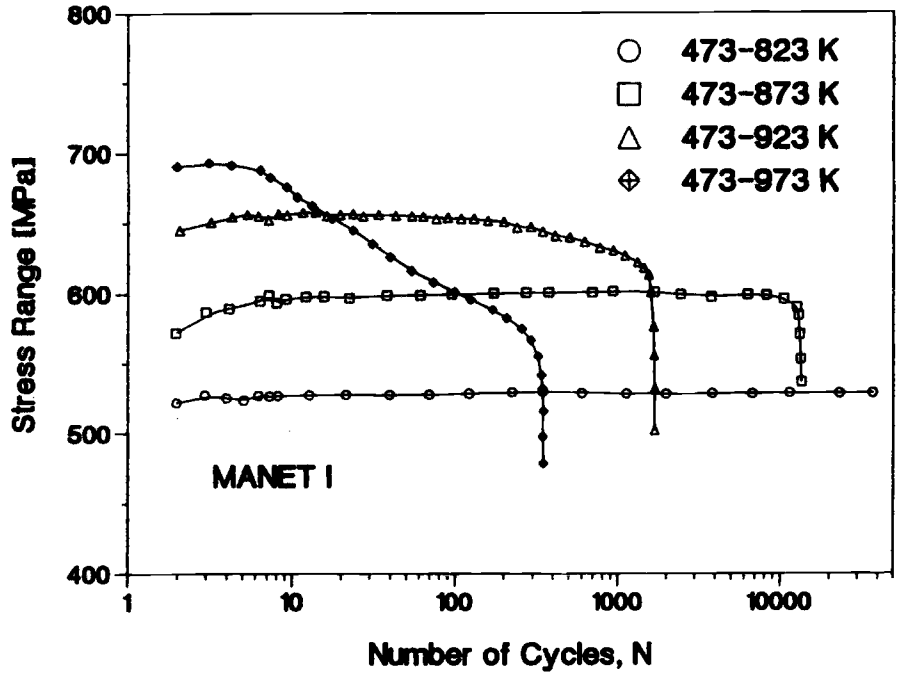

FIG. 16.34—Stress range versus number of cycles for the thermal fatigue-tested MANET I steel at the specified temperature ranges [84].

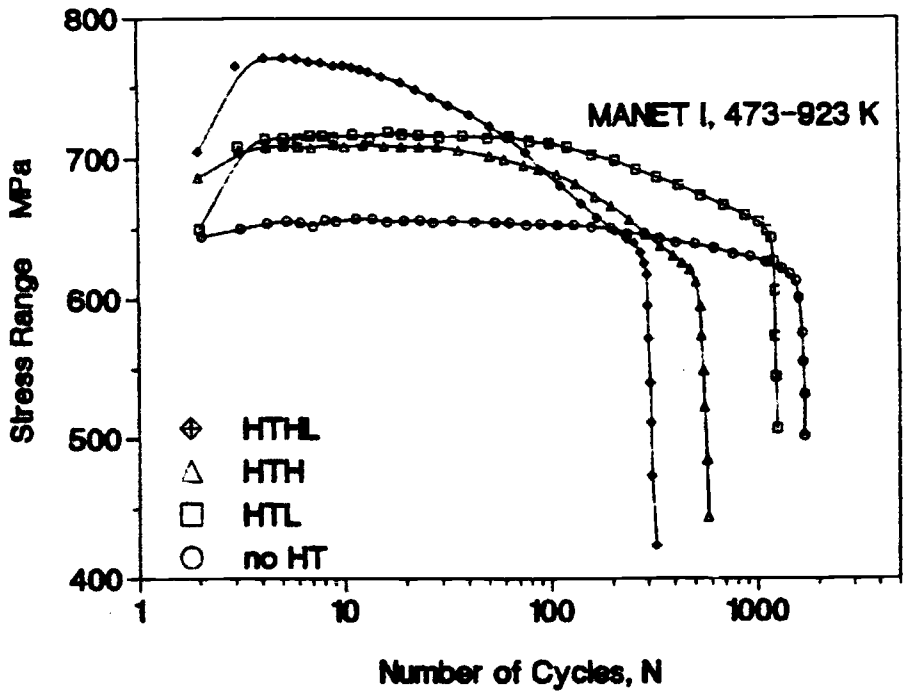

FIG. 16.35—Stress range versus number of cycles for the thermal fatigue-tested MANET I steel in the temperature range 200 to 650°C with and without hold times of 100 s at T_H, T_L, and at both T_H and T_L [81].

ever, all the OTMF and LCF data may be represented approximately in terms of $\Delta\varepsilon_{p,m}$ at $N_f/2$ by:

$$\frac{1}{N_f} = K\,(\Delta\varepsilon_{p,m})^m \qquad (16.24)$$

where K is strongly dependent on the ΔT but not on the mean cycle temperature and m is a constant.

FATIGUE CRACK GROWTH

In addition to the tensile, creep, and LCF properties, fracture toughness and fatigue and creep crack growth data are required for the advanced high-chromium martensitic steels being used or developed for the new high-efficiency boiler

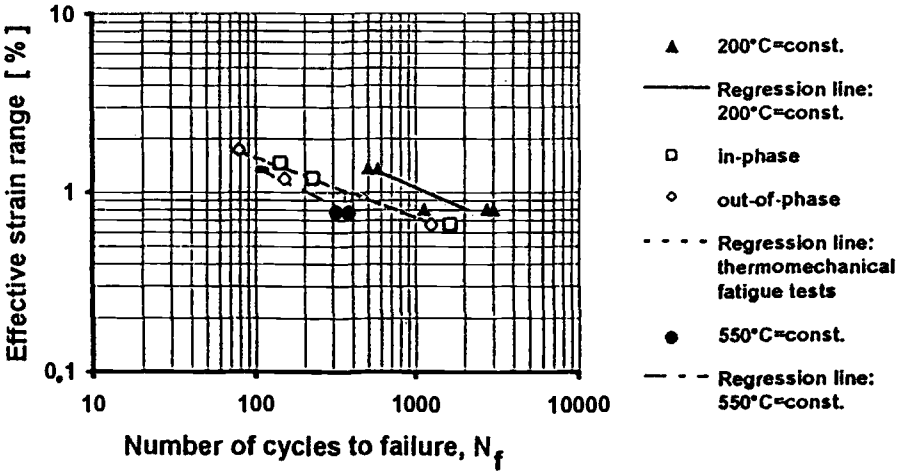

FIG. 16.36—Correlation between the effective strain range and numbers of cycles to failure for isothermal (200 and 550°C) and thermomechanical (200 to 550°C) fatigue-tested MANET I steel [90].

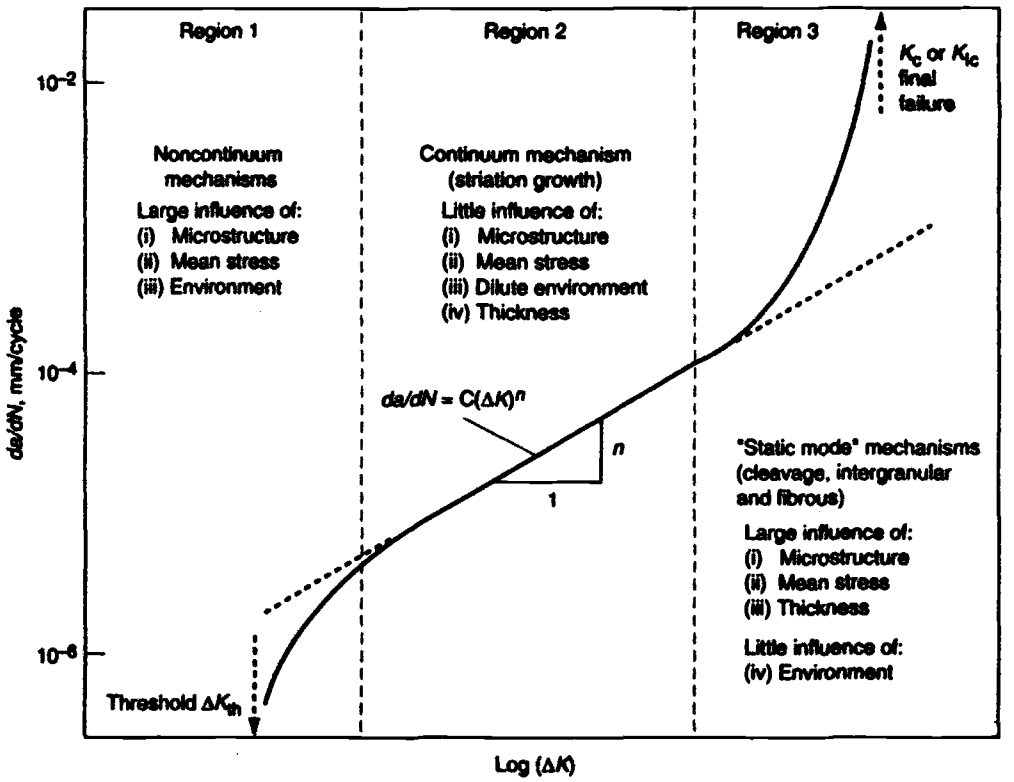

FIG. 16.37—Schematic illustration of the variation of the fatigue crack growth rate, da/dN, with alternating stress intensity, ΔK, in steels, showing the three primary crack growth regions [94].

units with more demanding steam conditions so as to provide a database for defect assessment studies, to establish maintenance scenarios, and for residual life assessments. Furthermore, the extension of cracks induced during fabrication (welding) by fatigue during normal operation or plasma disruptions is an important failure mode for the first wall of a tokamak fusion reactor [93].

The fatigue crack growth behavior is generally characterized using linear elastic fracture mechanics (LEFM) principles, and the Regions 1, 2, and 3 in the fatigue crack growth curves are illustrated schematically in Fig. 16.37 [94]. The fatigue crack growth rate (da/dN) in the subcritical Region 2 is related to the stress intensity factor range (ΔK) as follows (Paris law) [95,96]:

$$\frac{da}{dN} = C(\Delta K)^n \tag{16.25}$$

where C and n are material constants.

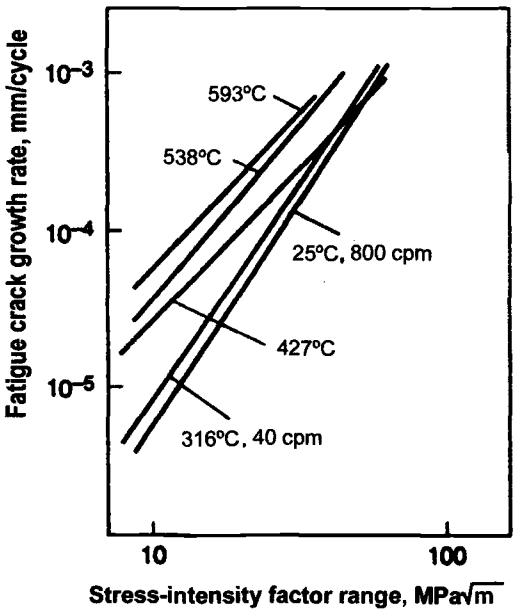

FIG. 16.38—Fatigue crack propagation behavior of the modified 9Cr-1Mo steel tested in air at ambient (800 cpm) and elevated (40 cpm) temperatures, R = 0.05 [15,97].

The fatigue crack growth rates (FCGRs) for several heats of the modified 9Cr-1Mo steel in air at ambient temperature and 315, 415, 540, and 593°C (600, 800, 1000, and 1100°F, respectively) and R = 0.05 have been documented [97] and are summarized in Fig. 16.38 [15]; the data were obtained in tests at frequencies of 800 cpm (ambient temperature) and 40 cpm (elevated temperatures). The FCGRs increase with increasing temperature, the effect being more pronounced at low ΔKs.

More recent data on the FCGRs of the modified 9Cr-1Mo steel and weld HAZ and E911 steel have been published [98,99]; the tests were performed at 600°C, R = 0.05 [98], and 0.1 [99] and cyclic frequencies ranging from 20 to 0.01 Hz. The FCGRs for the three materials under fast cycling conditions are very similar and in good agreement with other published data for the modified 9Cr-1Mo steel at about 600°C [97,100]. The FCGRs for the modified 9Cr-1Mo steel and HAZ show modest increases with decreasing frequency, the effect being enhanced at higher ΔKs, but those for the E911 steel appear to be independent of such frequency effects. The modified 9Cr-1Mo steel fractured transgranularly irrespective of the cyclic frequency, but a characteristic feature of the steel tested at the lowest frequencies is a significant softening in a 0.2 mm zone adjacent to the fracture surface. Such soft zones are not evident following testing at the highest frequencies.

The FCGRs of the quenched-and-tempered MANET I steel, determined in tests on small (W≤24 mm) C-T specimens machined from plates ranging in thickness from 8 to 12 mm at a frequency of 10 Hz at room temperature, 250 and 450°C, and with R values of 0.05 to 0.30, increase markedly with increasing test temperature but are not significantly affected by thermal aging and are not dependent on the steel plate thickness [101]. The FCGRs of the 1.4914 steel at ambient temperature and with R = 0.1 are plotted as a function of ΔK in Fig. 16.39 [102]; the FCGRs in the sub-critical (Paris) Region 2 are given by:

$$\frac{da}{dN} = 5.3 \times 10^{-9} (\Delta K)^3 \qquad (16.26)$$

where da/dN is in mm/cycle and ΔK is in MPa√m.

The FCGR of the MANET I steel is similar to that of the 1.4914 steel at ambient temperature but a little higher at 300°C [103].

It has been concluded, in agreement with the results of recent investigations on other materials, that the fatigue crack growth behavior at rates below approximately 1×10^{-5} mm/cycle (Region 1) is determined primarily by the microstructure of the steel and cannot be described by a continuum mechanics approach [102].

Small C-T specimens of the MANET I steel have been irradiated to 0.5 to 10 dpa at 250°C and to 10 dpa at 350 and 450°C [104–106]. The irradiated specimens could not be tested in the sub-critical (Paris) Region 2 because the large reductions in fracture toughness induced by the irradiation results in the fatigue crack growth curves exhibiting only Regions 1 and 3 (that is, direct transition from threshold behavior to critical crack growth) [101]. The FCGRs of the irradiated specimens at 250 and 450°C are no more than a factor of two to three different from those of the unirradiated thermal control specimens; thus, there is a small increase in the FCGR due to irradiation at 250°C (Fig. 16.40) and a small reduction at high ΔK in the 450°C irradiated and tested samples [101]. However, there are large reductions in the Paris region (reduction of ΔK_{max}) due to the strong decrease in the fracture toughness at 250°C, implying reductions in the allowable fatigue loading and, even more importantly, in the permitted crack extensions by fatigue ($\Delta K_{max} \leq 40$ MPa√m). Most of the samples fail by ductile fracture, but some brittle regions are often evident on the fracture surfaces of the 250°C irradiated and tested specimens.

LIFE PREDICTIONS

The principal approaches formulated to model the behavior and predict the long-term creep-fatigue and thermomechanical fatigue endurances from short-term, continuous cycling and hold-time LCF tests have been documented and reviewed [44,107–109]; they include the following:

(i) Linear Damage Summation (LDS) [110].
(ii) Strain Range Partitioning (SRP) [111, 112].
(iii) Ductility Exhaustion (DE) [113].
(iv) Frequency Modified Strain Range (FMSR) [114].
(v) Continuum Damage Mechanism (CDM) [108].
(vi) Overstress Method [115].

Although it has no physical basis, the LDS method has been used fairly extensively for creep-fatigue predictions as it is relatively simple to apply and has been incorporated in the ASME Code Case N-47, Sect. III, Subsection NH. The total fractional damage (D*) is given by:

$$D^* \geq \sum \frac{N_h}{N_f} + \sum \frac{t_h}{t_r} \qquad (16.27)$$

where N_h is the number of applied cycles and t_h and t_r are the hold period and creep-rupture times at a given load.

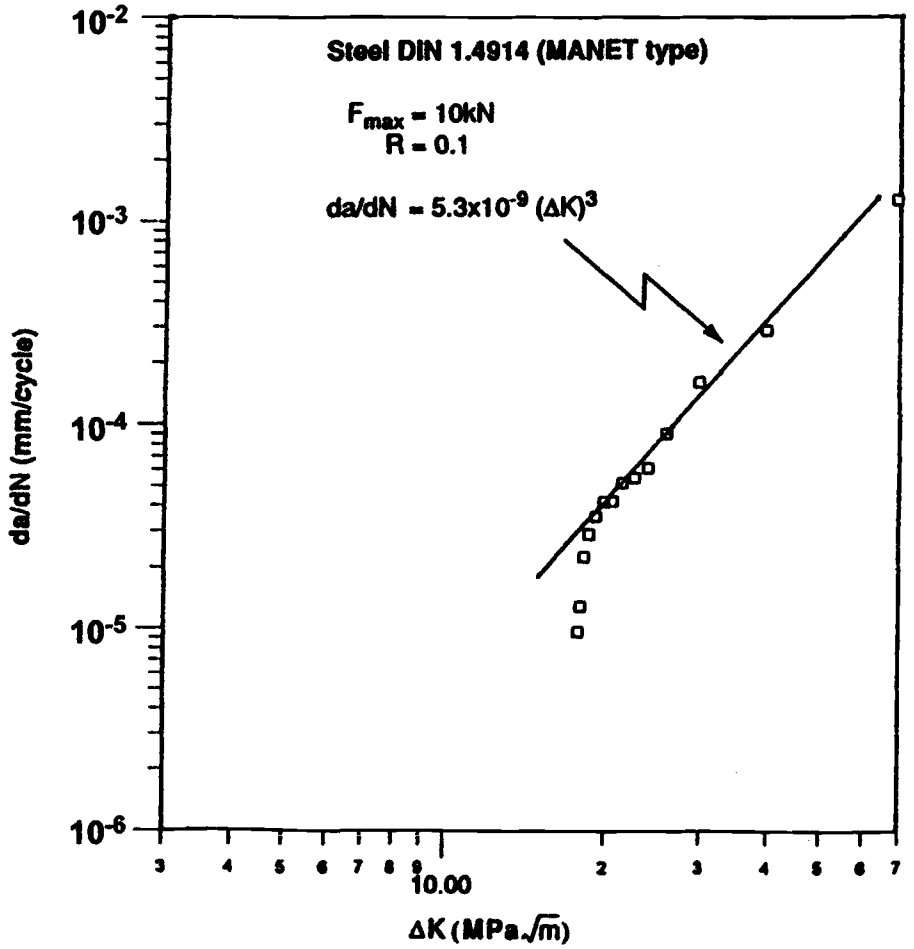

FIG. 16.39—Fatigue crack growth rate in the sub-critical Paris region 2 for the MANET-type steel at ambient temperature [102].

The LDS approach is conservative (D* > 1) when used to construct the creep-fatigue interaction diagram for 9Cr-1Mo steel tested at 520 [21] and 525°C [53,116]. However, this creep and fatigue damage fraction method is not appropriate for analyzing the effects of tensile hold periods on the endurances at 550°C of the modified 9Cr-1Mo steel, primarily due to its high resistance to intergranular fracture and high creep-rupture times and ductilities at this temperature [16].

The SRP method is now believed to be a more adequate procedure for the analysis of creep-fatigue data as it is potentially capable of handling any strain cycle composed of plastic flow (sum of all time independent inelastic strain components) and creep (sum of all time dependent strain components). Although rather complicated to use, this approach has met with some success in the case of low-alloy Cr-Mo and austenitic steels; however, there are fewer recorded instances of its application to the creep-fatigue of the high-chromium martensitic steels.

The DE and CDM approaches also aim to overcome the limitations of the traditional LDS method by incorporating coupling of the creep and fatigue damage, but the use of these methods to sum the fatigue and creep damage contributions in LCF tests with tensile hold times for the modified 9Cr-1Mo and E911 steels provides only a modest advantage over the LDS approach [108]. However, it is claimed that the overstress concept can be successfully applied to predict the creep-fatigue endurances of the modified 9Cr-1Mo steel in high (1×10^{-7} Pa) vacuum at 600°C [55].

The evaluation of the TF and TMF endurances of the high-chromium martensitic steels from the isothermal LCF data has not been extensively investigated. However, it is claimed, based on the results of a limited study, that the application of ductility normalized SRP to TMF of a 12Cr-MoWV steel has only been partially successful [117].

The creep deformation occurring at the maximum temperature is reversed by plastic strain at the minimum temperature in the TF and TMF cycles [44]. This situation is equivalent to that in which a hold time is introduced in an isothermal LCF test and the temperature cycling in-phase and out-of-phase can therefore be compared to LCF testing with symmetric cycles and hold periods in tension and compression, respectively. Based on the evidence presented in an earlier sub-section of this Chapter, out-of-phase cycling is expected to be the most damaging for Cr-Mo steels, but the limited data for the MANET steels (Fig. 16.36) [90] suggest that the in-phase and out-of-phase endurances in the temperature range 200 to 550°C are similar. In all probability, this is again due to the high resistance of these types of steels to intergranular creep fracture and the observation that significant

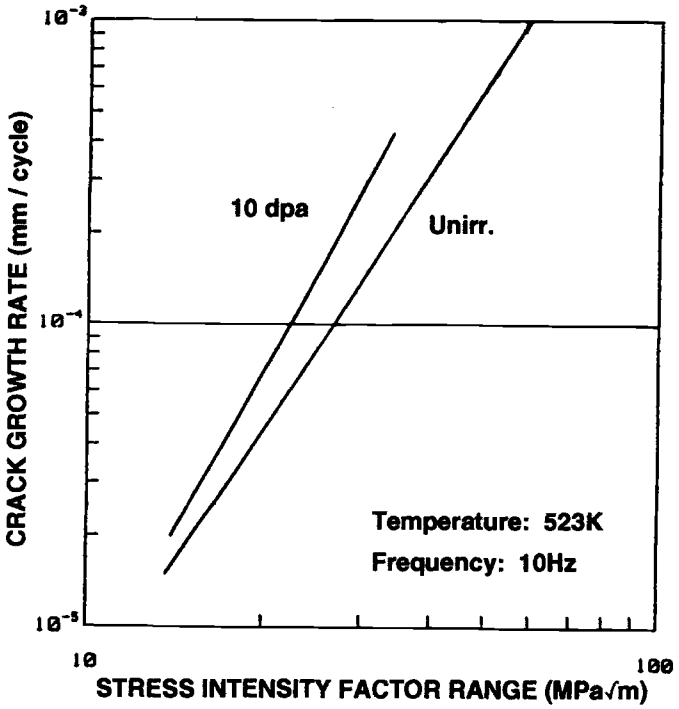

FIG. 16.40—Fatigue crack growth rate as a function of the stress intensity factor range for the MANET I steel before and after irradiation to 10 dpa at 250°C [101].

mean stresses are not developed during the in-phase and out-of-phase cycling.

A conceptual approach to generate thermomechanical failure data from isothermal LCF data at T_L and T_H of the thermal cycle has been presented [90,91]. The in-phase and out-of-phase TMF cyclic softening is represented by Eq 16.21, and the ΔF values are correlated with $\Delta\varepsilon_p$ as follows:

$$\Delta\varepsilon_p = \Delta\varepsilon_t - 100\frac{\Delta\sigma_t}{E} \qquad (16.28)$$

where $\Delta\sigma_t = \Delta F/A^*$ and A^* is the specimen cross-sectional area.

The $\Delta\varepsilon_p$ versus N relationship can thus be derived from Eqs 16.21 and 16.28, with the failure criterion for the in-phase and out-of-phase TMF being given by Eq 16.22. The iterative solution of Eq 16.22 yields a curve that intersects the $\Delta\varepsilon_p$-N curve at N_f. The predicted and experimental N_f values for the MANET I steel, obtained from a limited number of TMF screening tests between 200 and 550°C, have been found to be in reasonable agreement [91].

In addition, the prediction of the LCF lives using a damage model with $\Delta\varepsilon_p$, T, and $\dot{\varepsilon}_t$ as variables [see the sub-section on Strain Rate and Frequency (under the section on Strain Controlled Low-Cycle Fatigue) and Eq 16.8] has been extended to TMF loading [32]. The calculation of the damage is based on the Taira equivalence concept [118] and is performed on the stable hysteresis loop using a linear damage rule; the damage per cycle is given by:

$$\frac{1}{N_f} = \int_{T_L}^{T_H} d(\delta\varphi) + \int_{T_H}^{T_L} d(\delta\varphi) \qquad (16.29)$$

where $\delta\varphi$ is the incremental damage due to plastic deformation, temperature, and strain rate for each cycle.

The endurances calculated using this model are also in good agreement with the experimental data for the in-phase and out-of-phase TMF loading between 200 and 550°C for the MANET I steel [32].

A major problem in the development and application of the models to predict the creep- fatigue, thermal, and thermomechanical fatigue behavior of the high-chromium martensitic steels is that their microstructures are not stable during testing. Further development and validation of the predictive approaches require specific investigations of the role of microstructural stability and additional experimental testing in high vacuum to avoid the detrimental effect of oxidation on the fatigue failures and endurances at high temperatures.

Preliminary attempts [98,99] to model the behavior whereby the FCGRs of the modified 9Cr-1Mo steel and HAZ increase at low cyclic frequencies have been made using the following creep-fatigue crack growth interaction equation:

$$\left(\frac{da}{dN}\right)_{Total} = \left(\frac{da}{dN}\right)_{Fatigue} + \int\left(\frac{da}{dt}\right)_{Creep} \qquad (16.30)$$

The first term on the right-hand side of the equation represents the pure fatigue component (Paris equation) while the second term constitutes an appropriate creep crack growth law [54]:

$$\frac{da}{dt} = B' K_T^q \qquad (16.31)$$

where B′ and q are constants and KT represents a suitable crack tip parameter [99] and is integrated over the loading cycle so as to estimate the pure creep contribution. While some success has been achieved in this modeling, the predictions are, as expected, very sensitive to the analytical procedures and input parameters; additional long-term FCGR tests and analyses of the roles of primary creep and instantaneous crack tip plasticity need to be implemented to validate the approaches.

REFERENCES

[1] D. R. Harries, Rad. Effects 101 (1987) 3.
[2] D. R. Harries and E. Zolti, Nucl. Eng. and Design/Fusion 3 (1986) 331.
[3] G. Degallaix, S. Degallaix, and J. Foct, Mat. Sci and Eng. 58 (1983) 55.
[4] L. F. Coffin, Trans. ASME 76 (1954) 931.
[5] S. S. Manson, in: Proc. 1st. Int. Conf. on Fracture, Vol. 3 (Society for Strength and Fracture of Metals, Japan, 1965) 1838.
[6] L. F. Coffin, S. S. Manson, A. E. Carden, L. K. Severud, and W. L. Greenstreet, Time-Dependent Fatigue of Structural Alloys, Oak Ridge National Laboratory, ORNL-5073, January 1977.
[6] L. F. Coffin, S. S. Manson, A. E. Carden, and L. K. Severud, Oak Ridge National Laboratory, ORNL Report 5073, 1977.
[7] S. Kim and J. R. Weertman, Metall. Trans. A19 (1988) 999.
[8] K. Kanazawa, K. Yamaguchi, and K. Kobayashi, Mater. Sci. Eng. 40 (1979) 89.
[9] W. Baumgärtner, M. Boçek, C. Petersen, D. Rodrian, W. Scheibe, R. Schmitt, H. Schneider, and W. Schweiger, Pre- and Post-Irradiation Fatigue Properties of 1.4914 Martensitic Steel

(MANET), Kernforschungszentrum Karlsruhe, KfK Report 4677, 1989, p. 72.
[10] W. Baumgärtner, M. Boçek, C. Petersen, D. Rodrian, W. Scheibe, R. Schmitt, H. Schneider, and W. Schweiger, Pre- and Post-Irradiation Fatigue Properties of 1.4914 Martensitic Steel (MANET), Forschungszentrum Karlsruhe, KfK Report 4774, 1990, p. 97.
[11] W. Baumgärtner, M. Boçek, C. Petersen, D. Rodrian, W. Scheibe, R. Schmitt, H. Schneider, and W. Schweiger, Pre- and Post-Irradiation Fatigue Properties of 1.4914 Martensitic Steel (MANET), Forschungszentrum Karlsruhe, KfK Report 4944, 1991, p. 91.
[12] W. Scheibe and R. Schmitt, in: Proc. Annual Meeting on Nuclear Technology, Nurenberg, May 1990 (INFORUM Verlag, Bonn) 597.
[13] P. Marmy, Y. Ruan, and M. Victoria, J. Nucl. Mater. 179-181 (1991) 697.
[14] C. R. Brinkman, J. P. Strizak, and M. K. Booker, Smooth- and Notched-Bar Fatigue Characteristics of Modified 9Cr-1Mo Steel, Oak Ridge National Laboratory, ORNL Report 6330, February 1987.
[15] R. W. Swindeman and W. Ren, ASM Handbook, Vol. 19, Fatigue and Fracture (ASM International, Materials Park, OH, 1996) 704.
[16] J. Wareing and A.A. Tavassoli, in: Proc. 13th Intl. Conf. on Structural Mechanics in Reactor Technology (SMIRT, 1995) E08.
[17] P. Berge, J. Donati, F. Pellicani, and M. Weisz, in: Ferritic Steels for High Temperature Applications, Ed. A. K. Khare (American Society for Metals, Metals Park, OH, 1983) 100.
[18] H. J. Chang and J. J. Kai, J. Nucl. Mater. 191-194 (1992) 836.
[19] H. J. Chang, J. J. Kai, and C. H. Tsai, J. Nucl. Mater. 212-215 (1994) 574.
[20] D. S. Wood, in: Ferritic Steels for Fast Reactor Steam Generators, Eds. S. F. Pugh and E. A. Little (British Nuclear Energy Society, London, 1978) 189.
[21] B. K. Choudhary, K. Bhanu Sankara Rao, S. L. Mannan, and B. P. Kashyap, in: EUROMAT 96: Materials and Nuclear Power (The Institute of Materials, London, 1996) 289.
[22] T. Yukitoshi, K. Yoshikawa, K. Tokimasa, T. Kudo, Y. Shida, and Y. Inaba, in: Ferritic Steels for Fast Reactor Steam Generators, Eds. S. F. Pugh and E. A. Little (British Nuclear Energy Society, London, 1978) 87.
[23] G. Degallaix, J. Foct, C. Grabel, and A. Vanderschaeghe, Mém. Sci. Rev. Métall, 79 (1982) 21.
[24] V. K. Sikka, Substitution of Modified 9Cr-1Mo Steel for Austenitic Stainless Steel, Oak Ridge National Laboratory, ORNL Report 5841, April 1982.
[25] B. G. Gieseke, C. R. Brinkman, and P. J. Maziasz, in: Microstructures and Mechanical Properties of Aging Material, Eds. P. K. Liaw, R. Viswanathan, K. L. Murty, E. P. Simonen, and D. Frear (The Minerals, Metals and Materials Society, Warrendale, PA, 1993) 197.
[26] G. Ebi and A. J. McEvily, Fatigue Engng. Mater. Struct. 7 (1984) 299.
[27] Y. Asada, T. Nakamura, M. Yaguchi, A. Ishikawa, and G. Cao, in: Proc. 1992 Pressure Vessels and Piping Conf., Ed. C. Becht IV, PVP-Vol 230 (American Society of Mechanical Engineers, New York, 1992) 47.
[28] S. Matsuoka, S. Kim and J. R. Weertman, in: Topical Conference on Ferritic Alloys for Use in Nuclear Energy Technologies, Eds. J. W. Davis and D. J. Michel (The Metallurgical Society of AIME, Warrendale, PA, 1984) 507.
[29] J. C. Earthman, G. Eggeler, and B. Ilschner, Mat. Sci. Engng. A110 (1989) 103.
[30] K. Wellinger and R. Idler, Arch. Eisenhüttenwes. 48 (1977) 279.
[31] S. Kitade, K. Setoguchi, M. Yamauchi, and T. Igari, Cyclic Stress-Strain Behavior of Modified 9% Cr-1Mo Steel Under Creep-Fatigue Interaction, Mitsubishi Heavy Industries Ltd., Nagasaki R & D Center Report.
[32] C. Petersen, R. Schmitt, and D. Garnier, J. Nucl. Mater. 233-237 (1996) 285.
[33] L. F. Coffin, in: Creep-Fatigue Interaction, ASME-MPC-3 (American Society of Mechanical Engineers, New York, 1976) 349.
[34] J. F. Stubbins and D. S. Gelles, J. Nucl. Mater. 233-237 (1996) 331.
[35] G. Degallaix, J.-B. Vogt, and J. Foct, Mém. Sci. Rev. Métall. 87 (1990) 47.
[36] R. Schmitt and W. Scheibe, in: Fusion Technology, 1994, Eds. K. Herschbach, W. Maurer, and J. E. Vetter (North Holland, Amsterdam, 1995) 1321.
[37] M. L. Grossbeck, J. M. Vitek, and K. C. Liu, J. Nucl. Mater. 141-143 (1986) 966.
[38] D. S. Wood, Nuclear Tech. 55 (1981) 332.
[39] C. Petersen, M. Pfeifenroth, D. Rodrian, W. Scheibe, R. Schmitt, H. Schneider, and W. Schweiger, Pre- and Post-Irradiation Fatigue Properties of MANET Steel, Forschungszentrum Karlsruhe, Report FZKA 5515, January 1995, p. 85.
[40] J. Aktaa, M. Klotz, C. Petersen, M. Pfeifenroth, D. Rodrian, and R. Schmitt, Fatigue and Creep Properties of Base Material of LA Martensitic Steel F82H Mod., Forschungszentrum Karlsruhe, FZKA Report 5858, January 1997, p. 136.
[41] J. Bertsch, Mikroskopische Untersuchung der Bildung von Ermüdungsrissen an zwei ferritisch-martensitschen Stählen im unbestrahlten und vorbestrahlten Zustand, Forschungszentrum Karlsruhe, FZKA Report 5984, September 1997.
[42] V. Bicego, B. Brown, G. Fedeli, M. A. Roman, N. Taylor, and H. Van Wortel, in: Proceedings of the Seventh International Conference on Creep and Fracture of Engineering Materials and Structures, J. C. Earthman and F. A. Mohamed (Minerals, Metals, and Materials Society, Warrendale, PA, 1997) 545.
[43] D. Sunamoto, T. Endo, and M. Fujihara, in: Creep and Fatigue in Elevated Temperature Applications, Vol. 1 (Inst. Mech. Engng., London, 1974) C252.
[44] L. Lundberg and R. Sandström, Scand. J. of Metallurgy 11 (1982) 85.
[45] W. B. Jones, in: Production, Fabrication, Properties and Application of Ferritic Steels for High Temperature Applications, Ed. A. K. Khare (American Society for Metals, Metals Park, OH, 1983) 221.
[46] Y. Asada, M. Ueta, K. Douzaki, M. Sukekawa, K. Taguchi, and H. Koto, in: Proc. 1992 Pressure Vessels and Piping Conf., New Orleans, Ed. C. Becht IV, PVP-Vol. 230 (American Society of Mechanical Engineers, New York, 1992) 41.
[47] W. Baumgärtner, M. Boçek, C. Petersen, D. Rodrian, W. Scheibe, R. Schmitt, H. Schneider, and W. Schweiger, Pre- and Post-Irradiation Fatigue Properties of 1.4914 Martensitic Steel (MANET), Forschungszentrum Karlsruhe, KfK Report 5099, October 1992, p. 92.
[48] W. Baumgärtner, M. Boçek, C. Petersen, D. Rodrian, W. Scheibe, R. Schmitt, H. Schneider, and W. Schweiger, Pre- and Post-Irradiation Fatigue Properties of 1.4914 Martensitic Steel (MANET), Forschungszentrum Karlsruhe, KfK Report 5288, December 1993, p. 79.
[49] C. R. Brinkman, M. P. Strizak, M. K. Booker, and C. E. Jaske, J. Nucl. Mater. 62 (1976) 181.
[50] D. S. Wood, in: Experience of Structural Validation in the Nuclear Industry with Emphasis on High temperature Design (Institute of Mechanical Engineers, London, 1979) 23.
[51] D. C. Lord and L. F. Coffin, Metall. Trans. 4 (1973) 1647.

[52] B. J. Cane and R. S. Fidler, in: Ferritic Steels for Fast Reactor Steam Generators, Eds. S.F. Pugh and E. A. Little (British Nuclear Energy Society, London, 1978) 193.
[53] S. J. Sanderson, in: Ferritic Steels for High Temperature Applications, Ed. A. K. Khare, (American Society for Metals, Metals Park, OH, 1983) 85.
[54] E. Barker, G. J. Lloyd, and R. Pilkington, Mater. Sci. Eng. 84 (1986) 49.
[55] Y. Okamoto, M. Yaguchi, A. Ishikawa, Y. Asada, and T. Asayama, in: Proc. 11th Intl. Conf. on Structural Mechanics in Reactor Technology (SMIRT), 1991, 349.
[56] H. Teranishi and A. J. McEvily, Metall. Trans. 10A (1979) 1806.
[57] J.-B. Vogt, G. Degallaix, and J. Foct, Fatigue Fract. Engng. Mater. Structure 11 (1988) 435.
[58] P. Marmy and M. Victoria, J. Nucl. Mater. 191-194 (1992) 862.
[59] P. Marmy, J. Nucl. Mater. 212-215 (1994) 594.
[60] K. Wellinger and S. Sautter, Arch. Eisenhüttenwes 44 (1973) 47.
[61] R. Lindau and A. Möslang, J. Nucl. Mater. 191-194 (1992) 915.
[62] R. Lindau and A. Möslang, J. Nucl. Mater. 212-215 (1994) 599.
[63] J. Bertsch, R. Lindau, and A. Möslang, J. Nucl. Mater. 233-237 (1996) 276.
[64] P. Marmy, Plasma Devices and Operations 4 (1996) 211.
[65] J. F. Stubbins, B. A. Kschinka, and D. L. Marriott, J. Nucl. Mater. 141-143 (1986) 55.
[66] R. Gersinska, Microstructural Investigation of Fatigued 12% Cr Steel 1.4914 (X18CrMoVNb 12 1), Kernforschungszentrum Karlsruhe, KfK Report 5069, 1992.
[67] R. Lindau and A. Möslang, J. Nucl. Mater. 179-181 (1991) 753.
[68] D. Gavillet, P. Marmy, and M. Victoria, J. Nucl. Mater. 191-194 (1992) 890.
[69] A. F. Armas, I. Alvarez-Armas, M. Avalos, C. Petersen, and R. Schmitt, in: Fusion Technology 1996, Eds. C. Varandas and F. Serra (Elsevier, Amsterdam, 1997) 1359.
[70] A. F. Armas, M. Avalos, I. Alvarez-Armas, C. Petersen, and R. Schmitt, J. Nucl. Mater. 258-263 (1998) 1204.
[71] W. Vandermeulen, W. Hendrix, V. Massaut, J. Van de Velde, and Ch. De Raedt, Master Test Results, SCK/CEN Report MAT/P1/WVM/gm/92-11; FT/Mol/92-05, December 1992.
[72] A. Möslang, S. Cierjacks, and R. Lindau, in: Cyclotrons and their Applications, Eds. B. Martin and K. Ziegler (World Scientific, London, 1991) 545.
[73] P. Marmy, M. Daum, D. Gavillet, S. Green, W. V. Green, F. Hegedus, S. Proennecke, U. Rohrer, U. Stiefel, and M. Victoria, Nucl. Instr. and Methods in Phys. Res. B47 (1989) 37.
[74] A. Möslang, D. Preininger, and K. Ehrlich, in: Proc. All-Union Conf. on Effect of Irradiation on Materials for Fusion Reactors, Leningrad, September 1990.
[75] P. Marmy and M. Victoria, in: Proc. 9th Intl. Conf. On the Strength of Metals and Alloys, Eds. D. G. Brandon, R. Chaim, and A. Rosen (Freund Publishing House, London, 1991) 841.
[76] P. Marmy, J. L. Martin and M. Victoria, Plasma Devices and Operations 3 (1994) 49.
[77] A. Möslang, S. Baumgärtner, G. Burkle, R. Lindau, G. Przykutta, and K. Ehrlich, in: Fusion Tech. 1992, Vol. II, Eds. C. Ferro, M. Gasparotto and H. Knoepfel (North-Holland, Amsterdam, 1993) 1439.
[78] H. Ullmaier and N. Schmitz, J. Nucl. Mater. 169 (1989) 233.
[79] J. I. Shakib, H. Ullmaier, E. A. Little, W. Schmitz, R. G. Faulkner, and T. E. Chung, J. Nucl. Mater. 191-194 (1992) 1404.
[80] C. Petersen and G. H. Rubiolo, in: Fatigue 90, Eds. H. Kitagana and T. Tanaka, Vol. III (MCE Publications Ltd., Birmingham, 1990) 1559.
[81] I. Alvarez-Armas, A. F. Armas, and C. Petersen, Fatigue Fract. Engng. Mater. Structure 17 (1994) 671.
[82] C. Petersen, I. Alvarez-Armas, and A. F. Armas, Plasma Devices and Operations 3 (1994) 317.
[83] L. Belyaeva, O. Orychtchenko, C. Petersen, and V. Rybin, J. Nucl. Mater. 271 & 272 (1999) 151.
[84] I. Alvarez-Armas, A. F. Armas, and C. Petersen, J. Nucl. Mater. 191-194 (1992) 841.
[85] A. F. Armas, I. Alvarez-Armas, and C. Petersen, in: Low Cycle Fatigue and Elasto-Plastic Behavior of Materials, Ed. K.-T. Rie (Elsevier Applied Science, London, 1992) 275.
[86] I. Alvarez-Armas, A. F. Armas, and C. Petersen, in: Fatigue 93, Eds. J.-P. Bailon, and J. I. Dickson (Engineering Materials Advisory Services Ltd., Warley, UK, 1993) 903.
[87] C. Petersen, J. Nucl. Mater. 212-215 (1994) 584.
[88] C. Petersen in: Characterization and Assessment of Ferritic/Martensitic Steels, Eds. K. Ehrlich, D. R. Harries, and A. Möslang, Forschungszentrum Karlsruhe, FZKA Report 5626, February 1997.
[89] C. Petersen, J. Nucl. Mater. 258-263 (1998) 1285.
[90] F. Wolter and C. Petersen, in: Proc. Annual Meeting on Nuclear Technology '94, Stuttgart, (INFORUM Verlag, Bonn, 1994) 493.
[91] C. Petersen and F. Wolter, in: Fusion Technology 1994, Eds. K. Herschbach, W. Maurer, and J. E. Vetter (North-Holland, Amsterdam, 1995) 1285.
[92] A. Zisman, V. Rybin, C. Petersen, and R. Schmitt, J. Nucl. Mater. 264 (1999) 234.
[93] E. Diegele, T. Fett, D. Munz, and H. Stamm, J. Nucl. Mater. 155-157 (1988) 679.
[94] ASM Handbook, Vol. 19, Fatigue and Fracture (ASM International, Materials Park, OH, 1996) 632.
[95] P. C. Paris, Trend. Engng. 13 (1961) 9.
[96] P. Paris et al., J. Basic Engng. 85 (1963) 528.
[97] L. A. James and K. W. Carlsen, J. Pressure Vessel Tech. 107 (1985) 271.
[98] N. Taylor, V. Bicego, E. Lucon, and P. Bontempi, in: EUROMAT 97: Advanced Materials and Processes and Applications, Vol. I, Metals and Composites (Netherlands Society for Materials Science, Zwijndrecht, NL, 1997) 19.
[99] N. Taylor, E. Lucon, V. Bicego, and P. Bontempi, in: Advanced Steam Plant (Inst. Mech. Engng., London, 1997) 201.
[100] A. Vanderschaege, C. Gabrel-Cousaert, and J. Lecoq, in: Pressure Vessel Technology: Proceedings of the Seventh International Conference, Vol. I (Verband der Technischen Überwachungs-Vereine e.V., Essen, Germany, 1992) 802.
[101] M. I. de Vries, in: Effects of Radiation on Materials: 16th International Symposium, ASTM STP 1175, Eds. A. S. Kumar, D. S. Gelles, R. K. Nanstad and E. A. Little (American Society for Testing and Materials, Philadelphia, PA, 1993) 558.
[102] F. Müller, Experimentelle Ermittlung des Riβausbreitungsverhaltens verschiedener Werkstoffe mit Methoden der Bruchmechanik, Diploma Thesis, University of Karlsruhe, May 1994.
[103] F. Müller, Ergebnisbericht über Forschung und Entwicklung, Kernforschungszentrum Karlsruhe, KfK Report 5334, March 1994, p. 6.
[104] N. van der Kleij, Ed., Progress Report 1989 on Fusion Technology Tasks, ECN, Petten, Report C-90-041, August 1990.
[105] H. Th. Klippel, Ed., Progress Report 1989 on Fusion Technology Tasks, ECN, Petten, Report C-91-035, June 1991.
[106] H. Th. Klippel Ed., Progress Report 1989 on Fusion Technology Tasks, ECN, Petten, Report C-92-049, July 1992.
[107] G. A. Webster and R. A. Ainsworth, High Temperature Component Life Assessment (Chapman and Hall, London, 1994).
[108] V. Bicego, N. Taylor, and P. Bontempi, Fatigue Fract. Engng. Mater. Struct. 20 (1997) 1183.
[109] ASM Handbook, Vol. 19, Fatigue and Fracture, (ASM International, Materials Park, OH, 1996).

[110] S. Taira, in: Creep in Structures, Ed. N. J. Hoff, (Springer, Berlin, 1962) 96.
[111] S. S. Manson, G. R. Halford, and M. Hirschberg, in: Design for Elevated Temperature Environment (American Society of Mechanical Engineers, New York, 1971) 12.
[112] S. S. Manson, in: Fatigue at Elevated Temperatures, ASTM STP No. 520, Eds. A. E. Carden, A. J. McEvily, and C. H. Wells (American Society for Testing and Materials, Philadelphia, PA, 1973) 744.
[113] R. Hales, Fatigue. Fract. Engng. Mater. Struct. 6 (1983) 121.
[114] L. F. Coffin, Metall. Trans. 2 (1971) 3105.
[115] K. Taguchi, E. Kanno, S. Ozaki, and T. Uno, Int. J. Pres. Ves. & Piping 44 (1990) 99.
[116] D. S. Wood, A. B. Baldwin, and K. Williamson, in: Time and Load Dependent Degradation of Pressure Boundary Materials (International Atomic Energy Agency, Vienna, 1978); IAEA Report IWG-RRPC-79/2, p. 88.
[117] S. Taira, M. Fukjino, and R. Ohtani, Fatigue Engng. Mater. Struct. 1 (1979) 495.
[118] S. Taira, in: Fatigue and Elevated Temperatures, ASTM STP No. 520, Eds. A. E. Carden, A. J. McEvily and C. H. Wells (American Society for Testing and Materials, Philadelphia, PA, 1973) 80.

17

Recovery (Annealing) of Radiation Damage

Hardening of the ferritic/martensitic steels by irradiation damage processes (Chapter 12) occurs below 400 to 450°C (the temperature depends on the steel); it is caused by the irradiation-produced vacancies and interstitials and from irradiation-enhanced precipitation of new phases [1]. In general, below $\approx 0.3T_m$, dislocation loops form from interstitials and vacancies and increase the flow stress, which leads to hardening and embrittlement. Between ≈ 0.3 to $0.4T_m$, a void and dislocation structure forms (the dislocation loops are unstable and grow into a dislocation network), and diffusion is sufficient for the formation of precipitates. Above about $0.4\ T_m$, displacement damage can continuously anneal out, resulting in little change in strength (at these temperatures strength sometimes decreases because irradiation-enhanced diffusion accelerates the normal thermal aging process).

Just as irradiation hardening ceases at 400 to 450°C because irradiation damage anneals out, post-irradiation annealing can also reduce the effect of irradiation on tensile and impact properties. Annealing of pressure vessels of light-water fission reactors has been proposed and used as a method of extending the lifetime of the reactor. The annealing technique was used in 1967 on a U.S. Army reactor, in 1984 on a Belgian reactor, and since 1987 on 14 power reactors built by the former Soviet Union in Soviet Bloc countries [1]. Typically, the annealing of the pressure vessel steels used in fission plants has been carried out at 430 to 475°C for about 150 h. Annealing of the pressure-vessel steels is carried out after the vessel has reached a fluence of <1 dpa, which suffices to produce considerable hardening in these low-alloy steels [1].

A few annealing experiments have been carried out on the 9–12% Cr Cr-Mo steels considered for fusion applications [2–5]. Wassilew and Ehrlich [2] annealed for 0.5 h at 535°C one of the impact specimens of the MANET I steel irradiated to 5 dpa at 300°C in HFR (Fig. 17.1). When this specimen was tested at 500°C, almost half of the reduction in USE was recovered, which the authors attributed to, "a dissolution of the irradiation-induced defect structure . . . ." [2].

Zvezdin et al. [4] annealed three Russian steels 4 h at 550°C after irradiation to 4×10^{26} n/m^2 (E > 0.1 MeV) (around 20 dpa) at 350°C in the BOR-60 fast reactor. The steels (discussed

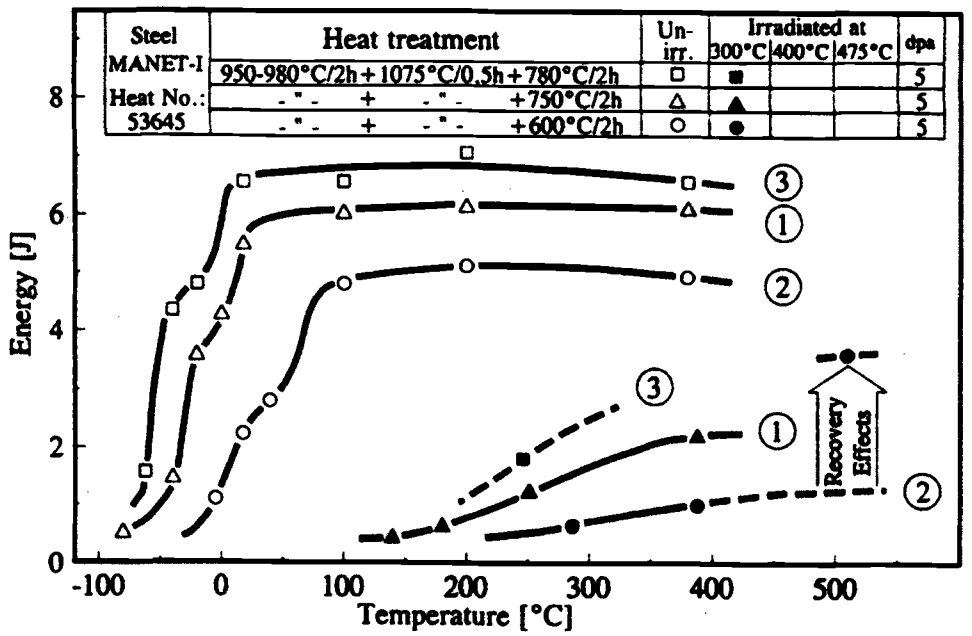

FIG. 17.1—Charpy impact curves for MANET steel irradiated to 5 dpa at 300°C in HFR after three different tempering treatments. One irradiated specimen was annealed 1 h at 535°C and tested; the change due to the anneal is labeled "Recovery Effects."

in Chapter 14) were 10X13M2FB (12Cr-2MoVNb), 10X9M2FB (9Cr-2MoVNb), and 10X9MFB (10Cr-1MoVNb) that were processed from pure materials in an open electric-arc furnace (OEAF) and in an OEAF with an electro-slag remelt (OEAF+ESR). Results are shown in Fig. 17.2 [4].

The 12Cr steel [(Fig 17.2(a)], which showed no effect of the processing, showed significant recovery after annealing. Re-irradiation to 2×10^{26} n/m^2 at 380°C did not cause embrittlement up to the level achieved after the initial irradiation. However, re-irradiation was at a lower fluence and a higher irradiation temperature (380 versus 350°C), so the level of embrittlement should be somewhat less. The two lower-chromium steels [Figs. 17.2(b) and 17.2(c)] showed substantially better recovery after annealing by practically recovering back to the original level. In both cases the OFAC+ESR was an improvement over the OFAC. Likewise,

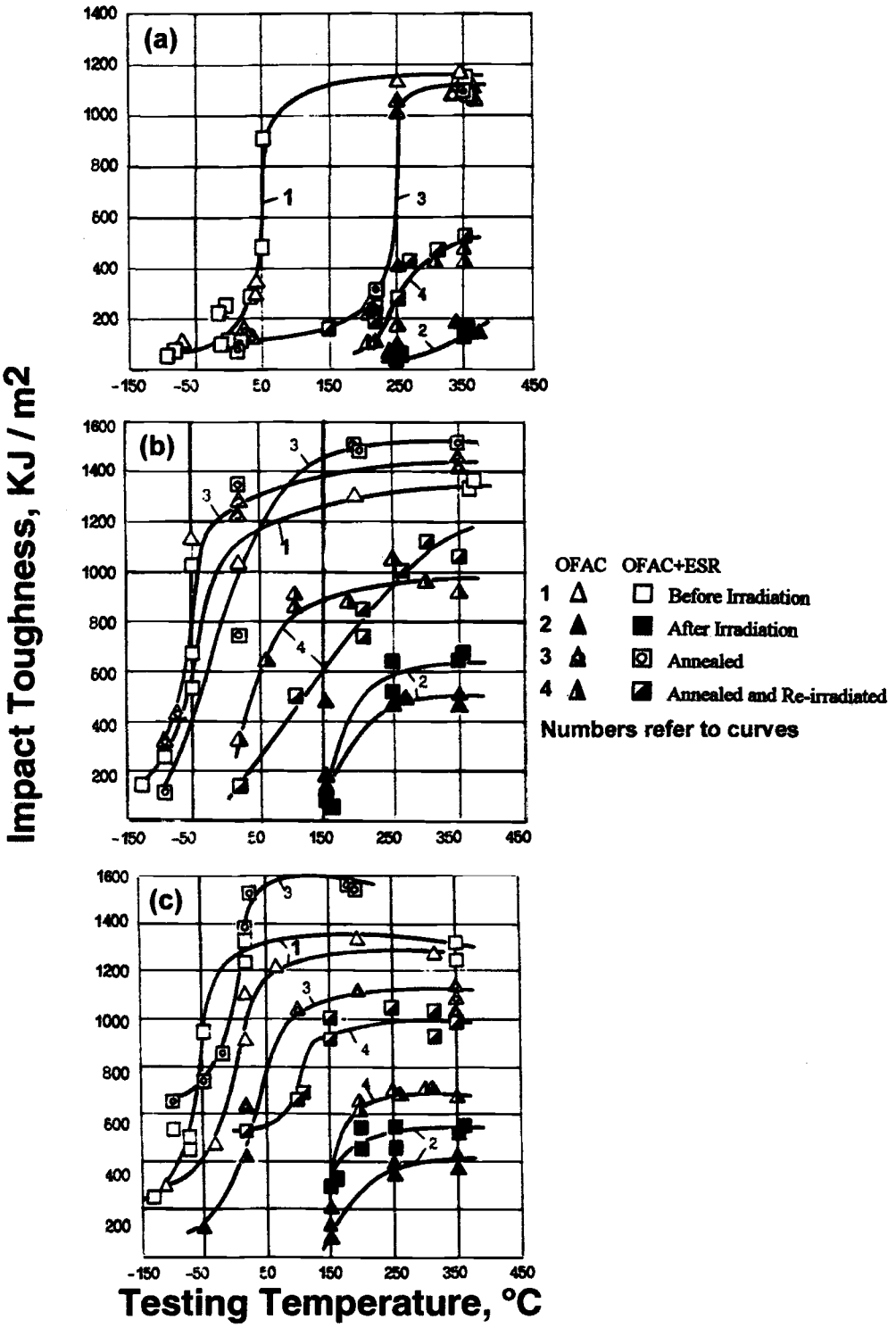

FIG. 17.2—Impact curves for (a) 10X13M2FB (12Cr-2MoVNb), (b) 10X9M2FB (9Cr-2MoVNb), and (c) 10X9MFB (10Cr-1MoVNb) steels.

after re-irradiating, the shift in DBTT of the OFAC+ESR material was not as large as that for the OFAC, which was also the case for the initial irradiation [4].

Khabarov et al. [5] performed 1-h annealing experiments on 13Cr2MoNbVB (13Cr-1.5MoVNbNi) steel removed from subassemblies in the BN-350 and BN-600 reactors after irradiation to 4 to 85 dpa at 280 to 350°C. The authors stated that recovery began at 450 to 470°C, and complete recovery of the USE to the pre-irradiation level occurred after annealing 1 h at 550°C.

Differences in the recovery processes would be expected for steels irradiated in a fast reactor and a fusion reactor because of the transmutation helium produced in the latter. The experimental work on the martensitic steels discussed above was for the recovery of irradiation effects caused primarily by displacement damage [1–5]. Helium bubbles would not anneal out, and they might grow at the annealing temperature. Since these steels are relatively immune to elevated-temperature helium embrittlement, the helium should not affect the steel after the recovery anneal for that reason, although that would need to be demonstrated.

In Chapter 14, the increase in the DBTT of the martensitic steels during irradiation and how this embrittlement that occurs at temperatures where hardening occurs may be affected by helium was discussed. When helium is produced in the steel during irradiation, an increment of the shift in DBTT over and above that due to displacement damage and precipitation that occur during irradiation was attributed to the helium. A recovery anneal may again produce a steel with improved impact properties (over the properties before recovery), because even in the presence of helium, hardening may be required for the increased DBTT, and most of the hardening entities (e.g., dislocation loops) are eliminated by the recovery anneal. However, there remains the question of whether helium bubbles would be agglomerated by the anneal and, if so, what effect this would have on the impact properties once hardening occurred during re-irradiation. The answer must await clarification of the mechanism by which helium affects the embrittlement process.

REFERENCES

[1] R. Pelli and K. Törrönen, State of the Art Review on Thermal Annealing, AMES Report No. 2, European Commission, DG XII-Institute for Advanced Materials, Joint Research Center, Brussels-Luxembourg, 1995.

[2] C. Wassilew and K. Ehrlich, J. Nucl. Mater. 191-194 (1992) 850.

[3] V. K. Shamardin, A. M. Pecherin, O. M. Vishkarev, V. P. Borisov, and G. A. Tulyakov, in: Proc. Int. Conf. on Radiat. Mater. Sc. (Alushta, USSR, May 22-25, 1990) 3.

[4] Y. I. Zvezdin, O. M. Vishkarev, G. A. Tulyakov, Y. G. Magerya, V. A. Smirnov, I. A. Shenkova, I. V. Altovski, A. A. Grigoryan, V. K. Shamardin, and U. M. Pecherin, J. Nucl. Mater. 191-194 (1992) 855.

[5] V. S. Khabarov, A. M. Dvoriashin, and S. I. Porollo, J. Nucl. Mater. 233-237 (1996) 236.

18

Summary: Past, Present, and Future

Ferritic/martensitic steels are considered for use in fast fission and fusion reactors. The viability of the steels for applications in the fast fission or fusion neutron environment depends mainly on its irradiation resistance. In the preceding chapters, the effect of irradiation on various properties was presented. In addition to the irradiation conditions (e.g., fluence, spectrum, irradiation temperature, etc.), steel composition and microstructure, which depend on how a steel is processed, are important in determining irradiation resistance. As shown in the previous chapters, many of these variables have been investigated in varying degrees for different mechanical and physical properties. In general, however, detailed, single-variable irradiation studies to comprehensively investigate these parameters have not been conducted. Because of space considerations in irradiation facilities and the expense of conducting such experiments, most irradiation experiments have been restricted to one steel composition in one condition irradiated over a temperature and fluence range that is limited by the conditions of the irradiation facility. Furthermore, space limitations in irradiation facilities mean that only a limited number of miniature mechanical property specimens can be irradiated, which can cause problems in evaluating the data. For example, only four to six Charpy specimens per irradiation condition are usually irradiated, thus possibly affecting the determination of an accurate Charpy curve; and in some cases, tension specimens have not been simultaneously irradiated with Charpy impact specimens, thus making a quantitative comparison between hardening and embrittlement difficult.

For any given application, the mechanical and physical properties in the unirradiated and irradiated condition will determine a design window for the use of the ferritic/martensitic steels. Figure 18.1 is a temperature-fluence diagram that illustrates how the design window for a fusion power plant might be determined for F82H in a water-cooled system [1]. The diagram indicates that irradiation hardening (an increase in yield stress) occurs up to 425 to 450°C, but that hardening itself does not define the design window. Hardening causes embrittlement (defined for Fig. 18.1 as an increase in DBTT) that defines the lower limit of the window out to ≈5 MW/m^2. For Fig. 18.1 [1], helium was postulated to cause further embrittlement, thus raising the lower limit at higher fluences as helium builds up in the fusion reactor first wall. The upper operating temperature limit is determined by creep, which is affected by thermal aging and, possibly, by irradiation-assisted thermal aging (Fig. 18.1). In other possible fusion reactor designs, the upper temperature limit could depend on compatibility of the steel with the coolant media (e.g., liquid lithium or Pb-Li eutectic) and, possibly, by thermal stress development and thermal fatigue in addition to creep strength and aging effects.

In the following, the detailed discussions on irradiation effects of the previous chapters will be used as the basis to summarize and correlate the properties of the ferritic/martensitic steels with conditions expected in a fusion power plant. The discussion also applies to the effects of the neutron environment on these steels in a fast reactor, the primary difference being that the high concentrations of helium and hydrogen produced by fusion neutrons will not form in the steels irradiated in a fast reactor. Most of the literature references to the material being summarized were given in earlier chapters, and only references not provided in previous chapters will be given here.

IRRADIATION EFFECTS

Neutron irradiation of ferritic/martensitic steels causes the formation of vacancies and interstitials (Frenkel pairs) in the steel matrix (Chapter 8). Excess vacancies collect to cause void swelling (Chapter 9), which has a maximum around 400°C, but in the ferritic/martensitic steels, swelling is low relative to other materials considered for nuclear applications. Swelling is not expected to limit the use of the steels, even up to a first wall service lifetime of 150 to 200 dpa, although the data obtained to this fluence level were from fast reactor irradiation, where little helium formed. In simulation studies, helium appeared to cause an increase in swelling for neutron irradiation at 300 to 400°C, and although the extent of this increase has not been quantified, total swelling is still not expected to limit the use of the steels.

In addition to swelling, the movement of vacancies and interstitials to the sinks can lead to changes in the precipitate structure (Chapter 10). Radiation-induced segregation (RIS) can cause the dissolution of existing precipitates and the formation of new precipitates. There can also be changes in composition at internal boundaries.

Excess irradiation-produced interstitials and vacancies can agglomerate into dislocation loops and a dislocation structure that causes hardening (Chapter 12), as measured by an increase in strength and a reduction in ductility. Likewise, new irradiation-enhanced or irradiation-induced precipitates can affect the strength. Hardening influences the fracture characteristics of steel as exhibited by changes in impact properties (Chapter 14) and fracture toughness (Chapter 15), leading to embrittlement. It can also affect the fatigue and fa-

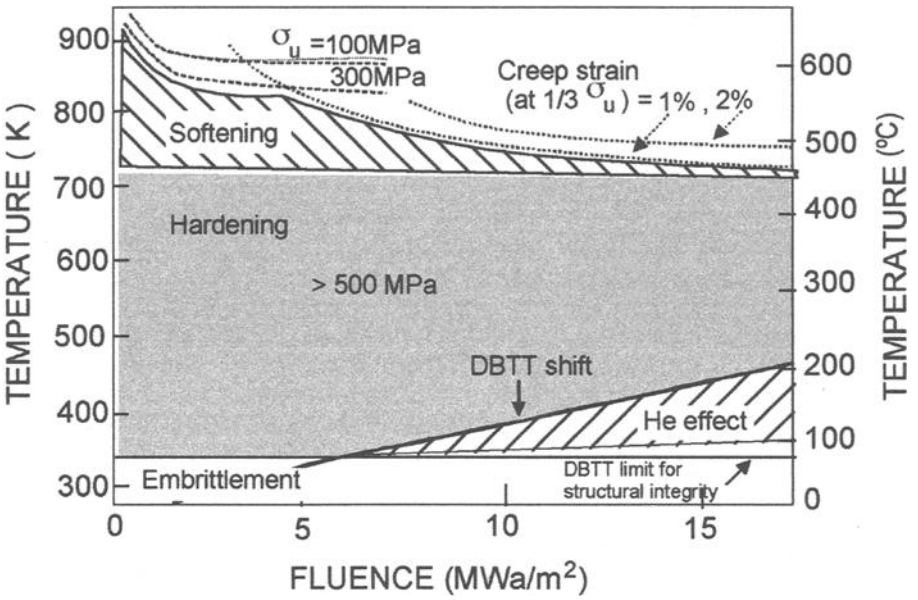

FIG. 18.1—Schematic diagram depicting the design window for a water-cooled tokamak-type fusion reactor constructed with the reduced-activation ferritic/martensitic steel F82H [1].

tigue crack growth (Chapter 16). The magnitude of the hardening decreases with increasing temperature and ceases at 400 to 500°C, depending on the steel.

Hardening generally saturates with fluence, although there is some evidence that hardening can go through a maximum at higher fluences and temperatures due to irradiation-enhanced thermal aging, which induces softening (i.e., irradiation-enhanced diffusion promotes dislocation recovery, sub-grain growth, and precipitate coarsening). Irradiation-enhanced thermal aging can also occur above the temperatures where hardening ceases, thus influencing thermally activated recovery and precipitate coarsening processes. The evidence for a hardening maximum is based primarily on observations on yield stress behavior with a limited amount of recent data indicating that the shift in DBTT might also go through a maximum. Since other mechanical properties (i.e., toughness, fatigue, etc.) are affected by the hardening, if hardening does pass through a maximum, a maximum in the effect of hardening on these other properties might be expected.

The most detrimental effect of hardening involves the irradiation embrittlement measured by an increase in DBTT and a decrease in USE in an impact test. Shifts in DBTT generally saturate with fluence, and shifts in excess of 150°C have been recorded for some steels irradiated in a fast reactor, while other steels show much smaller shifts for similar irradiation conditions. Depending on the DBTT before irradiation, the DBTT after irradiation can be well below or well above room temperature. The extent of the shift depends on irradiation temperature, just as hardening does. Because of the qualitative nature of an impact test, observations on DBTT shift cannot be applied to a fusion design. Although some information is available on irradiation effects on fracture toughness—a more quantitative fracture parameter—more such data are required.

Irradiation spectrum is important for fusion applications, but as yet the only studies on materials irradiated by the 14 MeV neutrons characteristic of a fusion spectrum from the deuterium-tritium fusion reaction were on small specimens to very low fluences. The high-energy neutrons of a fusion spectrum produce (n,α) and (n,p) reactions, resulting in high helium and hydrogen concentrations forming in the matrix of a first-wall structural material. At present, simulation techniques must be used to obtain the large concentrations of helium and hydrogen expected to form in a ferritic/martensitic steel during the irradiation of the first wall of a fusion reactor.

Simulations to produce helium in conjunction with displacement damage by neutron irradiation have been conducted by irradiating nickel- or boron-doped steels in a mixed-spectrum reactor. Little or no hardening due to helium has been reported from tension tests of nickel- and boron-doped steels, but from impact tests on such irradiated steel specimens, there is growing evidence that helium exacerbates the shift in DBTT. Under conditions where ≈200 to 400 appm He were present in the steel, shifts in DBTT of over 200°C have been observed. Such extensive embrittlement would severely limit the use of a steel (Fig. 18.1), but these results and their application to fusion conditions are fraught with uncertainty and controversy.

Simulation of hydrogen effects is difficult because relatively thin specimens must be used for hydrogen charging, and the gas rapidly diffuses from the steel, especially at the expected operating temperatures of a fusion reactor. Hydrogen-effects studies on the high-chromium ferritic/martensitic steels are in general agreement with that conclusion (Chapter 6).

Heavy- and light-ion irradiations have been used to simulate damage microstructures and helium effects on the microstructure. Mechanical properties tests can be carried out

both during and after irradiation in the accelerator. However, these techniques have limited use for mechanical property studies because of the expense involved with the irradiation of large numbers of large mechanical property test specimens. A 14 MeV neutron source is required with a large enough volume to irradiate mechanical property specimens to verify observations from fission reactor irradiations as applied to fusion.

In addition to spectrum effects, dose rate or flux affects swelling, as determined from comparative studies using neutron, electron, and ion irradiations. As the dose rate increases, the peak swelling temperature increases. Since these studies involve irradiations by ions and electrons and only small specimens can be irradiated, less is known about dose-rate effects on mechanical properties. However, work on low-alloy Mn-Mo-Ni pressure-vessel steels for light water reactors has demonstrated a complex but significant effect of dose rate on embrittlement for low doses (<0.1 dpa) at around 300°C [2]. At this temperature, the flux-dependent regime begins at about 10^{12} n cm^{-2} s^{-1}. The dose rate in the pressure-vessel steels apparently affects the fluence at which saturation of the changes in mechanical properties occurs and may be associated with precipitation of copper and interfacial segregation of other impurities. The minimum flux needed to have an effect probably increases at higher irradiation temperatures, but it may be significant for high-flux fusion conditions to 400°C. Thus, along with spectrum effects and the effect of helium, flux effects on microstructural evolution and mechanical property changes need to be experimentally determined for fusion-relevant materials and conditions.

EFFECT OF COMPOSITION AND MICROSTRUCTURE

Microstructure ultimately determines the properties of ferritic/martensitic steels in both the unirradiated and irradiated conditions. Differences in composition affect microstructure by changing the amount of austenite and δ-ferrite that form during austenitization and by changing the hardenability of the steel, which determines the section sizes that can be transformed to martensite. Composition also determines the martensite-start (M_s) and martensite-finish (M_f) temperatures, which determines how much austenite is retained after a normalizing or quenching treatment. Finally, composition determines the type and amount of carbides and other precipitates that form during heat treatment and during irradiation. Rarely have composition and microstructure been examined systematically in irradiation studies. Therefore, it is often difficult to separate how the irradiation behavior is affected by a change in microstructure.

Carbon is the most important alloying element in ferritic/martensitic steels, because in addition to affecting the precipitate types and amounts that form, it has the largest effect (per amount present) on hardenability and the M_s and M_f temperatures, and, as an austenite stabilizer, it affects the amount of austenite (and δ-ferrite) formed during austenitization. The effect of carbon on properties after irradiation is evident in the different behavior of 9Cr-1MoVNb (0.1% C) and 12Cr-1MoVW (0.2% C) steels. Twice as much carbon, along with the austenite stabilizer nickel, is added to the 12Cr-1MoVW steel to stabilize the austenite and minimize δ-ferrite. The primary precipitate in both steels is $M_{23}C_6$, but because of the higher carbon concentration in the 12Cr-1MoVW steel, it contains twice as much carbide precipitate. The larger irradiation-induced shift in DBTT in the 12Cr-1MoVW steel than in 9Cr-1MoVNb steel after irradiation at >300°C has been attributed to the larger amount of carbide in the 12Cr-1MoVW steel and to the irradiation-enhanced coarsening of these precipitates, under the assumption that the precipitates act as crack initiators. Irradiation-induced precipitation of α′-phase in the 12Cr steel can also contribute to the shift in the 12Cr steel and not the 9Cr steel because α′ is not generally found in steels with ≤10% Cr (it has not been observed in 9Cr-1MoVNb).

Duplex steels containing martensite and δ-ferrite contain higher concentrations of ferrite stabilizers (e.g., 9 to 10% Cr and 2% Mo in EM12, which contains 0.1% C) compared to the steels that are entirely martensitic. During the austenitization treatment, these elements promote δ-ferrite at the expense of the austenite, and the δ-ferrite is enriched in the ferrite-stabilizing elements. Duplex steels are often more susceptible to embrittlement during thermal aging and during irradiation. It has been proposed that the problem for duplex steels or steels containing small amounts of δ-ferrite is caused by carbides at the interface between the δ-ferrite and tempered martensite, although an effect of the property differences between martensite and δ-ferrite cannot be completely ruled out.

Precipitation of the chromium-rich α′ phase in the chromium-rich δ-ferrite can also play a role in higher-chromium (≥10%) duplex steels. Irradiation can promote the nucleation and growth of interface carbides and α′ precipitates and thus enhance the irradiation embrittlement. Although there are indications that the δ-ferrite swells more than the tempered martensite, neither constituent shows much swelling. Despite the propensity of the duplex steels to have these problems, EM12, a 9-10Cr-2Mo steel with 0.1% C and a 50% martensite-50% δ-ferrite microstructure, was more resistant to irradiation embrittlement (less shift in DBTT) when irradiated in the Phénix fast reactor at ≈390°C to ≈40 dpa than HT9 irradiated in FFTF at ≈420°C to ≈36 dpa, even though the latter steel was essentially 100% tempered martensite. The difference is probably that the larger carbides in the higher-carbon HT9 determines the embrittlement behavior of this steel, and the lower-carbon concentration in the EM12 does not allow for a critical buildup of detrimental interface carbides. Another difference might be that the formation of δ-ferrite can refine the austenite grain size during processing.

The effect of microstructure and carbon content was further elucidated when the duplex EM12 was compared with EM10, a 9Cr-1Mo steel with 0.1% C that was 100% tempered martensite, and with F17, a 17% Cr (0.06%C) non-transformable fully ferritic steel, after the three steels were irradiated in the Phénix reactor to 30 dpa at 386 to 525°C. The fully martensitic steel showed the least irradiation embrittlement at 390°C, followed by the steel containing 50% δ-ferrite and 50% tempered martensite (EM12), and then by the 100% ferritic steel (F17). More α′ formed in the high-chromium F17 steel to increase the irradiation hardening. TEM examination indicated a similar ranking for swelling resistance, with the

δ-ferrite—either in the F17 or the EM12—showing more swelling than the tempered martensite.

The effect of substitutional alloying elements on the irradiation behavior was examined during the development of reduced-activation ferritic/martensitic steels. Chromium concentration was varied by several investigators over the range 2 to 12%, and the substitutional alloying elements other than chromium were also often varied. For a series of Cr-2W-0.25V-0.1C steels with 2.25, 5, 9, and 12% Cr, there was a variation in the extent of irradiation hardening, with the smallest increase in strength and decrease in ductility occurring around 9% Cr after irradiation to 7 to 27 dpa at 365°C in FFTF. The DBTT and USE of Charpy specimens irradiated in FFTF to ≈7 to 28 dpa showed a pronounced minimum in the shift in DBTT at ≈9% Cr. Even with this systematic change in chromium composition (other elements remaining constant), the comparison among the martensitic steels (5 to 12% Cr—the 2.25% Cr steels transform to bainite and polygonal ferrite) was for different microstructures: the 5Cr and 9Cr steels were 100% martensite, and the 12Cr steel was 75% martensite and 25% δ-ferrite. Irradiation had the least effect on the DBTT and USE of the 5Cr and 9Cr fully martensitic steels, with the 9Cr-2WV being better than the 5Cr-2WV.

Swelling studies on Fe-Cr binary alloys with 0 to 15% Cr showed that the effect of chromium on swelling resistance was essentially inverse to the effect on hardening behavior: swelling was near a maximum around 9% Cr. Similar observations have been made for Cr-W steels with 2 to 12% Cr. Further, 9Cr martensitic steels have been consistently shown to be higher swelling than 12Cr steels. One explanation offered is that the α′ precipitates in the 12Cr steels act as vacancy sinks. However, this explanation is counter to the observation that δ-ferrite in duplex steels and in a 17% Cr ferritic steel F17 consistently swells more than the martensite in EM10 steel; δ-ferrite, because of its higher chromium concentration, is more prone to α′ formation than martensite.

In addition to the different matrix microstructures for different chromium concentrations, the type of precipitates present also depends on chromium. For the high-chromium steels (Cr ≳ 8%), the primary precipitate is chromium-rich $M_{23}C_6$ with a small amount of MC carbide or MX carbonitride. As the chromium concentration decreases, the amount of $M_{23}C_6$ decreases, and the dominant precipitate becomes chromium-rich M_7C_3. The amount of MC and/or MX also increases with decreasing chromium. For a 5Cr-2WV steel, the $M_{23}C_6$ disappears, and the precipitate is primarily M_7C_3 with much more MC than in a 9 to 12% Cr steel. Below ≈5% Cr, the hardenability is such that it is difficult to form martensite for section thicknesses of interest for nuclear applications.

The relative effect of these different precipitates during irradiation has not been determined. It has been speculated that the difference between the irradiation behavior of the martensitic reduced-activation 5Cr-2WV and 9Cr-2WV steels was caused by the different primary carbides (M_7C_3 and $M_{23}C_6$, respectively) in the two steels. For the duplex 12Cr-2WV steel, α′ and carbides on δ-ferrite/tempered martensite interfaces were postulated to play a role in producing the inferior impact properties of this steel relative to the 5Cr-2WV and 9Cr-2WV martensitic steels during fast reactor irradiation. As discussed above, steels with chromium concentrations ≳10% are prone to α′ precipitation during irradiation, and α′ forms during thermal aging of high-chromium ferritic stainless steels, such as F17 (17% Cr). Hardening by this phase can lead to enhanced embrittlement over that caused by displacement damage alone.

Changes in alloying elements other than chromium also affect irradiation behavior. Martensitic steels with 9% Cr and either 1% V or 2% W (both with ≈0.1% C) were irradiated in FFTF at 365°C to 10 dpa. Properties of these steels were inferior to those containing a combination of 0.25% V and 2% W. Other combinations of vanadium and tungsten have been examined, but of the compositions examined, the combination of ≈0.25% V and 2% W with 0.1% carbon appeared to provide the best combination of elevated-temperature strength and impact toughness for a steel in the unirradiated and irradiated conditions.

Molybdenum and tungsten can lead to the formation of laves phase (Fe_2Mo or Fe_2W) in the 9 to12 Cr-Mo or 9 to 12Cr-W steels during thermal aging, but irradiation appears to move its formation to higher temperatures (>600°C). It appears to form at lower temperatures during irradiation only at higher molybdenum (>1%) or tungsten (>2%) concentrations.

One alloying element that apparently imparts improved impact properties to the reduced-activation martensitic steels is tantalum. A 9Cr-2WVTa steel with 0.07% Ta had superior impact properties when compared to similar ferritic/martensitic steels (conventional or reduced-activation) tested in both the unirradiated and irradiated condition. Atom probe studies indicated that most of the tantalum remained in solution in the normalized-and-tempered condition. When the 9Cr-2WVTa steel was compared with 9Cr-2WV steel—the same steel composition but without tantalum—the only microstructural difference attributed to the tantalum was a smaller prior austenite grain size in the tantalum-containing steel. No significant difference in strength of the two steels was observed as normalized and tempered, after thermally aging to 20 000 h at 365°C, or after irradiation to 7 to 28 dpa at 365°C in FFTF. Part of the improvement in impact properties for the tantalum-containing steel was attributed to the reduced grain size and part to a tantalum-induced increase in the fracture stress or an effect of tantalum on the flow stress-temperature or flow stress-strain rate behavior. More work is required to determine the exact cause.

The impact behavior of the tantalum-containing steel showed two types of contrary behavior compared to other steels. First, for irradiations at 365°C in FFTF, there was a continuous increase in DBTT with fluence between 7 and 28 dpa, rather than the saturation with fluence observed for other steels. Second, the shift in DBTT for the 9Cr-2WVTa steel increased with irradiation temperature for irradiation at 350 to 450°C in HFR and 365 and 393°C in FFTF, whereas the opposite behavior has been observed for most other steels. A decrease is expected, because irradiation hardening decreases with temperature. A loss of tantalum from solution during irradiation to form precipitates or to be incorporated into existing precipitates was postulated to cause the contrary behavior, and other work found tantalum-rich precipitates that formed during irradiation. Based on the supposition that tantalum in solution affects the fracture stress or flow stress, the loss of tantalum from solution would cause the observed behavior.

EFFECT OF MELTING PRACTICE AND THERMOMECHANICAL TREATMENT

Little information is available on the effect of the melting practice used to produce high-chromium ferritic/martensitic steels on the subsequent behavior during irradiation. A study carried out in Russia indicates that melting practice can have a favorable effect by improving the irradiation resistance to embrittlement in the hardening regime. Electroslag remelted steel developed a much smaller shift in DBTT than the same steel without ESR. However, there was a difference in the effect of the ESR process, depending on the composition of the steel. A 9Cr steel with 2% Mo was less affected than a 9Cr steel with 1% Mo. On the other hand, there was no effect of ESR on a 12Cr steel. In work in Germany on reduced-activation steel, it was shown that increased oxygen content could result in an increased DBTT. The amount of oxygen present can depend on the processing, as demonstrated in the Russian work that indicated oxygen was decreased by the ESR process.

In the Russian work, a comparison of a steel made from high-purity charge materials with one made using a typical charge showed that the steel from the high-purity charge was embrittled less after irradiation. More work is needed in this area, especially to determine the effect of minor alloying elements on properties, since the reduced-activation steels are expected to be processed from high-purity charge materials.

The high-chromium ferritic/martensitic steels are generally used in the normalized-and-tempered or quenched-and-tempered condition, which produces a tempered martensite microstructure. The austenitizing conditions determine the prior-austenite grain size and the lath packet size of the martensite. Both parameters can affect the unirradiated and irradiated properties, especially the fracture behavior, although only limited work has been done to establish the relative effect of each parameter on properties. Tempering conditions affect the recovery of the dislocation structure and the size and distribution of the precipitates.

The enhanced resistance to irradiation embrittlement—smaller shifts in DBTT—at 300 to 500°C of the 9Cr-1MoVNb and 9Cr-2WVTa steels relative to the 12Cr-1MoVW steel would at first glance probably be attributed to the smaller prior austenite grain size and the smaller volume of smaller precipitates in the 9Cr steels relative to the 12Cr-1MoVW steel. The smaller prior-austenite grain size in the 9Cr steels is attributed to the niobium and tantalum, and the difference in carbide precipitates is due to the higher carbon concentration in the 12Cr-1MoVW steel (0.2% versus 0.1%). In reality, the interaction of these parameters is much more complicated than the effect caused by the prior austenite grain size and/or lath size and precipitate size alone, as indicated by the fact that the ΔDBTT for the 9Cr-1MoVNb was greater than that for the 12Cr-1MoVW steel when both were irradiated at 55°C, while just the opposite was observed after irradiation at 300 and 400°C. The switch at the higher temperatures was attributed to the larger amount of larger $M_{23}C_6$ precipitate particles in the 12Cr-1MoVW steel relative to 9Cr-1MoVNb steel and growth of that precipitate (perhaps at δ-ferrite/martensite boundaries) during the higher-temperature irradiation and, in addition, the possible formation of α′ precipitate that hardens the 12Cr-1MoVW steel matrix more than the hardening that occurs by displacement damage alone in the 9Cr steels (no α′ forms in the 9Cr steel). No explanation exists for why the 12Cr-1MoVW steel is inherently more irradiation resistant than the 9Cr-1MoVNb steel when irradiated at 55°C, despite the smaller grain size of the 9Cr steel. The 12Cr-1MoVW steel often contains small amounts of δ-ferrite and retained austenite, and it might be speculated that the presence of these more ductile constituents could improve the fracture properties for the low-temperature irradiation, although that remains speculation.

OPTIMIZATION OF FERRITIC/MARTENSITIC STEELS

Based on the limited amount of comparative data available on composition effects on unirradiated and irradiated properties, it appears that martensitic steels with 7 to 10% Cr have the best combination of mechanical properties after (and probably before) irradiation. Although 7 to 10% Cr steels exhibit more swelling than lower and higher chromium compositions, the amount of swelling is low (<2% for 9Cr-1MoVNb steel after 200 dpa in a fast reactor). Beyond limited efforts in the development of the MANET steels and the reduced-activation steels, no concerted efforts have been made to optimize the compositions for irradiation resistance.

One of the most interesting effects observed in the study of the reduced-activation steels was the effect of the small amount of tantalum (≈0.02 to 0.07%) on improving the impact toughness of 7 to 9Cr-2WVTa steels and that part of the improvement may be lost during irradiation. No mechanism for the tantalum effect has been established, but if it is assumed that tantalum affects the fracture stress, one possibility could be that tantalum acts as a getter for surface-active impurities (e.g., oxygen), and this causes an increase in the effective surface energy that gives rise to an increase in fracture stress. However, at this point it is not known whether the tantalum causes a change in the fracture stress or the flow stress.

Given that the resistance to embrittlement can be affected by alloying, one way to remedy the deterioration of impact toughness during irradiation would be to add an alloying element that raises the fracture stress or changes the flow stress as tantalum is postulated to do, but with the difference that the added element remains in solution during irradiation or thermal aging. Nickel and platinum additions to α-iron are thought to impart improved toughness by increasing the fracture stress, similar to that postulated for tantalum. Neither of these elements is overly prone to precipitate in carbides. However, nickel is not a reduced-activation element under some criteria, and platinum is expensive. Therefore, other elements need to be sought in place of tantalum.

The possibility of using heat treatment (or other processing techniques) to improve the properties needs to be explored. Systematic studies to elucidate the effect of heat treatment on prior austenite grain size, lath size, and precipitate size and distribution could go a long way toward the development of an optimized steel for nuclear applications. Indications are that prior austenite grain size affects the properties of the 9Cr-1MoVNb steel, even for a small change in grain size. Grain size variation may provide a way to develop impact properties in

the 9Cr-2WV steel similar to those obtained in the 9Cr-2WVTa steel. That is, if the prior austenite grain size of the 9Cr-2WV steel could be reduced to give a DBTT before irradiation similar to that of the 9Cr-2WVTa steel, the DBTTs of the two steels might approach similar values after irradiation. If another element is found to lower the fracture stress or change the flow stress and does not precipitate during irradiation, it could be combined with the heat treatment to produce a steel with a small prior-austenite grain size (developed by the heat treatment) and a reduced fracture stress or favorable flow stress behavior that does not deteriorate during irradiation. Alternatively, tantalum could be combined with the new element to produce a steel with a refined grain size and improved fracture resistance *after* high-dose irradiation.

Precipitates are a major source of the strength of ferritic/martensitic steels. The primary precipitate in the normalized-and-tempered 9–12% Cr steels is chromium-rich $M_{23}C_6$. As the amount of chromium is decreased to 7% in a Cr-2WV steel, some of this precipitate is replaced by M_7C_3, and in a 5% Cr steel, most of the precipitate is M_7C_3. Like the $M_{23}C_6$, the M_7C_3 is present as large globular carbides, and in this morphology it does not play its optimum role in the elevated-temperature strength. Further, because of their morphology, these two types of precipitates can play a detrimental role in the fracture behavior. Processing procedures that would decrease the size of the particles and increase their number density could enhance mechanical properties. Likewise, indications are that despite the presence of the MC carbide formers vanadium and tantalum in the 7 to 12% Cr reduced-activation steels and vanadium and niobium in the conventional Cr-Mo steels, a relatively small amount of fine MC is present in the microstructure. In the 9Cr-1MoVNb, 9Cr-2WV, and 9Cr-2WVTa steels, for example, the MC precipitate number densities were only 1 to 8×10^{18} m^{-3} for MC compared to ≈ 3 to 7×10^{19} m^{-3} for $M_{23}C_6$. The relative effect of the MC precipitates on elevated-temperature strength may be minimal, but this needs to be quantitatively assessed and ways to improve the precipitate morphology need to be pursued.

Helium effects were minimized in austenitic stainless steels by providing a high density of precipitates to act as nucleation sites for bubble formation. For such a microstructure, a high density of small helium bubbles form at the precipitate-matrix interfaces and not only minimize bubble swelling, they also minimize elevated-temperature helium embrittlement, because they reduce the amount of helium that reaches grain boundaries. If helium is proved to cause embrittlement in the temperature regime where the ferritic/martensitic steels harden ($\lesssim$400 to 450°C), a high density of fine precipitates might be a way to alleviate the problem. Since precipitates can act as crack nuclei, a buildup of helium bubbles on the larger precipitates of low number density in the present steels of interest might actually exacerbate embrittlement. It is known that as the chromium concentration of the Cr-W steels is decreased the amount of the MC increases. For example, a 2.25Cr-2WV steel has a considerably higher density of the fine MC precipitates than the 9Cr-2WV or 9Cr-2WVTa steels do, although these steels do not have good irradiation resistance. Other ways need to be found to produce steels with a precipitate morphology favorable to irradiation resistance.

THE FUTURE: OXIDE DISPERSION-STRENGTHENED STEELS?

Figure 18.1 illustrates how the potential operating temperature window for a water-cooled fusion plant is defined by embrittlement at the low temperatures and creep at elevated temperatures [1]. According to a fusion design study in Japan, higher operating temperatures are required for improved efficiency and safety [3]. To achieve higher operating temperatures for a ferritic/martensitic steel, a structural material is required with improved elevated-temperature strength relative to the conventional ferritic/martensitic steels being considered, for which the creep strength is probably adequate to about 550°C. With such a new material, the operating window could be opened wider. If ferritic/martensitic steels capable of use at higher temperatures could be developed, they would also be attractive for fusion power systems cooled by liquid metal or helium [4]. Such steels could also be used as fuel cladding in fast fission reactors.

A ferritic/martensitic steel with improved high-temperature properties for use in the power-generation industry has been a goal of the steel industry since the 1940s, when Cr-Mo steels were first introduced. As discussed in Chapter 2, progress has been made, and the new Cr-Mo-W steels have been code approved for thick section applications for operation at 620°C. The steels that show the most promise for operating at even higher temperatures are the oxide dispersion-strengthened (ODS) steels. The ODS steels are presently receiving an ever-increasing amount of attention as possible candidate materials for first wall and blanket structural materials for fusion [5–7] and for fuel cladding for fast fission reactors [8,9].

The ODS steels are not new to the nuclear industry. They were considered for fuel cladding applications for fast reactors as early as the 1960s [10]; some of that earlier work was referred to in Chapters 9 and 11. The problem that has hindered these steels for nuclear and other applications is the anisotropy of the properties that is the result of the processing procedures used to form the steels. In this section, we will briefly review the steels to demonstrate the promise and problems of these materials, with emphasis on the recent work.

The first ODS steels consisted of a high-chromium (12 to 17% Cr) non-transformable ferrite matrix with a high number density of small titania (TiO_2) and/or yttria (Y_2O_3) particles as the strengthening dispersion. Two early compositions that were studied extensively were [11]: Fe-13Cr-1.5Mo-2.9Ti-1.8Ti_2O_3 (DT2906) and Fe-13Cr-1.5Mo-2.2Ti-0.9Ti_2O_3-0.5Y_2O_3 (DT2203Y05). Elevated-temperature strength is provided by the titania and yttria particles and by χ-phase (70% Fe, 15% Cr, 7% Ti, 6% Mo) that forms at grain boundaries. These steels and variations on these steels generally showed excellent swelling resistance when irradiated by neutrons [11–15], electrons [16,17], and heavy ions [18,19]. Results from the accelerator irradiations indicated that swelling resistance was also excellent when helium was present [18,19]. The oxide particles are expected to act as a myriad of nucleation sites for a large number of small helium bubbles, thus ameliorating the effect of transmutation helium on mechanical properties as well as reducing swelling. Most of the irradiation studies on the early steels concerned swelling

(Chapter 9), and there was a limited amount of work on irradiation creep (Chapter 11). Irradiation-creep resistance was much better than for Type 316 stainless steel but not as good as EM12 [11].

The only extensive high-dose irradiation of mechanical properties specimens was in the Phénix reactor, where irradiations were up to 81 dpa at 400 to 580°C on the Fe-13Cr-1.5Mo-2Ti-0.45Y-0.3O (DT2203Y05) ODS steel (Chapter 12) [14]. Although swelling was suppressed by the oxide dispersion, there were problems caused by irradiation. Tension tests indicated that the steel was embrittled, and TEM showed numerous microstructural changes. These included: (a) the decrease in the matrix chromium and molybdenum content (the changes depended on the irradiation temperature), (b) the formation of α' below 480°C, (c) the formation of χ-phase (in addition to that present before irradiation) in high-dose regions above 500°C, (d) the formation of Laves phase in the low-dose regions, and (e) the dissolution of fine oxide particles during irradiation (attributed to ballistically ejected oxide atoms). Thus, the indications are that irradiation can cause problems for ODS steels, in addition to the anisotropy problem that has long plagued the steels.

In addition to the limited amount of data on the effect of irradiation on tensile behavior, there appears to be only one study that examined the effect of irradiation on Charpy impact behavior (Chapter 14) [20]. The ferritic ODS steel, labeled 1DS (Fe-11Cr-2.7W-0.4Ti-0.66Y_2O_3), irradiated in a fast reactor (JOYO) showed excellent resistance to embrittlement for small (1.5 × 1.5 mm^2 cross section) Charpy specimens. There were again indications of anisotropy in the properties.

In recent years, there have been ODS steel development programs in France [6] and Japan [7–9]. A primary objective of these programs is to solve the major problem of the ferritic ODS steels, namely, the [8] "bamboo-like grain structure and a strong deformation texture," which gives rise to anisotropic mechanical properties, especially an inferior biaxial creep-rupture strength. The development programs seek to process the presently available steels (e.g., commercial MA 957—Fe-14Cr-1Ti-0.3Mo-0.25Y_2O_3) to produce an equiaxed structure [6] and explore new alloy compositions [6–9]. As an example of a treatment used to try to eliminate the anisotropy of the 1DS steel, the processing (after the mechanical alloying through the extrusion steps) involved six warm rolling passes and a 1 h heat treatment at 1100°C [9].

Many of the new alloys use tungsten instead of molybdenum (making them reduced activation), and they usually use Y_2O_3 dispersions with lower titanium concentrations than were used for the earlier versions [6–9]. Aluminum and niobium additions have also been explored for grain refinement [9], but this has not solved the problem with anisotropy.

A second approach to solve the anisotropy problem is to use a 9 to 11% Cr, 2–3% W base with the yttria dispersion [6–9]. The objective here is to develop an equiaxed structure through the austenite-to-martensite transformation when the steel is cooled from the austenitization treatment temperature. This approach has produced steels with excellent tensile properties [6–8] and a significant decrease in the anisotropy of the microstructure [8]. However, the creep-rupture properties were significantly reduced from those of the high-chromium ODS steels [8].

It would appear that a problem with a martensitic ODS steel is that it will have to contain sufficient carbon to produce the austenite that is transformed to martensite. When the steel is tempered to impart toughness, $M_{23}C_6$ will form. As noted in earlier chapters, $M_{23}C_6$ can determine the properties of the high-chromium ferritic/martensitic steels—especially the impact toughness—and it would probably do the same in a martensitic ODS steel. Furthermore, operation at high temperatures would further coarsen the $M_{23}C_6$. High-chromium ferritic ODS steels avoid the $M_{23}C_6$ by keeping the carbon concentration low (0.01 to 0.03%). Finally, an ODS martensitic steel would have an upper-temperature limit set by the A_{C1} temperature. The steel could probably not be used above this temperature because the properties would change due to the austenite formation and the martensite that would form during shutdown.

There are other problems with the ferritic ODS steels besides the anisotropy. At present, the literature is devoid of information on the production of thick-walled parts or large-diameter tubing, and only recently have some reduced-activation compositions been made. Finally, the fabrication processes for these materials for the heavy sections of a fusion blanket structure will need to be established, and this means addressing the problem of joining the materials. In other words, much research and development is still required to determine if ODS steels can be used for future fusion first wall and blanket applications and fast reactor fuel cladding.

Two other non-commercial high-chromium ferritic/martensitic steel developments can be mentioned. The first is the development of 12Cr-8Mo steels for fuel cladding that are strengthened by intermetallic compounds [21]. These steels, produced by powder metallurgy techniques, have been shown to have creep-rupture strengths over twice that for HT9.

What is interesting about the second steel [22], which has good creep strength to 650 to 700°C, is that it achieves its excellent elevated-temperature properties by dispersion strengthening, but it is produced by more conventional techniques than the powder-metallurgy/mechanical alloying techniques used for ODS steels. The composition of the steel, called A21, is 9.5Cr-3Co-1Ni-0.6Mo-0.3Ti-0.07C. It is strengthened by tiny titanium carbides that are produced by hot working in the austenite region before cooling to form martensite. Hot working generates dislocations that provide nucleation sites for fine TiC particles to produce dispersion-strengthened martensite with high creep strength but without the anisotropy of the extruded ODS steels. By balancing the composition between the titanium and carbon and using up essentially all of the carbon to form TiC, it is possible to avoid the large $M_{23}C_6$ precipitates that can be detrimental to the toughness. Because of the high cobalt concentration, it would not be used for nuclear applications (cobalt causes high radioactivity after neutron irradiation). However, perhaps the processing technique can be adapted to produce steels with compositions that can be used for nuclear applications.

Both the 12Cr-8Mo and the A-21 steel are in a very early development stage. Even though the ODS steels have been around for over 30 years, they also have to be considered in an early development stage, as the problem with anisotropic properties still does not seem to be solved. Therefore, if high-

chromium ferritic/martensitic steels are to be used for nuclear applications at present and in the near future, all indications are that the conventional Cr-Mo steels and their reduced-activation counterparts will be the steels used. As discussed earlier, improvements have been made in the properties of these steels and, in some cases, there are now Cr-Mo steels approved for some non-nuclear operations up to 620°C.

For fusion, there is a dearth of materials presently viewed feasible for the first wall and blanket structures. Besides the ferritic/martensitic steels, vanadium and SiC/SiC composites are the only other materials being considered. However, the development of these latter two materials is probably not advanced beyond the stage of development achieved by the ODS steels. Therefore, barring the introduction of some new material, it appears that the high-chromium ferritic/martensitic steels produced by conventional processes are the only structural material available for fusion at present, and will probably be the only material available for well into the future.

REFERENCES

[1] A. Hishinuma, A. Kohyama, R. L. Klueh, D. S. Gelles, W. Dietz, and K. Ehrlich, J. Nucl. Mater. 258-263 (1998) 193.

[2] G. R. Odette, E. V. Mader, G. E. Lucas, W. J. Phythian, and C. A. English, in: Effects of Radiation on Materials: 16th International Symposium, ASTM STP 1175, Eds. A. S. Kumar, D. S. Gelles, R. K. Nanstad, and E. A. Little (American Society for Testing and Materials, Philadelphia, 1994) 373.

[3] M. Kikuchi, in: Proceedings of IEA Working Group Meeting on Ferritic/Martensitic Steels, Eds. K. Shiba and A. Hishinuma (Japan Atomic Energy Research, Tokai, Japan, 1998) 79.

[4] L. Giancari, M. Dalle Donne, and W. Dietz, Fusion Eng. Design 36 (1997) 3.

[5] B. van der Schaaf, Proceedings of IEA Workshop/Working Group Meeting on Ferritic/Martensitic Steels, Ed. R. L. Klueh, Oak Ridge National Laboratory, ORNL/M-6627, 1998.

[6] A. Alamo, Proceedings of IEA Workshop/Working Group Meeting on Ferritic/Martensitic Steels, Ed. R. L. Klueh, Oak Ridge National Laboratory, ORNL/M-6627, 1998.

[7] A. Hishinuma, Proceedings of IEA Workshop/Working Group Meeting on Ferritic/Martensitic Steels, Ed. R. L. Klueh, Oak Ridge National Laboratory, ORNL/M-6627, 1998.

[8] S. Ukai, M. Harada, H. Okada, M. Inoue, S. Nomura, S. Shikakura, K. Asabe, T. Nishida, and M. Fujiwara, J. Nucl. Mater. 204 (1993) 65.

[9] S. Ukai, M. Harada, H. Okada, M. Inoue, S. Nomura, S. Shikakura, T. Nishida, M. Fujiwara, and K. Asabe, J. Nucl. Mater. 204 (1993) 74.

[10] J.-J. Huet, H. Massaux, L. De Wilde, and J. Noels, Revue de Métallurgie (1968) 863.

[11] J.-J. Huet, L. Coheur, L. De Wilde, J. Gedopt, W. Hendrix, and W. Vandermeulen, in: Topical Conference on Ferritic Alloys for Use In Nuclear Energy Technologies, Eds. J. W. Davis and D. J. Michel (The Metallurgical Society of AIME, Warrendale, PA, 1984) 329.

[12] J.-J. Huet, A. De Bremaecker, M. Snykers, and Ph. Van Asbroeck, in: Irradiation Behavior of Metallic Materials for Fast Reactor Core Components, Vol. 1., Eds. J. Poirier and J. M. Dupouy (CEA, Gif-Sur-Yvette, France, 1979) 5.

[13] A. De Bremaecker and J. -J. Huet, in: Dimensional Stability and Mechanical Behavior of Irradiated Metals and Alloys, Vol. 1 (British Nuclear Energy Society, London, 1983) 117.

[14] P. Dubuisson, R. Schill, M. P. Hugon, I. Grislin, and J. L. Séran, in: Effects of Radiation on Materials: 18th International Symposium, ASTM STP 1325, Eds. R. K. Nanstad, M. L. Hamilton, F. A. Garner, and A. S. Kumar (American Society for Testing and Materials, West Conshohocken, PA, 1999) 882.

[15] D. S. Gelles, J. Nucl. Mater. 233-237 (1996) 293.

[16] H. Kinoshita, N. Akasaka, H. Takahashi, I. Shibahara, and S. Onose, J. Nucl. Mater. 191-194 (1992) 874.

[17] J. Saito, T. Suda, S. Yamashita, S. Ohnuki, H. Takahashi, N. Akasaka, M. Nishida, and S. Ukai, J. Nucl. Mater. 258-263 (1998) 1264.

[18] E. A. Little, D. J. Mazey, and W. Hanks, Scripta Metallurgica et Materialia 25 (1991) 1115.

[19] K. Asano, Y. Kohno, A. Kohyama, T. Suzuki, and H. Kusanagi, J. Nucl. Mater. 155-157 (1988) 928.

[20] T. Kuwabara, H. Kurishita, S. Ukai, M. Narui, S. Mizuta, M. Yamazaki, and H. Kayano, J. Nucl. Mater. 258-263 (1998) 1236.

[21] M. Tokiwai, M. Hori, K. Kako, and M. Fujiwara, J. Nucl. Mater. 204 (1993) 56.

[22] R. F. Buck and W. M. Garrison, Adv. Matls. & Processes 150 (2) (1996) 27.

Subject Index

About the authors

Dr. Ronald L. Klueh received a B.S. degree from Purdue University and an M.S. and Ph.D. from Carnegie Mellon University. He has been conducting research on materials at the Oak Ridge National Laboratory since 1966, when he began work on compatibility and corrosion. His work on ferritic steels began in 1970, when he studied the mechanical properties of 2 1/4Cr-1Mo steel for fast reactor steam generators. Beginning in 1980, he joined the fusion materials program to study irradiation damage of ferritic/martensitic steels. He led an effort to develop reduced-activation steels for fusion applications, which resulted in a 9Cr steel with the best irradiation resistance of any such steel developed for the fusion programs worldwide. A series of 3Cr-WV bainitic steels were also developed and patented. Since 1993, he has headed the U.S. delegation to the International Energy Agency Working Group on Ferritic/Martensitic Steel for Fusion, a committee that is coordinating an international collaboration to demonstrate the feasibility of these steels for fusion. He is a fellow of ASM International and has over 175 publications in the open literature, two patents, and has edited three books.

Dr. Donald R. Harries received the degrees of B.Sc. (Honors Metallurgy) from the University of Wales and a Ph.D. and Sc.D. from the University of Cambridge. He was Leader of the Core Components and Structural Materials Group, Metallurgy Division, Atomic Energy Research Establishment, Harwell, England, and subsequently Head of Technology, The NET Team, Garching, Germany, and Chief Metallurgist, British Nuclear Fuels plc, Fuel Division, Preston, U.K. He has also been a visiting scientist at the Oak Ridge National Laboratory, U.S.A., and Forschungszentrum Karlsruhe, Germany. Dr. Harries has worked as an independent metallurgical and nuclear consultant since retiring from BNFL.

He has published over 100 papers in scientific and technical journals and about 250 reports on the structure, deformation, mechanical properties, fracture behavior and irradiation effects in materials for nuclear fission and fusion power reactor systems. Dr. Harries is a member of The Institute of Materials, a Chartered Engineer and a Fellow of The Institution of Metallurgists; he is a recipient of the Charles Eichner Medal of the Société Française de Métallurgie for exceptional contributions in the field of nuclear power.

ISBN 0-8031-2090-7